A Study of the Mechanics of Ultrasonic Deep Drawing using a Simulative Test.

by

M.J.R. YOUNG, M.Sc., A.I.M.

Submitted in fulfilment of the requirements for the degree of Doctor of Philosophy, University of Aston in Birmingham, April 1973.

Faculty of Engineering
Department of
Mechanical Engineering

Supervisor
Dr. D.H. Sansome

DISTORTED PAGES IN ORIGINAL

DAMAGED TEXT IN ORIGINAL

Summary

The effects of ultrasonic vibrations on the mechanics of deep drawing have been examined using a mechanical analogue based on the wedge drawing test. An apparatus was designed which permitted the simultaneous deformation of two wedge shaped coupons constituting a test piece of biaxial symmetry. Vibrations were applied to the wedge dies so as to simulate a radial mode oscillation of the die in the equivalent axi-symmetric process. During tests on aluminium sheet it was found that by increasing the vibration amplitude, the effective friction force between the blank holder plate and upper test piece surface could be reduced to zero. This was accompanied by a decrease in the punch load which exceeded the magnitude of the friction force reduction. Indirect measurement of the friction force associated with the die profile radius, indicated that this was also reduced by the application of vibrations.

The experimental curves relating punch load reduction to vibration amplitude consistently revealed two distinct regions; an enhanced effect at low amplitudes giving way to a linear reduction in punch load with increasing amplitude. The initial non-linear effect was accurately accounted for by the measured reduction in friction forces and it was proposed that the linear effect was due to oscillatory force superposition.

Analysis of the oscillatory motion of the wedge test piece led to the derivation of mathematical models describing the mechanisms of friction reduction at the blank holder and die radius. The magnitude of these effects was found to be critically dependent upon the ratio of the oscillatory velocity amplitude to the mean drawing velocity. Models were also proposed describing the mechanics of force superposition

during radial drawing-in and plastic bending and unbending around the die radius. Good agreement was found between the theoretically derived sum of these component effects and the measured reduction in punch load.

The combined effect of vibrations on each phase of the drawing process led to an increase in the limiting draw ratio and it was concluded that similar effects would be achieved in the axisymmetric process.

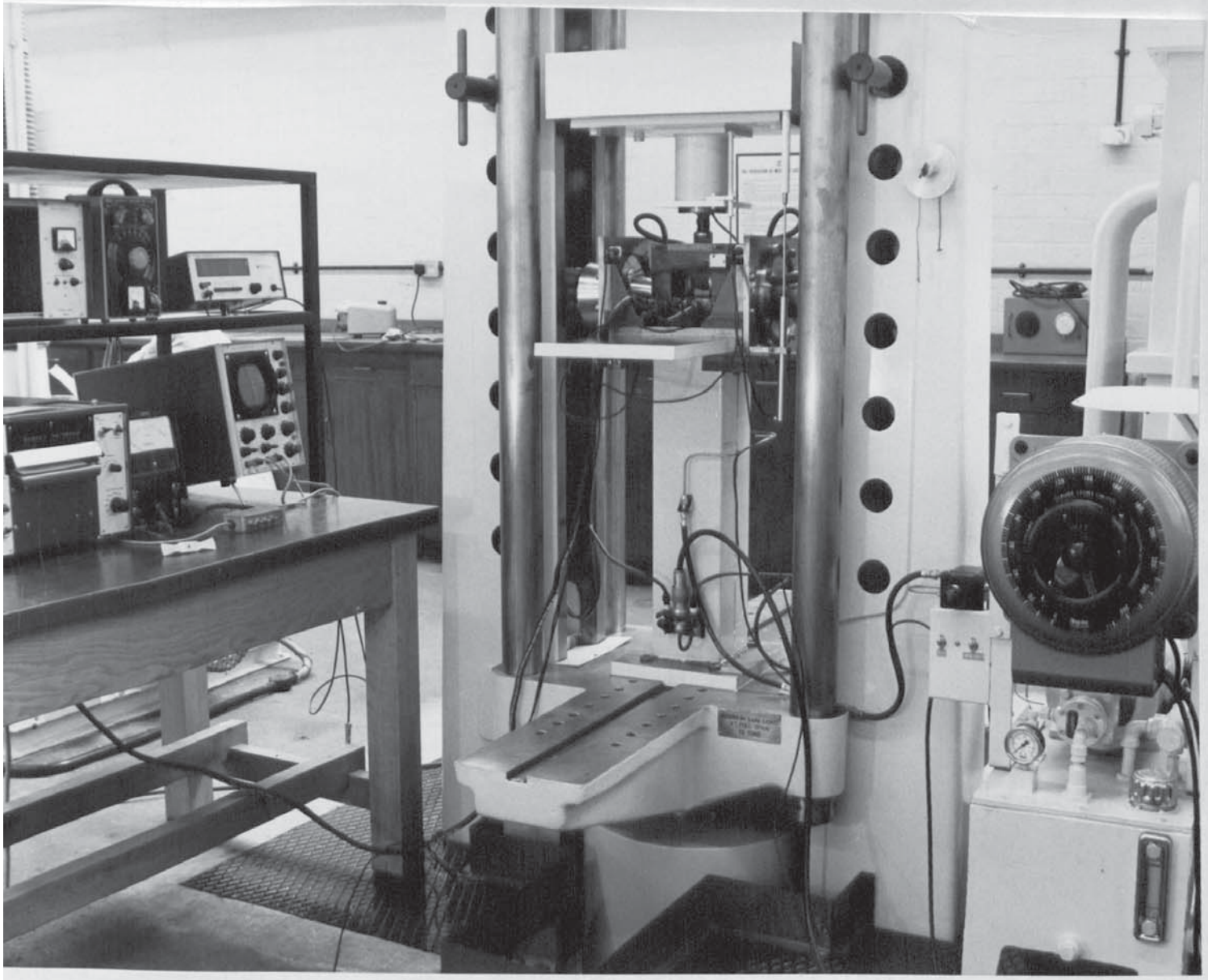

Frontispiece

A Study of the Mechanics of Ultrasonic Deep Drawing using a Simulative Test

CONTENTS

Nomenclature

Oscillatory parameters

ε_m - strain amplitude

σ_m - stress amplitude

ξ_m - displacement amplitude

ξ'_m - displacement amplitude of testpiece at any radius, r, during wedge drawing.

$\dot{\xi}_m$ - velocity amplitude

F_m - oscillatory force amplitude

$\hat{\tau}$ - oscillatory shear stress

Note:

(i) the subscripts 'mo' and 'ml' signify the amplitudinal values of the above parameters at the input and loaded ends of the acoustic system respectively.

(ii) subscripts r_m, θ_m and ϕ denote radial, circumferential and torsional amplitudes respectively.

(iii) instantaneous values of the above parameters are signified by the same symbols but with the subscript 'm' omitted.

ω - angular frequency given by $\omega = 2\pi f$ where f is the frequency.

C - velocity of compression waves in a given material

C_r - wave velocity in an annular ring.

E - Young's modulus (assumed to be the same under oscillatory and non-oscillatory conditions).

ν - Poisson's ratio.

ρ - density.

λ - wavelength of longitudinal waves in a particular material at a given frequency.

λ_b - wavelength of transverse (or bending) waves.

k - wave number, defined as $k = \frac{\omega}{C} = \frac{2\pi}{\lambda}$.

Z_H - complex mechanical impedance, $Z_H = R_H + i X_H$.

R_H - resistive load impedance .

X_H - reactive load impedance .

i - $\sqrt{-1}$

w - specific wave impedance defined by $w = \rho.c.$

w_o - acoustic impedance of a waveguide defined by:

$w_o = \rho.c.s$

γ - wave propagation constant in system with losses.

N - end diameter ratio of acoustic horn .

α - taper factor of conical horn, given by $\alpha = \frac{N-1}{Nl}$.

b - taper constant of exponential horn, $b = \frac{1}{l}.\ln N$

l - horn length; also unsupported length of partly drawn test piece.

R_1 - radius at wide end of horn.

R_2 - radius at narrow end of horn.

a - velocity amplitude; V_ρ / ξ_m

F_r - blank holder friction force under oscillatory conditions.

I_o - impulse associated with a complete cycle of the friction force acting on an element in contact with the die radius.

I - total impulse due to a complete cycle of the friction force integrated over the contact arc ϕ.

ΔF - reduction in blank holder friction force.

Δf - reduction in die radius friction force under oscillatory conditions .

σ_b' - bending stress increment under oscillatory conditions.

$\Delta\sigma_b$ - reduction in bending stress.

ΔT_b - strip tension decrement associated with reduction in bending stress.

ΔP - reduction in punch load under oscillatory conditions.

ΔT_u - strip tension decrement due to reduction in unbending stress at die radius exit plane.

ΔT_r - strip tension decrement due to reduction in radial drawing in stress at the die exit plane.

Non-oscillatory parameters.

$\sigma_1, \sigma_2, \sigma_3$ - principal stresses in descending order of algebraic magnitude.

σ_o - effective stress producing yielding in the annealed condition.

σ_b - stress increment producing plastic bending at radius b.

σ_u - stress increment producing plastic unbending at radius c.

$\bar{\sigma}$ - effective stress to produce yielding, equal to the yield stress in uniaxial tension.

ξ_1, ξ_2, ξ_3 - principal strains

$\bar{\varepsilon}$ - effective strain given by;

$$\bar{\varepsilon} = \sqrt{\frac{2}{3}\left\{(\varepsilon_1-\varepsilon_2)^2+(\varepsilon_2-\varepsilon_3)^2+(\varepsilon_1-\varepsilon_3)^2\right\}}$$

m - correction factor applied to Tresca Yield Criterion.

t - blank or strip thickness; also time in cyclic functions.

r - radial distance from punch axis.

x - axial distance.

R_o - initial rim radius.

r_o - current rim radius.

r - instantaneous radius of an element initially at radius R, in the undrawn blank.

Q_c - radius of central surface of blank during plastic bending.

Q_n - radius of neutral surface.

λ_N - displacement of neutral surface during plastic bending under tension.

ϕ - die contact angle; also phase angle associated with wave motion.

θ - angular displacement of an element over the die radius; defined in Fig. 3.6.

W - bending work per unit width.

μ - coefficient of friction.

f - stress increment due to friction around the die radius; also frequency.

F - friction force associated with blank holder load.

H - blank holder load.

P - punch load.

T - strip tension.

M - bending moment.

I - second moment of area.

V_r - mean velocity of element at radius r during wedge drawing.

V_p - mean punch velocity.

Note:

Subscripts t, r and θ denote normal, radial and circumferential values of stress and strain.

Subscripts a, b and c denote the values of stress strain and thickness at particular stages of drawing defined by the radial distance from the punch axis; a, b and c.

1. Introduction

It has been known for some time that when vibrations are applied to a metal forming operation certain effects may be produced which cause the process forces to deviate from those normally associated with the non-oscillatory deformation conditions. The exact nature of these effects and the circumstances under which they occur are not fully understood. However, considerable attention has been paid to the study of specific cold forming operations in which either the work piece or some part of the tooling is vibrated and this has led to a better understanding of the basic principles involved.

Oscillatory forming may be classified into two main groups according to the operating frequency, namely:

(i) low frequency - covering frequencies up to about 500 Hz.

(ii) high frequency - lying within the range 10-50 KHz.

The latter is broadly described as ultrasonic, although this term is not strictly accurate at the low end of the range. Its wider use stems largely from the extended range in which practical systems normally operate.

The distinction between high and low frequency operation is not necessarily related to the effects produced in each instance but to fundamental differences in the design criteria of the respective technological systems. At the low frequencies, it is appropriate to vibrate the tools bodily, using for example an eccentric drive or electro-hydraulic mechanism[1]. However, in order to achieve practical amplitudes at ultrasonic frequencies, the prime consideration is to maintain a resonant condition in the work tools. It is therefore necessary to consider the entire forming process with this objective in mind and to employ established acoustic principles in the design of the vibrational system.

Research into ultrasonic working processes has been mainly concerned with tube and wire drawing and to a lesser extent, with extrusion, forging, deep drawing and rolling. Such processes are characterised by a reduction in the forming forces and in some cases an improvement in the surface finish of the workpiece, compared with conventional metal working techniques. The reduction in process forces has been attributed to two effects, namely:

(i) acoustic force superposition - in which an oscillatory force component is superimposed onto the direct deformation force.

(ii) reduction in interfacial friction. The relative importance of these two effects varies according to the characteristics of the particular working operation and the vibrational mode induced in the mechanical system.

Direct absorption of ultrasonic energy at lattice imperfections was initially thought to be a substantial factor in accounting for the observed force reduction. It is now generally accepted, however, that the only effect produced by attenuation of the vibrations, is heating which occurs at high acoustic intensities. This, together with superposition phenomena are collectively described as 'volume effects', as distinct from the surface effect associated with the influence of vibrations on interfacial friction forces.

The current research programme is concerned with the process of ultrasonic deep-drawing, without ironing. It is hoped, by adapting a simulative test, to apply vibrations in such a way as to reproduce the phenomena observed in similar oscillatory processes. Particular attention will be paid to the measurement of friction forces during drawing, with the primary objective of evaluating the effect of tool vibration

on interfacial friction during plastic deformation.

2. Critical Review of Published Research Into Oscillatory Metal Forming

2.1. Introduction

The effects of applying both high and low frequency vibrations to a plastically deforming metal have been widely studied under many and varied circumstances[2]. The published results of this work provide a considerable fund of information from which to review the current status of the technique and assess the relevance of the mechanisms proposed in explanation of the practical observations. However, it is not intended to carry out an exhaustive review of the literature but rather to concentrate on those papers which, by virtue of their fundamental approach or scientific originality, contribute significantly to an understanding of the mechanics of oscillatory metal working.

Over the past 5 or 6 years studies in both pure and applied research have provided general support for the concept of volume and surface effects. The results of mechanical tests performed under oscillatory conditions have been confirmed in technological deformation processes, leading to a clearer understanding of the significance of the dynamic force superposition mechanism.

Although the friction characteristics of vibrated surfaces have been widely studied under conditions of elastic loading it has not yet been conclusively demonstrated that the observed reduction in friction force is relevant in conditions of bulk plastic deformation.

It is proposed in the following section, to consider the evidence supporting each of these basic phenomena and to illustrate the results of fundamental research by examples of

the application of these theories to technological deformation processes.

2.2. The Volume Effect

2.2.1 Tensile Testing with the Application of Low Intensity Vibrations

The effect of ultrasonic energy on the physical properties of metals was first demonstrated by Blaha and Langenecker in 1955[3]. Their early experiments were concerned with the application of ultrasound to single crystals of Al, Cd and Zn during tensile testing[4]. Details of this work are as follows: Specimens held in a specially adapted testing machine were immersed in CCl_4, contained in a glass vessel, resting on the head of an acoustic resonator which was tuned to 800 kHz. Energy was transmitted through the fluid, to the specimen and the effect on the deformation load of both continuous and intermittently applied vibrations examined. During intermittent tests the deformation stress decreased abruptly on activating the testpiece. The level of stress remained constant whilst the material continued to deform plastically and on switching off the ultrasonic generator it returned to a level slightly lower than that observed at the start of the oscillatory interval. This phenomenon is illustrated for the case of a pure zinc crystal in Fig. 2.1. Repeated bursts of ultrasound produced a series of yield values, the envelope of which showed a gradually decreasing stress level.

Most of the tests were carried out at the maximum power output of the resonator viz. 25 watts. On reducing the power by 50%, the reduction in deformation stress was observed to be proportionately decreased. Similar results were obtained on Pb and Cd crystals tested at the same frequency and on all

Fig. 2.1 Stress strain curves of a zinc crystal subjected to repeated ultrasonic vibration. (After Blaha and Langenecker[4]).

Fig. 2.2 Strain hardening curves of zinc at 19°C, 58°C and 93°c, curves a, b and c respectively. The effect of ultrasonic vibration at 19°C is illustrated by the superimposed curve d. (After Blaha and Langenecker[4]).

Fig. 2.3 Effect of vibration amplitude on the reduction in the static yield stress at room temperature. (After Nevill and Brotzen[5])

three materials irradiated over a range of frequencies between 15 and 10,000 Hz. The latter series of tests was carried out using an adapted electro-dynamic loud speaker.

During all of the tests the temperature of the transmitting fluid was measured. Precautions were taken to ensure that the radiating head was adequately water cooled to maintain a constant temperature.

It was suggested by the authors that there was a similarity between the stress strain curves obtained during continuous irradiation and corresponding curves obtained by straining at successively higher temperatures under non-oscillatory conditions. This is illustrated in Fig. 2.2 where curves a, b and c represent the strain hardening relationship for zinc tested at 19°C, 58°C and 93°C respectively. The superimposed curve, d, illustrates the effect of continuously applied ultrasonic vibrations at a temperature of 19°C. Blaha and Langenecker then carried out some approximate calculations of the thermal energy required to 'raise' the specimen temperature from 19 to 58°C, causing the stress reduction from curve (a) to curve (b), and also the acoustic energy to produce an equivalent reduction in shear stress, represented by curve (d). The shear stress amplitude in the testpiece was calculated making allowances for reflection of sound waves at the various interfaces, e.g. resonator head/container and transmission fluid/specimen. The calculated value of stress was found to be significantly less than the observed reduction in shear stress. Furthermore, the acoustic energy, on the basis of these calculations, was several orders of magnitude less than the corresponding thermal energy required to effect a similar reduction in shear stress.

In order to explain these observations, they proposed that the movement of oscillatory stress waves through the crystal lattice activated dislocations which during strain hardening in the earlier part of the tensile test had become blocked. The acoustic damping effect was therefore related to the energy absorbed in lifting the dislocations over the potential energy barriers associated with obstacles in the lattice. Since this effect is very much greater than that due to elastic hysteresis they argued that the acoustic energy was absorbed essentially at dislocation sites and was therefore more effective than thermal activation, which raises the energy level of the entire lattice.

Although this hypothesis seems feasible, doubt is cast on the accuracy of the acoustic stress estimates due to the authors' failure to take account of resonance causing stress concentrations at certain positions along the testpiece. In the presence of a standing wave, deformation would be expected to occur locally at stress antinodes when the amplitude was sufficiently high to activate dislocation movement. No attempt was apparently made to examine the strain distribution during this series of experiments.

In 1957 Nevill and Brotzen[5] reported the results of their experiments which attempted to verify the claims of Blaha and Langenecker. They conducted a series of oscillatory tests on low carbon steel wire at frequencies between 50 and 80 kHz, using a specially designed tensile testing rig which incorporated an acoustic concentrator and driving crystal in the lower head. The system was operated in the standing wave régime by varying the frequency of the electrical supply to the driving crystal. Resonance was detected in the wire specimen by measuring the magnetic flux change associated with

the inverse magneto-strictive effect [6], which was proportional to the oscillatory stress amplitude. This technique was used to obtain an arbitrary measure of the antinodal stress amplitude during testing, which together with the frequency, were the only oscillatory parameters monitored. Vibrations were applied both continuously and intermittently over a large total strain and at temperatures between 30 and 500°C. (This was controlled by passing a direct current through the testpiece.)

Their results were in general agreement with those of Blaha and Langenecker and indicated a stepwise reduction in static stress during the oscillatory testing interval. More importantly however, they were able to relate the magnitude of the observed stress reduction to the oscillatory stress amplitude. Tests over the frequency range 15-80 kHz indicated a linear relationship between the decrease in static yield stress and the oscillatory stress amplitude. Their results are shown for frequencies of 28 and 35 kHz in Fig. 2.3. This effect was also found to be independent of temperature in the range 30-500°C and was not affected by the level of permanent strain attained during the tensile test. It should be noted that these results indicated only a qualitative relationship between the measured yield stress reduction and oscillatory amplitude since no attempt was made to calibrate the acoustic stress measuring instrument.

The authors proposed that the observed results could be explained by considering a macroscopic superposition of steady and alternating stresses. In essence this implies that when the specimen is subjected to a longitudinal elastic wave, with an associated stress amplitude, σ_m, yielding will occur when

the direct stress rises to a value σ' which satisfies the relationship:

$$\sigma_m + \sigma' = \bar{\sigma} \qquad \text{---------- 2.1}$$

where $\bar{\sigma}$ is the current yield stress in uniaxial tension under non-oscillatory conditions.

This simple definition offered a qualitative explanation of the observed effects but did not consider the interaction between cyclic stress waves and the lattice imperfections which determine the mechanical characteristics of metals. Several possible mechanisms were considered by which dislocations might absorb energy and break free from the obstacles pinning them. However, none of these were compatible with the test conditions described and each was discarded by the authors.

Later work by Pohlman and Lehfeldt[7] provided quantitative confirmation of the macroscopic superposition effect. They conducted a series of ultrasonically activated tensile tests on pure polycrystalline copper at a frequency of 20 kHz. The ultrasonic power was provided by a magneto-strictive transducer. This was coupled to one end of the testpiece which was of an appropriate length for resonance to occur at the operating frequency of the transducer. Care was taken to attach the transducer and testpiece to the testing machine at planes of zero motional amplitude, in order to minimise acoustic power losses. The displacement amplitude was measured, at a cross section of the testpiece coincident with a motional antinode, by means of a non-contacting electrodynamic pick-up. The maximum stress amplitude in the testpiece was then determined from the familiar expression:

$$\sigma_m = k.E.\xi_m \qquad \text{---------- (2.2)}$$

where k and E are the wave number and Young's modulus of the

test piece material and ξ_m the motional amplitude.

They found that the observed reduction in yield stress was proportional to the oscillatory stress amplitude and showed good quantitative agreement with the applied acoustic stress calculated from equation 2.2.

More recently, Winsper and Sansome[8] studied the effects of low frequency vibrations on the yield stress in simple tension, of Duralumin and plain carbon steel. The tests were performed on a modified Haigh fatigue testing machine at a frequency of 100 Hz. This permitted the simultaneous measurement of direct and alternating stresses using a conventional Kelvin Hughes recorder with a series amplifier. They found that the yield stress was reduced abruptly on applying vibrations to the deforming testpiece and that the reduction in static stress was accurately accounted for by the measured alternating stress amplitude.

2.2.2 Tensile Tests at High Acoustic Intensities

In some of his later experiments Langenecker[9] examined the effects of much higher acoustic intensities on the stress strain curves obtained from tensile tests on high purity aluminium single crystals. Using high gain acoustic concentrators coupled efficiently to single crystal testpieces of only 0·080 in. diameter he was able to produce sound intensities of up to 650 watts/in^2 during plastic deformation. The effects of irradiation at these levels are shown in Fig. 2.4a, which illustrates the shear stress vs. elongation relationship at increasing levels of acoustic power, compared with the corresponding results of non-oscillatory tests carried out at 18^{o}C. Attention was drawn once more to the similarity between the results obtained with continuous irradiation and the effects

Fig. 2.4 Comparison of the effects of temperature and ultrasonic irradiation on the stress strain characteristics of aluminium single crystals. (After Langenecker (9)).

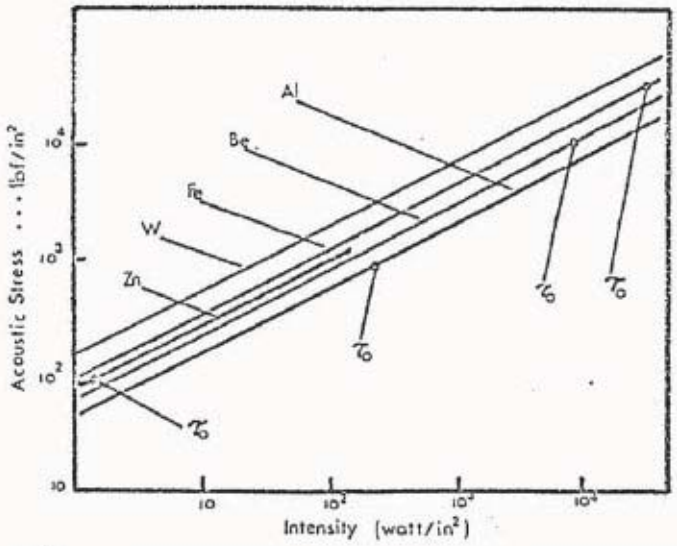

Fig. 2.5 Acoustic stress vs. ultrasonic intensity for different metals. The critical shear stress in each case is indicated by τ_0.

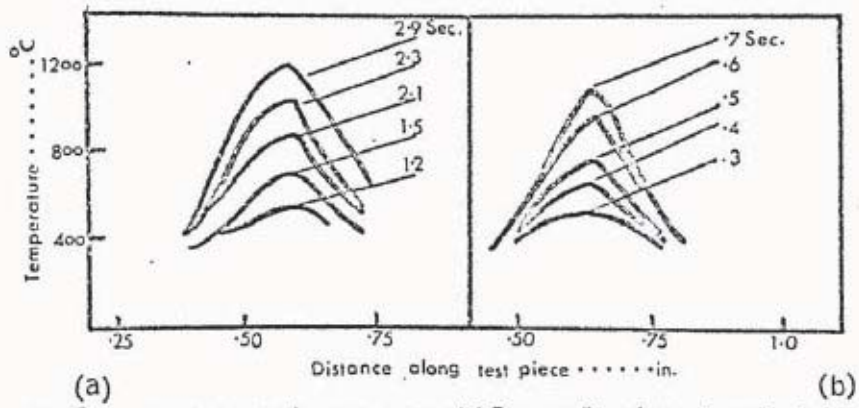

Fig. 2.6 Temperature profile of standard tensile samples at several increments of time after the beginning of ultrasonic irradiation. (a) Profile at 35 watts input.
(b) Profile at 80 watts input.

of increasing temperature, illustrated by the family of curves in Fig. 2.4b. As the intensity was increased the reduction in shear stress increased until at 325 watts/in^2 it approached 100%. Similar results were obtained on harder metals[10] notably W, Fe and Be. The reduction of the apparent yield stress to almost zero in each case could not be explained from consideration of the superimposed acoustic stress amplitude. This was demonstrated by the graphs shown in Fig. 2.5 where acoustic stress amplitude is plotted against intensity for each material, using the relationship:

$$\sigma_m = \xi .w = \sqrt{\frac{2.I.E}{C}} \qquad \text{---------- (2.3)}$$

where σ_m is the stress amplitude in the testpiece, $\dot{\xi}$ the travelling wave velocity amplitude, w the specific wave impedance, c the wave velocity, E Young's modulus and I_1 the sound intensity. The critical resolved shear stress τ_o which corresponds to the yield point, is indicated on each graph. Langenecker observed that for intensities up to 540 watts/in^2, the maximum level applied in his experiments, the acoustic stress associated with travelling waves was less than 1450 lbf/in^2 and only in the case of the softer materials was this sufficient to produce shear stress components of sufficient magnitude to activate pinned dislocation. Langenecker therefore proposed that some other mechanism must operate to account for the observed softening effects in the 'hard' materials. He conducted a series of experiments to determine whether or not standing waves were established in a steel testpiece irradiated at 20 kHz. Using infrared radiometry[9] he determined the temperature profile along the testpiece at several increments of time after the start of testing. The results are shown in Fig. 2.6a and b representing power inputs

of 35 and 80 watts respectively. These measurements indicated a sharp rise in temperature at the mid-length of the testpiece, which was considered therefore to be coincident with a stress antinode. Attempts to measure the stress amplitude in this region using the inverse magnetostrictive effect failed to reveal a stress concentration in the testpiece. Recourse was therefore made to approximate calculations based on the acoustic power absorption. This was determined from the heat conversion rate in the region of peak temperature indicated in Fig. 2.6. From these calculations the stress amplitude was found to be of the correct order but still a factor of 3 below the critical shear stress for the steel specimen under test.

Langenecker reviewed the possible mechanisms by which metals could absorb energy from sound waves[11] in an attempt to explain the softening effect at high acoustic intensities. These included thermoelastic energy conversion effects due to the motion of dislocations and energy transformation due to inelastic scattering. The mechanisms of absorption associated with dislocation motion are resonance, relaxation and hysteresis but the contribution of these effects was considered to be minimal under the test conditions employed.

Thermoelastic energy conversion effects were thought to be negligible at frequencies of 20 kHz and only become significant in the megacycle range. The final mechanism, inelastic scattering, would be expected to produce more pronounced effects in polycrystalline testpieces than in single crystals. This however, was not observed in Langenecker's experiments where both single crystals and polycrystalline materials were tested.

In the light of these considerations Langenecker proposed that the enhanced softening effect at high intensities could be explained by the action of sound waves on dislocations if the concept of localised heating around dislocations was introduced. He suggested that the heated areas would result in weakened regions, which would permit dislocation movement at much lower resolved shear stresses. The yield criterion under oscillatory conditions would then be expressed by the equation:

$$\sigma_m = \tau' \qquad \text{---------- (2.4)}$$

where τ' represents the apparent static shear stress at which flow is initiated at an elevated temperature.

Other workers have produced experimental evidence of 100% reduction in apparent yield stress under similar test conditions. Oelschlägel and Weiss[12] conducted tensile tests on aluminium single crystals with applied ultrasound at a frequency of 20 kHz and observed a reduction in yield strength of almost 100%. However, no attempt was made to measure the power input or oscillatory stress amplitude.

More recently, Lester and Whymark[13] examined the plastic flow threshold for nickel wires subjected to a static tensile load with superimposed longitudinal vibratory stress. The wires were suspended vertically from an acoustic concentrator driven at its resonant frequency of 18 kHz. Weights were attached at the lower end to ensure a standing wave régime and the wave length was made equal to $\frac{7}{4}\lambda$, where λ is the wave-length in nickel at 18 kHz. The oscillatory stress amplitude was calculated from measurements of the motional amplitude at the input end of the exponential concentrator. They plotted the oscillatory stress amplitude to produce plastic

flow over a range of static loads. Their results, shown in Fig. 2.7 indicated that the oscillatory stress was more effective in producing plastic flow than the equivalent static stress. They concluded that in the case of nickel it was incorrect to assume that the sum of static and oscillatory stresses at the flow threshold was equal to the static flow stress. It is suggested by the author, however, that the equation used by Lester and Whymark to determine the maximum stress amplitude in the wire is incorrect. The equation quoted in their paper, derived originally by Mason[14], described the strain variation along an exponential concentrator. It is appropriate in this case to determine the stress amplitude from the conditions of motional continuity between the specimen and output end of the concentrator.

The maximum stress is therefore given by[15]:

$$\sigma_{m_{max}} = k.E.\xi_{m_o}.e^{b\ell} \qquad \text{---------- (2.5)}$$

where k is the wave number $(\frac{2\pi}{\lambda})$, E Young's modulus, ξ_{m_o} the measured displacement amplitude at the input end of the concentrator of length, ℓ and exponential factor b.

It can readily be shown from acoustic theory, discussed in section 4, that the ratio of maximum stress amplitude in the wire to maximum stress amplitude in the concentrator is:

$$\frac{\sigma_{m_{max}}}{\sigma_{m_e}} = e^{b(\ell - x_n)\sqrt{(\frac{k}{b})^2 - 1}} \qquad \text{---------- (2.6)}$$

where x_n is the distance from the input end of the horn to the stress antinode.

Assuming a reasonable value for the ratio of the input to output diameter of the horn, (since this was not given) it is possible to estimate the order of error introduced.

Fig. 2.7 Onset of plastic flow in a vibrated nickel wire with a static load. (After Lester and Whymark[13]).

Fig. 2.8 Stepwise change in strain rate with increasing strain amplitude. (After Friedrich et al,[16]).

Fig. 2.9 Effect of amplitude change on the strain rate. (After Friedrich et al,[16]).

Fig. 2.10 For a non-linear function,

$\dot{\sigma}=\phi(\tau_s)$,

$|\dot{\sigma}(\tau_{s0}+\Delta\tau_s) - \dot{\sigma}(\tau_{s0})| > |\dot{\sigma}(\tau_{s0}-\Delta\tau_s) - \dot{\sigma}(\tau_{s0})|$

(After Friedrich et al[16]).

For a diameter ratio of 5:1, the true stress amplitude in the wire would be 3 to 4 times greater than the value calculated by Lester and Whymark. It therefore appears that their results indicate an approximately linear superposition effect in accordance with the findings of earlier researchers.

A programme of research undertaken by Friedrich and Kaiser[16] goes some way in providing an explanation of stress superposition effects on a sub-microscopical scale. They examined the effects of superimposed vibration on the creep strain rate and shear yield stress for copper and pure aluminium single crystals loaded in tension. Their tests were carried out over the frequency range 2.5 - 6.5 kHz and the results indicated once again an almost linear dependence of flow stress reduction on the superimposed oscillatory stress amplitude. Under creep conditions, that is, with a constant stress, the strain rate showed a sudden increase when ultrasonic energy was applied. This effect is illustrated in Fig. 2.8 which shows the shear strain as a function of time. At points A and B the stress amplitude was increased stepwise by the same factor but it will be seen that the increase in strain rate was much greater at the higher absolute value of amplitude. Friedrich and Kaiser illustrated this effect by plotting the shear strain rate ratio against amplitude ratio associated with each increase in amplitude. This relationship, shown in Fig. 2.9 indicated a markedly non-linear effect with increasing vibration amplitude.

They attempted to explain their observations by applying a generalised model describing the movement of dislocations in the slip plane. The strain rate, $\dot{a}$, is determined by the rate at which dislocations are freed from the pinning effect of short range obstacles in the slip plane. This has been

described by Seeger[17] as a thermally activated process in which the activation energy is expressed as a decreasing function of the shear stress, τ_s, acting on the dislocation. The strain rate is given by:

$$\dot{a} = c.\exp\left\{-(U_o - v\tau_s)/k_1T\right\} \quad \text{---------- (2.7)}$$

where U_o is the activation energy in the absence of a shear stress, v, the activation volume, k_1 Boltzman's constant, T the absolute temperature and c a constant relating to the dislocation model. At constant temperature the stress dependence of the strain rate becomes:

$$\dot{a} = c_1 \exp\,(v.\tau_s/k_1.T) \quad \text{---------- (2.8)}$$

If an oscillatory stress defined by $\hat{\tau}_s = \hat{\tau}\sin\omega t$, is superimposed on the steady stress, such that $\tau_s = \tau_{so} + \hat{\tau}_s$, then the mean strain rate under oscillatory conditions is found by substituting for τ_s in equation (2.8) and integrating the resultant expression over a complete cycle. The instantaneous strain rate under oscillatory conditions becomes:

$$\dot{a} = C_1 \exp\left\{v(\tau_{so} + \hat{\tau}\sin.\omega t)/k_1T\right\}$$

and the mean strain rate is given by:

$$\dot{a}_o = \frac{C_1}{2\pi} \exp(v.\tau_{so}/k_1T) \int_o^{2\pi} \exp\left(\frac{v\hat{\tau}\sin.\omega t}{k_1T}\right).d(\omega t) \quad \text{-- (2.9)}$$

Since $C_1.\exp(v\tau_{so}/k_1T)$ is the strain rate under the action of a constant shear stress τ_{so}, the variation in strain rate produced by a superimposed oscillatory component is

$$\frac{\dot{a}_o}{\dot{a}} = \frac{1}{2\pi} \int_o^{2\pi} \exp\left(\frac{v\hat{\tau}\sin.\omega t}{k_1T}\right).d(\omega t) = f(z) \quad \text{------ (2.10)}$$

where $z = \frac{v\hat{\tau}}{k_1T}$

Approximate solutions for f(z) were given by Friedrich and

Kaiser as:

$$f(z) = 1 + Z^2/4 \text{ for } Z < 1$$

and $f(z) = (1/\sqrt{2\pi Z})e^Z$ for $Z > 1$

The function f(z) is shown in Fig. 2.9 which indicates that the form predicted by equation (2.10) agreed closely with the four experimentally determined strain rate ratios:

The physical significance of the model was explained qualitatively in the following way. Due to the marked non-linearity of the relationship between shear stress and strain rate the increase in strain rate due to an increase in the shear stress $\Delta\tau_s$ is very much greater than the corresponding decrease caused by an equal shear stress decrement, $\Delta\tau_s$. This is illustrated in Fig. 2.10. Under oscillatory conditions it therefore follows that during the positive half cycle the increase in shear strain rate above the non-oscillatory value will be much greater than the decrease in the negative half period and the strain rate modulation becomes markedly anharmonic as illustrated in Fig. 2.11. Under the action of a constant mean shear stress the mean strain rate must therefore be greater than the non-oscillatory value, the deviation being expressed by equation 2.10.

Similar arguments were applied to define the mechanism operating in a tensile test with superimposed oscillatory shear stress. However, in order to maintain a constant shear strain rate normally imposed in this test, the mean shear stress, τ_{s_o} must be reduced. They deduced a mathematical model, based on equation (2.8) which predicted the reduction in critical shear stress (yield stress) $\Delta\tau_{s_o}$ with increasing oscillatory stress amplitude. At very low stress amplitudes the relationship showed a quadratic dependence of $\Delta\tau_{s_o}$ on

Fig. 2.11 Anharmonic modulation of the creep strain rate with superimposed oscillatory stress amplitude, $\hat{\sigma}_s$,. (After Friedrich, et al[16])

Fig. 2.12a. Reduction in yield stress as a function of the stress amplitude for aluminium single crystals. (After Friedrich et al[16]).

Fig. 2.12b. Reduction in yield stress with increasing stress amplitude for copper single crystals. (After Friedrich et al.[16]).

amplitude whereas higher values of $\hat{\tau}$ resulted in an almost linear effect. The results of practical measurements on Cu and Al single crystals showed good agreement with this general form as illustrated in Figs. 2.12a and 2.12b.

2.2.3. Effect of ultrasound on the post deformation properties of single and polycrystalline metals

Work hardening of zinc single crystals by high amplitude ultrasonic waves has been reported by Langenecker[18]. During tests in which sound waves, at a stress amplitude of 360 lbf/in^2 and frequency of 25 kHz were applied intermittently to specimens loaded in tension, the variation of shear stress with glide strain followed the form shown in Fig. 2.13. On initial application of ultrasound the shear stress fell abruptly to point b in the graph. It then increased quite sharply during subsequent glide until at c, when the vibrations were switched off, it rose almost instantly to a level d which was considerably above the initial non-oscillatory level, a. The shape of the stress strain curve during irradiation suggested that rapid hardening was occurring and that this appeared to reach a saturation level. The results of a series of tests were presented by plotting the increase in shear stress against acoustic stress amplitude - Fig. 2.14. This clearly indicated both a threshold and saturation value of stress, defined by p_1 and p_2 respectively. At stress amplitudes less than p_1 (360 lbf/in^2) the shear stress was reduced in the manner described in earlier references,[3,4,5] however beyond p_1 pronounced hardening was observed which increased upto stress amplitudes in the region of 800 lbf/in^2. Langenecker explained the effect by reference to the formation of vacancy rings in the lattice which were thought to be generated during the intersection of migrating

Fig. 2.13 Effect of repeated high-amplitude Ultrasonic Radiation on the stress-strain curve of zinc. (After Langenecker [18]).

Fig. 2.14 Relationship between acoustic stress amplitude and the shear stress increase, in zinc single crystals ultrasonically treated at room temperature. (After Langenecker [18]).

dislocations[19]. The presence of large numbers of vacancies was thought to hinder the movement of dislocations and hence increase the flow stress.

Kralik[20] examined the mechanical properties of polycrystalline copper treated ultrasonically at 90°K and observed a marked increase in yield stress when compared with untreated specimens. Exposure to a pressure amplitude of 1280 lbf/in^2 for 15 secs. increased the stress at a total elongation of 0.6% by a factor of 3.5 relative to the unirradiated specimens. This phenomenon was once again attributed to the formation of very large numbers of vacancies.

These results are confirmed by the work of Oelschlägel and Weiss[12] who carried out tests on zinc and aluminium single crystals. They also reported that in the case of zinc crystals recovery occurred after holding at room temperature for about 200 mins, resulting in the restoration of the original yield stress and ductility values. The rate and degree of recovery was found to be greater than observed for untreated specimens, which was compatible with the vacancy theory.

Considerable evidence exists, based on electrical resistivity measurements and electron-microscopy, which confirms the presence of high vacancy densities in material exposed to low frequency fatigue mechanisms[21]. Hardening mechanisms, although not fully understood, are considered to be similar to those found in materials quenched from a high temperature or irradiated with high energy nuclear particles, both of which produce high vacancy densities.

The similarity between metal exposed to high intensity ultrasound and low frequency fatigue has been demonstrated by

Severdenko and Elin.[22] Electron-microscopy studies of Armco iron, ultrasonically treated at 23.5 kHz, showed evidence of elastic slip and extrusion which occurs only during cyclic stressing and is characteristic of the fatigue process.

It appears from the results of research covering a wide range of materials and experimental conditions, that the observed reduction in yield strength under oscillatory conditions can be explained in terms of stress superposition. Both macroscopical and microscopical models predict an almost linear dependence of yield stress reduction on the superimposed oscillatory stress amplitude during tensile tests. However, a full understanding of the fundamental effects of stress waves on crystal plasticity and in particular on the movement of dislocations which determine the macroscopic phenomena, has not yet been achieved. It is in this area of study that an explanation will be found for the observed permanent effects of oscillatory stress on the mechanical and physical properties of irradiated test pieces.

It is now considered appropriate to examine the relevance of these observations to certain technological deformation processes. The following section reviews the results of applied research carried out in the United States, U.S.S.R., West Germany and the U.K. in an attempt to define the state of knowledge at the start of the current research programme.

2.2.4 Application of Oscillatory Energy to Metal forming Processes.

Since the early 1960's, considerable scientific effort has been devoted to studying the application of both high and low frequency vibrations to a wide range of forming processes. Much of the early work was concerned with the effects of

ultrasonic energy during wire and tube drawing. These processes were chosen primarily because of the relative ease of coupling the working tools to appropriate ultrasonic transducers and also due to their low energy requirements compared with, for example, rolling or extrusion, although these processes have also been considered.

2.2.4.1 Longitudinally activated processes

In 1963 Boyd and Maropis[23] reported on the results of wire drawing experiments in which the die was vibrated longitudinally at a frequency of 25 kHz. With electrical power inputs of upto 300 watts the drawing tension for a 7.5% area reduction of a tin alloy wire was reduced by up to 66 %. They observed that the effectiveness of the oscillatory process was markedly dependent upon the drawing velocity. This is illustrated in Fig. 2.15 where the reduction in drawing tension is shown to decrease rapidly at velocities greater than 300 ft/min. They attempted to summarise the qualitative effects of acoustic activation by developing a simplified model defining the drawing tension under oscillatory and non-oscillatory conditions. Considering only the homogeneous deformation and introducing an empirical efficiency factor to allow for redundant work and friction effects, they developed an elementary expression defining the drawing tension T in terms of the logarithmic strain and mean yield stress $\bar{Y}$, viz.

$$\frac{T}{S_2} = \frac{1}{\eta}.\bar{Y}.\ln \frac{S_1}{S_2} \quad \text{---------- (2.11)}$$

where S_1 and S_2 are the initial and final cross sectional areas of the wire and η an empirical constant defining the ratio of theoretical drawing tension (ignoring redundant work and friction work) to the actual drawing tension.

Fig. 2.15 Variation of drawing tension with drawing velocity for various levels of ultrasonic power. (After Boyd and Maropis[23]).

Fig. 2.16 Effect of acoustic power on drawing tension ratio, , for tin-alloy curve. (After Boyd and Maropis[23]).

They proposed that the efficiency under oscillatory conditions could be represented over a limited range of acoustic power, by a linear expression of the form:

$$\eta = \eta_o + \frac{k_o P}{V} \qquad \text{---------- (2.12)}$$

where η and η_o are the efficiencies under oscillatory and non-oscillatory conditions respectively, P the acoustic power, V the drawing velocity and k_o a constant of proportionality.

Then, if

$$\frac{T_o}{S_2} = \frac{1}{\eta_o} . \bar{Y} . \ln \frac{S_1}{S_2}$$

and

$$\frac{T}{S_2} = \frac{1}{(\eta_o + \frac{k_o P}{V})} . \bar{Y} . \ln \frac{S_1}{S_2}$$

it follows that $\frac{T_o}{T} = 1 + k^1(\frac{P}{V})$ ---------- (2.13)

The validity of equation 2.13 was examined by comparison with experimental values of drawing tension at various acoustic power levels and drawing velocities. Boyd and Maropis plotted the relationship between To/T and P/V and obtained an almost linear graph which was in general accord with equation 2.13, see Fig. 2.16. In fact the data indicated a non-linear relationship at low values of the ratio P/V which was not commented upon by the authors. This might be expected, however, from the experimental data shown in Fig. 2.15 relating drawing tension and drawing velocity at different acoustic intensities. This indicated that as the velocity increased, implying a decreasing value of P/V, the reduction in drawing tension became negligible. It therefore follows that a diminishing effect would be expected at low values of P/V.

Although the work of Boyd and Maropis established a

qualitative relationship between the electrical power input and primary deformation force, it did not contribute to an understanding of the mechanics of the oscillatory process. It is believed that this can only be achieved by accurate measurement of the relevant oscillatory parameters, viz. motional and strain amplitudes - preferably measured directly in the work piece. Boyd and Maropis suggested however, that the reduction in drawing force might be accounted for by lowering of interfacial friction between workpiece and tools and/or an increase in 'metal plasticity' based on the early observations of Langenecker[3] which were discussed in section 2.2.1.

A more detailed study of the application of ultrasound to wire drawing was undertaken by Pohlman and Lehfeldt[24]. They carried out a series of experiments on copper, aluminium and steel wires which were drawn through a longitudinally activated die at a frequency of 21 kHz. The drawing force and motional amplitudes of the die and drawn wire were monitored during the tests and they observed that the reduction in drawing force with ultrasound, varied periodically with the drawn length, reaching a maximum value at intervals corresponding to $\lambda/2$, the half wavelength of longitudinal waves in the wire material. The result confirmed the earlier experimental findings of Robinson et al[25] and Severdenko and Klubovich[26].

They also found that by inserting a second fixed drawing die at an optimum distance from the activated die, the reduction in drawing stress could be maximised at a value which did not vary with drawn length. The authors therefore concluded that the vibrator and drawn wire formed part of a common oscillatory system which could be tuned to resonance at the operating frequency of the drive unit. They found that the

system was described by the motional wave form shown in Fig. 2.17, which was confirmed experimentally. Force continuity was assumed in the deformation zone, between the tool and wire which, due to the virtually step-wise change in cross sectional area at this plane, implied a stress discontinuity producing enhanced stress and movement amplitudes in the wire. The resonant length 'a' was shown to be less than $\lambda/2$ and this was stated to be a function of the reactive component of the mechanical impedance of the wire. Resonance was therefore achieved when the distance between the dies was set at $(a+n\frac{\lambda}{2})$, where $a < \frac{\lambda}{2}$ and n = o, 1, 2, 3 etc.

Pohlman and Lehfeldt were able to calculate the antinodal stress amplitude from measured values of the displacement amplitude at the motional antinode using equation 2.2, viz:

$$\sigma_m = k.E.\xi_{m_\omega}$$

For which ξ_{m_ω} is the displacement amplitude in the drawn wire. They found good agreement between the measured reduction in drawing stress and the oscillatory stress amplitude although the latter was consistently some 10-15% lower. This discrepancy was assumed to be due to an additional reduction in the static drawing force brought about by a reduction in interfacial friction.

Later work by Winsper and Sansome[27] however, offered an alternative explanation. They carried out a series of oscillatory wire drawing experiments on brass, mild steel and aluminium using a single activated die. Tests were also carried out with two additional fixed dies positioned at specific locations on either side of the vibrated die. In each case the wire was drawn onto a coiler drum. The results of single die tests were in accord with those of Pohlman and Lehfeldt, showing

Fig. 2.17 Amplitude distribution in wire drawing with a tuned wire length. (After Pohlman and Lehfeldt[24]).

Fig. 2.18 Experimental data for different materials, plotted on the dimensionless curve relating reduction in drawing stress to the oscillatory stress amplitude.
(After Winsper and Sansome[29]).

a similar variation of mean load reduction with drawn length, the optimum value once more being defined by $(a + n\ \lambda/2)$. Winsper and Sansome calculated the oscillatory force amplitude induced in the drawn wire from measured values of the motional amplitude at the die and obtained close agreement with the observed reduction in mean drawing load. They concluded that force superposition was the only effect produced and presented the data for each material by plotting dimensionless parameters derived in the following way:

From equation 2.2 the oscillatory force amplitude is given by:

$$F_m = E.S.\ k\xi_{m_\omega} \qquad \text{---------- (2.14)}$$

where S is cross sectional area of the drawn wire.

Since ξ_{m_ω}, the antinodal amplitude in the drawn wire is directly proportional to ξ_{m_ℓ}, the die amplitude, equation (2.14) may therefore be written:

$$\frac{F_m}{E.S.} = K.k.\xi_{m_\ell} \qquad \text{---------- (2.15)}$$

where K is a constant of proportionality - which is determined experimentally from measured values of die and wire amplitudes. It may also be conveniently calculated from the following equation provided that the value of 'a' is specified:

$$K = \frac{\xi_{m_\omega}}{\xi_{m_\ell}} = \frac{1}{\text{Sin } k.a.} \qquad \text{---------- (2.16)}$$

where k is the wave number, given by $\frac{2\pi}{\lambda}$.

If the reduction in mean drawing force, ΔF, is accounted for entirely by force superposition, equation (2.15) becomes:

$$\frac{\Delta F}{E.S.} = K.k.\xi_{m_\ell} \qquad \text{---------- (2.17)}$$

By plotting the two dimensionless parameters contained in equation (2.17) a linear relationship, of 45 degree slope,

should be obtained irrespective of the test piece material. This result was confirmed by Winsper and Sansome whose data are reproduced in Fig. 2.18.

Tests with two additional fixed dies showed a reduction in mean drawing load which was greater than the oscillatory force amplitude induced in the deformation zone of the vibrated die. In tandem drawing the tension between each pair of dies exerts a back pull on the front die which increases the total drawing force. Winsper and Sansome argued that if one of the dies was vibrated and the distance between the dies and drawing drum chosen so as to establish a stress antinode in each deformation zone, successive reductions in the mean drawing force would be experienced at each die. The final reduction in drawing tension between the last die and drum would therefore be greater than the induced force amplitude. Their analysis of the mechanics of this process was based on the work of Thompson[28] who established a simple linear relationship between the die load and applied back-pull and drawing force and applied back-pull, for conventional wire drawing, viz:

$$\left.\begin{aligned} P' &= P'_o + (1-b)Q \\ \text{and } F' &= F'_o - bQ \end{aligned}\right\} \quad \text{----------(2.18)}$$

where P' and F', P'_o and F'_o are the drawing and die loads with and without back-pull respectively, Q the applied back pull and b is the back-pull factor, which is less than unity and constant for a given set of conditions. Winsper and Sansome used equations (2.18) to develop an expression predicting the reduction in total mean drawing load $\Delta P'_3$, and the mean die load, $\Delta F'_3$, for the drawing arrangement illustrated in Fig.2.19.

The validity of their analysis was examined experimentally using three multi-die arrangements which are shown in Table 2.1.

Fig. 2.19 (a) Relative position of dies for three-die ultrasonic drawing.

(b) Diagram showing the back tension effect combined with force superposition, giving a true reduction in drawing force. (After Winsper and Sansome[27]).

Fig. 2.20 Effect of plug amplitude on the reduction in draw force. (After Winsper and Sansome[29]).

Table 2.1 Showing correlation between experimental and theoretical values of the total mean drawing force, and the load on the second fixed die (after Winsper and Sansome[27]).

Comparison of measured die loads and drawing forces indicated close agreement with predicted values also shown in Table 2.1.

The conclusions drawn from this study provide what is considered to be a more rational explanation of the earlier observations made by Pohlman and Lehfeldt, in their two die experiments. Their experimental arrangement was similar to that described by Winsper and Sansome in the third system given in Table 2.1. Under these conditions the reduction in mean drawing load is readily shown to be given by:

$$\Delta P_2' = (2-b_2)\Delta F' \quad \text{---------- (2.19)}$$

and since b_2, the back pull factor, is less than unity the value of $\Delta P_2'$ exceeds the force amplitude by a factor of between 1 and 2.

It is not possible to comment on the back-pull factor in the experiments of Pohlman and Lehfeldt since insufficient data is provided. However, using the above analysis, their results could be explained if the back-pull factor obtained a value of 0.88.

The significance of Winsper and Sansome's work lies in the implication that greater area reductions can be achieved in multi-die oscillatory drawing than in the equivalent non-oscillatory process or in single die drawing with axial vibrations. In the latter case the limiting condition is reached when the peak stress in the drawn wire is equal to the yield stress. According to the superposition theory, this value is the same under both oscillatory and non-oscillatory conditions and the presence of a dynamic stress component affects only the mean stress. In multi-die drawing it has been shown that the reduction in mean stress can exceed the

oscillatory stress amplitude indicating a true reduction in the peak stress level which influences the limiting area reduction.

Winsper and Sansome subsequently studied the effects of ultrasound on the tag load during fixed plug drawing.[29] In these experiments the plug was vibrated longitudinally and simultaneous records taken of die and tag loads and oscillatory plug amplitude. They found that for stainless steel the drawing force was reduced by up to 45% and that the reduction in both draw force and die load varied linearly with the plug amplitude. Also, the relationship between force reduction and plug amplitude was found to be independent of the area reduction. Their results are summarised in Fig. 2.20 which shows the reduction in draw force with increasing plug amplitude for area reductions between 5 and 24.3%. Examination of the oscillatory force amplitude induced in the drawn tube as a result of plug bar activation, showed a periodic variation with increasing drawn length. The maximumamplitude occurred at intervals equivalent to the half wavelength for stainless steel at the operating frequency. It was found however, that the peak amplitude was significantly lower than the observed reduction in mean draw force. The authors therefore concluded that an additional mechanism operated under the conditions of their tests and it was speculated that this might have led to friction reduction between the tools and workpiece. No direct evidence of this was reported. However they established that the surface finish was improved under oscillatory conditions, compared with the unactivated process, which might be explained by enhanced relative motion between the contacting surfaces.

Fig. 2.21 Different die excitation systems. (After Lehfeldt[30]).

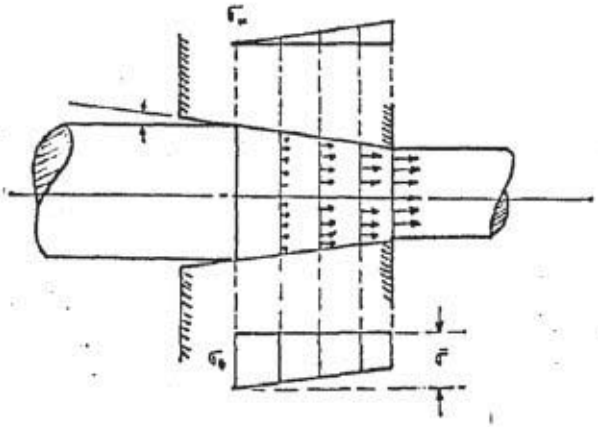

Fig. 2.22 (a) Stress distribution in a drawing die using the Tresca yield criterion,

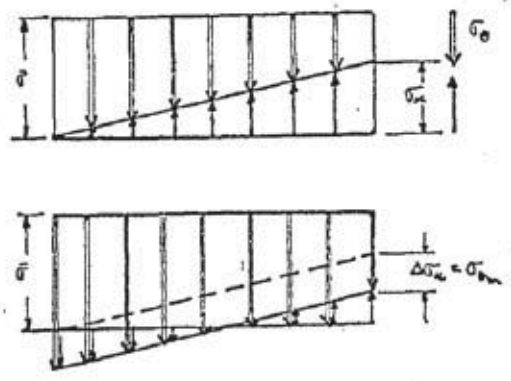

(b) Stress superposition in drawing die under the conditions in 2.21(b).

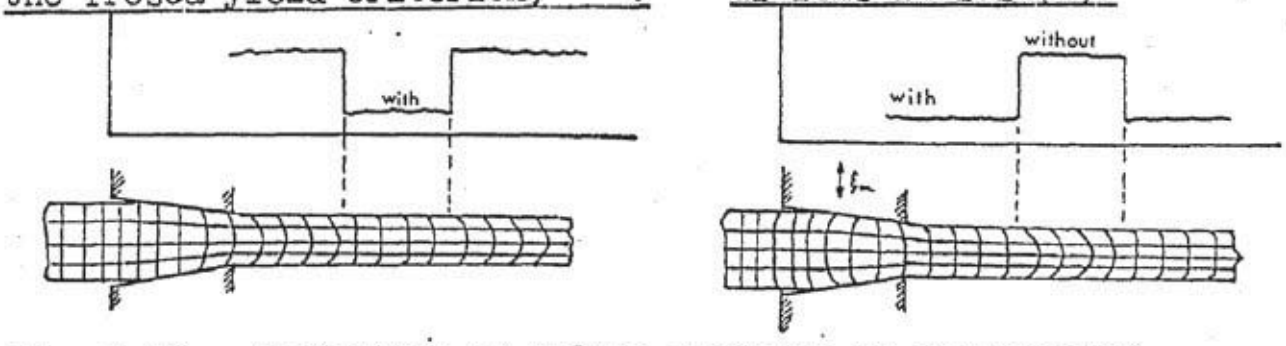

Fig. 2.23 Distortion of volume elements in rod drawing with and without vibrations.

This aspect will be discussed further in section 2.3.

2.2.4.2 Alternative systems of excitation

Each of the references cited above were concerned with longitudinally resonant systems in which the tool was vibrated parallel to the drawing axis and was positioned at a motional antinode in the vibrator. Several alternative configurations have been used in practical oscillatory wire drawing experiments described by Lehfeldt[30]. These are summarised in Figs. 2.21a - 2.21d. Although each system adopts a longitudinal oscillatory mode, the position of the die with respect to the standing waves established in the acoustic guide and also the orientation of the drawing axis relative to the oscillatory axis, differ from the basic systems described earlier. In Fig. 2.21a the die is located at a motional node with the drawing axis parallel to the direction of wave propagation. This arrangement led to a very low coupling between the vibrator and wire since only the transverse strain, associated with the longitudinal stress antinode, contributed to the deformation forces. Lehfeldt's experiments confirmed that this method was ineffective in lowering the drawing stress, only a slight reduction being achieved.

An alternative arrangement, proposed initially by Oelschlägel and Weiss[31], is shown in Fig. 2.21b. With the die mounted transversely at a motional node so that the drawing axis was perpendicular to the direction of vibration, it was argued that the die would experience a cyclic distortion, causing the cross section to become elliptical as the oscillatory strain increased during each half cycle. The periodic change in profile therefore imposed a cyclic

transverse stress on the deforming wire which lowered the mean drawing stress. This is illustrated in Fig. 2.22a, which shows schematically the distribution of transverse and longitudinal stresses in the deformation zone. Adopting the Tresca criterion, the condition of yielding is defined by

$$\sigma_x + \sigma_\theta = \bar{\sigma} \quad \text{---------- (2.20)}$$

where σ_x and σ_θ are the longitudinal and transverse stresses respectively. Under oscillatory conditions the compressive transverse stress is periodically increased by the addition of an oscillatory component as illustrated in Fig. 2.22b. Lehfeldt claimed that this resulted in a net compressive strain at the die entry plane and a reduction in the drawing stress σ_{x_b}, at the exit plane, by an amount equal to the transverse stress amplitude, σ_{θ_m}. This was calculated from the following expression:

$$\sigma_{\theta_m} = k.\xi_{m_\ell} E.\ S_k \quad \text{---------- (2.21)}$$

where k and ξ_{m_ℓ} are the wave number and motional amplitude of the acoustic waveguide respectively, E the Young's modulus of the workpiece material and S_k a correction factor which allows for the strain distribution around the die insert.

Comparison of measured and calculated values of drawing stress reduction using equation 2.21 showed close agreement. Confirmation of the enhanced compressive stress during deformation was provided by observing the distortion in a square network engraved on one face of a longitudinally sectioned length of wire. The results of these tests showed that under oscillatory conditions the vertical lines within the deformation zone were bent against the drawing direction at the entry plane and on passing through the die experienced

further distortion but this time in the direction of drawing. The net result was a set of near vertical lines distorted only near the surface. In contrast, conventional drawing produced a grid in which the vertical lines were markedly curved in the drawing direction. These effects are illustrated in Fig. 2.23.

Similar results were obtained with the arrangements shown in Fig. 2.21c. In this instance a split die was used with one half rigidly fixed and the other attached to the vibrator at a motional antinode. This resulted in a swaging action, which produced reductions in drawing force of up to 50%. It was explained that in none of the transverse drawing experiments did the draw force reduction vary with drawn length, indicating the absence of a longitudinal standing wave in the drawn wire.

The final system examined is shown in Fig. 2.21d. In this arrangement the drawing die is mounted transversely at a motional antinode and under these circumstances the die and wire are vibrated bodily, setting up a bending wave in the wire as it passes through the die. Experiments showed that once again the reduction in drawing force varied periodically but in this case the maximum reduction occurred at intervals equal to the halfwavelength of bending waves in the wire material. On this basis the reduction in axial drawing stress was related to the bending stress at the plane of the die. This was evaluated approximately by applying the relationship for a freely supported beam loaded at its centre.[32] On substituting the motional amplitude ξ_m for the static displacement, the mean axial stress amplitude, averaged over half the cross section, is readily shown to be given by:

$$\bar{\sigma}_m' = \frac{32}{\pi} \cdot \xi_{m_\ell} \frac{E.d}{\lambda_b^2} \quad \text{---------- (2.22)}$$

where d is the wire diameter and λ_b the half wavelength of bending waves in the wire. ξ_{m_ℓ} and E are as defined earlier. The value of longitudinal oscillatory stress in the deformation zone calculated from equation 2.22 showed good agreement with the measured draw force reduction confirming once again the basic superposition mechanism.

The effect of ultrasound on the strip drawing process was examined by Rozner,[33] using the apparatus shown in Fig. 2.24. From measurements of the drawing stress and die separation force he concluded that the process forces were lowered as a result of superposition effects and also due to a reduction in the coefficient of friction, μ, between the strip and each die. However since the friction force was not measured directly but calculated from the normal and axial forces the latter assumption may be in error. This is particularly the case since the values of normal and axial forces were likely to be affected by ultrasound, independently of μ which was determined from the following equation:

$$\mu = \frac{\frac{T'}{2Q'} - \tan\alpha}{\frac{T'}{2Q'}.\tan\alpha + 1} \quad \text{---------- (2.23)}$$

where T′ and Q′ are the drawing force and normal force respectively and α the angle of inclination of each die to the drawing axis.

These results indicate however, that a transverse oscillatory mode is effective in reducing the drawing force and although insufficient data were given regarding oscillatory force amplitudes, the work adds at least qualitative support to the researches of Lehfeldt.

Fig. 2.24 Apparatus for oscillatory strip drawing. (After Rozner (33)).

Fig. 2.25 Effect of drawing speed on stress reduction. (After Lehfeldt (30)).

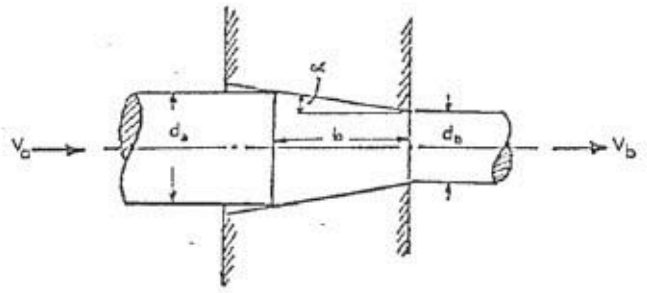

Fig. 2.26 Rod drawing deformation geometry.

2.2.4.3 Velocity Effects

The effect of increasing drawing velocity on the reduction in process forces, under given oscillatory conditions, has been reported by several workers[23,24] but little attempt was made to provide a qualitative explanation until quite recently. Lehfeldt, in 1969,[30] examined the reduction in drawing force while drawing copper wire at a constant vibration amplitude over a speed range of from 0.5 to 12 in. per second. He observed that beyond a certain drawing velocity the effectiveness of ultrasonic vibrations was rapidly reduced, becoming negligible at a velocity of about 9 in. per second, see Fig. 2.25.

It was proposed that this phenomenon could be explained by comparing the mean strain rate, for the particular reduction and draw speed, with the acoustic strain rate associated with a particular vibration amplitude. The mean strain rate, using the legends of Fig. 2.26 may be found by considering the distance travelled by respective elements in the entry and exit planes, during a small time interval dt, if the initial and final velocities are Va and Vb.

The mean strain rate $\bar{\dot{\varepsilon}}$ then becomes:

$$\bar{\dot{\varepsilon}} = \frac{(V_b dt - V_a dt)}{\ell_o} \frac{1}{dt} \quad \text{---------- (2.24)}$$

where ℓ_o is the axial length of the deformation zone. Applying the condition of constancy of volume and expressing ℓ_o in terms of the initial and final wire diameters and die semi-angle, α, after rearranging, the mean strain rate is found from

$$\bar{\dot{\varepsilon}} = \frac{V_b}{V_a} \left(1 + \frac{db}{da}\right) 2 \tan\alpha \quad \text{---------- (2.25)}$$

Lehfeldt considered that the oscillatory energy would

only be effective in reducing the drawing load when the acoustic strain rate was greater than the mean deformation rate expressed by equation 2.25.

In a standing wave regime the acoustic strain rate may be found by considering the displacement waveform defined by:

$$\xi = \xi_m \cos kx . \cos \omega t \quad \text{---------- (2.26)}$$

where x is the distance from the end of the longitudinal system and the other variables are as defined earlier.

The strain rate is therefore found by differentiating equation (2.26) first with respect to distance, x and then with respect to time, viz:

$$\dot{\varepsilon} = k\omega\xi_m \sin kx . \sin \omega t \quad \text{---------- (2.27)}$$

and the amplitudinal value is therefore simply:

$$\dot{\varepsilon}_m = k . \omega . \xi_m \quad \text{---------- (2.28)}$$

The acoustic strain was considered to be effective only during a quarter of the vibrational cycle and Lehfeldt therefore concluded that the effective mean acoustic strain rate was equal to a quarter of the root mean square value, viz:

$$\bar{\dot{\varepsilon}}_m = \frac{1}{4}\sqrt{2} . k . \omega \xi_m \quad \text{---------- (2.29)}$$

The results shown in Fig. 2.25 were then discussed in relation to the above criterion. For the reduction quoted, Lehfeldt calculated that the deformation rate, $\bar{\dot{\varepsilon}}$ at 1.0 in/sec was greater than the effective acoustic strain rate associated with the motional amplitude induced in the wire, the values being 13.5 sec^{-1} and 10 sec^{-1} respectively. It was therefore argued that the observed decrease in drawing stress reduction would be anticipated at speeds in excess of 1.0 in/sec and that the stress reduction over the range 1.0 - 9.0 in/sec was due

to surface effects and not to stress superposition. However, no explanation was given as to why interfacial friction should be reduced beyond a certain drawing speed when no effect was apparent at speeds below this critical value. It is also pointed out that the proposed criterion, defining the limiting speed at which acoustic force superposition is effective, implies a dependency upon the area reduction. Such an effect was not observed in tests carried out independently by Pohlman and Lehfeldt[24] and Winsper and Sansome[29]. Doubt therefore exists as to the validity of this explanation.

The effect of drawing velocity on the force reduction during ultrasonic wire drawing was also examined by Winsper and Sansome[34]. Using a similar set-up to that described for their earlier experiments they measured the reduction in drawing force produced by a given vibration amplitude over a range of drawn speeds from 0.5 - 66 ft/min. These results are summarised in the graph shown in Fig.2.27 which indicates a continuous decrease in the effectiveness of vibrations with increasing drawing speed.

Winsper and Sansome attempted to explain this by considering the motional and elastic characteristics of the coupling between the die and wire. They proposed that provided the oscillatory velocity amplitude of the die exceeded the mean linear velocity of the wire, then during a portion of the vibration cycle the die would overtake the wire, drawing would cease, and part of the drawing tension would be relaxed producing a force superposition effect. The problem was discussed quantitatively by reference to Fig. 2.28 which shows the die displacement and velocity waves in relation to the

Fig. 2.27 Effect of drawing velocity on the reduction in mean drawing stress under oscillatory conditions. (After Winsper and Sansome[29]).

Fig. 2.28 Die velocity and displacement waves in relation to mean drawing velocity. (After Winsper and Sansome[29]).

mean drawing velocity. Examination of the velocity wave reveals that during the interval t_1 the die overtakes an element of wire moving at velocity V, and at this point drawing ceases. During the interval between t_1 and t_2, the motion of the element coincides with that of the die as elastic strain is released in the drawn wire. At t_2 the peak to peak displacement amplitude in the wire is defined by C_1 C_2 which is less than that of the die by an amount related to the speed of coiling on the drawing block. The elastic strain released by this displacement is subsequently taken up partly by the motion of the die and partly by the block until at t_3 drawing commences again.

If the die displacement and velocity are given by $\xi = \xi_m \cos\omega t$ and $\dot{\xi} = \dot{\xi}_m \sin\omega t$ respectively, then drawing ceases when:

$$V_1 = \dot{\xi}_m \sin\omega t_1$$

$$\text{or } t_1 = \frac{1}{\omega} \sin^{-1}\left(\frac{V_1}{\dot{\xi}_m}\right) \qquad \text{---------- (2.30)}$$

At t_2, after a time defined by $(\pi/\omega - t_1)$ the die and wire will have travelled a distance

$$= 2\xi_m \cos\omega t_1 \qquad \text{---------- (2.31)}$$

and the drawing block will have coiled a length of wire

$$= V_1\left|\frac{\pi}{\omega} - 2t_1\right| = \frac{V_1}{\omega}\left|\pi - 2\omega t_1\right| \qquad \text{-------- (2.32)}$$

The peak to peak elastic deformation of the wire is thus

$$2\xi_{m\omega} = 2\xi_m \cos\omega t_1 - \frac{V_1}{\omega}\left|\pi - 2\omega t_1\right| \qquad \text{---------- (2.33)}$$

The oscillating force induced in the wire is determined by substituting for ξ_{m_ω} in the familiar equation:

$$F_m = k.E.\xi_{m_\omega}.S \qquad \text{---------- (2.34)}$$

where S is the cross-sectional area of the drawn wire. In order to determine the reduction in drawing force it is necessary to calculate the oscillatory force amplitude in the deformation zone. This can readily be done provided that the position of the motional and stress antinodes in the drawn wire, are defined in relation to the deformation zone. Winsper and Sansome determined this experimentally as described in section 2.2.4.1.

The authors compared experimental values of drawing stress reduction with those calculated from equation (2.34) and found good agreement, particularly at higher drawing speeds. The theory predicted that as the drawing speed increased to that of the amplitudinal oscillatory velocity of the die, the oscillatory force induced in the wire tended to zero. This was accurately confirmed by the experimental data, See Fig. 2.27. In physical terms this implies that a motional discontinuity is established between the die and wire as the drawing velocity is increased and less energy is transmitted into the deformation zone.

2.3 The effect of vibrations on interfacial friction

Friction between two contacting surfaces stems from the interaction of asperities[35]. These local high spots form points of initial contact and are deformed plastically by normal and shear stresses until the total contact area is sufficient to support the applied forces without further deformation. Relative sliding motion between the surfaces then occurs by shearing of the contacting areas and the shear stress necessary to produce this movement constitutes the frictional force. This simple picture must be modified to take account of the effects of such factors as the presence of a lubricant

film between the surfaces and the magnitude of the applied forces. When the latter are sufficiently large, bulk plastic deformation of the contacting bodies occurs generating fresh surfaces free from protective oxide films and hence more reactive and likely to form weldments at the points of contact.[36] This effect is offset however by the heat produced at high shearing rates, which causes local melting or softening of the asperities.

Clearly any factor which affects the chemical activity of the contacting surfaces or the strength of the asperities or mechanics of asperity deformation must influence the nature and magnitude of the frictional force. The application of vibrations to rubbing surfaces might under certain circumstances, produce each of these effects. Considerable attention has therefore been paid to studies of the effects of vibration on interfacial friction under conditions of elastic and plastic deformation and these are reviewed in the following section.

2.3.1. Friction reduction under conditions of elastic loading.

The effect of vibrations on the coefficient of static friction was first examined by Fridman and Levesque[37]. Using a simple inclined plane with a sliding steel block they demonstrated that by exciting standing waves in the latter, the block could be made to slide at very low angles of inclination. This indicated a reduction in the friction force acting between the block and slider.

The inclined plane was excited at different frequencies from 6.6 kHz to 41 kHz, resulting in overtone modes. No attempt was made to measure the vibration amplitude directly

but this was inferred from measurements of the transducer exciting current. Typical results are shown in Fig. 2.29 which indicate the effect of transducer power on the percentage reduction in the coefficient of static friction for three different frequencies. The general characteristic was a rapid rate of decrease in friction at low power levels falling off slightly as the power was increased. These results appeared to indicate that lower frequencies were more effective in reducing friction at a given power level. However, examination of the vibration field using Chladni figures[38] indicated variations in the nodal patterns established at different frequencies and it was probable also that widely varying amplitudes were established in the region of the slider. It was therefore not possible to make any quantitative assessment of the mechanism underlying the friction reduction. Fridman and Levesque considered however that movement was initiated due to the breaking of weldments when subjected to the acceleration associated with the oscillatory wave form.

In 1966 Pohlman and Lehfeldt[27] examined the effect of vibrations on the kinetic friction force between two metal surfaces using a rotating disc on which rested an ultrasonically activated ball. This was subjected to a normal load which was applied by the addition of weights, upto a maximum of 40 lb. Vibrations were applied in four different ways:

(a) and (b) tangentially at an 8^{o} angle of inclination to the plane of the disc which was moving first in a clockwise direction and then anticlockwise.

(c) normal to the direction of rotation and in the plane of the disc.

(d) normal to both the disc and direction of rotation.

Fig. 2.29 The effect of transducer power on the coefficient of static friction for ground steel surfaces. (After Fridman and Levesque [37]).

Fig. 2.30 Examination of the effect of oscillation direction on the coefficient of kinetic friction. (After Pohlman and Lehfeldt [7])

Fig. 2.31 Friction reduction in relation to contact speed for several oscillation directions. (After Pohlman and Lehfeldt [7]).

These are illustrated in Fig. 2.30. The effectiveness of the various arrangements was demonstrated by determining the reduction in friction force between the ball and disc over a range of surface speeds at a constant vibration amplitude. The results are shown in Fig. 2.31 where the friction reduction, represented by the ratio of oscillatory to non-oscillatory friction force is expressed as a percentage. The graph shows that arrangements a, b and c are much more effective in reducing the friction force than method d in which the vibration axis was normal to the plane of the disc. This was explained by the fact that during the downward portion of the cycle the load on the ball would be increased which, it was argued, would offset the reverse effect experienced during the upward vibration cycle. The mean normal load and hence the friction force would therefore be virtually unchanged.

The friction reduction observed in methods a, b and c was attributed to fatigue fracture of microwelds under the action of high alternating stress amplitudes. No evidence in support of this mechanism was given however.

More recently, Godfrey[39] measured the effect of vibration at frequencies between 20 and 1000 Hz, on the kinetic friction between a steel slider and flat steel plate. The latter was driven by a conventional 20 watt loud speaker and a piezoelectric pickup was used to monitor the acceleration, velocity and displacement of the beam. The slider, resting on three fixed balls was loaded by weights totalling 2.2 lb.

The results of lubricated tests, in which the beam was smeared with oleic acid in white oil, were presented as plots of the kinetic coefficient of friction against beam acceleration, for different frequencies and a constant sliding

speed. These curves are shown in Fig. 2.32 and indicate that vibration has a negligible effect on the friction coefficient at low values of acceleration but beyond a certain value it is rapidly reduced. Tests at different sliding velocities indicated that the effect of vibrations on friction was independent of this factor under the test conditions described. Godfrey observed that the threshold value of acceleration at which friction reduction was initiated coincided approximately with the value due to gravity. This suggested that the load between slider and plate was reduced when the plate was pulled down faster than the slider assembly could fall under gravity. Electrical resistance measurements between slider and plate revealed an open circuit during a portion of the cycle at high accelerations, indicating that the two surfaces in fact separated. At lower intensities, decreased friction was accompanied by an increase in the electrical resistivity. This was explained in terms of reduced contact area due to the fracture of some of the weldments. Comparison of these results with the data of Pohlman and Lehfeldt suggests that a different mechanism operated at high frequencies. Acceleration clearly does not have the same simple effect as at low frequencies. This is illustrated by the small reduction in friction achieved with arrangement 'd' in Fig. 2.30, in spite of the very high acceleration applied to the rider (i.e. 23,000 g.). It is clear that in the latter case separation did not occur due it is thought to the low vibration amplitude. Separation would not be possible unless the amplitude exceeded the elastic spring-back of the two contacting surfaces. It appears therefore that in this test configuration two criteria must be satisfied for significant friction reduction to be achieved, viz.

Fig. 2.32 Effect of vibration on the coefficient of kinetic friction, μ (After Godfrey[39]).

Fig. 2.33 Friction vector reversal associated with relative cyclic motion at an interface. (After Sirotyuk et al[41]).

Fig. 2.34 Variation of friction force as a function of β, the velocity ratio. (After Golubev and Dyadechko[43]).

(a) The acceleration of the rider or beam must exceed that due to gravity.

(b) The oscillatory displacement amplitude must be greater than the elastic strain released during off-loading, in order for separation to occur. Elastic strain release which does not result in the fracture of micro weldments formed between the surfaces, would not be expected to reduce the mean load or the shearing force necessary to cause bulk relative motion.

Later work by Lenkiewicz[40] in which a vibrated sample, in the form of a flat strip, was held tangentially against a rotating drum, confirmed the dependence of friction reduction on the sliding velocity. These tests were carried out at low frequencies (20-120 Hz) and sliding speeds between 0 and 60 in. per sec. It was found that in order to reduce the friction at high sliding velocities it was necessary to employ higher vibration amplitudes. In this respect the results were in accord with those of Pohlman and Lehfeldt[27]. Lenkiewicz also observed that forced vibrations, under the particular test conditions described, were effective in eliminating stick-slip vibrations.

2.3.2 Friction reduction during plastic deformation

Sirotyuk et al[41] examined the mechanism of friction reduction when drawing through an ultrasonically activated die. Their analysis of the oscillatory process was based on two assumptions; (a) that the die could be considered to vibrate bodily (each particle moving in phase and experiencing the same motional amplitude) and (b) that relative axial motion occurred between the die and workpiece. They argued that provided the oscillatory amplitude of the vibrated die exceeded the linear drawing velocity then during some portion of the

cycle the die would overtake the workpiece causing an effective reversal of the friction vector. If the interfacial friction conditions are assumed to be the same during oscillatory and non-oscillatory working, only a mean value of friction force will contribute to the drawing load. This situation is illustrated in Fig. 2.33 a and b. The upper figure indicates the cyclic velocity of the die in relation to the drawing velocity. Reversal of the friction vector occurs after an interval t_1, and the portion of the cycle during which the friction force assists the body motion is given by $T/2 - 2t_1$. Similarly, during the interval $T/2 + 2t_1$, the friction force hinders the body motion. The force acting during each part of the cycle is shown in the lower figure and provided that the friction conditions remain constant, the factor by which the mean friction force is reduced is found from the ratio of the oscillation period to the difference between the intervals of 'assisted' and 'hindered' motion. viz.

$$\frac{Fr}{F} = \frac{(T/2 - 2t) - (T/2 + 2t)}{T} = \frac{4t_1}{T} \quad \text{----- (2.35)}$$

where Fr and F denote the mean friction force under oscillatory and non-oscillatory conditions respectively.

t_1 in equation (2.35) is found from the condition:

$$V = \dot{\xi}_{m\ell} \sin \omega t_1$$

$$\text{therefore } \omega t_1 = \sin^{-1} V/\dot{\xi}_{m\ell}$$

$$\text{and since } T = \frac{2\pi}{\omega}$$

$$\frac{Fr}{F} = \frac{2}{\pi} \sin^{-1}\left(\frac{V}{\dot{\xi}_{m\ell}}\right) \quad \text{---------- (2.36)}$$

where V is the mean drawing velocity and $\dot{\xi}_{m\ell}$ the oscillatory velocity amplitude of the die.

The authors attempted to verify this theory by applying

vibrations to the fixed plug, during tube drawing and comparing the drawing force under oscillatory and non-oscillatory conditions. They assumed that the friction force associated with the plug was approximately 20-25% of the draw force. Choosing oscillatory parameters calculated to virtually eliminate the plug friction they found however that the draw force was reduced by 25-30%. They attributed the enhanced effect to additional friction reduction at the die/tube interface.

Further work concerned with tube sinking in which the die was ultrasonically vibrated in an axial direction was reported by Nosal and Rymsha[42]. They modified the above theory to take account of the resolved component of the die oscillation parallel to the die/tube interface and used the model to calculate the reduction in draw force based on the following relationship:

$$P_z = P_d + P_f = P_d(1 + \mu\cot\alpha) \quad \text{---------- (2.37)}$$

where Pz is the total drawing force.

Pd, the proportion of the drawing force used to overcome the resistance to deformation.

P_f, the force to overcome external friction.

μ, the coefficient of friction.

α, the semi-die angle.

Under oscillatory conditions the term $\mu\cot\alpha$ is reduced by a factor 'n' (defined by an equation similar to (2.36)), and the oscillatory drawing force then becomes:

$$P_{zy} = P_d\left(1 + \frac{\mu\cot\alpha}{n}\right) \quad \text{---------- (2.38)}$$

The reduction in total drawing force is then found from:

$$\frac{P_z - P_{zy}}{P_z} \cdot 100 = \frac{\mu\cot\alpha}{1 + \mu\cos\alpha} \cdot \left(1 - \frac{1}{n}\right) \cdot 100 \text{ per cent} \quad (2.39)$$

This equation was found to show good agreement with measured force reductions of 20 and 35%. However, the validity of this apparent correlation is based on two assumptions which are considered to be incorrect, viz:

(a) The application of oscillatory energy affects only the interfacial friction.

(b) That relative cyclic motion occurs between the die and tube.

It is apparent from the published work on oscillatory wire drawing[27] that axial activation of the die leads to the superposition of an alternating force upon the static deformation load, with a consequent reduction in the mean forming load. Since the oscillatory configuration used by Nosal and Rymsha is essentially the same, a similar phenomenon would be anticipated. It cannot therefore be claimed that the observed reduction in drawing force is attributable solely to reduced friction. In fact, during oscillatory wire drawing, force superposition has been found, by a number of independent workers, to account entirely for the observed reduction in draw force. It is concluded therefore that oscillation of the die merely imparts a cyclic motion to the work piece under these conditions, producing intermittent deformation without separation or relative cyclic motion at the interface, as described by Winsper and Sansome[34].

Golubev and Dyadechko[43] analysed the effect of torsional vibrations on the interfacial friction during wire drawing. They considered the relative motion between the wire and die to have two velocity components, viz: V_k, the component of the mean axial velocity parallel to the die surface, and $\dot{\xi}_\phi$, the tangential velocity amplitude, related to the cyclic rotation

of the die by the expression:

$$\dot{\xi}_\phi = \phi_m . r . \omega \cos\omega t \quad \text{---------- (2.40)}$$

where ϕ_m is the maximum angular rotation, r the average die radius and ω the angular frequency.

The die motion imparted a tangential component to the sliding velocity between the die and wire, which rotated the vector through an angle, defined by γ. If the resultant sliding velocity is given by:

$$V_c = \sqrt{V_k^2 + \dot{\xi}_\phi^2} = \sqrt{V_k^2 + \phi_m^2 . r^2 \omega^2 \cos^2\phi}$$

$$\text{then } \cos\gamma = \frac{V_k}{\sqrt{V_k^2 + \phi^2 r^2 \omega^2 . \cos^2\phi}} \quad \text{---------- (2.41)}$$

The effect of vector rotation on the friction force was determined by considering the friction force impulse acting parallel but in the opposite direction to V_c, during a period of time dt. This was defined by $dI = N\mu dt$.
where N is the normal force and μ the friction coefficient. The effective friction force under oscillatory conditions is thus found from the projection of the friction vector onto the drawing axis, viz: $dI_o = N\mu\cos\gamma dt$ ---------- (2.42)
Thus total friction force impulse during a complete cycle is therefore:

$$I_o = N\mu \int_o^T \cos\gamma dt = N_1 \mu_1 T$$

$$\text{hence } \frac{N_1\mu_1}{N_\mu} = \frac{1}{T} \int_o^T \cos\gamma dt \quad \text{---------- (2.43)}$$

Substituting for γ in equation 2.43 and writing $t = \frac{\phi}{\omega}$ and $T = \frac{2\pi}{\omega}$ the proportional change in friction force is found from:

$$\frac{N_1\mu_1}{N_\mu} = \frac{2}{\pi} \frac{V_k}{\phi . r . \omega} \int_o^{\frac{\pi}{2}} \frac{d\phi}{\sqrt{\left(\frac{V_k}{\phi r \omega}\right)^2 + \cos^2\phi}}$$

putting $\beta = \frac{V_k}{\phi r \omega}$ and rearranging gives:

$$\frac{N_1\mu_1}{N_\mu} = \frac{2}{\pi}\frac{\beta}{\sqrt{\beta^2+1}}\int_0^{\frac{\pi}{2}}\frac{d\phi}{\sqrt{1-\frac{1}{1+\beta^2}\sin^2\phi}} = \frac{2}{\pi}\frac{\beta}{\sqrt{\beta^2+1}}\,.\,k \quad - (2.44)$$

where k is the complete elliptical integral given by

$$k = \int_0^{\frac{\pi}{2}} \frac{d\phi}{1 - c^2\sin^2\phi} \; ; \; C^2 = \frac{1}{1+\beta^2}$$

The theoretical effectiveness of rotational oscillations in reducing friction was illustrated by plotting $\frac{N_1\mu_1}{N_\mu}$ as a function of β see Fig. 2.34. When $\beta < 0.1$ the friction is reduced by about 80%. No attempt was made by the authors to verify this analysis experimentally.

An analysis of the effect of transverse die oscillations on the friction force during tube sinking was later carried out by Severdenko and Reznikov[44]. Using similar arguments to those given above they considered the rotation of the friction vector during each half cycle of the die vibration. This may be deduced from the velocity vector diagram shown in Fig. 2.35 where $\dot{\xi}m_t$ is the transverse velocity amplitude, V_o the mean sliding velocity and α the die semi-angle.

The resultant velocity V_k is rotated through an angle ρ_1 to the sliding direction during one half cycle and ρ_2 during the reverse half cycle. From Fig. 2.35 these angles are readily shown to be given by:

$$\tan\rho_1 = \dot{\xi}m_t \cos\alpha \,/(V_o + \dot{\xi}m_t \sin\alpha) \text{ ---------- } (2.45)$$

and $$\tan\rho_2 = \dot{\xi}m_t \cos\alpha \,/(V_o - \dot{\xi}m_t \sin\alpha) \text{ ---------- } (2.46)$$

The friction force under oscillatory conditions was determined once again by considering the impulsive force acting during a complete cycle and taking account of the vector rotation which occurred in each half cycle.

Writing the friction force impulse as:

Fig. 2.35 Determination of the resultant velocity of a particle moving with a mean velocity Vo, in contact with an oscillating surface. (a) during half cycle 0 - $\frac{T}{2}$ (b) during half cycle $\frac{T}{2}$ - T. (After Severdenko and Reznikov[44]).

Fig. 2.36 The effect of different directions of die oscillation, in relation to the drawing axis, on the friction force.

(After Severdenko and Reznikov[44]).

Fig. 2.37 Systems of ultrasonic excitation for tube sinking. (a) Longitudinal, (b) Transverse.

(After Severdenko and Reznikov[44]).

$$dI = N\mu\cos\rho_1 \, dt$$

We obtain $$I = N\mu\left[\int_0^{T/2} \cos\rho_1 \, dt + \int_0^{T/2} \cos\rho_2 \, dt\right] \quad \text{--- (2.47)}$$

where $$\cos\rho_1 = (V_o + \dot{\xi}_{mt}\sin\alpha)/\left\{(V_o + \dot{\xi}_{mt}\sin\alpha)^2 + (\dot{\xi}_{mt}\cos\alpha)^2\right\}^{1/2}$$

and $$\cos\rho_2 = (V_o - \dot{\xi}_{mt}\sin\alpha)/\left\{(V_o + \dot{\xi}_{mt}\sin\alpha)^2 + (\dot{\xi}_{mt}\cos\alpha)^2\right\}^{1/2}$$

(2.48)

but $$I = N_1\mu_1 T \quad \text{----------} \quad (2.49)$$

where $N_1\mu_1$ is the average friction force during period T;

the proportional change in friction force, N, is therefore found by substituting equations (2.48) and (2.49) in 2.47), viz:

$$\int = \frac{N_1\mu_1}{N\mu} = \frac{1}{\pi}\left[\int_0^{\pi/2} \frac{\beta' + \sin\alpha\cos\phi}{\sqrt{(\beta' + \sin\alpha\cos\phi)^2 + \cos^2\alpha\cos^2\phi}} \, d\phi\right.$$

$$\left. + \int_0^{\pi/2} \frac{\beta' - \sin\alpha\cos\phi}{\sqrt{(\beta' - \sin\alpha\cos\phi)^2 + \cos^2\alpha\cos^2\phi}} \, d\phi\right] \text{--(2.50)}$$

where $$\beta' = \frac{V_o}{\dot{\xi}_{mt}}$$

Equation (2.50) was solved using Simpson's formula[45] and the solution presented by plotting the relationship between $\int$ and β, see Fig. 2.36 curve 1. Curves 2 and 3 represent the friction reduction effect produced by torsional and longitudinal vibrations respectively and it is clearly seen that the latter is the most efficient means of influencing the friction forces. Severdenko and Reznikov attempted to demonstrate the relative

efficiencies of transverse and longitudinal modes experimentally by applying ultrasonic vibrations to the drawing die during tube sinking. Two arrangements were used, Fig. 2.37a and 2.37b; the first exciting the die longitudinally and the second causing the die to move bodily in a transverse direction relative to the drawing axis. Comparison of the draw force under oscillatory and non-oscillatory conditions for each mode showed load reductions of 30-35% for the longitudinal system compared with only 12-19% with transverse oscillations. Although these results appear to confirm the theoretical predictions they are considered to be misleading on two counts, viz.

(1) The transverse vibration system described would not result in vector rotation because both the die and tube are excited in phase, being vibrated bodily. The sliding velocity vector does not therefore change direction and the friction force must remain the same as under non-oscillatory conditions.

(2) It was considered that transverse oscillation would lead to bending waves in the drawn tube causing stress superposition related to the oscillatory bending moment established in the deformation zone.

This possibility was examined in greater depth by the present author, using arguments similar to those proposed by Lehfeldt.[30] The mean axial stress amplitude due to the oscillatory bending moment induced in the tube, within the deformation zone, is found using the relationship:

$$\sigma_1 = \frac{M}{I} \cdot r \qquad \text{---------- (2.51)}$$

where σ_1 is the fibre stress at distance r from the neutral axis, M the bending moment and I the moment of inertia of a hollow cylinder about a diameter. The mean axial stress

amplitude is found by integrating over half the section and dividing by the cross sectional area, viz.

$$\bar{\sigma}_m = \frac{M}{I} \int_{r_1}^{r_2} \frac{16y\sqrt{(\frac{d_2}{2})^2 - r^2}}{\pi(d_2^2 - d_1^2)} \cdot dr$$

$$= \frac{M}{I} \cdot \frac{4}{3\pi} \left[(\frac{d_2}{2})^2 - (\frac{d_1}{2})^2 \right]^{1/2} \quad \text{---------- (2.52)}$$

where d_1 and d_2 are the inner and outer diameters of the tube. M is found approximately from static bending theory assuming that the waveform in the tube can be represented by a centrally loaded beam freely supported at its ends,[32] viz:

$$M = \frac{12.E.I.y}{\ell^2} \quad \text{---------- (2.53)}$$

where E is Young's modulus and y the deflection at the centre of the beam of length ℓ between supports.

In the present case y is replaced by ξ_{mt}, the displacement amplitude of the die (acting transverse to the drawing axis) and ℓ by the half wavelength of bending waves in the tube. This is found from the solution to the wave equation, defining the transverse motion of the tube, which satisfies the specified end conditions,[46] viz.

$$n \frac{\lambda_b}{2} = \pi \quad \text{---------- (2.54)}$$

where n is given by; $n = \left(\frac{4k}{\sqrt{d_2^2 + d_1^2}} \right)^{1/2}$.

The drawing stress reduction due to longitudinal and transverse stress superposition may now be compared from equations (2.17) and (2.52).

On substituting for M and λ_b in equation (2.52) the ratio

of the mean axial oscillatory stress amplitudes induced in the deformation zone by longitudinal and transverse excitation modes is given by:

$$\frac{\sigma_m}{\bar{\sigma}_m} = \frac{\pi k \cdot \lambda_b^2}{\sin.ka.64\left\{\left(\frac{d_2}{2}\right)^2-\left(\frac{d_1}{2}\right)^2\right\}^{1/2}} \quad \text{---------- (2.55)}$$

On inserting the experimental data of Severdenko and Reznikov into equation (2.55) the longitudinal superposition effect is found to exceed the transverse effect by a factor of 1.75 which compares quite closely with the reported factor of 2.10. It therefore appears likely that the observed draw force reduction was in fact due to force superposition and not to friction reduction, as claimed.

2.4. Deep drawing with applied Vibrations

Although several workers have examined the effects of ultrasound on the characteristics of the cup forming, draw ironing and dimpling processes, this area of research has until now received relatively scant attention. Balamuth[47] considered the dimpling process using an axially vibrated punch at a frequency of 13.5 kHz and found that titanium alloy sheet could be formed satisfactorily at room temperature whereas without ultrasound it was necessary to preheat the dies. He claimed that the forming forces were reduced, due to the high impact force associated with a peak punch acceleration of about 15,000 g. He claimed that during deformation the zone of motion, illustrated in Fig. 2.38 prevented permanent contact between the punch and blank, effectively reducing the friction forces and causing deformation by a series of high frequency impacts. Later research[27] reviewed in the preceding sections has cast serious doubt on this explanation. It is now

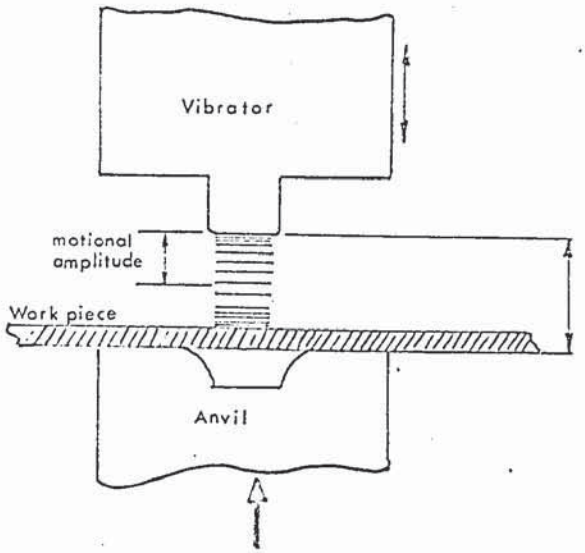

Fig. 2.38 'Zone of Motion' concept in dimpling with applied ultrasonics. (After Balamuth[47]).

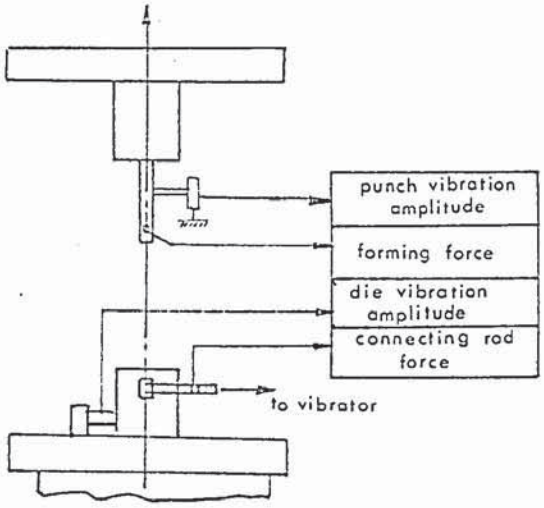

Fig. 2.39 Low frequency forming sub-press and instrumentation. (After Kristoffy[49]).

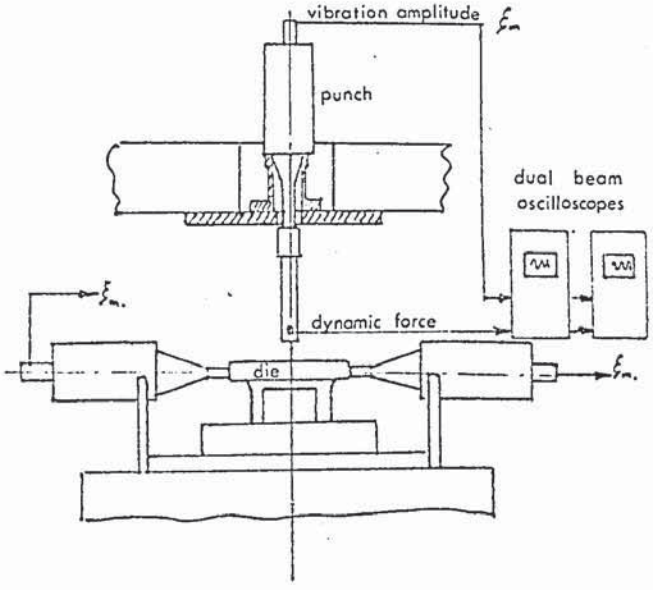

Fig. 40 High frequency forming sub-press with radial mode die. (After Kristoffy[49]).

generally agreed that separation of the surfaces does not occur under conditions of bulk plastic deformation unless the vibration amplitude is greater than the elastic strain recovery in the deforming work piece. The amplitudes employed by Balamuth (0.0008 in.,peak to peak) clearly did not meet this requirement and it is more probable that his observations can be explained in terms of force superposition.

Similar results were reported by Langenecker et al[48] who used an axially vibrated punch or die to deep draw copper cups. Macrosound at intensities of upto 450 watts/in^2 was claimed to reduce the forming load from 200-70 lbf. They attributed this effect to acoustic force superposition but added that at very high intensities enhanced effects could be produced by acoustic heating of the work piece.

More recently, Kristoffy[49] carried out a series of detailed experiments on the deep drawing and draw ironing of aluminium and steel cups. Vibrations were applied at 20 kHz and 20 Hz using two independent systems which permitted the punch to be excited axially in both cases, see Fig. 2.39 and 2.40. At the higher frequency facility was also provided to vibrate the die in a radial mode and at 20 Hz in a tangential mode. Both static and dynamic forming forces were monitored, the latter using a strain gauge attached close to the end of the punch. During high frequency tests, with axial punch vibration, this location was designed to coincide with a stress mode in the unloaded condition, see Fig. 2.41. On loading, any energy transmitted to the work piece resulted in travelling waves of both displacement and force; the strain gauge therefore produced a signal proportional to the dynamic force component applied to the work piece. The output from the gauge was monitored using two dual beam oscilloscopes connected in

Fig. 2.41 Ultrasonic stress and displacement distribution along punch assembly. (After Kristoffy [49]).

Fig. 2.42 Effect of 20kHz punch vibration on the forming force in deep drawing. (After Kristoffy [49]).

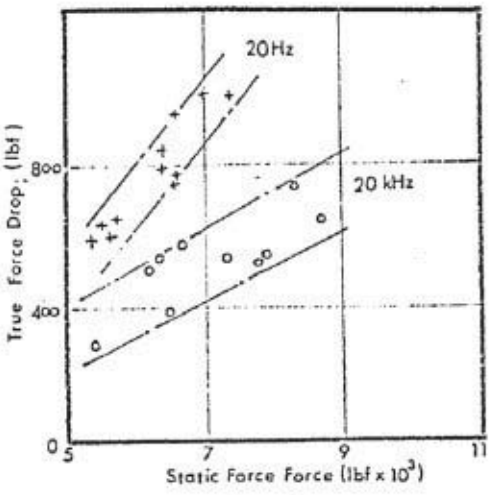

Fig. 2.43 True forming force drop in ironing with superimposed 20Hz and 20kHz die vibration.

parallel. One had a compressed time scale giving a conventional force - time function and the other, an expanded scale monitored the dynamic force and displacement amplitudes. The direct forming force was also monitored on a conventional load displacement recorder.

The results of tests at 20 Hz and 20 kHz with vibrated punch showed a significant reduction in the mean forming forces, as indicated by the load displacement recorder, compared with equivalent non-oscillatory tests. The oscilloscope traces revealed however, that the peak force applied to the blank under oscillatory conditions was equal to the non-oscillatory value at each stage of drawing. This is illustrated in Fig. 2.42. By contrast, tests with high and low frequency die activation showed a true reduction in punch load. This is illustrated for the case of ironing by the graph showing true force reduction against static forming force in Fig. 2.43. Under the conditions of these tests the low frequency vibration appeared more effective, producing a load reduction of 14% compared with 8% at 20 kHz.

Kristoffy did not attempt a detailed analysis of the process but proposed that true force reduction was due to radial force superposition in the case of high frequency tests and at low frequencies, using the tangentially vibrated die, to additional tangential shear and friction reduction. He concluded that friction reduction would not occur with radial vibration, since the die oscillation was perpendicular to the punch motion. However, his argument did not consider the effect of radial oscillations on the blank as it passed beneath the blank holder and around the die radius. It will be shown in the current research programme that friction reduction can occur in these

regions under circumstances similar in principle to those employed by Kristoffy and that such effects significantly influence the forming load.

3. The Application of Ultrasonic Energy to the deep Drawing Process.

3.1 The Mechanics of Deep Drawing - Chung and Swift Analysis.

The analysis carried out by Chung and Swift[50] considered the instantaneous distribution of drawing stress and the strain undergone by any particular element in the flange during drawing.

From a series of stress distribution plots representing various stages of drawing the progress of any particular element through the complete process can be traced, leading in its most comprehensive form to a plot of punch load vs. punch travel.

The analysis is developed by considering several distinct regions of drawing and in each case deriving expressions for the associated increment of radial stress. Five regions of drawing are considered and the instantaneous radial stress associated with each is shown in Fig. 3.1.

(I) The component of radial stress due to drawing-in of the flange.

(II) A contribution to the above stress attributed to the blank holding load, assumed to act at the periphery of the blank.

(III) Plastic bending under tension at the start of the die profile radius.

(IV) Friction and radial stress components related to the motion of the blank over the die profile radius.

(V) Unbending under tension at exit from die radius.

The cup wall forces related to each of the stress increments are considered to be simply additive and the punch load is derived directly from the cup wall stress at radius r_c.

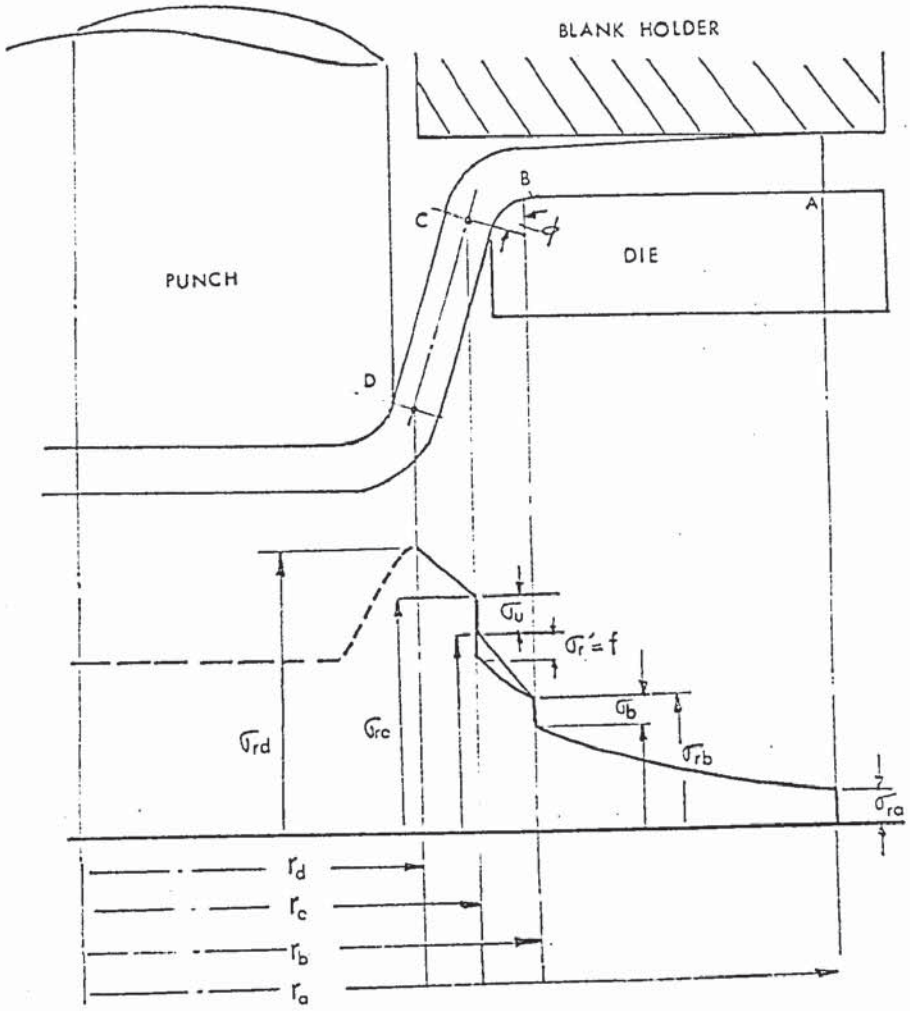

Fig. 3.1 Radial stress distribution during deep drawing.

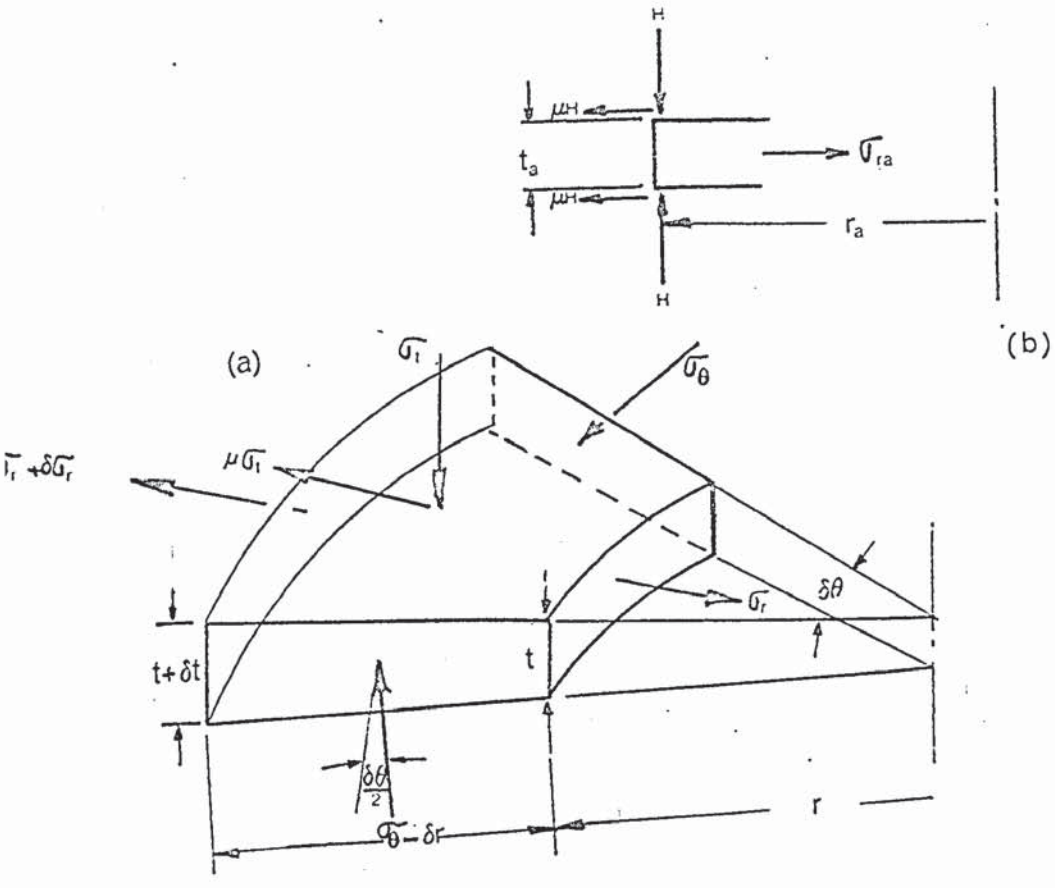

Fig. 3.2 a) Stresses acting on a circumferential element in the flange.

b) Component of radial drawing in stress due to blank holder friction.

3.1.1 Plane Radial Drawing

The instantaneous stresses acting in the flange on a radial element of width dr at radius r are shown in Fig. 3.2(a) The equilibrium equation may be determined by resolving the associated forces in a radial direction.

After some simplfication the equation is written:-

$$d\sigma_r = -\sigma_r \frac{dt}{t} - (\sigma_r + \sigma_\theta)\frac{dr}{r} + \frac{2\mu\sigma_r}{t} \quad \text{---} \quad (3.1)$$

In a plastically deforming material it is necessary to relate the stress system to the plastic properties of the workpiece by applying an appropriate yield criterion. The one which most nearly represents the behaviour of many common metals is that due to Von Mises, namely

$$\frac{1}{\sqrt{2}} \left\{(\sigma_1 - \sigma_2)^2 + (\sigma_2 - \sigma_3)^2 + (\sigma_3 - \sigma_1)^2\right\}^{1/2} = \bar{\sigma} \quad (3.2)$$

where σ_1, σ_2 and σ_3 are the three principal stresses in descending order of algebraic magnitude and $\bar{\sigma}$ is the effective stress which is physically equal to the yield strength in uniaxial tension.

If it is assumed that the blank holder force acts only at the periphery of the blank, then σ_t, equivalent to σ_2 in equation (3.2) is zero over the remainder of the flange. Equation (3.2) then reduces to the biaxial yield criterion, which on substituting σ_r andσ_θ for the maximum and minimum principal stresses may be written:-

$$\sigma_r^2 - \sigma_r \sigma_\theta + \sigma_\theta^2 = \bar{\sigma} \quad \text{----------} \quad (3.3)$$

Equation(3.3) is difficult to apply in practice but may be closely approximated by a modified Tresca yield criterion[51] Fig. 3.3 illustrates the two dimensional yield plane for the Tresca and Von Mises criteria. In the lower right hand quadrant which represents the stress system in the flange, the maximum

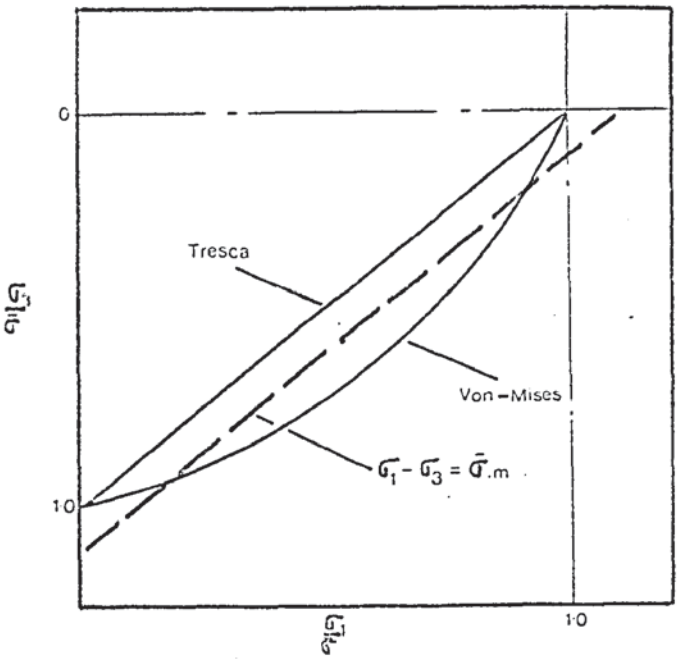

Fig. 3.3 Modified Yield Criterion

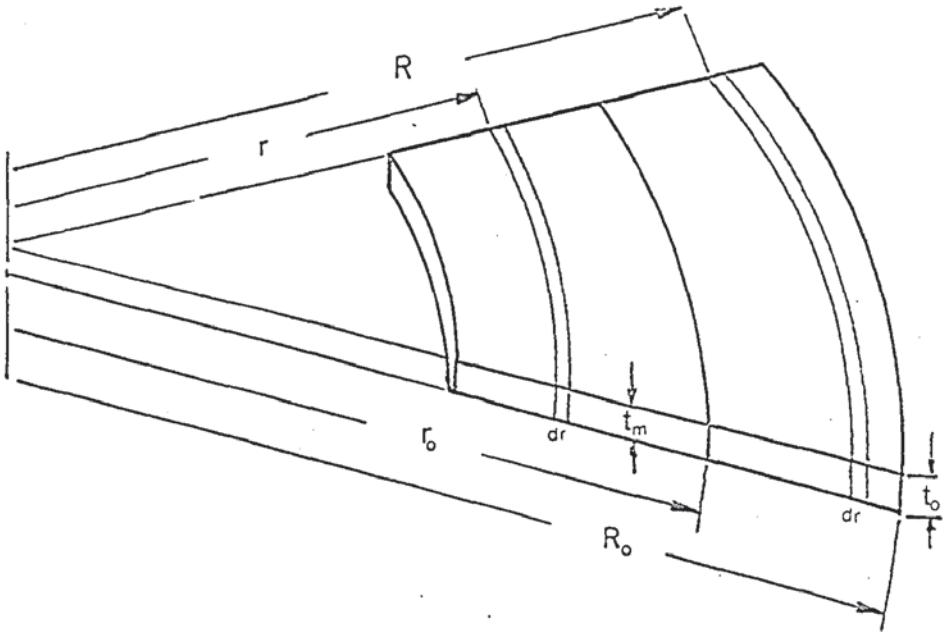

Fig. 3.4 Geometrical relationship between the initial and current radii of a circumferential element, dr, during radial drawing in.

divergence between the Tresca and Von Mises criteria is approximately 15%. This can be halved by applying a factor, m to the Tresca criterion which is then written;

$$\sigma_1 - \sigma_3 = m\bar{\sigma} \qquad \text{---------- (3.4)}$$

where m is some value between 1 and $\frac{2}{\sqrt{3}}$, say 1·08[51].

The yield criterion written in terms of the radial and circumferential stresses acting on an element in the flange then becomes;

$$\sigma_r - (-\sigma_\theta) = 1{\cdot}08\bar{\sigma} \qquad \text{---------- (3.5)}$$

At any instant, the blank thickness has been shown by Hill[52] to vary by not more than 3% across the flange; it is therefore a reasonable approximation in equation (3.1) to consider the term $\sigma_r \frac{dt}{t} \simeq 0$. Substituting equation (3.5) in (3.1) the equilibrium equation for a non-work hardening material then becomes:

$$d\sigma_r = -1{\cdot}08\ \bar{\sigma}\ \frac{dr}{r} \qquad \text{---------- (3.6)}$$

The instantaneous stress distribution is found by integrating between the limits $\sigma_r = \sigma_{r_a}$ at $r = r_a$ and σ_r at radius r; where r_a is the instantaneous rim radius, σ_{r_a} the radial stress due to the blank holder force assumed to act at the periphery and σ_r the radial stress at any radius r, between r_a and r_b. We may therefore write:

$$[\sigma_r]_{\sigma_{r_a}}^{\sigma_r} = 1{\cdot}08\bar{\sigma} \int_r^{r_a} \frac{dr}{r} \quad \text{and} \quad \sigma_r = 1{\cdot}08\bar{\sigma}\ \ln \frac{r_a}{r} + \sigma_{r_a} \qquad \text{(3.7)}$$

The radial stress acting at the rim is then found from the expression:

$$\sigma_{r_a} \cdot 2\pi . r_a . t_a = 2H\mu \quad \text{and} \quad \sigma_{r_a} = H\mu/\pi\ r_a . t_a \qquad \text{--------- (3.8)}$$

where H is the blank holder force and t_a the blank thickness at the periphery as illustrated in Fig. 3.2b.

In many practical instances it is desirable to make some

allowance in the analysis for the work hardening which occurs during deformation.

If elastic strains are ignored the effective strain can be expressed in terms of the principal strains, by an analogous expression to equation (3.2) by assuming that the effective stress is entirely dependent upon the effective strain.

We may therefore write:

$$\bar{\varepsilon} = \sqrt{\frac{2}{3}\left\{(\varepsilon_1 - \varepsilon_2)^2 + (\varepsilon_2 - \varepsilon_3)^2 + (\varepsilon_1 - \varepsilon_3)^2\right\}} \quad \text{----- (3.9)}$$

The effect of work hardening may be considered by inserting an empirical expression, describing the relationship between effective stress and strain, into the equilibrium equation (3.6). The stress strain characteristics of many common engineering alloys can be described by a power law of the form[53]:

$$\bar{\sigma} = \sigma_o + B\bar{\varepsilon}^n \quad \text{---------- (3.10)}$$

where B and n are arbitrary constants and σ_o represents the effective stress producing yielding, in the annealed condition.

The effective strain $\bar{\varepsilon}$ in any element during radial drawing, for ratios <2, has been shown by Hill[52] never to vary from the value of circumferential strain, $\ln \frac{R}{r}$ by more than 3%. In order to determine the distribution of radial stress at any stage of drawing it is necessary to consider the strain history of each element by relating its current radius to the initial radius. This is illustrated in Fig. 3.4 for a circumferential element dr, initially at radius R, and having moved to current radius r. The initial and current radii may be related to the initial and current blank periphery, R_o and r_o respectively by applying the condition of constancy of volume to the portion of the blank between R and R_o as it moves to the current position defined by r and r_o, see Fig. 3.4. We may therefore write:

$$\pi t_o(R_o^2 - R^2) = \pi . t_m(r_o^2 - r^2) \quad \text{---------- (3.11)}$$

where t_o is the initial blank thickness and t_m the current mean blank thickness.

On rearranging this gives:

$$\frac{R}{r} = \left[\frac{t_m}{t_o}\left(\frac{1}{r^2}\left(R_o^2\,\frac{t_o}{t_m} - r_o^2\right) + 1\right)\right]^{1/2} \qquad (3.12)$$

and the circumferential strain therefore becomes:

$$\varepsilon_\theta = \frac{1}{2}\ln\left(\frac{t_m}{t_o}\left(\frac{c}{r^2} + 1\right)\right) \qquad (3.13)$$

where

$$\frac{c}{r^2} = \frac{1}{r^2}\left(R_o^2\left(\frac{t_o}{t_m}\right) - r_o^2\right)$$

Substituting for $\bar{\varepsilon}$ in equation (3.10) the effective stress is given by:

$$\bar{\sigma} = \sigma_o + B\left[\frac{1}{2}\ln\left(\frac{t_m}{t_o}\left(\frac{c}{r^2} + 1\right)\right)\right]^n \qquad (3.14)$$

and the radial drawing stress distribution in the flange is found by substituting for $\bar{\sigma}$ from (3.14) in (3.6) viz:

$$\sigma_r = m\sigma_o \cdot \ln\frac{r}{r_b} + mB \cdot \int_{r_b}^{r_a}\left[\frac{1}{2}\ln\left(\frac{t_m}{t_o^2}\left(\frac{c}{r^2} + 1\right)\right)\right]^n \frac{dr}{r} + \sigma_{r_a} \qquad (3.15)$$

The second term on the right hand side must be solved by numerical integration inserting values of t_m determined from (51)

$$\frac{dt}{t} = -\left[2 + \frac{3}{\frac{H\mu}{\pi\, r_a \cdot t_a m\bar{\sigma}} + \ln\frac{r_a}{r} - 2}\right]\frac{dr}{r} \qquad (3.16)$$

3.1.2 Plastic Bending Under Tension

When an element of metal in the flange reaches the die profile radius it is bent to conform to the curvature of the die profile. The distributions of stress and strain induced in an element experiencing plastic bending under tension are shown in Fig. 3.5. In determining the stress increment $\sigma'_{r_b} - \sigma_{r_b}$, necessary to deform the element the following assumptions are made:

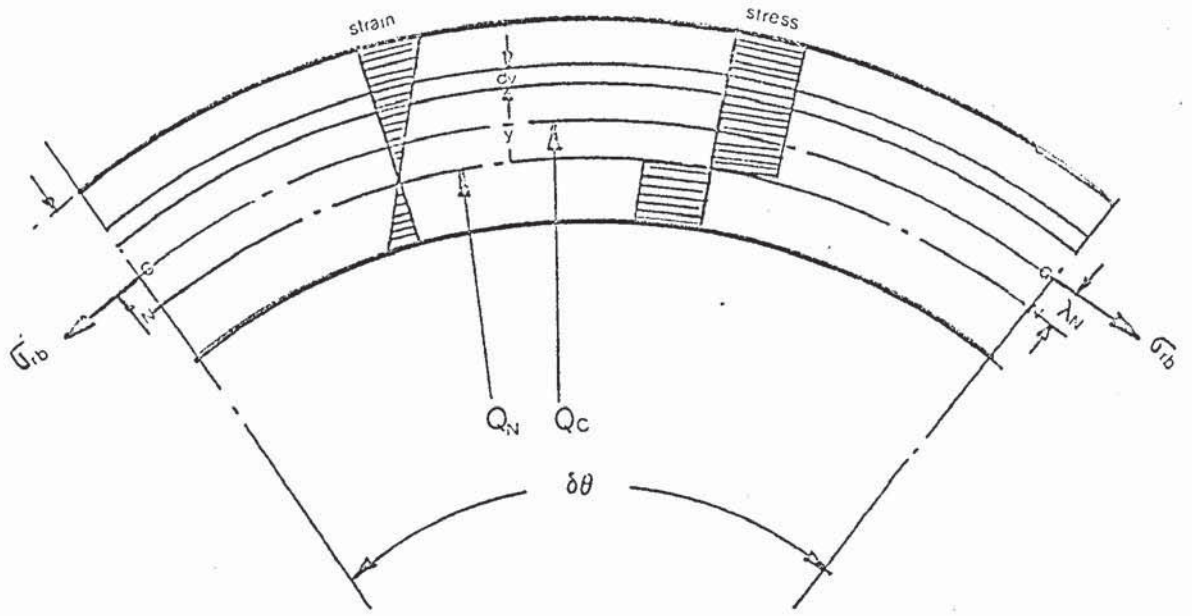

Fig. 3.5 Plastic bending under tension.

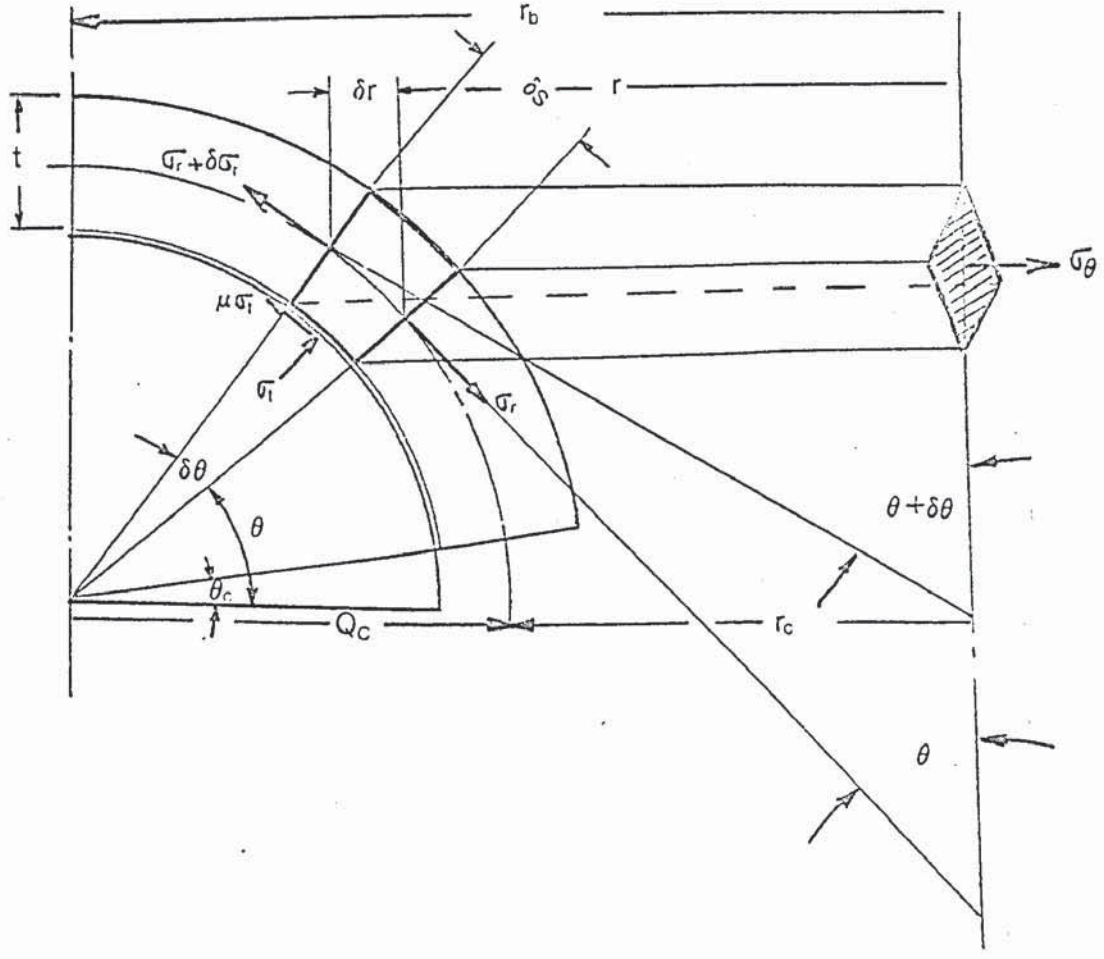

Fig. 3.6 Stresses acting on an element passing around the die profile radius.

(i) The yield stress can be represented by a mean value. This is a reasonable approximation if the material shows a linear rate of work hardening over the strain interval represented by plastic bending.

(ii) Bending is assumed to be instantaneous and the circumferential strain, $\varepsilon_\theta = 0$

(iii) From (ii) above and assuming the normal stress σ_t, to be small compared with the other principal stresses, bending occurs under plane strain conditions. Hence yielding occurs when $\sigma_r = \frac{2}{\sqrt{3}}\bar{\sigma}$.

(iv) Elastic strain may be neglected.

(v) Plane sections normal to the neutral axis remain plane after bending.

Plastic bending under tension results in a displacement of the neutral surface NN from the central surface CC by an amount λ_N, which is related to the difference between the bending tension and compression across the section. The imbalance of stress is due to the tensile back stress σ_{r_b} and the displacement of the neutral surface may be determined by equating the total force per unit width with the difference between bending tension and compression. From Fig. 3.5 we may therefore write:

$$\sigma_{r_b} \cdot t_b = \int_{\frac{t_b}{2} - \lambda_N}^{\frac{t_b}{2} + \lambda_N} \frac{2}{\sqrt{3}} \cdot \bar{\sigma}_1 \cdot dy$$

$$= \frac{2}{\sqrt{3}} \cdot \bar{\sigma}_1 \cdot 2\lambda_N$$

$$\text{and } \lambda_N = \frac{\sqrt{3}}{4} \cdot \frac{\sigma_{r_b}}{\bar{\sigma}_1} \cdot t_b \qquad \text{---------- (3.17)}$$

where $\bar{\sigma}_1$ is the mean yield strength, in uniaxial tension, determined with regard to the effective strain experienced by the element in moving to the plane of bending, $\simeq \ln \frac{R}{r_b}$ and the slope of the stress strain relationship, assumed to be linear over the strain interval associated with plastic bending.

The increase in drawing stress, σ_b due to bending may be determined by equating the work done in bending to the work done by the drawing stress. The work done in bending per unit width is given by the product of stress x elementary strain x elementary volume, which is written:

$$dw = \sigma_1 . d\varepsilon \ (Q_N + y) \ d\theta . dy \quad \text{---------- (3.18)}$$

where $d\theta$ is the angle subtended by the element at the centre of the radius of curvature.

Expanding equation (3.18) the total work per unit width becomes:

$$\frac{W}{d\theta} = \int_0^{\frac{t_b}{2} + \lambda_N} (Q_N + y) \cdot \int_0^{\ln(1+\frac{y}{Q_N})} \frac{2}{\sqrt{3}} \bar{\sigma}_1 . d\bar{\varepsilon} . dy + \int_0^{\frac{t_b}{2} - \lambda_n} (Q_N - y) \int_0^{\ln(1+\frac{y}{Q_N})} \frac{2}{\sqrt{3}} \bar{\sigma}_1 . d\bar{\varepsilon} . dy \ \text{---} \quad (3.19)$$

In equation (3.19) the elementary strain is given by $\ln(\frac{Q_N + y}{Q_N})$, from Fig. 3.5, and the effective strain is thus

$$\bar{\varepsilon} = \frac{2}{\sqrt{3}} \ln \left(\frac{Q_N + y}{Q_N}\right) \simeq \frac{2}{\sqrt{3}} \frac{y}{Q_N}$$

Substituting the above expression for the effective strain in (3.19) this may be rewritten:

$$\frac{W}{d\theta} = \frac{4}{3} \bar{\sigma}_1 \cdot \int_0^{\frac{t_b}{2} + \lambda_N} (Q_N + y) \frac{y}{Q_N} . dy + \frac{4}{3} \bar{\sigma}_1 \int_0^{\frac{t_b}{2} - \lambda_N} (Q_N - y) \frac{y}{Q_N} . dy \ \text{--------} (3.20)$$

The additional drawing stress, σ_b, to provide the bending

work per unit width is given by:

$$W = \sigma_b . t_b . Q_c . d\theta \quad \text{---------- (3.21)}$$

and from (3.20) we may write:

$$\sigma_b = \frac{4}{3} \frac{\bar{\sigma}_1}{t_b . Q_c} \left| \frac{t_b^2}{4} \left(1 + 2\frac{\lambda_N}{Q_N}\right) + \lambda_N^2 \right| \quad \text{---------- (3.22)}$$

The stress increment producing plastic unbending at radius r_c Fig. 3.1 may be found from equations (3.16) and (3.22) by substituting the appropriate values for the radial drawing stress blank thickness and mean yield strength.

3.1.3. Stress due to Friction and Radial Drawing over the Die Profile Radius

As each element passes around the die profile radius it is subject to a further radial drawing-in effect and an interfacial friction force related to the normal stress, σ_t. The stresses acting on an elementary ring of mid-plane length $Q_c d\theta$ at an angle θ to the drawing axis are defined in Fig. 3.6.

If the thickness is assumed to be constant over the die radius and an appropriate mean value of yield stress determined, the drawing stress increment associated with this region may be evaluated as follows:

Resolving the forces acting on the elementary ring in the vertical direction, we may write:

$$(\sigma_r + d\sigma_r)t.2\pi(r + dr)\cos(\theta + d\theta) - \mu\sigma_t.2\pi r \frac{dr}{\sin\theta} \cdot \cos\theta$$

$$= 2\pi(r + d_r)\, \sigma_t . \frac{dr}{\sin\theta} + \sigma_r t.\cos\theta.2\pi r \quad \text{---------- (3.23)}$$

Ignoring products of small increments this may be re-arranged to give:

$$t \frac{d}{dr}(\sigma_r . r . \cos\theta) - \sigma_t . r(1 + \mu\cot\theta) = 0 \quad \text{---------- (3.24)}$$

Similarly resolving forces horizontally by considering

one half of the elementary ring and taking the projected rather than circular area we have:

$$2\sigma_\theta \frac{dr}{\sin\theta}.t + \sigma_r.t.\sin\theta.2r = \mu\sigma_t.\frac{dr}{\sin\theta}\ \sin\theta.2r + \sigma_t\frac{dr}{\sin\theta}.\cos\theta\ .2r$$

$$+ (\sigma_r + d\sigma_r).t.(r + dr)2.\sin(\theta + d\theta)$$

which on rearranging and simplifying becomes:

$$t\frac{d}{dr}(\sigma_r.r.\sin\theta) + r\sigma_t(\cot\theta - \mu) = \frac{\sigma_\theta.t}{\sin\theta} \qquad \text{------ (3.25)}$$

Eliminating σ_t between equations (3.24) and (3.25) after some rearranging finally yields:

$$\sigma_\theta(1 + \mu\cot\theta) - \mu\sigma_r\, r.\frac{d\theta}{dr} - \frac{d}{dr}(\sigma_r.r) = 0 \qquad \text{-------- (3.26)}$$

Substituting into equation (3.26) the modified Tresca yield criterion, in which $\sigma_\theta = \sigma_r - m\bar{\sigma}$ we may write:

$$d\sigma_r = -m\bar{\sigma}\frac{dr}{r} - \mu\frac{d\theta}{r}Q_c\left[m\bar{\sigma}\cos\theta - \sigma_r(\cos\theta - \frac{r}{Q_c})\right]$$

therefore,

$$\sigma_r' = -\int_{r_c}^{r_b} m\bar{\sigma}\frac{dr}{r} - \int_{\pi_2}^{\theta_c}\frac{\mu Q_c}{r}\left[m\bar{\sigma}\cos\theta - \sigma_r(\cos\theta - \frac{r}{Q_c})\right]d\theta \qquad \text{--- (3.27)}$$

where $\sigma_r' = \sigma r_c - \sigma r_b$

The first term in equation (3.27) is the component of stress due to radial drawing and the second relates to friction over the die profile radius.

The latter may be rewritten, on substituting for r, from the relationship $r = r_b - Q_c\cos\theta$, viz.

$$df = \mu\left[\frac{(m\bar{\sigma} - \sigma_r)\cos\theta}{\frac{r_b}{Q_c} - \cos\theta} + \sigma_r\right]d\theta \qquad \text{---------- (3.28)}$$

This must be solved by numerical integration since σ_r and r are both functions of θ.

An approximate solution for the die profile friction is found for the special case when $\sigma_\theta \to 0$ and $r \to \infty$. This

situation represents the conditions which apply to the problem of belt-pulley friction. Inserting the limits in the above analysis, equation (3.26) becomes:

$$\frac{-d\sigma_r}{\sigma_r} = \mu d\theta$$

This may be integrated between the limits $\sigma_r = \sigma_{r_c}$ at $\theta = \theta_c$ and $\sigma_r = \sigma r_b$ at $\theta = \pi/2$.

Therefore $\ln \frac{\sigma_{r_c}}{\sigma_{r_b}} = -\mu(\theta_c - \pi/2)$

but $\sigma_r = \sigma_{r_b} + f$, where f is the radial stress increment due to the profile radius friction force. We may therefore write:

$$f = \sigma_{r_b} \left[e^{\mu(\pi/2 - \theta_c)} - 1 \right] \quad \text{---------- (3.29)}$$

The total drawing stress is then found from the sum of the components associated with each specific aspect of the process defined above, viz:

$$\frac{P}{A} = (\sigma_{r_a} + \sigma_{r_c} + \sigma_u + \sigma_b + f) \sin\theta$$

where P is the punch load and A the cup wall area given by $A = 2\pi r_c t_c$ in which r_c is the radius at which the metal leaves the die profile and t_c the thickness of the blank for the particular stage of drawing considered.

3.2 Oscillatory Cup Drawing - Choice of Vibrational Mode

From the basic understanding of the mechanics of cup-drawing which the Chung and Swift[50] analysis affords, it was possible to consider the likely effects of particular vibrational modes on the process forces. At the start of the investigation the results of much of the work reviewed in section 2 were known and it is against this background that

the oscillatory configuration was selected.

In spite of the inherent experimental difficulties it was decided that the greatest benefits were to be achieved by exciting either the die or blank holder in a radial mode. Five major considerations led to this conclusion.

(I) Research into ultrasonic tube drawing, with an activated plug or die, consistently indicated significant force reductions which were claimed to result in an increase in the maximum area reduction possible, for a given material. If the die or blank holder plate used in cup drawing, are vibrated in a radial mode the relative motion between the tools and workpiece becomes analagous to that achieved in tube drawing with an axially excited plug.

(II) One possible mechanism of friction reduction discussed in section 2 is that of friction vector reversal which has been predicted to occur under conditions of relative cyclic motion between the surfaces at the friction interface. A radial oscillatory mode would permit such a mechanism to operate at the testpiece/die and test piece/blank holder interfaces.

(III)Longitudinal vibration of the punch was felt likely to result in a superposition effect similar to that observed in wire drawing at both low and high frequencies. This would be of limited benefit if in addition to lowering the deformation forces, it caused a reduction in mean breaking load since this might preclude the possibility of increasing the limiting draw ratio.

(IV) Longitudinal vibration of the punch was considered unlikely to have a significant effect on the blank holder friction force which could readily be monitored during cup-drawing. The

opportunity of examining known friction reduction mechanisms would therefore have been lost.

(V) Analysis of the cup drawing process indicated that the radial drawing-in stress constitutes the major proportion of the cup wall stress. It was therefore considered desirable to adopt a vibrational mode which offered the possibility of influencing either the stress system or material properties during this phase of drawing.

Considerable difficulty was experienced in designing a radial resonator with a sufficiently uniform motional field to facilitate accurate analysis of the results of oscillatory cup drawing tests. It was therefore decided to consider the possibility of adapting the wedge drawing test in order to provide a two dimensional analogue of the cup drawing process. Some of the theoretical aspects of radial resonators are discussed in greater depth in section 4.6. and in Appendix I.

3.3 The Sachs Wedge Drawing Test

3.3.1 Basic Characteristics

In the wedge drawing test a tapered sample of strip is drawn through a similarly shaped die using a tensile testing machine. The initial shape of the test piece is a close approximation to a segment from a plane circular disc and the deformation effected during drawing is therefore closely representative of that undergone by the blank during the 'cupping' test. The maximum length or width of wedge drawable under given conditions is taken as the criterion of drawability and this may be expressed as the ratio of the initial to final width, or as the ratio of the radii defining the circular extremities of the wedge. This is illustrated in Fig. 3.7.

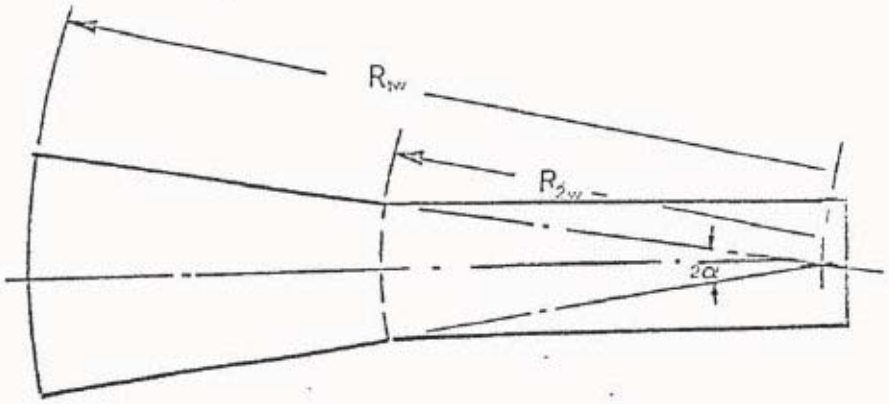

Fig. 3.7 Geometry of wedge drawing test piece.

Fig. 3.8 Forces acting during wedge drawing.

(after Loxley and Swift[58])

The test was originally described by Sachs[54] in 1930 and later by a number of independent workers including Eisenkolb[55] and Kayseler[56]. In 1942 Brewer and Rockwell[57] carried out an extensive series of wedge and cup drawing tests. For the former, they used a hydraulic press, designed, by virtue of its smooth rapid action, to overcome the inherent problem of edge friction observed in earlier tests. They claimed that good correlation could be obtained between the two tests under the appropriate conditions of lubrication and strain rate. Their results on a range of aluminium alloys gave values of L.D.R. for the wedge test varying between 1·68 - 1·92 compared with corresponding cup test results of 1·85 - 2·04. The consistently lower ratios obtained for wedge drawing seemed hardly to justify the claim. A later study by Loxley and Swift[58] confirmed the divergence between the two tests. They compared the results of wedge and cupping tests on aluminium bronze and mild steel, with two different lubricants and also unlubricated. The limiting draw ratio for the wedge tests on mild steel increased from 1·50 without lubrication to 1·81 with Aquadag compared with corresponding ratios for cup drawing of 2·08 and 2·18. Hardness tests at the centre and edge of the wedge testpieces were made at various stages during drawing and in each case a significant increase in hardness was observed towards the edge. They concluded that the usefulness of the wedge test was limited by its extreme sensitivity to changes in the frictional conditions associated with the testpiece edges.

A simple analysis of the forces acting during wedge drawing enabled them to illustrate the effects of wedge angle and edge friction on the drawing load. Fig. 3.8. If

P_o is the side reaction and Q_w the horizontal force to produce yielding in the wedge, then the drawing load, R_w, for frictionless conditions is given simply by:

$$R_{ow} = 2Q_w \tan \alpha \quad \text{---------- (3.30)}$$

where α is the semi-wedge angle.

The presence of edge friction causes the line of action of P to be rotated through an angle ϕ and the drawing load then becomes:

$$R_f = 2Q_w \tan (\alpha + \phi) \quad \text{---------- (3.31)}$$

where $\tan \phi = \mu$, the coefficient of edge friction.

The effect of wedge angle and friction coefficient can be examined by considering the ratio:

$$\frac{R_f}{R_{ow}} = \frac{\tan(\alpha + \phi)}{\tan\alpha} = 1 + \frac{\tan\phi}{\tan\alpha} \quad \text{---------- (3.32)}$$

For a semi-wedge angle of 10^o, a value of μ 0·1 causes the drawing force to exceed the frictionless value by 60 per cent. Increasing the wedge angle would reduce the effect of edge friction but would also tend to concentrate the stress in the neck of the testpiece, leading to premature failure.

The increased wedge drawing load due to edge friction must to some extent be offset by the absence of load increments related to the motion of the testpiece over the die profile radius. Frictionless wedge drawing would therefore be expected to result in a higher limiting draw ratio relative to the equivalent cupping test. Complete removal of edge friction is not considered possible even with the best available lubricants, viz. polythene or proprietory plastic coatings. The wedge test as a direct assessment of drawability is therefore always likely to yield results which differ significantly from the equivalent cupping test.

3.3.2. The Wedge Test as an oscillatory deep drawing Analogue

One might be tempted to conclude, from the previous section, that the fundamental problem of edge friction disqualifies the wedge test as a deep drawing analogue, for most practical purposes. However, on close examination it is apparent that this test might prove a most convenient means of indicating, at least qualitatively, how the process forces are influenced by the application of vibrations to the tools.

The wedge drawing test may be adapted so that it includes each phase of drawing present in the axisymmetric process, by designing the testpiece so that it represents two diametrically opposed segments from a plane circular blank. The biaxial symmetry then permits simultaneous drawing of the two ends through individual wedge dies, by applying a force in a direction normal to the radial axes of the testpiece. This arrangement described in detail, in section 5, may readily be employed to examine the effects of different vibrational modes on the drawing load. In particular, radial mode vibrations of an annular cup drawing die may be simulated by vibrating both wedge dies longitudinally. A resonant system based on axial symmetry may be readily designed and offers considerable simplification of both experimental and analytical techniques, compared with the corresponding radial system. In addition to simplifying the problem of acoustic design the simple 'biaxial' test readily permits the direct measurement of the blank holder friction force. This aspect is discussed in Section 5.

In the oscillatory wedge drawing test two basic situations might be envisaged:

(i) Axial oscillation of the dies and/or blank holder plate might result in partial or complete removal of edge friction and in addition influence the remaining punch load components common to both cup and wedge drawing tests. If this were the case the L.D.R. would be expected to be equal or greater than the corresponding value for cup drawing and the wedge test might therefore become a much closer approximation to the cupping test.

(ii) A reduction in forming load may be produced without affecting the friction conditions at the edges of the test piece. Under these circumstances although the results could not be compared directly with corresponding cup drawing data, any reduction in punch load must be associated with a phase of drawing which has a direct counterpart in the cupping test. The results would therefore be expected to indicate qualitatively the effects produced in cup drawing with radially resonant tooling.

4. Acoustic Theory

4.1 General characteristics of ultrasonic systems.

4.1.1 Introduction.

Ultrasonic systems involve the generation and transmission of elastic waves in a mechanical structure. In order to transmit energy efficiently from the power source to the work piece or load it is important to appreciate certain basic properties of elastic media which influence the vibrational mode and transmission characteristics.

The wave motion in an extended elastic medium may be either dilatational or distortional. In the former, the particle motion is parallel to the direction of propagation and in the latter it is perpendicular to it. These types of wave motion facilitate various vibrational modes, namely, longitudinal, torsional and flexural or transverse. It is also possible, under certain circumstances to excite radial vibrations which represent a special case of longitudinal wave motion[59] in a system having radial symmetry.

The frequency of elastic oscillations may vary infinitely but in the present context it is useful to define the ultrasonic range as lying between 8 kHz and 100 kHz. It is possible, however, to operate well into the mHz range but until now the technological process has found greatest scope below 100 kHz.

An important parameter, which is determined by the operating frequency for a given material, is the wavelength of the elastic disturbance. This property becomes of critical importance when the dimensional scale of the technological process encompasses several wavelengths at the operating frequency. Tuning effects must then be considered in order to maintain resonance and ensure an adequate oscillatory amplitude. This aspect of

ultrasonic systems represents a fundamental departure from the general characteristics of low frequency oscillatory processes, and involves an appreciation of new concepts in the design of practical apparatus.

4.1.2 Elements of Ultrasonic Systems.

Ultrasonic systems consist essentially of two parts; the electrical apparatus for producing a suitable alternating power supply and the electro-mechanical and mechanical elements. The electrical generator is commonly either a valve or solid state unit depending to some extent on the operating frequency and on the type of transducer used in the main part of the ultrasonic system. Valve generators operate at high anode voltages and may be used to drive either magneto-striction or piezo ceramic transducers, provided that the appropriate impedance matching output transformer is used. Solid state generators are based on silicon control diodes which are triggered high current rectifiers operating at low voltages. This reduces the capital cost compared with valve equipment. Also, the impedances of semi-conductor devices are of the same order as those of transducers, which simplifies the problem of impedance matching[60].

The main part of the ultrasonic system consists of three basic components:

(i) a transducer which converts the electrical signal into mechanical vibrations of the same frequency.

(ii) a radiating head or working tool, coupling the ultrasonic system to the load.

(iii) an acoustic waveguide linking the transducer and working head.

It is possible to connect the transducer directly to the

working head but the characteristics of such a system would not be appropriate to most technological applications. In practice some attempt is made to control the oscillatory régime in order to increase the effectiveness of the transducer under specific operating conditions. This is done by inserting a mechanical transformer between the transducer and head. In the general case, a transforming device is employed in order to match the mechanical impedance of the transducer to that of the load, whilst satisfying the tuning criteria which ensure resonance at the design frequency. In rod systems, impedance transformation is normally achieved by varying the cross section of the wave guide, according to certain established criteria[61]. This subject will be dealt with in more detail in section 4.3. Transformers of the above type are also used to increase the deformation and motional amplitudes at the working head, thus increasing the acoustic intensity in this region.[62]

4.2. Propagation of elastic waves in homogeneous rod systems

The term rod system implies a waveguide of normally circular section whose transverse dimensions are less than the half wavelength for longitudinal waves in a given material. The simplest rod system therefore consists of a tuned cylinder whose diameter is less than $\frac{\lambda}{2}$ (the half wavelength). When considering the characteristics of such a waveguide it is necessary to examine the motion and deformation of each transverse element in time and space, in relation to the origin of the system. This approach leads to the formation of the wave equation which is a partial differential equation in the variables time (t) and distance (x). Specific solutions are

determined by applying boundary conditions defining the state of loading at the output end of the system and by considering the wave form of the acting force and the initial condition of the system. From these solutions it is possible to determine the three fundamental characteristics of the system, viz:

(i) The input impedance;

(ii) The location of nodal and antinodal planes and the distribution of oscillatory values throughout the system.

(iii) The natural frequency of the system (assuming one degree of freedom).

The forcing function is generally of a sinusoidal form and the particle motion thus obeys a harmonic law in which the particle acceleration is proportional to its displacement from the mean position, viz:

$$\frac{\partial^2 \xi}{\partial t^2} = \omega \xi \quad \text{---------- (4.1)}$$

where ω is the angular velocity related to the frequency f, by the expression: $\omega = 2\pi f$

If we assume plane wave propagation in an ideal elastic medium, i.e. one which is loss free and of uniform physical properties, then under steady state conditions, the wave equation may be derived in the following way[63].

Consider an element dx of mass m, in a rod of cross sectional area S, Fig. 4.1. Then, if the stresses acting on the element are as shown and the displacement of its centre of gravity is denoted by ξ, the resultant force acting on the element may be written:

$$F = s\sigma_x - S\left(\sigma_x + \frac{\partial \sigma_x}{\partial x}. \, dx\right) \quad \text{---------- (4.2)}$$

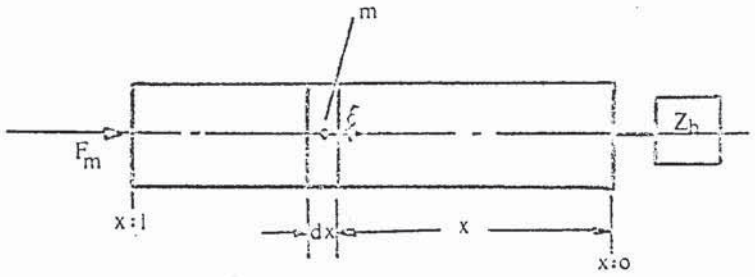

Fig. 4.1 Oscillatory motion of an element in an ideal elastic medium

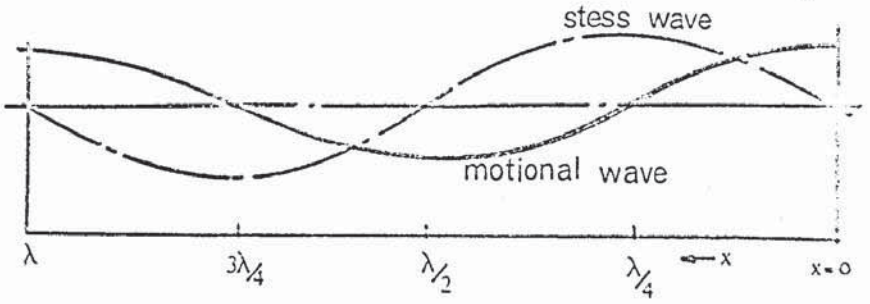

Fig. 4.2 Stress displacement distribution in the standing wave regime.

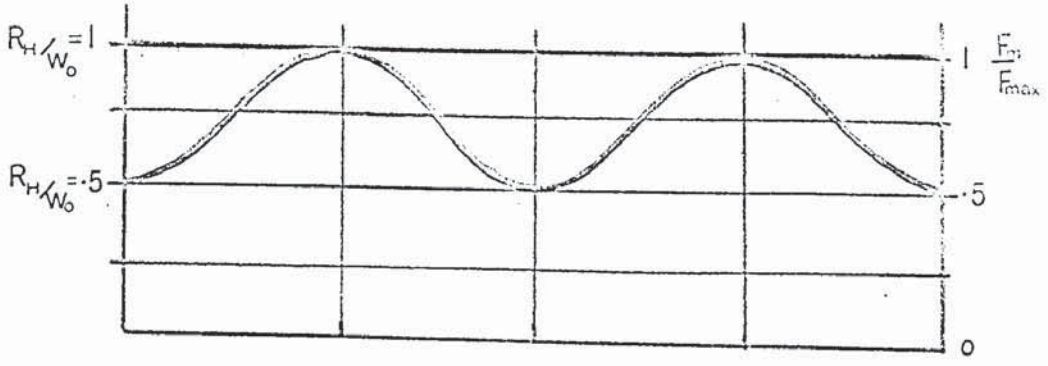

Fig. 4.3 Distribution of force amplitude in travelling wave regime for different values of the ratio, R_H/W_o.

From Newton's second law, $F = m\ddot{\xi}$

it follows that:

$$\rho . s . dx \frac{\partial^2 \xi}{\partial t^2} = -S \frac{\partial \sigma_x}{\partial x} \cdot dx \qquad \text{---------- (4.3)}$$

where ρ is the density of the rod.

Since stress and strain are related by the expression

$$\sigma = \varepsilon E = \frac{\partial \xi}{\partial x} . E$$

where E is Young's modulus, equation 4.3 may be written:

$$\frac{\partial^2 \xi}{\partial t^2} = \frac{E}{\rho} \frac{\partial^2 \xi}{\partial x^2} \qquad \text{---------- (4.4)}$$

and substituting $c^2 = \frac{E}{\rho}$ in 4.4 above we obtain:

$$\frac{\partial^2 \xi}{\partial t^2} = c^2 \frac{\partial^2 \xi}{\partial x^2} \qquad \text{---------- (4.5)}$$

where c is the wave velocity in the material under consideration.

The general solution of this equation (defining the instantaneous particle displacement ξ at any plane x, in the system) is of the form:

$$\xi = A_1 \phi_1 (t - \frac{x}{c}) + A_2 \phi_2 (t + \frac{x}{c}) \qquad \text{---------- (4.6)}$$

where A_1 and A_2 are arbitrary constants of integration and ϕ_1 and ϕ_2 are functions determined by the form of the oscillatory driving force.

If we adopt the original assumption that the forcing function has a harmonic form, then introducing complex notation we may write:

$$\xi = \xi_m e^{i\omega t} \quad \text{where } i = \sqrt{-1}$$

and $\frac{\partial^2 \xi}{\partial t^2} = -\omega^2 \xi_m e^{i\omega t}$

or $\frac{\partial^2 \xi}{\partial t^2} = -\omega^2 \xi \qquad \text{---------- (4.7)}$

substituting equation (4.7) into equation (4.5) gives:

$$\frac{d^2\xi}{dx^2} = \frac{-\omega^2}{c^2}\xi \qquad \text{---------- (4.8)}$$

It is convenient to consider only the variation of amplitudinal oscillatory values throughout the system and to note that the displacement and force at each plane vary with time according to a harmonic law. This does not limit the scope of the analysis in any way. Therefore replacing ξ by the complex amplitude ξ_m in equation 4.8 we obtain;

$$\frac{d^2\xi_m}{dx^2} = \frac{-\omega^2}{c^2}\xi_m \qquad = -k^2\xi_m \qquad \text{---------- (4.9)}$$

where k is the wave number or propagation constant given by $\frac{\omega}{c} = \frac{2\pi}{\lambda}$.

The general solution to the wave equation is of the form:

$$\xi_m = A\cos kx + B.\sin kx$$

where A and B are arbitrary constants.

Teumin, in a rigorous treatment of this subject[64], has shown that an identical expression to equation (4.9) can be derived by considering the rod system as a collection of elementary systems with lumped constants, each element possessing a characteristic mass, elasticity and damping factor. This analysis leads to the following wave equations defining the amplitudinal force and oscillatory velocity characteristics in a rod system with losses.

Using amplitudinal values of force and velocity the equations are written:

$$\left.\begin{aligned} \frac{d^2F_m}{dx^2} &= \gamma^2 F_m \\ \frac{d^2\dot{\xi}_m}{dx^2} &= \gamma^2 \dot{\xi}_m \end{aligned}\right\} \qquad \text{---------- (4.10)}$$

In this case the propagation constant γ is complex and

may be represented by the equation;

$$\gamma = \beta + i\alpha$$

where β is the damping constant and α the phase shift constant.

These constants are expressed in terms of the elementary parameters of mass, m_1, elasticity c_1, and internal resistance R_1, by the following expressions;

$$\beta = \frac{R_1}{2}\sqrt{\frac{C_1}{m_1}}$$

$$\alpha = \sqrt{\frac{1}{2}\omega^2 m_1 C_1 + \frac{1}{2}\left((R_1^2+\omega^2 m_1^2)\omega^2 C_1^2\right)^{\frac{1}{2}}}$$

It can be seen that when the resistance is small, i.e. $\omega m_1 >> R_1$ then $\beta \to 0$ and $\alpha \to \omega\sqrt{m_1 C_1} = \frac{\omega}{c} = k$, the wave number in a loss free system.

Since $m_1 = S\rho$ and $C_1 = \frac{1}{ES}$ $\therefore \sqrt{m_1 C_1} = \frac{1}{c}$

where S is the cross sectional area, ρ the density and E Young's Modulus.

In most practical systems this approximation is justified, since the only significant absorption of energy is associated with the load attached to the end of the waveguide. This may be considered as a lumped mechanical impedance possessing both reactive and resistive characteristics[64] viz.

if the impedance is denoted by Z_H, then

$$Z_H = R_H + i\,X_H \qquad \text{---------- (4.11)}$$

where R_H is the resistive part of the load impedance resulting in energy absorption and X_H is the reactive load which contributes to the stored energy in the system and determines the phase shift between the force and motional waves.

Mechanical impedance is defined as the inverse ratio of the particle velocity to the oscillatory force producing the motion. Therefore at a given section along the rod system

the mechanical impedance is given by:

$$Z_1 = \frac{F_{m_1}}{\dot{\xi}_{m_1}}$$, using complex amplitudinal values of force and velocity.

It will be shown that the use of this concept permits the rational design of both loaded and unloaded systems, based on the determination of the complex input impedance. Using this parameter the natural frequency of the system is readily found from the condition that the reactive part of the input impedance is zero at resonance, i.e.

$$X_{IN} = 0 \qquad \text{---------- (4.12)}$$

when f = fo, the resonant frequency.

Returning to equation (4.9) and considering the analogous expression for particle velocity $\dot{\xi}_m$, we may write the general solution as follows:

$$\dot{\xi}_m = A_1 \cos kx + B_1 \sin kx \qquad \text{---------- (4.13)}$$

and since $F_m = S\sigma_m = SE.\frac{d\xi_m}{dx} = -i.S.\frac{E}{\omega}\frac{d\dot{\xi}_m}{dx} = -i.\frac{w_o}{k}.\frac{d\dot{\xi}_m}{dx}$

where w_o is the wave impedance of the rod at any section, we may write the equivalent expression defining the oscillatory force distribution as follows:

$$F_m = iw_o.(A_1 \sin kx - B_1 \cos kx) \qquad \text{---------- (4.14)}$$

Constants A_1 and B_1 may be determined for the general loaded condition by examining the boundary conditions at each end of the rod system.

For convenience we shall consider the oscillatory force to be applied at the end, x = ℓ and a load Z_H to be attached at x = 0. See Fig. 4.1.

Then if $F_m = F_{m1}$ and $\dot{\xi}_m = \dot{\xi}_{m1}$ at x = 0,
From equation (4.13) we may write: $\dot{\xi}_{m1} = A_1$

and from equation (4.14):

$$F_{m1} = iw_o B_1 \text{ or } B_1 = i\frac{F_{m1}}{w_o}$$

Substituting for A_1 and B_1 in equation (4.13) and (4.14) we have:

$$\left.\begin{aligned} \dot{\xi}_m &= \dot{\xi}_{m1}\cos kx - i\frac{F_{m1}}{w_o}.\sin kx \\ \text{and } F_m &= F_{m1}\cos kx + iw_o\dot{\xi}_{m1}.\sin kx \end{aligned}\right\} \quad \text{---------- (4.15)}$$

but since $\frac{F_{m1}}{\dot{\xi}_{m1}} = Z_H$, equations (4.15) became:

$$\left.\begin{aligned} \dot{\xi}_m &= \dot{\xi}_{m1}\left[\cos kx + i\frac{Z_H}{w_o}.\sin kx\right] \\ F_m &= F_{m1}\left[\cos kx + i\frac{w_o}{Z_H}.\sin kx\right] \end{aligned}\right\} \quad \text{---------- (4.16)}$$

The input impedance of the system is given by:

$Z_{IN} = \frac{F_{mo}}{\dot{\xi}_{mo}}$, therefore applying the boundary condition $F_m = F_{mo}$ and $\dot{\xi}_m = \dot{\xi}_{mo}$ at $x = \ell$, to equations (4.16), we may write:

$$Z_{IN} = \frac{F_{m1}\left[\cos kl + i\frac{w_o}{Z_H}\sin kl\right]}{\dot{\xi}_{m1}\left[\cos kl + i\frac{Z_H}{w_o}\sin kl\right]} \quad \text{---------- (4.17)}$$

When the load is purely resistive, i.e. $Z_H = R_H$ the real and imaginery parts of equation (4.17) are readily separated giving:

$$Z_{IN} = R_{IN} + iX_{IN} = \frac{R_H}{\cos^2 kl + \left(\frac{R_H}{w_o}\right)^2 \sin^2 kl} - i\frac{w_o\frac{1}{2}\left(1-\left(\frac{w_o}{R_H}\right)^2\right)\sin 2kl}{\left(\frac{w_o}{R_H}\right)^2\cos^2 kl + \sin^2 kl} \quad (4.18$$

To determine the length of system compatible with resonance, we set $X_{IN} = 0$. It therefore follows from equation (4.18) that:

$$\frac{1}{2}w_o\left(1-\left(\frac{w_o}{R_H}\right)^2\right)\sin 2kl = 0$$

This condition is satisfied when $w_o = R_H$ and when $\ell = o$ or $\frac{n\lambda}{4}$.

The former case represents the travelling wave régime in which there is no reflected wave at the end of the system, all the energy being absorbed in the load. Under these circumstances, the length of waveguide is not critical and the input impedance is the same as that for a system of infinite length. For any other value of the ratio $\frac{w_o}{R_H}$ resonance occurs when ℓ is equal to an integral number of quarter wave lengths.

If we consider the unloaded condition, then from equation (4.17) we may write:

$$Z_{IN} = i w_o . \frac{\sin kl}{\cos kl} = i w_o . \tan kl \qquad \text{----------(4.19)}$$

At resonance, $X_{IN} = w_o . \tan kl = 0$

which is satisfied by $\ell = o$ or $n\lambda/2$

Therefore a standing wave régime will be maintained in a system with a free end if its length is an integral number of half wavelengths at the operating frequency.

It is important to appreciate the physical significance of the system described by equations (4.15) and (4.16). Generally, in a waveguide of finite length, two sets of waves travel simultaneously through the material, viz. the incident and reflected waves. Reflections occur at any plane in the guide which is characterised by a change in acoustic impedance. A clear example of this is at the free end of a wave system with an interface bounded by air. The metal/air boundary represents a pronounced change in impedance which results in virtually complete reflection of the incident wave and leads to the establishment of a standing wave, under the appropriate conditions of tuning. A standing wave is characterised by the formation of planes in which the oscillatory quantitites have maximum or minimum values. These locations are referred to as

antinodes and nodes respectively, and they occur at set intervals of 180 degrees or $\lambda/2$. Only the instantaneous values of the oscillatory quantities vary with time and thus at the points where the antinodes occur the instantaneous values during the oscillation period pass through the full cycle from zero to the maximum amplitude. At any other plane the instantaneous values vary with the same frequency from zero to the maximum value defined by the position of the plane being considered somewhere along the system. A standing wave results from the addition of the incident and reflected waves. When both waves are in phase, the maximum oscillatory amplitudes of the force and velocity waves become twice that at the source and the distribution of oscillatory quantities is such that the phases vary stepwise through zero and remain unchanged in the interval between adjacent nodes. The distribution of both force and velocity waves for such a condition is illustrated in Fig. 4.2. These wave forms are readily derived, for a free system, by inserting the condition $F_{ml} = 0$ into equation (4.15).

When a resistive load is attached to the end of a tuned system only partial reflection occurs at the interface, and a proportion of the energy passes into the load. The general case therefore represents a transitional state in which both standing and travelling waves exist. This situation is illustrated in Fig. 4.3. in which the moduli of force and velocity waves are plotted against fractional wavelength for some arbitrary value of the ratio R_H/w_o. A special case exists when the wave impedance of the guide is matched to the load, i.e. when $w_o = R_H$. This results in complete transmission of the incident wave into the load so that there is no reflected wave. If this condition is applied to equation (4.16), the expressions for oscillatory force and velocity amplitude become:

$$\left.\begin{aligned} \dot{\xi}_m &= \dot{\xi}_{ml}\,[\cos kx + i \sin kx] \\ \text{and} \quad F_m &= F_{ml}\,[\cos kx + i \sin kx] \end{aligned}\right\} \text{---------- (4.20)}$$

which may be rewritten: $\dot{\xi}_m = \dot{\xi}_{ml} e^{\,i\,kx}$

$$F_m = F_{ml} e^{\,i\,kx}$$

or changing to instantaneous values;

$$\dot{\xi} = \dot{\xi}_m e^{\,i\omega t} = \dot{\xi}_{ml} e^{\,i(kx + \omega t)}$$

$$F = F_m e^{\,i\omega t} = F_{ml} e^{i(kx + \omega t)}$$

which represents a system in which only the incident wave is present.

In trigonometrical form we may therefore write:

$$\left.\begin{aligned} \xi &= \xi_{ml} \cos(\omega t + kx) = \dot{\xi}_{ml} \cos\omega\left(t + \frac{x}{c}\right) \\ F &= F_{ml} \cos(\omega t + kx) = F_{ml} \cos\omega\left(t + \frac{x}{c}\right) \end{aligned}\right\} \text{--- (4.21)}$$

In this situation there is clearly no phase shift between the force and velocity waves and each particle in the system experiences the same oscillatory cycle, although there is a time difference in relation to the position of each particle, represented by the factor $\frac{x}{c}$.

The foregoing discussion provides the basis for a rational approach to the acoustic problems involved in this research programme and these principles are employed in subsequent sections dealing with specific design aspects of the oscillatory apparatus.

4.3 Acoustic impedance and velocity transformers

In practical ultrasonic systems the need generally arises for a specific oscillatory régime lying somewhere between the standing wave and travelling wave states. The extent to which either of these predominates in a particular system can be controlled to some degree by the inclusion of transforming devices at some appropriate position in the wave system. For example, the criterion for a predominantly travelling wave state, is that the wave impedances at the junctions between adjacent links comprising the wave system, should be closely matched and that the impedance of the final link should be matched to the load which is applied at the end of the system. This condition is ensured by the inclusion of suitably designed transforming links, so that the impedance at the output end of the matching link is transformed at its input to that of the preceding link. Such a transforming device normally takes the form of a rod of varying cross section.[64] The variation may be either continuous or stepped. In the former case tapered profiles are adopted, the most commonly used obeying either a linear, exponential or catenoidal law.

In addition to their impedance transforming properties, tapered sections of the above type are characterised by a continuous variation along their length of the oscillatory quantities, viz. strain particle velocity, force, etc. The effect of this property is to intensify the oscillatory energy in passing from the large to the narrow end of the tapered section. In many applications, requiring a standing wave state, this characteristic is employed in order to increase the motional amplitude to some value appropriate to the particular technologica process. In such cases the transforming device is referred to

specifically as a velocity transformer.

4.3.1 Analysis of the wave motion in a rod of varying cross-section.

The distribution of elastic waves along a rod system with continuously varying cross section, is described by a linear differential equation having variable coefficients. The general form of this, which is applicable to any law defining the taper of the rod, may be determined analytically, either by considering the oscillatory stresses acting on an element within the system[65] or from the assumption that the rod may be regarded as a system composed of an infinite number of elements having lumped mechanical constants[64]. The latter method is particularly useful when considering systems having high damping characteristics. However, since it is sufficiently accurate to ignore internal damping in many practical cases, identical expressions may be derived using stress analysis.

Provided that the length of rod is considerably greater than the cross sectional dimension it may be assumed that the wave front remains plane, and that there is no significant variation in stress across the section. Considering only steady state sinusoidal vibrations, in which amplitudinal values of the oscillatory quantities are used, the distribution of particle velocity may be derived as follows:[65]

If the stresses acting on an elementary section dx at a distance x from the narrow end of a tapered rod system are as shown in Fig. 4.4. then under the action of an oscillatory force, Fm, the equation of motion of the element may be written:

$$\sigma x_m S - (\sigma x_m + \frac{\delta s}{\delta x} dx) \cdot (S + \frac{\delta s}{\delta x} \cdot dx) = Fm \quad \text{------} \quad (4.22)$$

where S is the cross sectional area and σ_{x_m} the oscillatory stress amplitude at any distance x from the narrow end. Expand-

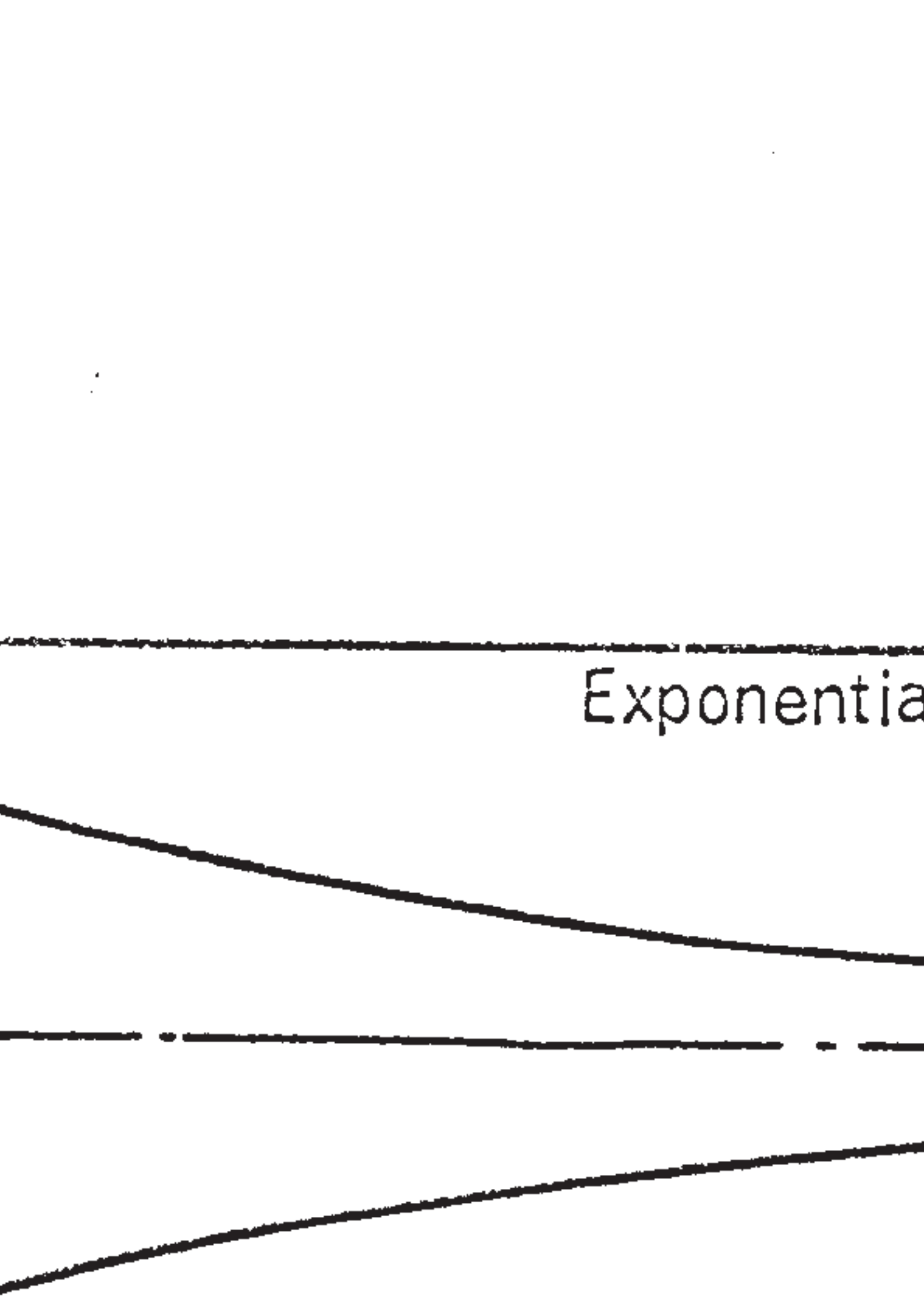
Exponentia

ing equation (4.22) and expressing Fm in terms of the acceleration and mass of the element the equation may be re-written:

$$\sigma_{x_m}.S - (\sigma_{x_m}.S + \sigma_{x_m}\frac{\partial S}{\partial x}.dx + S\frac{\partial \sigma_x}{\partial x}.d_x + \frac{\partial S}{\partial x}.\frac{\partial \sigma_{x_m}}{\partial x}.dx^2)$$

$$= S.dx\rho.\frac{\partial^2 \xi}{\partial t^2}$$

where ρ is the density of the rod material and ξ the mean instantaneous displacement of the element.

Ignoring products of small increments we obtain the following expression:

$$\sigma_{x_m}.\frac{\partial S_x}{\partial x}\,dx + S\frac{\partial \sigma_{x_m}}{\partial x}.dx = Sdx.\rho.\frac{\partial^2 \xi}{\partial t^2} \quad \text{---------- (4.23)}$$

If, as stated above we assume simple harmonic motion then $\frac{\partial^2 \xi m}{\partial t^2} = -\omega^2 \xi_m$ where ω is the angular velocity in radius per sec. and equation (4.23) becomes:

$$\frac{1}{S}.\frac{\partial S}{\partial x}.\sigma_{x_m} + \frac{\partial \sigma_{x_m}}{\partial x} = -\rho \xi_m.\omega^2 \quad \text{---------- (4.24)}$$

but since the stress σ_{x_m} is given by: $\sigma_{x_m} = E.\frac{\partial \xi}{\partial x}$ ----- (4.25a)

then $$\frac{\partial \sigma_{x_m}}{\partial x} = E\frac{\partial^2 \xi}{\partial x^2} \quad \text{---------- (4.25b)}$$

where E is the elastic modulus; substituting equations (4.25a) and (4.25b) into (4.24) we obtain the general equation of motion

$$\frac{d^2 \xi_m}{dx^2} + \frac{1}{S}.\frac{dS}{dx}.\frac{d\xi_m}{dx} + k^2 \xi_m = 0 \quad \text{---------- (4.26)}$$

where $K = \frac{\omega}{c}$ and c the wave velocity, is given by:

$$c = \sqrt{\frac{E}{\rho}}$$

Since the particle velocity $\dot{\xi}_m$ is given by $\dot{\xi}_m = \frac{\partial \xi_m}{\partial t}$ then the expression defining the velocity distribution is analogous to equation (4.26) and is written:

$$\frac{d^2\dot{\xi}_m}{dx^2} + \frac{1}{S} \cdot \frac{dS}{dx} \cdot \frac{d\dot{\xi}_m}{dx} + k^2\dot{\xi}_m = 0 \qquad \text{---------- (4.27)}$$

The wave equation defining the velocity distribution in a particular transforming device is derived by substituting the appropriate taper law into equation (4.27). For example, in the case of a tapered section obeying an exponential law in which the variation in cross sectional area is defined by:

$$S = S_o e^{-bx} \qquad \text{---------- (4.28)}$$

the substitution is readily shown to be:

$$\frac{1}{S} \cdot \frac{ds}{dx} = \frac{-bS_o e^{-bx}}{S_o e^{-bx}} = -b$$

where b is a constant and S_o the cross sectional area at the wide end.

The wave equation then becomes:

$$\frac{d^2\dot{\xi}_m}{dx^2} - b.\frac{d\dot{\xi}_m}{dx} + k^2\dot{\xi}_m = 0 \qquad \text{---------- (4.29)}$$

For which the general solution is:

$$\dot{\xi}_m = e^{-\frac{bx}{2}} \cdot (A_2 \cos k'x + B_2 \sin k'x) \qquad \text{------ (4.30)}$$

where A and B are arbitrary constants of integration and k' is the wave number modified to take account of the wave dispersion in the horn, given by $k' = \sqrt{k^2-(\frac{b}{2})^2}$. Equation (4.30) is solved by applying boundary conditions which define the acoustic load at each end of the system. The strain and motional amplitude distribution in an unloaded exponential horn have been reported in detail by Merkulov,[65] Neppiras[66] and Teumin[64] and are summarised graphically by the curves in Fig. 4.5 which show the distribution of particle velocity and oscillatory stress along an unloaded exponential velocity transformer. Similar relationships have been deduced for conical, stepped and catenoidal transformers and these are

illustrated by the curves in Fig. 4.6.

It will be apparent from Fig. 4.6 that the transforming characteristics of each type of tapered horn are different, and it is usual to relate them by comparison of the proportional increase in motional amplitude in passing from the wide to the narrow end. The 'gain', which expresses this characteristic is related in each case to the ratio of the end face diameters. This feature is illustrated for each of the transformers mentioned, by plotting the gain, $\dot{\xi}_{m1}/\dot{\xi}_{m_o}$, against the diameter ratio, N as shown in Fig. 4.7.[65] It will be seen that the exponential and catenoidal types are much more effective velocity transformers than the conical horn, which has a theoretical limit to the gain, in the fundamental mode, of approximately 4.6:1.

Velocity transformation is also achieved by the use of integral parallel rod sections incorporating a stepped diameter change, normally coincident with the mid-point of the system. The characteristics of such devices are readily derived by the application of appropriate boundary conditions to the equations developed in section 4.2 describing parallel rod systems. The characteristic curves for this type of transformer are also shown for comparison, in Figs. 4.6 and 4.7.

It was mentioned earlier in this section that transforming devices of the types described above are used in travelling wave systems to ensure efficient transmission of acoustic energy between successive links and between the wave guide and load. This application stems from the impedance transforming characteristics associated with tapered and stepped rod systems which will be considered fully in sections 4.4 and 4.5 where expressions for the input impedance of loaded conical, exponential and stepped horns will be derived.

4.4 Acoustic properties of exponential and stepped horns

4.4.1 Input impedance of a loaded exponential horn.

The distribution of strain and motional amplitude in a loaded exponential horn has been analysed by Teumin[67] using the concept of lumped mechanical elements to describe the system. He derived a set of equations defining the acoustic force and particle velocity distribution in a medium with internal damping and used these to determine an expression for the input impedance under various conditions of loading. It was also shown that in certain limiting conditions, the equation for the input impedance of an exponential horn differed from that of a parallel rod system only by the inclusion of a multiplying factor, e^{bl}, where l is the length of the horn and b the taper constant.

Identical equations may be derived from the general solution to the wave equation given in the previous section; equation (4.30), in which internal losses were assumed to be negligible.

If a complex load Z_H is applied to the narrow end of an exponential horn, as shown in Fig. 4.8, then the distribution of complex force and motional amplitudes along the transformer are derived in the following way:

The general solution to the wave equation describing the velocity distribution, was previously given as:

$$\dot{\xi}_m = e^{\frac{-b}{2}x} (A_2 \cos k'x + B_2 \sin k'x) \quad \text{-------} \quad (4.30)$$

where it will be recalled, x is the distance from the narrow end and A_2 and B_2 are arbitrary constants which may be determined for given operating conditions. The equivalent expression for the oscillatory force distribution may be obtained using equation (4.30) and bearing in mind that, $F_m = S\sigma_m$ and $\sigma_m = E.\varepsilon_m =$

$$E \frac{d\xi_m}{dx} = \frac{E}{i\omega} \cdot \frac{d\dot{\xi}_m}{dx} \quad \text{----------} \quad (4.31)$$

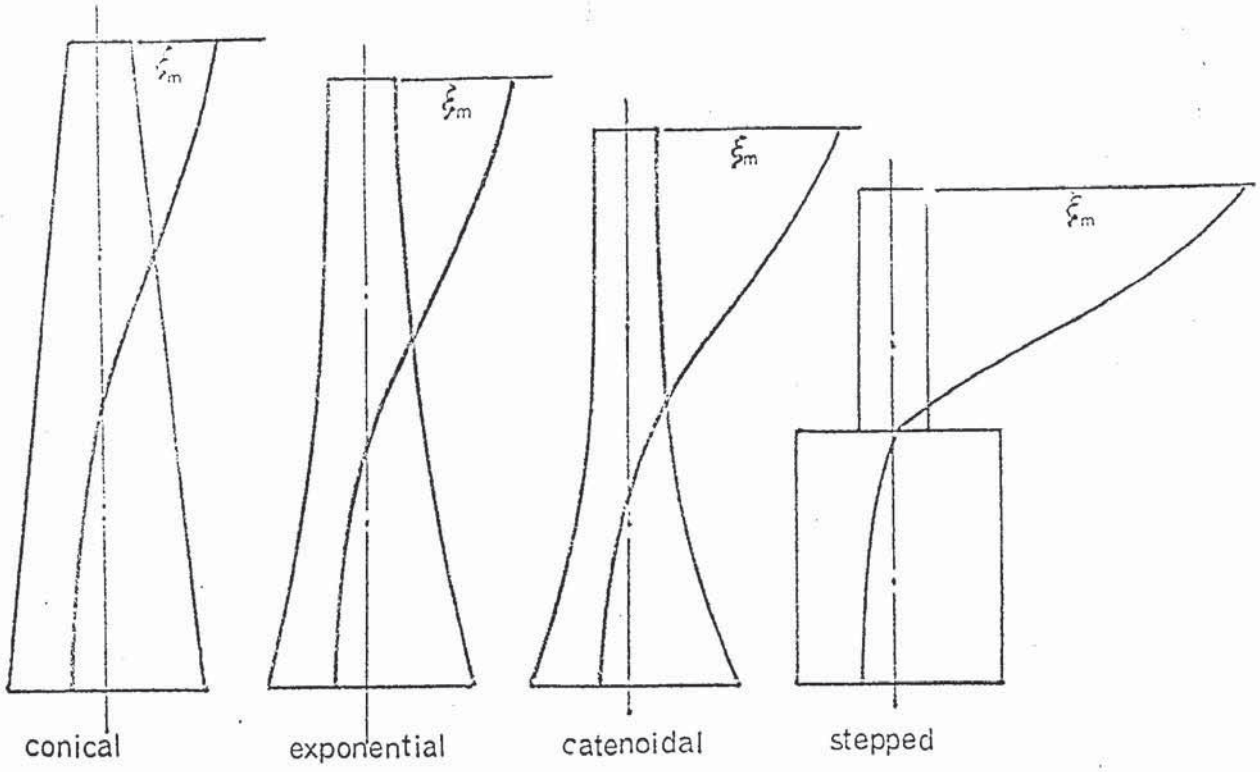

Fig. 4.6 Velocity transformation characteristics of various tapered horns. (After Heppiras[66])

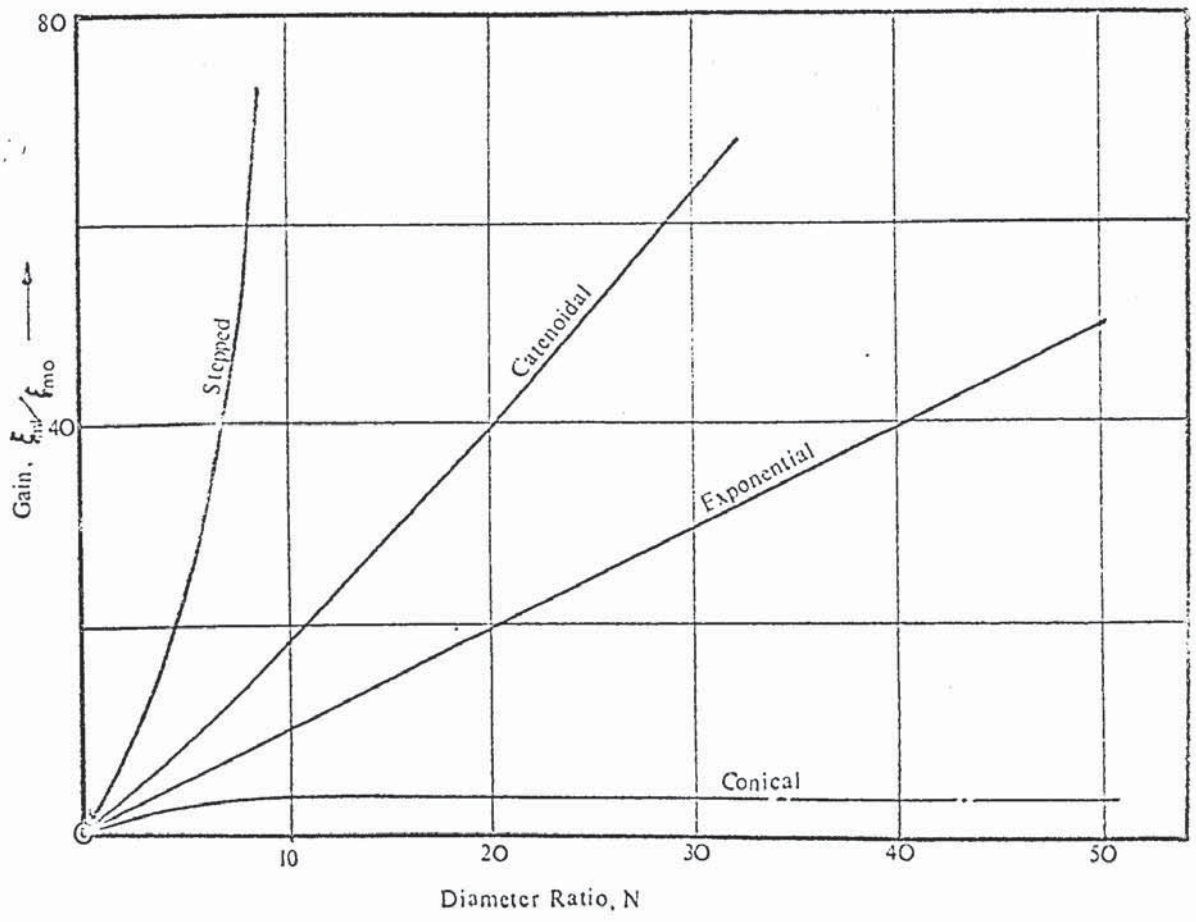

Fig. 4.7 Relationship between diameter ratio N and gain for various tapered horns. (After Merkulov[65])

$$\therefore \quad F_m = -i \frac{w_{o1}'}{k} \cdot e^{bx} \cdot \frac{d\dot{\xi}_m}{dx} \qquad \text{---------- (4.32)}$$

where w_{o1}' is the wave impedance of the horn at the wide end at distance 1 from the origin.

The first derivative of $\dot{\xi}_m$ with respect to distance x gives:

$$\frac{d\dot{\xi}_m}{dx} = e^{-\frac{b}{2}x} \left\{ -\frac{b}{2}[A_2 . \cos k'x + B_2 . \sin k'x] + k'[-A_2 \sin k'x + B_2 . \cos k'x] \right\} \text{---------- (4.33)}$$

and substituting for $\frac{d\dot{\xi}_m}{dx}$ in equation (4.32), after re-arranging we get:

$$F_m = i . \frac{w_{o1}'}{k} . e^{\frac{b}{2}x} . \left[A_2 (\frac{b}{2} \cos k'x + k' \sin k'x) - B_2 (\frac{b}{2} \sin k'x - k' \cos k'x) \right] \text{--- (4.34)}$$

The input impedance Z_{IN} is given by, $Z_{IN} = \frac{F_{mo}}{\dot{\xi}_{mo}}$ where F_{mo} and $\dot{\xi}_{mo}$ are the force and velocity amplitudes at the wide end. Therefore, from equations (4.30) and (4.34) we may write:

$$Z_{IN} = \frac{i . \frac{w_{o1}'}{k'} . e^{\frac{b1}{2}} \left[(\frac{b}{2} \cos k'1 + k' \sin k'1) + \frac{B_2}{A_2} (\frac{b}{2} \sin k'1 - k' \cos k'1) \right]}{e^{-\frac{b}{2}1} (\cos k'1 + \frac{B_2}{A_2} \sin k'1)} \qquad \text{- (4.35)}$$

If we now consider the boundary condition at x = 0, the narrow end, where the force and velocity amplitudes satisfy the equation, $Z_H = \frac{F_{m1}}{\dot{\xi}_{m1}}$, from equations (4.30) and (4.34) we may write:

$$Z_H = \frac{i \frac{w_{o1}'}{k'} \left[A_2 . \frac{b}{2} - B_2 k' \right]}{A_2} = i \frac{w_{o1}'}{k'} \left| \frac{b}{2} - k' \frac{B_2}{A_2} \right| \therefore \frac{B_2}{A_2} =$$

$$i \frac{Z_H}{w_{o1}'} - \frac{b}{2k'} \qquad \text{---------- (4.36)}$$

and substituting for $\frac{B_2}{A_2}$ in equation (4.35) we have;

$$Z_H = \frac{i . \frac{w_{o1}'}{k'} . e^{b1} \left[\frac{b}{2} . \cos k'1 + k' \sin k'1) + (i \frac{Z_H}{w_{o1}'} - \frac{b}{2k'}) (\frac{b}{2} \sin k'1 - k' \cos k'1) \right]}{(\cos k'1 + i \frac{Z_H}{w_{o1}'} . \sin k'1 - \frac{b}{2k'} . \sin k'1)} \qquad \text{- (4.37)}$$

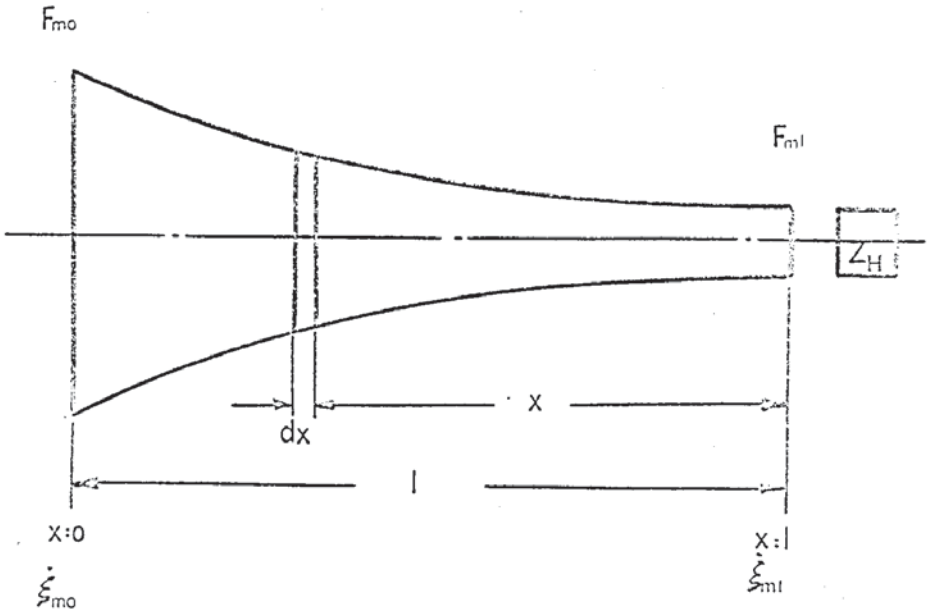

Fig. 4.8 Definition of boundary conditions in a loaded exponential horn.

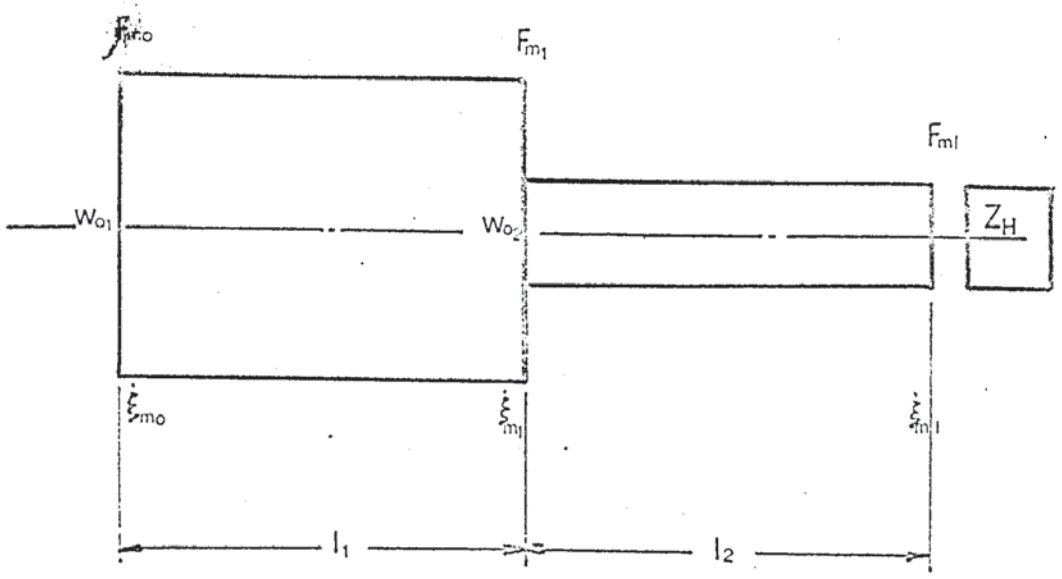

Fig. 4.9 Definition of boundary conditions in a loaded quarter-wave stepped horn.

which after rearranging gives:

$$Z_{IN} = w_{o1}' . e^{b1} \frac{\frac{Z_H}{w_{o1}'} (\cos k'1 - \frac{b}{2k'} . \sin k'1) + i . \sin k'1 \left[1 - (\frac{b}{2k'})^2\right]}{(\cos k'1 - \frac{b}{2k'} . \sin k'1) - i \frac{Z_H}{w_{o1}'} . \sin k'1} \quad \text{---- (4.}$$

If we consider the limiting case when $b << k'$ that is, for a transformer having a gradual taper, or designed for high frequencies then equation (4.38) becomes:

$$Z_{IN} = w_{o1}' . e^{b1} \frac{\frac{Z_H}{w_{o1}'} \cos k'1 + i . \sin k'1}{\cos k'1 - i \frac{Z_H}{w_{o1}'} . \sin k'1} \quad \text{-------- (4.39)}$$

which with slight rearranging is readily seen to be identical to equation (4.17), giving the input impedance of a parallel rod system, with the exception of the multiplier e^{b1}.

If an exponential transformer is connected to a parallel rod section then the input impedance of the latter becomes the load Z_H applied to the horn. Therefore from equations (4.17) and (4.39) it can be seen that the load is transformed at the input end by the factor e^{b1} and we may write:

$$Z_{IN} = e^{b1} . Z_H = N^2 Z_H \quad \text{---------- (4.40)}$$

This property can be employed in order to match the impedances of successive elements in a rod system.

4.4.2 Input impedance of a loaded stepped horn

If the force and velocity amplitudes at the ends and mid-section of a stepped horn are as shown in Fig. 4.9 then the equations defining the distribution of force and particle velocity amplitude in the two parallel sections can be written directly from consideration of equation (4.17), (Section 4.2)

$$\left.\begin{aligned} F_{mo} &= F_{m_1} \left[\cos kl_1 + i . w_{o1} \frac{\dot{\xi}_{m_1}}{F_{m_1}} \sin kl_1\right] \\ \dot{\xi}_{mo} &= \dot{\xi}_{m1} \left[\cos kl_1 + \frac{F_{m_1}}{\dot{\xi}_{m_1}} . \frac{1}{w_{o1}} \sin kl_1\right] \end{aligned}\right\} \quad \text{------ (4.41a)}$$

$$\left.\begin{aligned} F_{m_1} &= F_{ml}\left[\cos k\ell_2 + i\frac{w_{o_2}}{Z_H}\sin k\ell_2\right] \\ \dot{\xi}_{m_1} &= \dot{\xi}_{ml}\left[\cos k\ell_2 + i\frac{Z_H}{w_{o_2}}.\sin k\ell_2\right] \end{aligned}\right\} \quad \text{--------- (4.41b)}$$

where w_{o_1} and w_{o_2} are the wave impedances of the wide and narrow sections respectively; ℓ_1 and ℓ_2 the respective lengths and Z_H the load impedance applied at the narrow end. F_{m_1} and $\dot{\xi}_{m_1}$ may be eliminated between equations (4.41a) and (4.41b) giving the following expression for force and motional amplitudes at the input to the system:

$$F_{mo} = F_{ml}\left[\cos k\ell_2 + i\frac{w_{o_2}}{Z_H}.\sin k\ell_2\right]\cos k\ell_1 + i\dot{\xi}_{m\ell}\left[\cos k\ell_2 + i\frac{Z_H}{w_{o_2}}\sin k\ell_2\right]w_{o_1}\sin k\ell_1$$

$$\dot{\xi}_{m_o} = \dot{\xi}_{m_\ell}\left[\cos k\ell_2 + i\frac{Z_H}{w_{o_2}}.\sin k\ell_2\right]\cos k\ell_1 + i.F_{ml}\left[\cos k\ell_2 + i.\frac{w_{o_2}}{Z_H}\sin k\ell_2\right]\frac{1}{w_{o_1}}.\sin k\ell_1 \quad \text{--- (4.42)}$$

The above expression may be simplified by considering particular values of the lengths ℓ_1 and ℓ_2, viz. when $\ell_1 = \ell_2 = \lambda/4$ that is for a quarter wavelength stepped horn, then since $k = \frac{2\pi}{\lambda}$, $\cos k\ell_1 = \cos k\ell_2 = 0$ and $\sin k\ell_1 = \sin k\ell_2 = 1$ equations (4.42) become:

$$F_{mo} = -\dot{\xi}_{ml}\frac{Z_H}{w_{o_2}}w_{o_1} \quad \text{--------- (4.43)}$$

and $\dot{\xi}_{m_o} = -F_{m_\ell}.\frac{w_{o_2}}{Z_H}.\frac{1}{w_{o_1}}$

The input impedance is given by $Z_{IN} = \frac{F_{m_o}}{\dot{\xi}_{mo}}$ and we may therefore write the equation for the input impedance of a quarter wave stepped horn as:

$$Z_{IN} = Z_H \cdot \left(\frac{w_{o_1}}{w_{o_2}}\right)^2 \qquad \text{---------- (4.44)}$$

but since $w_{o_1} = S_o \rho c$ and $w_{o_2} = S_1 \rho c$ where S_o and S_1 are the area of the large and small ends respectively it is readily seen that the load impedance is transformed at its input by the fourth power of the diameter ratio N i.e.

$$Z_{IN} = N^4 Z_H \qquad \text{---------- (4.45)}$$

4.5 Analysis of a conical horn

4.5.1 Determination of the velocity and strain distribution along an unloaded conical horn.

The distribution of amplitudinal velocity and strain along a conical rod system, may be derived from the general wave equation (equation (4.26)) by substituting into this the appropriate taper law. If we measure distance along the horn from the wide end then the variation in area is given by the expression: $S = S_o(1 - \alpha x)^2$ ---------- (4.46)
where $\alpha = \frac{R_1 - R_2}{R_1 \ell}$, and R_1 and R_2 are the wide and narrow end diameters respectively.

Substituting for $\frac{1}{S} \cdot \frac{dS}{dx}$ in equation (4.26) we therefore obtain the wave equation defining the particle velocity distribution:

$$\frac{d^2\dot{\xi}_m}{dx^2} + \frac{2}{x - \frac{1}{\alpha}} \cdot \frac{d\dot{\xi}_m}{dx} + k^2\dot{\xi}_m = 0 \qquad \text{---------- (4.47)}$$

The general solution to this equation is readily found by series substitution assuming an expression of the general form

$$\dot{\xi}_m = \sum_{n=0}^{\infty} a_n \rho^{\lambda+n}$$

This gives, after some manipulation[65]:

$$\dot{\xi}_m = \frac{\alpha}{\alpha x + 1} [A_1 \cos kx + A_2 \sin kx] \qquad \text{-------- (4.48)}$$

where once again, A_1 and A_2 are arbitrary constants and k the wave number given by: $k = 2\pi/\lambda$.

A_1 and A_2 may be determined by considering the boundary conditions at each end of the unloaded horn. If we assume that the horn is driven at the wide end by a matched transducer which induces a velocity $\dot{\xi}_{mo}$ at X = 0, see Fig. 4.10, and also that the oscillatory strain is zero at both ends of the horn, then

$$\frac{d\dot{\xi}_m}{dx} = 0 \text{ when } x = 0 \text{ or } \ell \qquad \text{---------- (4.49)}$$

Differentiating equation (4.48) we obtain:

$$\frac{d\dot{\xi}_m}{dx} = -\frac{1}{(x-\frac{1}{\alpha})}\left\{(kA_1 \sin kx - kA_2\cos kx)+\frac{1}{x-\frac{1}{\alpha}}(A_1\cos kx + A_2\sin kx)\right\} \qquad \text{---- (4.50)}$$

Applying the boundary condition at $x = \ell$ to equation (4.50) gives: $-kA_1\sin k\ell + kA_2 \cos k\ell + \frac{\alpha}{1-\alpha\ell}(A_1\cos k\ell + A_2 \sin k\ell) = 0$

and on rearranging we obtain:

$$A_2 = A_1\left\{\frac{k(1-\alpha\ell)\sin k\ell-\alpha\cos k\ell}{k(1-x\ell)\cos k\ell+\alpha\sin k\ell}\right\} \qquad \text{---------- (4.51)}$$

Similarly, considering the boundary condition at x = 0 we have from equation (4.50)

$$kA_2.\alpha + A_1\alpha^2 = 0$$

or $A_2 = -A_1\frac{\alpha}{k}$ ---------- (4.52)

and from equations (4.51) and (4.52) we may write:

$$-\frac{\alpha}{k} = \frac{k(1-\alpha\ell)\sin k\ell - \alpha\cos k\ell}{k(1-\alpha\ell)\cos k\ell + \alpha\sin k\ell} \qquad \text{---------- (4.53)}$$

Substituting $\alpha = \frac{N-1}{N\ell}$, where $N = \frac{R_1}{R_2}$ and rearranging we obtain a transcendental function relating the transformer length and end diameter ratio for a given value of wave number, k. Viz.

$$\tan k\ell = \frac{k\ell}{\frac{(k\ell)^2 N}{(1-N)^2}+1} \qquad \text{---------- (4.54)}$$

Graphical solutions may be obtained expressing $k\ell$ as a function

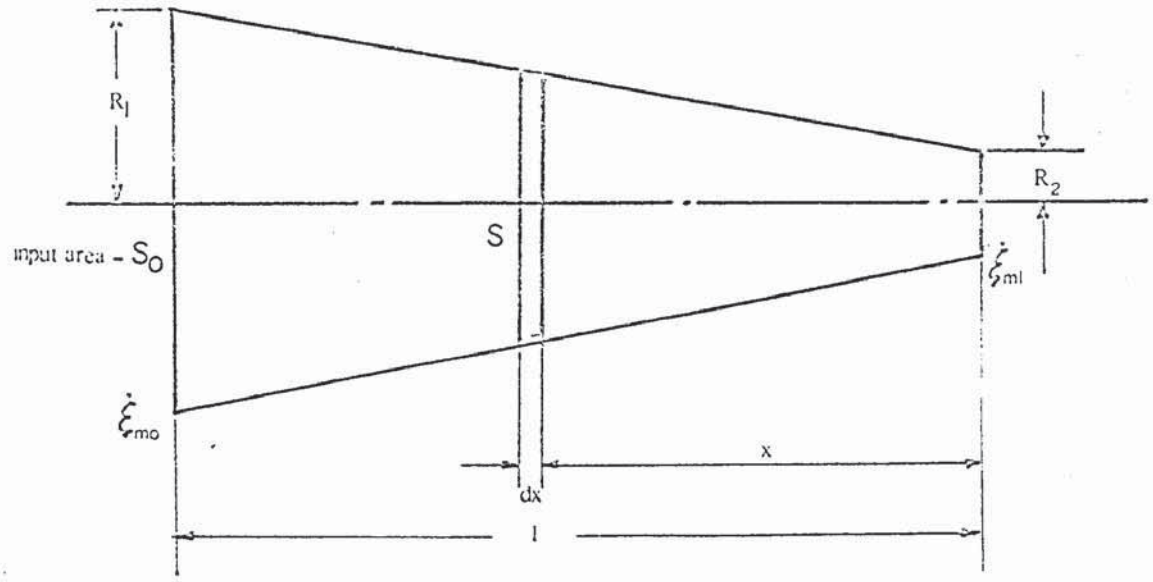

Fig. 4.10 Oscillatory motion of an element in a conical horn under the action of a sinusoidal force.

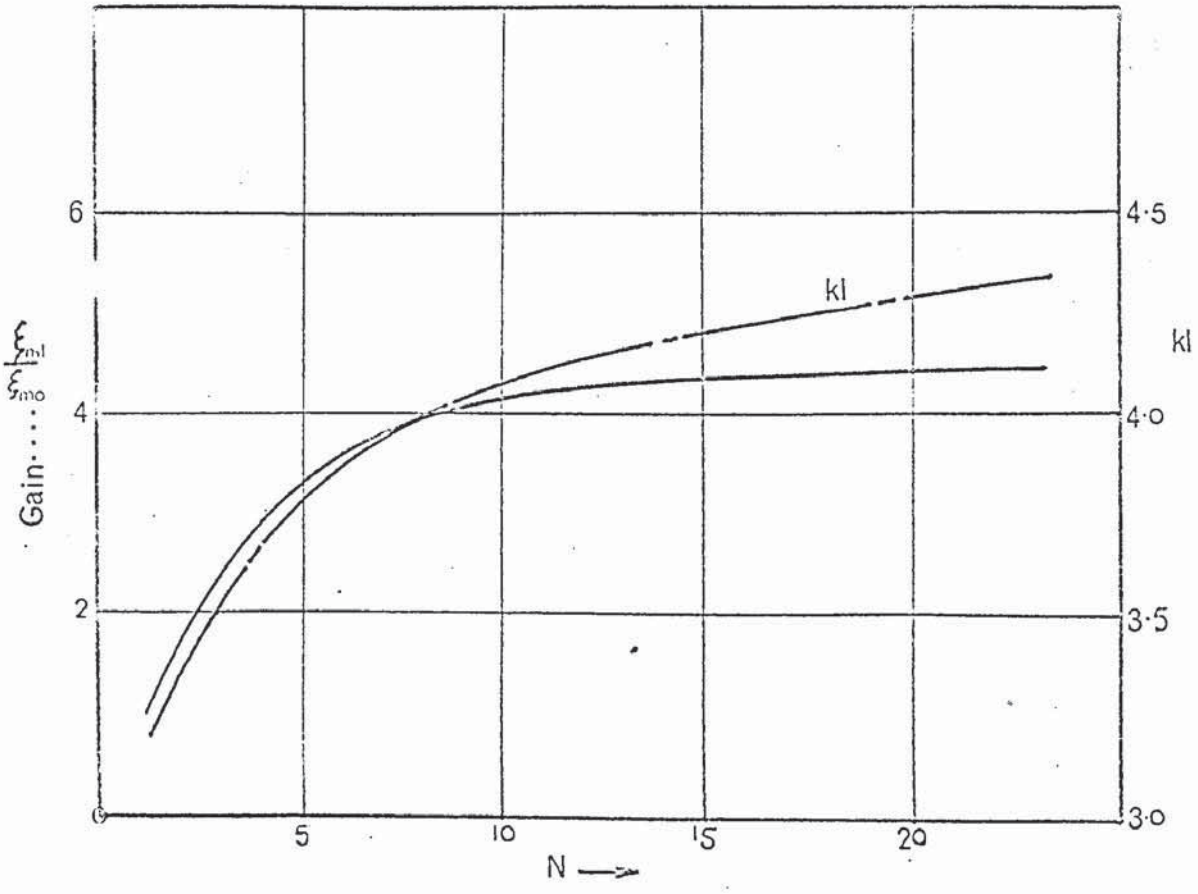

Fig. 4.11 Design characteristics of conical horn.

of N. The resulting curve thus defines the conditions under which resonance occurs when the horn is unloaded.

The velocity distribution may be found from the condition that $\dot{\xi}_m = \dot{\xi}_{mo}$ at $x = 0$

Substituting this value into equation (4.48) gives:

$$\dot{\xi}_{mo} = -\alpha A_1$$

and from equation (4.52):

$$A_2 = A_1 \cdot \frac{\alpha}{k} = \frac{\dot{\xi}_{mo}}{k}$$

∴ Equation (4.48) may be rewritten:

$$\dot{\xi}_m = \frac{\dot{\xi}_{mo}}{1-\alpha x} \cdot \left(\cos kx - \frac{\alpha}{k} \cdot \sin kx \right) \quad \text{---------- (4.55)}$$

The gain may be determined by considering the velocity amplitude at the narrow end of the system, from equation (4.55) this becomes:

$$\dot{\xi}_{m\ell} = \frac{\dot{\xi}_{mo}}{1-\alpha\ell} \left(\cos k\ell - \frac{\alpha}{k} . \sin k\ell \right) \quad \text{---------- (4.56)}$$

on rearranging and writing $\alpha = \frac{N-1}{N\ell}$,

$$\frac{\dot{\xi}_{m\ell}}{\dot{\xi}_{mo}} = N\left(\cos k\ell - \frac{N-1}{N.k\ell} . \sin k\ell\right) \quad \text{---------- (4.57)}$$

The relationship between gain and diameter ratio N may be determined graphically from a plot of N against the function $k\ell$ derived from equation (4.54). These basic design curves for an unloaded conical horn are shown in Fig. 4.11.

It is important, when operating in the standing wave régime, to attach the resonant wave guide to the external structure at some point of minimum motional amplitude. The displacement node on a half wave-length tapered rod does not coincide with the mid-plane but may be found by equating the formula for velocity distribution, to zero.

Thus, from equation (4.55) we obtain:

$$\dot{\xi}_m = \frac{\xi_{mo}}{1-\alpha x}\left(\cos kx - \frac{\alpha}{k}\sin kx\right) = 0$$

and $\tan kx = \frac{k}{\alpha}$

$$\therefore x_{node} = \frac{1}{k}\tan^{-1}\frac{k}{\alpha} \quad \text{---------- (4.58)}$$

4.5.2 Derivation of the force distribution and impedance transformation characteristics of a loaded conical horn.

It is convenient in considering a tapered rod system loaded at the narrow end, to measure distance along the x-axis from the plane of application of the load. If a complex load Z_H is applied to the narrow end of a conical horn, and the force and velocity amplitudes at each end of the system are as indicated in Fig. 4.12 the oscillatory force and velocity distribution may be determined from the general solution to the wave equation in the following way:

The taper law is modified by the change in origin of the system and the expression defining the variation in cross sectional area becomes: $S = So\ (1 + \alpha x)^2$ ---------- (4.59)

in which $\alpha = \frac{R_1 - R_2}{R_2 \ell} = \frac{1-N}{\ell}$

Equation (4.48) the general solution to the wave equation, is written:

$$\dot{\xi}_m = \frac{\alpha}{\alpha\ x+1}(A_1 \cos kx + A_2 \sin kx) \quad \text{------- (4.60)}$$

The analogous expression for the oscillatory force distribution is obtained from the relationship:

$$Fm = \frac{S.E.}{i\omega} \cdot \frac{d\dot{\xi}_m}{dx}$$

which on substituting for S from equation (4.59) gives:

$$Fm = S_o(1 + \alpha x)^2 \cdot \frac{E}{i\omega} \cdot \frac{d\dot{\xi}_m}{dx}$$

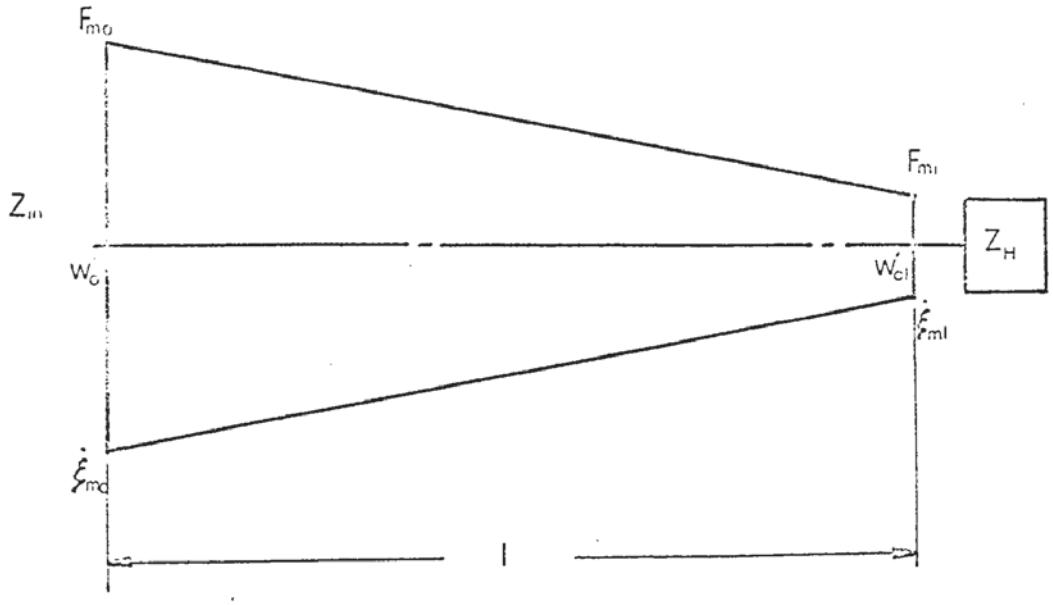

Fig. 4.12 Boundary conditions for loaded conical horn.

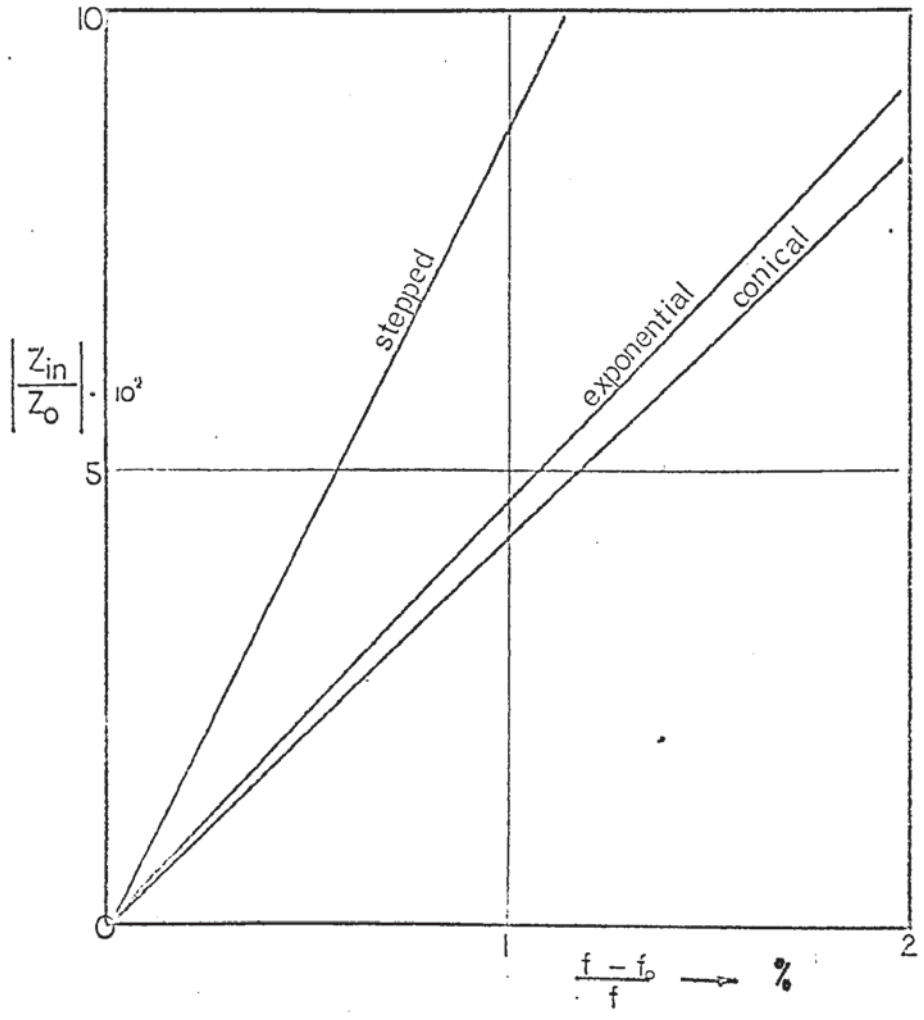

Fig. 4.13 Frequency dependance of reactive impedance of stepped, experimental and conical horns, (after Merkulov and Kharitonov (55))

$$= - i \frac{w'_{o\ell}}{k} \cdot (1 + \alpha x)^2 \cdot \frac{d\dot{\xi}_m}{dx} \quad \text{---------- (4.61)}$$

where $w'_{o\ell}$ is the wave impedance of the horn at the narrow end.

Substituting for $\frac{d\dot{\xi}_m}{dx}$ in equation (4.61) we may write:

$$Fm = i\frac{w'_{o\ell}}{k} (1 + \alpha x)^2 \cdot \frac{\alpha}{(\alpha x + 1)} \left(k(A_2 \cos kx - A_1 \sin kx) - \dot{\xi}_m\right)$$

$$= i \frac{w'_{o\ell}}{k} \alpha(1+\alpha x)\left(k(A_2 \cos kx - A_1 \sin kx) - \dot{\xi}_m\right) \text{-------- (4.62)}$$

The values of the arbitrary constants A_1 and A_2 may be determined by considering the boundary conditions at each end of the system. Viz. $Fm = Fm\ell$ and $\dot{\xi}m = \dot{\xi}m\ell$ at $x = 0$ and $Fm = Fmo$ and $\dot{\xi}m = \dot{\xi}mo$ at $x = \ell$.

Considering the loaded end of the horn we may write:

$$Fm\ell = - i \cdot \frac{w'_{o\ell}}{k} \cdot \alpha \ (kA_2 - \dot{\xi}m\ell) \text{ and } \dot{\xi}m\ell = \alpha A_1$$

$$\therefore A_2 = i \frac{F_{m\ell}}{w'_{o\ell} \cdot \alpha} + \frac{\dot{\xi}_{m\ell}}{k} \quad \text{---------- (4.63)}$$

but since $\frac{F_{m\ell}}{\dot{\xi}_{m\ell}} = Z_H$, the load impedance, then

$$A_2 = \frac{\dot{\xi}_{m\ell}}{\alpha}\left(i \frac{Z_H}{w_{o\ell}} + \frac{\alpha}{k}\right)$$

$$\text{or } \frac{A_2}{A_1} = i \cdot \frac{Z_H}{w'_{o\ell}} + \frac{\alpha}{k} \quad \text{---------- (4.64)}$$

using the relationship $\dot{\xi}_{m\ell} = \alpha A_1$

Substituting for $\dot{\xi}m$ in equation (4.62) and dividing by A_1 we may write:

$$F_m = - i \frac{w'_{o\ell}}{k} \cdot \alpha(1 + \alpha x)A_1 \left[k\left(\frac{A_2}{A_1} \cos kx - \sin kx\right)\right.$$

$$\left. - \frac{\alpha}{\alpha x+1} \left(\cos kx + \frac{A_2}{A_1} \sin kx\right)\right] \text{---------- (4.65)}$$

Eliminating $\frac{A_2}{A_1}$ between equations (4.64) and (4.65) and substituting for A_1 gives:

$$F_m = -i \frac{\dot{\xi}_{m\ell}}{k} \cdot w'_{o\ell}(1 + \alpha x)\left(k\left(i\frac{Z_H}{w'_{o\ell}} + \frac{\alpha}{k}\right)\cos kx - k\sin kx - \left(\frac{\alpha}{\alpha x+1}\right)\cos kx\right.$$

$$- \frac{\alpha}{\alpha x+1} \left(i\frac{Z_H}{w_{o\ell'}} + \frac{\alpha}{k} \right) \sin kx \Big\}$$

which on separating the real and imaginery terms gives:

$$F_m = \frac{\dot{\xi}_m}{k} w_{o\ell'} \cdot (1+\alpha x) \left[\left(k\frac{Z_H}{w_{o\ell'}} \cdot \cos kx - \frac{\alpha}{\alpha x+1} \cdot \frac{Z_H}{w_{o\ell'}} \sin kx \right) \right.$$

$$\left. - i \left(\alpha\left(1 - \frac{1}{\alpha x+1}\right) \cos kx - \left(k + \frac{\alpha^2}{k(\alpha x+1)}\right) \sin kx \right) \right] \quad (4.66)$$

The input impedance is given by $Z_{IN} = \frac{F_{mo}}{\xi_{mo}}$ at $x = \ell$ and from equations (4.66) and (4.60) we may write:

$$Z_{IN} = \frac{\frac{w_{o\ell}'}{k}(1+\alpha\ell)^2 \left[\left(k\frac{Z_H}{w_{o\ell'}} \cos k\ell - \frac{\alpha}{\alpha\ell+1} \cdot \frac{Z_H}{w_{o1}} \cdot \sin kl \right) - i\left(\frac{\alpha^2}{(\alpha\ell+1)} \cdot \cos k\ell - \left(k + \frac{\alpha^2}{k\alpha\ell+1}\right) \right. \right.}{\left. \left. \sin k\ell \right) \right]}$$

$$(\cos k\ell + \frac{\alpha}{k} \sin kl) + i\frac{Z_H}{w_{o\ell'}} \cdot \sin k\ell \quad - (4.67)$$

when α is set equal to zero in the above equation the expression reverts to that of a parallel rod system, viz.

$$Z_{IN} = \frac{\frac{w_{o\ell'}}{k}\left[k \cdot \frac{Z_H}{w_{o\ell'}} \cos kx + i \cdot k \sin kx \right]}{\cos kx + i \frac{Z_H}{w_{o\ell'}} \cdot \sin kx}$$

which on rearranging is readily seen to yield equation (4.17), the input impedance of a homogeneous rod system.

$$Z_{IN} = w_{o\ell} \cdot \frac{\cos k\ell + i\frac{w_{o\ell}}{Z_H} \cdot \sin k\ell}{\frac{w_{o\ell}}{Z_H} \cos k\ell + i \cdot \sin k\ell} \quad \text{----------} \quad (4.17)$$

where $w_{o\ell}$ is the wave impedance of the rod.

The reactive component of the input impedance of an unloaded conical horn is found from equation (4.67) by setting $Z_H = 0$ thus:

$$Z_{IN} = -i \cdot w_o' \cdot \frac{\alpha \cdot \cos k\ell \left(\frac{\alpha\ell}{\alpha\ell+1}\right) - \sin k\ell \left(k + \frac{\alpha^2}{k[\alpha\ell+1]}\right)}{\cos k\ell + \frac{\alpha}{k} \sin k\ell}$$

and writing $\alpha\ell = N-1$ we have:

$$\frac{Z_{IN}}{w_o'} = \frac{(N-1)^2 \left(\frac{1}{k\ell} - \cot k\ell\right) + k\ell}{k\ell . \cot k\ell + N-1} \qquad \text{-------- (4.68)}$$

where w_o' is the wave impedance at the wide end of the horn.

This expression agrees with the solution for the impedance of an unloaded conical horn, given by Merkulov and Kharitonov[68]. It should be noted that at resonance the reactive impedance is zero and that it only assumes a positive value when either the frequency, defined by k, or the length, doesnot satisfy the conditions for resonance, viz. Fmo = 0.

This feature is important when considering the design of a system which is required to operate at frequencies slightly above or below f_o (the resonant frequency). Under these circumstances the frequency dependance of the reactive part of the input impedance limits the load which can be applied to the transformer, for satisfactory operation. This characteristic is illustrated in Fig. 4.3 for exponential conical and stepped horns and it will be seen that the stepped transformer is particularly sensitive to small shifts in operating frequency[68]. For a given amplification a conical horn shows the minimum frequency dependence and is consequently more suitable in certain applications.

The properties of a conical horn will be considered later in relation to the design of the oscillatory apparatus.

4.6 Design of Radial resonators

In section 3, the choice of vibrational mode for the deep-drawing process was discussed and it was concluded that radial oscillation of the die would produce beneficial effects which could not be achieved with a longitudinal mode. However, such an objective is less easily achieved since, when considering radial systems, it is necessary to regard the tool as an integral

part of the waveguide rather than an 'attached mass' as in the axial counterpart[69]. The acoustic system must therefore satisfy not only the criteria for radial resonance but also the geometric constraints imposed by the technological requirements of the working process.

For some cold drawing operations, involving dies of circular section, the basic acoustic problem may be considered as one of radial wave motion in an annular disc. Consideration has been given to two concepts which led to independent solutions to the wave equations defining radial mode vibration. The first involved a detailed analysis which took account of both radial and circumferential strains in an annular section and led to a solution which predicted the ring geometry for true radial resonance at a given frequency[70].

The problem was also posed in slightly different terms, by considering the wave motion in isolated segments of an annular disc, namely by ignoring the circumferential strains[71]. This concept is justified in practice if the plate under examination is divided into segments, by machining narrow slots extending to within a short distance of both circular extremities.

These solutions are derived in Appendix I and experimental evidence of the validity of the analyses is discussed.

4.7 Summary

The original intention of this research programme, as discussed in sections 1 and 3.2, was to examine the axisymmetric problem of cup drawing using a radial resonator designed specifically for that application. However, it proved impracticable to produce a pure radial mode within the time schedule of this investigation and it was therefore decided to adopt a two dimensional test for which axial oscillatory

systems were appropriate. The development of high intensity radial resonators was undertaken concurrently with the construction of the oscillatory apparatus and it is only recently that a sufficient understanding has been achieved to permit the design of suitable axisymmetric oscillatory apparatus.

The review of acoustic theory and in particular the analysis of a conical transformer, were considered essential to an understanding of the operating principles and design criteria of the oscillatory apparatus described in section 5. The analyses and solutions considered above also contribute to an understanding of the physics and mechanics of the process being studied and permit a rational evaluation of the oscillatory phenomena observed during this research programme. Reference to the theories described above will therefore be made in the following sections.

5. Design of Oscillatory Wedge Drawing Sub-press and Ancillary Equipment.

5.1 General requirements of the apparatus.

Three principal objectives were considered in the design of the oscillatory sub-press, namely:

(i) the test should embody the basic forming characteristics of the cup drawing process and should be closely analogous to this operation within the limits imposed by certain inherent features of the wedge test.

(ii) the apparatus must provide a facility for the accurate measurement of the friction force associated with the blank holder load. It should also incorporate some means of assessing the die radius friction component of the punch load.

(iii) the size and disposition of the forming tools employed in the wedge test should be compatible with the acoustic requirements of the system.

Apart from these fundamental considerations an attempt was made to incorporate two other important features into the sub-press design. These were:

(i) an hydraulically activated blank holder system giving constant blank holder force throughout the drawing cycle, and

(ii) a means of ultrasonically activating the pressure plate or wedge die whilst monitoring all of the relevant process parameters.

It was concluded after careful evaluation of the above requirements that these conditions could best be satisfied by a wedge test having bi-axial symmetry. Such a test would therefore represent the simultaneous deformation of two diametrically opposed radial segments from a plane circular blank and would involve a sub-press having two pairs of die and blank holder

tools. It is readily seen that such a system permits the measurement of the blank holder friction force associated with each end of the wedge test piece, by placing a load cell of suitable design between the two horizontally opposed pressure plates. This general arrangement also allows the test piece to be drawn through the wedge dies using a punch whose axis lies in a plane normal to that of the die axes and thus closely represents the situation in axisymmetric cup drawing.

In this system, the two dies or blank holder plates may be attached to the output ends of identical axial resonators which are driven in phase, by the same electrical power source. This general arrangement is shown in Figs. 5.1 and 5.2. The blank holder plates are loaded by separate hydraulic cylinders which apply a thrust to each end of a stiff beam supported on the upper surfaces of the pressure plates, by roller bearings. Details of this design will be given in Sections 5.3 and 5.4 describing the friction load cell and blank holder assemblies.

In Fig. 5.1 the sub-press is shown mounted on the movable crosshead of a 100 tonf Avery mechanical testing machine. The punch assembly is attached to a fixed crosshead at a convenient height and located so that it passes between the dies when the sub-press is raised. The capacity of the testing machine in no way reflects the anticipated drawing loads in the present test, but the machine was chosen for its convenient dimensions and ram velocity characteristics.

5.2 Design of the Acoustic System.

5.2.1 General considerations.

The acoustic system, consisting of magnetostrictive transducers and coupling waveguides, was designed to fulfil certain oscillatory requirements whilst bearing in mind the wedge test geometry.

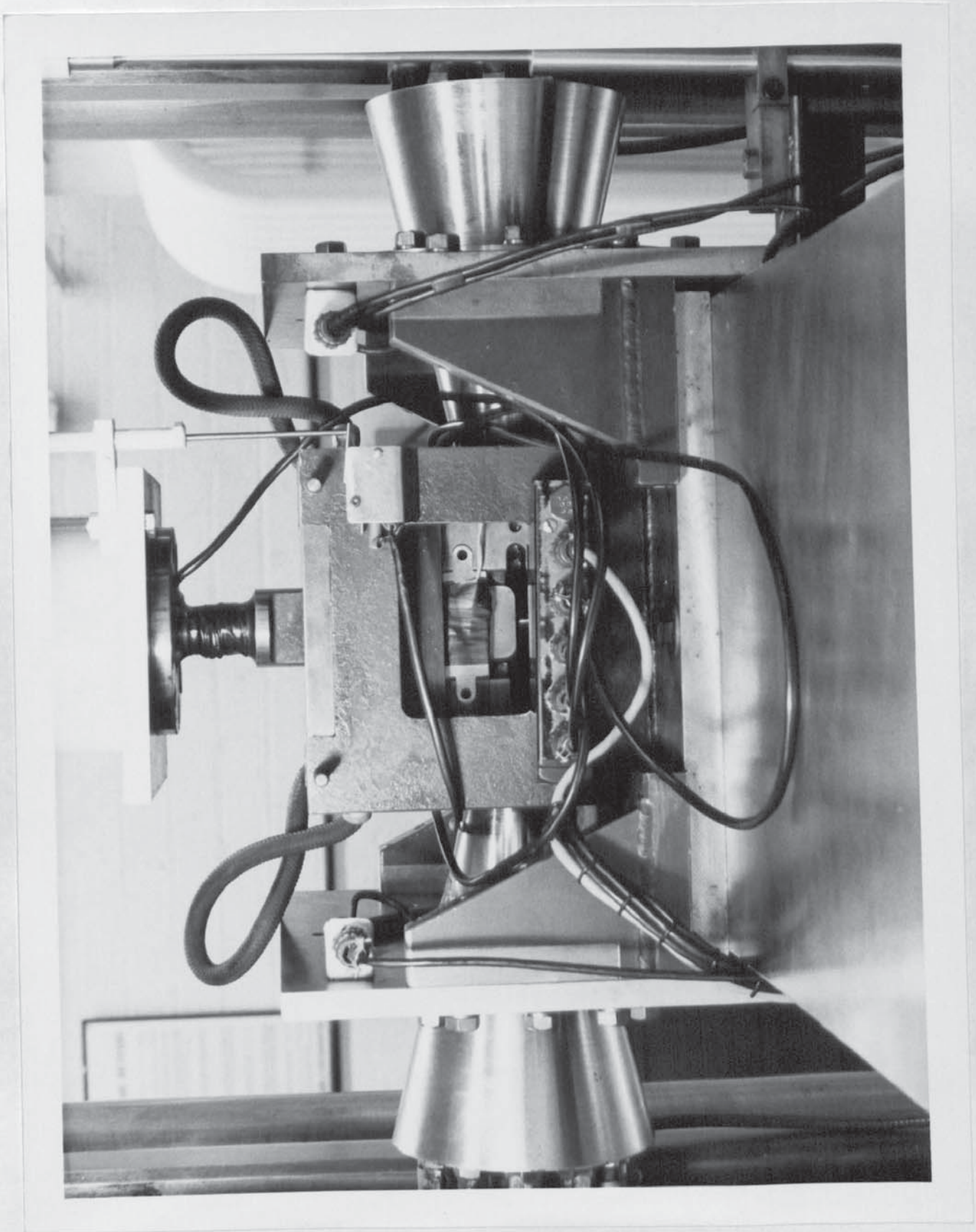

Fig. 5.1 Wedge Drawing Sub-press

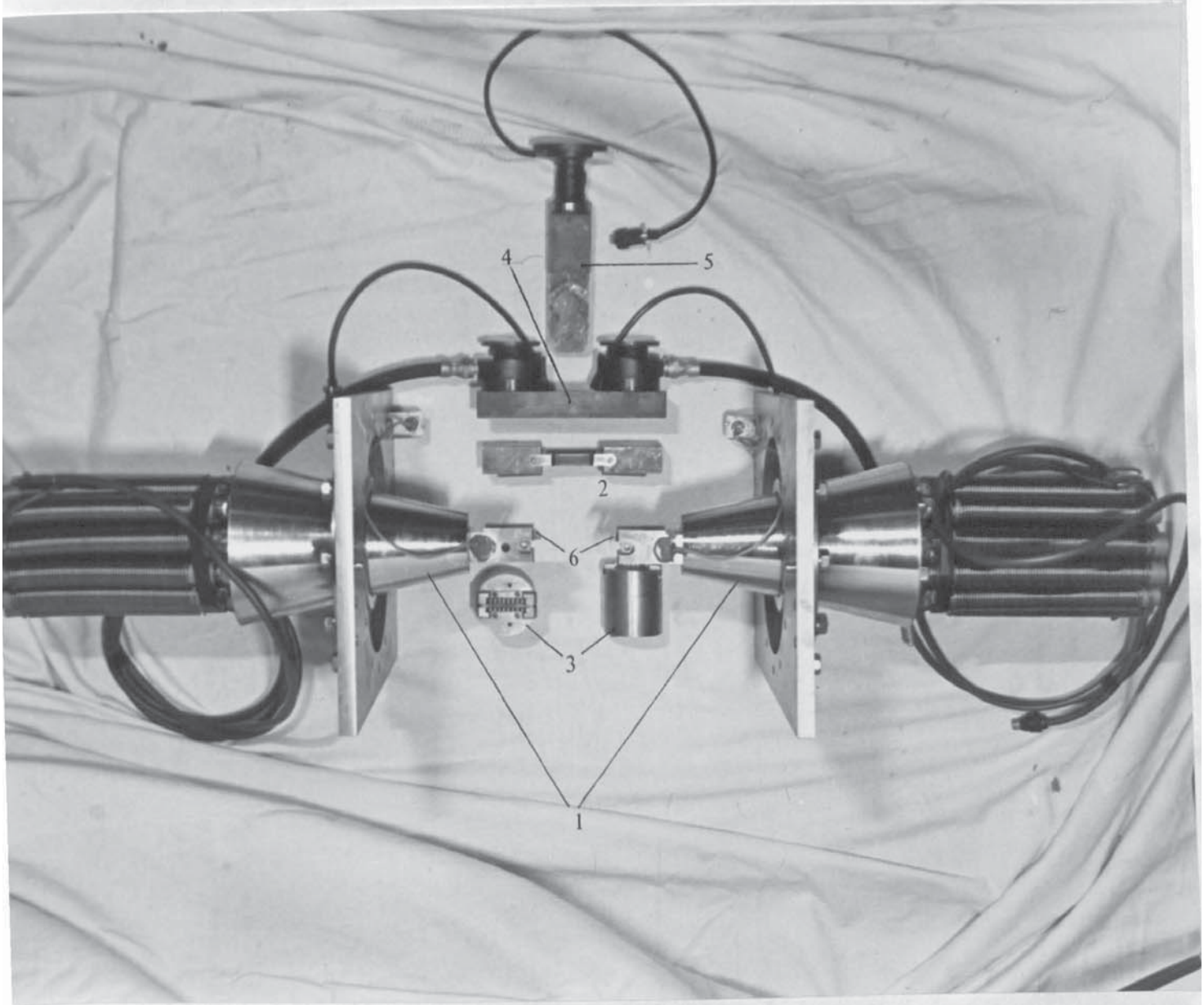

Fig. 5.2 Components of oscillatory sub-press

1. Concentrators
2. Blank holder plates
3. Die support blocks
4. Blank holder assembly
5. Punch
6. Wedge drawing dies.

The general shape and dimension of wedge test pieces, used by other researchers,[54] were considered in Section 3.3 and the scale of the present test was decided largely in accord with the capacity of available electrical generator equipment used to drive the oscillatory units. The design and manufacture of the test pieces is described in Section 6, where it will be seen that the dimensions were such as to permit a maximum drawing ratio of 2·50:1 using tools of 2 in. overall length.

With this parameter in mind the acoustic system was designed to fulfil the following requirements:

(i) Longitudinal resonance should be maintained at the design frequency, with the tools attached to each wave system.

(ii) the unloaded motional amplitude in the attached tools should be of the order of 0·002 in peak to peak.

(iii) the variation in displacement amplitude along the wedge tools should be minimal.

In order to achieve a P-P displacement amplitude of 0·002 in. it was clear that the system must be designed to operate in the standing wave régime and that some appropriate form of velocity transformer must be used to couple the transducer and tool assemblies. From the properties of such devices, discussed in Section 4.3, it was considered that the conical transformer was most appropriate to the present application. This choice will be fully justified in the following section.

The operating frequency of the system was chosen as 13·0 kHz in order to utilise readily available magnetostrictive transducers of a suitable design for attachment to the transformers.

5.2.2 Design of the Velocity Transformer.

The maximum motional amplitude that can be achieved in an

unloaded magnetostrictive transducer is of the order of 6×10^{-4} in[7.2]. A transformer with a velocity ratio of approximately 4:1 was therefore required to produce the specified output amplitude in the wedge tool. From the characteristic curves derived for conical, stepped and exponential concentrators, Fig. 4.7, section 4.3, it is apparent that this gain may be produced with diameter ratios of 9, 2 and 4 respectively for the above types of transformer. The corresponding curves showing the velocity distribution along the respective halfwave transformers are shown in Fig. 5.3. This illustrates that the variation in particle velocity over the end 1.50 in. assuming a resonant frequency of 13.0 kHz, is 18.5% for stepped and exponential horns compared with only 9.0% for the equivalent conical horn.

A second important consideration was the frequency dependence of the reactive input impedance of the three transformers considered. This factor was discussed in sections 4.4 and 4.5 where it was shown that in the case of the stepped horn, the input impedance is extremely sensitive to small variations in the driving frequency (in relation to the resonant frequency), see Fig. 4.13. Since it was proposed to use two resonant systems in the oscillatory wedge test, this feature was considered to be a distinct disadvantage, the implications of this characteristic being:

(i) that any deviation from the resonant frequency of a system raises the reactive input impedance above zero and hence reduces the maximum values of the oscillatory quantities for a given power input to the transducers.

(ii) a small difference between the resonant frequencies of the two oscillatory systems could result in a significant

Comparison of motional characteristics of conical and stepped concentrators.

Fig.5·3

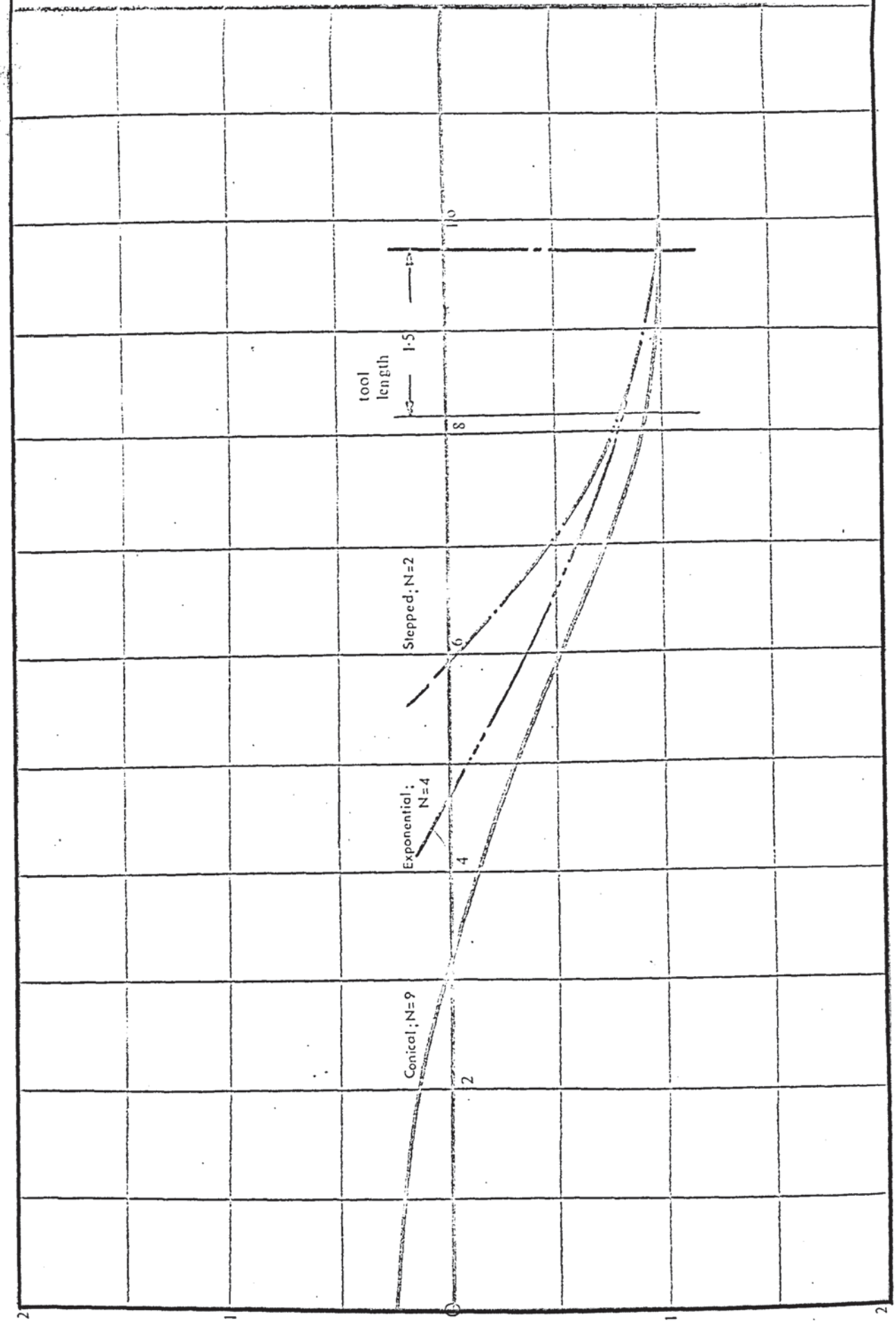

variation in the motional amplitude of each wedge tool, if stepped horns were used. This is related to the discrepancy between the resonant and driving frequencies of each horn and its effect on their respective reactive input impedances.

It was therefore apparent that in this low gain application the conical horn represented the most satisfactory transforming device, also offering the advantage of reduced machining costs compared with the exponential type.

The length of the conical horn was determined from the graph of N against kl in Fig. 4.11 (section 4.5.1) where k is the wave number given by $2\pi/\lambda$ and λ is the wavelength of longitudinal waves in a parallel section at the design frequency. The large diameter of the horn was fixed at 5 in. so as to accommodate 16 Ni-Cr-Co magnetostrictive transducers which were compatible with a power input to each vibrator, of up to 1·5 kW. It was then a simple matter to determine the small diameter and apex angle of the conical horn. Details of these calculations are given in Appendix II. A photograph of the transformers with wedge drawing dies and transducers attached is shown in Fig. 5.4. Details of the transformer construction are given in Fig. 5.5.

5.2.3 Material

In order to simplify the problems associated with acoustic matching of the tools and transformers and to ensure that the vibrator units were as nearly identical as possible, the same material was used in the production of all items comprising the wave guide and work tools.

A conventional deep drawing die steel was selected, which was readily available in a number of suitable heat treated

Fig. 5.4 Concentrator with transducers and wedge drawing die.

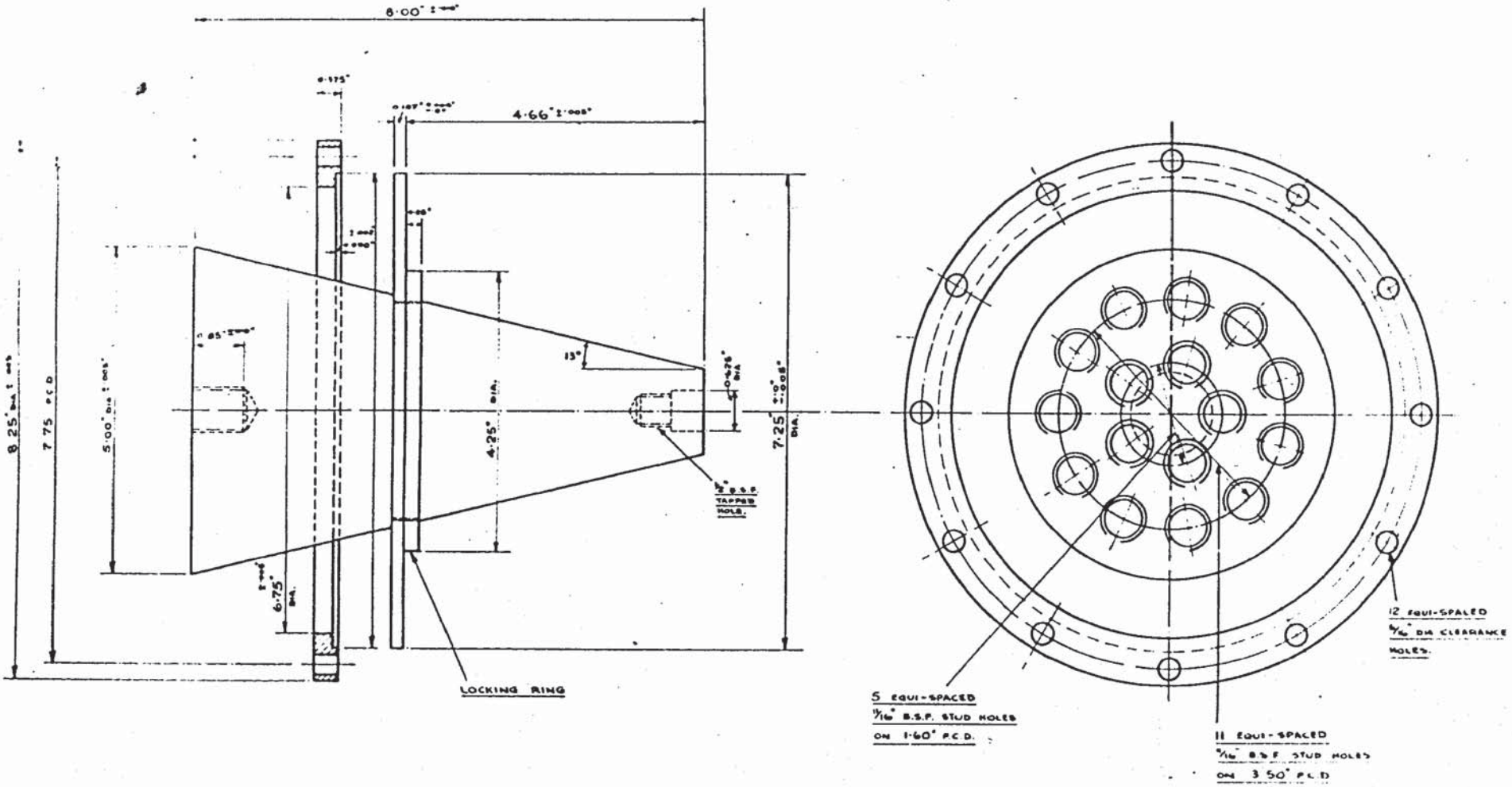

Fig. 5·5 ACCOUSTIC CONCENTRATOR AND MOUNTING RING.

conditions. The steel chosen was Carr's P552, a 110-tonf U.T.S. material capable of case hardening to 54-56 Rockwall C.

Details of the composition and heat treatment of each component of the sub-press are given in Appendix III.

5.2.4 Transducers.

Magnetostrictive transducers with an operating frequency of 13 kHz were chosen since they were of a robust construction and readily available, together with the necessary electrical generators. The transducers, supplied by Ultrasonics Ltd., were made of nickel alloy laminations which were bonded together using an epoxy resin, and brazed into steel stubs. The stubs were threaded at the free ends to facilitate attachment to the main elements of the oscillatory system. Each laminated core was surrounded by an insulated copper coil having a predetermined number of turns and supported on a paxolin former.

5.2.5 Mounting system.

The attachment of the oscillatory system to the main structural elements of the apparatus required special consideration in order to avoid excessive damping of the elastic waves. In the standing wave régime rigid attachment of the wave system may be made at a nodal plane, of minimum displacement. However, in the travelling wave régime in which there are no motional nodes, rigid attachment inevitably leads to attenuation unless a specially designed isolating member is used. This normally takes the form of a tuned sleeve which fits around the wave guide and is metallurgically bonded to it at one end. The isolating sleeve may be either a quarter wave-length or half wave-length long. In the former case, under resonant conditions, a nodal plane occurs at the end of the sleeve not attached to the waveguide, when this is rigidly clamped to the supporting

structure, see Fig. 5.6(a). When a half wave-length sleeve is used, rigid attachment is made at the displacement node formed at its mid-plane. This is shown in Fig. 5.6(b). Although the present system is designed to operate in the standing wave regime some energy will be transmitted out of the system at the working head causing a travelling wave to move through the wave guide. Under these circumstances, there will be some oscillatory motion in the nodal plane of the transformer. It is therefore appropriate to employ some form of tuned isolating system.

A convenient method in the present case involves the use of a circular disc or flange, tuned to resonate in a flexural node at the design frequency of the longitudinal system[73]. The dimensions of the disc are chosen so that a flexural node is produced at the outer circumference when the inner edge is excited by the axial system to which it is attached. Such a device is normally attached at a motional node to minimise the effects of a change in frequency during operation. The arrangement is illustrated in Fig. 5.6(c).

Even when the above factors are considered in the design of the isolating system, losses can still occur, by the propagation of radial vibrations through the mounting flange. Since a longitudinal displacement node is coincident with a force antinode, under standing wave conditions, maximum transverse strain occurs in this plane, its value being related to the Poisson characteristic of the material. If the dimensions of the mounting flange attached at the nodal plane are such that radial resonance occurs at the operating frequency, then considerable damping of the wave motion will be caused by clamping the plate to a rigid structure. It is therefore important when designing the mounting flange, to ensure that

Fig. 5·6a · Quarter wave isolating sleeve

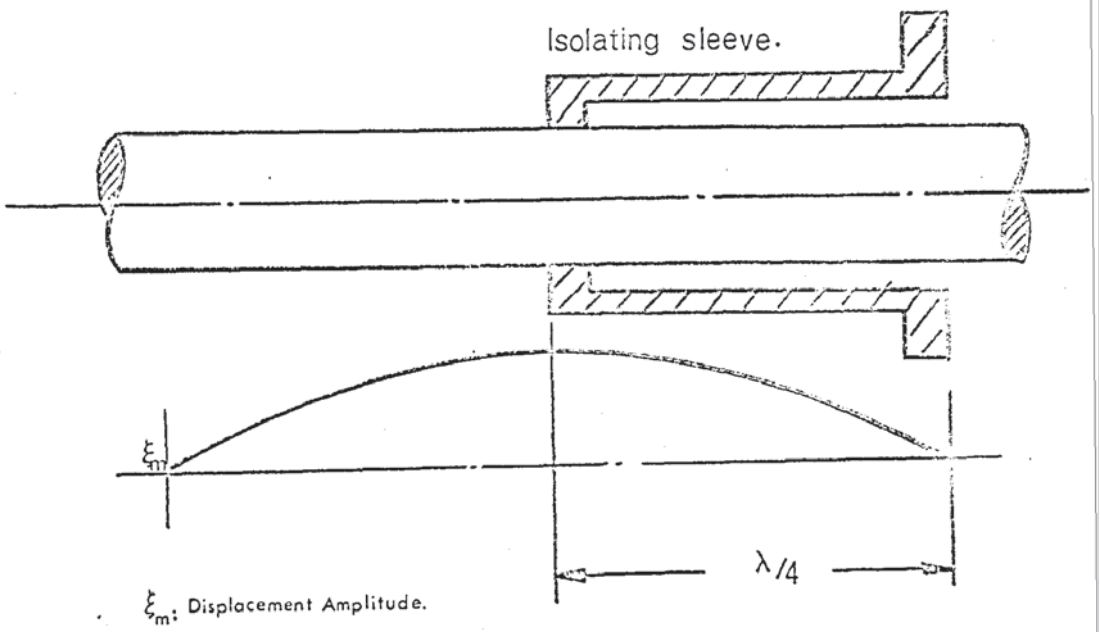

Fig. 5·6b Half wavelength isolating sleeve

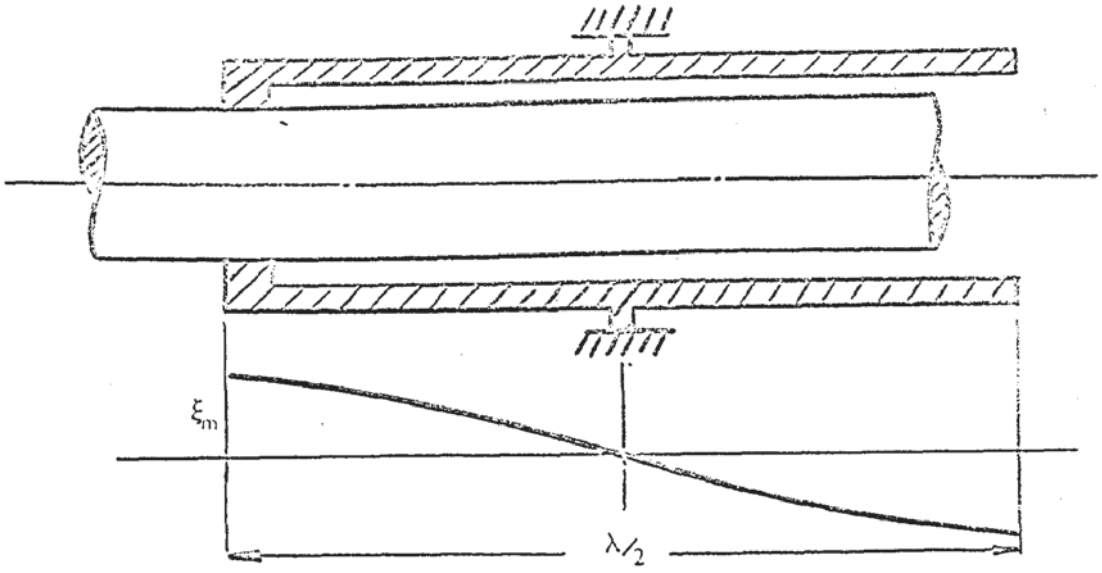

Fig. 5·6c Flexural mode mounting plate.

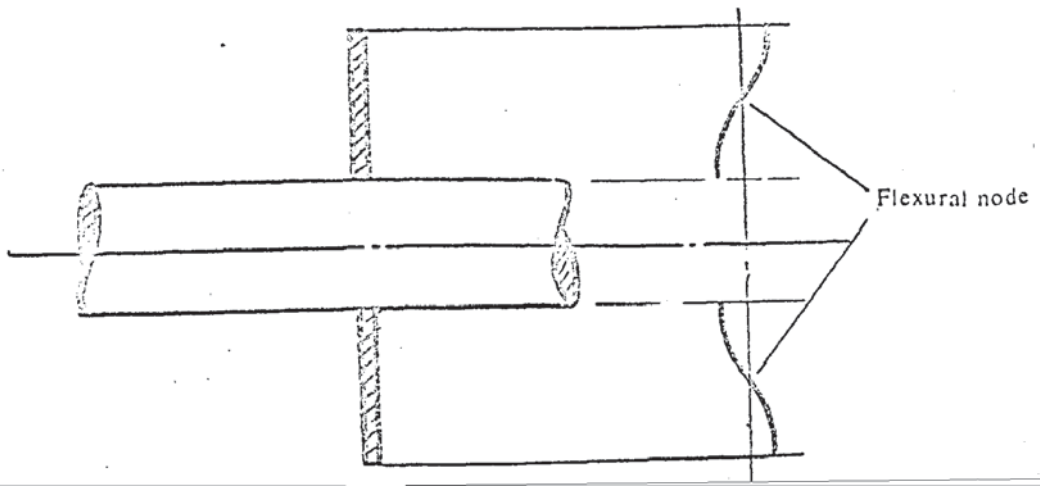

its dimensions are not compatible with radial resonance.

Calculations determining the mounting plate dimensions are given in Appendix IV, where it will be noted that overtone modes are used to ensure that the plate dimensions are compatible with the horn profile at the nodal plane of attachment.

The mounting plate was attached to the conical transformer using a threaded connection and locking plate. This arrangement is shown in Fig. 5.5.

5.2.6 Tuning of the oscillatory systems

The dimensions of the conical transformers were calculated so as to satisfy the requirements for resonance at 13 kHz in the unloaded condition using the relationships derived in section 4.5.1. However, no allowance was made in these calculations for the attachment of the wedge drawing tools, and since each tool represented a marked departure from the calculated horn geometry, it was not possible to incorporate the wedge dies within the tapered profile of the concentrators. The attachment of such a mass constituted a reactive load, having inertial characteristics which resulted in a reduction in the resonant frequency of the loaded system, relative to the unloaded condition and produced a corresponding drop in the motional amplitude along the horn. This feature was related to the change in operating conditions of the transducers which were designed to function within a specific frequency range. In order to restore the optimum resonant conditions it was therefore necessary to tune each system by shortening the concentrator lengths until resonance occurred at the design frequency of 13 kHz, with the wedge tools attached.

The problem of tool attachment has been considered by

several researchers in the field of high intensity ultrasonics (62) and it is apparent that two significant factors influence its effect on the oscillatory characteristics of the waveguide, namely;

(i) the change in wave velocity associated with the differing physical properties of the tool and waveguide materials.

(ii) inertial effects related to the distribution of mass at the end of the waveguide.

In the present case both tools and concentrators were made from the same material which ensured that the wave velocity remained constant in relation to the physical properties of the tools. It also served to minimise the discrepancy in wave impedance between the two components; a sudden change in impedance results in spurious reflections of elastic waves, causing energy absorption and local heating of the waveguide. Provided that the length of the tool is less than $\lambda/4$ (a critical length with associated impedance transformation characteristics), three possible situations relating to this problem have been defined[73];

(i) when the cross-sectional area of the tool is approximately equal to that of the output end of the waveguide.

(ii) when the tool cross-section is much smaller than that of the waveguide, and

(iii) when the mass of the tool is large in relation to that of the waveguide.

In the first case, compensation for the attached tool may be made solely in terms of the wave velocity. Therefore, when tool and concentrator are of the same material, as in the present case, compensation is made by removing from the concentrator a length equal to that of the tool.

In the second case when the tool is short and its cross-sectional area is small, allowance may be made by considering the ratio of the mass per unit length of tool to the mass per unit length of concentrator[73] (computed at a constant diameter equal to the small end dimension). The appropriate correction factor, $d\ell$ is therefore given by the following expression

$$d\ell = \frac{\rho_t S_t}{\rho_c S_c} . h \qquad \text{---------- (5.1)}$$

where ρ is the material density, S the Cross-sectional area and h the tool length. The subscripts 't' and 'c' refer to tool and concentrator respectively.

When the materials are the same, equation 5.1 becomes simply;

$$d\ell = \frac{S_t}{S_c} \; h \qquad \text{---------- (5.2)}$$

This correction is considered appropriate for tools of approximately cylindrical form.

In the third case involving a tool whose mass is large in relation to that of the concentrator, it has been suggested[66] that allowance can be made by removing from the small end of the concentrator a mass equal to that of the tool. However, two criteria have been specified in this case; the length of the tool should not exceed $\lambda/10$ and the mass of the tool should not be greater than $S\rho.\lambda/10$, where ρ is the concentrator material density and S the end face area.

In the present case the tool length was 2.00 in. ($\equiv\frac{2\lambda}{15}$) and the cross section; 1.00 in. x 1.50 in. The tool mass was found by weighing, to be 0.738 lbs. compared with the specified factor, $M = S\rho\lambda/10 = 0.102$ lbs. It was decided therefore to tune the system experimentally by successively removing metal from the small end and noting the resonant frequency of the

concentrator with the tool attached. Resonance could not be achieved at the original length of 9.61 in. determined from equation 4.54, and it was necessary to shorten the concentrator to 7.75 in. when resonance occurred at a frequency of 11.58 kHz. Further decrements were removed until resonance occurred at the design frequency corresponding to a length of 6.935 in. The experimental tuning curve is shown in Fig. 5.7 in which the resonant frequency of the system is plotted against the reduction in length.

The total length of concentrator removed was 2.675 in. which showed poor agreement with the wave velocity criterion, condition (1). The equivalent mass criterion was then considered, by calculating the volume of the frustum removed from the concentrator, to replace the tool mass.

The mass of a frustum is given by the expression:

$$M = \frac{\pi}{3\rho} (R^2 h_2 - R_1^2 h_1) = \frac{\pi}{3\rho} (\tan^2\alpha . h_2^3 - R_1 h_1) \quad \text{----- (5.3)}$$

where R, R_1, h_1 and h_2 are as defined in Fig. 5.8. The value of h_2 was determined by substituting in equation (5.3) the tool mass for m, and the appropriate values of R_1 and h_1 defined by the original concentrator dimensions. The correction factor $d\ell = h_2 - h_1$, calculated by this method was found to be 2.494 in. which corresponded to a resonant frequency of 12.70 kHz. The error involved in making this assumption would therefore have been 2.3 per cent which is within the operating frequency range.

Other systems examined by the author[69] showed good agreement using the equivalent mass criterion and in cases where the tool mass complied with the condition $m/M < 1$ (where $M = S\rho\lambda/10$), the experimental errors in predicting the resonant frequency of the system were less than 1 per cent.

Fig.5·7 Variation of resonant frequency with length removed from concentrator.

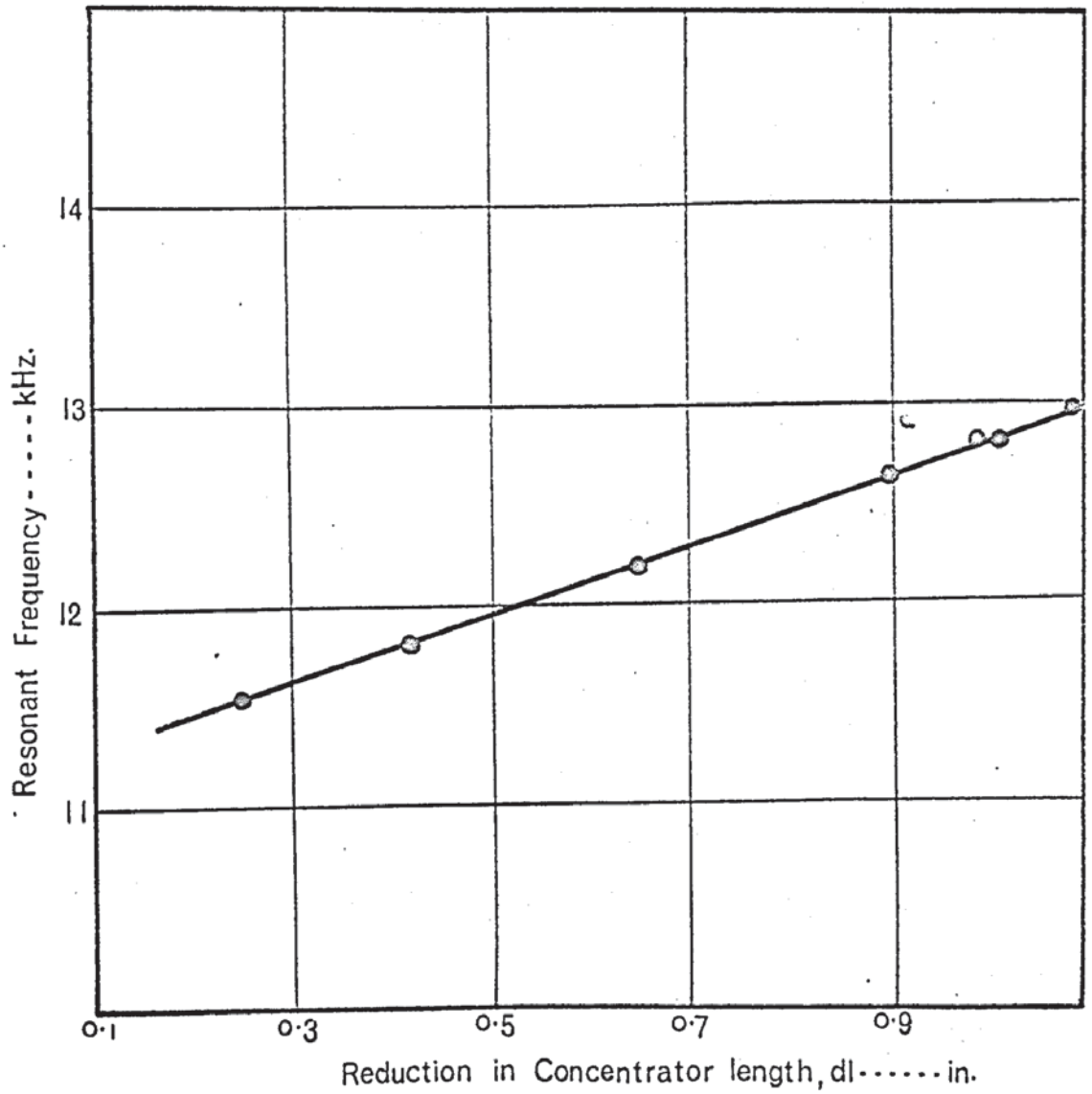

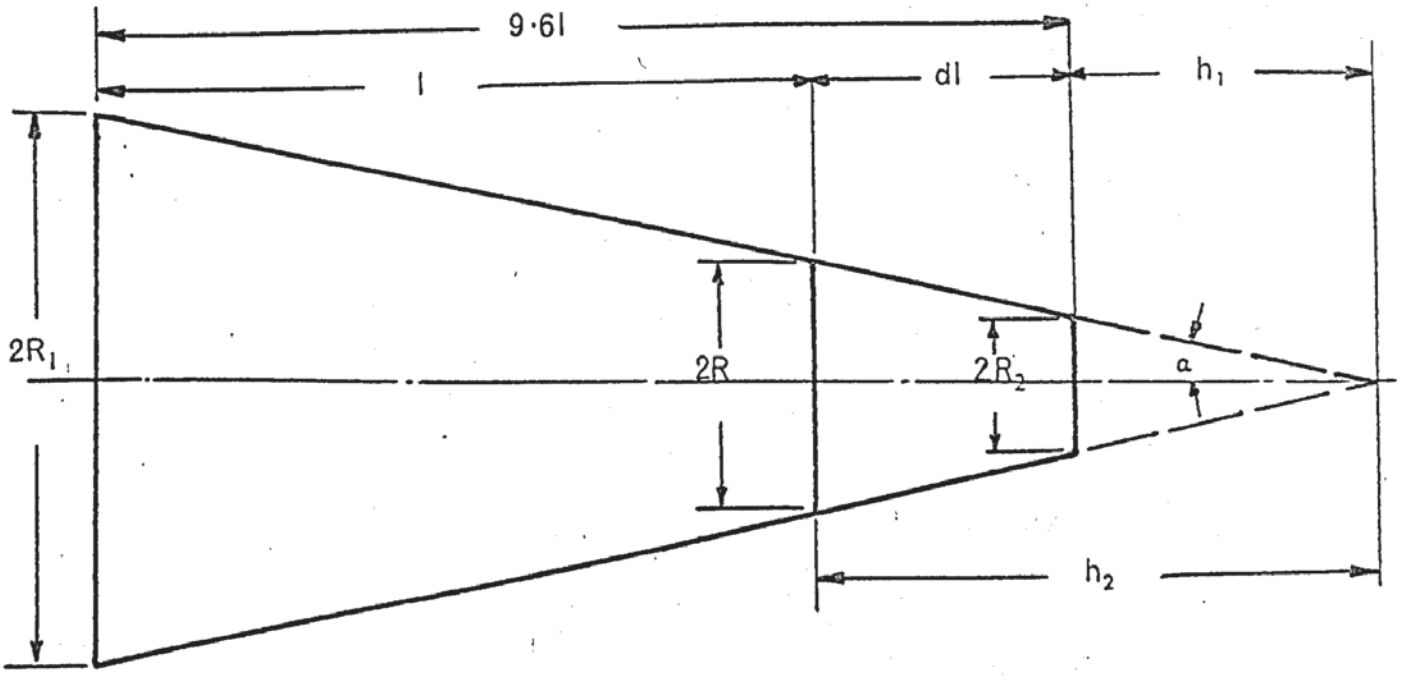

Fig.5·8 Determination of tuning correction for conical concentrator.

The second concentrator was made to the same dimensions as the first leaving 1/8 in. on the length for final tuning adjustments.

The blank holder plates were weighed and found to be within 1.5 per cent of the die weights. On attaching them to the tuned concentrators, a shift in frequency of less than 50 Hz was noted. The experimental data for the tuning procedure is given in table 5.1.

In each case the attachment of wedge dies and blank holders to the concentrators was effected using a threaded stud and to ensure good contact of the mating surfaces, copper washers, cut from annealed 0.005 in. strip, were inserted between the ground faces before fitting.

The final consideration after tuning, was the location of the motional node on each concentrator. This was found using a jockey wire in the form of a circular ring which was allowed to rest freely on the surface of the concentrator. Under resonant conditions the ring moved towards the plane of minimum motion which was then identified as the node. The position of this plane was found to have been displaced towards the 'small' end of the concentrator as a result of the tool attachment, compared with the calculated position for the original conical transformer.

5.3 Design and construction of the wedge drawing tools.

5.3.1 Wedge drawing dies

The dies consisted essentially of a tool steel block with a wedge shaped recess machined into the upper surface, leading at the narrow end to a radiused protrusion, Fig. 5.9. The included wedge angle was 28° and the recess depth 0.125 in. Recesses were machined into the front of the die block (beneath the die radius) into which could be located corres-

Table 5.1 Tuning data for Conical Concentrators.

Reduction in concentrator length, al (in)	Resonator Frequency kHz
0.246	11.56
0.420	11.82
0.648	12.19
0.901	12.62
0.982	12.78
1.011	12.78
1.085	12.96

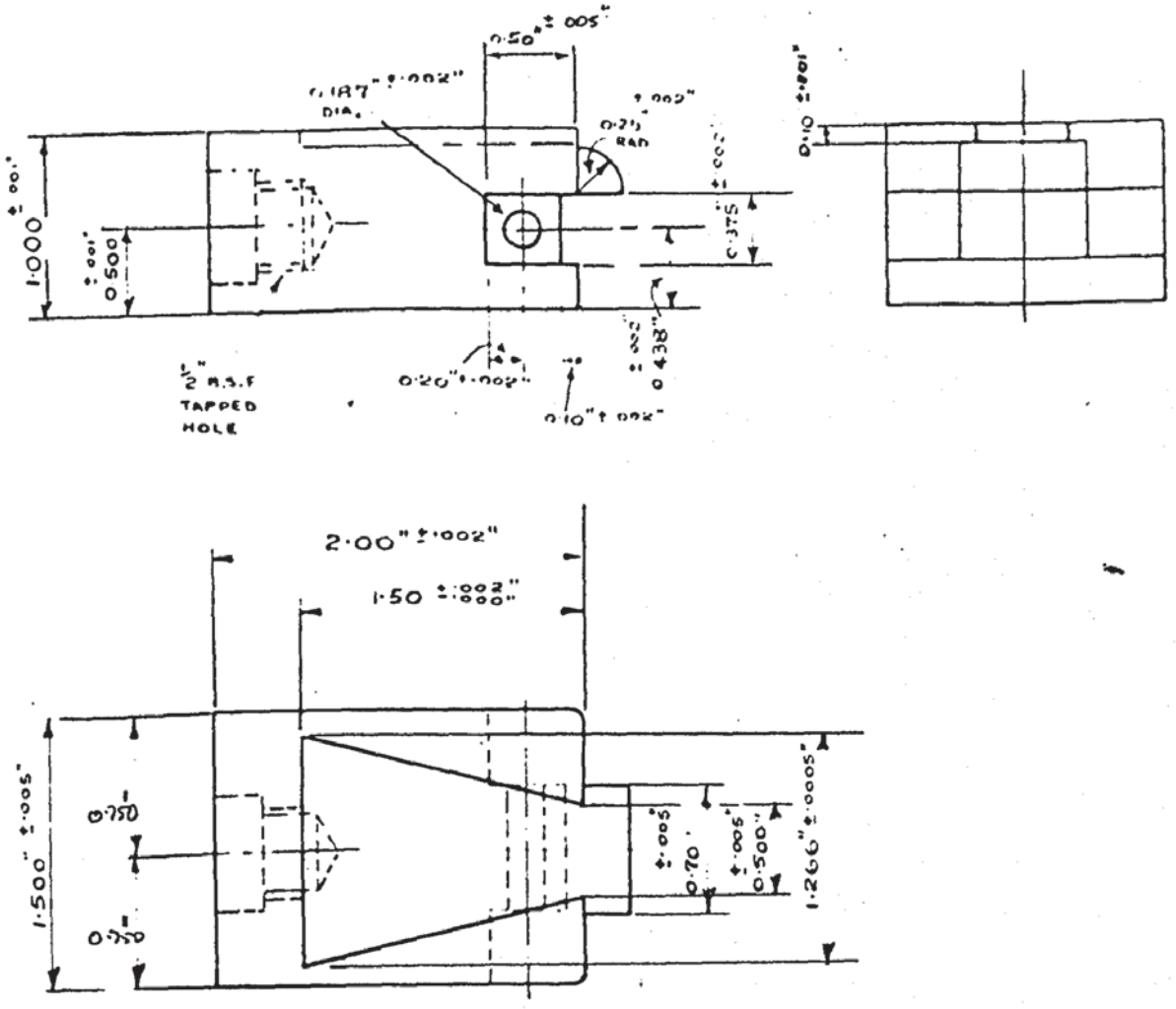

Fig. 5·9 Wedge Drawing Die.

ponding lugs on the friction load cell when operated using activated blank holder plates. The dies were attached to the narrow end of the concentrator using threaded dowels which located into counter-bored and threaded recesses in the dies and transformer end faces. Care was taken to ensure that the axes of the threaded holes in both dies and transformers were perpendicular to the end faces so that good contact was achieved between the mating surfaces. To this end the mating faces were surface ground after heat treatment. The ground surfaces of the wedge profile were finally polished to a 3μin. finish.

5.3.2 Pressure Plates.

The pressure plates were machined from steel blocks of the same overall dimensions as the dies. In the primary operating mode, i.e. with activated dies, they were designed to 'float' on top of the wedge test piece, being held apart by the friction load cell located between them, figs. 5.10 and 5.14. The machining tolerances ensured that sufficient clearance existed between the adjacent edges of the corresponding wedge profiles, to allow.005. in. relative axial motion of the die and blank holders before interference occurred between the respective wedge surfaces. Accurate location of the blank holder plates was finally achieved by adjusting the concentrator mounting saddles with the friction load cell in position. Any greater clearance was considered likely to lead to extrusion of the blank between the adjacent edges of each pair of tools. The blank holder plates were designed to be interchangeable with the dies so that either pair of tools could be vibrated. Attachment holes were therefore located in the rear end faces of the blank holders corresponding to those in the dies.

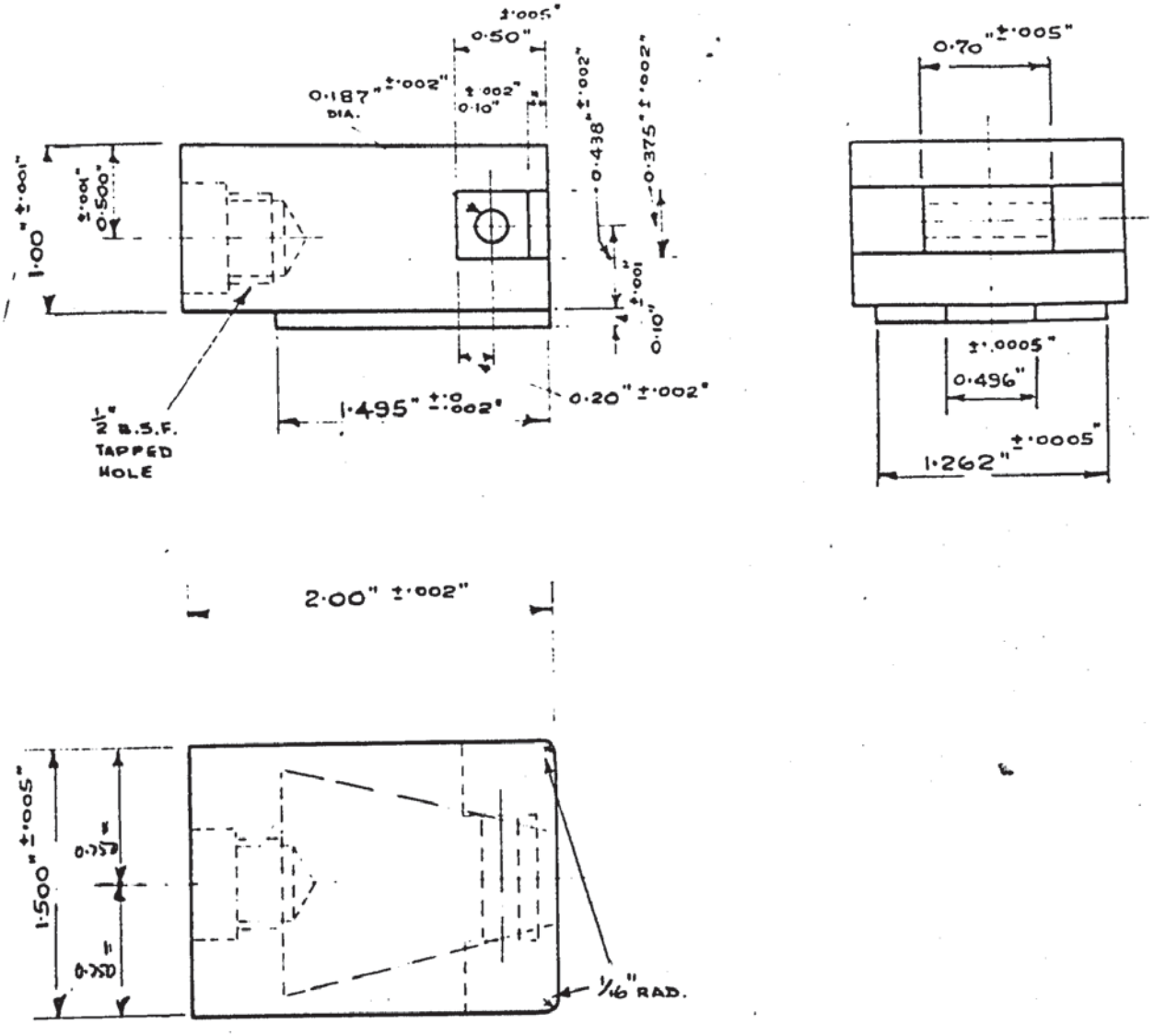

Fig. 5·10 Pressure Plate.

Die and pressure plate blanks were machined from the same annealed bar stock as the conical transformers, the dimension being left .001 in oversize to allow for final surface grinding after heat treatment.

The tools were case hardened in a cyanide bath to a hardness of 54/56 Rockwell C. Details of the heat treatment and material specification are given in Appendix III.

5.4 Hydraulic Blank Holder Assembly.

5.4.1 General description.

The load was applied to each blank holder plate by two hydraulic cylinders situated symmetrically over the die blocks and connected via a common line to a hydraulic pump unit. The general disposition of the blank holder assembly is indicated in Fig. 5.11 where it will be seen that the cylinders are located in a flat plate supported by plane vertical members welded to the base of the sub-press. The lower surface of each die is supported on a cylindrical thrust block fitted with a continuous track "Tychaway" roller bearing.

Details of the blank holder assembly are shown in Figs. 5.11 and 5.12. Each cylinder body incorporated a hollow cylindrical section surmounted by a mounting flange which was located in the upper supporting plate. The reduced sections formed load cells on which were mounted strain gauge bridges. To avoid tilting of the pistons during drawing, each piston was attached to a rigid beam passing over the two pairs of wedge tools.

This beam was subjected to a gradually increasing bending moment as the test piece was drawn through the wedge dies. It was therefore made sufficiently rigid to reduce the deflection at its ends to negligible proportions. The thrust was transmitted to the blank holder plates through specially

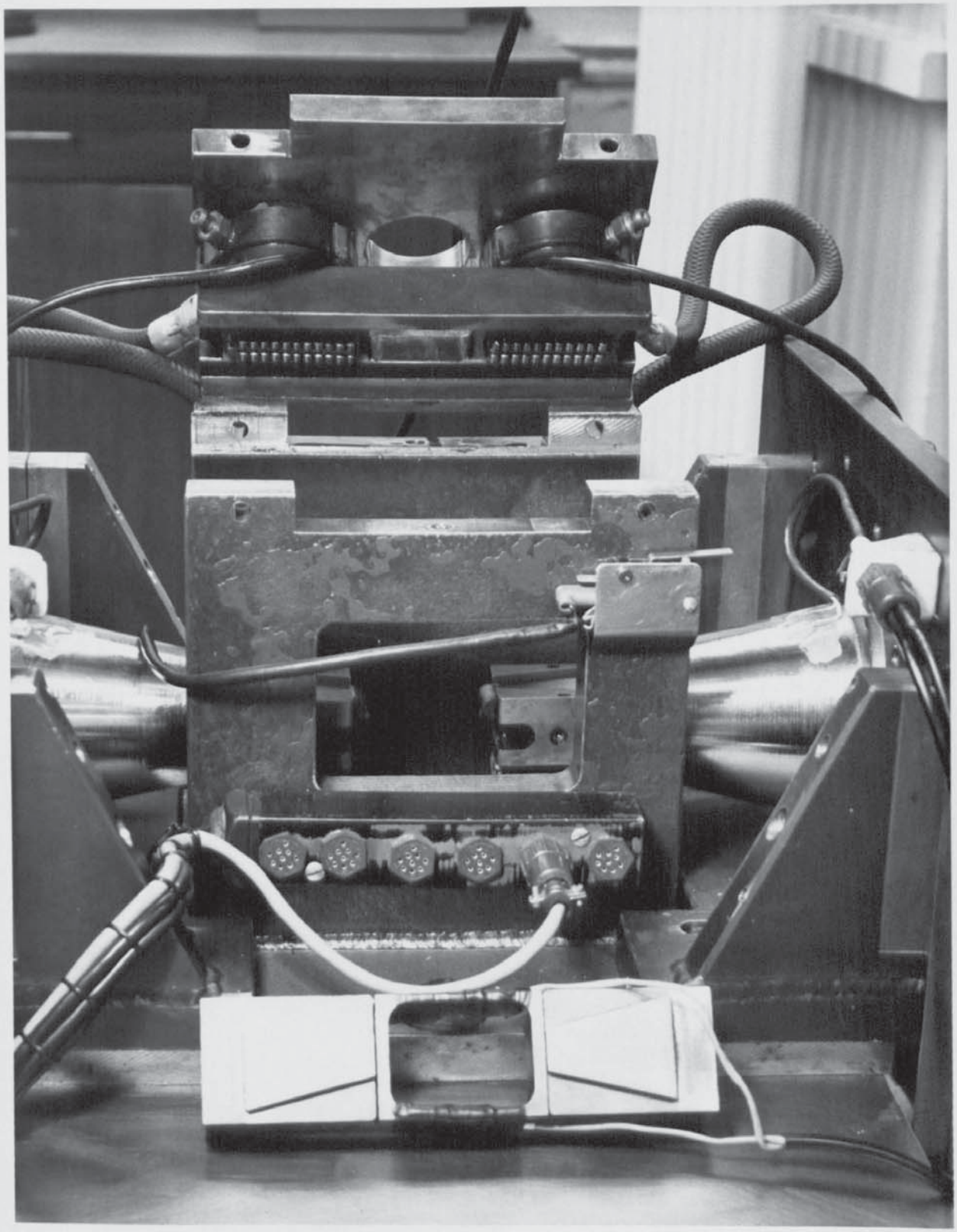

Fig. 5.11 Blank holder assembly

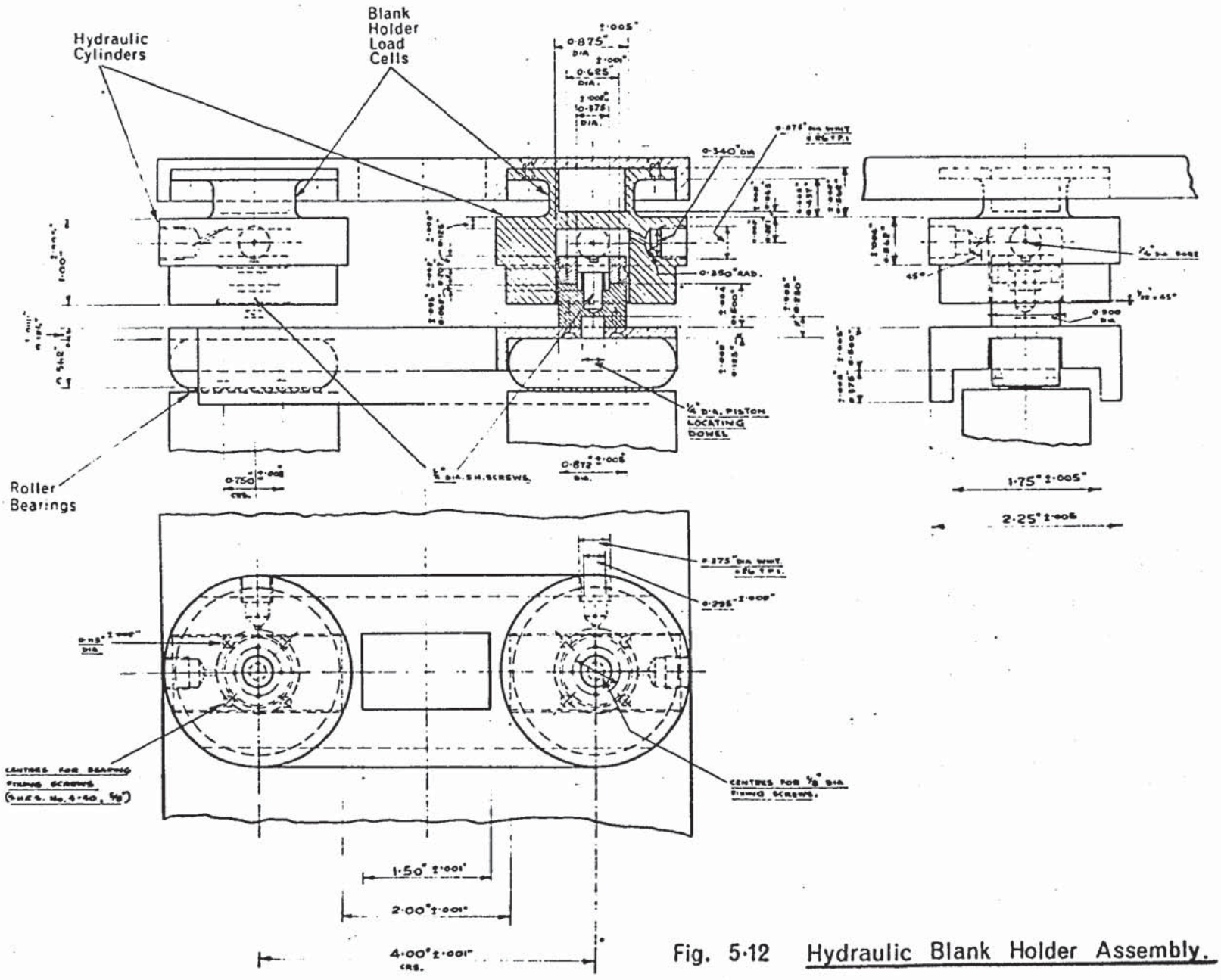

Fig. 5·12 Hydraulic Blank Holder Assembly.

designed roller bearings which were fitted to the underside of the beam at each end. These bearings were incorporated to minimise the degree of acoustic coupling and to reduce the frictional drag on the upper surface of the blank holder plate. The design of the bearings will be discussed in section 5.5 dealing with the friction load cell.

All of the components for the hydraulic blank holder assembly were manufactured in p552 alloy steel. Details of the heat treatments and surface finish are given in Appendix III.

5.4.2 Blank holder load cells.

The blank holder load cells incorporated in each of the cylinder bodies are shown in Fig. 5.12. They consisted essentially of hollow cylinders situated between the mounting flange and main cylinder body of each unit. The inner and outer radii were chosen to give a cross sectional area consistent with a maximum strain requirement of 0.01% for a blank holder load of 1000 lbf which was the maximum load attainable. Eight 120 ohm foil gauges were mounted as shown in Fig. 5.13(a) using "Araldite" epoxy resin to attach them. Four gauges were aligned axially and four circumferentially, taking careto position them symmetrically at 45° intervals, thus ensuring full compensation for bending due to possible non-axial loading. The use of transverse and axial gauges mounted consecutively gave maximum sensitivity and also provided satisfactory temperature compensation when appropriately connected. After allowing 24 hours for the cement to cure at room temperature the continuity and resistance to earth of each gauge was checked before wiring the bridge using the circuit shown in Fig. 5.13b. At this stage, the resistance to earth of the bridge was again checked before

Fig. 5·13 Blank holder load cells :- Bridge details.

(a) Positions of strain gauges on the cylindrical column.

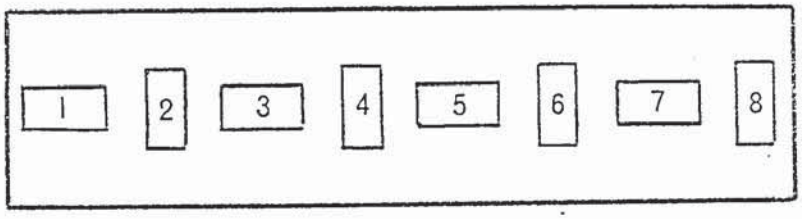

(b) Bridge circuit.

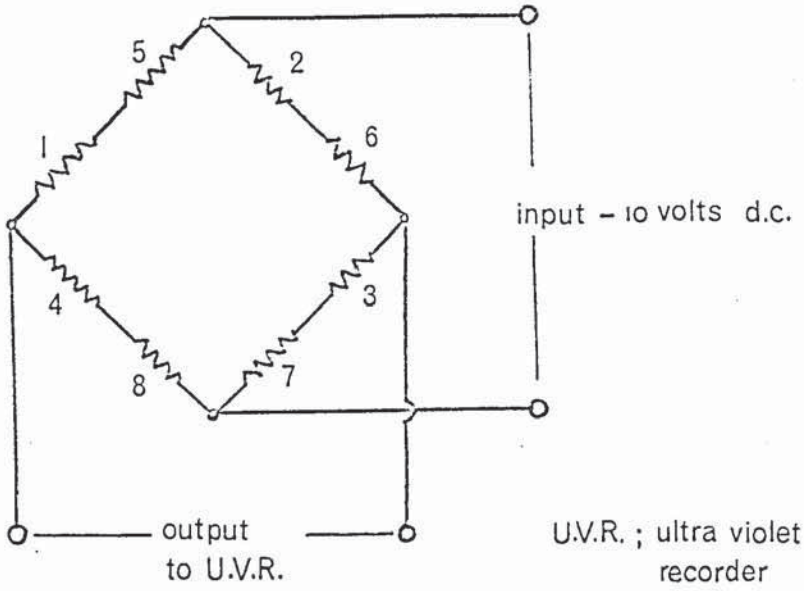

Fig. 5·15 Friction Load Cell:- Bridge details.

(a) Positions of gauges.

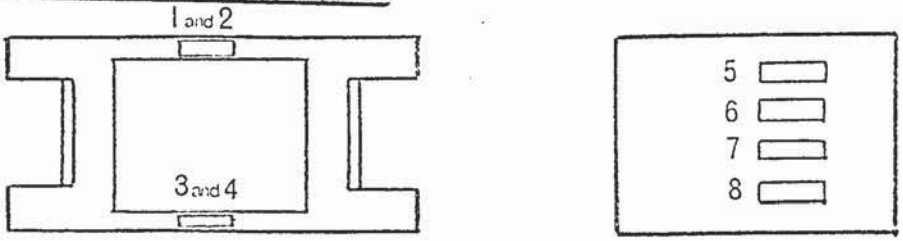

(b) Bridge circuit.

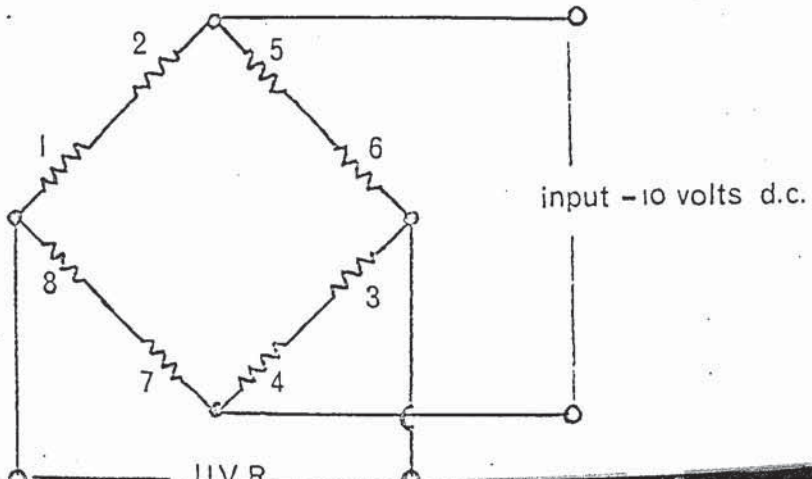

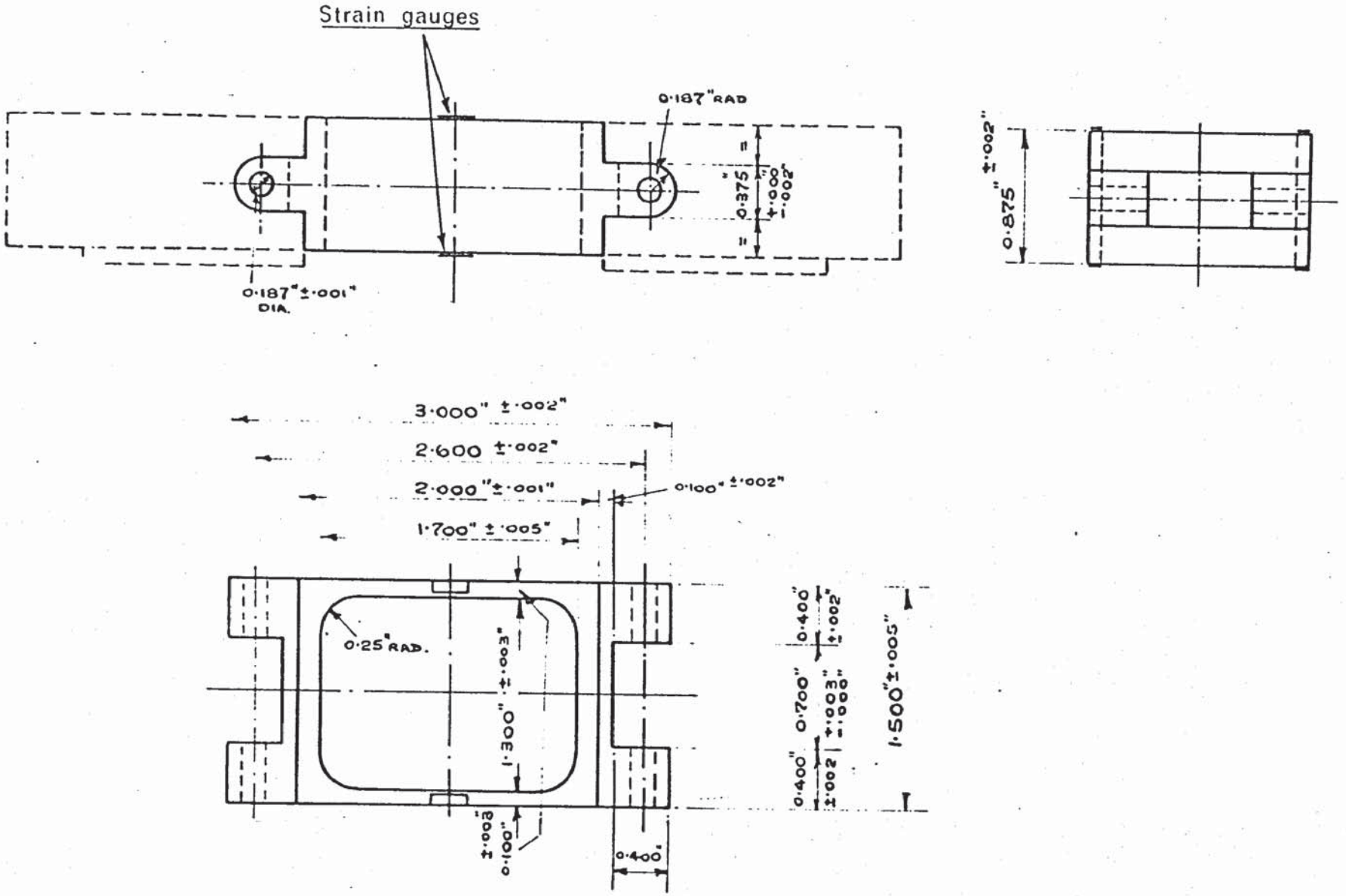

Fig. 5·14 Friction Load Cell.

applying a coating of di-gel to waterproof the instrument. The insulation test indicated a resistance of greater than 10 Mohm which was considered to be satisfactory.

5.5 Design and Construction of the Friction Load Cell

5.5.1 Mechanical aspects.

The purpose of the load cell was to measure the friction force acting at the interface between the test piece and the blank holder plates. By placing between the pressure plates a suitable mechanical link, it was considered possible to measure the compressive force induced in it by the mutually opposed friction forces associated with the deforming ends of the test piece. The link was also designed to locate the blank holder plates so that no contact occurred between the corresponding edges of the blank holder and die wedge profiles, during drawing. In principle therefore, the pressure plates and link formed a single unit which 'floated' on the upper surface of the testpiece in such a way that the load cell was subjected only to a compressive strain. In order to ensure that this was the case, the coupling between the blank holder plates and load cell and also the method of applying the hold down pressure were designed to eliminate bending, as far as possible.

The basic design of the load cell is shown in Fig. 5.14. It will be seen that the load cell is essentially a hollow rectangular cylinder with radiused lugs protruding from each corner. The lugs were designed to locate in equivalent recesses machined into both blank holder and die tools. In the original load cell design the depth of the side members did not exceed the lug height which made it possible to insert the link between either the dies or blank holder plates according to which pair of tools the vibrators were attached.

This design also made provision for pinning the tools to the load cell by inserting 3/16 in. dowels through the drilled lugs and body of each tool. It was found however, that significant bending stresses were induced in the load cell using this arrangement. This problem was overcome by introducing three modifications;

(i) increasing the depth of the side members from 0.375 in. to 0.875 in.

(ii) providing a clearance around the upper and lower lug surfaces to permit ± 0.020 in. vertical movement of the blank holder plate ends relative to the load cell.

(iii) modification of the roller thrust races attached to the underside of the cross beam, carrying the hydraulic cylinders, so that the line of contact of the inner rollers was close to the end of the upper surface of each blank holder. This is shown in Fig. 5.11.

The net effect of these alterations was to permit the blank holder plates to tilt slightly as the test piece ends were drawn past the mid-plane, without transmitting a bending moment to the central link. Any slight deflection of the pressure plates from the horizontal plane resulted in the load being applied at the inner end of the blank holder plates by virtue of the design and location of the roller bearings. Under these circumstances no further deflection of the plates could occur until the test piece reached the die exit plane.

5.5.2 Strain Gauge Bridge.

The compressive strain induced on the link was measured by attaching four identical 120 ohm foil gauges to the upper and lower surfaces of the side members, as shown in Fig. 5.14. The gauges were located symmetrically and connected so as to provide full bending compensation. It was considered that this

could be more readily achieved with the indicated gauge positions than by attaching these at the neutral axes of the link, which would have required much greater accuracy in locating each gauge, in order to reduce bending sensitivity. The gauges on each side of the link were connected in series and formed the active arms of the bridge, see Fig. 5.15. The remaining two arms were provided by four 'dummy' gauges mounted on a separate piece of steel bar of similar section and thermal mass to that of the link. This unit is shown in Fig. 5.16 together with the blank holder plates and completed load cell.

The external instrumentation used in conjunction with this load cell is considered in Appendix V.

5.5.3 Master load cell.

In order to ensure accurate calibration of the friction load cell it was concluded that this should be carried out under loading conditions which closely represented those experienced in operation. This was achieved by constructing a special load cell which in effect replaced the test piece. The design of this instrument is shown in Fig. 5.17. It consisted essentially of two parallel strips of hardened steel with integral cylindrical ends, threaded in the opposite sense, and a hollow sleeve screw cut internally with left and right hand threads at opposite ends, into which the plates were screwed. A hollow cylindrical portion, serving as the gauge length of a load cell, was incorporated in one half of the unit. This device was then inserted beneath the hydraulic blank holder assembly with the blank holder plates, connected to the friction load cell, resting on the upper surfaces of the parallel strips whose lower surfaces were supported by the continuous track roller bearings, mounted in the die

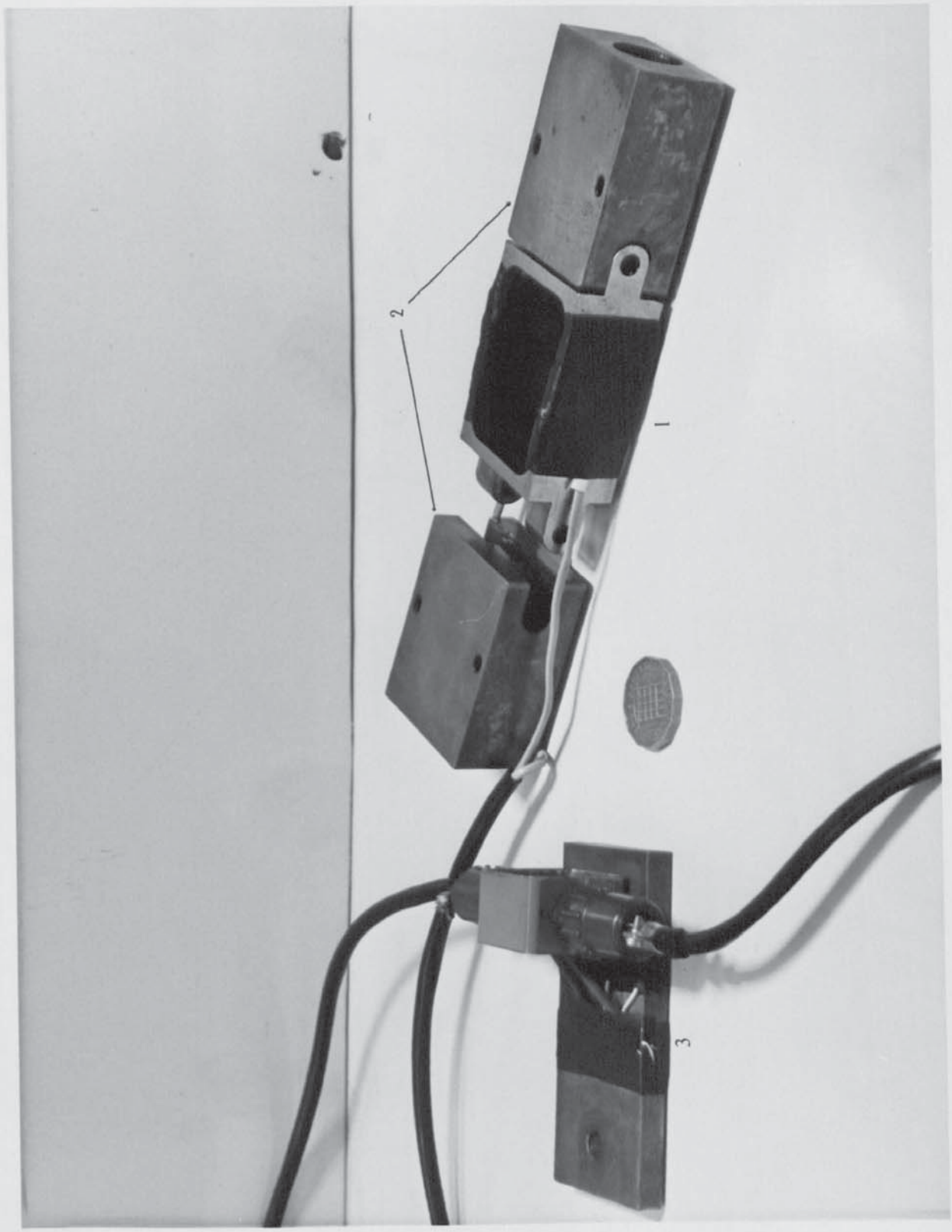

Fig. 5.16 Friction load cell (1) with blank holder plates (2) and 'dummy' gauges.(3)

Fig. 5.17 Master load cell.

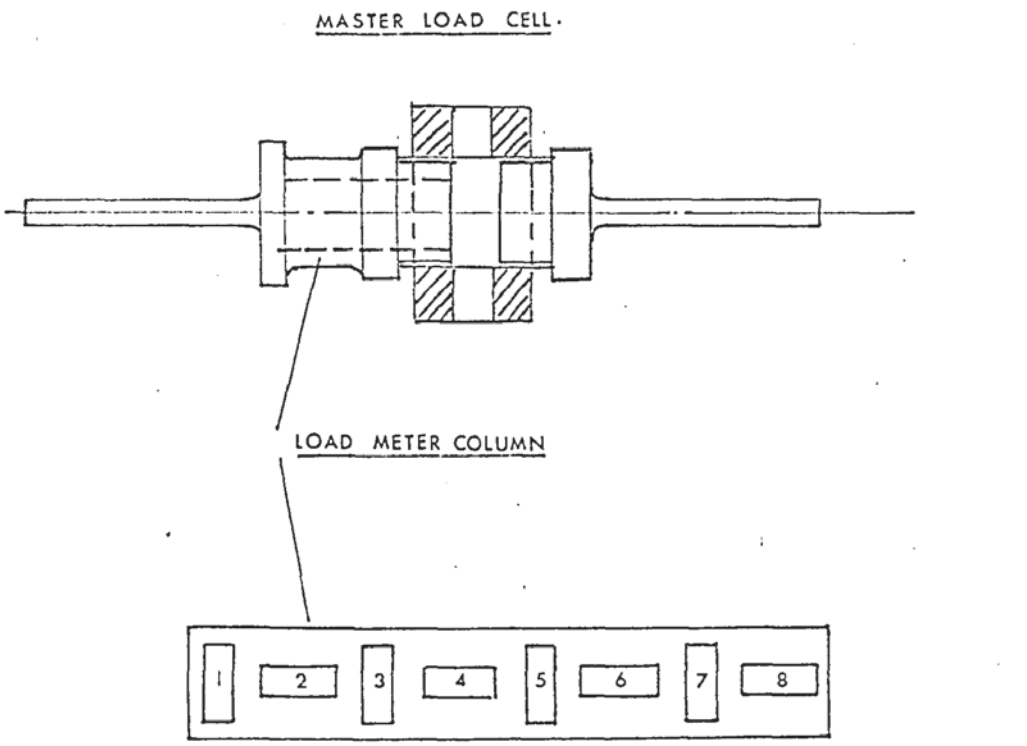

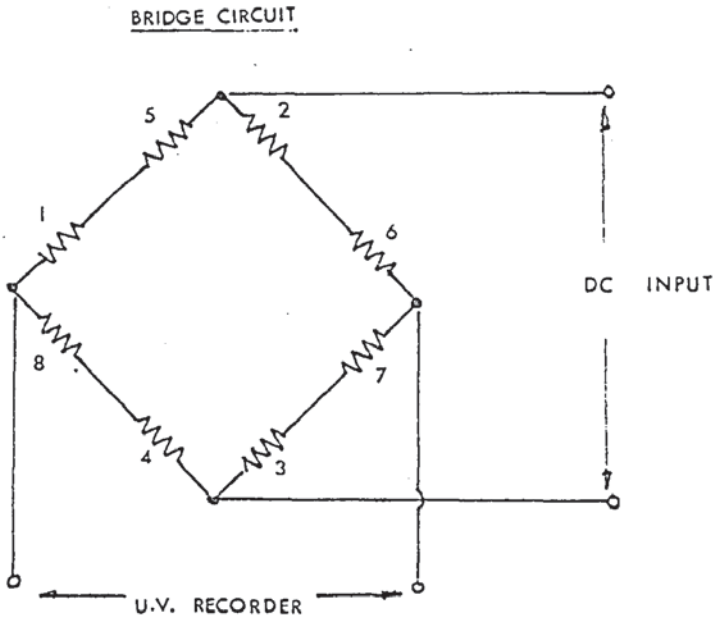

Fig. 5.18b Details of master load cell bridge.

thrust blocks, Fig. 5.18a. By rotating the cylindrical threaded sleeve in a clockwise or anticlockwise direction, the hardened steel ends could either be drawn together or moved apart. When a load was applied to the blank holder plates, rotation of the sleeve induced either a compressive or tensile stress in the cylindrical link, which represented the frictional force acting between pressure plates and steel strips. This in turn was directly related to the force transmitted to the friction load cell held between the blank holder plates. The load induced in the cylindrical link was measured by a strain gauge bridge consisting of 8, 120 ohm matched foil gauges mounted as shown in Fig. 5.18b. The bridge circuit and gauge connections were the same as used for the blank holder load cells - Fig. 5.13, and were designed as before, to give full compensation for bending and temperature variation. However, the method of loading and design of the 'master' load cell, in particular the thickness of the parallel plates, ensured that bending couples were minimised.

5.6 Punch and punch load-cell assembly.

The punch, with its integral load cell and mounting ring, was manufactured from P552 steel to the drawing shown in Fig. 5.19. The lower portion of the punch was made detachable to permit the use of various width tools and so accommodate different gauges of test piece material. No attempt was made in the original design of the punch assembly to consider acoustic tuning effects and the overall length of the system was therefore chosen arbitrarily from this viewpoint. The punch assembly was mounted on a rigid cylinder which in turn was firmly bolted to the fixed cross head of the testing

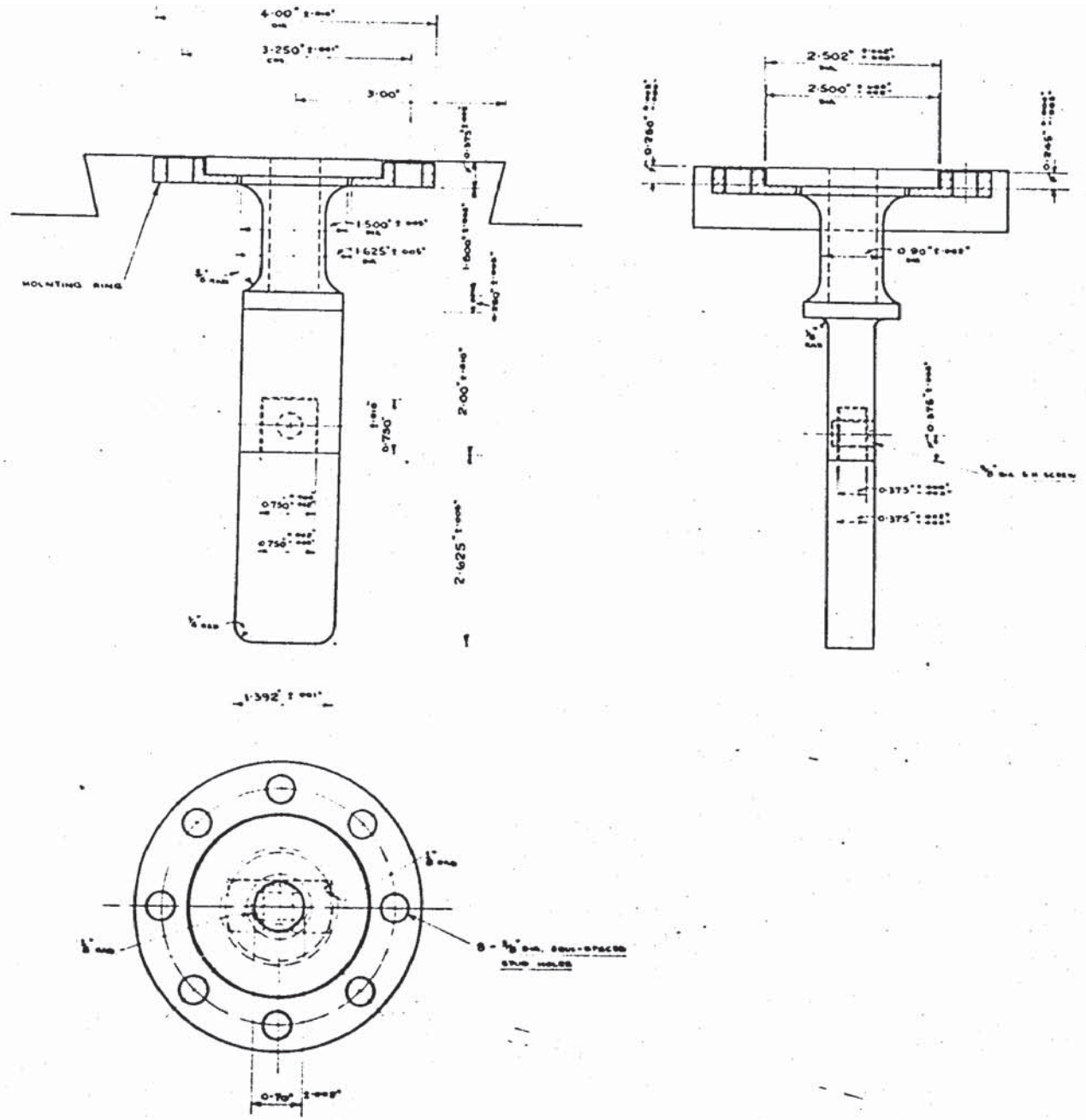

Fig. 5·19 PUNCH ASSEMBLY AND MOUNTING RING

machine, Fig. 5.1. The load cell was once again based on a hollow cylindrical section to which were attached eight 120 ohm foil gauges in a similar manner to that previously described. The dimensions of the loadcell were largely determined by the scale of the test piece and hence the general tool geometry. However, the cross sectional area of the load cell element was made appropriate to the required sensitivity, by calculating the maximum load based on the breaking stress of an aluminium wedge test piece.

The instrumentation used in conjunction with the punch load cell and each of the other load meters considered in this section will be described in Appendix V.

5.7. Instrumentation

The instrumentation employed on the oscillatory wedge drawing apparatus is summarised in the block diagram shown in Fig. 5.20. Details of oscilloscopes, AC millivoltmeter, DC power packs etc. are given in Appendix V, Table A.5.1, together with a brief description of function and associated circuitry in each case. A list of the galvanometers used in the ultraviolet recorder is given in Appendix V, Table A.5.2.

5.7.1 Load measurement

Each load cell formed a bridge circuit requiring an input voltage which was applied across two opposite corners. The out of balance condition produced a signal which was monitored across the remaining corners of the bridge. A stabilised DC voltage supply, variable between 0 and 30 volts and with a meter display, was used as the common input source to the blank holder, friction and punch load cells. A separate supply was used for the master friction load cell which was required only during calibration. The output from each of the strain

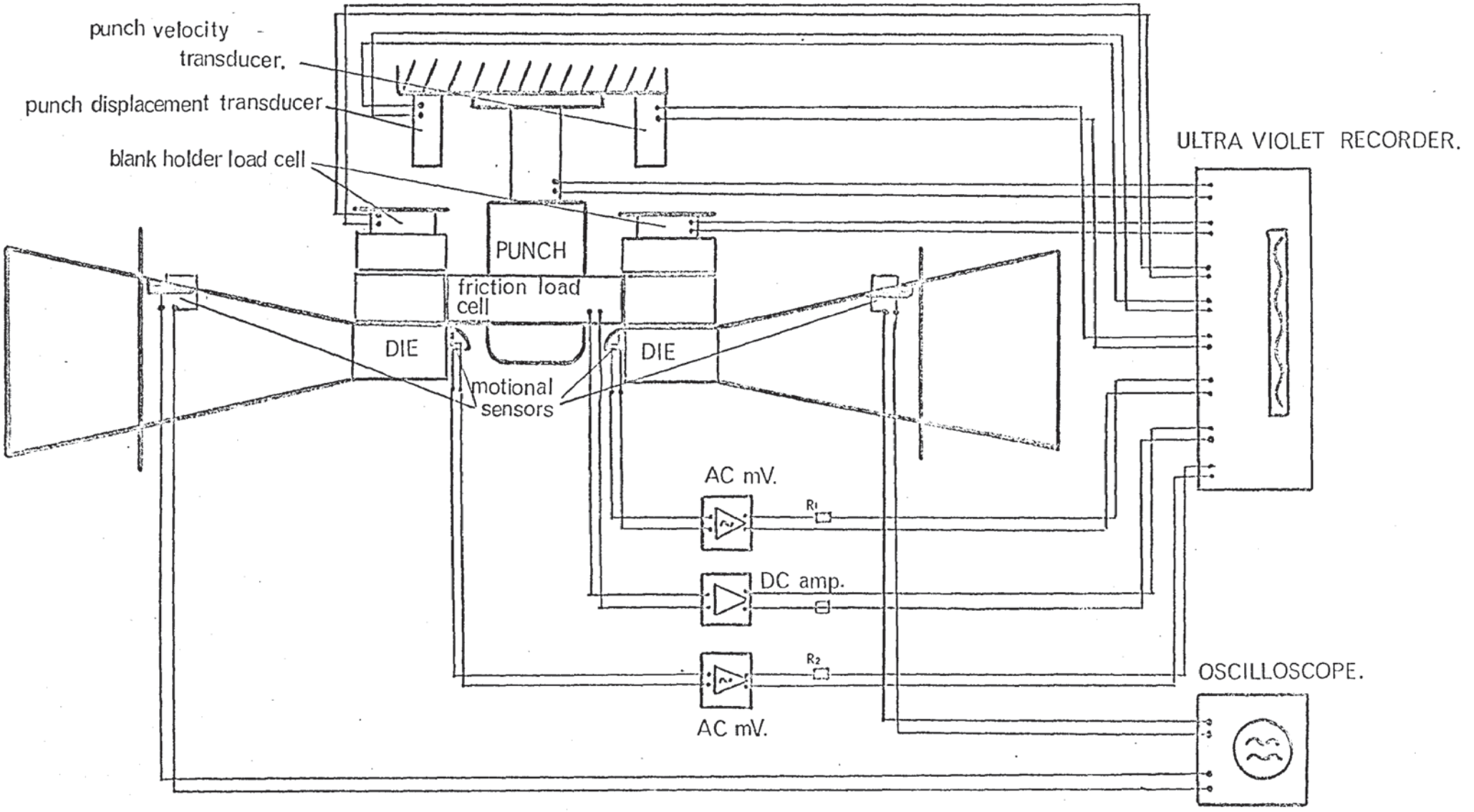

Fig. 5·20 Instrumentation for oscillatory wedge drawing sub-press.

gauge bridges was ultimately connected to a galvanometer of appropriate sensitivity, in an ultra-violet recorder. However an essential preliminary involved matching the resistance of the bridge arms in the unloaded condition, so that a state of electrical balance was achieved, giving zero output voltage. This was done by connecting a potentiometer between one of the output 'corners' of the bridge and either the positive or negative input terminal. The correct value of resistance and its appropriate location were simply found by experiment using a spot galvanometer with variable sensitivity in place of the galvanometer in the U/V recorder. This technique was applied to each load cell bridge in turn and the correct value of potentiometer determined in each case. It was desirable to replace a certain proportion of the potentiometer balancing resistance by a fixed resistance in order to increase the sensitivity of the final balancing control. The circuit diagram for the five load meter bridges is shown in Fig. 5.21. It was necessary in the case of the friction and 'master' load cells, to amplify the bridge output voltage in order to achieve the required sensitivity. This was done using a Southern Instruments 4 channel DC amplifier, type M1266. It should be appreciated that the load cells described were intended to measure only direct stresses and no attempt was made at this stage to monitor oscillatory stresses. The frequency response of the galvanometers and amplifiers was therefore not critical beyond the requirement to follow the normal load cycle associated with this deformation process. However, the amplifier gain characteristics were linear between 1.0 and 100 kHz which made them suitable for the ultrasonic stress measurements subsequently considered.

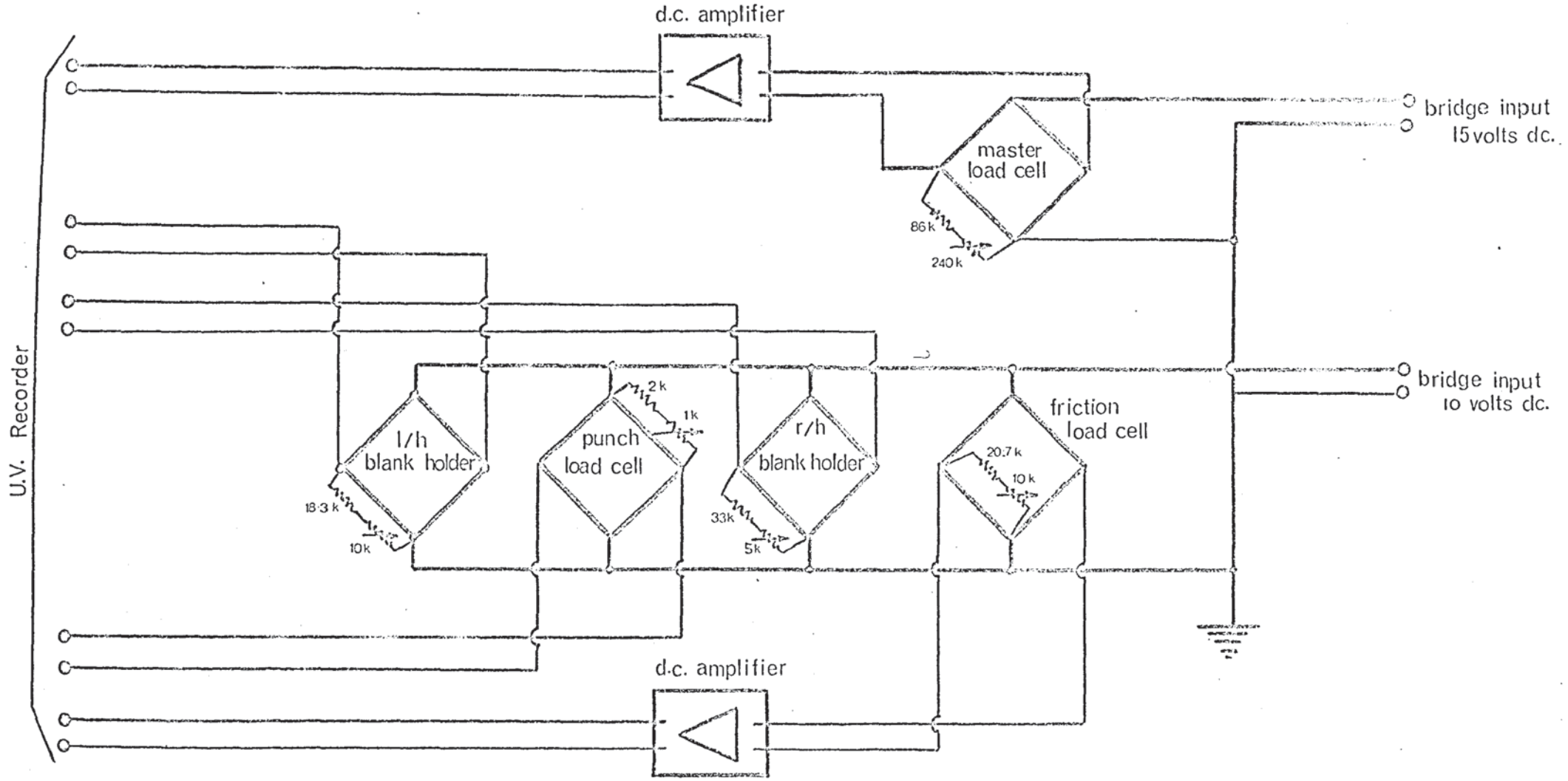

Fig. 5·21 Load Meter Circuits.

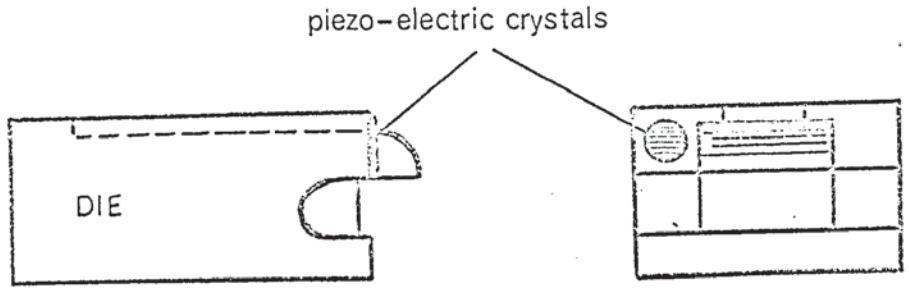

Fig. 5·22 Location of die amplitude sensors.

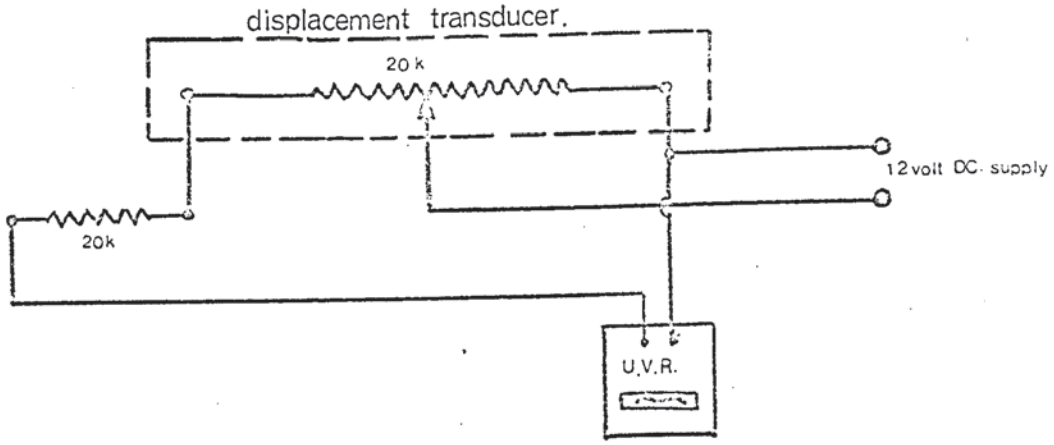

Fig. 5·23 Punch displacement transducer circuit.

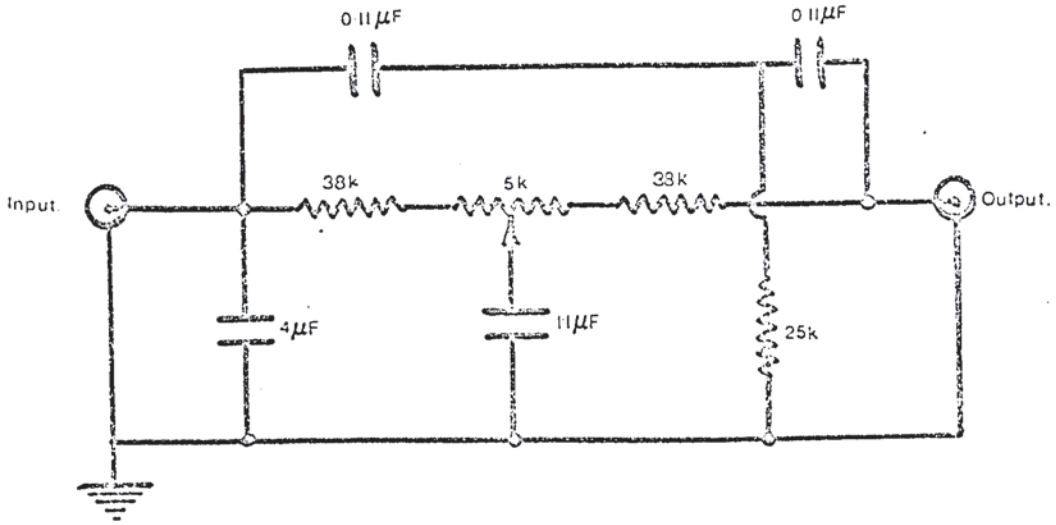

Fig. 5·24 Filter circuit for punch velocity transducer.

5.7.2 Die Motional Amplitude Sensors

One of the most important oscillatory parameters was the displacement amplitude of the wedge dies. This was measured by piezo-electric crystals which were cemented, using an epoxy-resin, to the end face of each tool as shown in Fig. 5.22. The crystals used were Mullard type PXE5 No. MB1048, which were axially polarised discs of 10 mm dia x 1 mm thick, with plane silvered surfaces forming the two electrodes. The crystals responded to an axial strain which induced a proportional potential difference between the two plane surfaces. In practice, the strain may be produced directly by attaching the crystal to a mechanical element which is subjected to an elastic deformation or it may result from the inertial forces associated with high acceleration or deceleration rates experienced by the crystal. In the present mounting location the latter case applied. Crystals were originally mounted parallel to the transformer surface, adjacent to the displacement node, which presented a region of maximum oscillatory strain. However, the output voltage was found to vary non-linearly with the die amplitude (measured optically). This was considered to be due to shear strains associated with the amplitude variation along the transformer surface and consequently the alternative method of attachment was considered. Although this proved to be less sensitive, the crystal voltage/displacement relationship was linear. The original crystals mounted adjacent to the nodal plane of each concentrator were used to give a visual display of the oscillatory amplitude on a dual trace oscilloscope. However, in addition to this it was considered essential to devise a system for continuously monitoring the output from the die mounted crystals. In order to correlate the process forces

and oscillatory parameters the output from each load cell and transducer should ideally be linked by appropriate circuitry to the U/V recorder so that all the data would then be available on a single trace.

Under operating conditions the crystal output was a sinusoidal voltage with a frequency close to 13 kHz. This frequency was beyond the range of available galvanometers and it was therefore necessary to consider only amplitudinal displacements, or some proportional signal. It was concluded that owing to the sinusoidal wave form of the crystal output it would be appropriate to consider the root mean square voltage, derived by rectifying this signal. This was conveniently achieved using an AC millivoltmeter made by Advance Electronics (Model VM 78). The instrument in question had 12 ranges covering 1mV f.s.d. to 300 V f.s.d. with attenuator and amplifier circuits designed to give a flat frequency response from 1 Hz to 1 MHz. The output from the amplifier fed a meter via a rectifier circuit and it was therefore a simple matter to take the RMS output from the meter terminals and feed it through a suitable matching circuit, to a galvanometer in the U.V. recorder. This arrangement is shown in the block diagram given in Fig. 5.20. The value of the series resistance, R affected not only the sensitivity of the galvanometer but also the response time of the output circuit. A compromise was therefore reached which permitted accurate monitoring of amplitude fluctuations throughout the testing cycle. This system was duplicated to provide amplitude data on both concentrators.

5.7.3. Punch Displacement Transducer

It was required to monitor the punch travel over a displacement of up to 2.0 in. This was achieved using a linear potentiometric transducer which consisted of a uniformly wound

resistance coil of 20 kohm and a concentric spring loaded slider attached to a 1/16 in. diameter rod. The body of the instrument was fastened by a suitable clamp to the rear vertical support member of the sub-press and the slider was activated by a spring loaded rod mounted on the punch support column. Spring loading was necessary to accommodate punch displacements beyond the anticipated depth of draw, which were outside the range of the transducer. The spring stiffness was such that depression of the thrust rod did not occur until the limit of the transducer travel was reached. The positions of transducer and thrust assembly were adjusted so that initial contact coincided with the onset of drawing; that is, at the first contact between punch and test piece.

The input to the transducer was provided by a stabilised DC supply which was adjusted to 12 volts. Leads were then taken from either end of the potentiometer and connected via a 20 K.ohm resister to a galvanometer in the U/V recorder. The purpose of the fixed resister was to prevent overloading the galvanometer at the lower limit of the potentiometer resistance. Details of the circuit are shown in Fig. 5.23.

5.7.4 Punch velocity transducer

The punch velocity was monitored using a Hewlett Packard linear velocity transducer Model 6LV2, which gave a DC voltage output proportional to the linear velocity. The unit consisted of a high coercive force permanent magnet core which induced a DC voltage while moving concentrically within shielded coils. The coils and housing were mounted on the sub-press support frame and the case attached by a threaded connector to a nimonic rod, of similar cross section, which was screwed into the fixed crosshead of the testing machine - Fig. 5.1. The length of the mounting rod was chosen so that the drawing displacement could

be accommodated within the working stroke of the transducer, which was 2.0 in..

The output from the transducer was taken directly to a galvanometer in the U/V recorder. Under operating conditions however, it was found that a significant alternating voltage component was superimposed on the DC signal from the transducer. Investigation showed this to be a function of the testing machine hydraulic unit and it was concluded that it would be necessary to filter the electrical signal in order to minimise the effect of the small velocity variations on the recorder trace. The hydraulic pulses were not considered likely to produce any significant mechanical effects in the proposed deformation process.

A Muirhead tunable filter was used to remove the alternating signal component. Adjustments of the filter controls were made until the required degree of attenuation was obtained. The final circuit was then noted and a separate filter constructed. Details of this circuit are given in Fig. 5.24.

5.8 Calibration of Instrumentation

Full details of instrument calibration are given in Appendix V. This describes the procedure carried out for each of the load cells, the punch velocity and displacement transducers and the displacement sensors. Calibration curves are given in each case.

5.9 Determination of the Progressive rim Velocity

A knowledge of the relative motion of the test piece and punch was considered essential to an understanding of the mechanics of the oscillatory wedge test. It was therefore necessary to determine the relationship between the punch velocity and test piece motion through the wedge drawing dies. Clearly, at any instant in the drawing cycle, the radial velocity of

each element of the test piece will increase from the outer radius, towards the die exit plane, at which point the test piece cross section remains virtually constant and the elementary linear velocity equals that of the punch.

The relationship was determined experimentally by performing intermittent tests during which the punch displacement was noted after each drawing increment, and also the corresponding movement of the outer test piece radii. The test piece displacement was determined by measuring the length of test piece within the wedge dies at each interval. A fine line was scribed on each side of the test piece across the die exit plane after each drawing increment and the distance between successive lines and the outer radius of the test piece ends measured using a vernier height gauge. Duplicate tests were performed with test pieces representing four drawing ratios, Viz. 1.50,1.60; 1.70 and 1.80:1. The relationship between punch displacement and progressive draw ratio, defining the motion of the test piece, was plotted from this data and found to yield the family of curves shown in Fig. 5.25. By considering the ratio of the punch and test piece displacements at specific draw ratios this data yielded the curves in Fig. 5.26 which show the relationship between the instantaneous rim velocity and punch velocity at each stage of drawing. The displacement ratio corresponding to each value of the progressive drawing ratio was determined graphically by constructing tangents to the curves at set intervals. Except at the start of drawing, the slope of the tangent was found to vary very little with drawing ratio. The progressive velocity ratio for each reduction is therefore represented quite accurately in the later stage of drawing, by the single curve plotted in Fig. 5.26.

Relationship between punch displacement and current rim radius for different draw ratios.

Fig 5·25

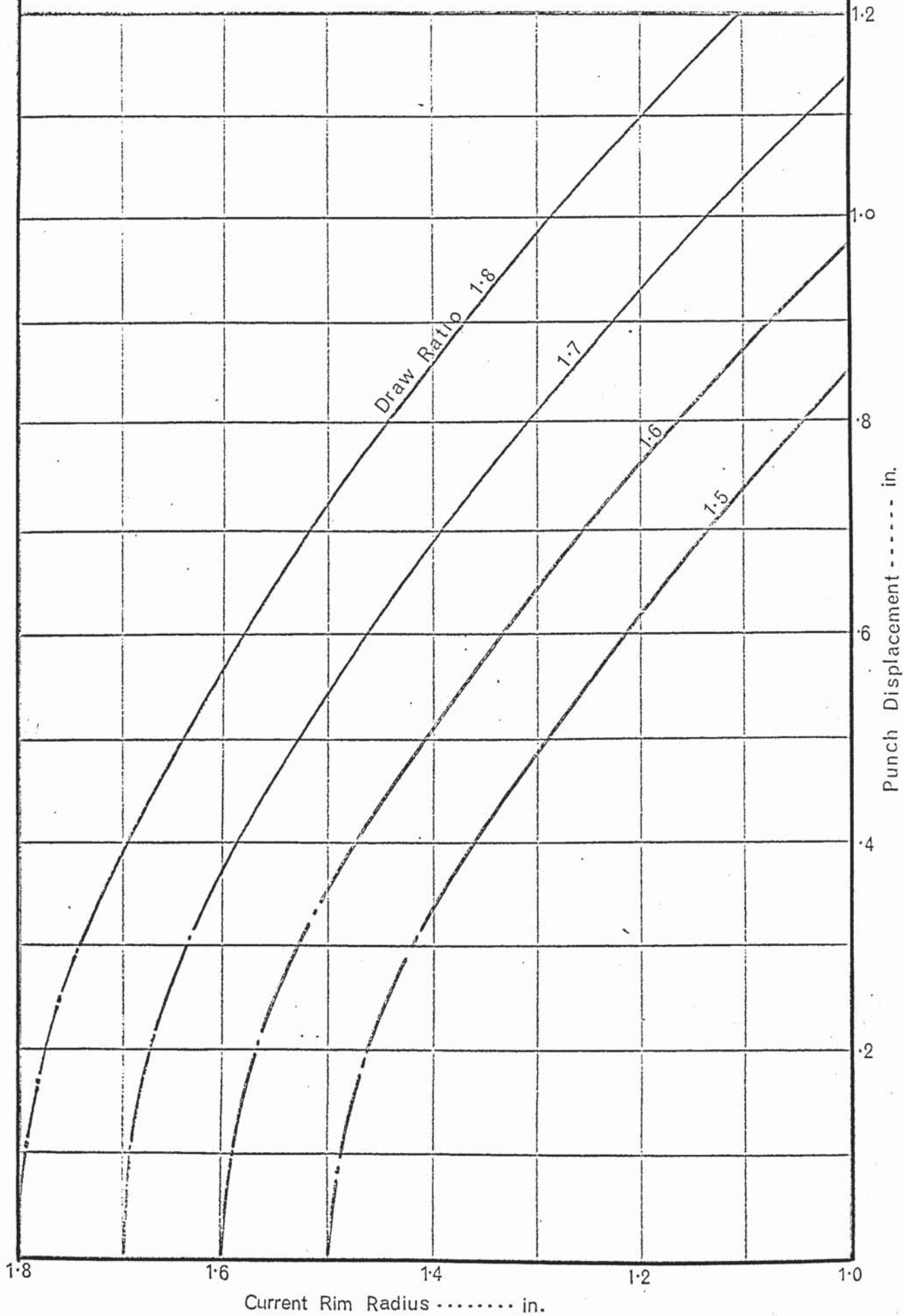

Ratio of rim velocity to punch velocity as a function of current rim radius for different drawing ratios.

Fig. 5·26

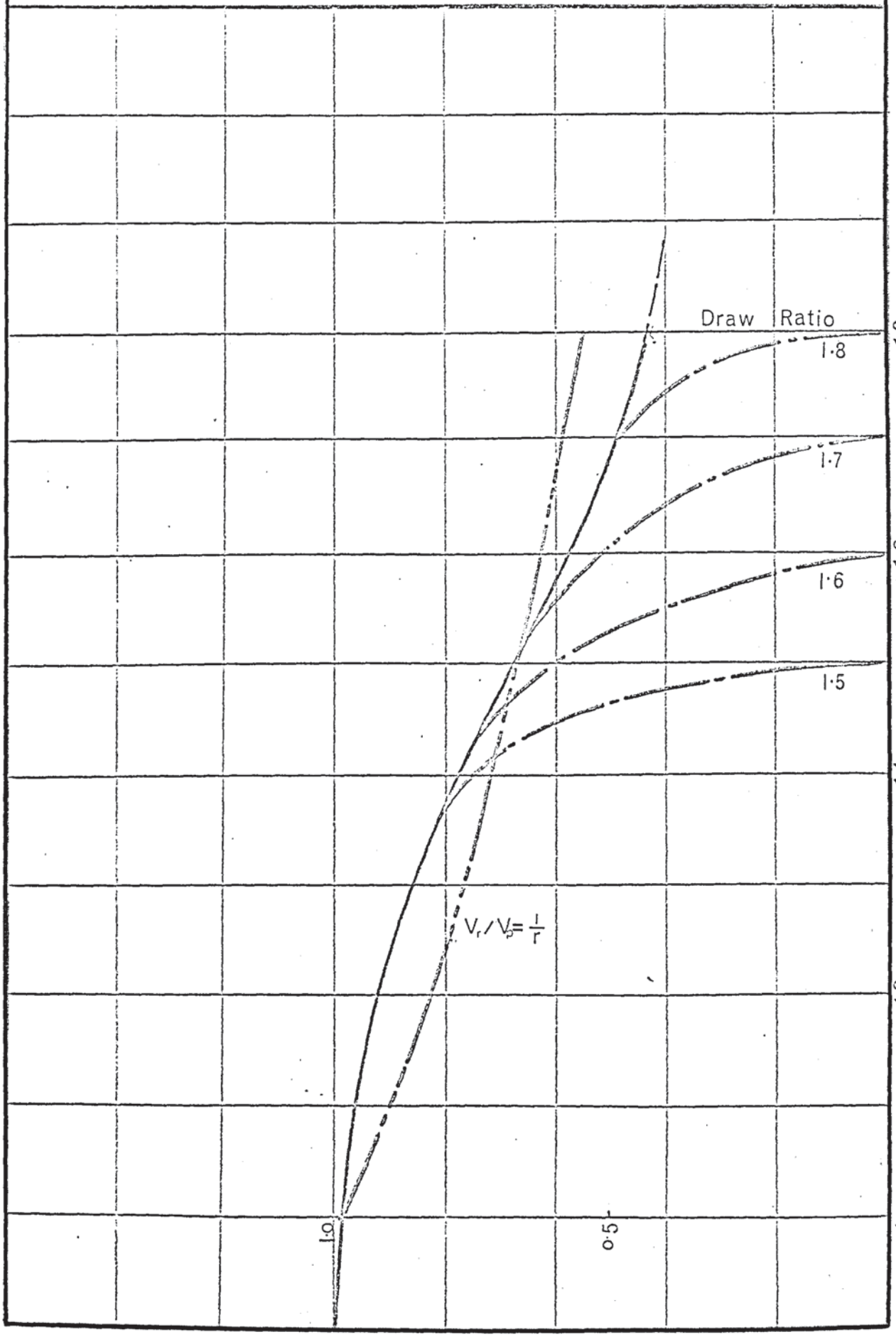

5.10 Electrical Generator

The electrical generator, Fig. 5.27, was a "Rapiclean" model 32/3000 made by Ultrasonics Ltd. This was a valve type unit, with a power rating of 3000 kw. It consisted essentially of a power amplifier and oscillator with an independent DC supply providing the magnetic bias current necessary for the magnetostrictive transducers. The robust construction of this unit and wide operating frequency range made it ideal for experimental work.

A brief description of the generator is given in Appendix VI which includes details of circuit modifications made in order to adapt the equipment to the present application.

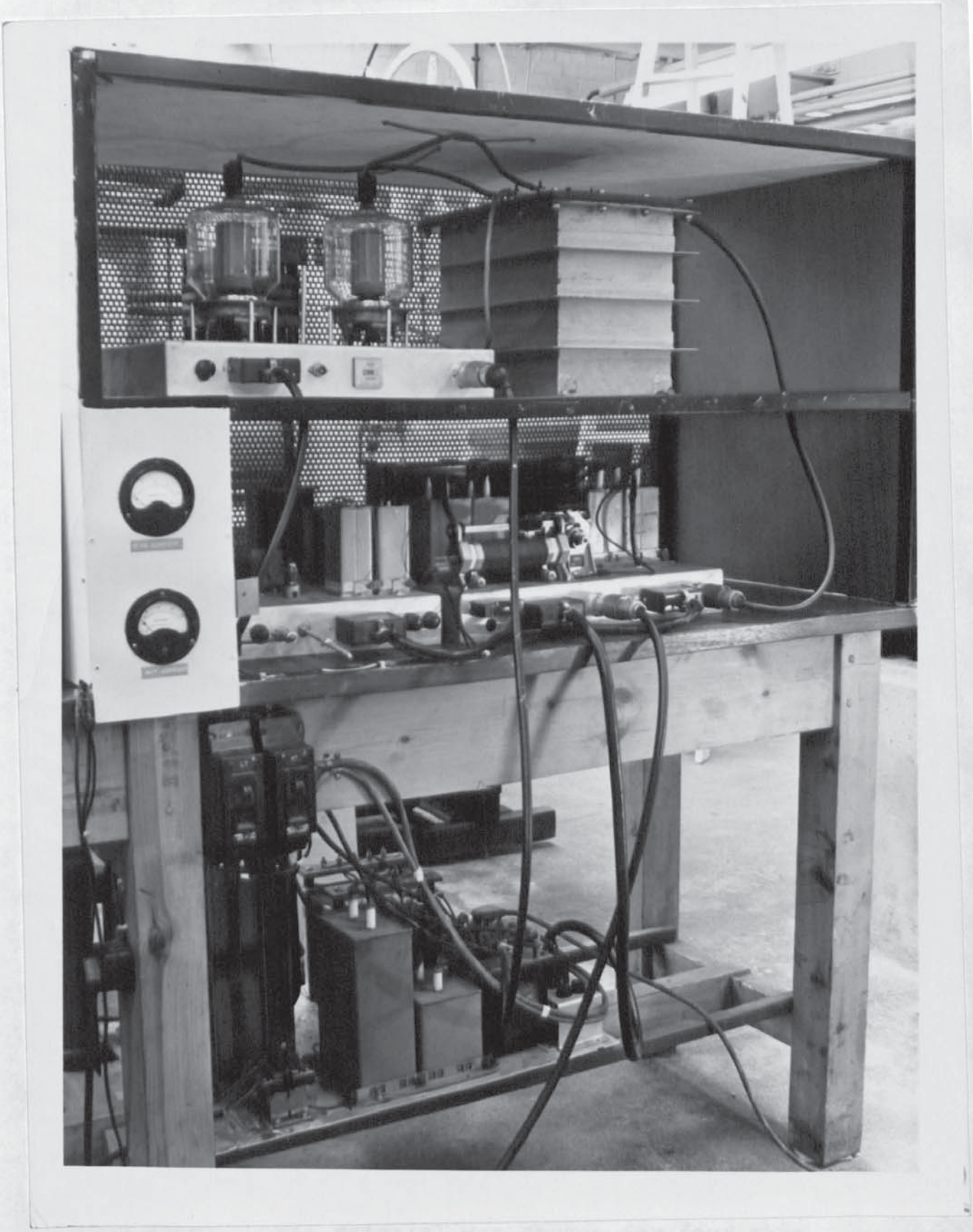

Fig. 5.27 Ultrasonic generator.

6. Wedge Drawing Test Pieces.

6.1 Test Piece Design.

The shape of the test piece was based on that adopted by Sachs[54] in his wedge drawing work. However, the dimensional scale was dictated by acoustic design considerations discussed in Sections 4.5 and 5.2. Details of the dimensions are given in Fig. 6.1, where it will be seen that the inner radius was made equal to 1.0 in. The drawing ratio R/r, was therefore numerically equal to the outer radius dimension and was closely analogous to the drawing ratio in the axisymmetric process. However, in this test there is no radial drawing-in component of stress associated with the test piece motion over the die radius, as in the case of cup drawing. The depth of draw in relation to the punch width also has a different significance to the height: diameter ratio of a drawn cup, and is not directly comparable. These aspects are considered fully in Section 9.

In order to prevent uneven deformation in the wedges resulting in lateral motion of the test piece relative to the bottom face of the punch, a 3/16 in. diameter pin was attached to the base of the punch, and located in a corresponding hole in the centre of the test piece, see Fig. 6.1. Premature failure at the site of the locating hole was prevented by the increased test piece width in this region.

6.2 Test Piece Material.

It was decided to perform the tests on commercially pure aluminium sheet. This material was chosen for four main reasons:

(i) it is a metallurgically simple material uncomplicated by yield phenomena or strain induced transformations.

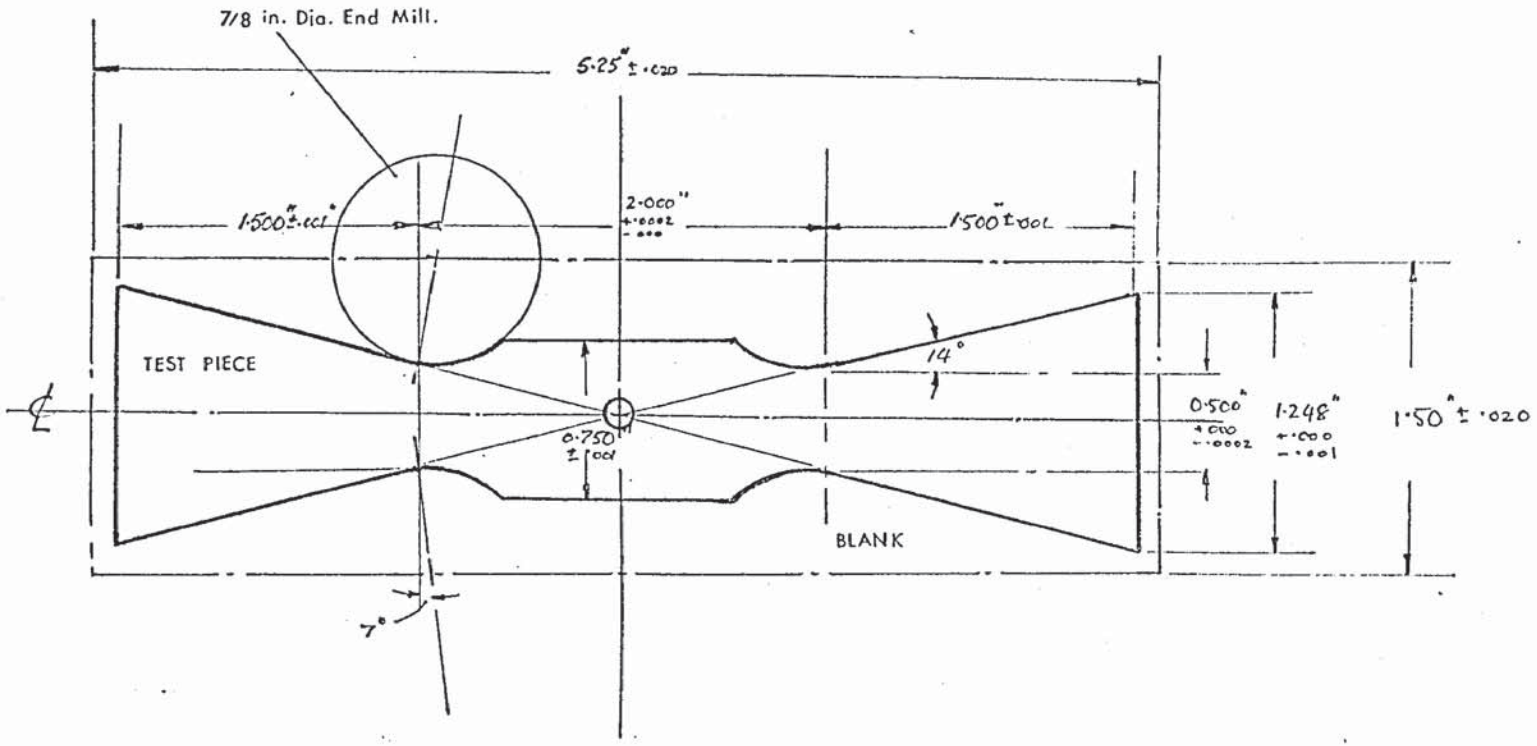

Fig. 6.1 Standard wedge drawing testpiece.

(ii) there are no frictional problems which might cause excessive die wear, necessitating the use of carbide dies. These, as discussed in Section 5.1, were incompatible with the acoustic design criteria of the oscillatory sub-press.

(iii) commercially pure aluminium is of technological importance as a deep drawing material.

(iv) it was readily available.

The test material was supplied by Aluminium Corporation Ltd. in the form of 1 ft. square sheets of fully annealed 20 gauge commercially pure aluminium.

6.3 Manufacture of Test Pieces

It was estimated that between 500 and 1000 test pieces would be used during the course of the investigation, which indicated the need for a streamlined method of production. The following procedure was therefore adopted:

(i) rectangular coupons, measuring 1.5 in. x 5.0 in., were sheared from the raw material, taking care to align the major axis with the rolling direction.

(ii) the central locating hole was drilled using a special jig which accepted upto 15 blanks at a time.

(iii) the final test piece profile was produced using an Elliott NC milling machine. Details of the programme and blank holding jigs are given in Appendix VII.

Using this technique the test piece dimensions were controlled to a tolerance of ±.0002 in.

7. Experimental Procedure.

7.1 General Description.

A general procedure was used for each series of tests performed. This is summarised under separate headings as follows:

7.1.1 Instrumentation

Prior to each test programme the power supply to each transducer load cell and measuring instrument was switched on and sufficient time allowed for steady state conditions to be reached. This applied particularly to the strain gauge bridges which required a minimum warm up period before final adjustments were made to the balancing potentiometers in each circuit.

7.1.2 Electrical Generator and Hydraulic Systems

A minimum period of 15 minutes was allowed for the generator to warm up prior to carrying out oscillatory tests. This ensured that the oscillator output was stable and allowed sufficient time for the heaters of the output valves to warm up. At this stage an almost instantaneous power output was obtained from the generator on applying the mains voltage to the primary of the H.T. transformers. This was done using a relay which was activated either manually or via a microswitch positioned appropriately on the sub-press.

The hydraulic power units for both the blank holder system and the tensile test machine were run for 30 minutes to allow the oil to warm up prior to testing.

7.1.3 Lubrication

One lubricant was used for all the tests performed on aluminium. This was a mineral oil with E.P. additives, Macoma 275, which was chosen for its high viscosity whilst permitting good consistency of application. The testpieces were lubricated prior to testing by dipping each end into a

container of oil and allowing the surplus to drain off. Finally, to ensure a consistent amount of lubricant during successive tests, the wedge drawing dies and blank holder plates were wiped clean before each test.

7.1.4 Hold down pressure

The hold down force applied to each blank holder plate was controlled by adjusting the hydraulic line pressure from the auxil iary power unit. The criterion used throughout the tests on aluminium was to apply an initial specific pressure of 450 lbf/in^2 to the undeformed coupon which was found to be sufficient to prevent wrinkling. The line pressure, indicated on a bourdon gauge, was therefore adjusted according to the drawing ratio, from the relationship defined by the graph in Fig. 7.1. This shows the variation of line pressure with drawing ratio for different values of initial specific pressure.

7.1.5 Operation of Test Rig.

A lubricated testpiece was placed in the sub-press with each end located in its respective wedge die. The blank holder plates and connecting friction load cell were then placed in position and the hydraulic assembly clamped to the main supporting frame above them. Fig. 5.1 shows the general test configuration. The appropriate blank holder pressure was selected, using the control valve on the auxiliary hydraulic power unit, and applied to the subpress. The punch speed was selected using the adapted by-pass valve on the test machine. Under oscillatory conditions care was taken not to switch on the H.T. supply to the generator until drawing had commenced in order to avoid burning the testpiece. For continuous tests a micro-switch was used but when it was required to switch the vibrators on and off several times during the test, it was found more convenient to use a manual system. In some cases minor

Relationship between hydraulic line pressure and initial blank holder pressure for various reduction ratios.

Fig. 7.1

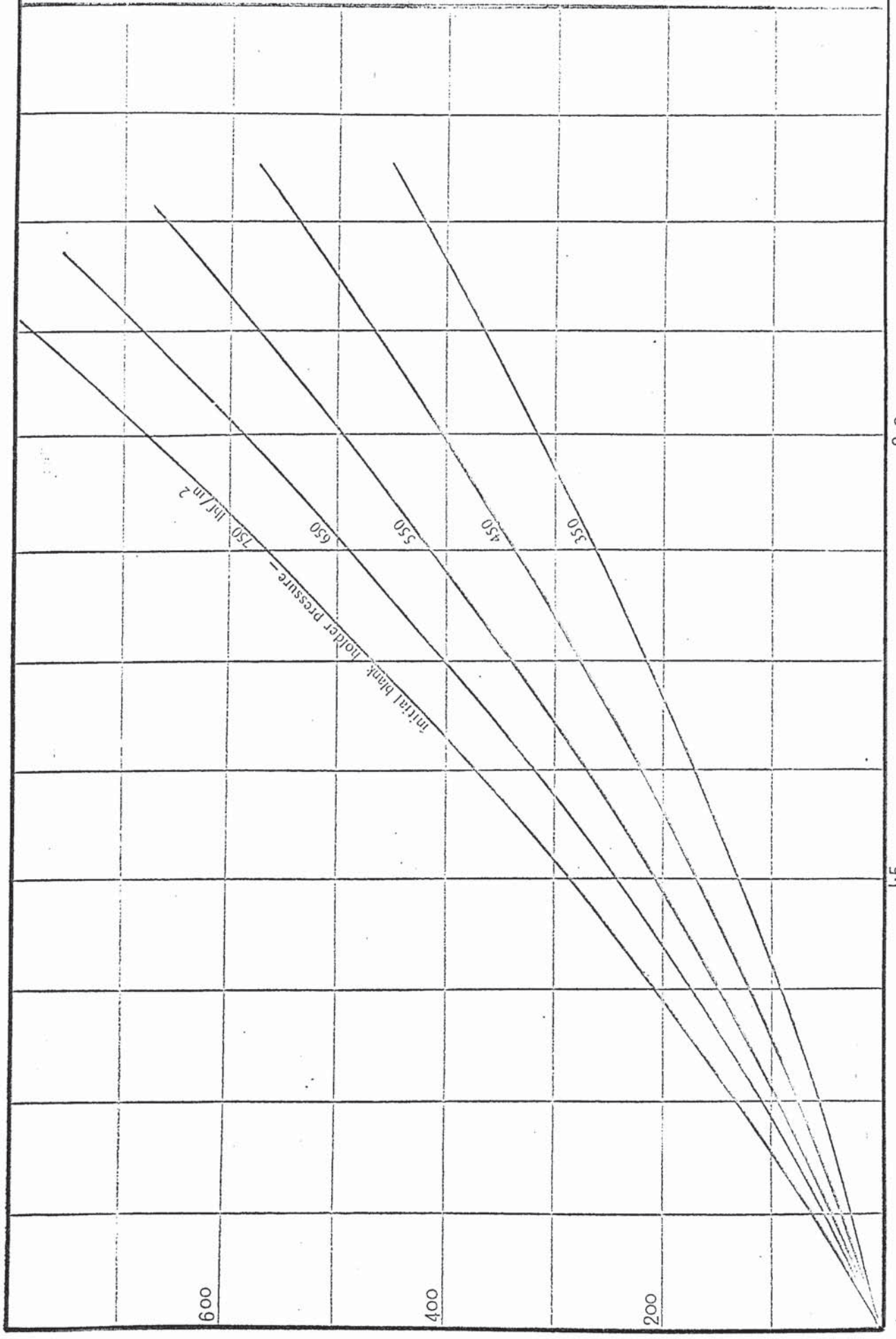

tuning adjustments were carried out during the initial part of the test in order to compensate for a slight shift in resonant frequency of one or other, of the vibrators. The motional amplitude was then balanced using a twin channel oscilloscope to monitor the output signal from two piezo-electric crystals attached to the vibrators. The die amplitude was controlled by varying the generator output voltage. This in turn was determined by the H.T. applied to the output stage which was controlled by a Variac Mains transformer.

7.2 Examination of the Effects of die amplitude on blank holder Friction force - Test Series 01.

These tests were carried out, using the above procedure, to investigate the effect of various levels of die amplitude on the measured value of blank holder friction force. Three drawing ratios were examined, viz. 1.60, 1.65 and 1.70 using a constant punch speed of nominally 0.15 in/sec. Die amplitudes were varied between zero and 5×10^{-5} in. by adjusting the H.T transformer primary voltage between zero and 60 volts A.C.

During each test the U.V. recorder was used to monitor the following parameters; blank holder friction force, punch load, left and right hand blank holder loads, punch displacement and velocity and the displacement amplitude of each vibrator.

Each test was performed initially with vibrations applied intermittently and then with continuously vibrated dies, in order to evaluate any error related to the response time of the instrumentation.

7.3 Examination of the Effects of Die Amplitude on Punch Load for Various Drawing Ratios:- Test Series 02

The second series of tests was carried out using the same test configuration but examining a wider range of drawing ratios A constant speed of 0.32 in/sec was used for the majority of

tests and as before these were carried out with both intermittently and continuously applied vibrations.

A much wider range of die amplitudes was examined, viz. from zero to 30 x 10^{-5} in. and the drawing ratio successively increased in order to determine the limiting reduction under oscillatory and non-oscillatory conditions. Further data was also obtained on the effects of die amplitude on blank holder friction force.

7.4 Evaluation of the Effect of Tool Vibrations on the Friction force Associated with the Testpiece Motion over the Die Radius. Test Series 03.

7.4.1 Design of Roller Die Assembly.

In order to obtain an indirect measure of the die radius friction force component, the basic die assembly was modified by the insertion of a pair of low friction transverse rollers which were mounted on a supporting frame, close to the fixed radius of each wedge die. The arrangement, shown in the photograph of Fig. 7.2, was designed to eliminate the die radius friction force whilst retaining the essential features of the test. It was therefore possible with certain allowances, to deduce the die radius friction force at each stage of drawing by a comparison of the punch load displacement curves for drawing over a fixed radius and over a roller, for a given drawing ratio.

The roller sub-assembly consisted of two $\frac{1}{2}$ in. diameter rolls free to rotate on coaxial $\frac{1}{8}$ in. diameter hardened steel shafts secured at each end in the vertical plates of the support frame. The whole assembly was designed to locate between the wedge drawing dies with an overall clearance of .005 in. The frame was not secured to the sub-press as it was intended to be self-aligning during drawing.

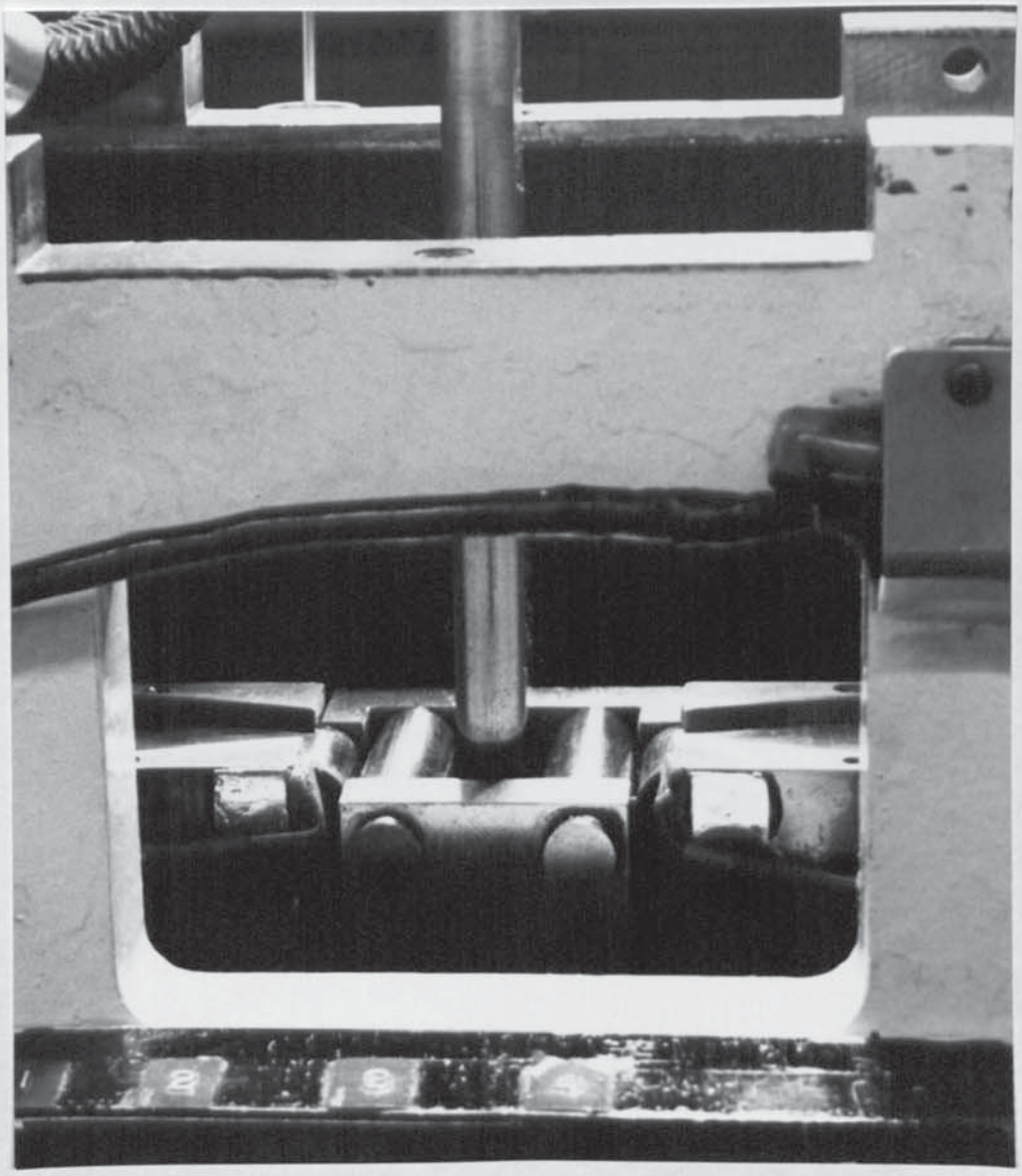

Fig. 7.2 'Frictionless' die radius assembly located between wedge drawing dies.

In order to employ this component, modifications were required to the punch and test piece as follows:

(a) a special punch was constructed with the width reduced so as to pass between the rolls whilst leaving the required clearance, namely 1.5 t_o, between punch and rolls. The dimensions of this unit are shown in Fig. 7.3.

(b) the design of test piece had to be modified in order to maintain the original test conditions.

The use of the 'roller radii' with the original design of test piece would result in an increased component of bending and unbending stress during the initial phase of drawing, as the wider central portion of the testpiece passed over the die radius. The testpiece design was therefore modified by inserting a $\frac{1}{2}$ in. long parallel portion between the wedge profile and the central region. This design is shown in Fig. 7.4.

7.4.2 Test Procedure

Tests were carried out as before for drawing ratios of 1.50 to 2.00, with die amplitudes from zero to 25 x 10^{-5} in. and at a constant punch speed of 0.32in/sec. In the majority of cases ultrasonic energy was applied intermittently. A limited number of tests were performed at higher drawing ratios in order to determine the limiting draw ratio.

This test arrangement was also used for a short series of unlubricated tests designed to examine the effect of die amplitude on punch load in order to establish whether the effectiveness of the oscillatory energy was enhanced or decreased by the presence of a lubricant. These tests were conducted at a drawing ratio of 1.80 with the punch speed constant at 0.32 in/sec.

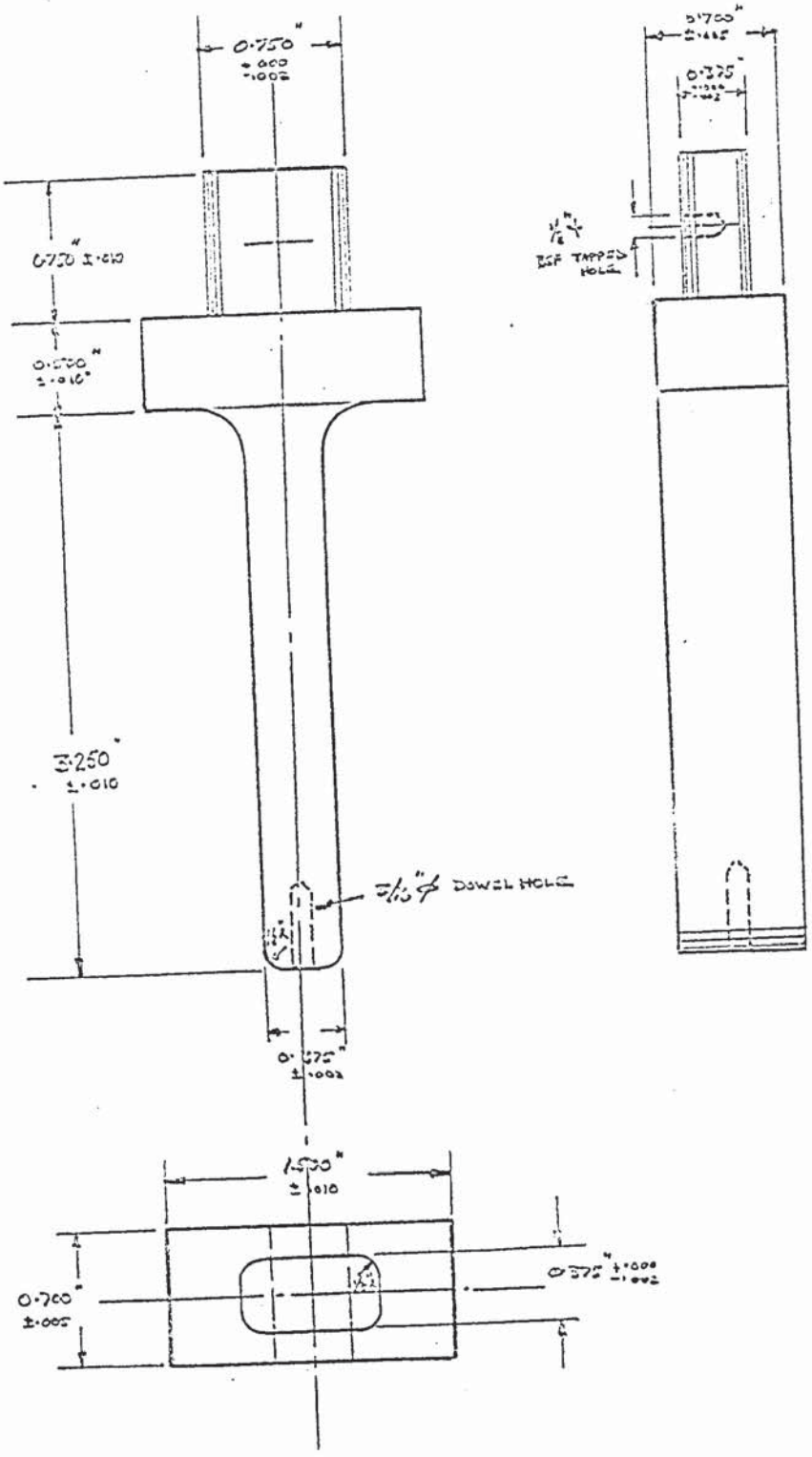

Fig. 7.3 Dimensions of modified punch for roller die assembly.

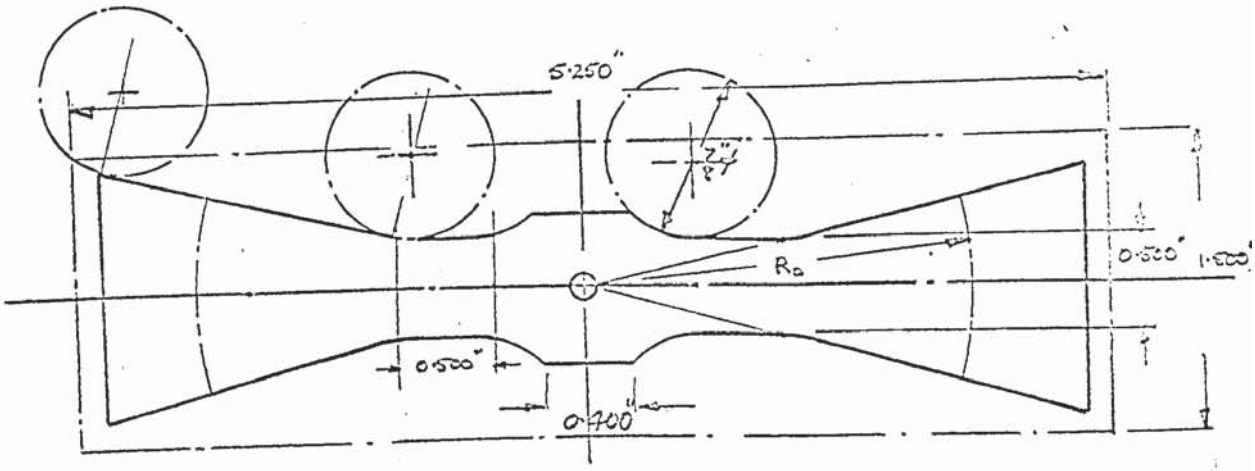

Fig. 7.4 Modified test piece design for 'roller radius' tests.

7.5 The effect of Die Amplitude on Punch load and Blank Holder friction force for a drawing ratio of 1.0, i.e. for a parallel test piece. Test Series P.02 and P.03.

A number of parallel testpieces were machined to dimension: 0.495 in x 4.00 in. This gave a 0.005 in. clearance in the wedge drawing dies and ensured that the only plastic deformation occurring in this zone was due to the blank holder force. The tests were conducted at a nominal drawing speed of 0.32 in/sec and in each case lubricant was applied.

7.5.1 Fixed radius - (P.02)

The first series was carried out using the standard wedge drawing dies without the roller assembly. The effect of vibrations on the blank holder friction force and punch load were determined over a range of die amplitudes using a hold down force of 250 lbf (equivalent to an initial pressure of 500 lbf/in^2).

7.5.2 Roller Radius (P.03)

In the second series of tests the above conditions were examined but this time with the roller assembly inserted.

7.6 Measurement of Oscillatory Forces

In order to obtain a complete knowledge of the forces acting on the deforming test piece it was considered desirable to measure the oscillatory force amplitude at the die exit plane and also in the partially drawn test piece. Several methods were considered and although they proved unsuccessful, a brief outline of each technique is given below with a more detailed account in Appendix VIII.

7.6.1 Measurement of the input impedance of the loaded vibrators.

From a knowledge of the impedance transformation characteristics of a conical horn it is possible to relate the values of oscillatory force and velocity at the input and output ends under loaded conditions, see section 4.5.2. Since the oscillatory force at the die exit plane is essentially that at the output end of the horn, it should be possible to determine this value by measuring the force amplitude at the input end. Direct strain measurements at the die exit plane were ruled out due to poor accessibility and plastic deformation of the test pieces in this region.

7.6.2 Measurement of the oscillatory force amplitude in the partially drawn test piece

Two methods were examined:

(a) direct measurement of oscillatory force using strain gauges attached to the surface of the partially formed test piece.

(b) measurement of the travelling wave amplitude in the test piece using a tuned punch assembly. Strain gauges, forming a full bridge were attached to the punch at a section coincident with a stress node under unloaded conditions. Any oscillatory force component occurring during drawing would then be due to travelling waves passing through the test piece and punch.

The results of tests using these techniques are described in Appendix VIII.

8. Experimental Results.

8.1 General description of Recorder Trace.

With the exception of the generator frequency all experimental parameters were continuously monitored and recorded on ultraviolet recorder charts. Typical traces are shown in Figs. 8.1a and b. The first illustrates the load and displacement variations during the deformation cycle for continuously applied vibrations. Fig. 8.1b shows a typical trace obtained under intermittent oscillatory conditions. Certain general characteristics of the traces are worthy of note:

8.1.1 Comparison of Oscillatory and non-Oscillatory data.

It will be seen in Fig. 8.1b that the punch load shows a step-wise decrease and increase respectively at the start and finish of periods of oscillatory drawing and a similar effect was noted, in the case of the friction force record. The technique of 'intermittent' testing permitted a direct comparison of oscillatory and non-oscillatory drawing parameters under identical test conditions. The intermittent traces for punch and blank holder friction force and die amplitude readily permitted the construction of continuous curves representing both oscillatory and non-oscillatory conditions. It was however recognised that the non-oscillatory loads might be influenced by previous intervals of vibrational drawing and for this reason additional tests were always performed without ultrasonic activation , at each drawing ratio. This aspect will be considered in greater detail during the discussion of results.

8.1.2 Punch Load Trace.

The general characteristic of the punch load trace was a gradual rise to a maximum value at which it levelled off

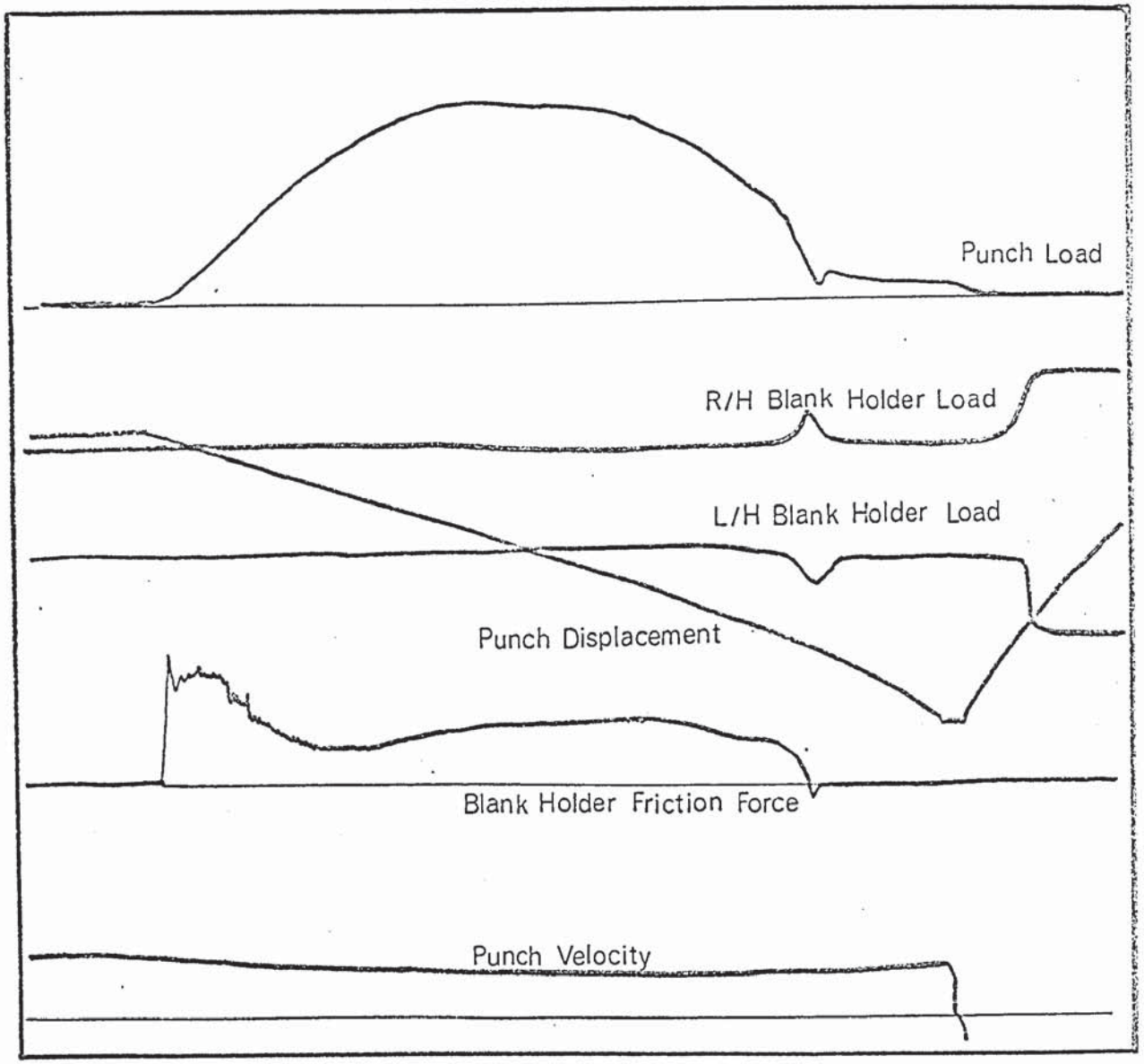

Fig. 3.1a. Typical u.v. recorder trace showing load cell and transducer outputs under non-oscillatory conditions.

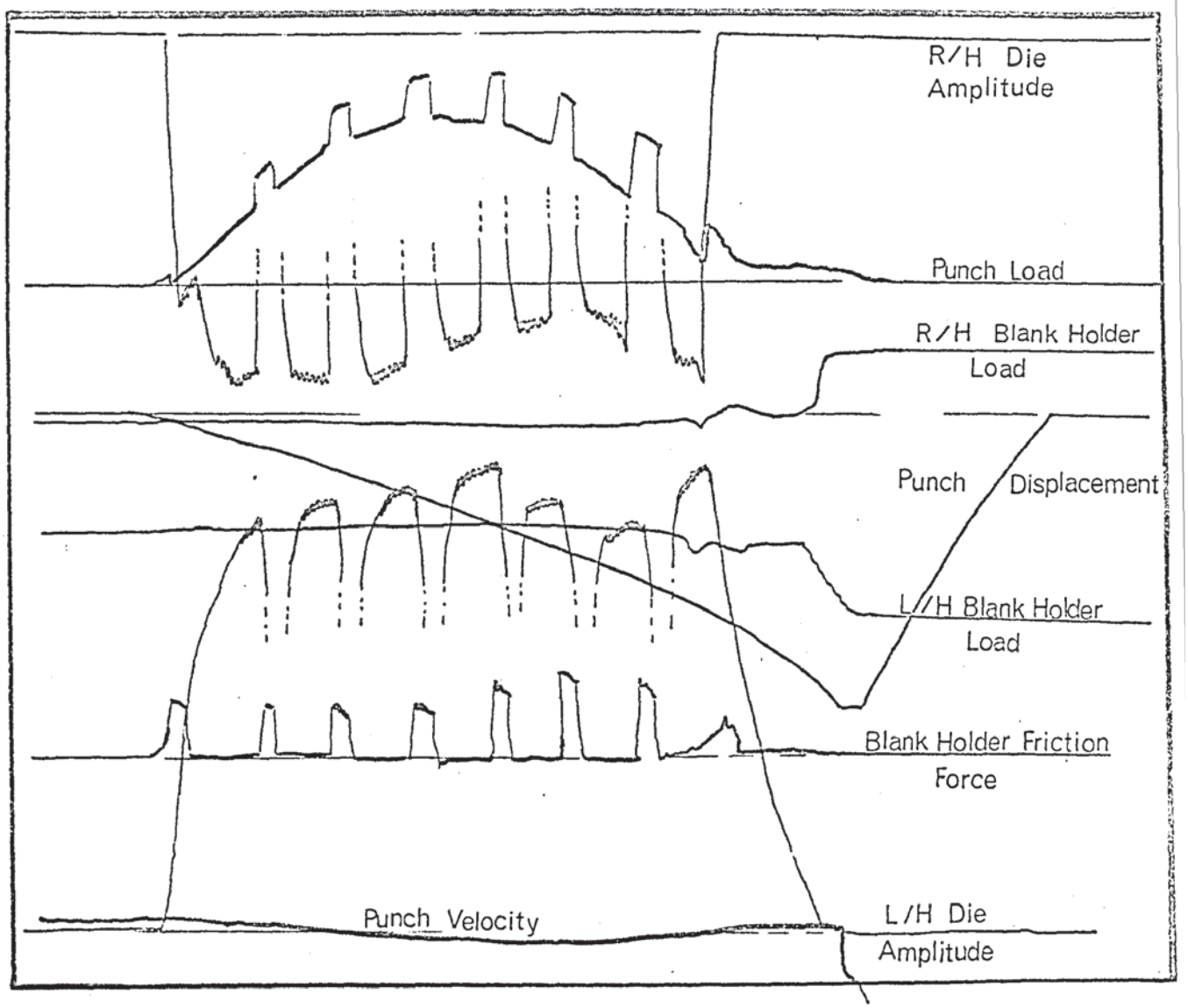

ig. 8.1b Typical u.v. recorder trace, illustrating the load cell and transducer outputs under intermittent oscillatory test conditions.

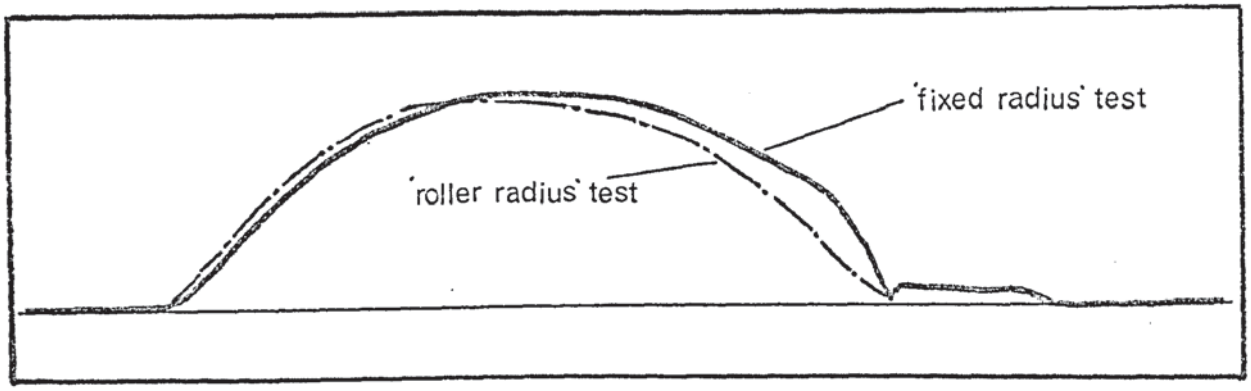

ig. 8.2 Comparison of non-oscillatory punch loads using standard wedge drawing dies and with the roller radius inserted.

and began to reduce slowly before rapidly falling to zero at the completion of radial drawing. The load then rose slightly to a steady level as the ends of the testpiece partially unbent and were drawn between the punch and die radii. In the case of drawing over the "frictionless die radii" the reduction in punch load beyond the maximum value was more uniform. This is illustrated qualitatively in Fig. 8.2.

8.1.3 Friction Load Trace

The friction force trace indicated the sum of the friction forces acting at the upper interface at both ends of the testpiece.

At the start of drawing the friction force rose rapidly to a high value, reduced gradually to a minimum and then rose again towards the end of drawing. (Figs. 8.6 - 8.8 illustrate the general shape of the trace which was observed in all lubricated tests.) Under oscillatory conditions the friction force was reduced to zero beyond a certain value of die amplitude. At amplitudes less than this only a partial reduction in friction force was noted and under these conditions the trace showed a periodicity not accounted for by spurious 'noise' pick-up. It was assumed under these conditions that a state of dynamic equilibrium was reached in which the blank holder plates were subjected to slightly varying friction forces as the conditions at the respective interfaces fluctuated during the test. It will be recalled that the pressure plates with connecting load cell were designed to 'float' on the upper surface of the testpiece, their positions being determined by the relative magnitude of the friction forces drawing them together.

8.1.4 Blank Holder Force

The blank holder load traces were used mainly to

indicate that a constant load was in fact applied to the pressure plates during drawing. In practice this was found to rise slightly before falling momentarily to zero at the end of the radial drawing stage and then returning to the original value as the pressure plates came into contact with the upper die surface. This feature served as a useful indication of the end of drawing. The slight increase in blank holder load was attributed to thickening of the test piece during drawing which resulted in movement against the frictional drag of the hydraulic pistons.

8.1.5 Die Amplitude.

A significant variation in the motional amplitude of both vibrators was noted during drawing. This followed a general form for each vibrator and resulted in a reduction in amplitude giving rise to a minimum value after the maximum punch load had been reached. This effect was more pronounced at the slower drawing speeds and was observed to be related to the magnitude of the punch load reduction. The phenomenon was therefore considered as an indication of the acoustic energy absorption by the load. It might also have been due in part to a change in the resonant frequency of the system due to small variations in the reactive component of the acoustic load. Because of this factor it was not considered practicable to attempt to quantify the effect.

Throughout the tests the resonant frequency of the vibrators was found to vary by ± 1.5 per cent from the design frequency of 13 kHz. However, due to the relatively low Q value of the concentrators (around 200 unloaded) no difficulty was experienced in maintaining resonance at near peak amplitudes during testing. This might have presented a serious problem had the system been designed using stepped

Q = quality factor

or exponential concentrators.

The response time of the instrumentation used to monitor the die motional amplitudes was found to be adequate to permit intermittent testing at speeds upto 0.35 in. per sec. Under these conditions continuous amplitude traces could be constructed by joining the peaks as shown in Fig. 8.1b. The experimental error introduced by this technique was estimated to be less than 1%.

8.1.6 Punch Velocity and Displacement.

The punch velocity was found to decrease by upto 20 per cent during testing at 0.15 in/sec, depending upon the maximum load. This was a feature of the test machine when operating with the by-pass valve in the partly closed position. At the higher speed, used for the majority of the tests the valve was almost fully open and the velocity variation was generally insignificant.

The punch displacement trace was non-linear and in order to facilitate the extraction of data, in which it was required to relate all parameters to punch movement, an appropriately calibrated gauge was used.

8.2 Examination of the Effects of Die Amplitude on Blank holder Friction Force. Test Series 01.

Test data relating friction force reduction to the mean displacement amplitude for drawing ratios of 1.60, 1.65 and 1.70 is presented in Tables 1 - 26 and Figs. 8.3 - 8.5. In each table the punch load friction force and die amplitudes are noted at intervals equivalent to a punch displacement of 0.1 in. throughout the drawing cycle. The difference between non-oscillatory and oscillatory punch and friction loads, ΔP and ΔF respectively, are also tabulated. Finally, the mean die velocity amplitude, $\dot{\xi}_m$ has been determined at each punch

displacement (from the relationship $\dot{\xi}_m = 2\pi f.\xi_m$) and expressed as the ratio of $V_p/\dot{\xi}_m$ where V_p is the mean punch velocity. When the punch velocity was found to vary significantly during the draw, the current value of V_p, appropriate to the particular stage of drawing was taken.

The results are also presented graphically, in order to illustrate the variation of friction force throughout the drawing process under oscillatory and non-oscillatory conditions - Figs. 8.6 - 8.8.

8.3 Examination of the effects of Die Amplitude on Punch Load: Test Series 02.

The results of tests carried out at drawing ratios of 0.50 - 2.00 are presented in Tables 27 - 84. The data is also presented graphically in Figs. 8.9 - 8.12 which show punch load/displacement curves for oscillatory and non-oscillatory tests and in Figs. 8.13 - 8.21 showing the reduction in punch load with increasing die amplitude. The maximum punch load and corresponding blank holder friction force under oscillatory and non-oscillatory conditions are plotted as a function of die amplitude, for each drawing ratio in Figs. 8.22 - 8.25.

8.4 Examination of the Effects of Motional Amplitude on die radius friction: Test Series 03.

The results of tests performed at drawing ratios from 1.50 - 2.30 are given in Tables 85 - 134 and graphically in Figs. 8.26 - 8.40. Figs. 8.9 - 8.12 show the punch load/displacement traces for 'frictionless' drawing, superimposed on the traces for normal drawing. The effect of die amplitude on the reduction in punch load is shown in Figs. 8.26 - 8.35 and the variation in maximum punch load and corresponding friction force with increasing die amplitude are plotted for each drawing ratio in Figs 8.36 - 8.40.

8.5 Examination of the Effect of Lubrication on Friction Reduction. Test Series 03N

Unlubricated tests were carried out using the roller radius assembly to establish whether friction reduction occurred at the blank holder test piece interface in the absence of a lubricant. The results are shown in Tables 86 - 88 and 135 - 139.

8.6 The Effect of Die Amplitude on Friction force and punch load for parallel testpieces.

The result of tests carried out using normal dies (series 02P) are given in Table 140 and graphically in Fig. 8.41.

Data relating to 'frictionless' tests (series 03P) is given in Table 141 and Fig. 8.42.

Test Series OI

Effect of die amplitude on percentage reduction in blank holder friction force.

Fig. 8.3

D.R.= 1.6

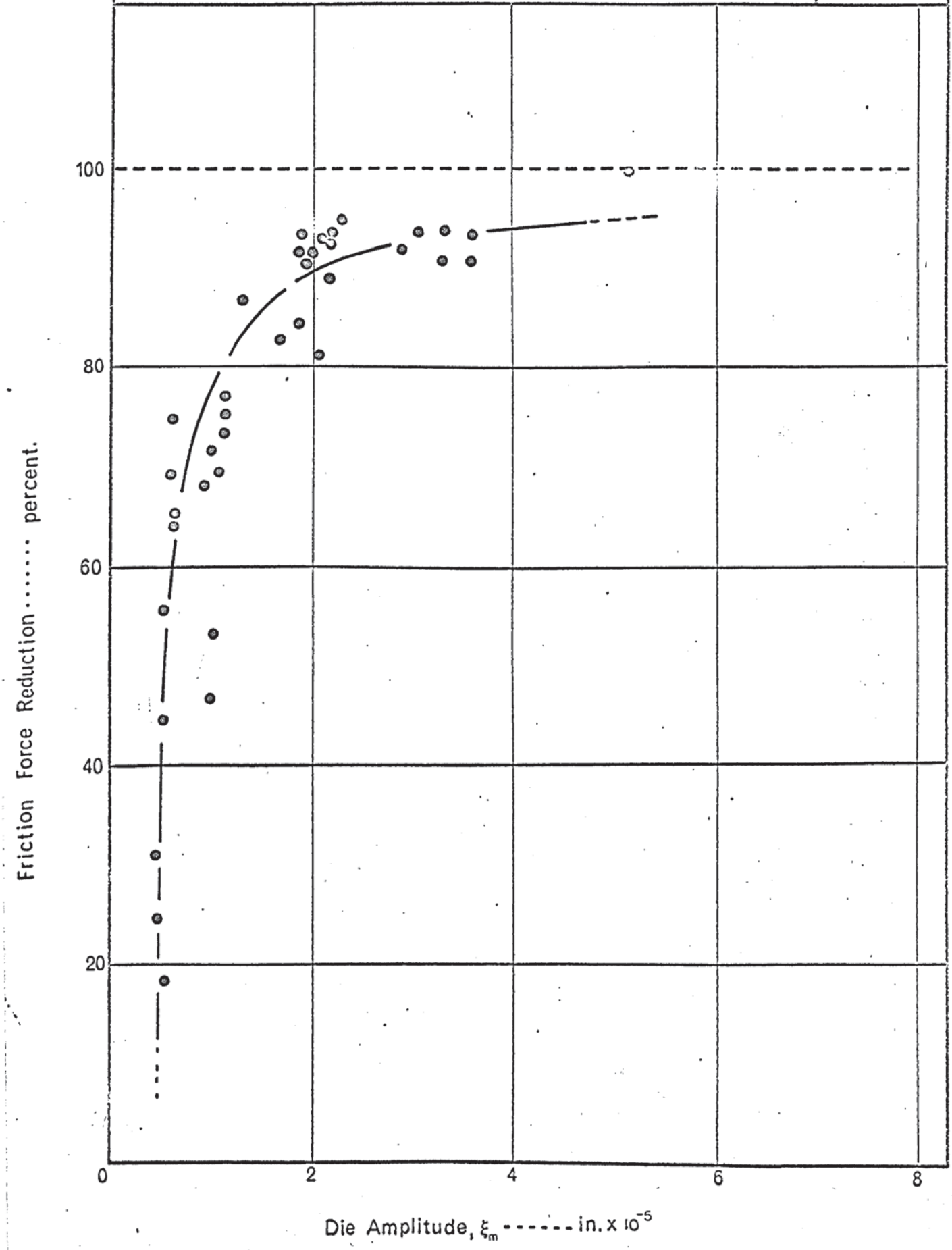

Test Series O1

Effect of die amplitude on percentage reduction in blank holder friction force.

Fig. 8.4

D.R.=1.65

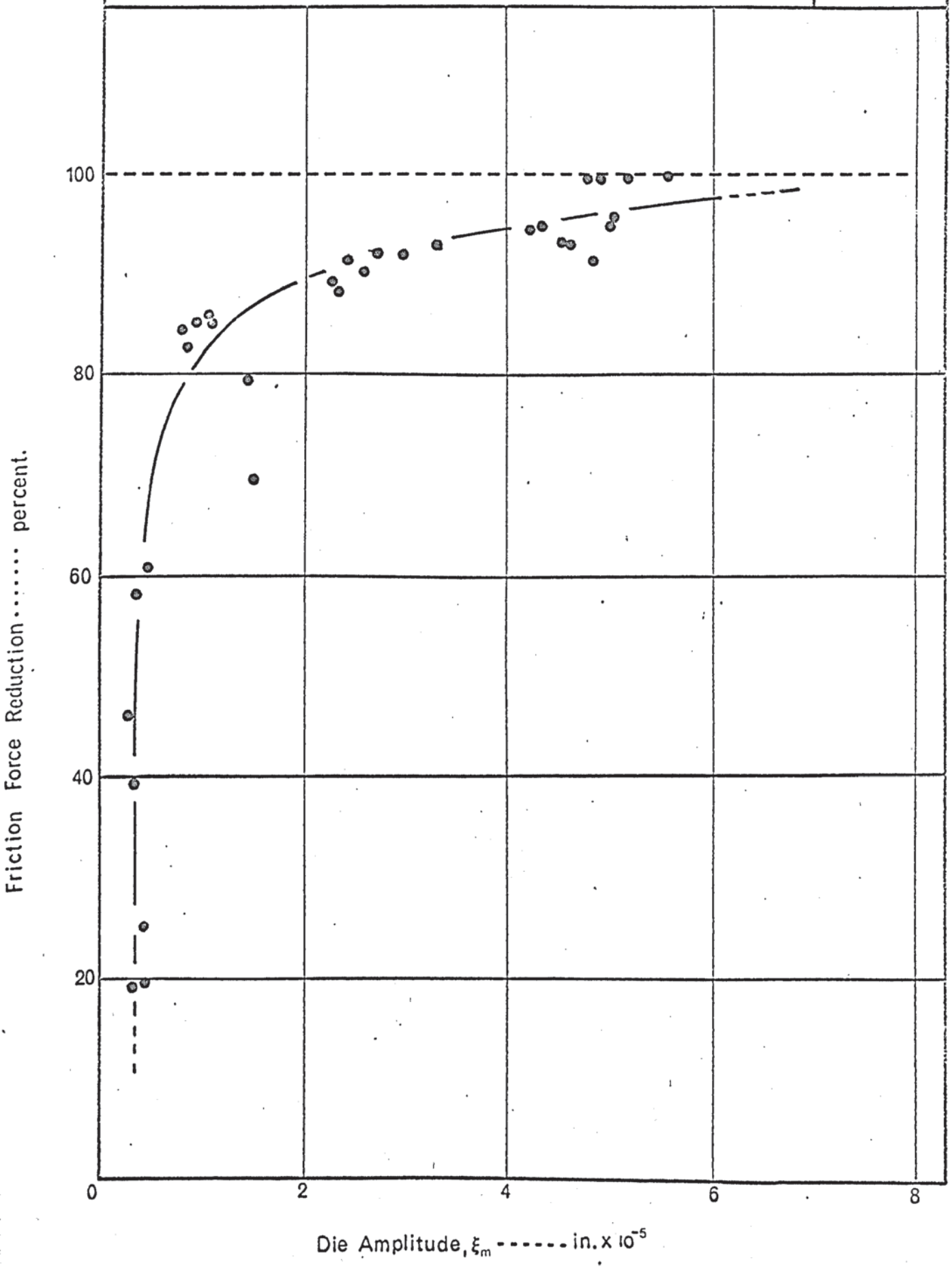

Test Series OI

Effect of die amplitude on percentage reduction in blank holder friction force.

Fig. 8.5

D.R.= 1.7

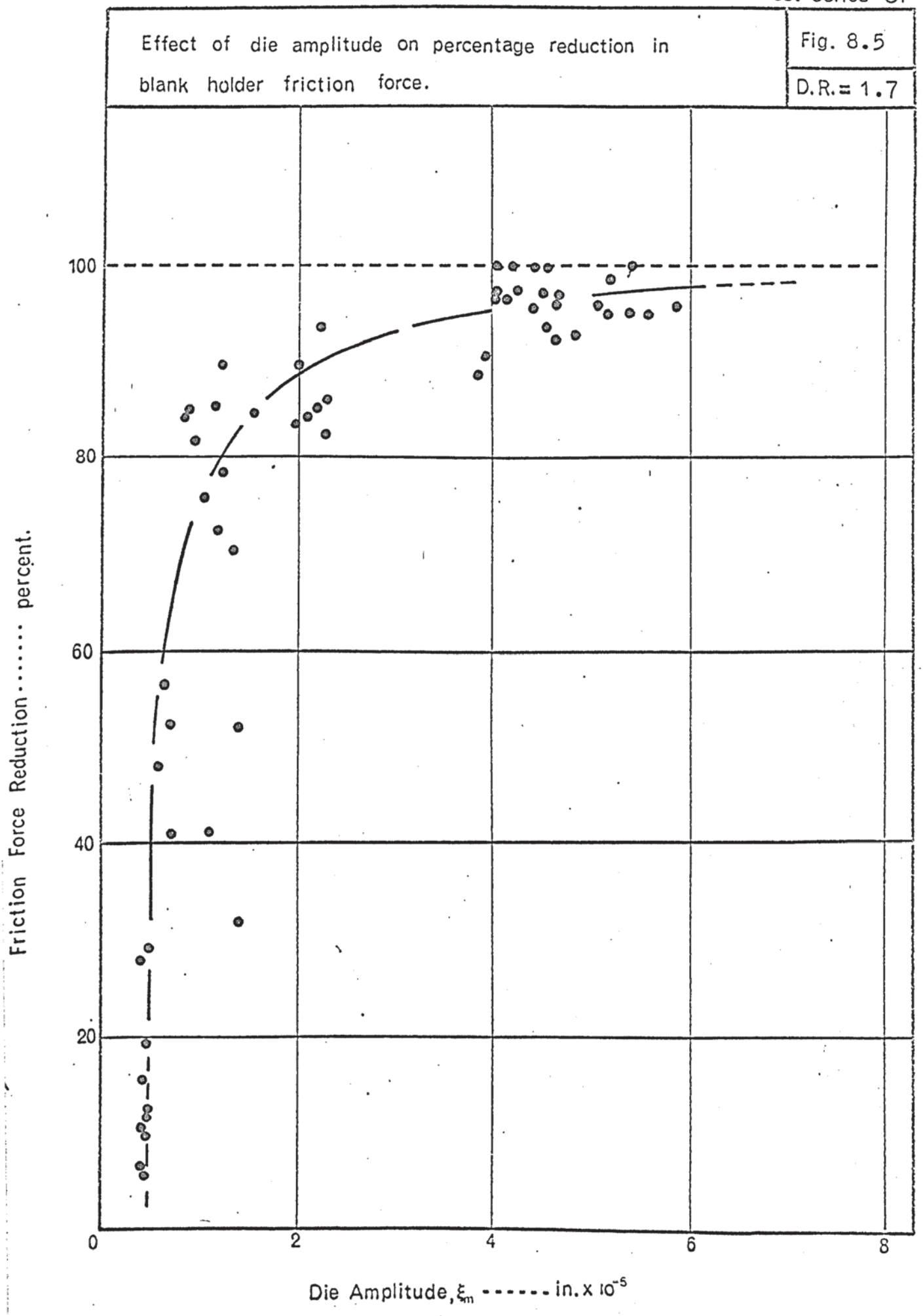

Test Series 01

Variation in friction force with punch displacement at different die amplitudes.

Fig.8.6a

D.R.= 1.6

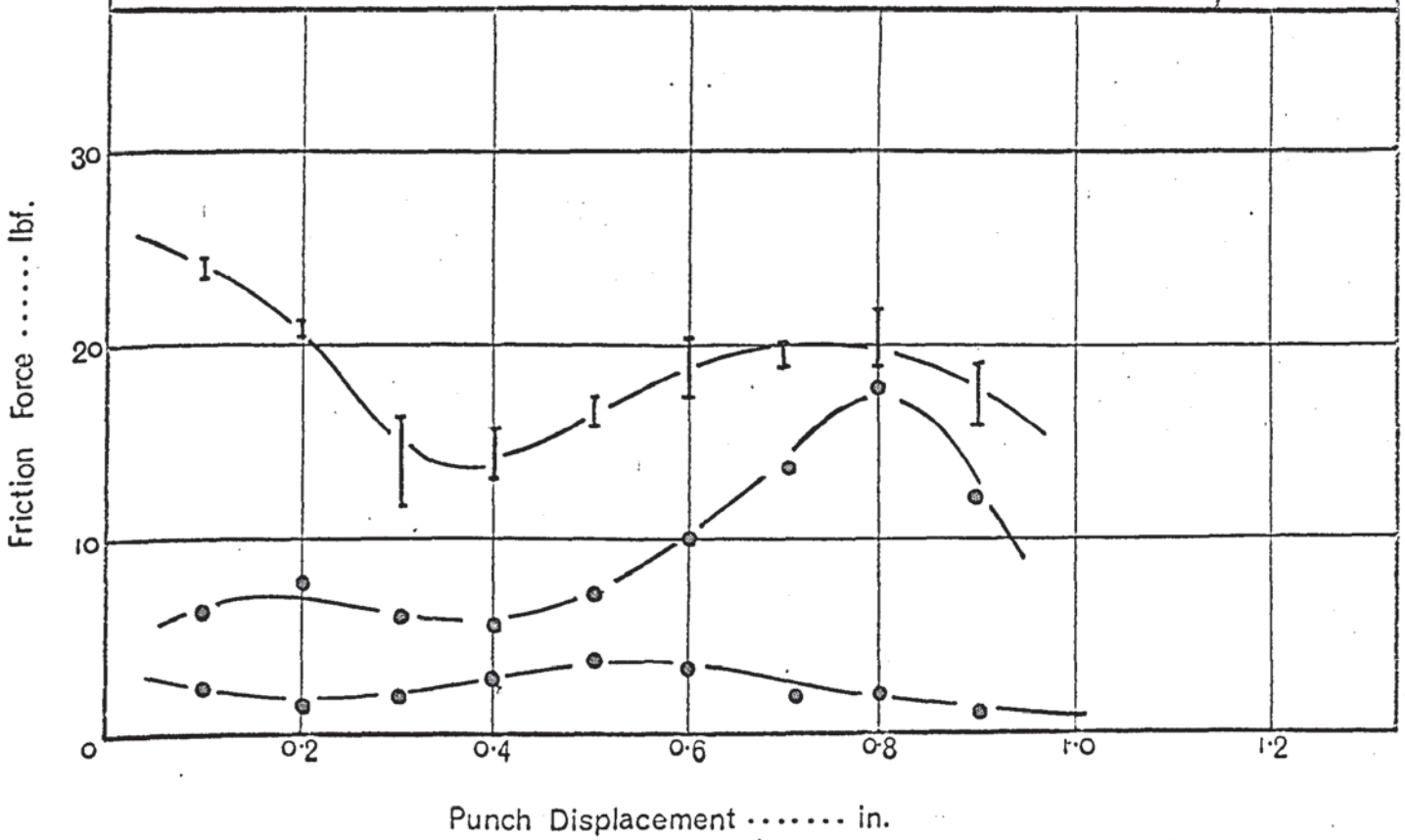

Test Series 01

Effect of punch displacement on blank holder friction force reduction at different die amplitudes.

Fig.8.6 b

D.R. = 1.6

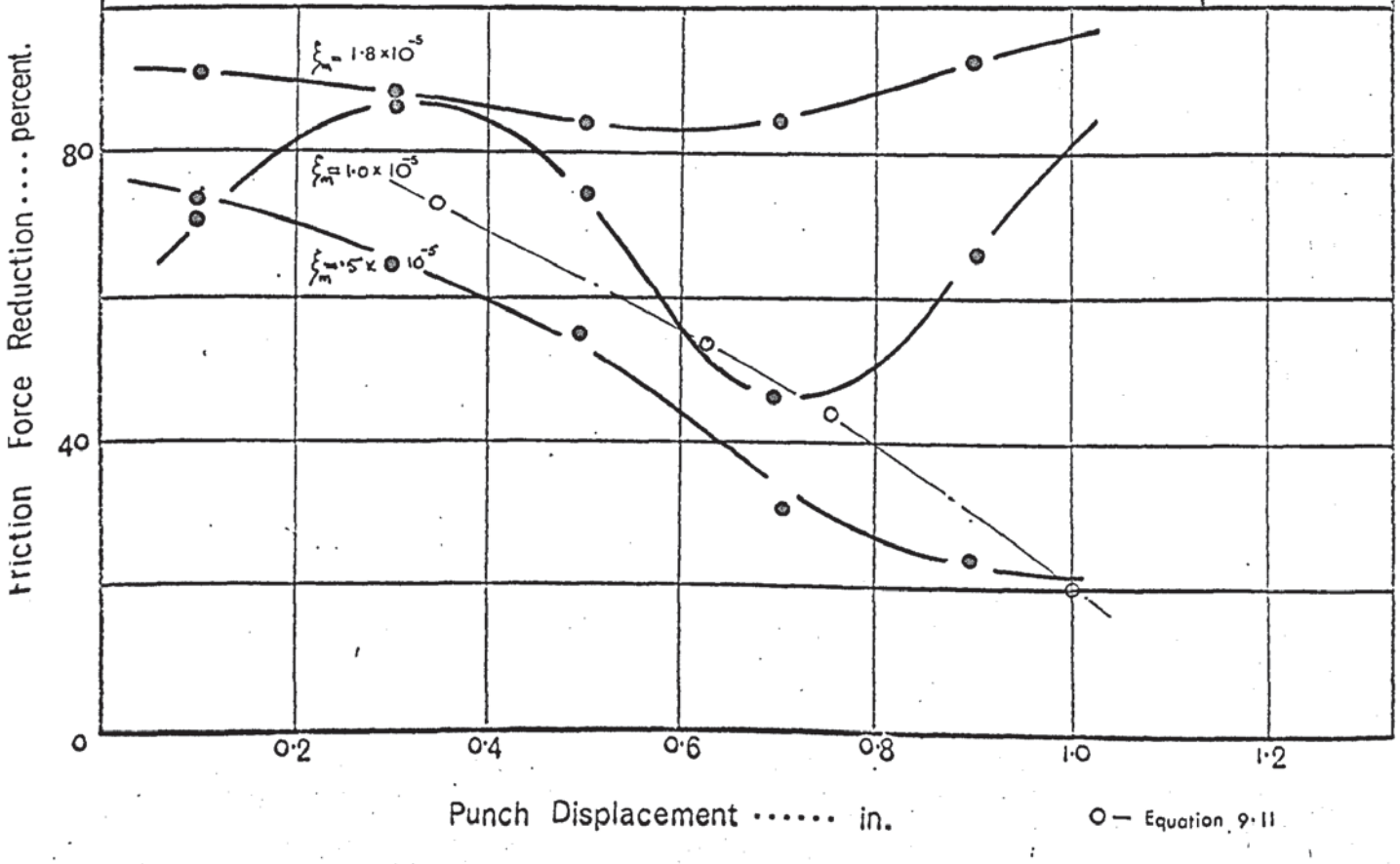

Test Series 01

Variation in friction force with punch displacement at different die amplitudes.

Fig.8.7a

D.R.= 1.65

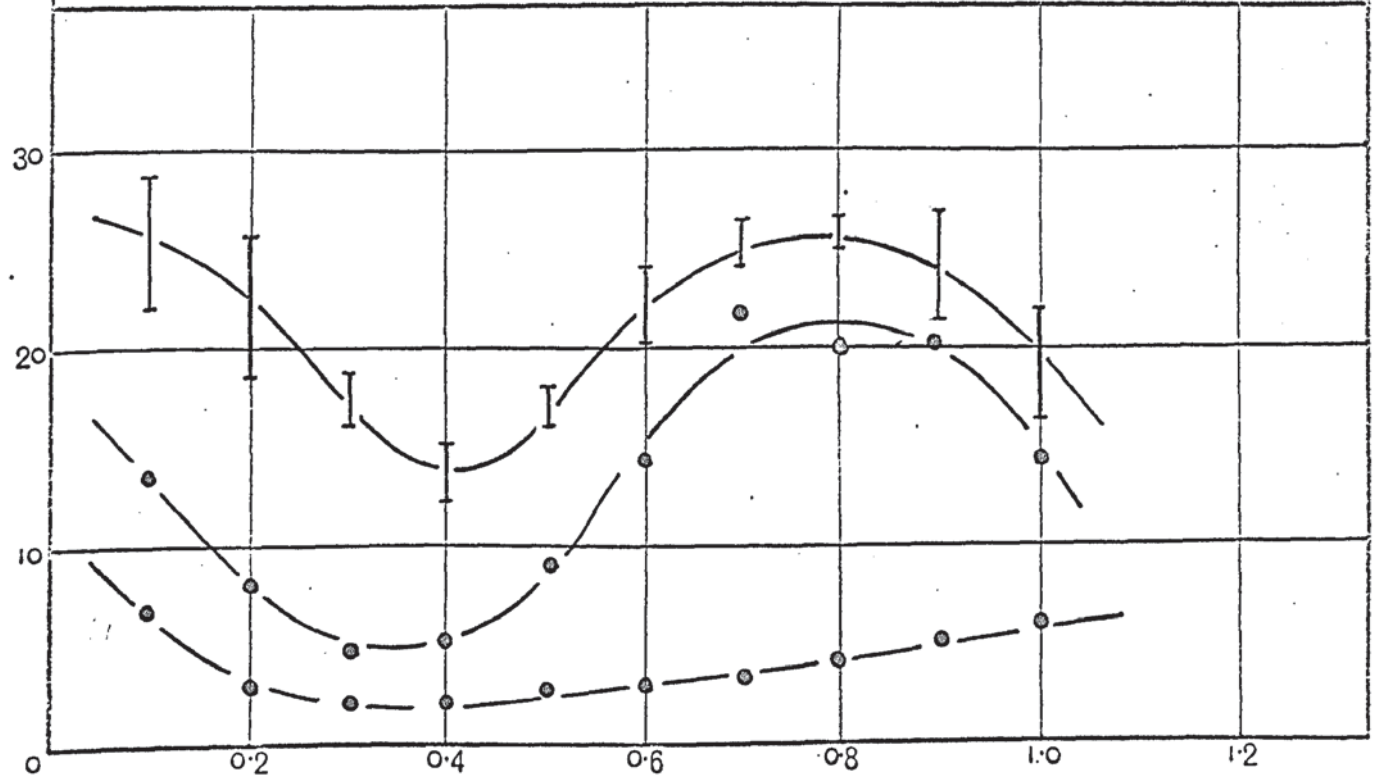

Punch Displacement ····· in.

Test Series 01

Effect of punch displacement on blank holder friction force reduction at different die amplitudes.

Fig. 8.7b

D.R. =1.65

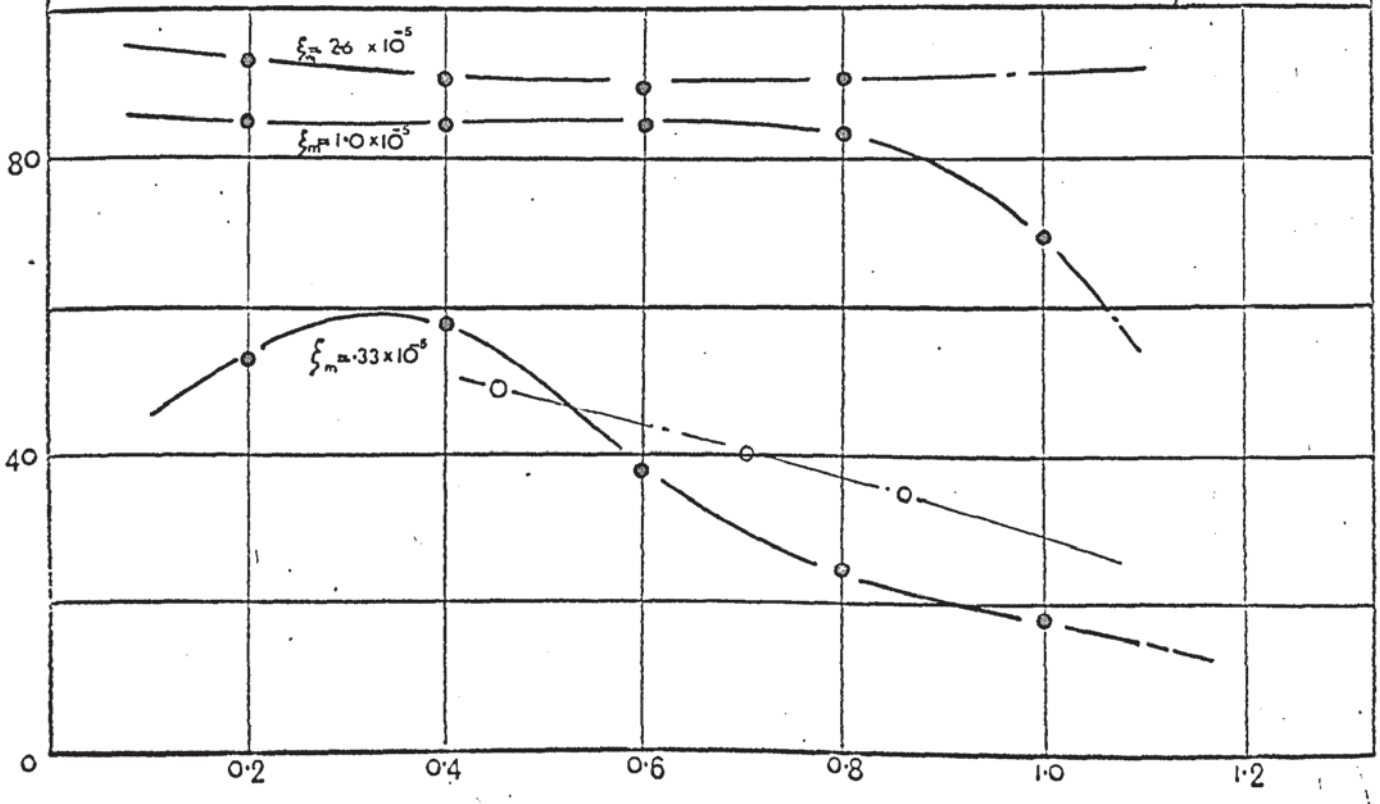

Punch Displacement ····· in.

O — Equation 9·11

Test Series O1

Variation in friction force with punch displacement at different die amplitudes.

Fig.8.8a

D.R.= 1.7

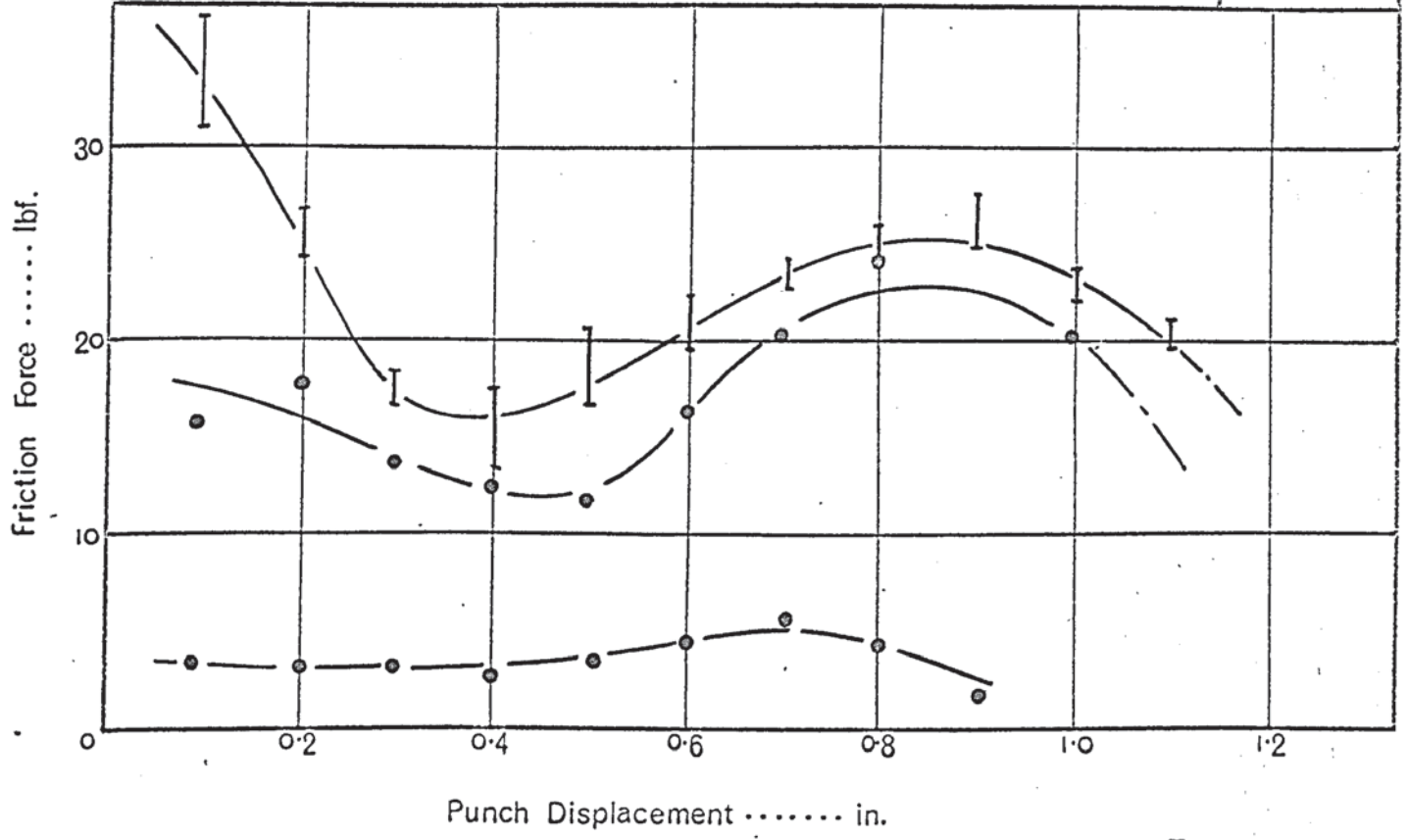

Test Series O1

Effect of punch displacement on blank holder friction force reduction at different die amplitudes.

Fig. 8.8b

D.R. = 1.7

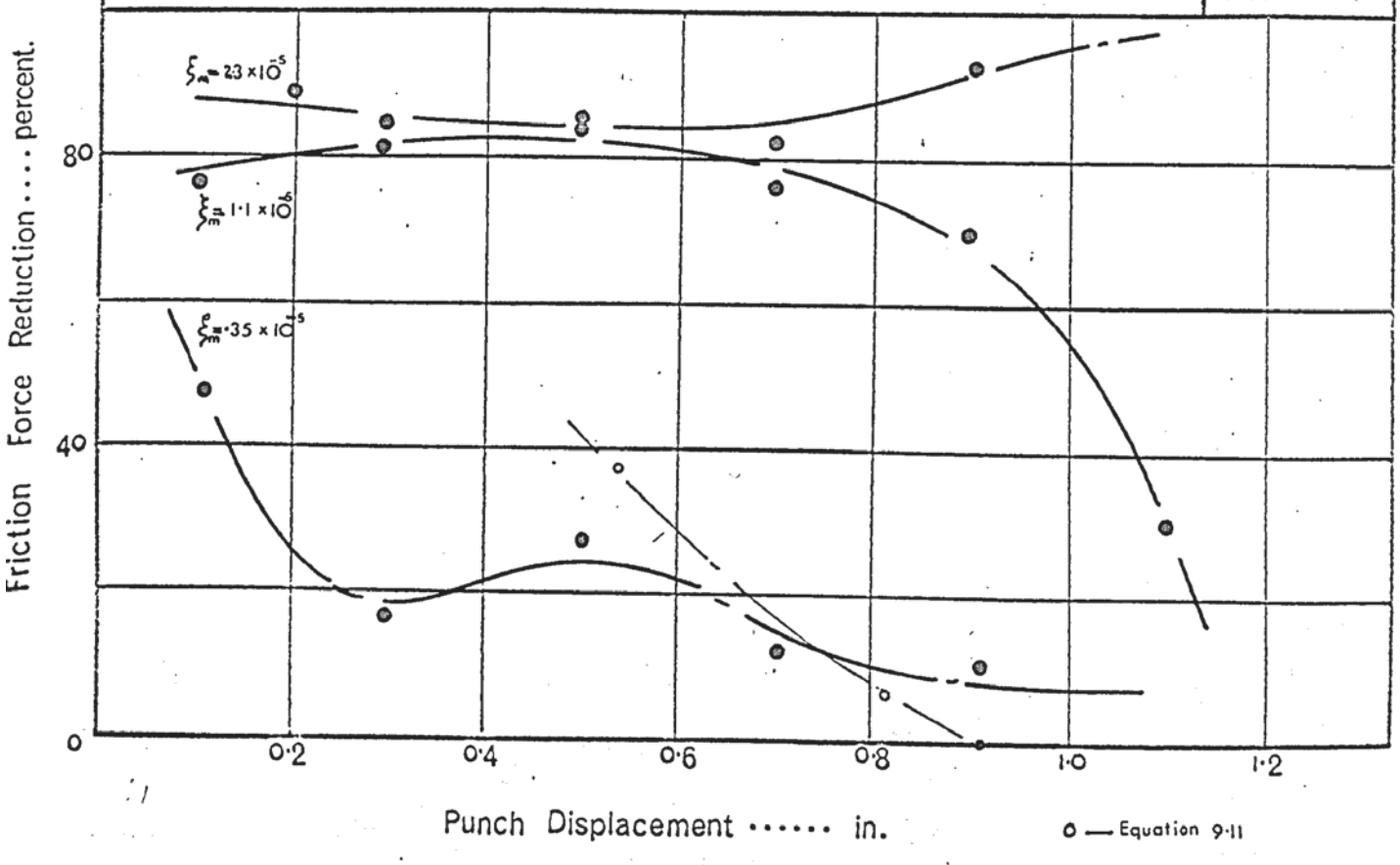

Test Series 02

Variation in Punch Load and Blank Holder Friction Force with Punch Displacement.

Fig. 8.9

D.R.1.5

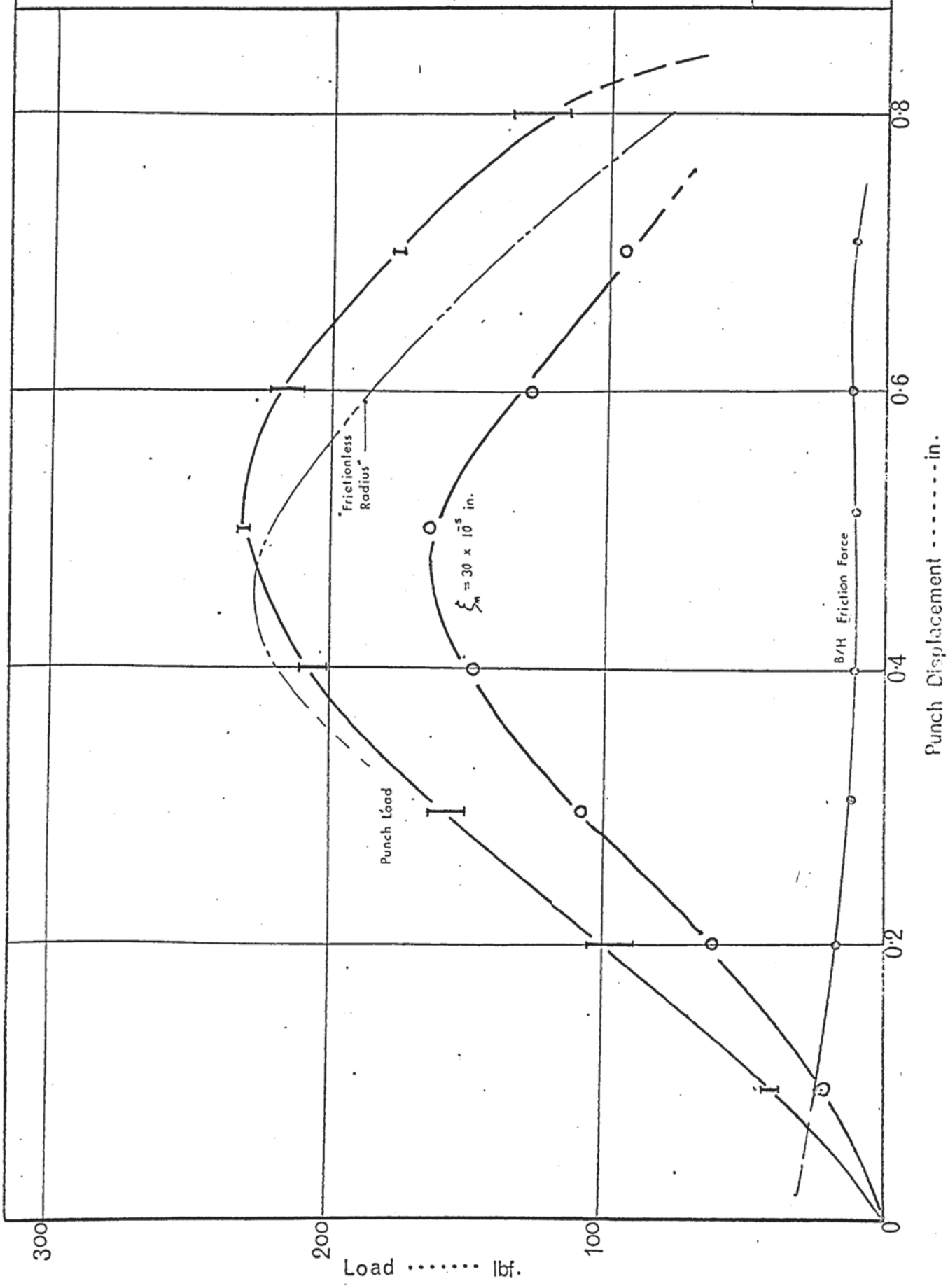

Test Series 02

Variation in Punch Load and Blank Holder Friction Force with Punch Displacement.

Fig. 8.10

D.R.1.6

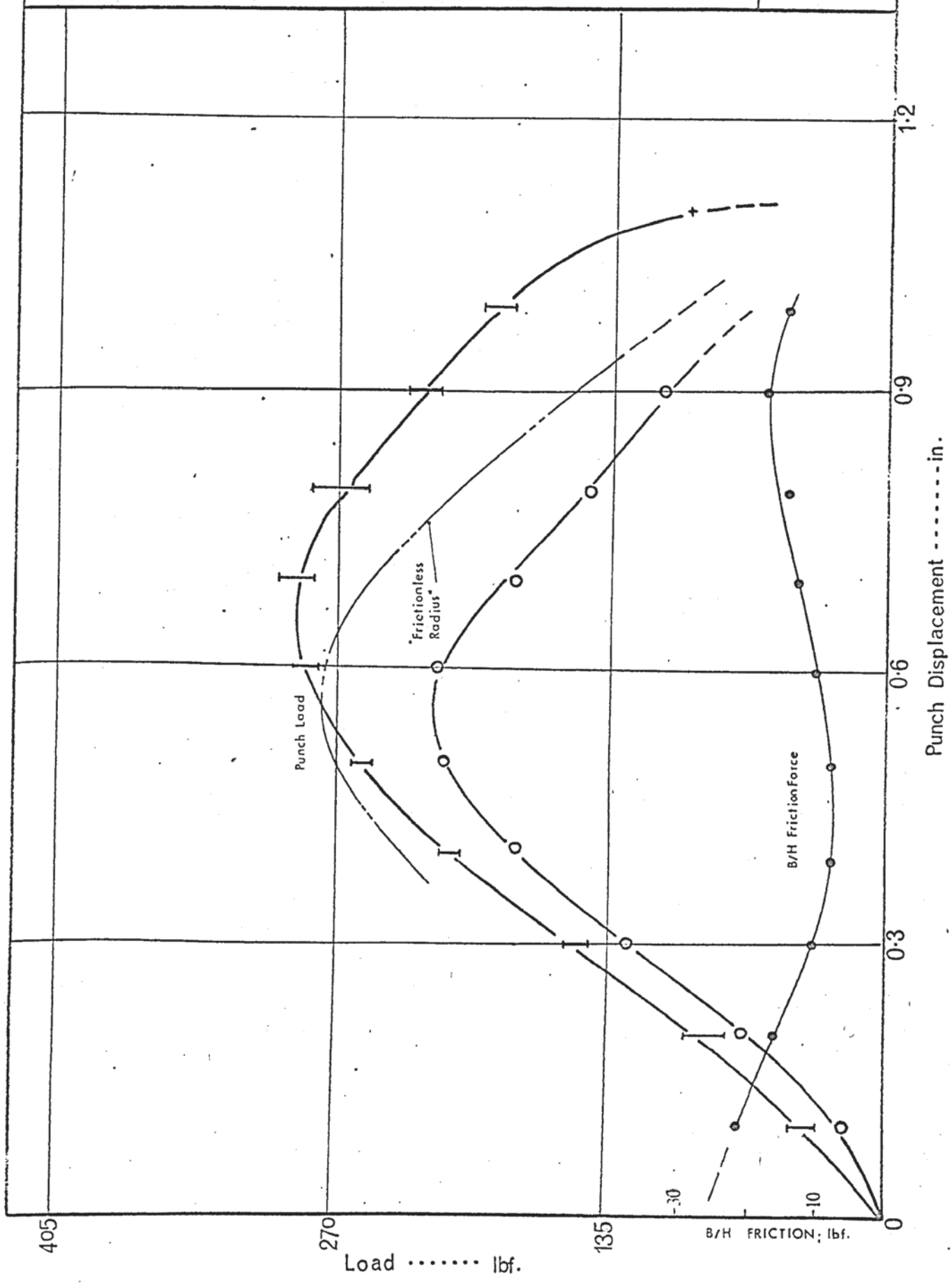

Variation in Punch Load and Blank Holder Friction Force with Punch Displacement.

Fig. 8.11

D.R.1.7

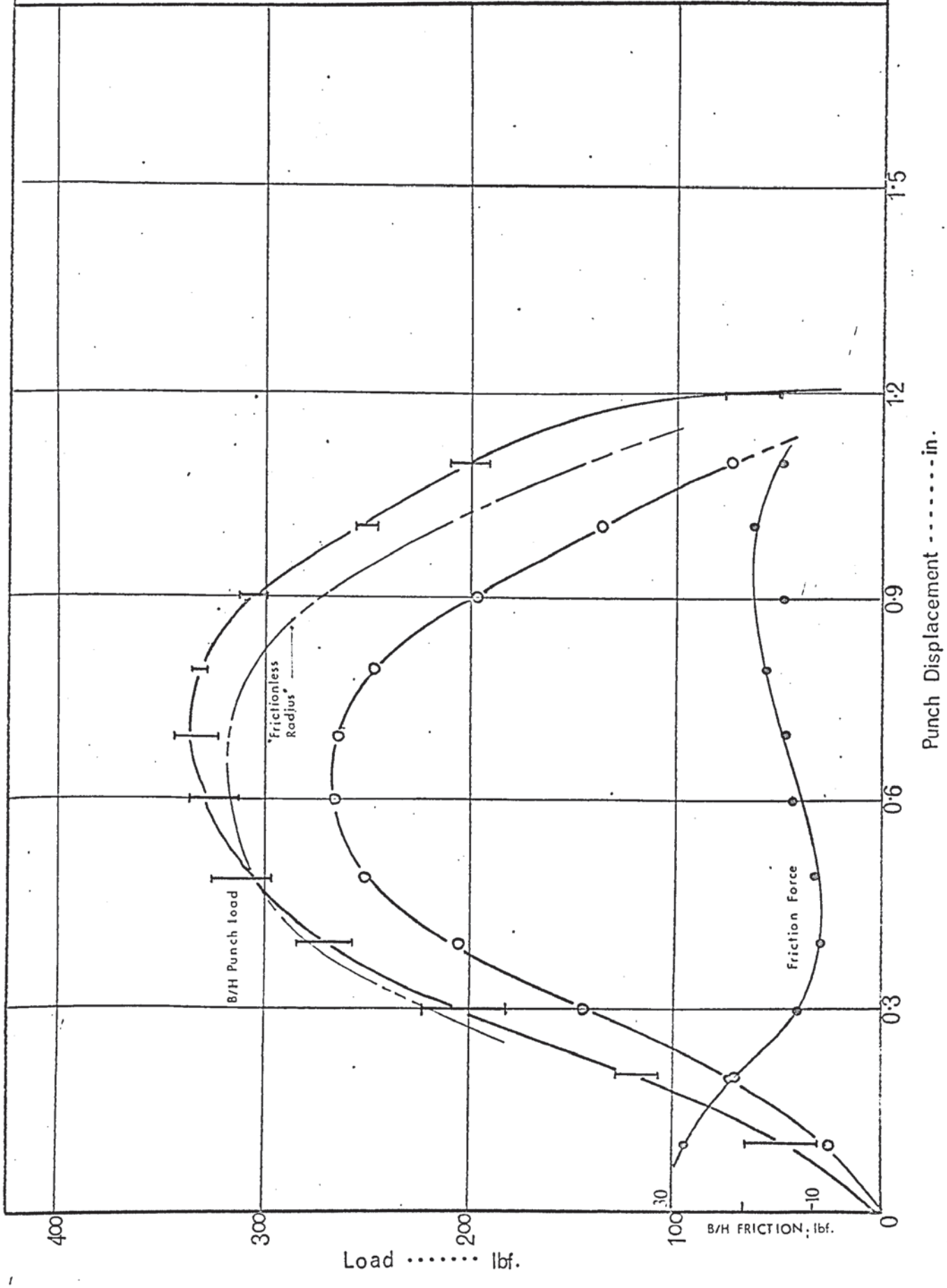

Variation in Punch Load and Blank Holder Friction Force with Punch Displacement.

Fig. 8.12

D.R. 1.8

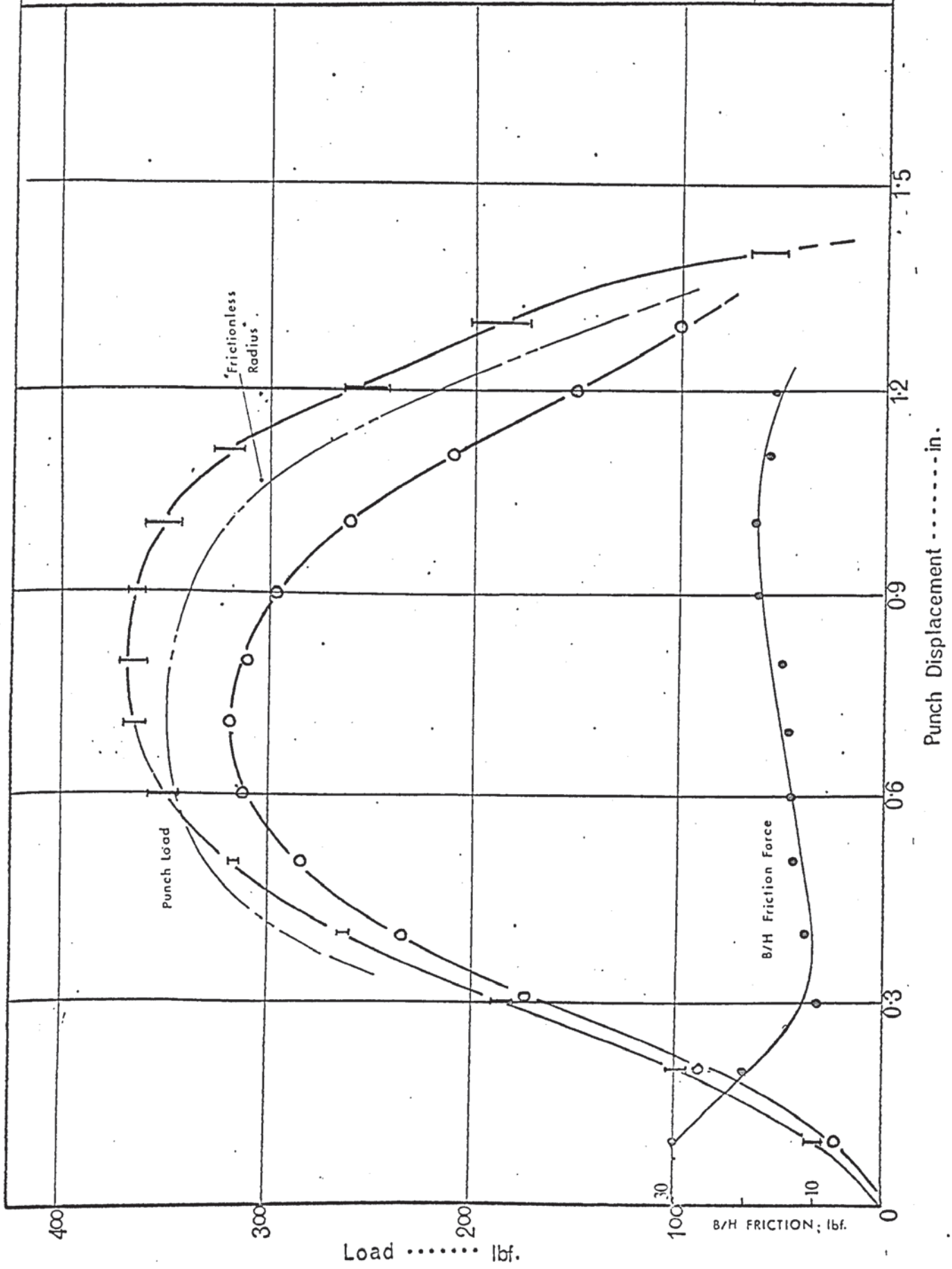

Test Series O2

The effect of increasing die amplitude on the reduction in maximum punch load..

Fig. 8.13

D.R. = 1.5

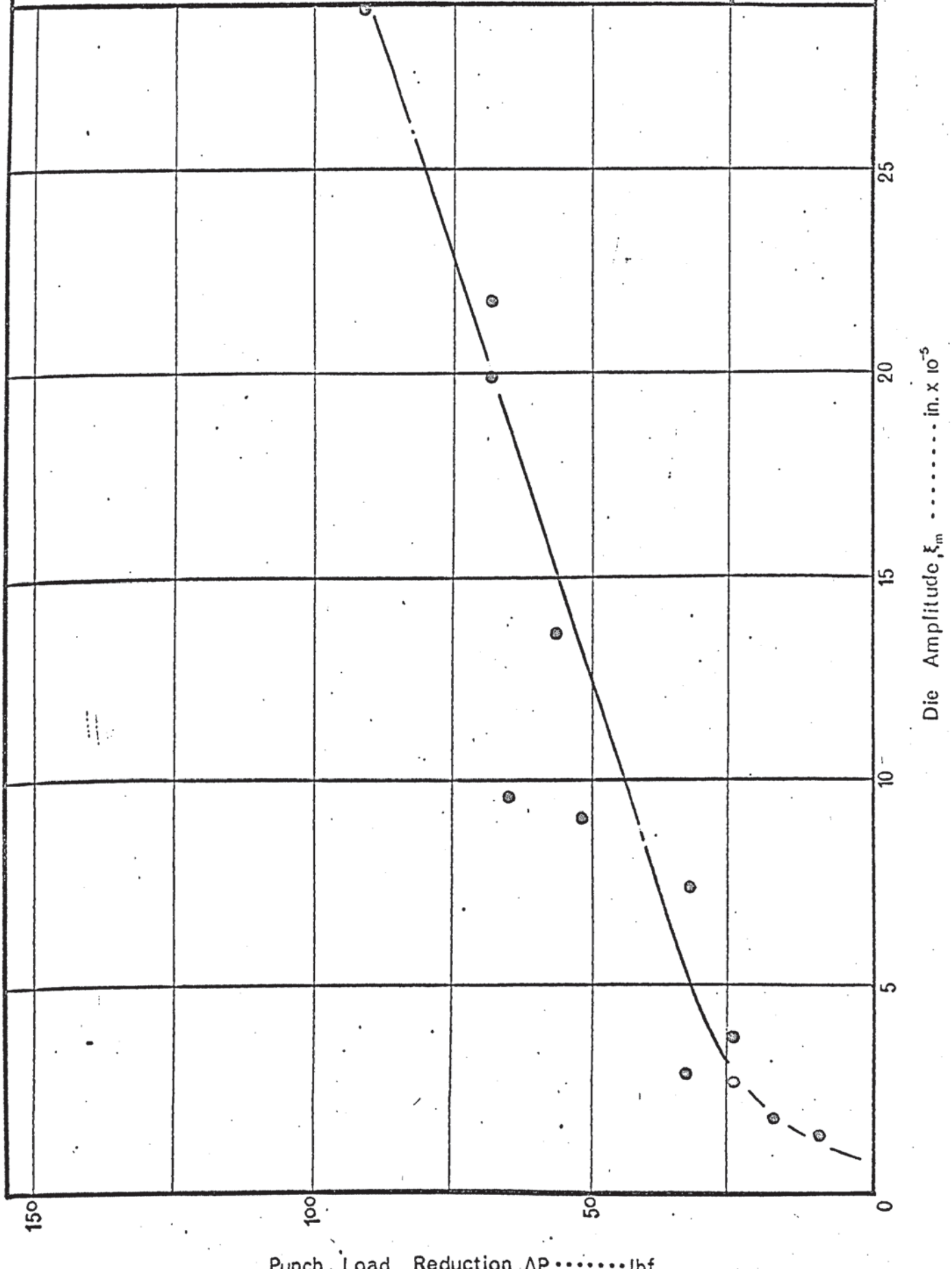

Test Series O2

The effect of increasing die amplitude on the reduction in maximum punch load.

Fig. 8.14

D.R. = 1.6

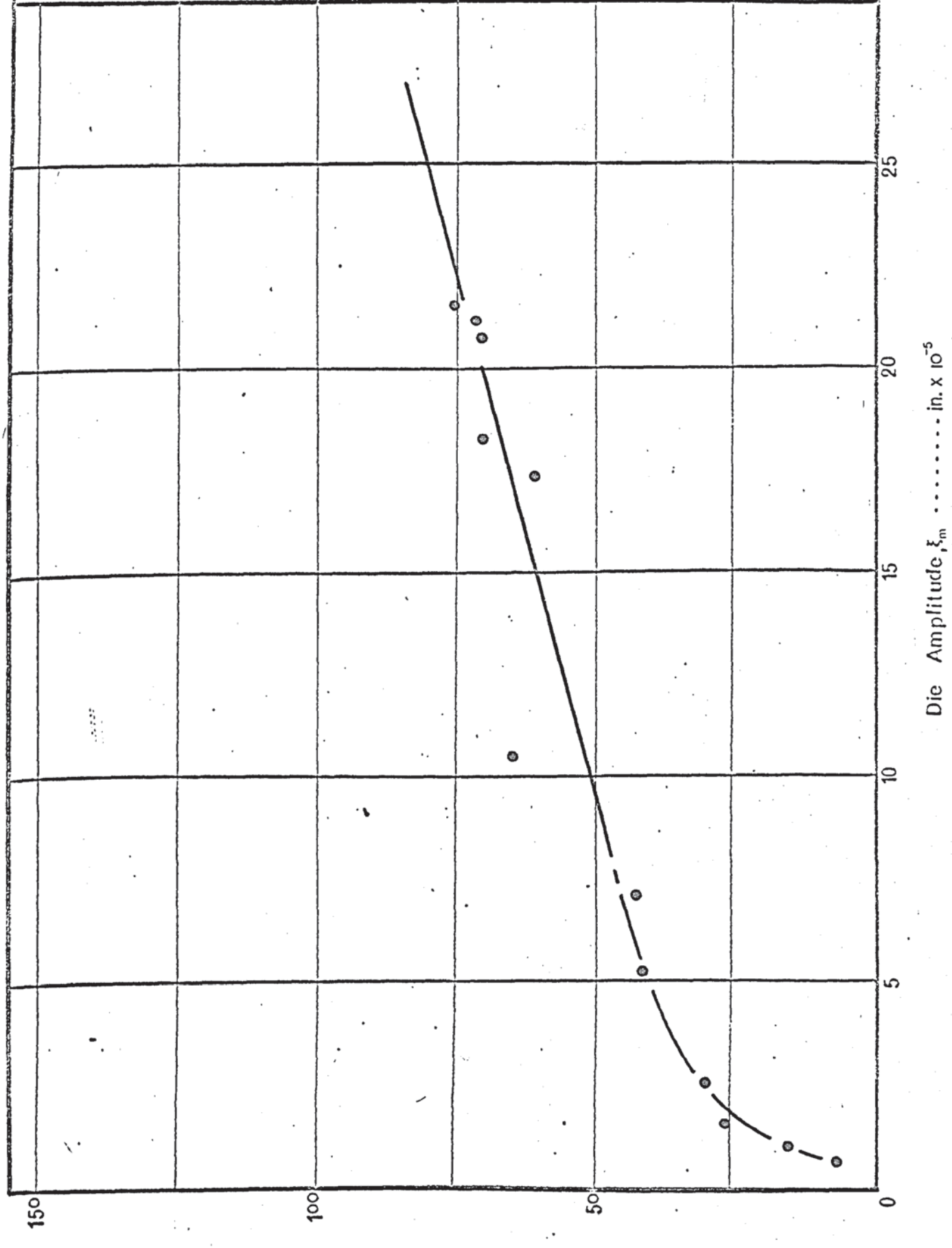

Test Series 02

The effect of increasing die amplitude on the reduction in maximum punch load.

Fig. 8.15

D.R. = 1.7

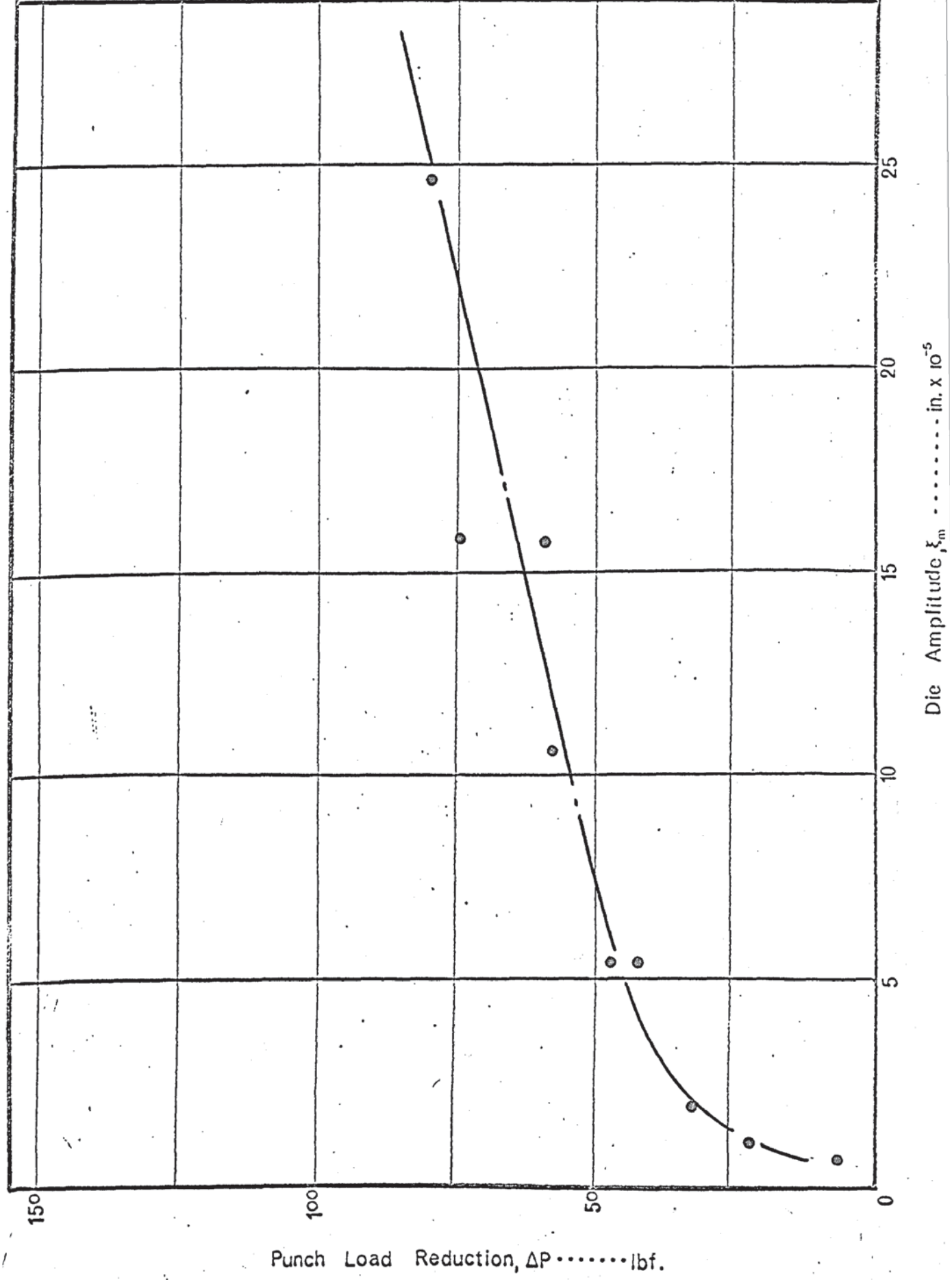

Test Series O2

The effect of increasing die amplitude on the reduction in maximum punch load.

Fig. 8.16

D.R. = 1.8

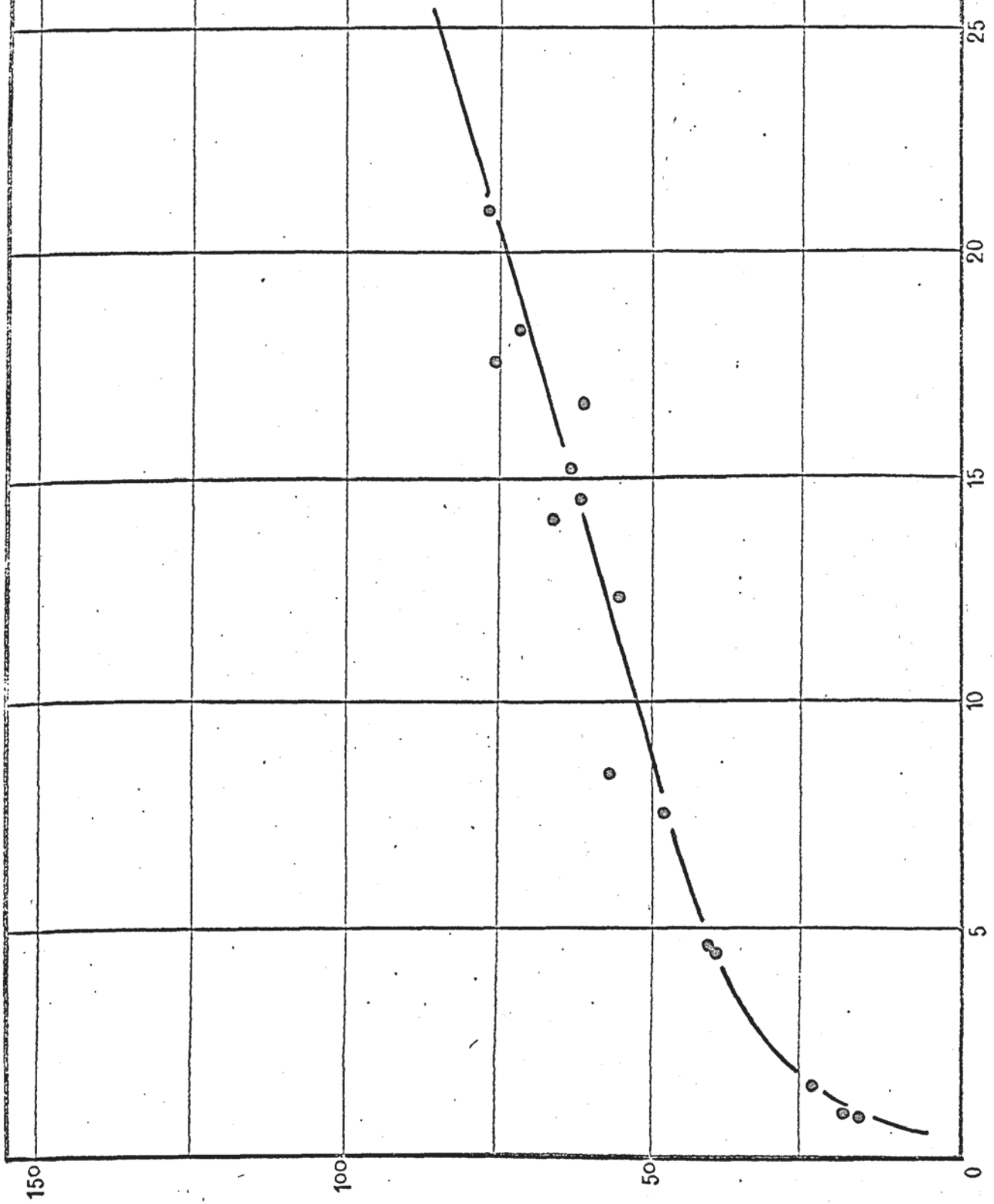

Test Series O2

The effect of increasing die amplitude on the reduction in maximum punch load.

Fig. 8.17

D.R. = 1.9

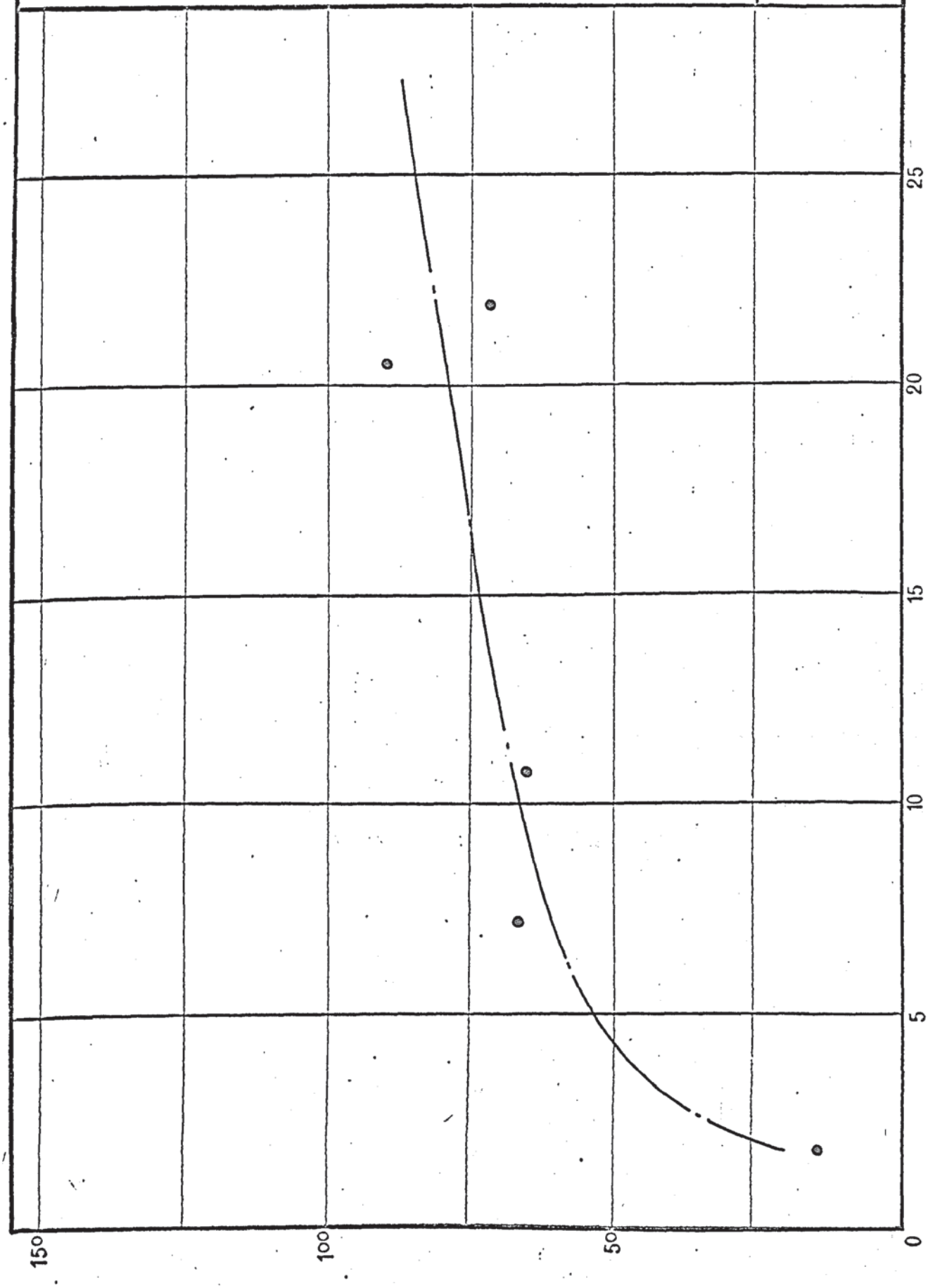

Test Series 02

Variation of punch load reduction with die amplitude at different stages of drawing.

Fig. 8.18

D.R. = 1.5

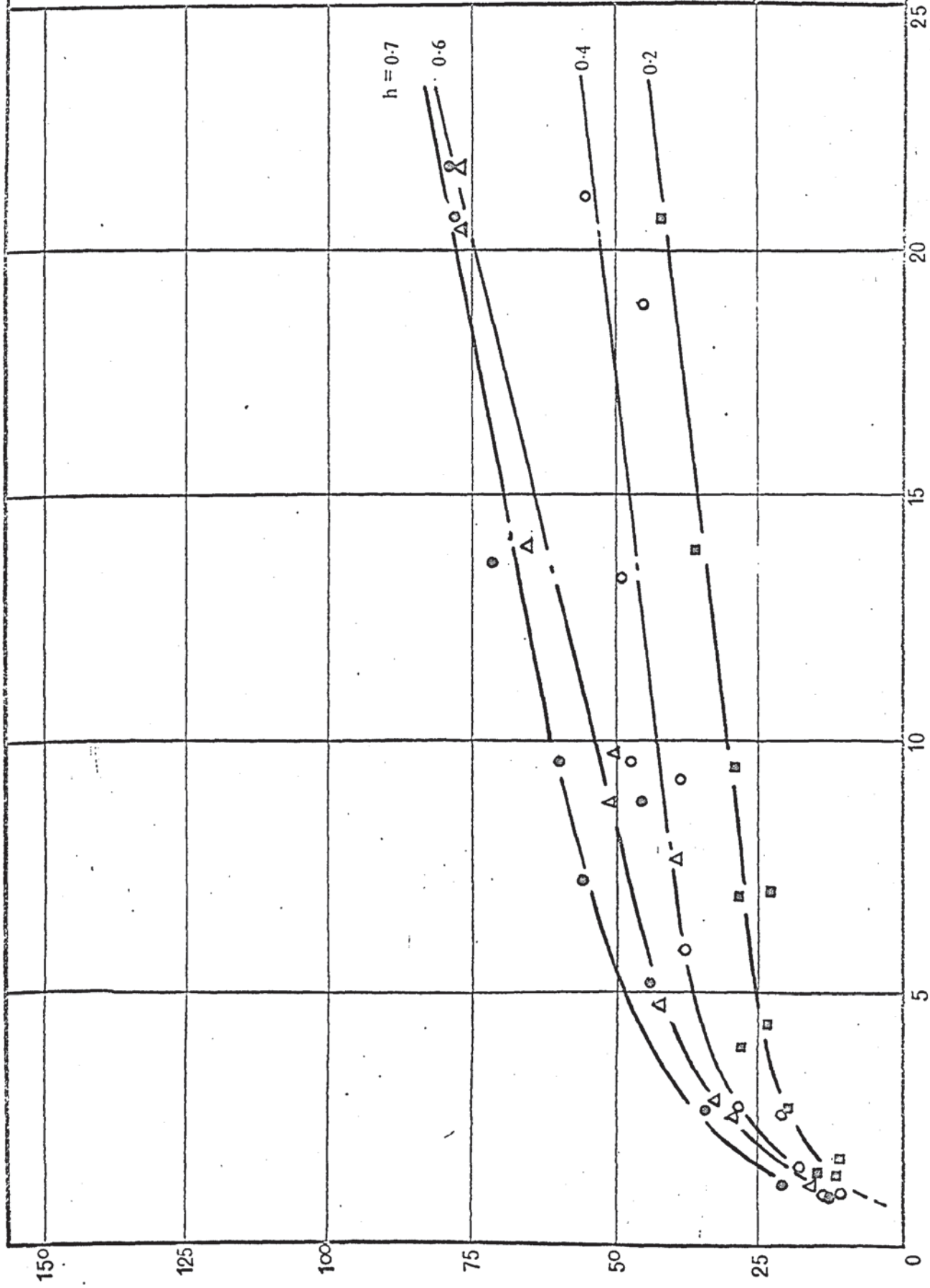

Test Series '02

Variation of punch load reduction with die amplitude at different stages of drawing.

Fig. 8.19

D.R. = 1.6

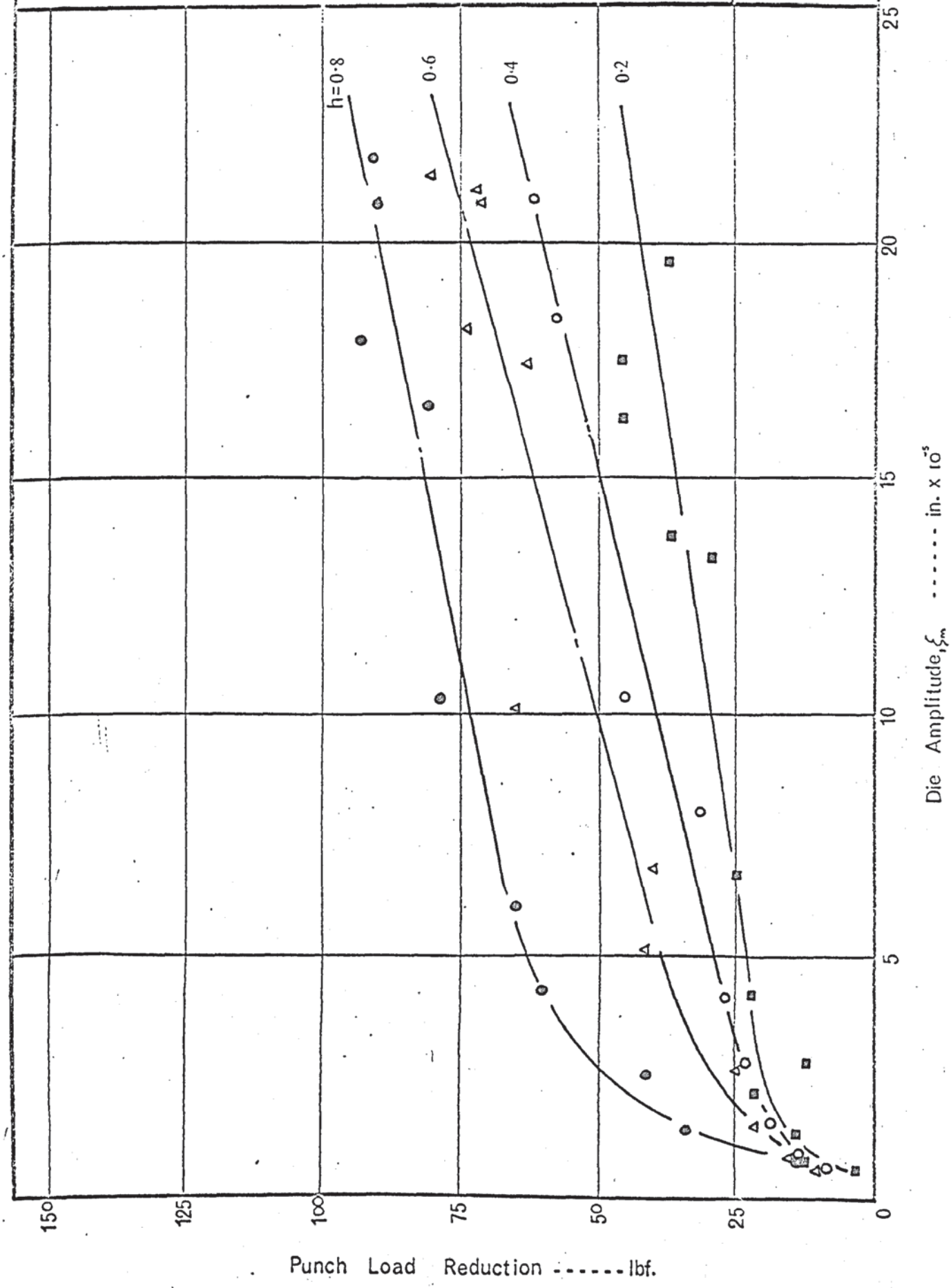

Test Series O2

Variation of punch load reduction with die amplitude at different stages of drawing.

Fig. 8.20

D.R. = 1.7

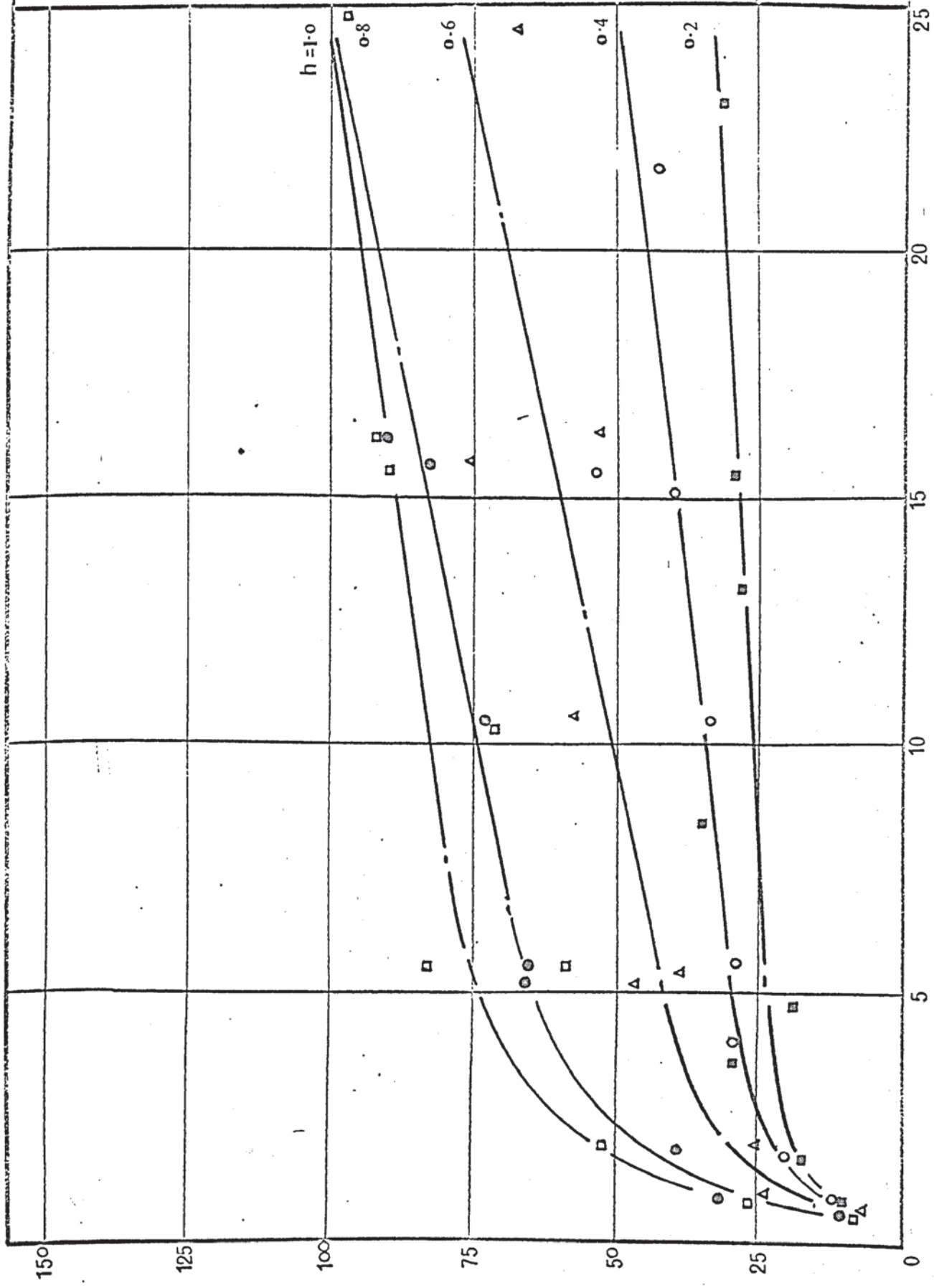

Test Series O2

Variation of punch load reduction with die amplitude at different stages of drawing.

Fig. 8.21

D.R. = 1.8

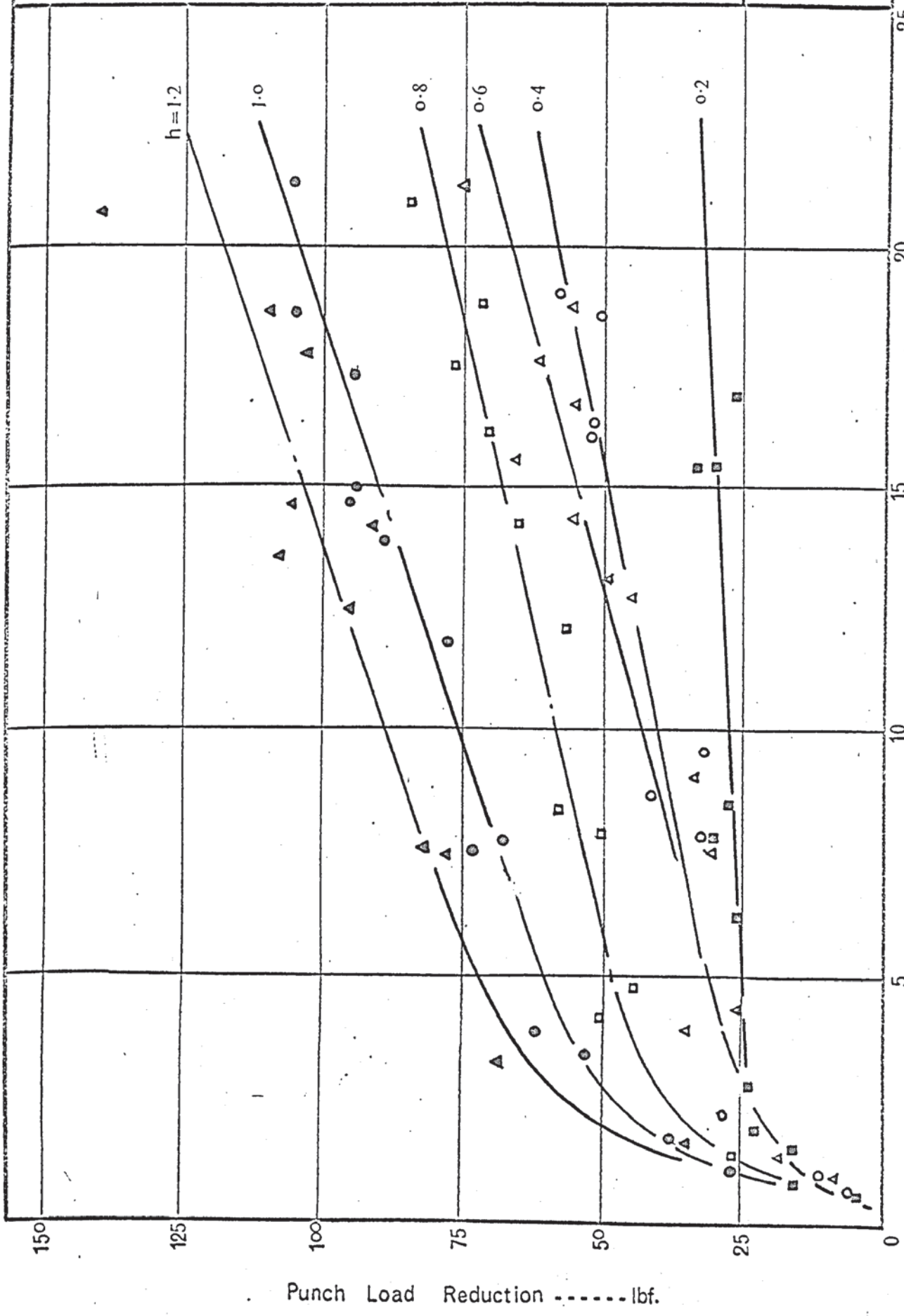

Effect of vibration amplitude on the maximum oscillatory and non-oscillatory punch loads, during interrupted oscillatory tests.

Fig 8.22a

D.R 1.5

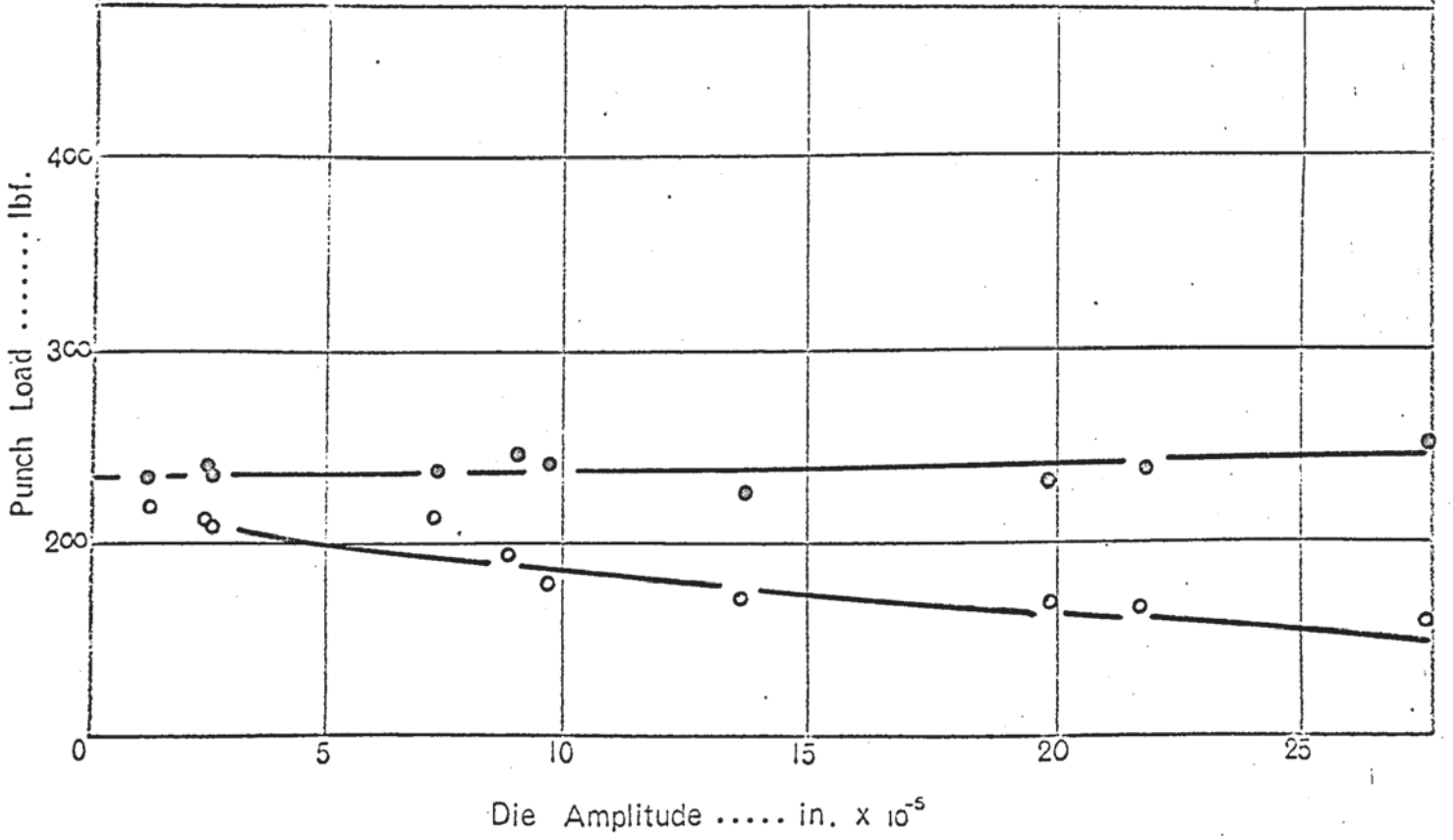

Variation in the corresponding blank holder friction force with increasing die amplitude.

Fig. 8.22b

D.R. 1.5

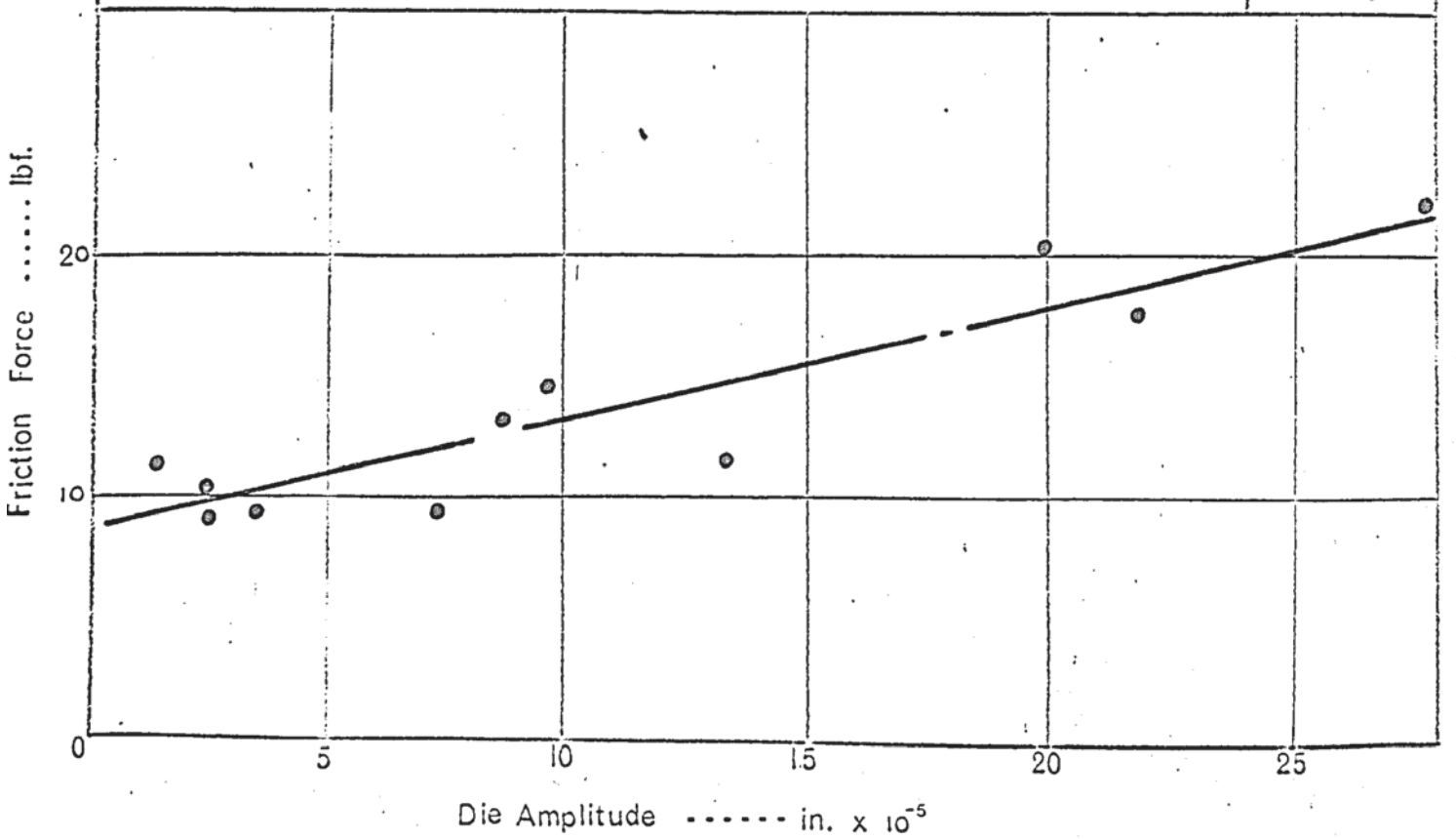

Test Series-02

Effect of vibration amplitude on the maximum oscillatory and non-oscillatory punch loads, during interrupted oscillatory tests.

Fig 8.23a
D.R 1.6

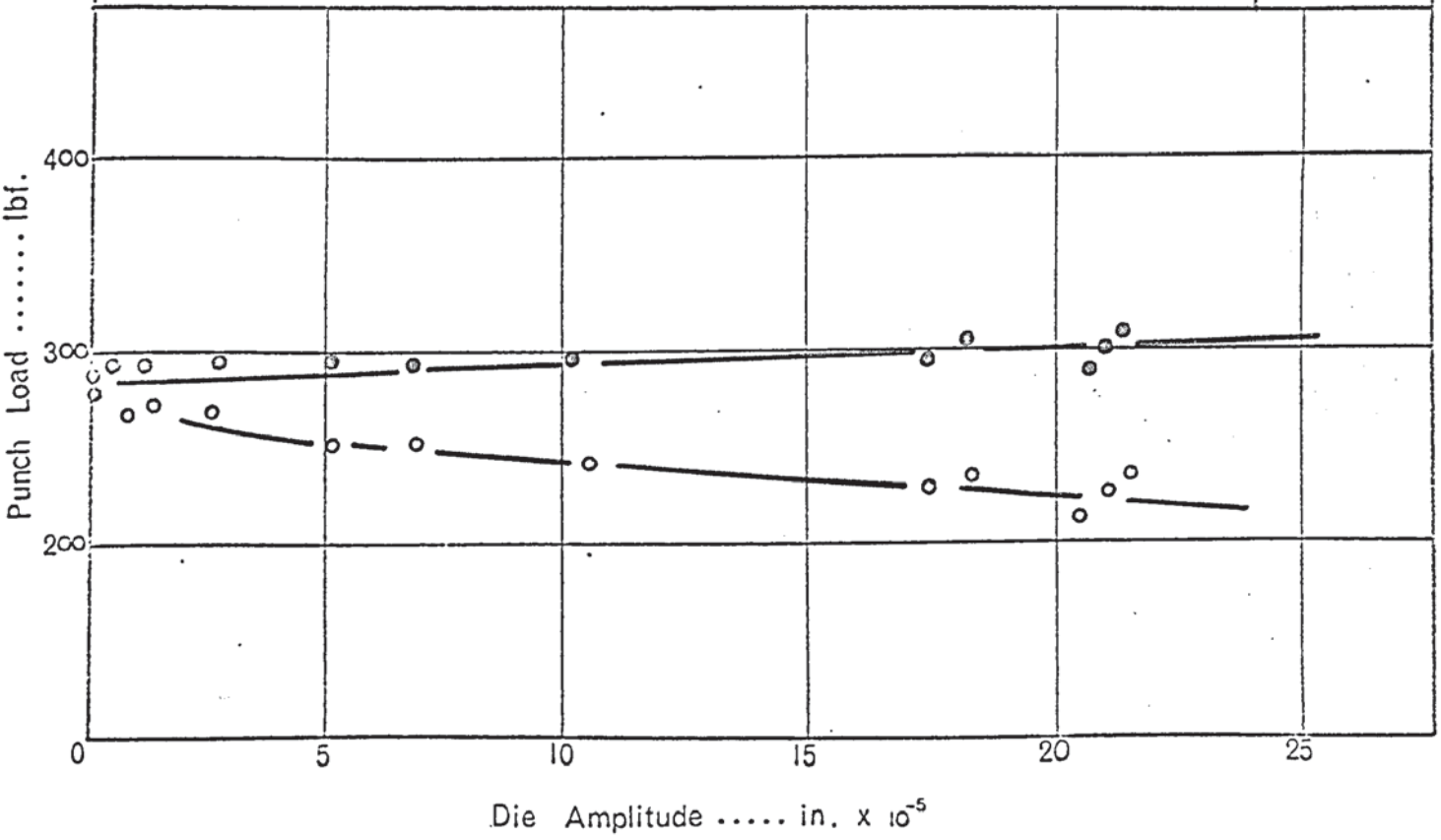

Variation in the corresponding blank holder friction force with increasing die amplitude.

Fig. 8.23b
D.R. 1.6

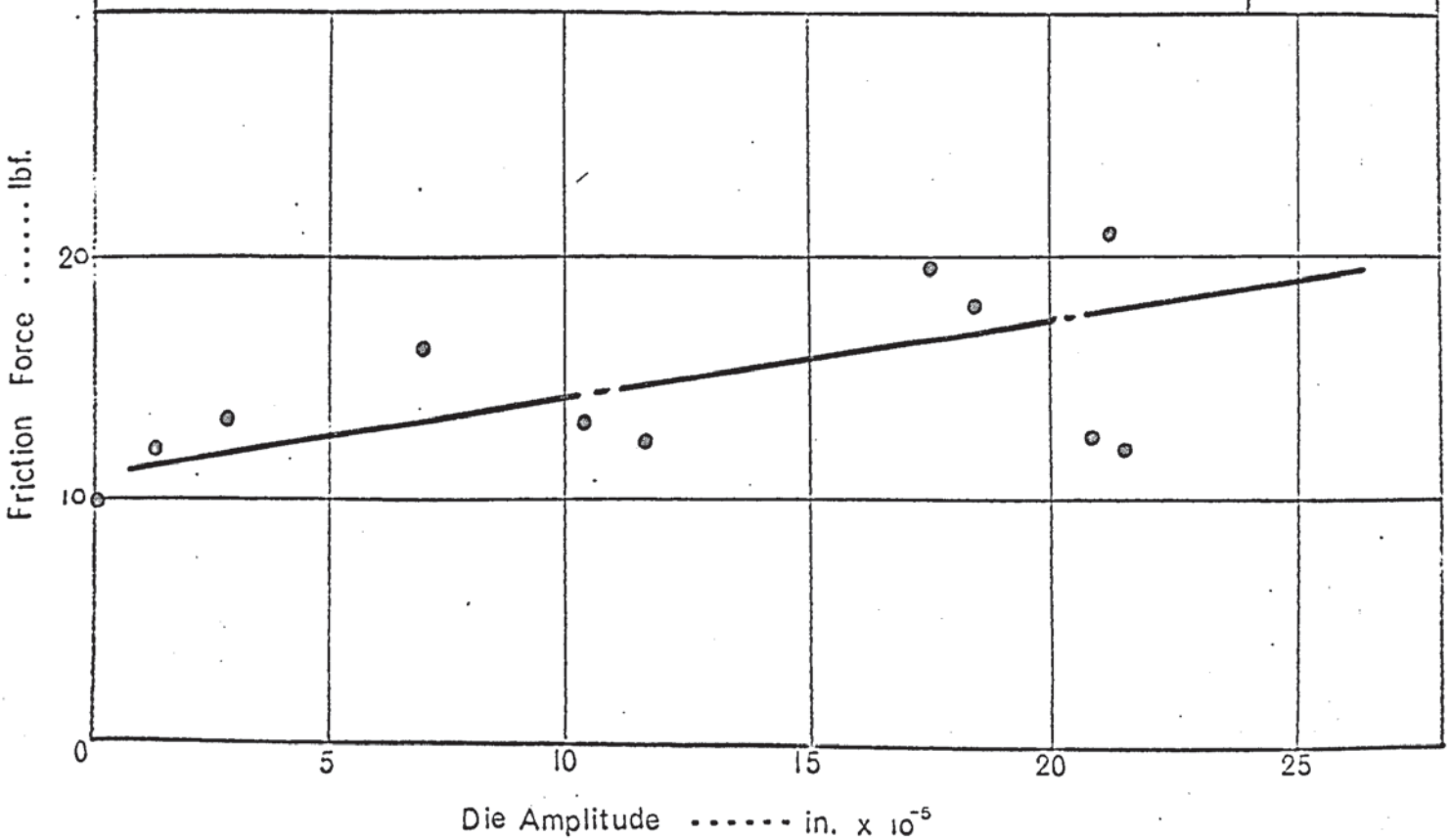

Test Series-02

Effect of vibration amplitude on the maximum oscillatory and non-oscillatory punch loads, during interrupted oscillatory tests.

Fig 8.24a

D.R 1.7

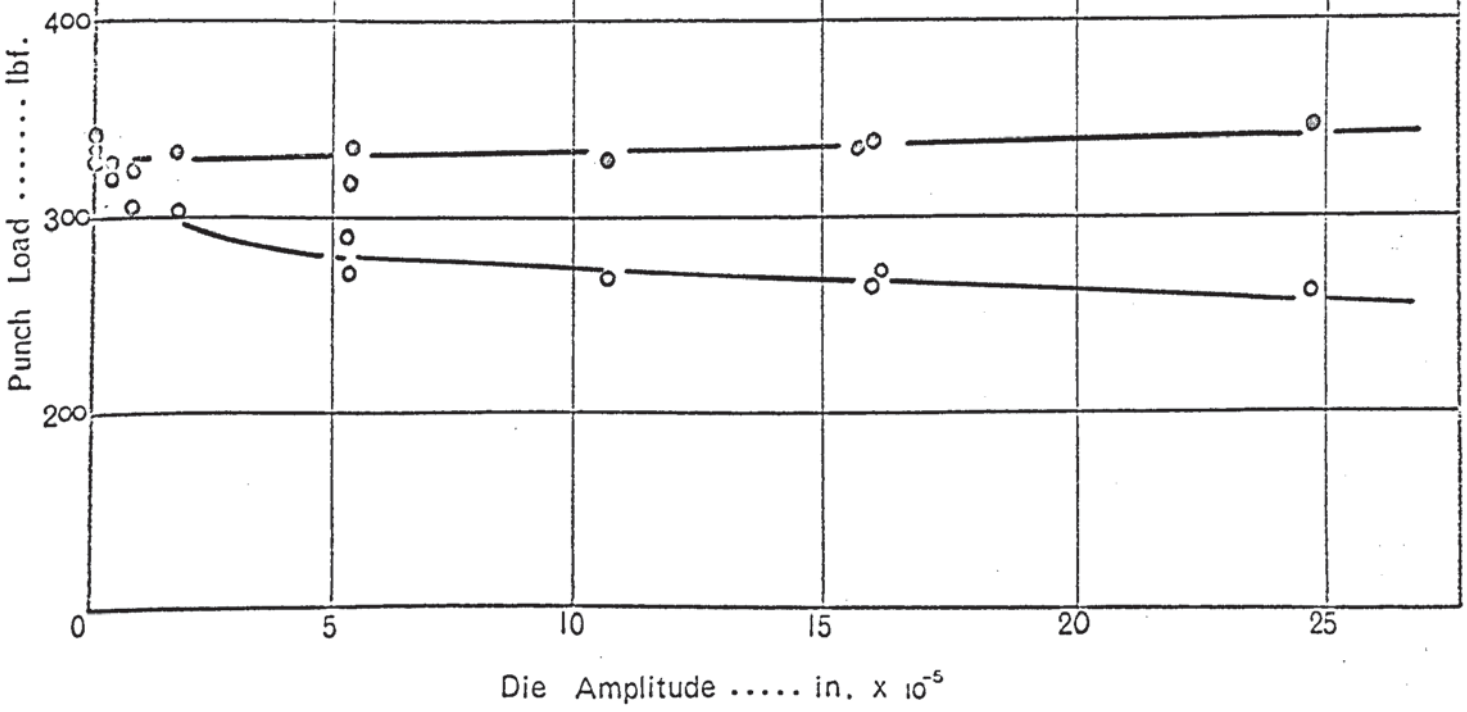

Variation in the corresponding blank holder friction force with increasing die amplitude.

Fig. 8.24b

D.R. 1.7

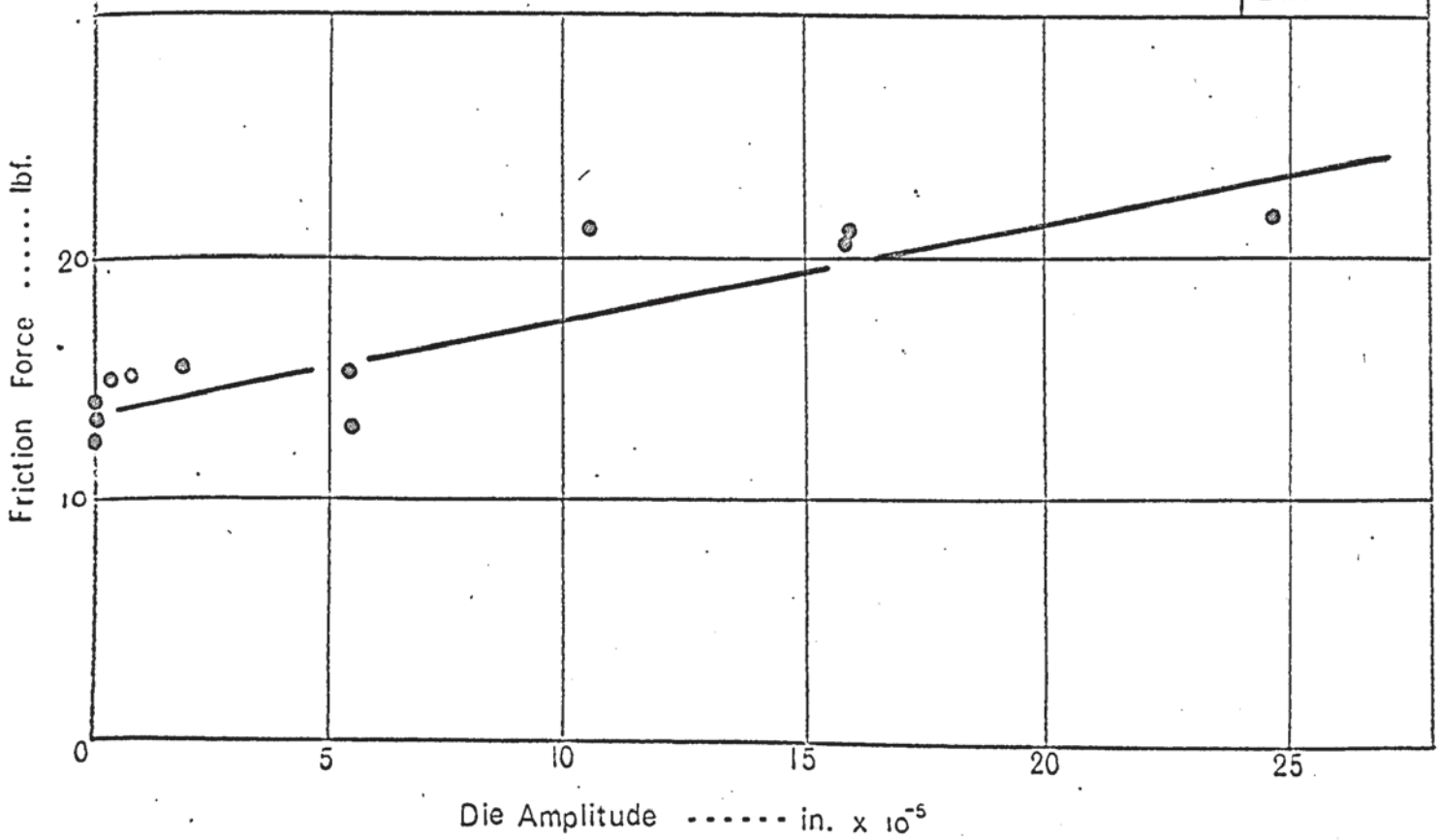

Test Series-02

Effect of vibration amplitude on the maximum oscillatory and non-oscillatory punch loads, during interrupted oscillatory tests.

Fig 8.25a

D.R 1.8

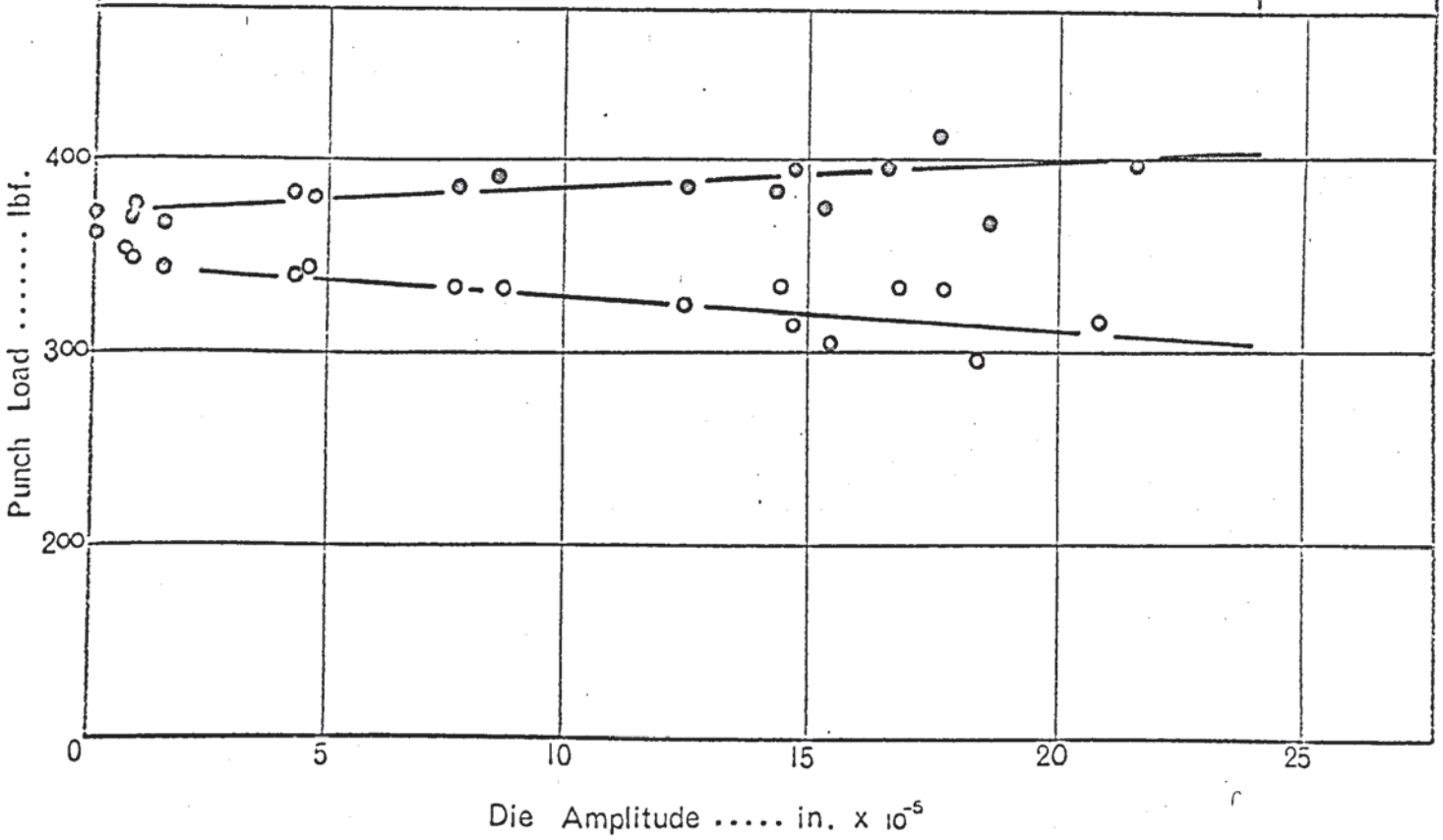

Variation in the corresponding blank holder friction force with increasing die amplitude.

Fig. 8.25b

D.R. 1.8

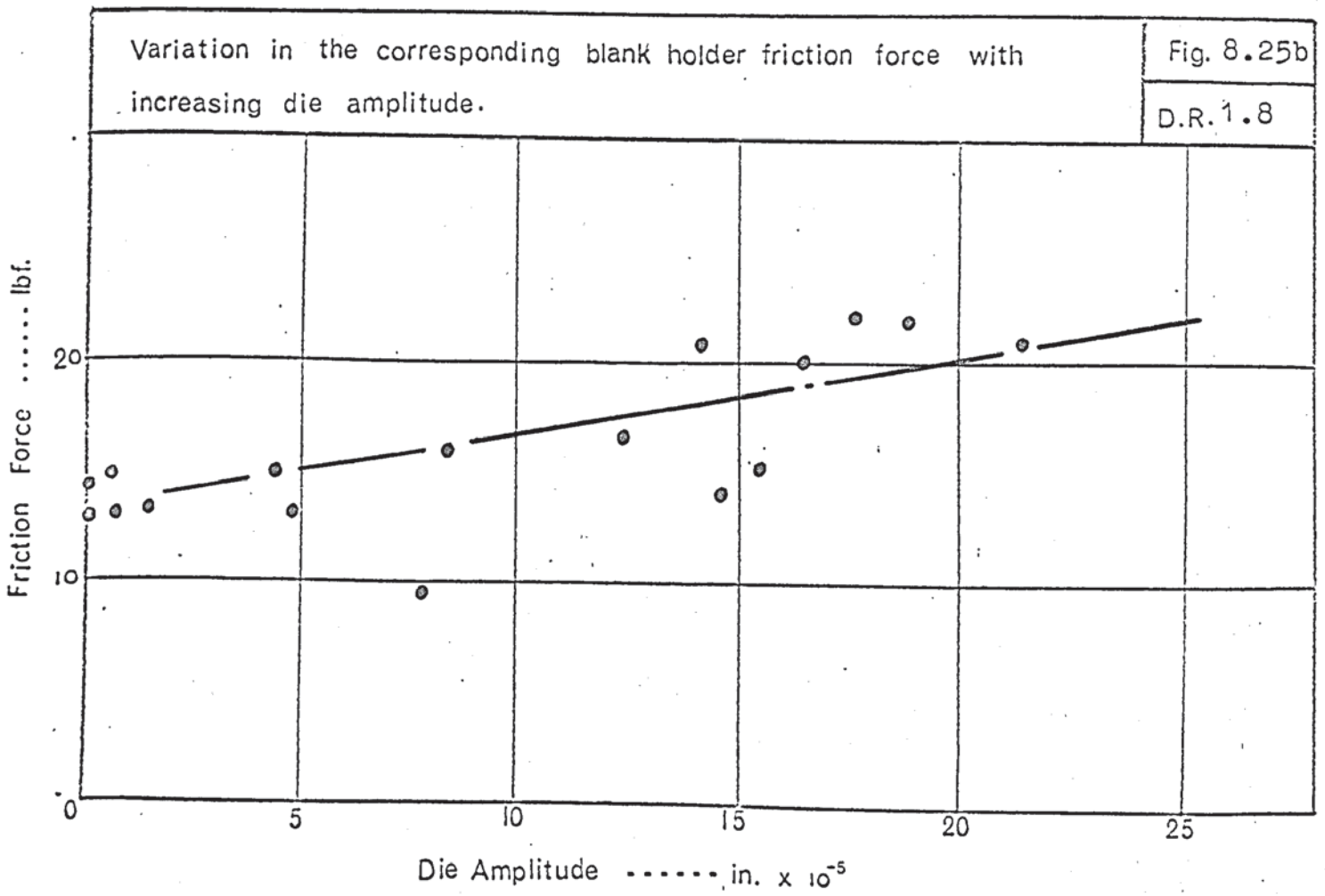

Test Series 03

The effect of increasing die amplitude on the reduction in maximum punch load.

Fig. 8.26

D.R. = 1.5

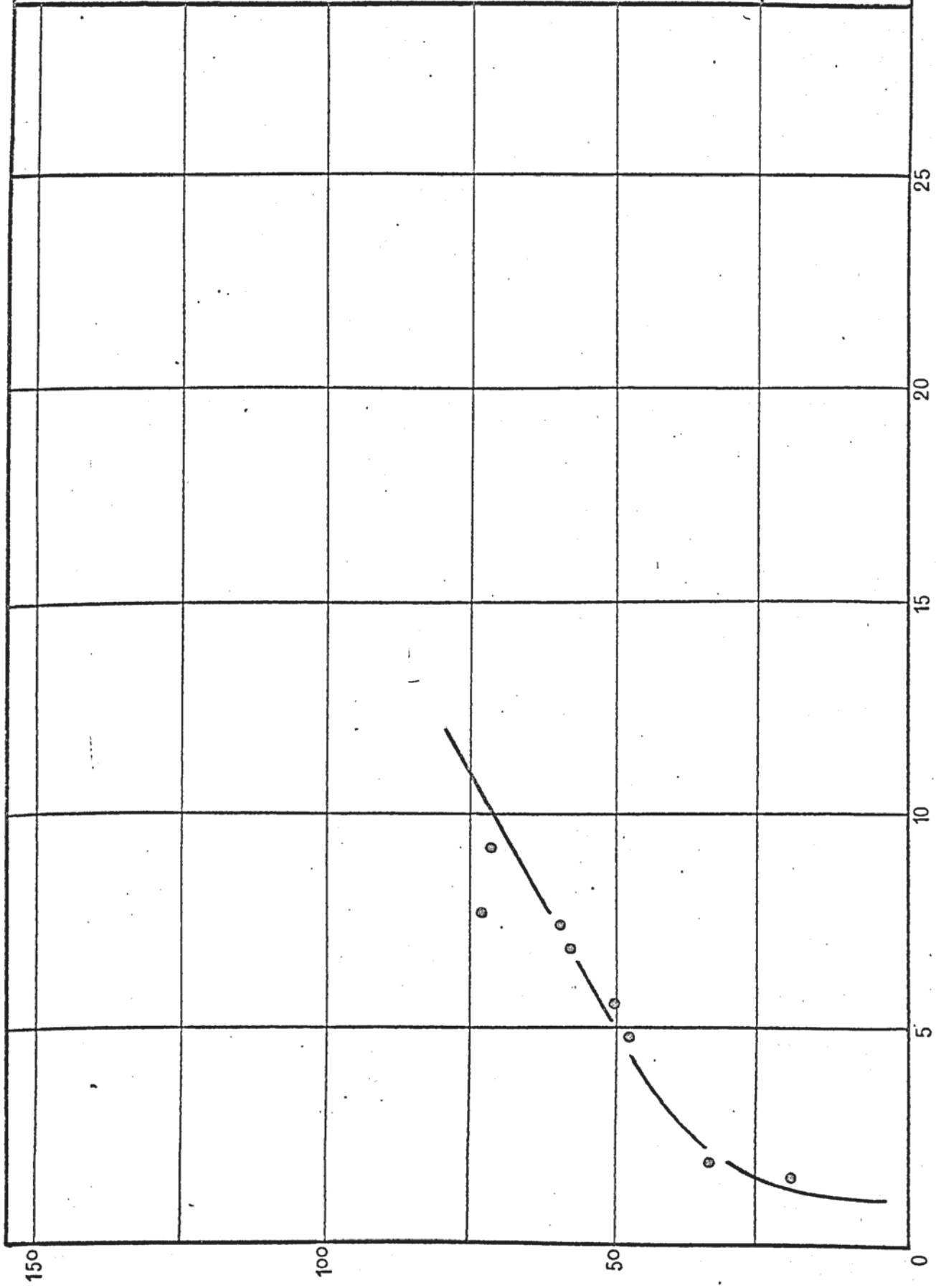

Test Series 03

The effect of increasing die amplitude on the reduction in maximum punch load.

Fig. 8.27

D.R. = 1.6

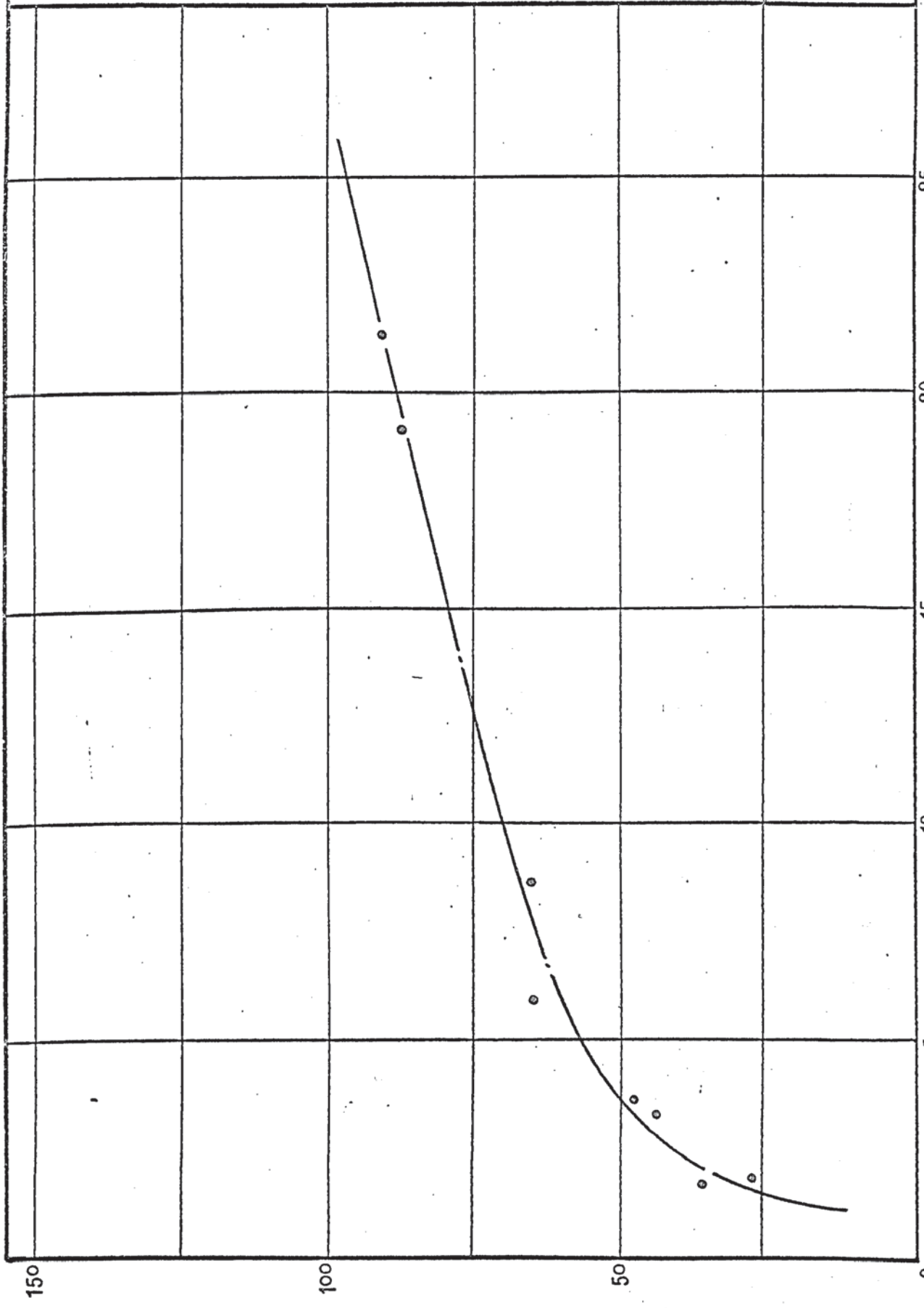

Test Series 03

The effect of increasing die amplitude on the reduction in maximum punch load.

Fig. 8.28

D.R. = 1.7

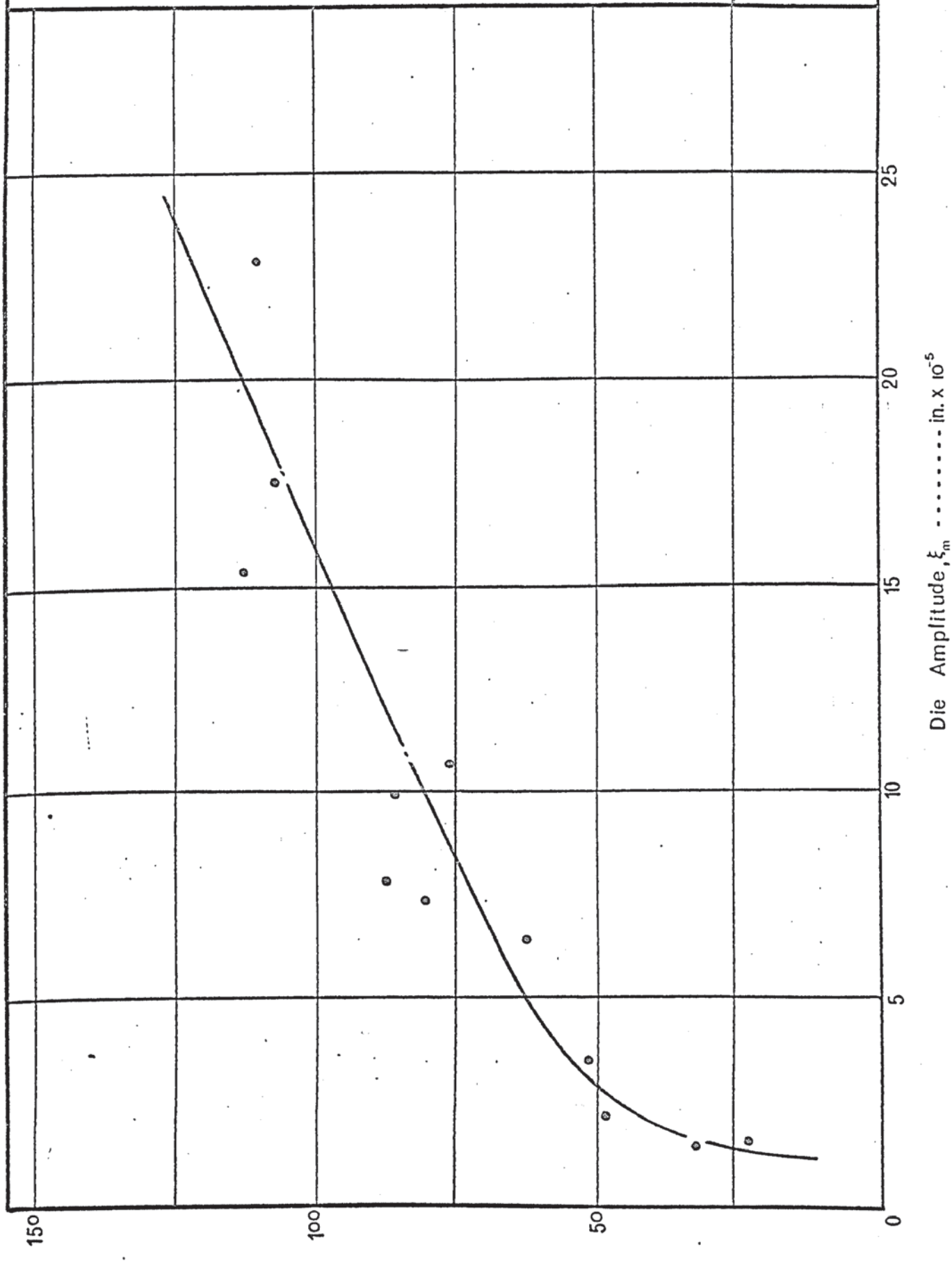

Test Series O3

The effect of increasing die amplitude on the reduction in maximum punch load.

Fig. 8.29

D.R. = 1.80

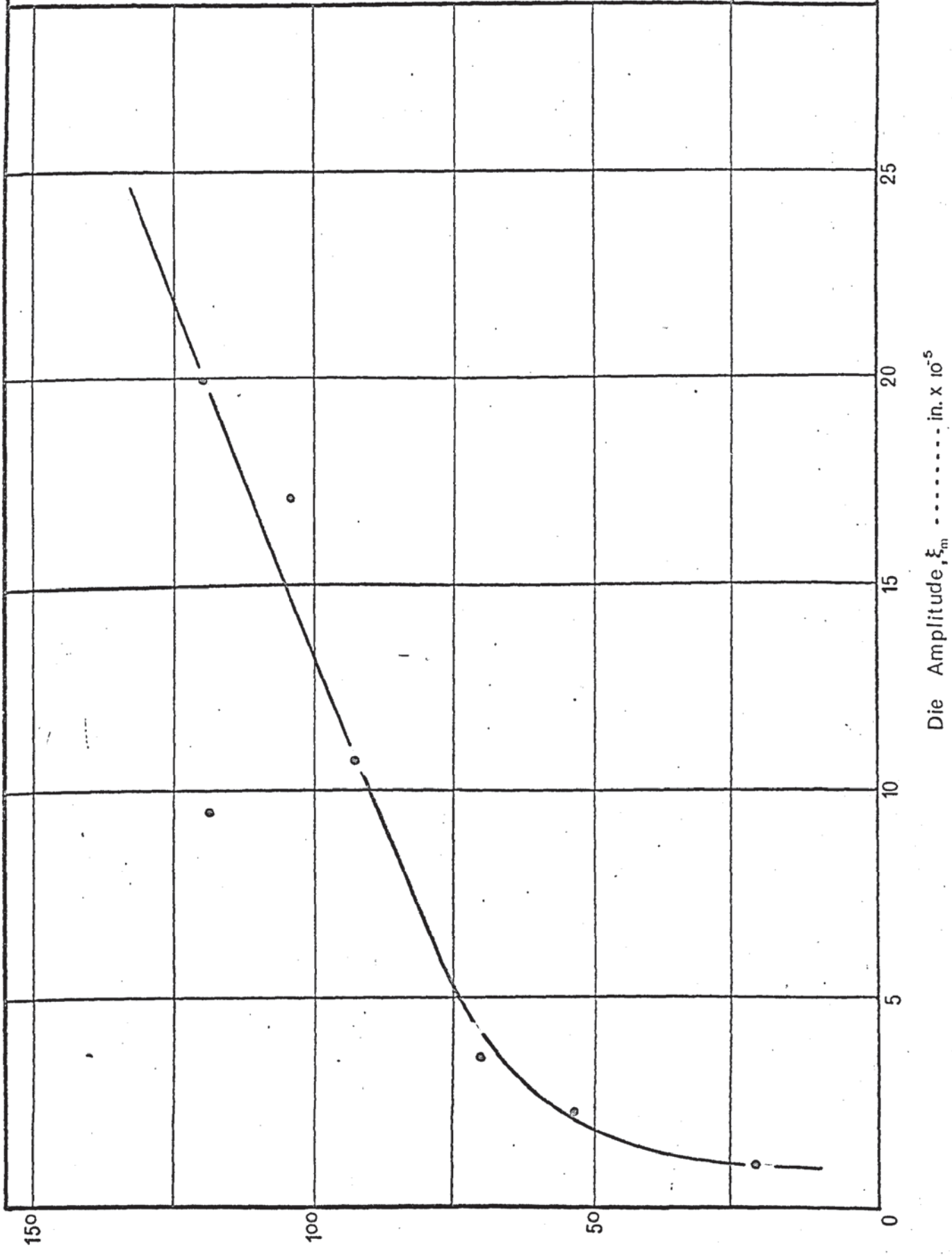

Test Series 03

The effect of increasing die amplitude on the reduction in maximum punch load.

Fig. 8.30

D.R. = 1.90

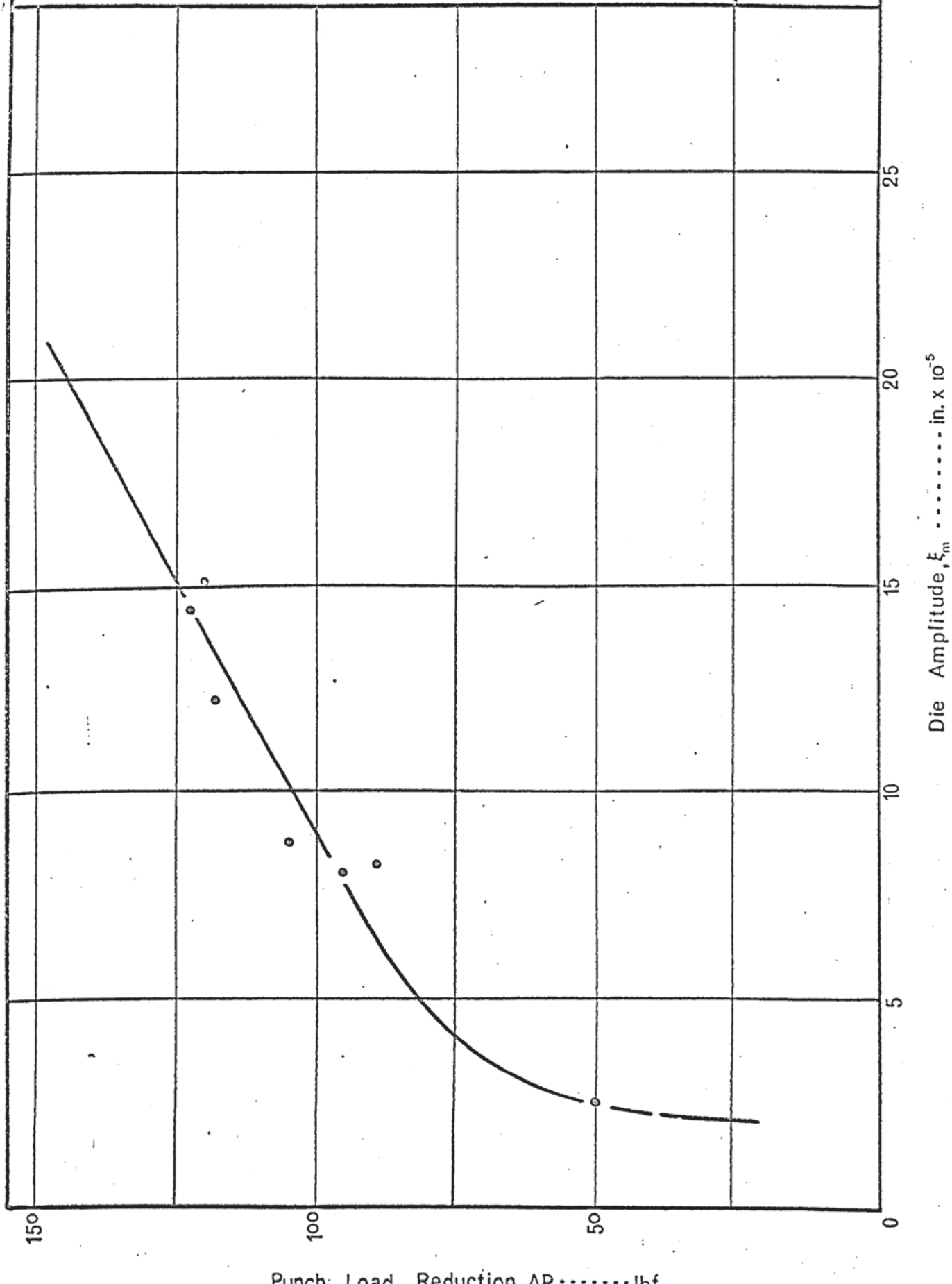

Test Series 03

Variation of punch load reduction with die amplitude at different stages of drawing.

Fig. 8.31

D.R. = 1.5

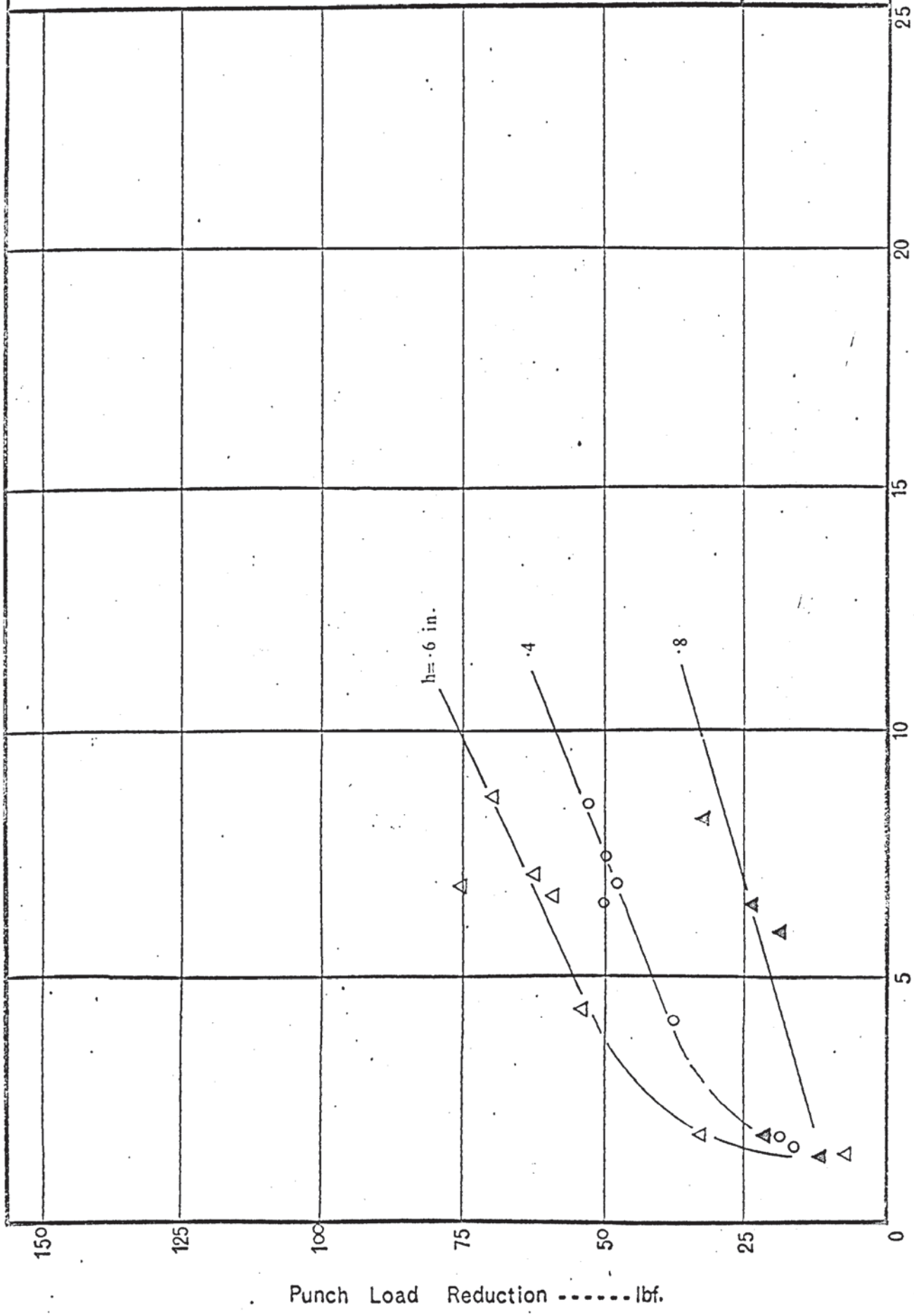

Test Series 03

Variation of punch load reduction with die amplitude at different stages of drawing.

Fig. 8.32

D.R. = 1.6

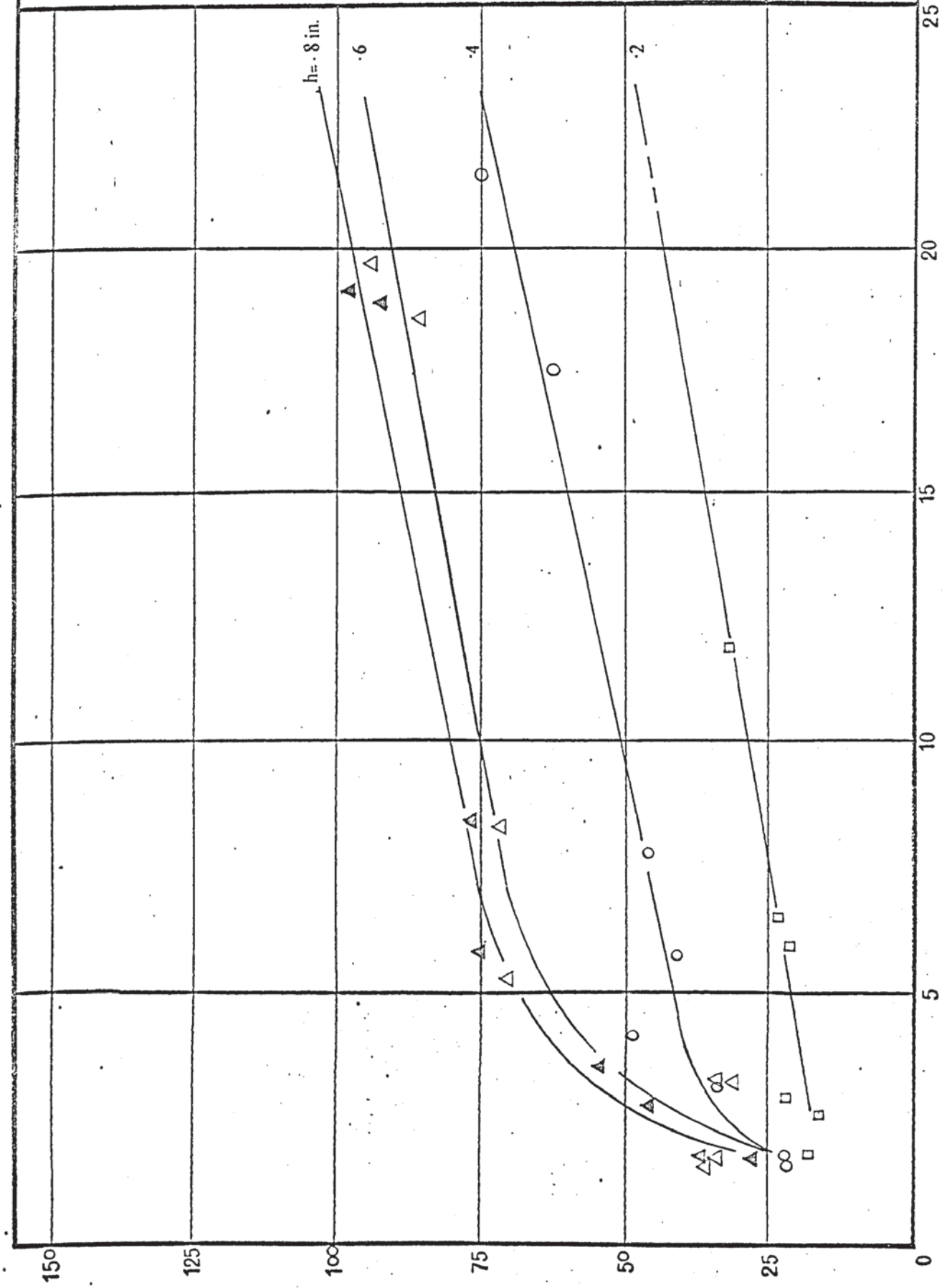

Test Series 03

Variation of punch load reduction with die amplitude at different stages of drawing.

Fig. 8.32

D.R. = 1.6

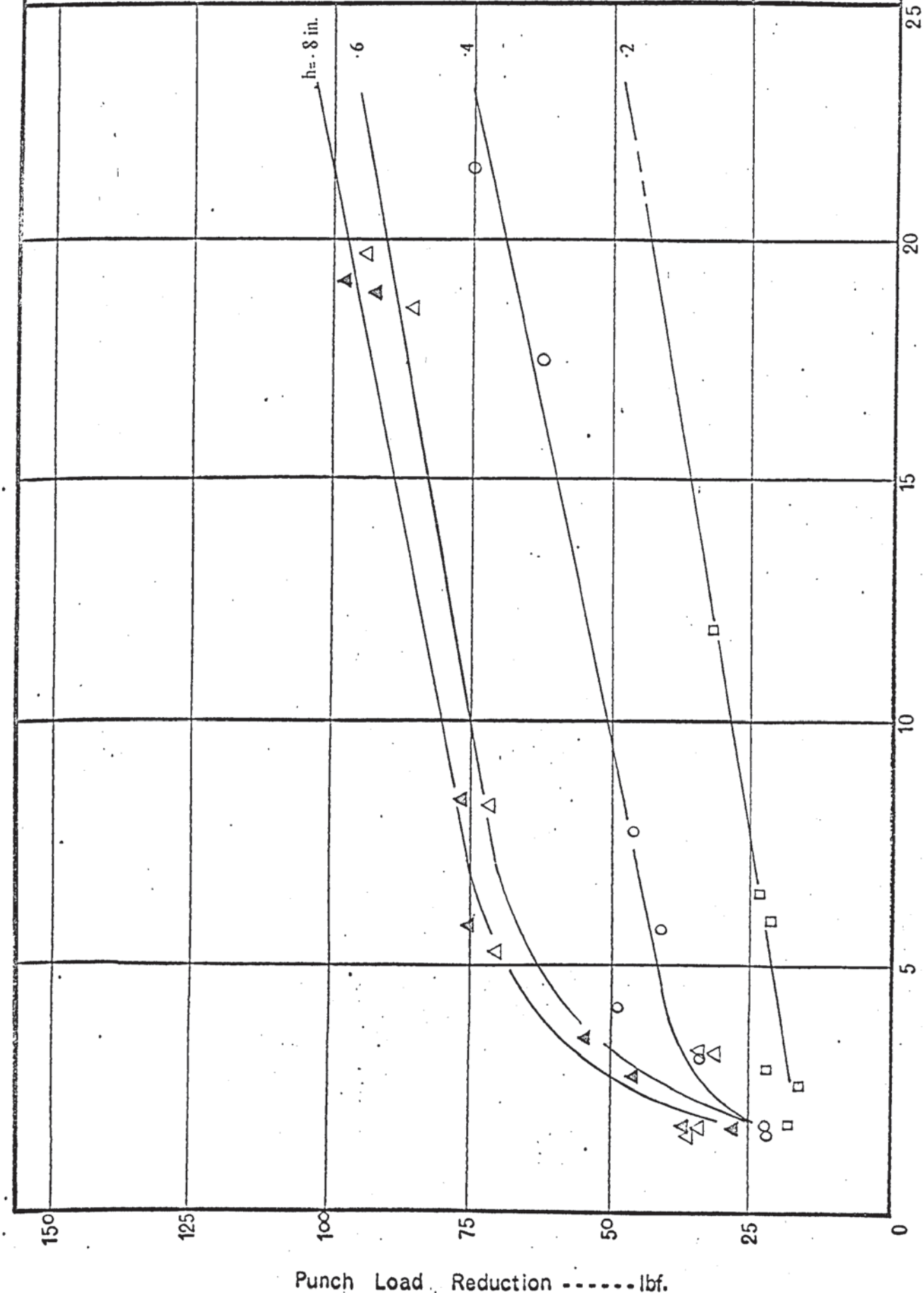

Test Series 03

Variation of punch load reduction with die amplitude at different stages of drawing.

Fig. 8.33

D.R. = 1.7

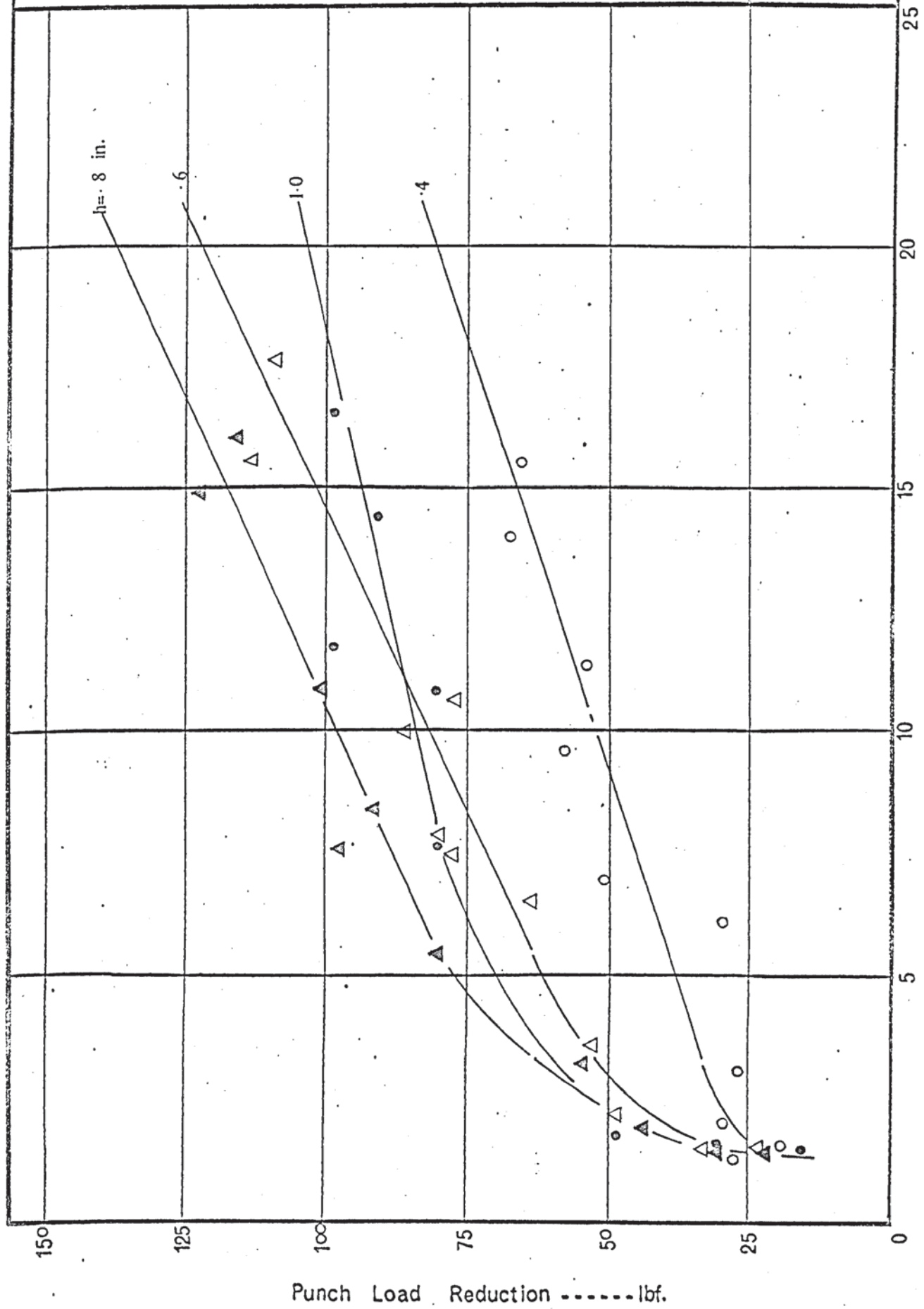

Test Series 03

Variation of punch load reduction with die amplitude at different stages of drawing.

Fig. 8.34

D.R. =1.80

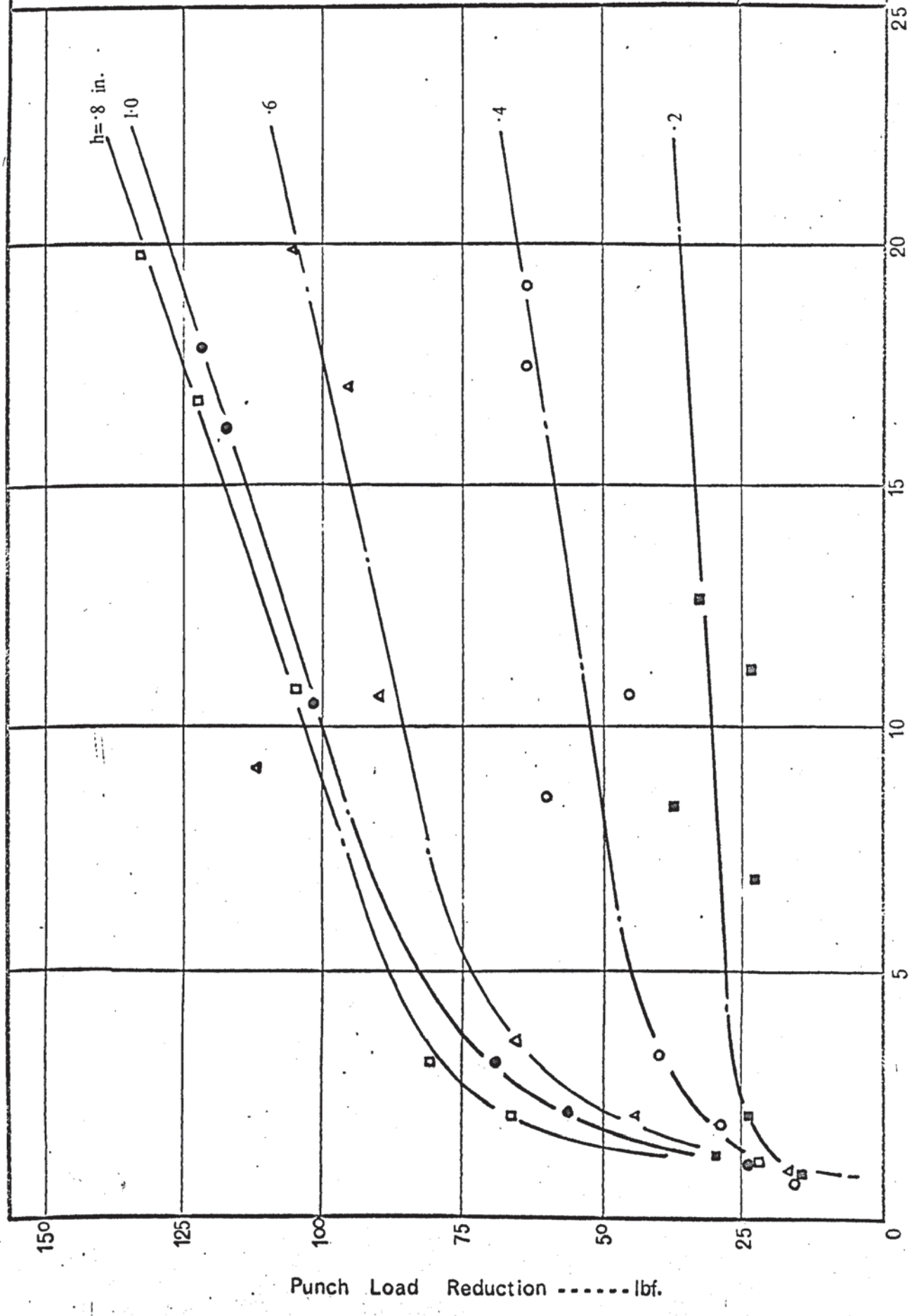

Test Series 03

Variation of punch load reduction with die amplitude at different stages of drawing.

Fig. 8.35

D.R. = 1.9

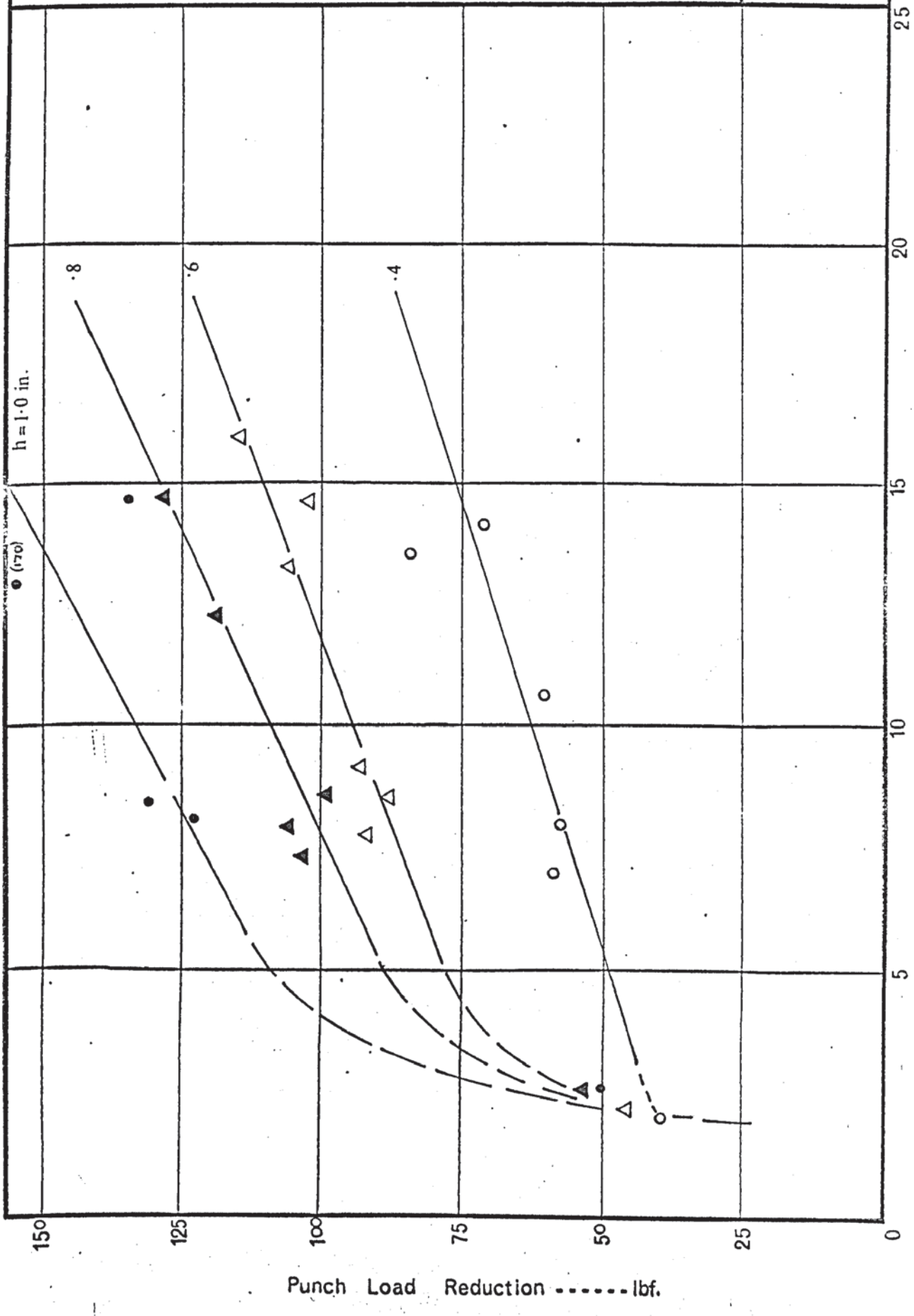

Test Series-03

Effect of vibration amplitude on the maximum oscillatory and non-oscillatory punch loads, during interrupted oscillatory tests.

Fig 8.36a

D.R 1.50

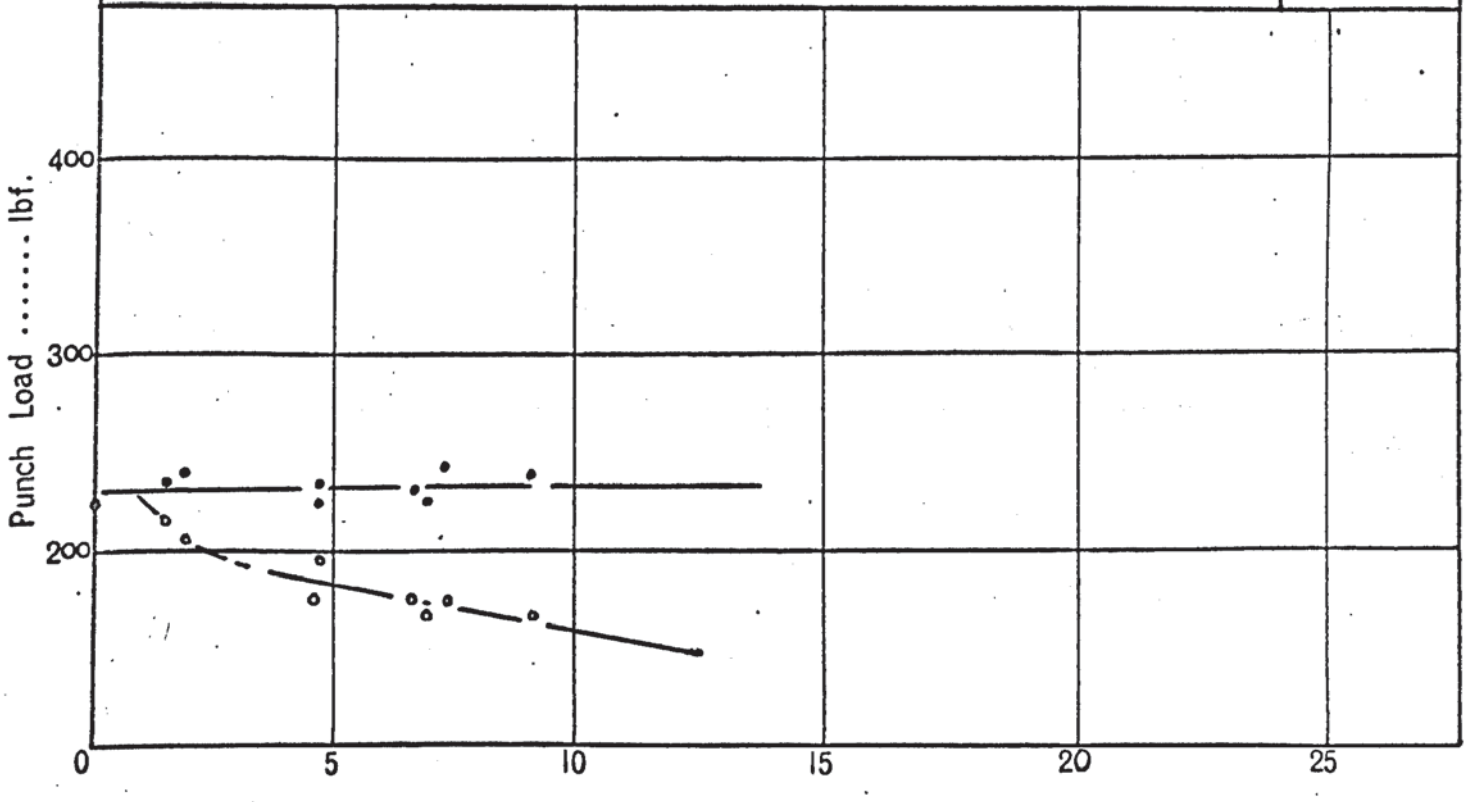

Variation in the corresponding blank holder friction force with increasing die amplitude.

Fig.8.36b

D.R.1.50

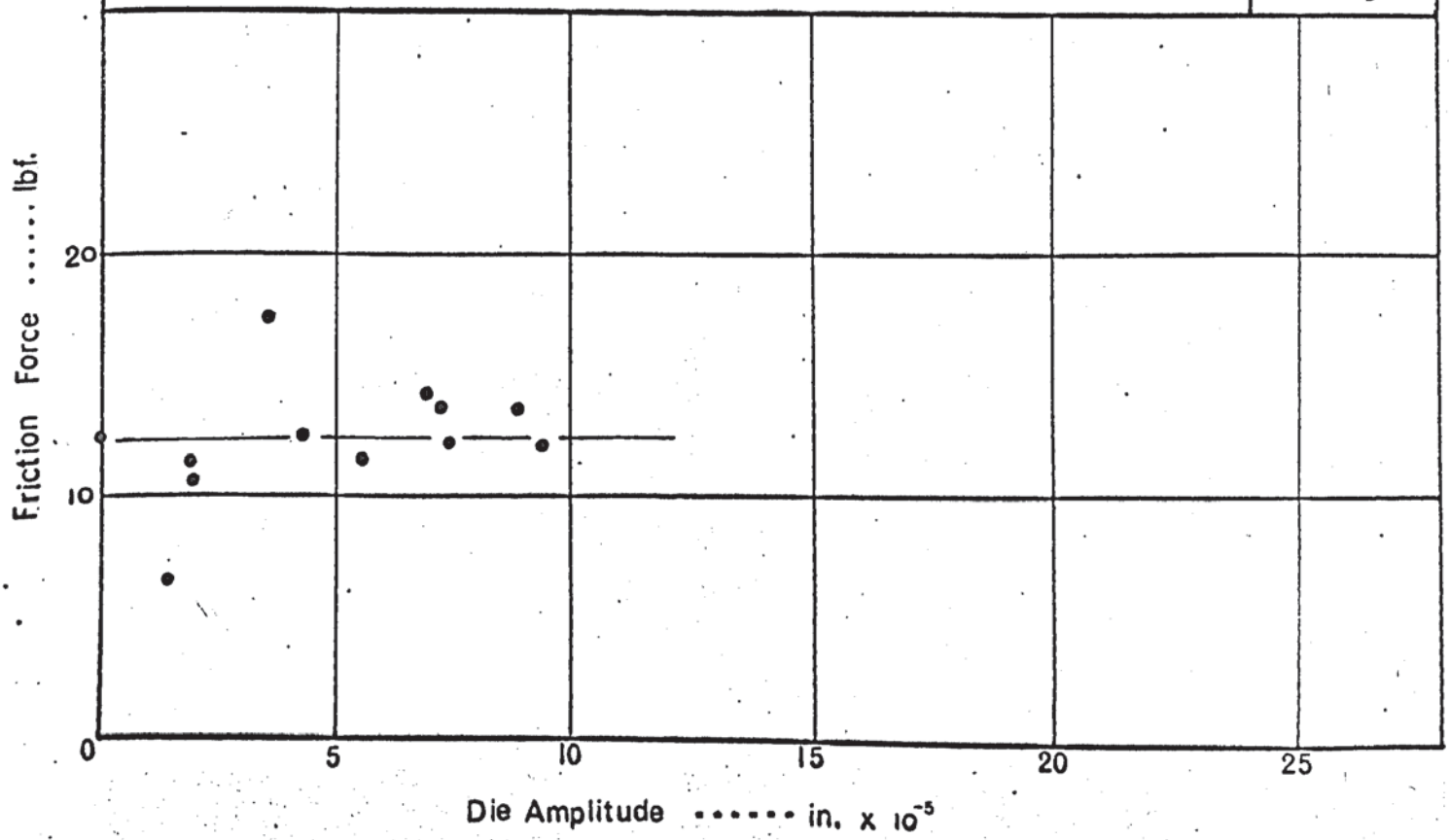

Test Series-03

Effect of vibration amplitude on the maximum oscillatory and non-oscillatory punch loads, during interrupted oscillatory tests.

Fig 8.37a

D.R 1.60

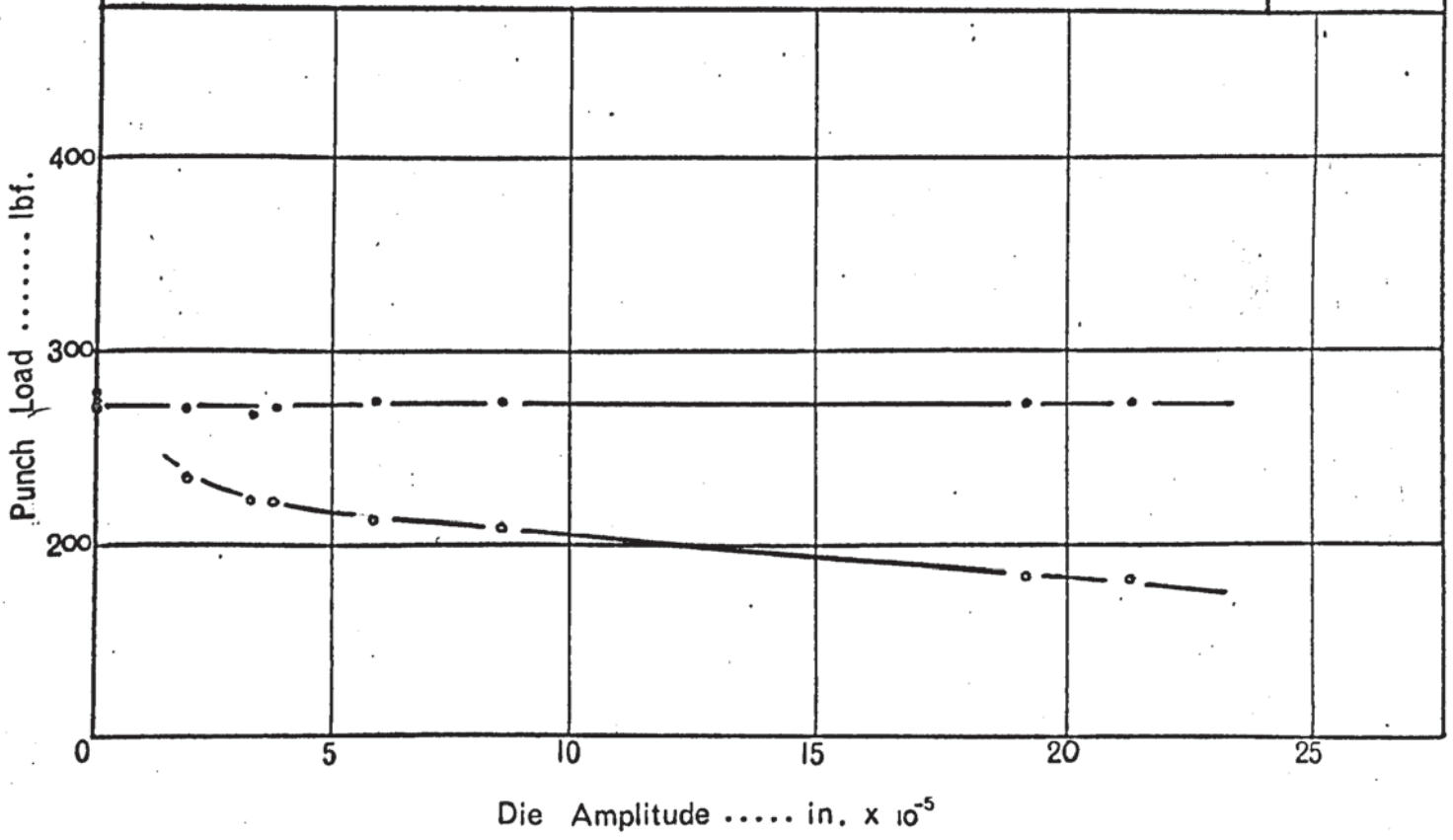

Variation in the corresponding blank holder friction force with increasing die amplitude.

Fig.8.37b

D.R.1.60

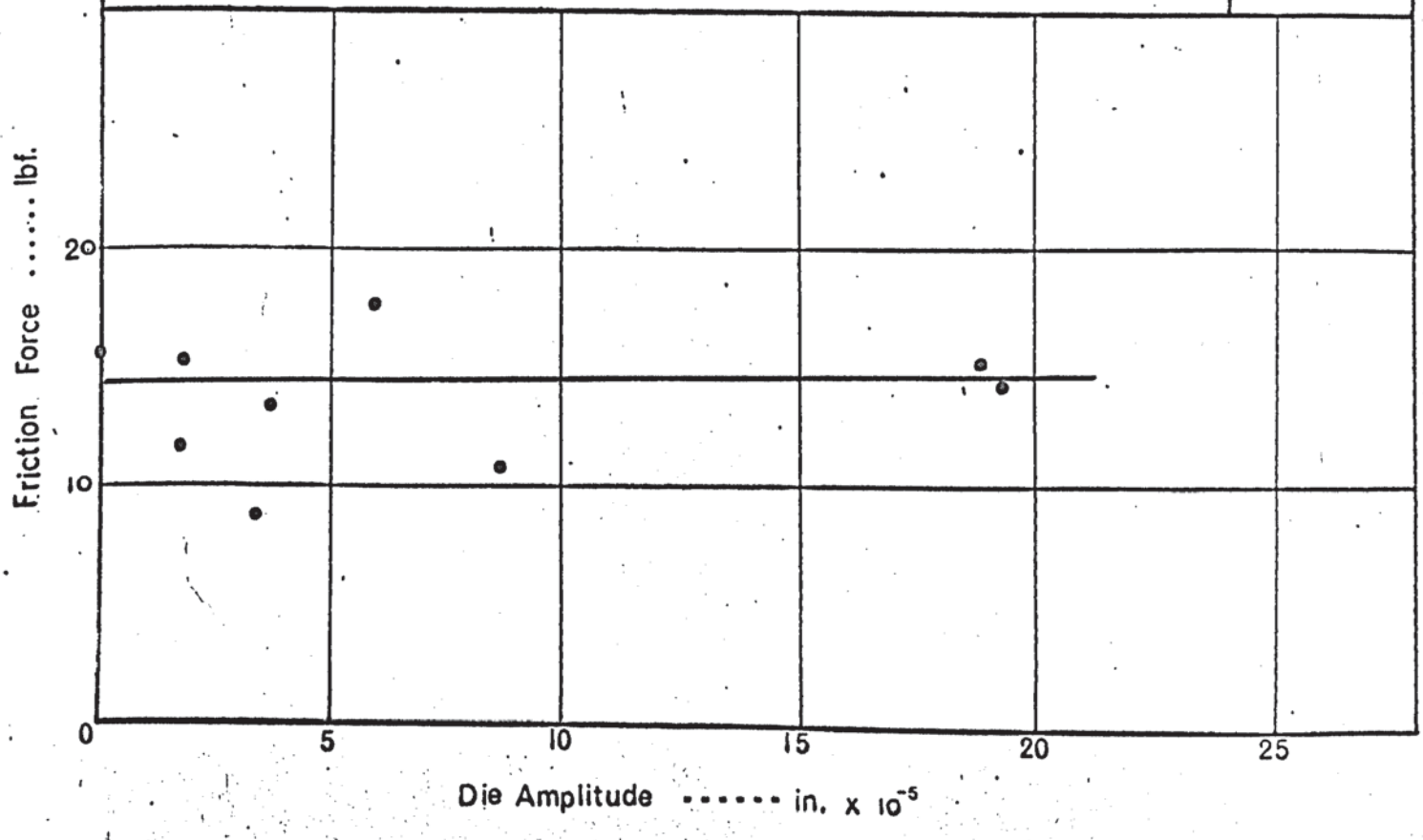

Effect of vibration amplitude on the maximum oscillatory and non-oscillatory punch loads, during interrupted oscillatory tests.

Fig 8.38a

D.R 1.70

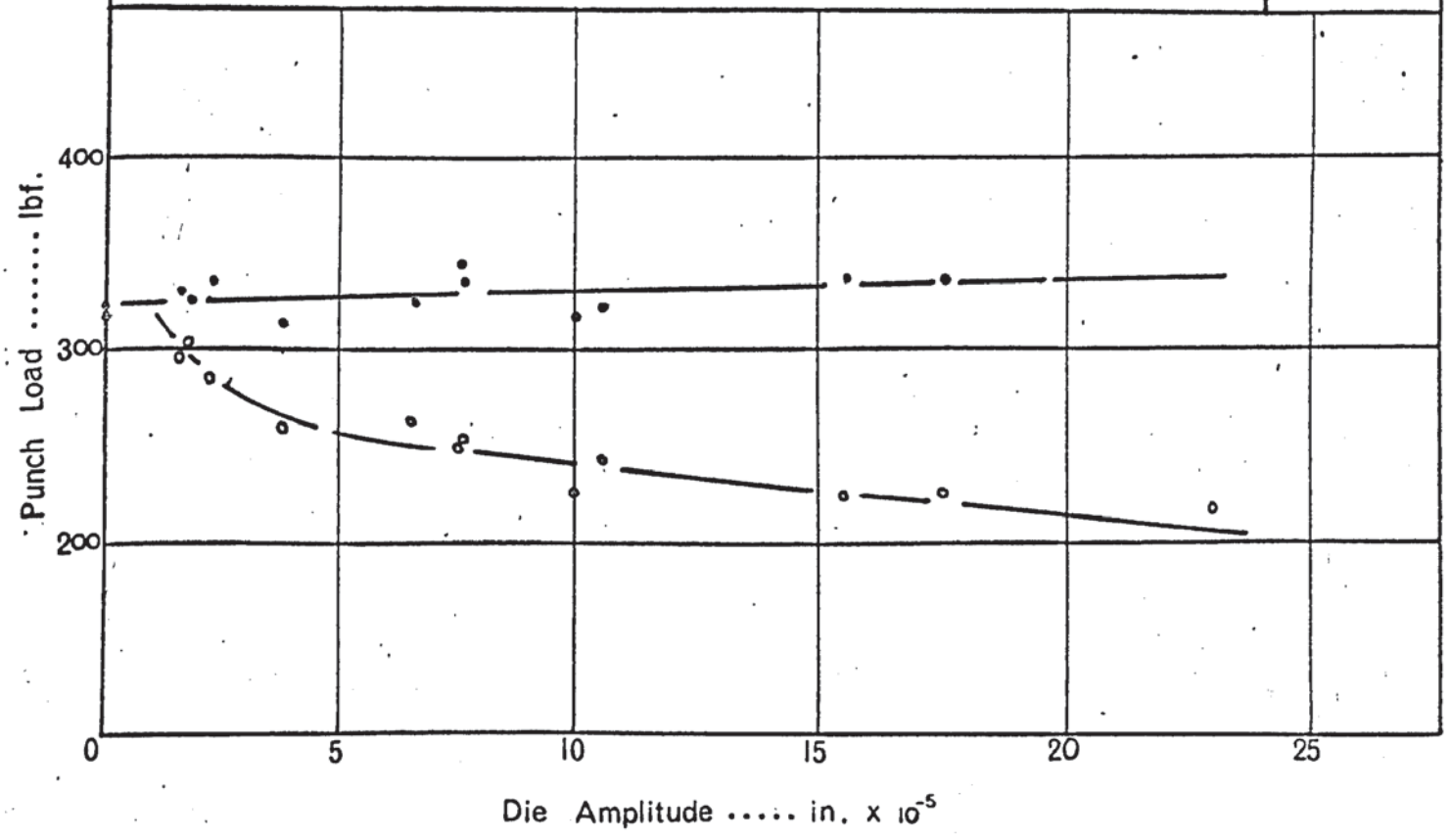

Variation in the corresponding blank holder friction force with increasing die amplitude.

Fig. 8.38b

D.R. 1.70

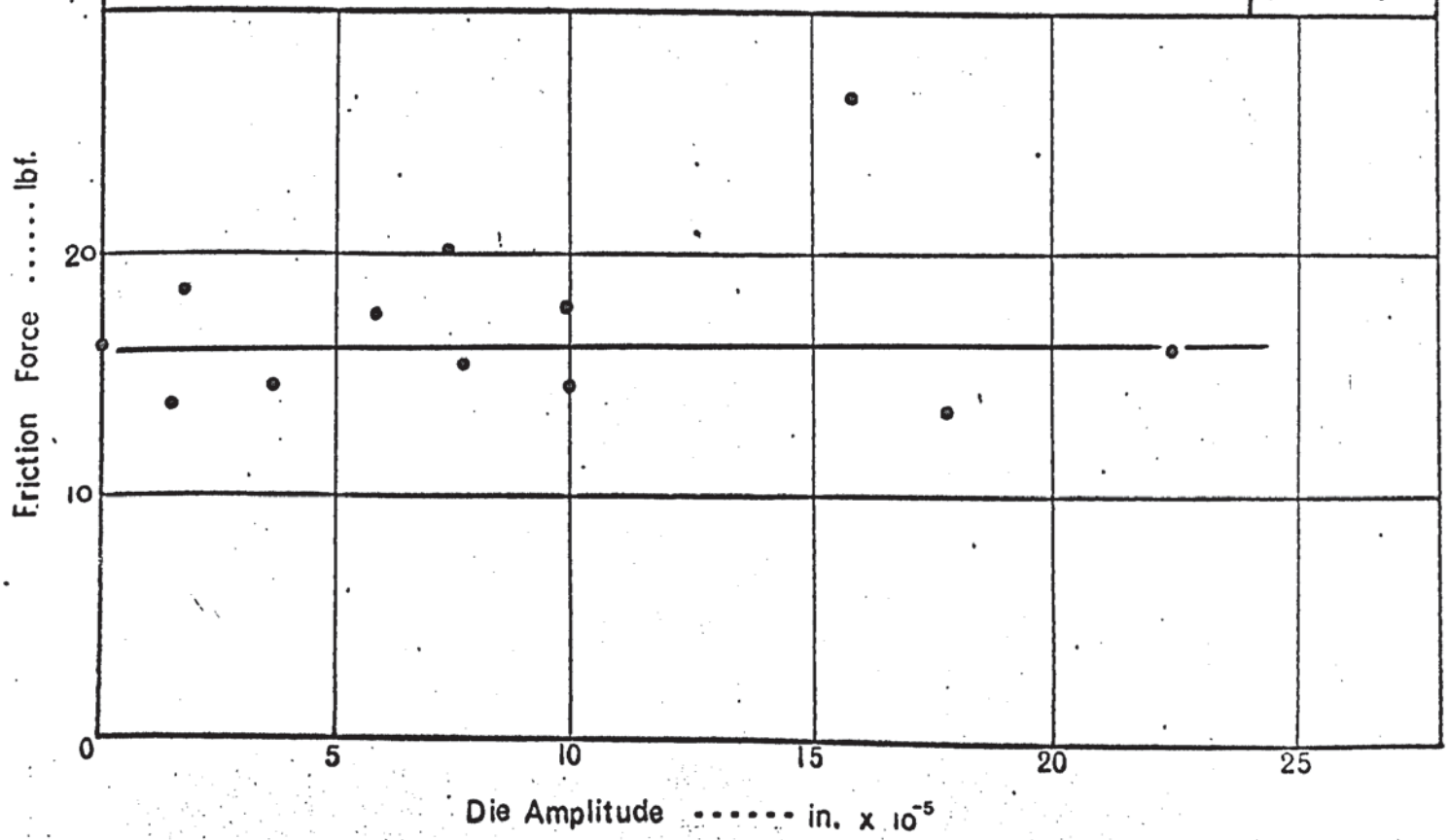

Test Series – 03

Effect of vibration amplitude on the maximum oscillatory and non-oscillatory punch loads, during interrupted oscillatory tests.

Fig 8.39a

D.R1.80

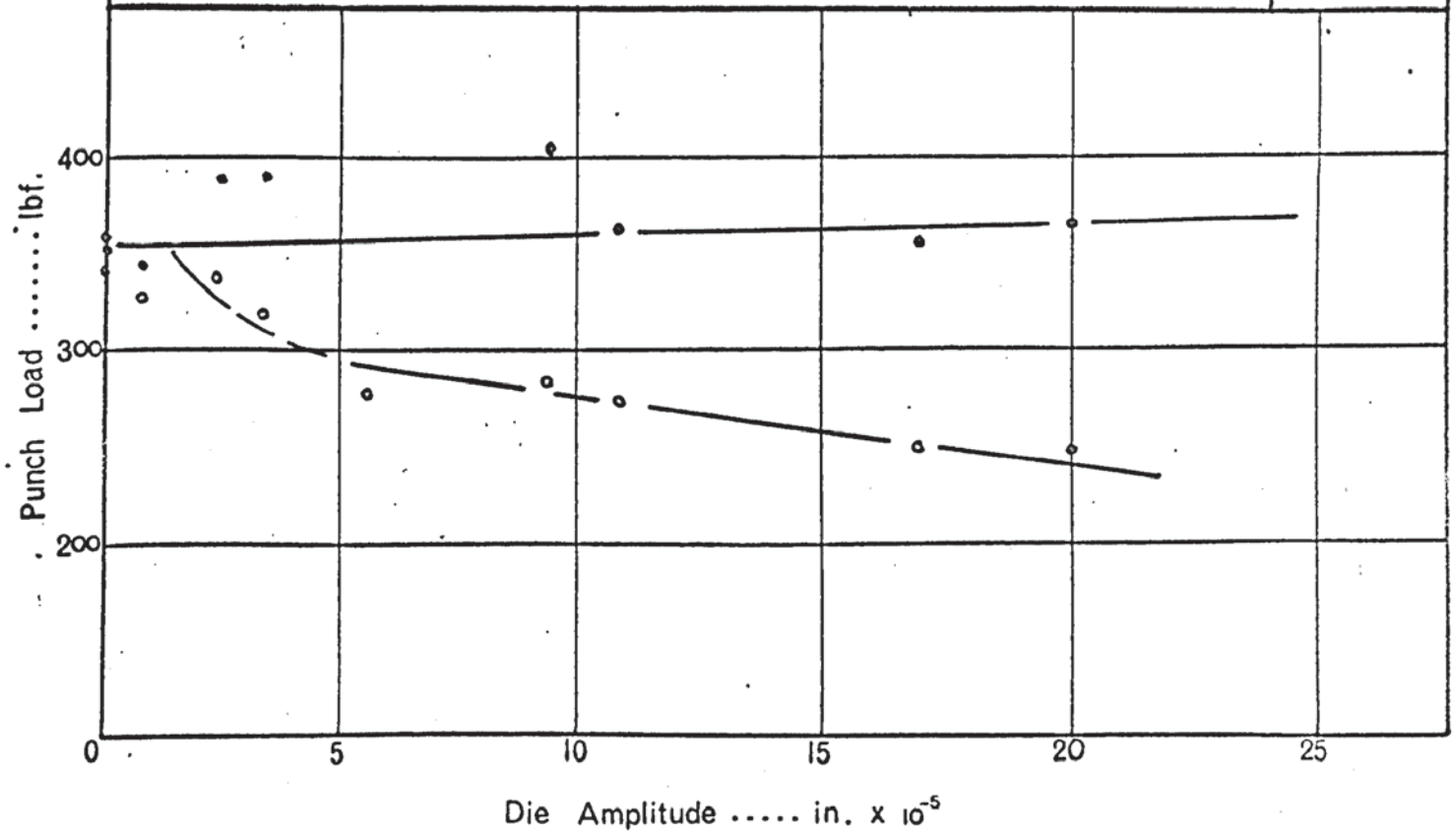

Variation in the corresponding blank holder friction force with increasing die amplitude.

Fig. 8.39b

D.R.1.80

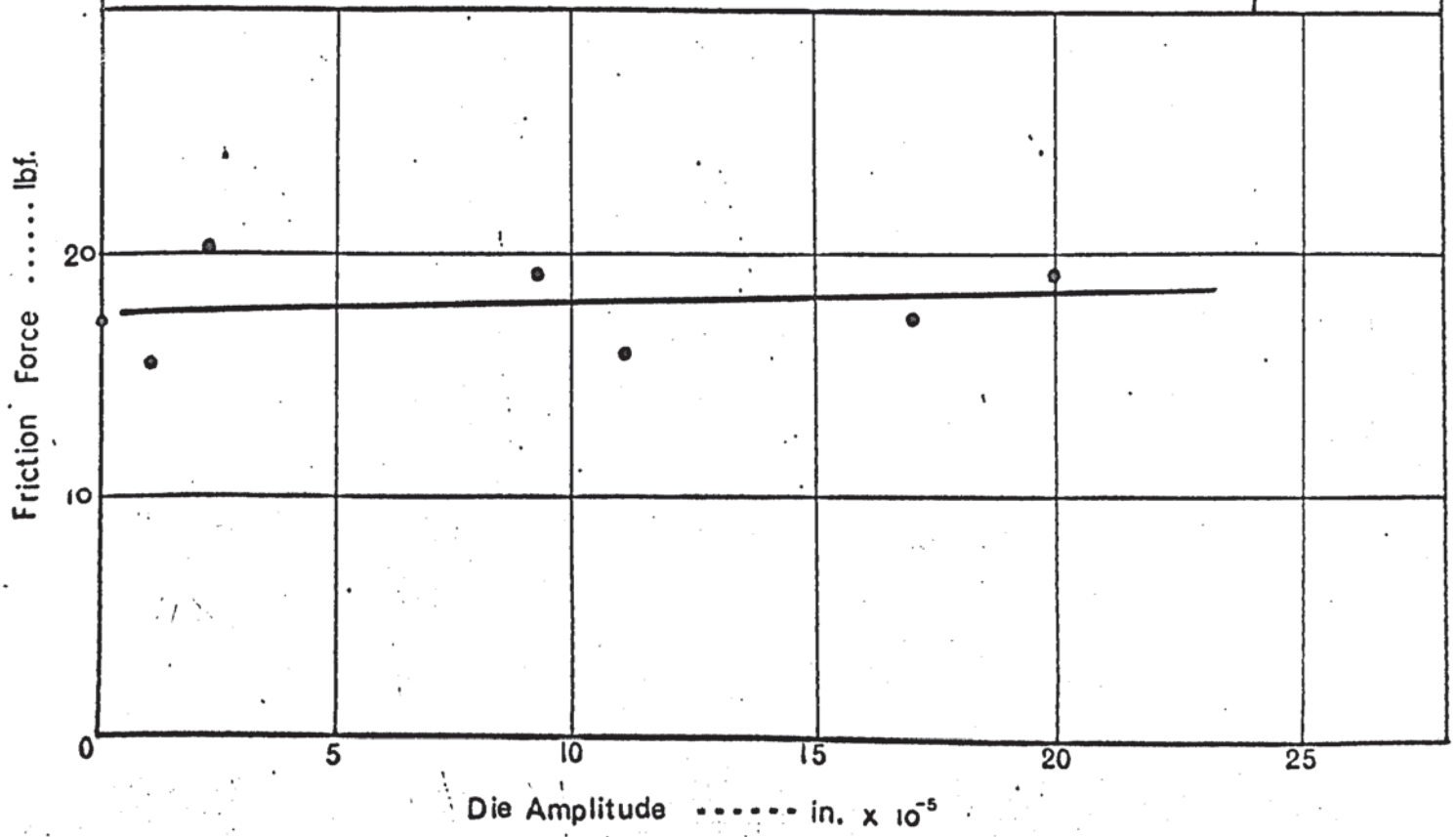

Effect of vibration amplitude on the maximum oscillatory and non-oscillatory punch loads, during interrupted oscillatory tests.

Fig 8.40a

D.R 1.90

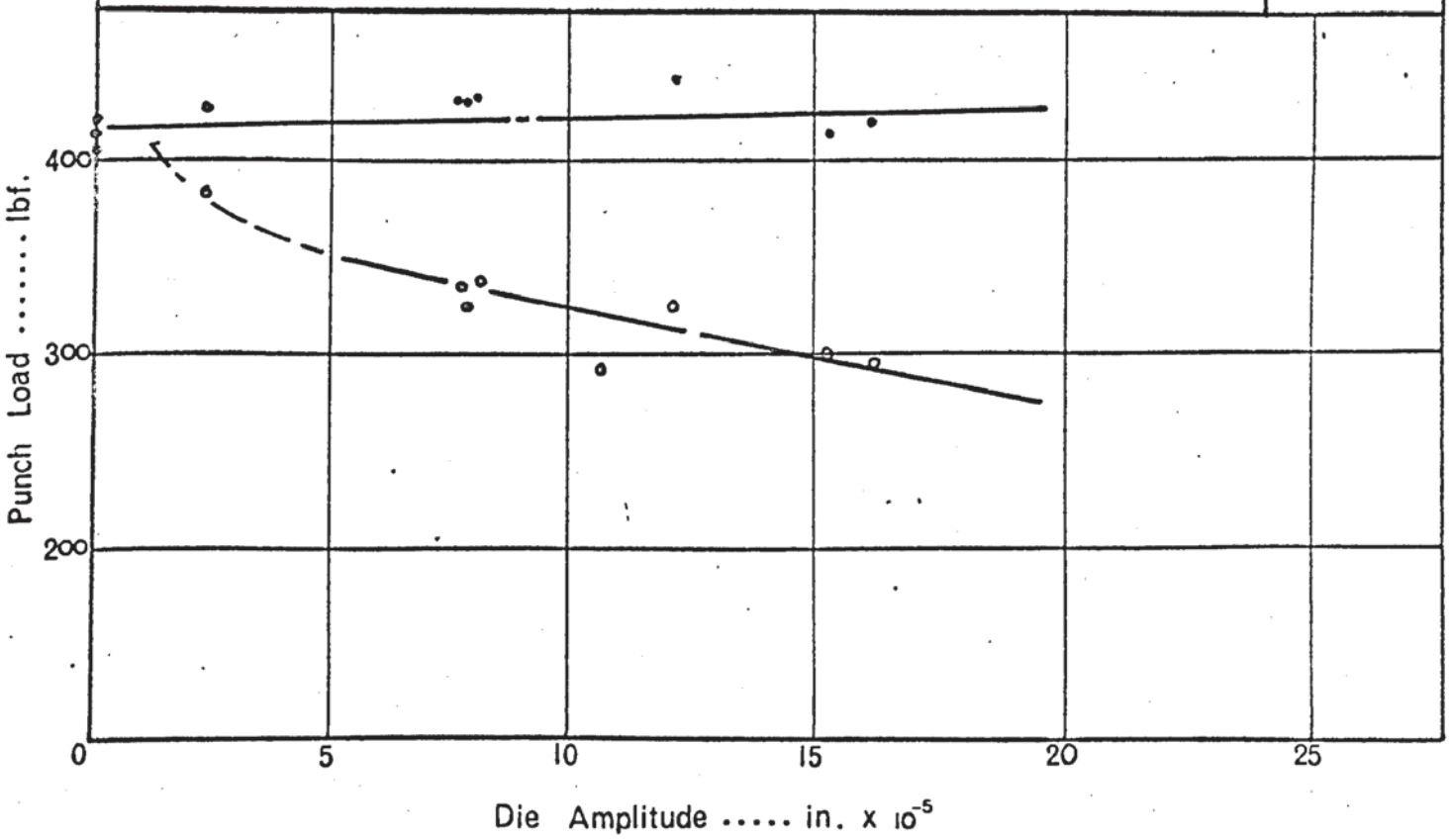

Variation in the corresponding blank holder friction force with increasing die amplitude.

Fig.8.40b

D.R.1.90

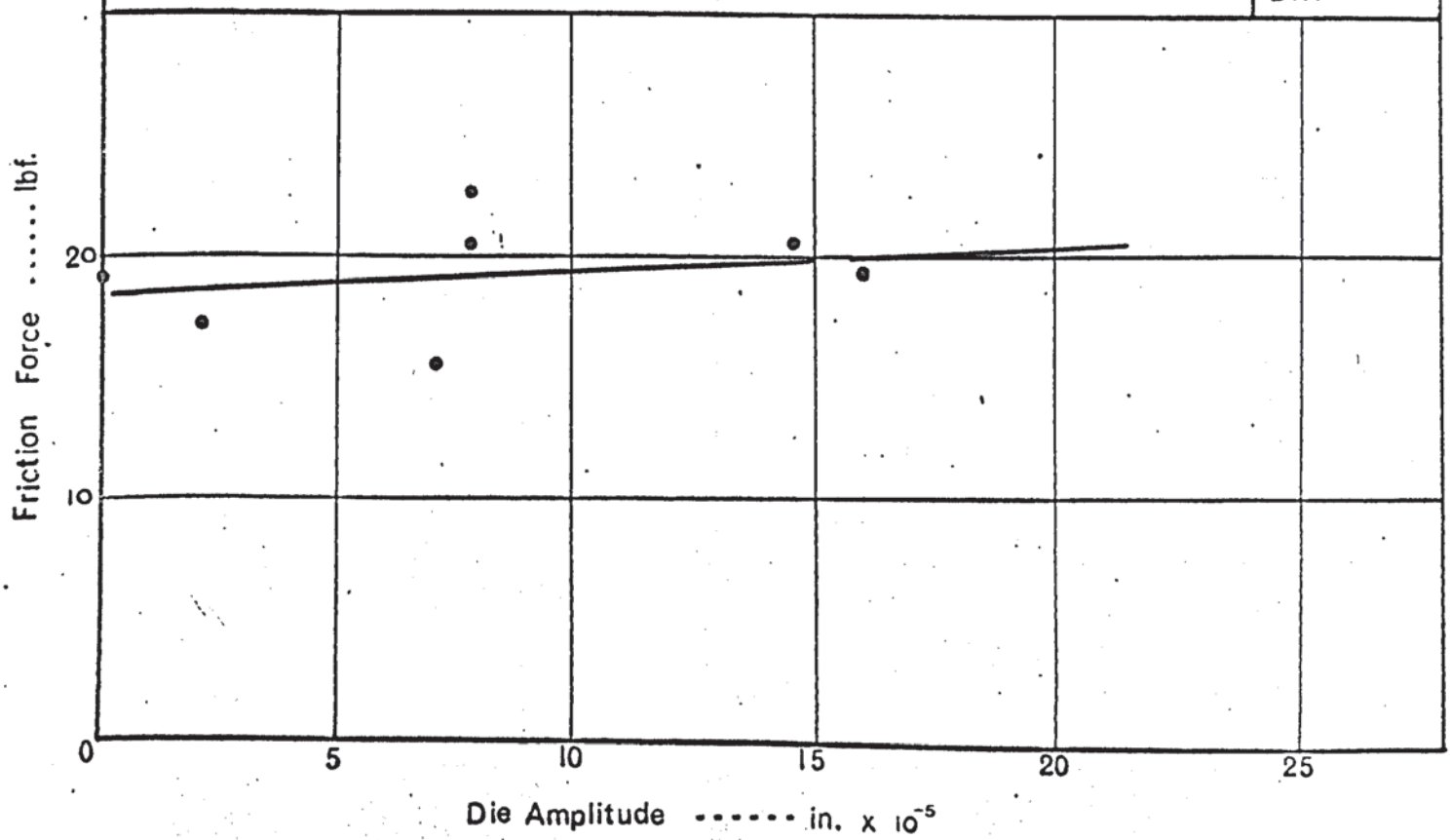

The effect of Die Amplitude on Punch Load for parallel test pieces drawn with normal wedge dies.

Fig.8.41a

D.R = 1·0

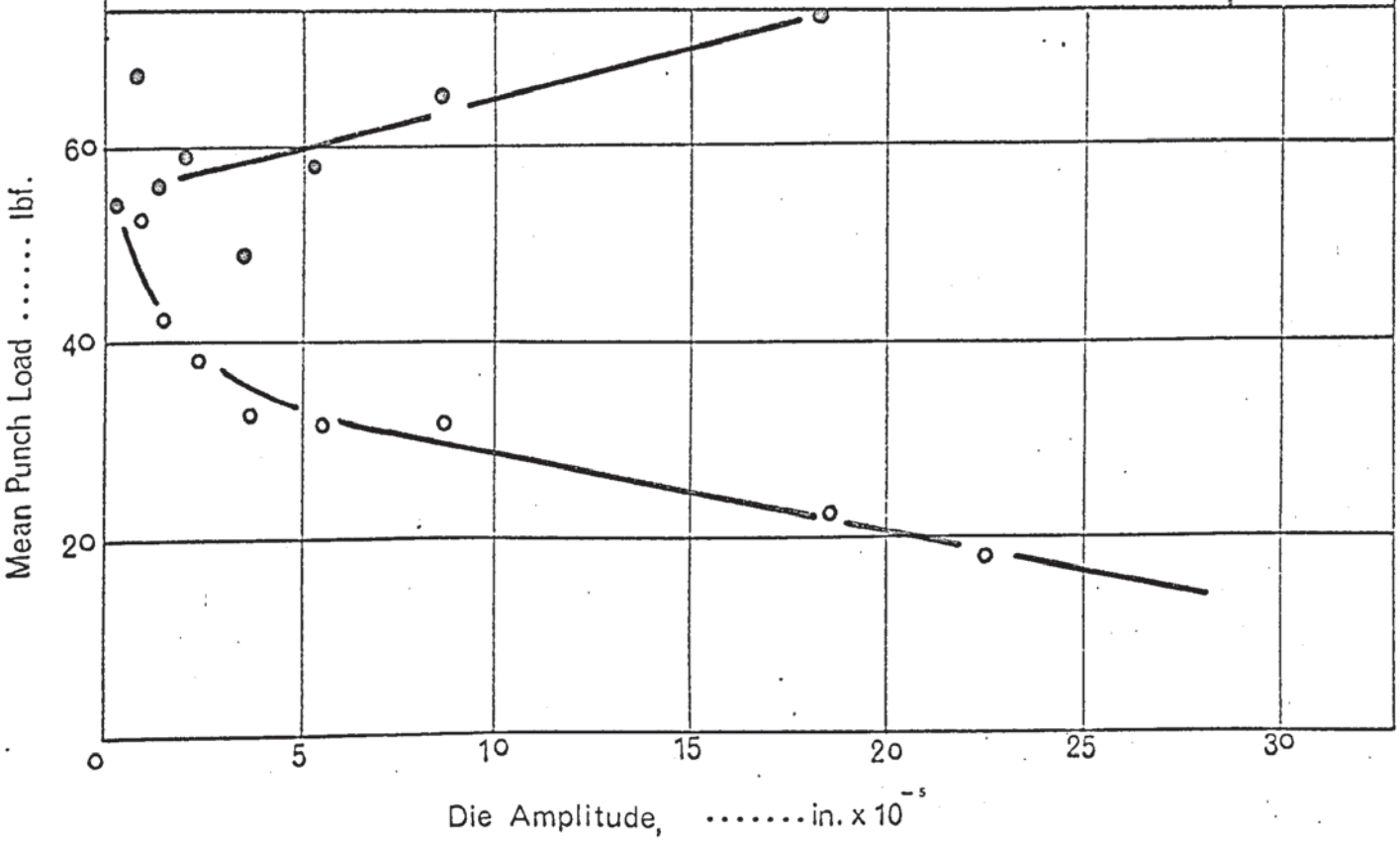

The effect of Die Amplitude on the Reduction in mean Punch Load and mean Blank Holder Friction Force.

Fig.8.41b

D.R.=1·0

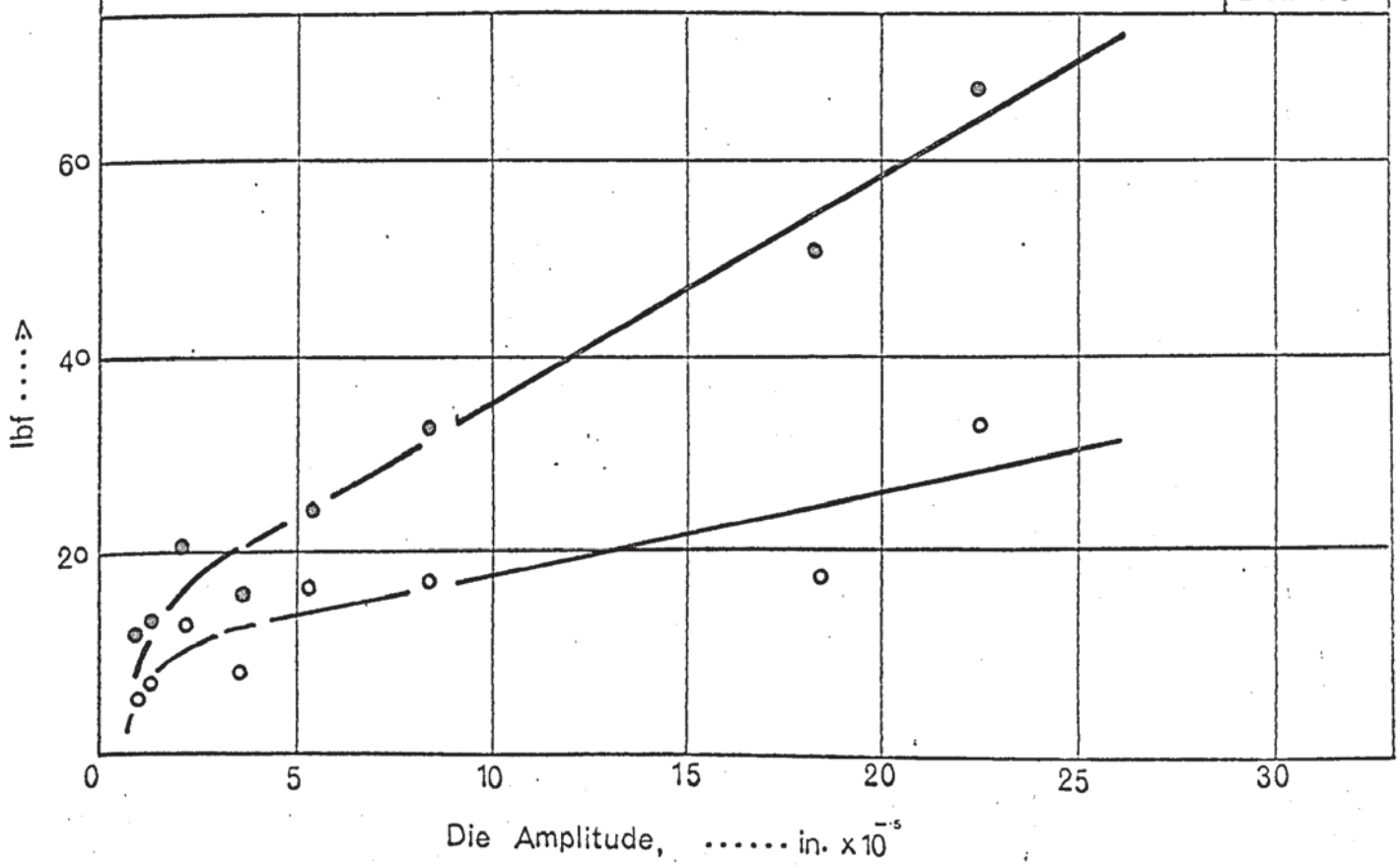

The effect of Die Amplitude on Punch Load for parallel test pieces drawn with the 'Roller Radius' assembly.

Fig.8.42a

D.R=1·0

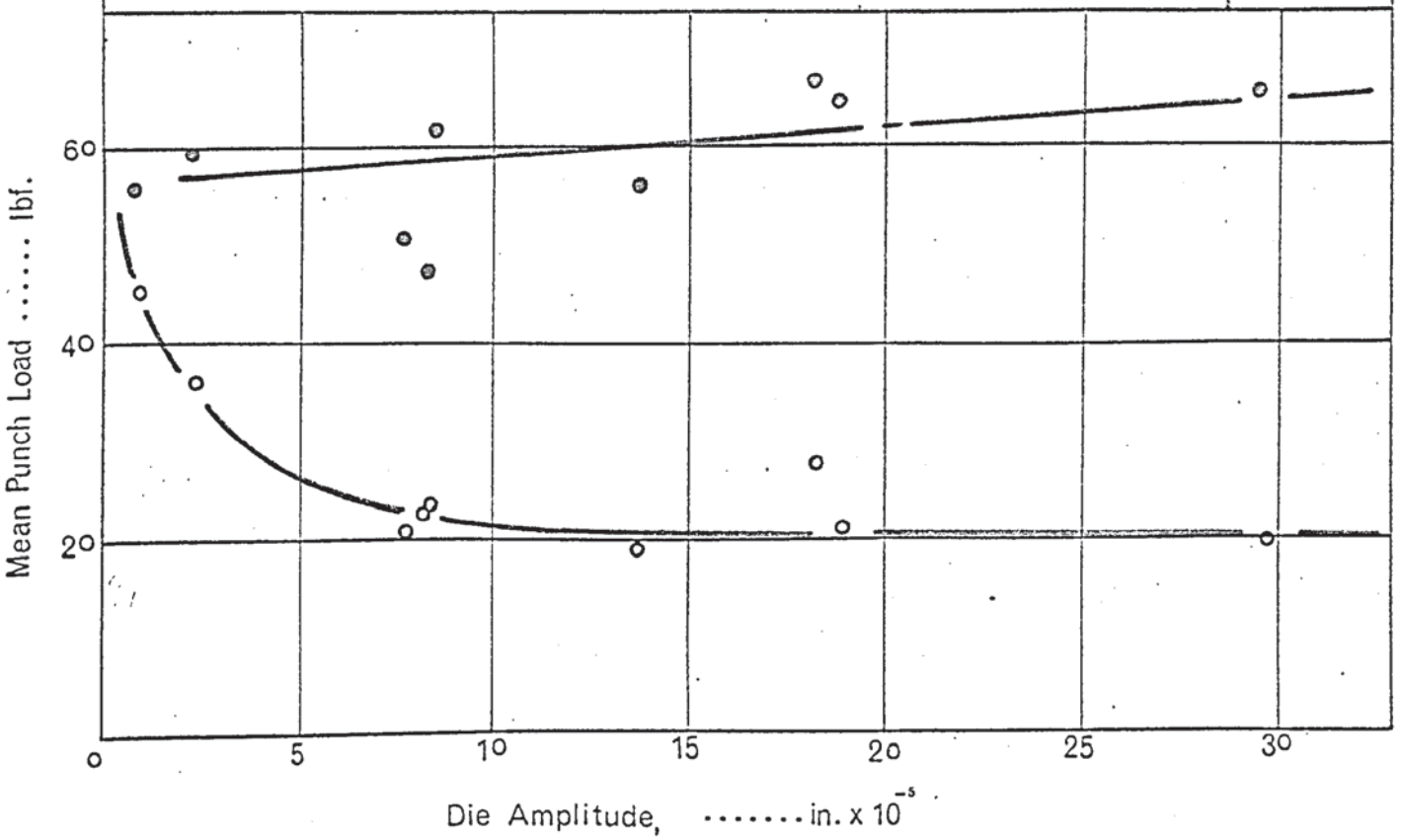

The effect of Die Amplitude on the Reduction in mean Punch Load and mean Blank Holder Friction Force.

Fig.8.42b

D.R.=1·0

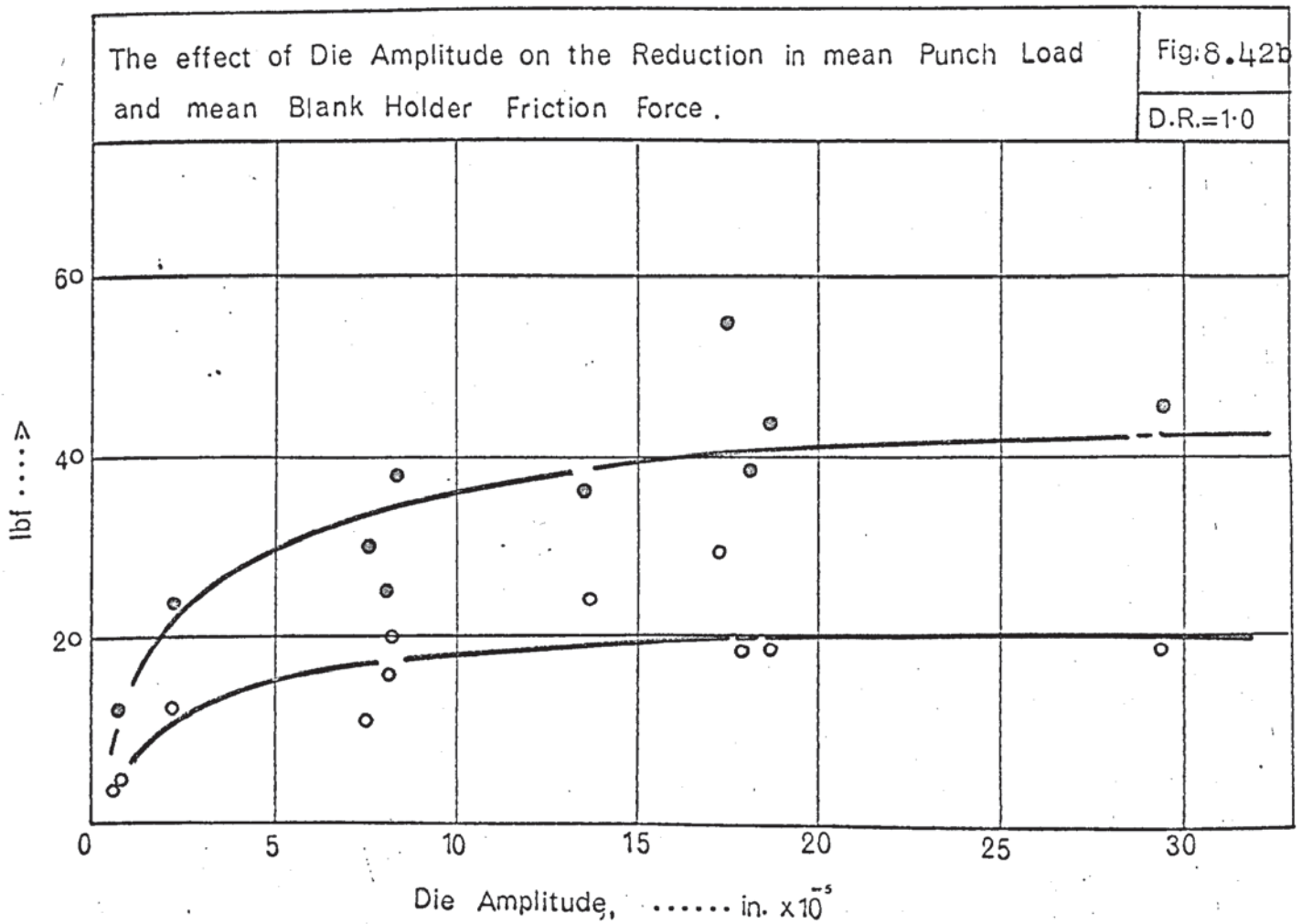

9 Discussion

9.1 General Characteristics of Oscillatory Test Data for Fixed Radius Drawing

9.1.1 Punch Load Data

Examination of the punch load/displacement curves, plotted from intermittent oscillatory test data at various drawing ratios, revealed several significant and consistent features. These are summarised as follows:

(i) a comparison of oscillatory and non-oscillatory punch load/displacement curves indicated an increasing reduction in punch load towards the end of the drawing cycle. This phenomenon was common to all reductions examined and became more pronounced with increasing die amplitude. Figs 8.9 - 8.12 illustrate the effect for drawing ratios from 1.5:1 to 1.8:1.

(ii) the reduction in punch load at the stage of drawing coincident with the maximum non-oscillatory punch load was observed to increase with increasing die amplitude. This is illustrated in Figs. 8.13 - 8.17 where it will be seen that the reduction in punch load increases rapidly upto a die amplitude of around 5×10^{-5} in. and at higher displacement amplitudes shows a linear relationship. A similar characteristic was observed at all reduction ratios.

(iii) examination of the punch load reduction/die amplitude relationship at various stages of drawing revealed the same features viz. a rapid non-linear reduction followed by a linear effect, for amplitudes greater than 5.0×10^{-5} in.. However, it was observed that at low drawing ratios the slope of the linear portion decreased as drawing progressed beyond the maximum punch load, whereas at higher ratios it remained virtually constant. This is illustrated for a drawing ratio of 1.50:1 in Fig. 8.18 which shows a family of curves representing

the variation in punch load reduction with increasing die amplitude at various stages of drawing, indicated by the punch displacement, h. Similar characteristics are shown in the set of graphs in Fig. 8.21, relating to a drawing ratio of 1.80:1.

(iv) from the data plotted in Figs. 8.18 - 8.21 it was also noted that the magnitude of the non-linear effect increased as drawing progressed beyond the maximum punch load.

(v) in order to correlate the force reduction at all stages of drawing, it was necessary to consider the strip tension, rather than the punch load. The punch load is a measure of the vertical component of the strip tension and if ϕ defines the arc of contact around the die radius, the tension in the partly drawn strip is given by:

$$T = P/\sin \phi \quad \text{---------- (9.1)}$$

where T is the total strip tension. See Fig. 9.1.

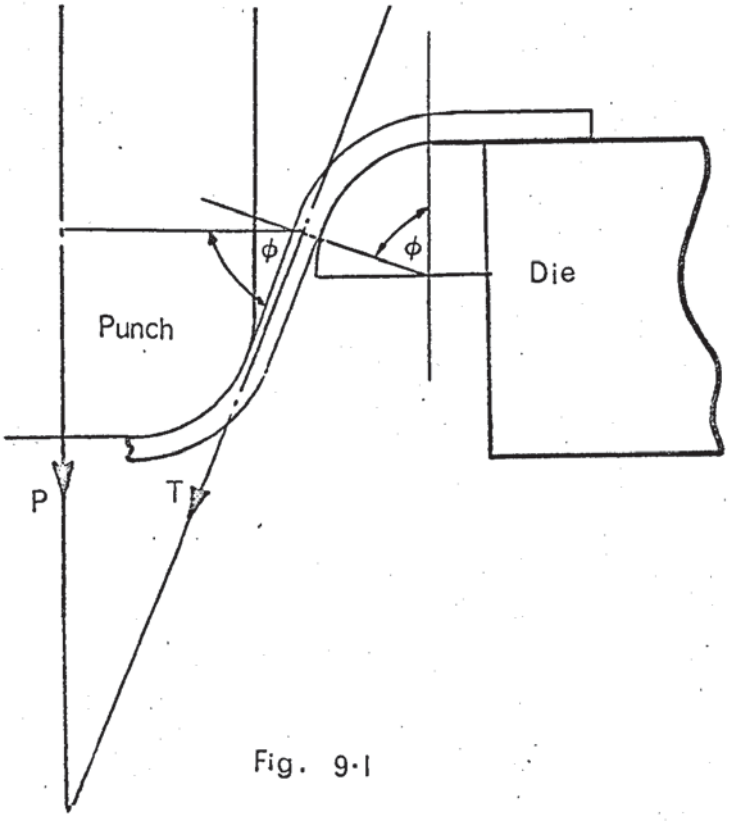

Fig. 9.1

Fig. 9.1. Relationship Between Punch Load, P and Strip Tension, T.

Variation in the reduction in strip tension during drawing at different die amplitudes.

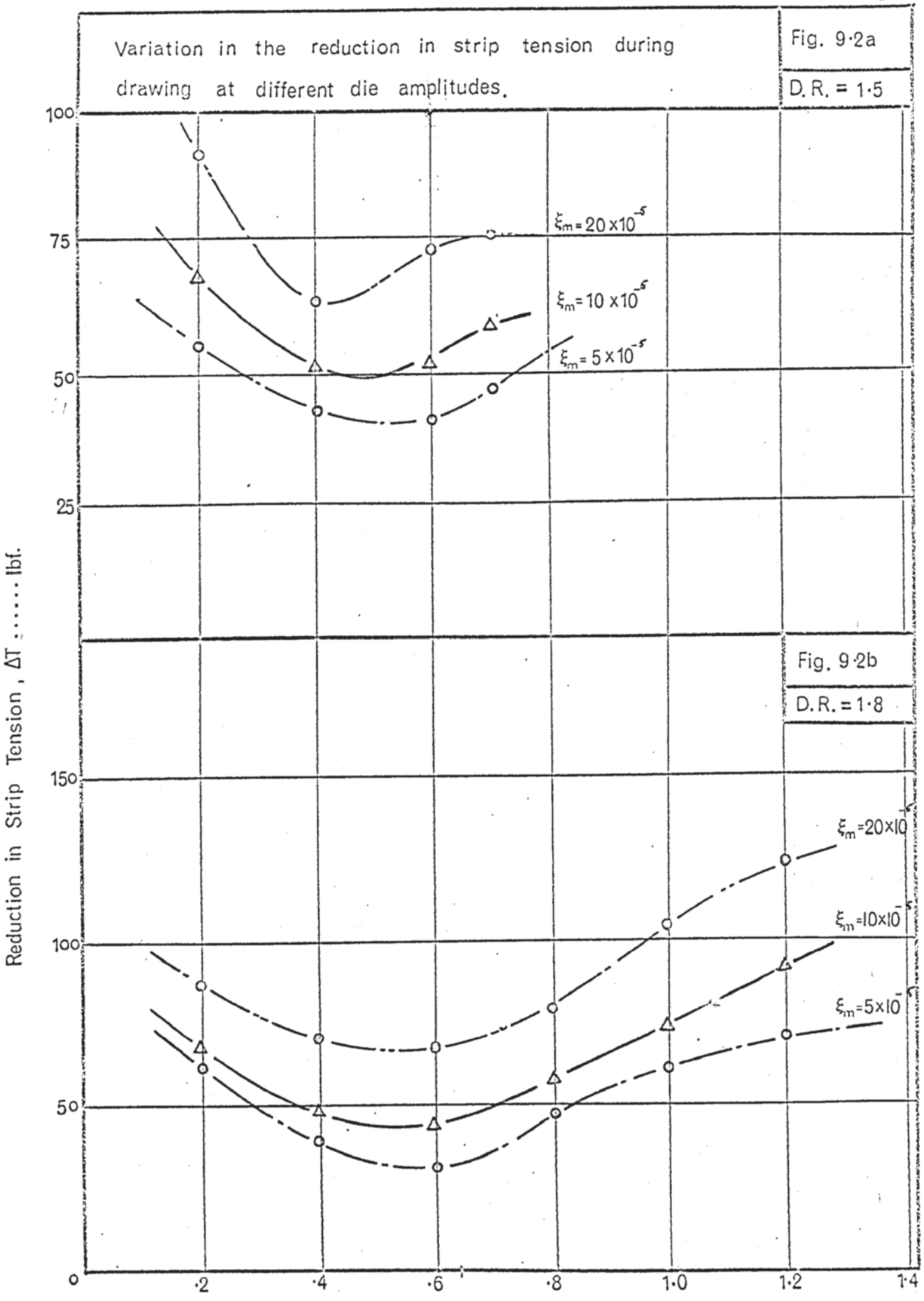

The contact angle at any stage of drawing is readily determined from consideration of the geometrical relation of the punch and die during drawing. Details of this analysis are given in Appendix 9 where the relationship between punch displacement and contact angle has been calculated. Using this information the experimental data has been transposed in order to plot the reduction in strip tension against punch displacement for drawing ratios of 1.50 and 1.80 at die amplitudes of 5×10^{-5}in. to 20×10^{-5}in.. These graphs are shown in Figs. 9.2a and 9.2b which indicate a large reduction in tension during the initial drawing stages. This falls to a minimum value at a punch displacement of around 0.4 in. and finally rises towards the end of the drawing cycle.

9.1.2 Friction Force Data

9.1.2.1 Test series 01

The friction force data from test series 01 was examined by plotting the percentage reduction in friction force against die amplitude for each of the drawing ratios considered. viz, 1.60:1, 1.65:1 and 1.70:1. This data is shown in Figs. 8.3 - 8.5 respectively. In each case the reduction in friction force increased rapidly with increasing die amplitude upto 2×10^{-5}in. At this level the friction force was reduced by 80-90%. Complete 'removal' of the friction was observed at amplitudes exceeding 5.0×10^{-5}in..

From the experimental data in this series it was also noted that extrapolation of the friction reduction curves indicated zero reduction at die amplitudes less than 0.50×10^{-5}in.

The variation in friction force with punch displacement under oscillatory and non-oscillatory conditions was also plotted, at various die amplitudes, for each reduction. This is shown in the graphs of Figs. 8.6 - 8.8. The upper graph in

each figure shows the friction force traces for individual tests carried out at different levels of die amplitude. The mean non-oscillatory friction trace is included in each case. The lower graph shows the percentage reduction in friction force as a function of punch displacement at various amplitudes. Each curve was determined from the trace of an individual oscillatory test carried out with interrupted die activation.

It will be seen from these graphs that at low vibration amplitudes the reduction in friction force decreases during drawing, the greatest effect being produced at the start of drawing. At higher amplitudes the variation becomes less marked until at values of 2×10^{-5} in. the reduction in friction force is almost constant at between 80 and 95 per cent. This general pattern was repeated for each drawing ratio.

9.1.2.2 Test Series - 02

Blank holder friction force data at drawing ratios of 1.50 - 1.90 was also obtained in the tests carried out at a nominal punch speed of 0.32 in/sec. The variation of friction force throughout the drawing cycle at various vibration amplitudes is given in Fig. 8.9 - 8.12. These results show the same general characteristics as in the original series with one notable exception. During these tests the die amplitudes were increased considerably beyond the level necessary to reduce the friction force to zero. It was noted, during interrupted oscillatory tests, that the friction force during the non-oscillatory interval was higher than the corresponding value obtained under non-oscillatory conditions. This effect was found to increase with increasing die amplitude and is illustrated by the graphs in Fig. 8.22b - 8.25b. A similar increase in the punch load during the non-oscillatory interval, relative to the normal non-oscillatory value was also observed. The

effect is illustrated in Fig. 8.22a - 8.25 a, which relate to the maximum oscillatory and non-oscillatory punch loads. The characteristics of both the punch load and friction force traces will be discussed in greater detail in the following analysis of the mechanics of the oscillatory process.

9.2 Theoretical Analysis

9.2.1 Introduction

In section 3, which considered the mechanics of the deep-drawing and wedge-drawing processes, it was shown that the drawing load could be broken down into a number of components each related to a specific feature of the process, namely:

(i) the force attributed to radial drawing;

(ii) force increments due to plastic bending at the entry to the die radius and unbending at the plane of exit;

(iii) the blank holder friction force which may be assumed to act at the radial extremity of the wedge test piece during radial drawing;

(iv) friction forces acting at the edges of the test piece during radial drawing;

(v) the friction force associated with the motion of the test piece over the die radius.

The effect of die oscillations on each of these force components will now be considered in detail and models proposed to account for the observed force reductions.

9.2.2 Oscillatory motion of the test piece during drawing

The conical concentrators, with attached drawing dies, were designed to operate in the standing wave regime so that the transfer of energy through the supports was minimal. During drawing however, it is clear that part of the wave motion reaching the tools was absorbed by the test piece and blank holder assembly instead of being reflected from the end

faces of the concentrators. This resulted in a reduction in the measured amplitude of the standing wave, referred to qualitatively in section 8.1.5. Part at least of the energy transmitted out of the vibrators was absorbed in generating a forced vibration in the test piece and it is proposed that the characteristics of this wave form may be used to predict the effects of die oscillations on the punch load and to account for the specific mechanisms affecting each component of the punch load defined in section 9.2.1.

The vibrational mode of the test piece within each deformation zone may be determined by considering the motion of a circumferential element of width dr constrained at its ends by a portion of the wedge die, as shown in Fig. 9.3a. Using the concept of elastic strain release proposed by Winsper and Sansome[34], then provided that the die velocity amplitude at the point of contact with the element, exceeds the linear velocity of the element Vr, the die will overtake the test piece at this section and the element will move forward with a superimposed cyclic velocity component as the drawing strains are released. It is desirable to consider the oscillatory state at each stage of drawing since it is a non-steady state process. The assumption is therefore made that at high frequencies the deformation strains and stresses will remain virtually constant during the small time interval represented by a single vibration cycle. At any stage, the displacement amplitude of each element may then be determined by integrating the expression for the relative velocity between die and element over the interval during which the die velocity exceeds that of the linear element velocity.

If the linear velocity of the element is Vr and that of the contacting portion of die is given by $\dot{\xi} = \dot{\xi}_m . \sin\omega t$, taking

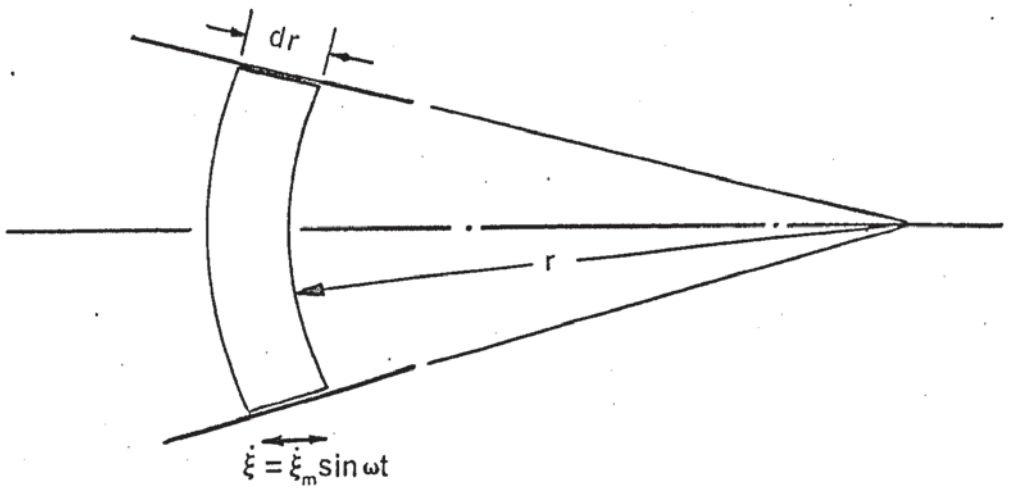

Fig. 9.3a Oscillatory motion of a circumferential element dr, during radial drawing-in.

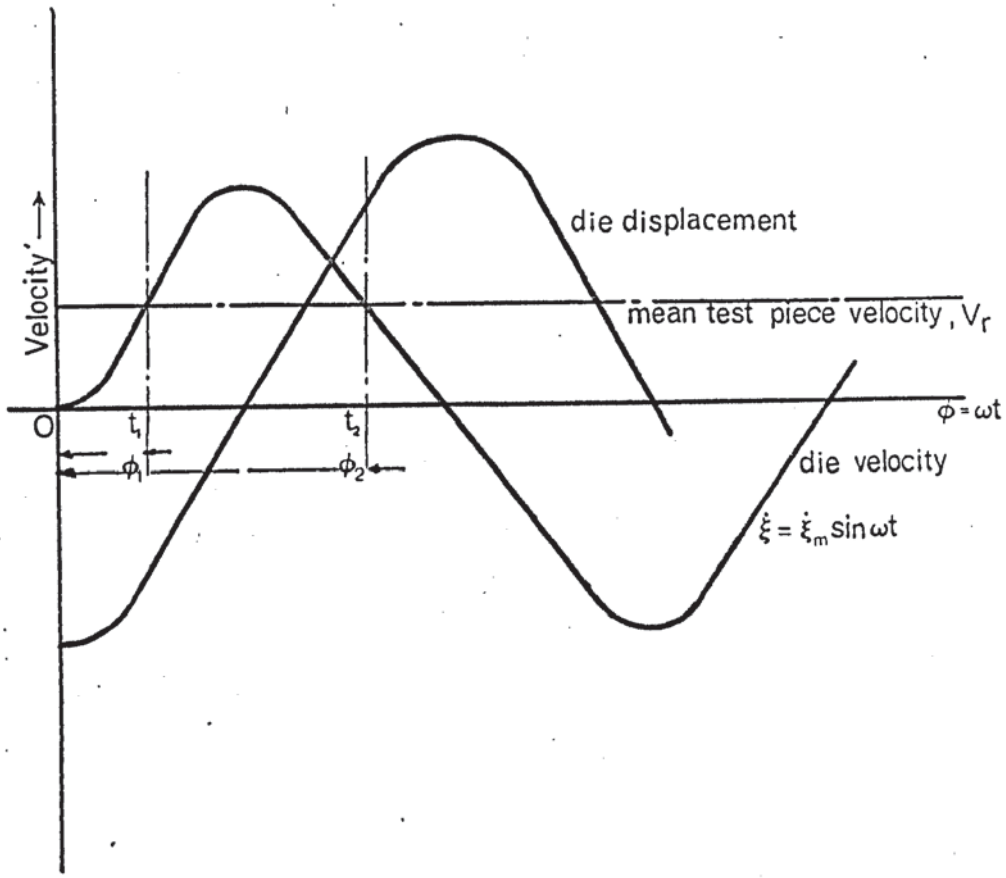

Fig. 9.3b Schematic illustration of relative motion between the die and testpiece during an oscillation cycle.

the time base from the maximum backward displacement for convenience, then during the interval t_1 to t_2, Fig. 9.3b, the relative velocity is given by

$$V = \dot{\xi}_m \sin\omega t - V_r \quad \text{----------} \quad (9.2)$$

At t_1 the die overtakes the testpiece element, releasing elastic strain until the velocities are equal again at t_2, corresponding to the maximum element displacement. During this interval, the die displacement passes through zero, coincident with the maximum oscillatory velocity, and the displacement of the element at t_2 is therefore the peak to peak value denoted by $2\xi'_m$. This may be found by integrating equation (9.2) between the limits t_1 and t_2;

$$2\xi'_m = \int_{t_1}^{t_2} (\dot{\xi}_m \sin\omega t - Vr)\, dt \quad \text{----------} \quad (9.3)$$

writing $\omega t = \phi$

and $dt = \frac{1}{\omega}.d\phi$ equation (9.3) becomes

$$2\xi'_m = \int_{\phi_1}^{\phi_2} (\xi_m \sin\phi - \frac{V_r}{\omega})\, d\phi \quad \text{----------} \quad (9.4)$$

where ϕ_1 and ϕ_2 are the phase angles defined in Fig. 9.3b. integrating (9.4) gives

$$2\xi'_m = \left[-\xi_m \cos\phi - \frac{V_r}{\omega}\phi\right]_{\phi_1}^{\phi_2}$$

$$= -\xi_m[\cos(\pi-\phi_1) - \cos\phi_1] - \frac{V_r}{\omega}(\pi-\phi_1-\phi_1)$$

$$= 2[\xi_m \cos\phi_1 - \frac{V_r}{\omega}(\tfrac{\pi}{2} - \phi_1)] \quad \text{----------} \quad (9.5)$$

but ϕ_1 is found from the condition:

$$V = \dot{\xi}_m \sin\phi_1 - V_r = 0 \quad \therefore \quad \phi_1 = \sin \frac{-V_r}{\dot{\xi}_m}$$

and on substituting for ϕ_1 in equation (9.5) we obtain after rearranging,

$$\xi_m' = \xi_m\left[\sqrt{1-\left(\frac{V_r}{\xi_m}\right)^2} - \frac{V_r}{\xi_m}\left(\frac{\pi}{2} - \sin^{-1}\frac{V_r}{\xi_m}\right)\right] \text{ --- (9.6)}$$

From equation (9.6) it can be seen that the displacement amplitude of each element, ξ_m', is a function of the ratio of the linear velocity of the element and the velocity amplitude of the die at that section. As this ratio tends to zero the motion of the element coincides with that of the die. Since the linear velocity of the testpiece increases across the deformation zone, approaching that of the punch at the die exit plane, then if the displacement amplitude of the die is constant in this region, the motional amplitude of the testpiece will decrease towards the die exit plane.

The variation in drawing velocity across the deformation zone may be determined by considering the displacement of a circumferential interface at a radius r with respect to a similar interface at the die exit plane. If it is assumed at any stage of drawing, that the thickness variation across the deformation zone is small, we may equate the volumes contained by the movement of an interface at radius r with that at radius r_b, the die exit plane, in a short time interval dt. If V_r is the velocity at radius r and Vp the velocity at r_b, equal to the punch velocity, we may write:

$$r.\theta V_r\, dt = r_b.\theta.\, Vp.dt \text{ ---------- (9.7)}$$

where θ is the included angle of the wedge drawing dies.

From equation (9.7) we obtain

$$V_r = \frac{r_b}{r}.\, V_p \text{ ---------- (9.8)}$$

This simple expression was found to agree quite well with the rim velocity determined experimentally at various stages of

drawing for different draw ratios. The relationship is superimposed on the family of curves shown in Fig. 5.26.

The displacement amplitude at any section of the test piece during radial drawing, may now be found by combining equations (9.6) and (9.8); writing $\frac{V_p}{\dot{\xi}_m} = a$ and setting $r_b = 1$, as in the present series of tests, we have:

$$\xi_m' = \xi_m \left[\sqrt{1-(\frac{a}{r})^2} - \frac{a}{r} (\frac{\pi}{2} - \sin^{-1} \frac{a}{r}) \right] \text{ ---------- } (9.9)$$

Equation (9.9) is used in the subsequent analysis of the oscillatory mechanisms which influence each component of the punch load.

The oscillatory motion of the test piece is summarised qualitatively in Fig. (9.4a). It is postulated that the longitudinal wave motion established in each drawing die is damped in the portion of the test piece passing over the die radius, and as the contact angle approaches 90^o a flexural waveform is established in the drawn test piece, between the planes of contact with the punch and die radii.

In the absence of die radius friction however, it is proposed that a compressional standing wave is established in the drawn test piece. When the total length of the test piece is equal to a quarter wave length, at the operating frequency, some interaction will occur between the transmitted waves from each vibrator resulting in reinforcement. If it is assumed that complete absorption of the incident wave takes place in each opposing deformation zone, the wave form will be as shown in Fig. 9.4b. This is discussed further in section 9.3.2.4.

9.2.3 Mechanisms of Friction reduction during drawing

It is necessary to consider the effects of the proposed oscillatory mode on each component of friction force operating during the wedge drawing test, viz:

(i) friction due to the blank holder force

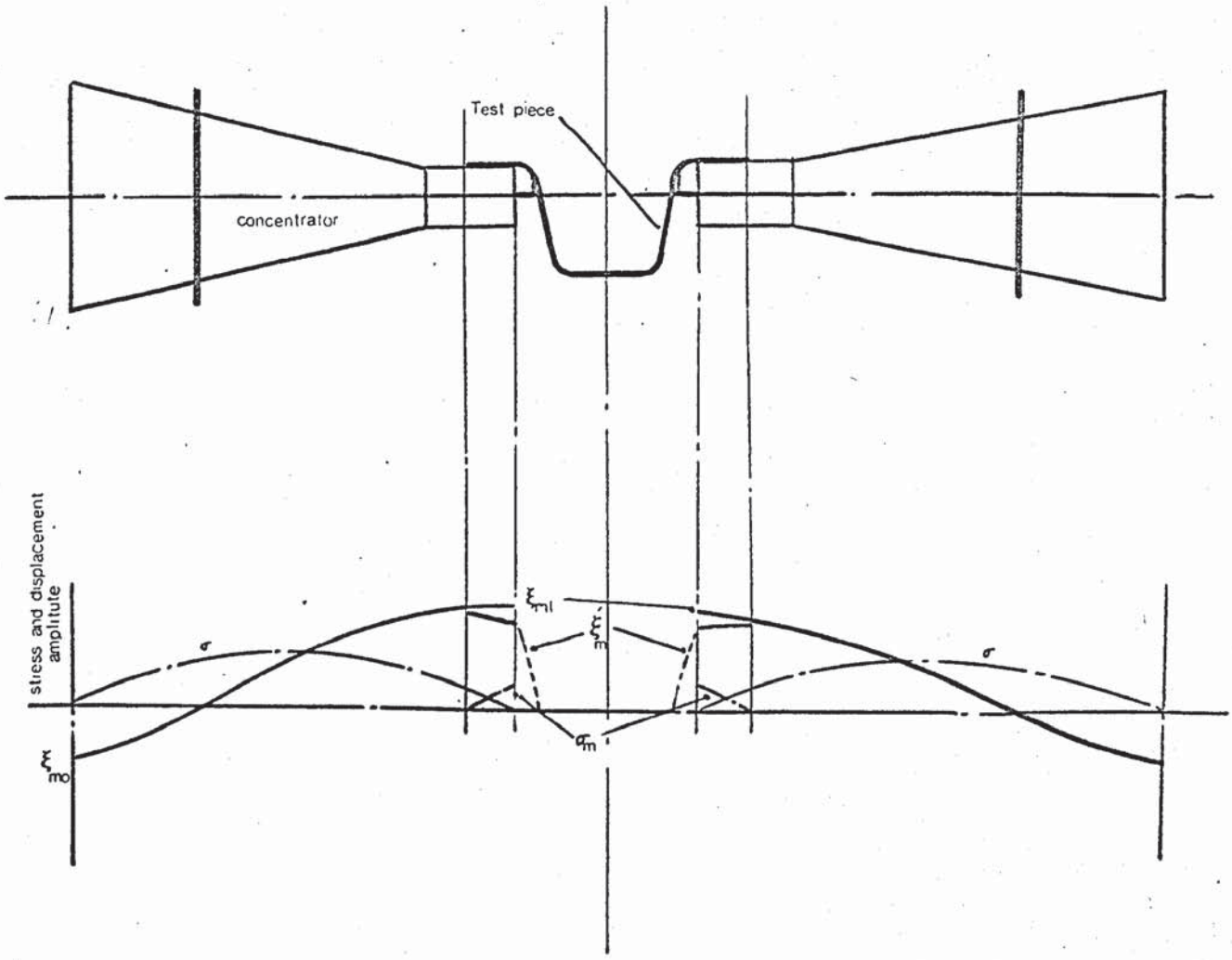

Fig. 9.4a Waveform associated with normal dies.

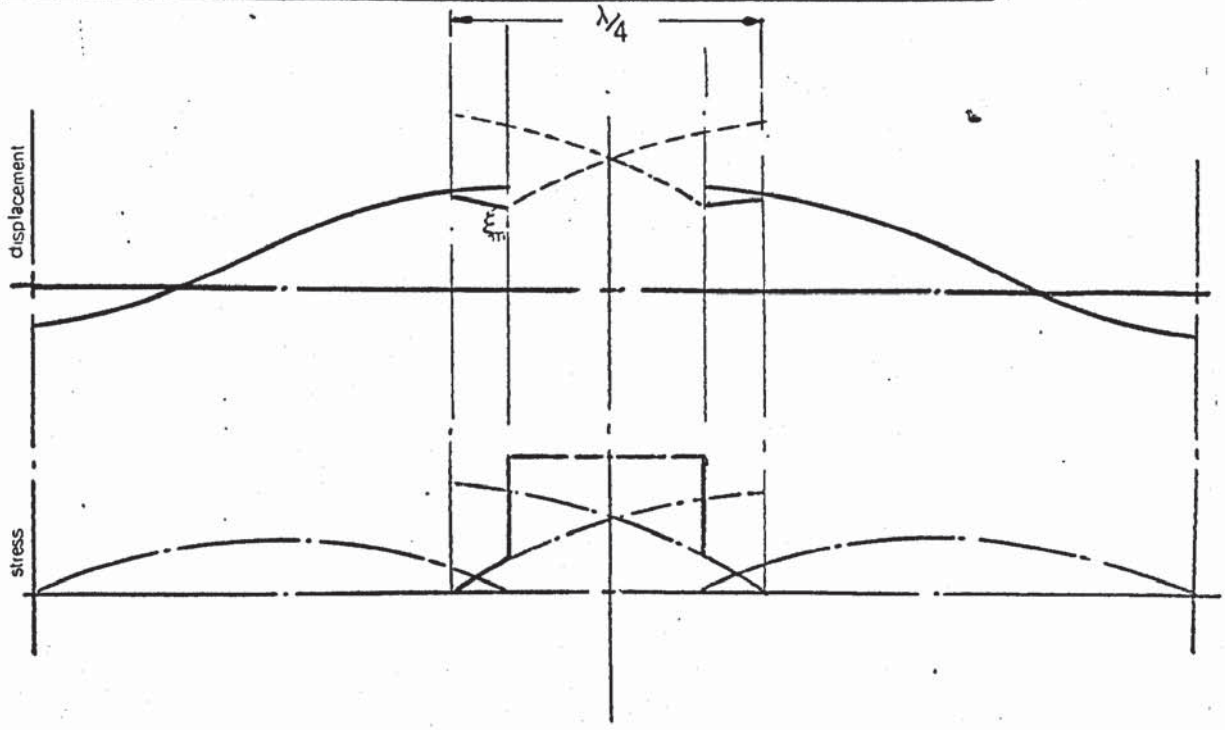

Fig. 9.4b Waveform in the absence of die profile friction.

(ii) friction between the edges of the test piece and the wedge die

(iii) friction related to the motion of the test piece over the die radius

Several possible mechanisms have been proposed for the reduction of friction in oscillatory deformation processes. These are:-

(i) friction vector reversal

(ii) activation of the drawing lubricant

(iii) shearing of asperity weldments

(iv) pumping of lubricants

(v) separation of the surfaces during part of the deformation cycle.

The relevance of these mechanisms to the present oscillatory process are considered in the following section.

9.2.3.1 Blank Holder Friction

The simple model proposed by Sirotyuk[41] which was discussed in Section 2.3.2, may be applied in this instance. It will be recalled that the mechanism was based on the reversal of the friction vector during part of the oscillatory cycle when one surface of the friction interface was vibrated relative to the other.

In the wedge drawing test, considering the interface between each blank holder plate and the upper testpiece surface, the blank holder is considered to be stationary whilst the testpiece moves with a linear velocity onto which is superimposed an oscillatory motional component. Both the linear velocity and the oscillatory amplitude vary across the friction interface at each stage of drawing. However by using the approximate relationship for the testpiece velocity given in equation (9.8) and applying equation (9.9) defining the test-

piece motion at any section in the deformation zone the friction reduction may be determined as follows:

If the blank holder friction force may be assumed to act at the testpiece periphery at any instant during drawing, the effect of vibrations may be deduced by considering the relative motion of the interface at this particular section only.

Fig. 9.5a illustrates qualitatively the testpiece motion at any section within the deformation zone. Provided that the velocity amplitude of the oscillatory component is greater than the linear test piece velocity at the section under consideration, V_r, the motion of the testpiece will be reversed during part of the vibration cycle. During this interval the friction vector will be reversed and if the friction force is the same under oscillatory and non-oscillatory conditions, only the mean friction force will contribute to the deformation load. This is illustrated in Fig. 9.5b where the shaded area represents the interval during which the test piece motion is effectively reversed.

The reduction in friction force under oscillatory conditions is readily determined as follows:

If the velocity of the testpiece is given by

$$V = \dot{\xi}'_m \sin\omega t + V_r$$

then $V = 0$ when $V_r = -\dot{\xi}'_m \sin\omega t$

Let θ_1 represent the phase angle during which the oscillatory velocity increases to match the linear velocity, then the friction force may be summed over a complete vibration cycle to give:

$$F_r = \frac{F}{2\pi}\left\{(\pi+2\theta_1) - (\pi-2\theta_1)\right\} = \frac{F.2\theta_1}{\pi} = \frac{2F}{\pi}\sin^{-1}\frac{V_r}{\dot{\xi}'_m} \quad - (9.10)$$

where F_r and F represent the mean friction force under

Fig. 9.5a Testpiece motion at radius r.

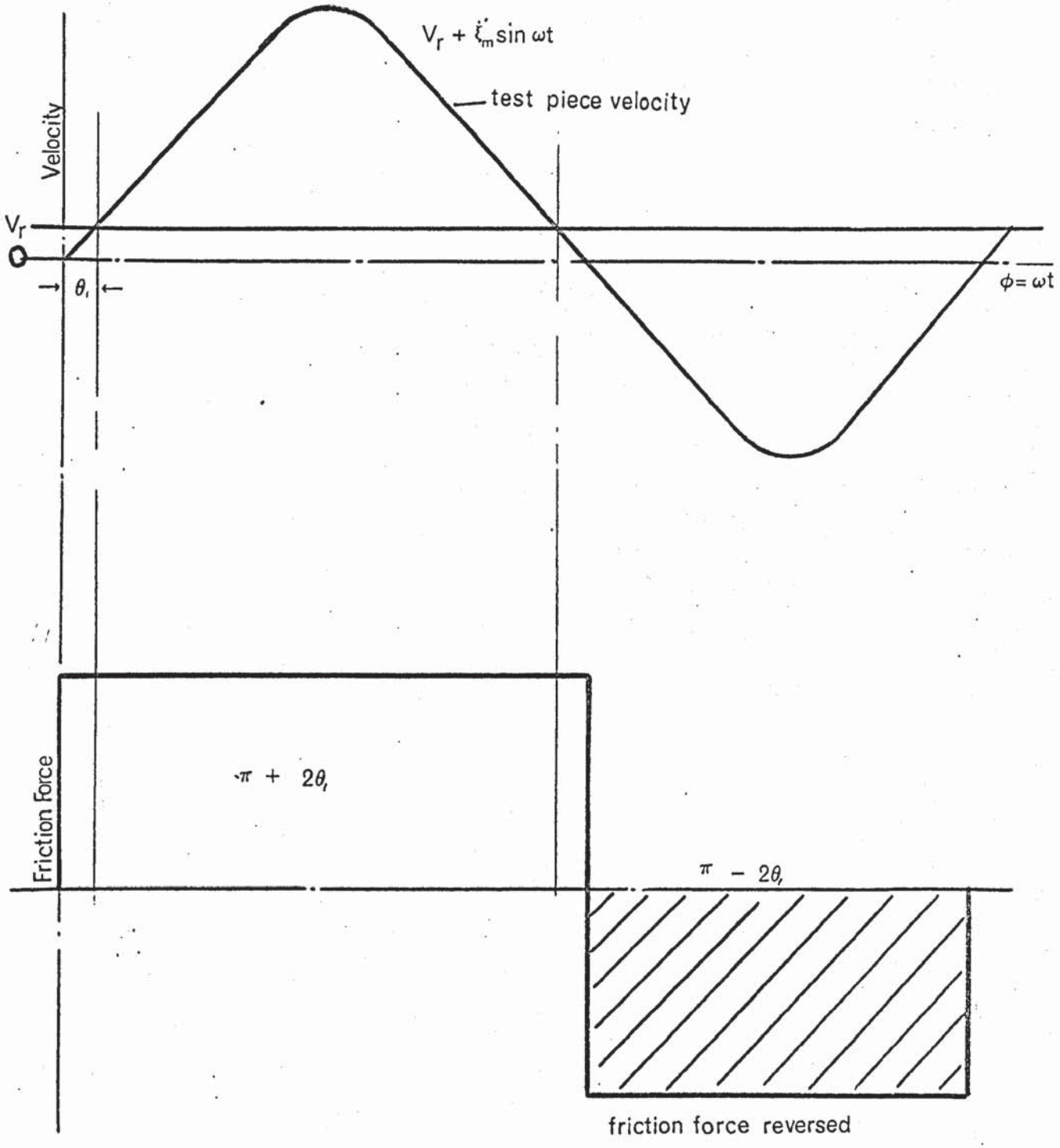

Fig. 9.5b Friction force reduction at the blank holder/ testpiece interface.

oscillatory and non-oscillatory conditions respectively.

But $V_r = \frac{V_p}{r}$

and $\dot{\xi}'_m = \dot{\xi}_m \left[\sqrt{1 - (\frac{a}{r})^2} - \frac{a}{r}(\frac{\pi}{2} - \sin^{-1} \frac{a}{r}) \right]$

therefore equation (9.10) becomes:

$$\frac{F_r}{F} = \frac{2}{\pi} \sin^{-1} \frac{a}{\left[\sqrt{r^2 - a^2} - a(\frac{\pi}{2} - \sin^{-1} \frac{a}{r})\right]} \quad \text{-------} \quad (9.11)$$

9.2.3.2. Comparison with Experimental data

The effectiveness of this mechanism is illustrated in Fig. 9.6 where the percentage reduction in friction force is plotted as a function of the velocity ratio, $a = \frac{V_p}{\dot{\xi}_m}$ for different values of r/r_b. The experimental results from test series 01 and 02 have been plotted on the same ordinates and it will be seen that the majority of points lie between the limits $1 > r/r_b < 2.00$, the maximum drawing ratio being 1.90:1. In order to examine the validity of the model in greater depth the theoretical reduction in friction force was calculated using data from individual tests. The predicted values of percentage friction force reduction were then superimposed on the graphs in Fig. 8.6a - 8.8a, showing the variation in friction reduction during drawing for draw ratios of 1.60, 1.65 and 1.70. The model was found to predict the general decrease in friction reduction from start to finish of drawing but the calculated reduction was consistently higher than the measured values. This is considered to be due largely to the inaccuracy in the assumption that the blank holder friction force acts at the testpiece perimeter. Thickening of the test piece was observed to occur at the edges during drawing which would result in part of the blank holder load being supported in these regions. If the friction force acts over an extended region

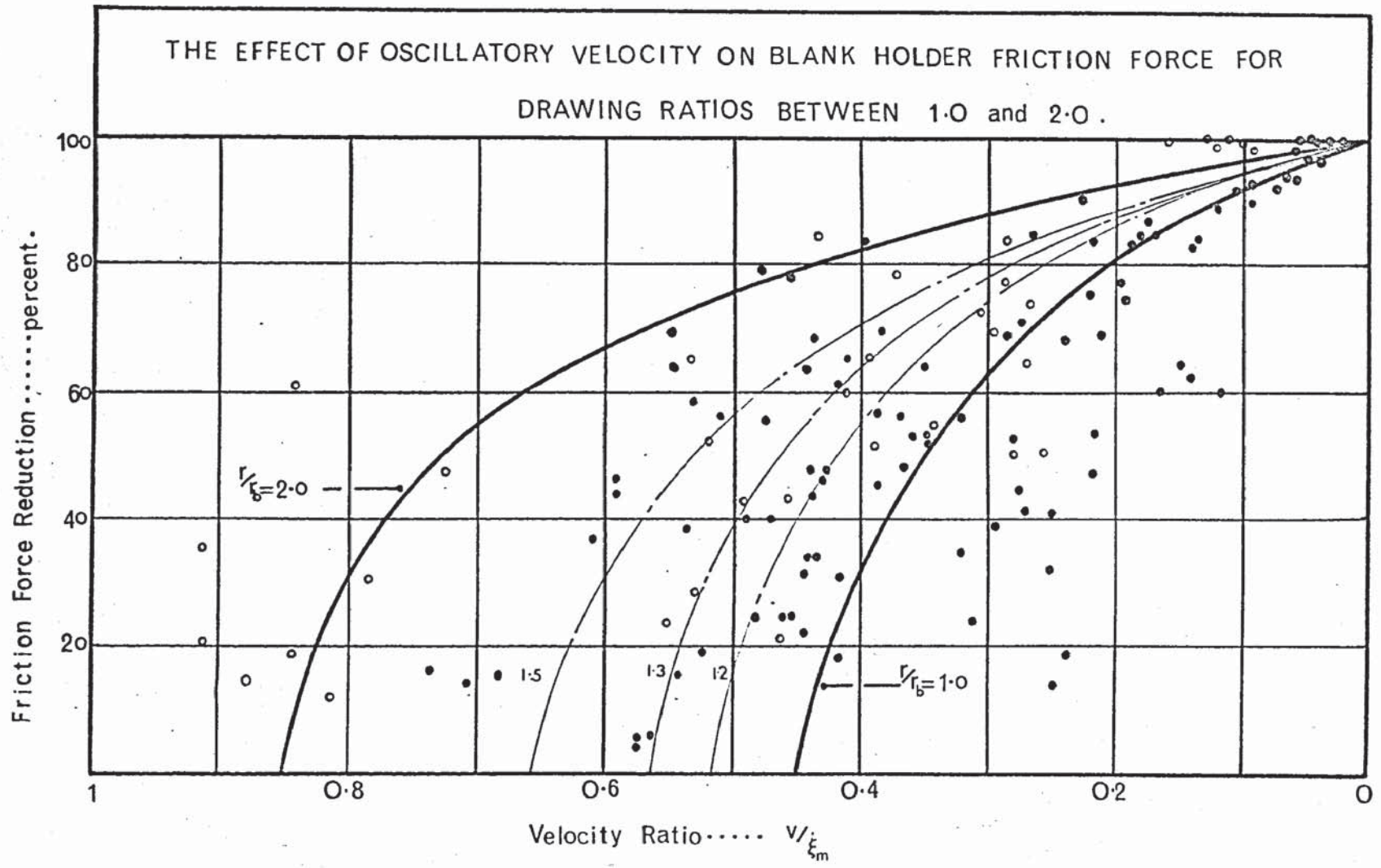

Fig. 9·6

Solid lines represent theoretical values calculated from equation 9·11

Nominal Punch Velocity (in/sec.): 0·15 — ● 0·35 — ○

of the testpiece then, since the effectiveness of the mechanism becomes less as the die exit plane is approached the total reduction in friction force at any stage of drawing would be less than predicted on the initial assumption.

From Fig. 9.6 it can be seen that the model predicts a 95% reduction in friction force for a velocity ratio of 0.1. This agreed closely with experimetnal data at both punch velocities examined. Also examination of the punch load reduction data, plotted in Fig. 8.13 - 8.21, indicates that the limit of the non-linear effect coincides with values of die amplitude which correspond to a velocity ratio of 0.1. However, the magnitude of the non-linear force reduction was greater than the measured reduction in blank holder friction force, indicating the presence of a further effect.

9.2.3.3 Reduction in friction forces between testpiece and die

The possibility of friction reduction at the lower test piece surface and at the interface between the die and edges of the test piece was considered. In order for the reversal mechanism to operate at the edges of the testpiece the motion of the die would have to be such that it assisted the testpiece motion during part of the vibration cycle. However, in the analysis defining the testpiece vibrational mode it was proposed that during the interval in which the die velocity exceeded that of the linear testpiece velocity, each element of the testpiece remained in contact with the die as the elastic strain was released. Friction vector reversal was therefore considered impossible. It was concluded also that the relative motion of the die and testpiece did not permit separation of the surfaces during the vibration cycle since the rate of strain release in the testpiece would be several orders of

magnitude greater than the oscillatory velocity, being equal to the velocity of compressional waves in the material.

9.2.3.4 Surface examination of Drawn Testpieces

In an attempt to verify the friction reduction mechanism and to confirm the oscillatory mode of the testpiece, a series of observations was carried out using a stereoscan electron microscope. It was intended to examine various portions of the testpiece to determine whether oscillatory drawing produced any distinctive surface characteristics. The occurrence of a cyclic relative motion at the tool/work piece interface would be expected to produce some evidence of surface disruption or flow. Should this be the case, such a feature would only be expected on the upper testpiece surface, if the proposed oscillatory mode of the testpiece is correct. A number of testpieces were prepared by etching in a 10% solution of sodium hydroxide (NaOH). This ensured a uniform surface finish by producing a thick oxide film. The tests were carried out at a drawing ratio of 1.70:1 over a range of die amplitudes. In order to produce clearly defined regions drawn either under oscillatory or non-oscillatory conditions the following sequence was adopted:

Testing was commenced with the vibrators switched off; after completing half the draw, they were switched on for a period of approximately 1 sec. and the test completed under non-oscillatory conditions. The effect was to produce a narrow transverse band on the testpiece, representing the oscillatory interval, which was clearly observed by visual examination.

Sections were taken from the upper and lower surfaces and from the edges of the testpieces within and adjacent to the oscillatory band. These were mounted on conventional specimen holders and examined at various magnifications upto x 1,150

using an electron microscope with oblique beam scanning facilities. The depth of focus possible using this arrangement provided a three dimensional view of the selected field which greatly facilitated detailed comparison of the surfaces.

Examination of sections subjected to low amplitude vibrations revealed no significant difference between regions drawn with and without vibrations. However at amplitudes in the region of 20×10^{-5} in. specimens taken from the upper surface showed a distinct transition across the 'oscillatory' band. In each case examined, the region drawn under oscillatory conditions was characterised by a high level of debris and evidence of oxide film break up. The effect is illustrated in the photographs in Figs. 9.7a and b, which show oscillatory and non-oscillatory regions at magnifications of x 200 and x 900 respectively. Corresponding regions taken from the lower surface of the testpiece and from the edges showed no evidence of oxide film breakup. This is illustrated in Fig. 9.8. The absence of this effect on the edges and lower surface of the testpiece indicated that the oscillatory conditions in these areas were essentially different from those affecting the upper surface. The results were therefore consistent with the proposed vibrational mode of the test piece.

9.2.3.5 Unlubricated Tests

In order to assess the possibility of mechanisms (ii) and (iv) contributing to the observed friction reduction, a series of tests were carried out without lubrication. Care was taken to degrease the tools thoroughly before drawing under both oscillatory and non-oscillatory conditions. Standard traces were obtained for a range of die amplitudes at drawing

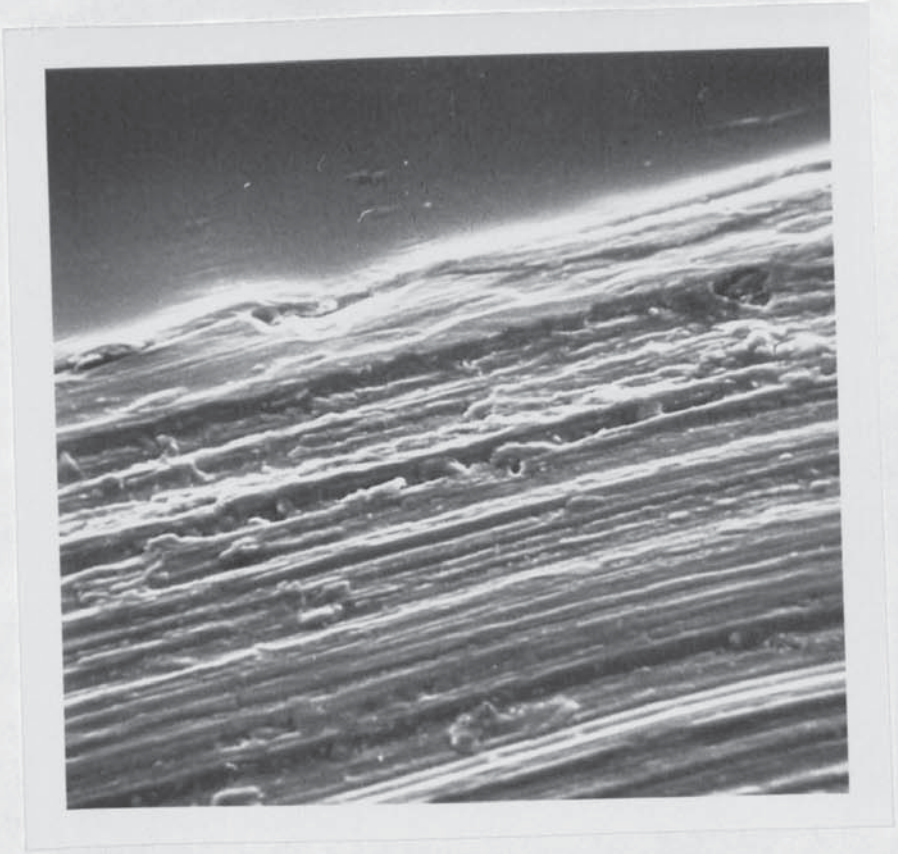

Oscillatory

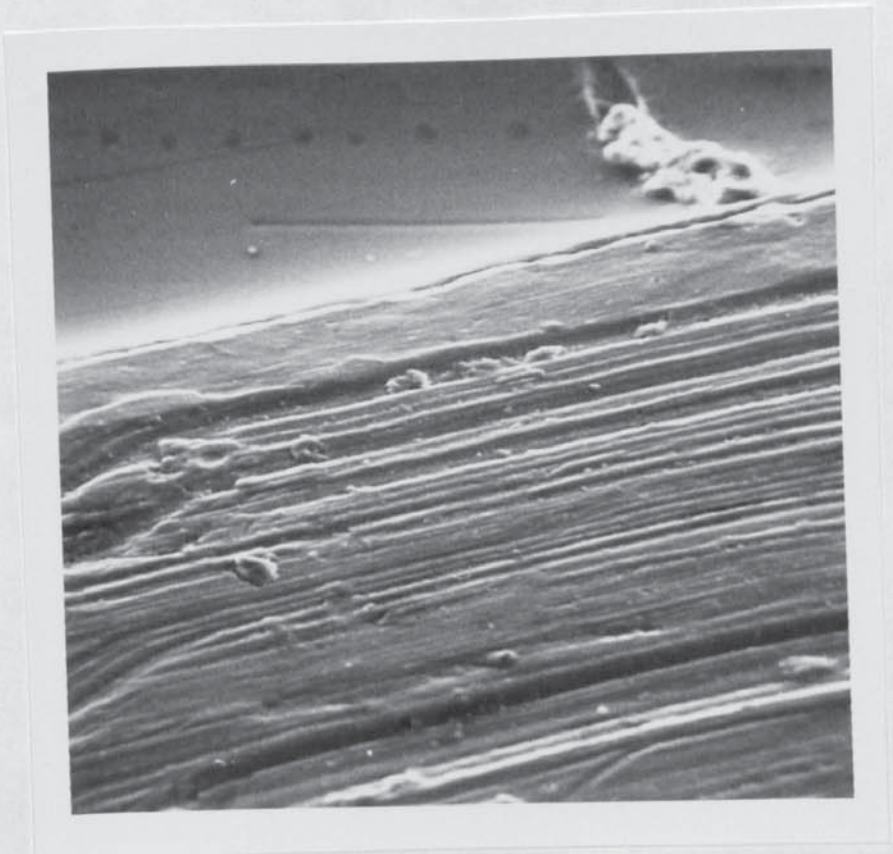

Non-oscillatory

Fig. 9.7a. Upper testpiece surface showing difference between oscillatory and non-oscillatory regions.

Magnification x 200

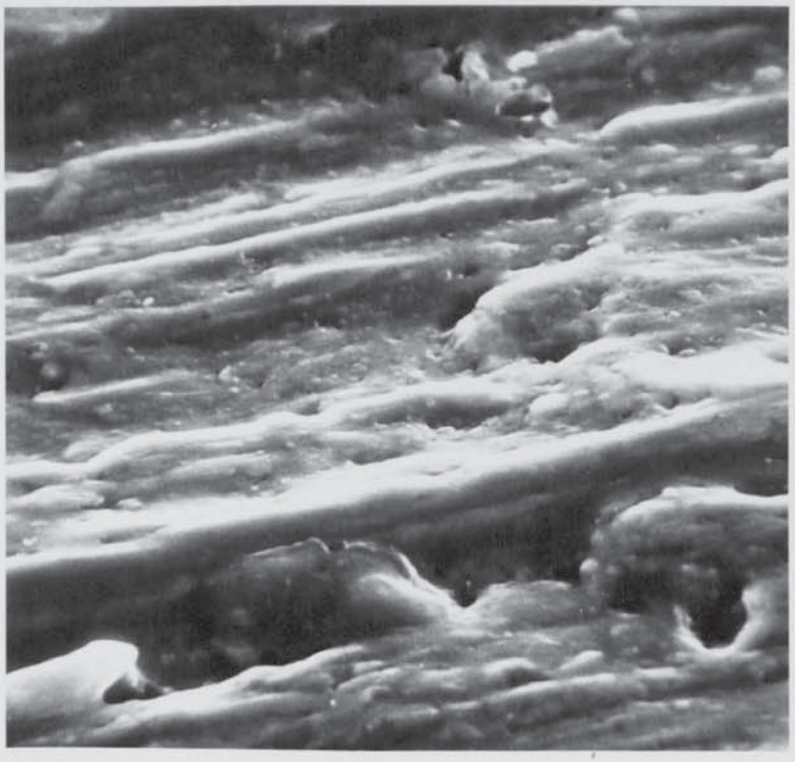

Oscillatory

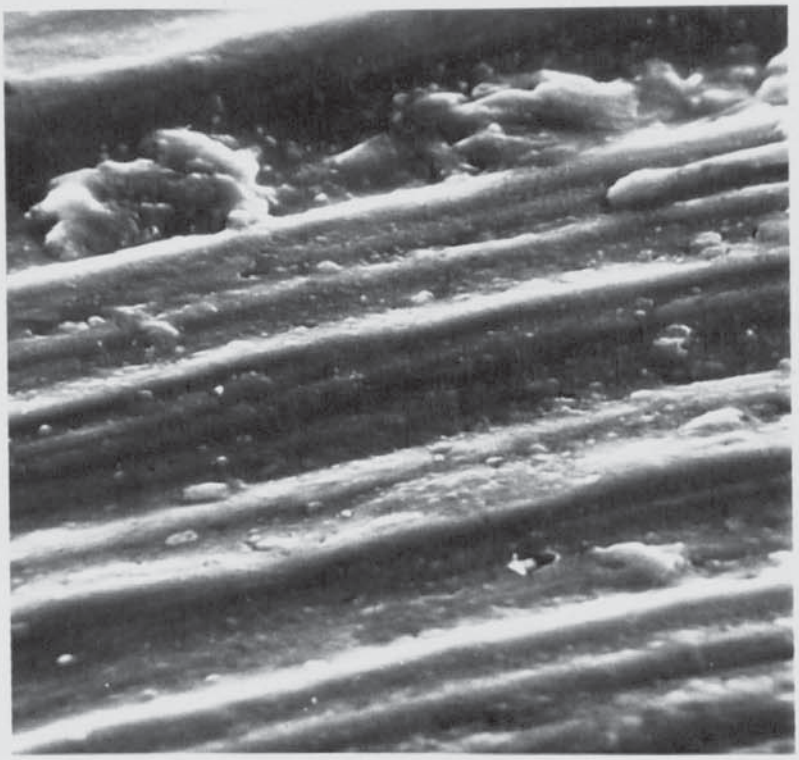

Non-oscillatory

Fig. 9.7b Upper testpiece surface showing difference between oscillatory and non-oscillatory regions.

Magnification x 900

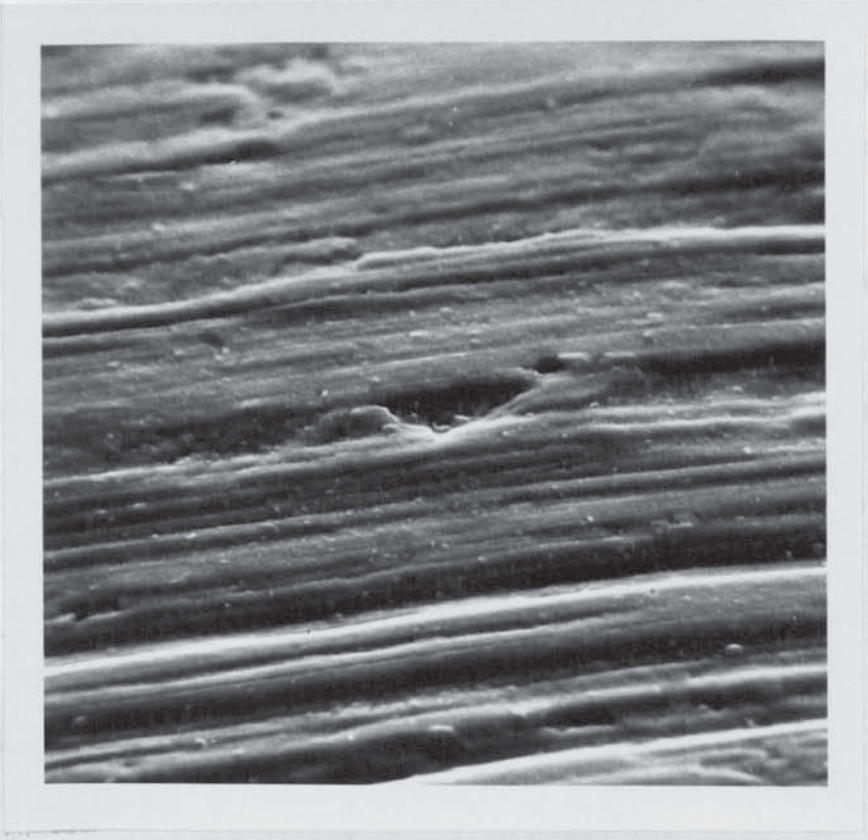

Oscillatory

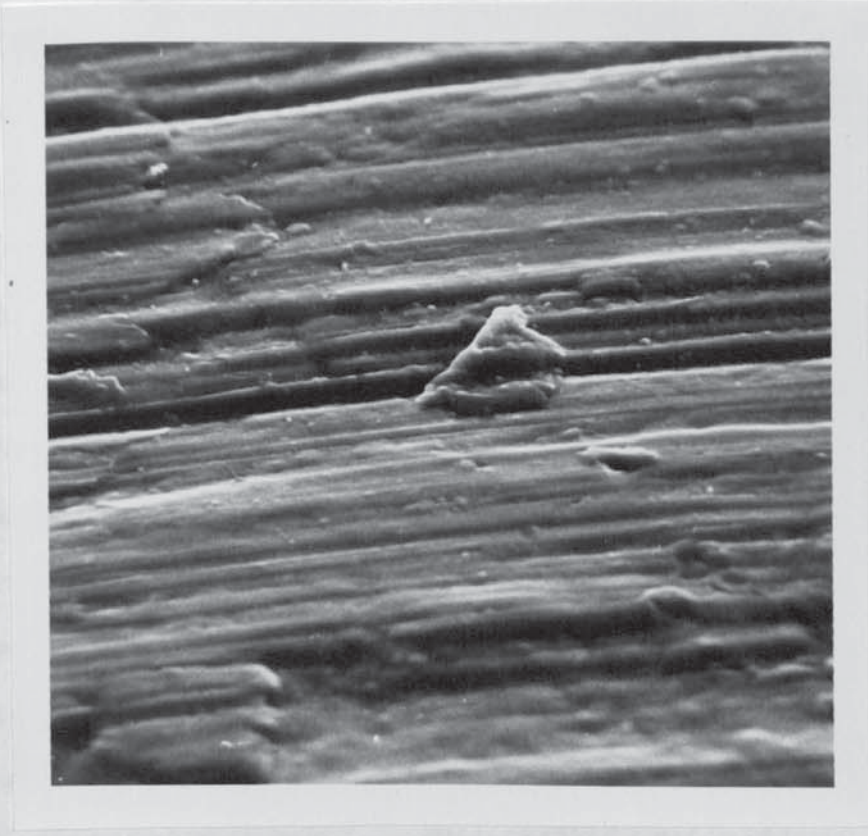

Non-oscillatory

Fig. 9.8 Regions from the edge of the testpiece drawn under oscillatory and non-oscillatory conditions.

Magnification x 900

ratios of 1.60, 1.70 and 1.80:1. The results indicated similar effects to those produced in the lubricated test series. However at die amplitudes in excess of 6×10^{-5} in. the friction force, which was reduced to zero during the early stages of drawing, was found to increase towards the end of the draw. This was attributed to welding which was considered more likely in the absence of a lubricant film. From the general characteristics of the lower amplitude tests it was therefore concluded that any effect due to pumping or activation of the lubricant was of negligible magnitude.

9.2.3.6. Low velocity ratio tests

In order to examine the effects of low velocity ratios on the friction characteristics, several tests were carried out at slow punch speeds, of the order of 0.03 in/sec. with die amplitudes upto 8×10^{-5} in. ($\dot{\xi}_m$ in 14.8 in/sec). This gave a velocity ratio ($a = \frac{v}{\dot{\xi}_m}$) of 0.002:1, which was much lower than achieved in the main series of tests. A striking characteristic of the deformation process under these conditions was that severe galling occurred between the test piece and blank holder and to a lesser extent between the lower test piece surface and the die. In extreme cases the testpiece was actually welded to the die which resulted in premature failure. For this reason, coupled with the need to minimise die wear, only limited testing was carried out at very low ratios. Blank holder friction force measurements were erratic when welding occurred but for less severe conditions, down to ratios of 0.01, the friction force recorded during intermittent testing at a drawing ratio of 1.70:1 was observed to be approximately twice the equivalent non-oscillatory value. This observation was consistent with the general phenomenon observed in the main series of tests and

might be explained by the additional friction work expended during oscillatory drawing.

If it is assumed that the energy expended in effecting the additional oscillatory frictional work is degraded to heat, then a further friction effect might be expected at low velocity ratios due to enhanced welding of asperities.

It is suggested that under conditions of large relative motion, the heat generated at the interface is sufficient to facilitate atomic diffusion resulting in welding of the contacting surface asperities. Provided that the junctions are isolated they will be sheared during the motional cycle. However as the heating effect increases, producing a reduction in yield stress, the true contact area becomes greater in order to support the constant blank holder load and it becomes increasingly more difficult to shear the surface weldments. This tendency develops as more oscillatory energy is expended, until the reversal mechanism fails to operate and welding occurs between the contacting surfaces.

The observations relating to intermittent oscillatory tests can be explained using similar arguments. During the oscillatory intervals heating occurs, resulting in an increased contact area. However, provided the velocity ratio is not too low, the mean frictional force is reduced by the vector reversal mechanism. When the vibrators are switched off the additional heat input ceases and the contacting surfaces are rapidly chilled. This raises the shear strength and since the increased area of contact is maintained, causes an increase in the frictional force necessary to shear the junctions. Therefore, the greater the relative motion the more heat is produced which causes a corresponding increase in true contact area leading to an

increased non-oscillatory friction force during the 'off' period of the test. This explanation is consistent with the observed phenomena over a range of velocity ratios corresponding at one extreme to zero friction reduction and at the other to extensive welding between testpiece and blank holder plate.

9.2.3.7. The Effect of Vibrations on Die Radius Friction

It is proposed that the effect of vibrations on the die radius friction force may be determined by considering the cyclic rotation of the relative velocity vector, associated with each element in contact with the die surface. As the angle of rotation varies periodically, the effective friction force also varies. The effect of superimposed oscillations can be determined, as proposed by Severdenko and Reznikov,[44] by comparing the impulsive force, acting during a vibration cycle, under oscillatory and non-oscillatory conditions.

The relative motion of the testpiece and die at any position around the die radius may be determined as follows:-

Let the elementary contact angle be $d\theta$, at a position on the die surface defined by θ, see Fig. 9.9. If the motion of the die in contact with the element is $\dot{\xi} = \dot{\xi}_m \cos \omega t$, then the testpiece, moving initially with constant velocity V_p, will be given a cyclic motional component. This may be defined by taking the normal and tangential components of the die velocity;

The testpiece motion perpendicular to the radius at the point of contact defined by θ is $\dot{\xi}_m = \dot{\xi}\cos\theta$ and in a tangential direction, $V_p + \dot{\xi}_T = V_p + \dot{\xi}\sin\theta$. The normal component, $\dot{\xi}_N$ results in rotation of the relative velocity vector V_R, the angle of rotation varying between two extreme limits corresponding to the amplitudinal velocity in each half period.

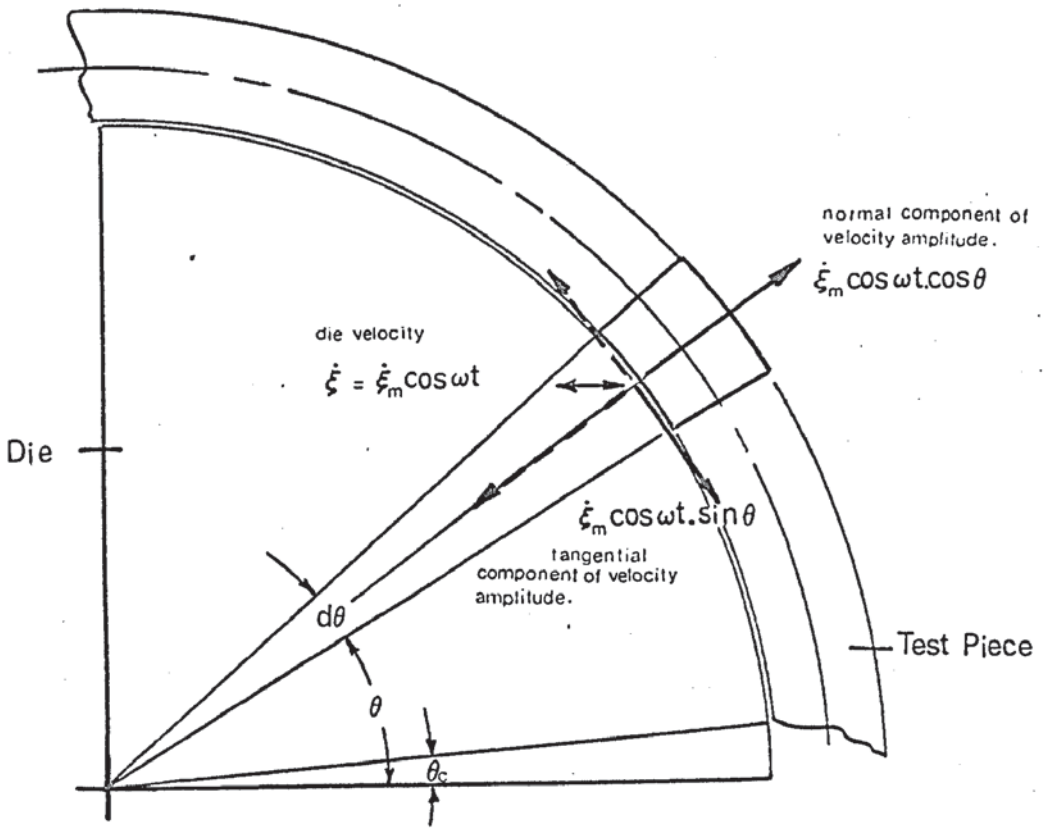

Fig. 9.9 Oscillatory motion of an element $d\theta$, passing around the die profile radius.

Considering the half cycle in which the die motion is to the right in Fig. 9.9, the resulting velocity of the testpiece is given by:

$$V_R = \left\{(V_p + \dot{\xi}_m \cos\omega t.\sin\theta)^2 + \dot{\xi}_m^2 \cos^2\omega t \cos^2\theta\right\}^{\frac{1}{2}} \quad \text{-- (9.12)}$$

$$= (\dot{\xi}_m^2 \cos^2\omega t + 2\dot{\xi}_m \cos\omega t.\sin\theta + V_p^2)^{\frac{1}{2}} \text{ ------ (9.13)}$$

which acts at an angle δ_1 to the tangent.

$$\text{where } \tan\delta_1 = \frac{\dot{\xi}_m \cos\omega t.\cos\theta}{V_p + \dot{\xi}_m \cos\omega t \sin\theta}$$

Similarly, considering the cyclic motion to the left in Fig. 9.9,

$$V_R = (\dot{\xi}_m^2.\cos^2\omega t - 2\dot{\xi}_m \cos\omega t.\sin\theta + V_p^2)^{\frac{1}{2}} \text{ ------- (9.14)}$$

and δ_2 is given by: $\tan\delta_2 = \dfrac{\dot{\xi}_m \cos\omega t.\cos\theta}{V_p - \dot{\xi}_m \cos\omega t.\sin\theta}$

If the friction force vector normally acting tangentially at 180^o to the relative velocity vector, is rotated through an angle δ, then the effective impulsive force during a small interval dt is:

$$dI_\theta = df_\theta \cos\delta.dt \quad \text{---------- (9.15)}$$

and the force impulse associated with a complete cycle is given by:

$$I_\theta = df_\theta \int_0^T \cos\delta.\, dt \quad \text{---------- (9.16)}$$

where df_θ is the friction force acting on the element.

Substituting for $\cos\delta$ in equation (9.16) from equations (9.13) and(9.14) we may write:

$$I_\theta = df_\theta \left[2 \int_0^{T/4} \frac{V_p + \dot{\xi}_m \cos\omega t \sin\theta}{\sqrt{\dot{\xi}^2 \cos^2\omega t + 2\dot{\xi}_m V \cos\omega t.\sin\theta + V_p^2}} .dt\right.$$

$$+ 2 \int_0^{T/4} \frac{V_p - \dot{\xi}_m \cos\omega t . \sin\theta}{\sqrt{\dot{\xi}^2 \cos^2\omega t - 2\dot{\xi}_m V_p \cos\omega t . \sin\theta + V_p^2}} . dt \Bigg] \quad - (9.17)$$

If we now express t in terms of the phase angle ϕ from the relationships:

$$\omega t = \phi$$

and $$dt = \frac{d\phi}{\omega}$$

then, putting $\frac{V_p}{\dot{\xi}_m} = a$, equation 9.17 becomes:

$$I_\theta = \frac{2df_\theta}{\omega} \Bigg[\int_0^{\pi/2} \frac{a + \cos\phi \sin\theta}{\sqrt{\cos^2\phi + 2a . \cos\phi \sin\theta + a^2}} . d\phi$$

$$+ \int_0^{\pi/2} \frac{a - \cos\phi \sin\theta}{\sqrt{\cos^2\phi - 2a \cos\phi \sin\theta + a^2}} . d\phi \Bigg] \quad ---------- (9.18)$$

From the simple belt pulley friction model given in section 3, the friction force acting at the die radius exit plane is found for any stage of drawing from the expression:

$$f_\theta = \sigma_{r_b} \left[e^{\mu(\pi/2 - \theta)} - 1 \right] \quad ---------- (9.19)$$

and $$df_\theta = - \mu \sigma_{r_b} . e^{\mu(\pi/2 - \theta)} . d\theta$$

This implies that the friction force varies around the die radius between the limits $f_\theta = 0$ for $\theta = \pi/2$ and $f_\theta = f_{\theta_c}$ for $\theta = \theta_c$.

It is therefore possible to determine the impulsive friction force under oscillatory conditions at any point around the die radius, by substituting the expression for df_θ, in equation (9.18) viz.

$$I_\theta = \frac{2\mu\sigma'_{r_b}}{\omega} \left[e^{\mu(\pi/2 - \theta)} \right] \Bigg[\int_0^{\pi/2} \frac{a + \cos\phi \sin\theta}{\sqrt{\cos^2\phi - 2a \cos\phi \sin\theta + a^2}} . d\phi \; +$$

$$+ \int_{o}^{\pi/2} \frac{a - \cos\phi\sin\theta}{\sqrt{\cos^2\phi - 2a.\cos\phi\sin\theta + a^2}} d\phi \Bigg] \quad \text{---------- (9.20)}$$

where σ'_{r_b} is the radial stress at the die unit plane under oscillatory conditions. The total friction force impulse is then found by integrating equation (9.20) with respect to θ over the contact arc, and the final equation becomes:

$$I_T = \frac{2\mu\sigma'_{r_b}}{\omega} \left[\int_{\theta_c}^{\pi/2} \left[e^{\mu(\pi/2 - \theta)}\right] \int_0^{\pi/2} \frac{a + \cos\phi\sin\theta}{\sqrt{\cos^2\phi + 2a.\cos\phi\sin\theta + a^2}} . d\phi . d\theta \right.$$

$$\left. + \int_{\theta_c}^{\pi/2} \left[e^{\mu(\pi/2 - \theta)}\right] \int_0^{\pi/2} \frac{a - \cos\phi\sin\theta}{\sqrt{\cos^2\phi - 2a\cos\phi.\sin\theta + a^2}} d\phi . d\theta \right] \quad (9.21)$$

The reduction in friction force may be determined by comparing the impulsive forces under oscillatory and non-oscillatory conditions. Considering a complete vibration period, the latter is readily found from equation (9.19), viz:

$$I'_T = \sigma_{r_b} \left[e^{\mu(\pi/2 - \theta_c)} - 1 \right] \frac{2\pi}{\omega} \quad \text{---------- (9.22)}$$

where I'_T is the total non-oscillatory friction force impulse. The friction force reduction is then given by:

$$\Delta f = \left[1 - \frac{I_T}{I'_T} \right] \quad \text{---------- (9.23)}$$

which may be solved by substituting for I_T and I'_T from equations (9.21) and (9.22).

In view of the computational difficulty in determining the complete solution to equation (9.23) it is proposed to examine the friction reduction effect at the two boundaries of the contact arc, for a stage of drawing at which θ_c tends to zero. The friction force reduction at the exit plane can then be determined, to a first approximation, by assuming a linear

relationship for the variation in the elliptical integral over this interval.

At the entry plane the friction force is zero and from equation (9.18) the integral defining the effective vector rotation is also zero.

At the exit plane, assuming $\theta_c = 0$ and substituting for df_θ in equation (9.18), the friction force impulse may be written:

$$I_\theta = \frac{2\sigma'_{rb}}{\omega} \left(e^{\mu \cdot \pi/2} \right) \int_0^{\pi/2} 2 \cdot \frac{a}{\sqrt{\cos^2\phi + a^2}} \cdot d\phi \quad \text{------ (9.24)}$$

which may be rearranged to give:

$$I_\theta = \frac{4\sigma'_{r_b}}{\omega} \left(e^{\mu \cdot \pi/2}_{\mu} \right) \frac{a}{\sqrt{1 + a^2}} \cdot \int_0^{\pi/2} \frac{d\phi}{\sqrt{1 - \left(\frac{1}{1 + a^2}\right)\sin^2\phi}} \quad \text{- (9.25)}$$

For $0 \leqslant \left(\frac{1}{1+a^2}\right)^{1/2} \leqslant 1$ this equation may be evaluated from standard tables of complete elliptical integrals: the general form being:-

$$K = \int_0^{\pi/2} \frac{d\phi}{\sqrt{1 - k^2\sin^2\phi}} = F(k, \pi/2)$$

If we now consider the vector rotation effect to vary linearly throughout the contact arc, from zero at the entry plane to Ψ_o at the exit plane, where Ψ_o is given by:

$$\Psi_o = \frac{4}{\omega} \cdot \frac{a}{\sqrt{1 + a^2}} \cdot F(k, \pi/2) \quad \text{---------- (9.26)}$$

then the total friction force impulse under oscillatory conditions, given by equation (9.21) may be rewritten in simplified form as:

$$I_T = \Psi_o \, \sigma'_{rb.\mu} \int_0^{\pi/2} \left[e^{\mu(\pi/2 - \theta)} \right] \cdot \left[1 - \frac{2}{\pi}\theta \right] d\theta \quad \text{---------- (9.27)}$$

On expanding, this expression becomes:

$$I_T = \Psi_o \sigma'_{rb} \mu \left[\int_o^{\pi/2} (e^{\mu\pi/2} . e^{-\mu\theta}) d\theta - \frac{2}{\pi} \int_o^{\pi/2} (e^{\mu\pi/2} . e^{-\mu\theta} . \theta - \theta) d\theta \right]$$

which on integration gives:

$$I_T = \Psi_o \sigma'_{rb} \mu \left\{ -\left[e . \frac{e}{\mu}^{-\mu\theta} \right) \right]_o^{\mu . \pi/2} \Bigg]_o^{\pi/2} - \frac{2}{\pi} \left[-\frac{e^{\mu\pi/2}}{\mu} \left\{ \theta . e^{-\mu\theta} - \int_o^{\pi/2} e^{-\mu\theta} . d(\theta) \right\} \right]_o^{\pi/2}$$

$$= \Psi_o \sigma'_{rb} \mu \left[- \left\{ e^{\mu\pi/2} . \frac{e}{\mu}^{-\mu\theta} \right\} - \frac{2}{\pi} \left\{ - \frac{e^{\mu(\pi/2-\theta)}}{\mu^2} (\mu\theta+1) \right\} \right]_o^{\pi/2}$$

$$= \Psi_o \sigma'_{rb} \mu \left[(e^{\mu\pi/2} - 1) . \left(\frac{1}{\mu} - \frac{2}{\pi\mu^2} \right) + \frac{1}{\mu} \right] \quad \text{---------- (9.28)}$$

The friction force reduction may now be found from equation (9.23) on substituting for I'_T and I_T from equations (9.22) and (9.28) respectively. This may be written:

$$\Delta f = 1 - \frac{\omega \sqrt{\frac{4a}{1+a^2}} . F(k, \pi/2) . \sigma'_{rb} \left[(e^{\mu\pi/2} - 1) . (1 - \frac{2}{\mu\pi}) + 1 \right]}{\sigma_{rb} (e^{\mu\pi/2} - 1) . \frac{2\pi}{\omega}}$$

$$= 1 - \frac{2}{\pi} . \frac{a}{\sqrt{1+a^2}} . F(k, \pi/2) \left[(1 - \frac{2}{\mu\pi}) + 1/(e^{\mu\pi/2} - 1) \right] \frac{\sigma'_{rb}}{\sigma_{rb}} \quad \text{------ (9.29)}$$

The magnitude of the friction force reduction has been determined from equation (9.29) for different values of the velocity ratio a, taking μ = 0.05 and 0.10 and assuming initially that $\sigma'_{rb} \simeq \sigma_{rb}$. It will be shown in section 9.2.4. that this approximate is justified. The relationship is shown in Fig. 9.10, where the friction force reduction is plotted against the reciprocal velocity ratio for each value of μ. It will be seen that the effectiveness of vibrations increases with increasing

Theoretical Reduction in Die Radius Friction Force with Increasing Values of Reciprocal Velocity Ratio.

Fig. 9·10

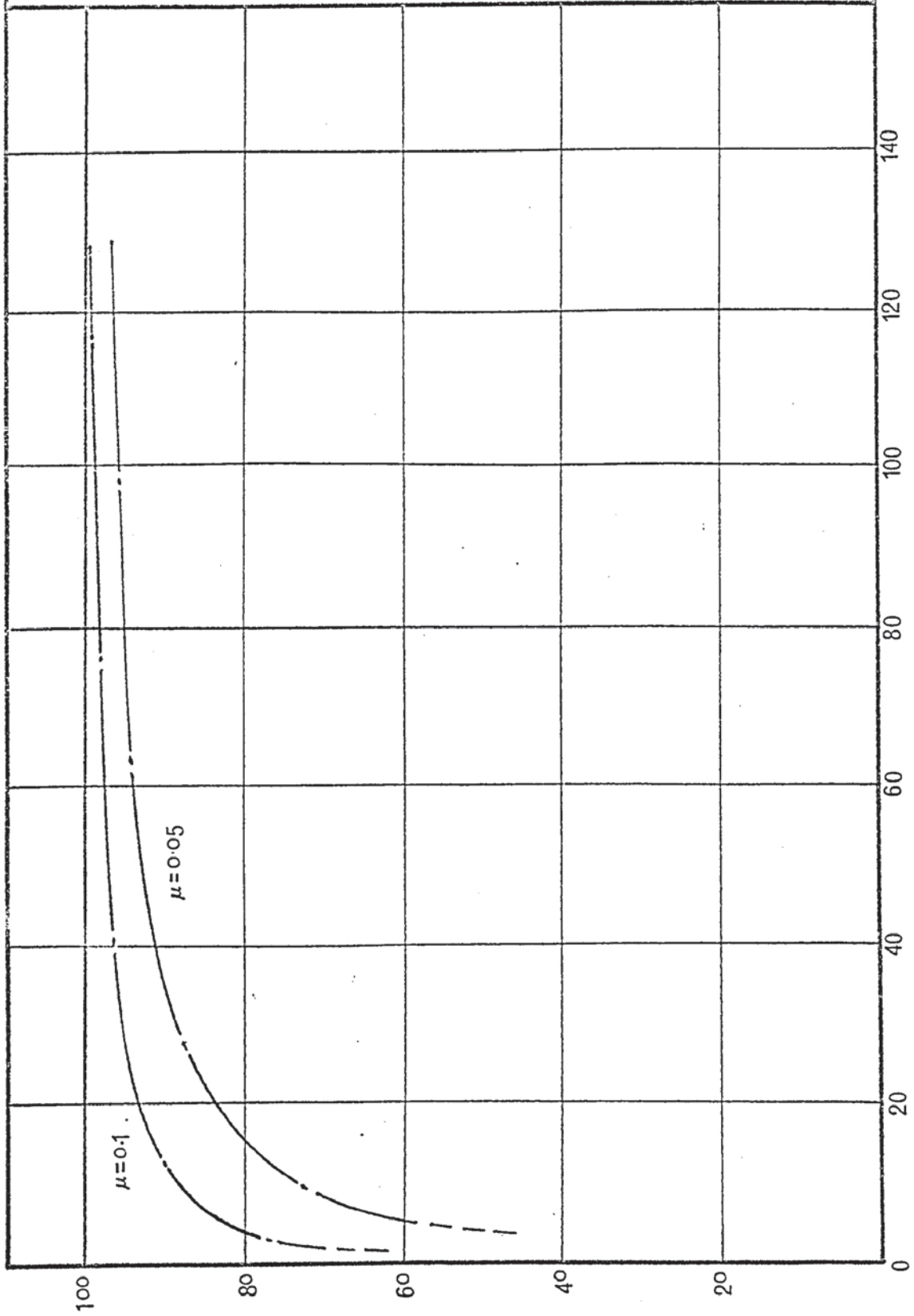

Draw Ratio	Blank holder friction force, (lbf). (From Figs. 8.22b-8.25b)	Die radius friction force, (lbf). (From Figs. 9.11 and 9.12)	Magnitude of non-linear punch load reduction, (lbf). (From Figs. 8.13-8.16)	Reduction in sum of blank holder and die radius friction forces - predicted from equations 9.11 a and 9.28.
1.50	11.0	15	25	24.1
1.60	12.5	14	29	24.6
1.70	15.5	20	35	32.9
1.80	15.0	20	33	32.4

Table 9.1 Comparison of theoretical and measured values of blank holder and die radius friction force reduction, at the position of maximum punch load.

values of μ and that for $\mu = 0.05$ the friction force is reduced by 90% at a velocity ratio of 0.025. For $\mu = 0.1$ the corresponding effect is produced at a velocity ratio of 0.10. For increasing values of the reciprocal velocity ratio the reduction in friction force approaches 100% over the range of friction coefficients considered.

The effect of increasing values of μ on the reduction in friction force would be expected since the increase in friction force towards the exit plane of the die radius coincides with the maximum rotation of the friction vector.

9.2.3.8 Experimental determination of die Radius Friction Force

It was not possible to measure the die radius friction force directly. However, by comparing the punch load/displacement curves for drawing with and without the roller assembly, as described in section 7.4, a fairly accurate estimate was possible at each ratio. In order to eliminate any inconsistency related to the reduced punch radius used with the roller assembly, the strip tension was plotted instead of punch load. This data is presented in Figs. 9.11 and 9.12. Evaluation of the die radius friction force at each stage of drawing depends upon the accuracy with which the displacement axes are aligned for each pair of curves. The most accurate value will therefore be that coinciding with the maximum strip tension. This value has been determined for each drawing ratio from 1.50 to 1.80 and the results presented in Table 9.1.

The accuracy of the friction model derived in section 9.2.3.7 may be examined using the punch load reduction data from test series 02; Fig. 8.13 - 8.17. If the non-linear portion of the punch load reduction curve is assumed to be accounted for by the reduction in blank holder and die radius friction forces, the

Strip Tension / Punch Displacement Curves For Draw Ratios of 1·5 and 1·8, Showing The Effect of Die Radius Friction.

Fig. 9·11

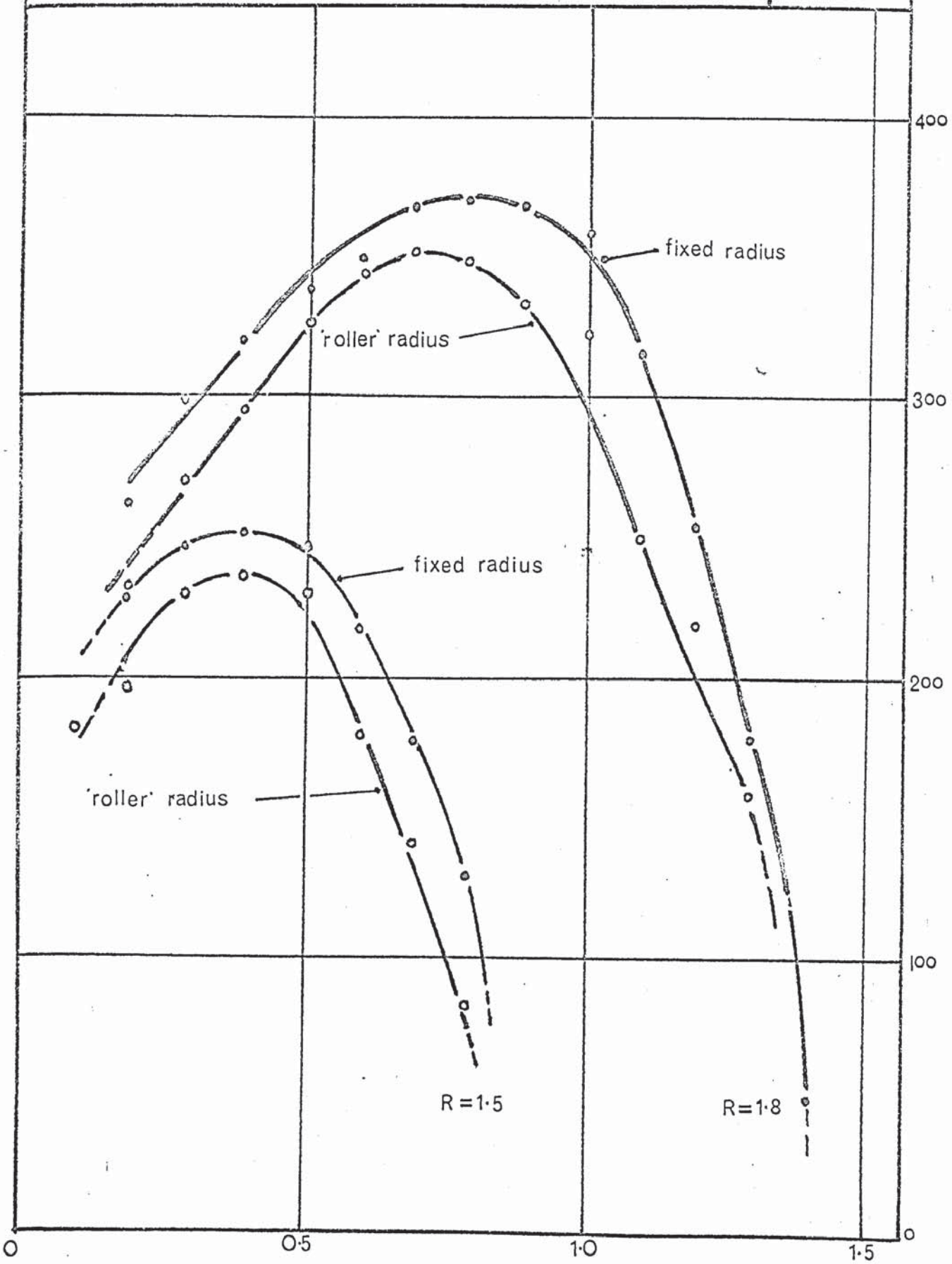

Strip Tension / Punch Displacement Curves for Draw Ratios of 1·6 and 1·7
Showing the effect of Die Radius Friction.

Fig. 9·12

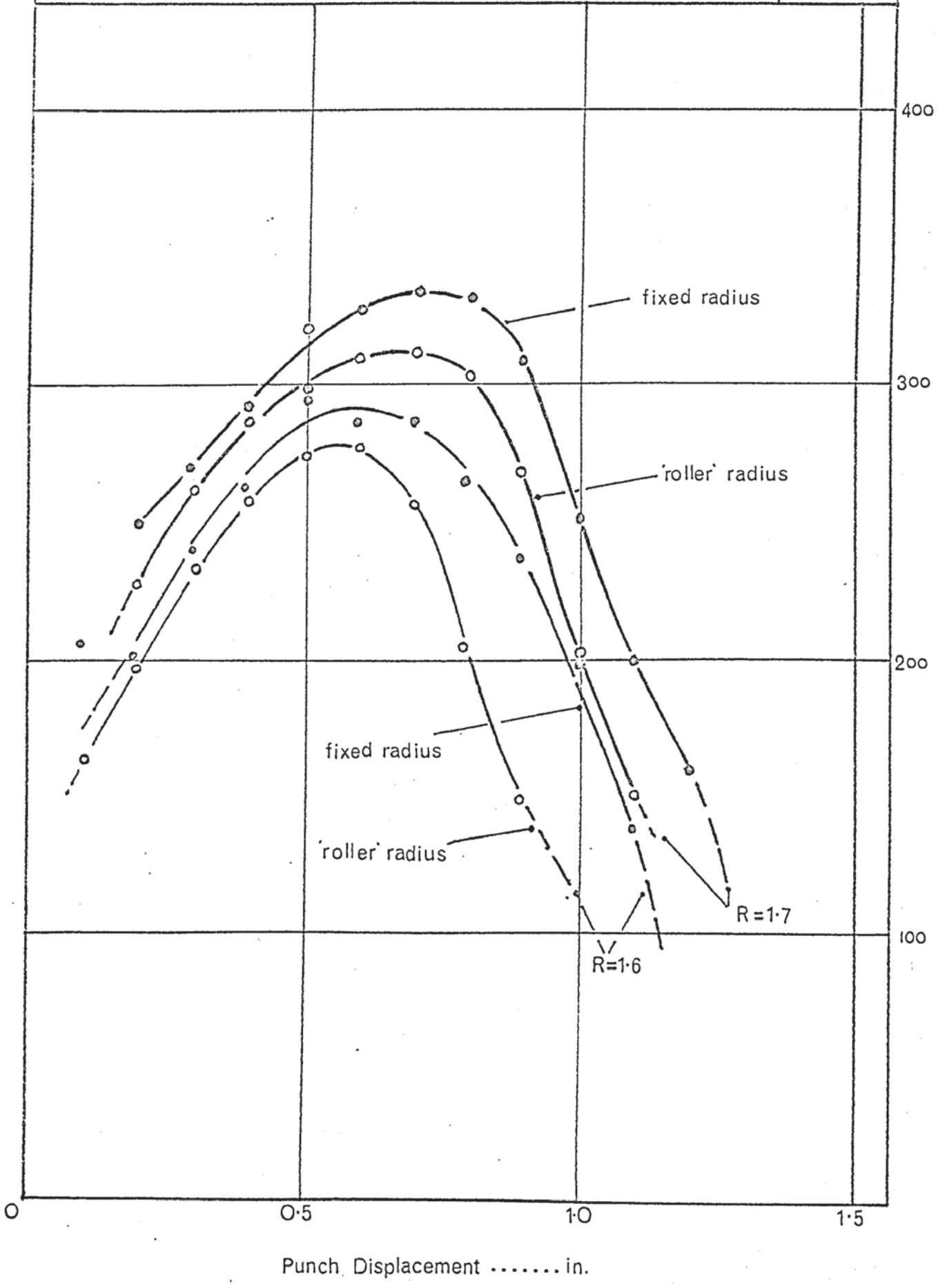

total friction force reduction and the limiting velocity ratio at which this is achieved may be readily determined from the experimental data.

Values corresponding to the maximum punch load have been plotted in Fig. 9.13 where they are superimposed on the curve representing the theoretical reduction in blank holder and die radius friction force at the limiting velocity ratio. The latter figure was based on the data plotted in Figs. 9.11 and 9.12 and the theoretical reduction determined at the critical velocity ratio, from equation 9.29. It will be seen from Fig. 9.13 that good agreement exists at all drawing ratios. Also the limiting velocity ratio, beyond which the friction reduction effect becomes negligible, was found to lie between 0.095 and 0.105 which agrees closely with the theoretical value at the 90% saturation level assuming a friction coefficient of 0.10.

9.2.3.9 Summary of Friction Effects.

Measurement of the blank holder friction force acting at the upper surface of the testpiece, during both oscillatory and non-oscillatory tests, indicated that the friction force could be effectively eliminated beyond a certain level of the die amplitude. It was also apparent that friction reduction did not occur at amplitudes below a certain value. Both limits were dependent on the drawing velocity.

A mathematical model based on the concept of friction vector reversal, was derived. This was found to predict the observed reduction in friction force, in both test series, with good accuracy. It was also found to predict the critical die amplitude defining the threshold and saturation limits for both drawing velocities considered. The threshold value, expressed in terms of the velocity ratio, was found experimentally to lie between

Reduction in the sum of Blank Holder and Die Radius Friction Forces, at the position of maximum Punch Load, predicted from equations 9·11 and 9·28.

Fig. 9·13

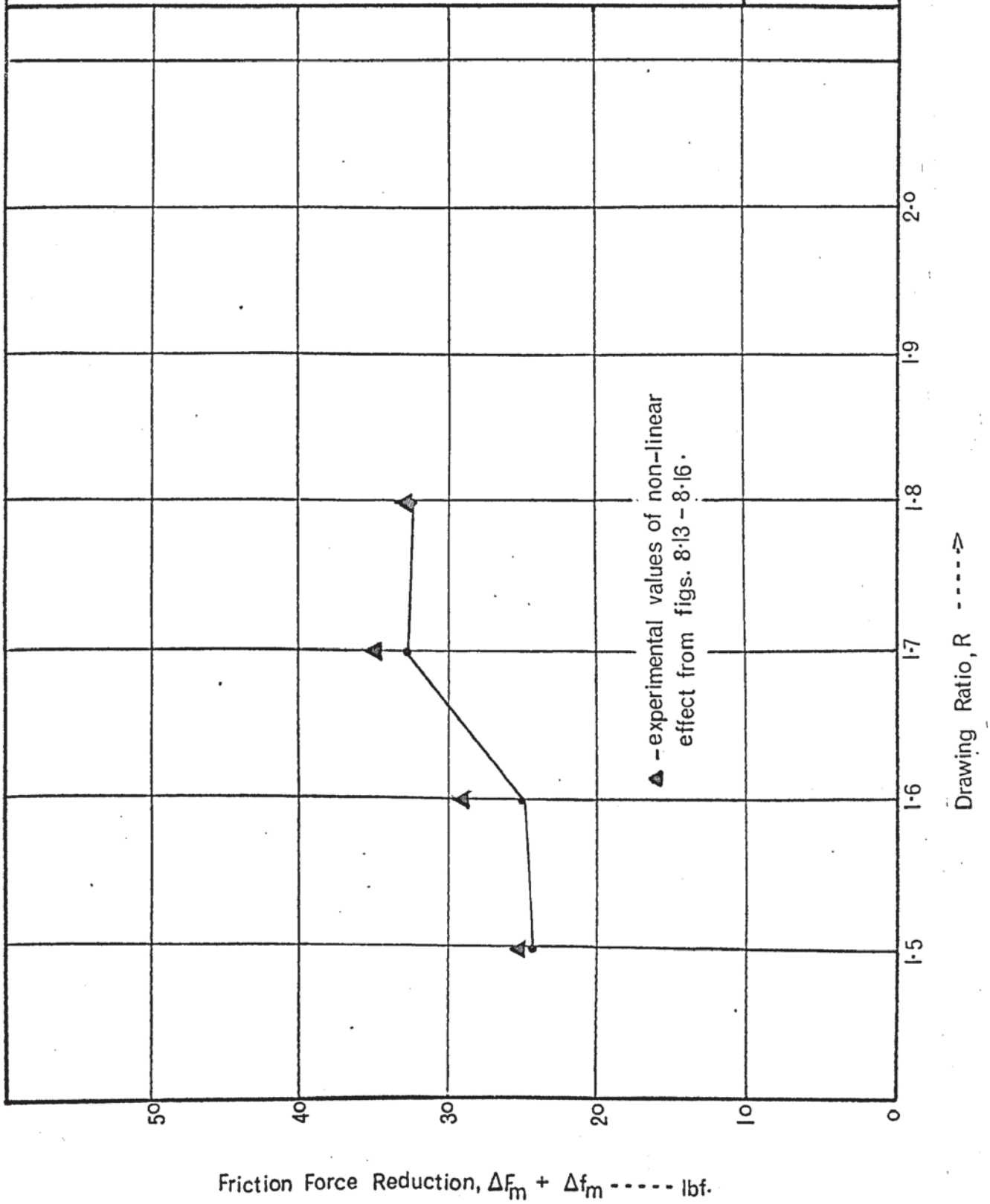

0.4 and 0.8 compared with the theoretical ranges for the drawing ratios considered, of 0.45 - 0.85. A reduction in friction force of 95% was predicted at a velocity ratio of 0.1 which coincided accurately with the experimental results.

A model was proposed for the reduction in die radius friction force under oscillatory conditions, based on rotation of the relative velocity vector. This predicted a 100% reduction in friction force as the velocity ratio approached zero. At a velocity ratio of 0.1 the reduction was 90%, indicating the effectiveness of this mechanism at low die amplitudes.

The non-linear portion of the punch load reduction curves for various drawing ratios, was accounted for by the reduction in die radius and blank holder friction forces, the former being calculated from equation (9.29) using measured values of the non-oscillatory friction force. Examination of various regions of the testpiece surface provided further confirmation of the oscillatory motion of the test piece during drawing. It was concluded therefore that the major friction reduction effects were confined to the upper surface of the testpiece and the die radius region. Furthermore, the effects were found to be similar in the absence of lubricants which indicated that activation and pumping of lubricants could only have been minor effects under the present test conditions.

9.2.4 Force Superposition Effects

In order to explain fully the measured reduction in punch load, it is necessary to account for the linear portion of the graphs in Figs. 8.13 - 8.21. It was proposed in section 9.1 that this effect was due to force superposition which is likely to influence two components of the punch load, viz. the radial drawing stress and the stress increment due to plastic bending and unbending. These will now be considered in the following

sections.

9.2.4.1 The effect of die oscillation on the radial drawing in stress

From earlier discussions[24][27], it is apparent that the presence of oscillatory stresses can influence the level of mean stress at which deformation occurs and in many cases the observed reduction in mean stress under oscillatory conditions agrees closely with the stress amplitude acting in the deformation zone. The circumstances of the present test are considered compatible with this mechanism and the following analysis has been carried out in order to predict the magnitude of the superposition effect during radial drawing-in. The oscillatory stresses acting on any cross section within the deformation zone during radial drawing in, may be determined by considering the motion of an elementary wedge, of width dr experiencing an amplitudinal displacement $\dot{\xi}_m$, see Fig. 9.14. If r is the current radius of the element and dθ the angle subtended at the drawing axis, the radial and circumferential stresses resulting from a radial displacement $\dot{\xi}_m$ are determined as follows:

Since the blank holder force is considered to act only at the periphery and edges of the testpiece the thickness stress may be considered as zero over the remainder of the radial portion and in the case of a thin plate we may consider the stress strain system to be biaxial, i.e. plane stress.

The radial and circumferential strains may be written as[74]:

$$e_1 = \sigma_1/E - \nu\sigma_2/E \quad \text{and} \quad e_2 = \sigma_2/E - \nu\sigma_1/E \text{ ----- (9.30)}$$

Substituting the amplitudinal values of oscillatory stress and strain these may be re-written:

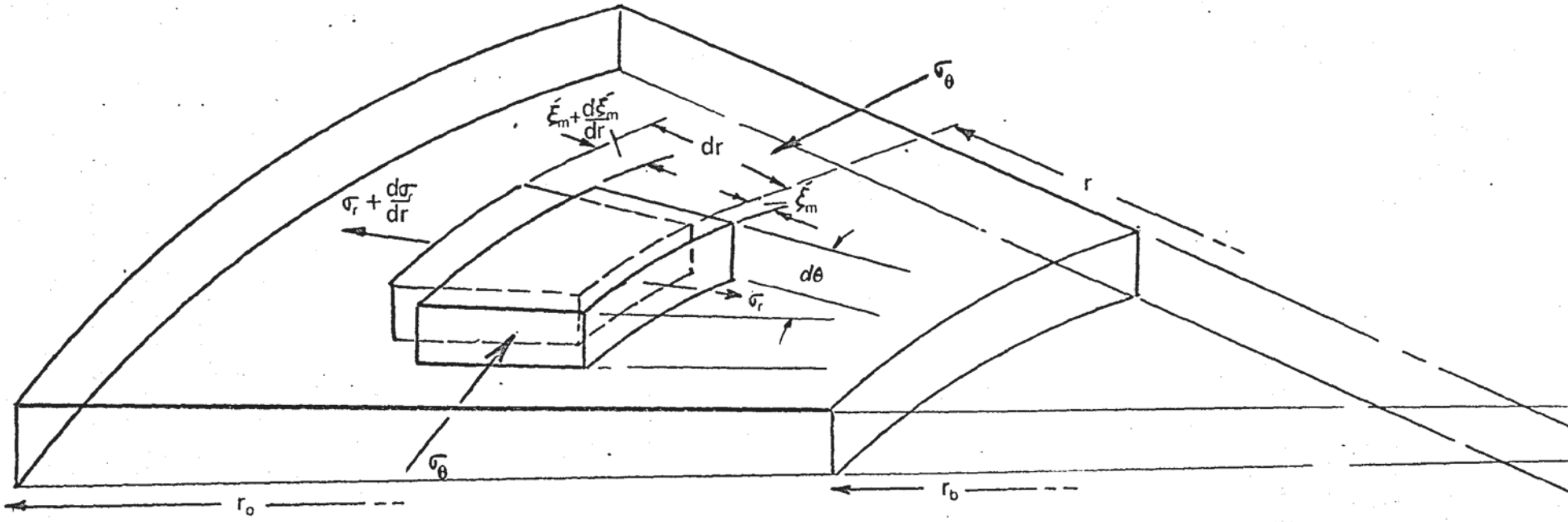

Fig. 9.14 Oscillatory motion of an elementary wedge of width dr, during radial drawing-in.

$$\sigma_{r_m} = \frac{E}{1-\nu^2}(\acute{\xi}_{r_m} + \nu\acute{\xi}_{\theta m}); \quad \sigma\theta_m = \frac{E}{1-\nu^2}(\acute{\xi}_{\theta_m} + \nu\acute{\xi}_{r_m}) \quad \text{-- (9.31)}$$

where $\acute{\xi}_{r_m}$ and $\acute{\xi}_{\theta m}$ are the radial and circumferential strain amplitudes respectively, E is Young's modulus and ν Poisson's ratio. From Fig. 9.14 $\acute{\xi}_{r_m}$ = change in $\delta r/\delta r$, which in the limit = $\frac{d\acute{\xi}_m}{dr}$

and $\acute{\xi}_{\theta_m} = \frac{(r + \acute{\xi}_m)\delta\theta - r\delta\theta}{r\delta\theta} = \frac{\acute{\xi}_m}{r}$

we may therefore re-write equation (9.31)

$$\left.\begin{aligned} \sigma_{r_m} &= \frac{E}{1-\nu^2}\left(\frac{d\acute{\xi}_m}{dr} + \nu.\frac{\acute{\xi}_m}{r}\right) \\ \sigma_{\theta_m} &= \frac{E}{1-\nu^2}\left(\frac{\acute{\xi}_m}{r} + \nu.\frac{d\acute{\xi}_m}{dr}\right) \end{aligned}\right\} \quad \text{---------- (9.32)}$$

It is now required to examine the effect of radial and circumferential elastic stresses on the yield criterion appropriate to this stage of the deformation process. The modified Tresca criterion can be applied with reasonable accuracy as discussed in section 3. This is written:

$$\sigma_1 - \sigma_3 = m\bar{Y} \quad \text{---------- (9.33)}$$

where σ_1 and σ_3 are the maximum and minimum principal stresses, which are replaced by σ_r and σ_θ in order to define the yield condition during radial drawing in.

If it is assumed that yielding occurs at the same value of effective stress under oscillatory conditions and that the oscillatory motion induced in the testpiece at any section results in relaxation of the deformation strains with corresponding reduction in the respective stresses, the yield criterion under oscillatory conditions may be defined as

$$(\sigma_r + \sigma_\theta) = (\bar{\sigma}_r + \sigma_{r_m}) + (\bar{\sigma}_\theta + \sigma_m) = m\bar{Y} \quad \text{------ (9.34)}$$

where $\bar{\sigma}_r$ and $\bar{\sigma}_\theta$ are the mean radial and circumferential stresses

acting on any element under oscillatory conditions. Experimenta evidence indicates that the edge friction conditions are unchanged by the application of vibrations. The reduction in radial drawing stress at the exit plane of the wedge drawing die may therefore be determined by substituting equation (9.34) into the equilibrium equation defining the radial stress distribution across the flange in the axisymmetric process.

In section 3 this was given as:

$$d\sigma_r = -(\sigma_r + \sigma_\theta)\frac{dr}{r}$$

which under oscillatory conditions becomes:

$$d\sigma_r = -(\bar{\sigma}_r + \bar{\sigma}_\theta)\frac{dr}{r} = -m\bar{Y}\frac{dr}{r} + (\sigma_{r_m} + \sigma_{\theta_m})\frac{dr}{r} \quad \text{--------- (9.35)}$$

The stress at the die exit plane (equivalent to the plane of entry to the die radius) using the same nomenclature as in the earlier derivation is readily shown to be:

$$\sigma_{r_b} = m\bar{Y}\,\ell n\frac{r}{r_b} - \int_{r_b}^{r}(\sigma_{\theta m} + \sigma_{r_m})\frac{dr}{r} + \sigma_{r_a} \quad \text{--------- (.36)}$$

where σ_{r_a} represents the blank holder friction force which is assumed to act at the blank periphery.

The second term in this expression represents the reduction in mean drawing stress at any stage of drawing and is numerically equal to the oscillatory stress amplitude at the die exit plane.

If the reduction in mean stress is denoted by $\Delta\sigma_r$ then on substituting for σ_{r_m} and σ_{θ_m} from equation (9.32) in equation (9.36), this may be found from the following expression:

$$\Delta\sigma_r = \frac{E}{(1-\nu^2)}\int_{r_b}^{r}\left\{(1+\nu)\frac{d\xi_m}{dr} + (1+\nu)\frac{\xi_m}{r}\right\}\frac{dr}{r} \quad \text{---- (9.37)}$$

If we consider the oscillatory motion of the testpiece in

contact with the die, as defined by equation (9.9) section 9.2.2, then we may substitute for ξ_m' and $\frac{d\xi_m'}{dr}$ in equation (9.37) above.

The testpiece oscillatory amplitude at any radius r, was shown to be given by:

$$\xi_m' = \xi_m\left[\sqrt{1 - \left(\frac{a}{r}\right)^2} - \frac{a}{r}\left(\pi/2 - \sin^{-1}\frac{a}{r}\right)\right] \quad \text{---------- (9.9)}$$

where a is the velocity ratio, $Vp/\dot{\xi}_m$ and ξ_m the displacement amplitude of the die, assumed to be approximately constant over the upper face of the wedge drawing dies.

From (9.9) the first derivative of displacement amplitude with respect to r, defining the particle displacement at radius r, is:

$$\frac{d\xi_m'}{dr} = \xi_m\left[\frac{a}{r^2}\left(\pi/2 - \sin^{-1}\frac{a}{r}\right)\right] \quad \text{----------(9.38)}$$

Substituting equations (9.9) and (9.38) into equation (9.37) we have:

$$\Delta\sigma_r = \frac{E.\xi_m}{(1-\nu^2)}\int_{r_b}^{r}\left[(1+\nu)\left\{\frac{a}{r^2}\left(\pi/2 - \sin^{-1}\frac{a}{r}\right)\right\} + \frac{(1+\nu)}{r}\cdot\right.$$

$$\left.\left\{\sqrt{1 - \left(\frac{a}{r}\right)^2} - \frac{a}{r}\left(\pi/2 - \sin.\frac{a}{r}\right)\right\}\right]\frac{dr}{r} \quad \text{----------(9.39)}$$

$$= \frac{E\xi_m}{1-\nu}\int_{r_b}^{r}\frac{1}{r^3}(r^2 - a^2)^{\frac{1}{2}}\,dr \quad \text{---------- (9.40)}$$

which on integrating gives:

$$\Delta\sigma_r = \frac{E\xi_m}{1-\nu}\left[-\frac{\sqrt{r^2 - a^2}}{2r^2} + \frac{1}{2a}\cos^{-1}\frac{a}{r}\right]_{r_b}^{r} \quad \text{------- (9.41)}$$

Inserting the end conditions into equation (9.41) and writing $r_b = 1$ as in the present test series, we obtain the expression for the reduction in drawing stress at any stage of the process defined by the current rim radius r_o;

$$\Delta\sigma_r = \frac{1}{2}.\frac{E.\xi_{ml}}{(1-\nu)}\left[\left(\sqrt{1-a^2} - \frac{\sqrt{r_o^2 - a^2}}{r_o^2}\right) + \frac{1}{a}\left(\cos\frac{-1}{r_o}a - \cos^{-1}a\right)\right]$$

-- (9.42)

9.2.4.2 General Comparison with experimental results

The effect of die amplitude on the reduction in radial drawing stress is illustrated graphically in Fig. 9.15. For convenience, the reduction in strip tension due to the change in radial drawing-in stress, ΔT_r is plotted against 1/a, for different values of r_o, the current rim radius. ΔT_r is determined from the equation, $\Delta T_r = 2\Delta\sigma_r.t_m.b$ where t_m is the mean strip thickness (assumed constant at 0.036in.) and b is the width, also constant at 0.5 in. This shows a near linear relationship at all stages of drawing with a slightly enhanced effect upto reciprocal values of 10. Below this value the slope of each curve increases slightly as the reciprocal tends towards a value of 1 at which the drawing stress reduction becomes zero. It will be noted also that the effect of die oscillations on the drawing stress decreases as drawing progresses.

These general characteristics are consistent with the experimental punch load data at low drawing ratios. However at a ratio of 1.8 the linear portion of the punch load reduction curves showed a sudden increase towards the end of drawing which is not predicted by the above model, Fig. 8.21. Figs. 9.2a and 9.2b show the reduction in strip tension with increasing die amplitude at drawing ratios of 1.5 and 1.8

Theoretical Relationship between the Reduction in Strip Tension, Due to change in Radial Drawing-in Stress, Δ_r, and the reciprocal value of the Velocity Ratio, 'a'.

Fig·9·15

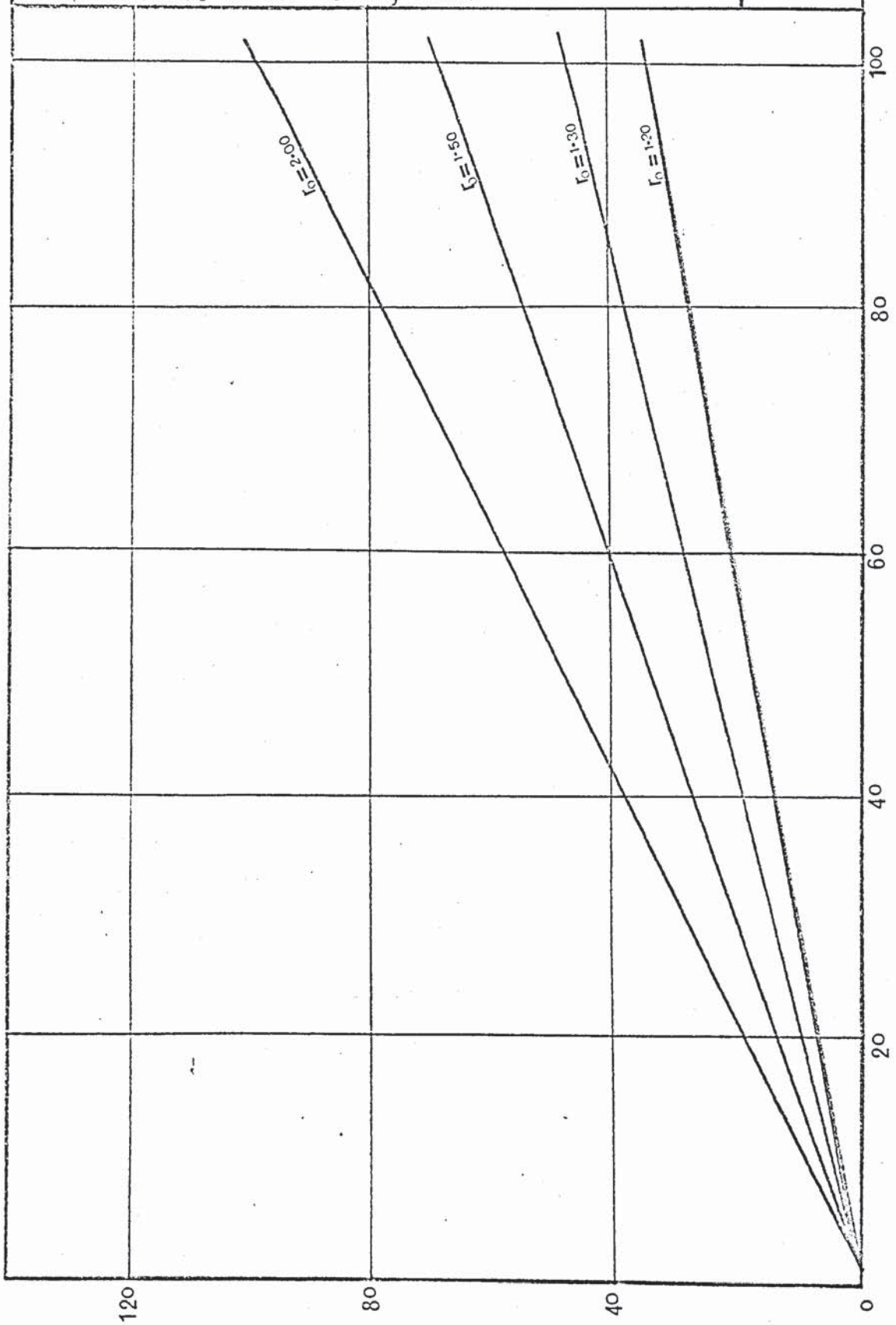

respectively. The enhanced reduction in strip tension towards the end of drawing can be explained, in the case of the lower draw ratio, by an increased friction reduction effect. Both the blank holder and die radius friction forces rise towards the end of the draw and at high vibration amplitudes they are effectively eliminated. This effect does not fully account for the increased tension reduction at the higher draw ratio however. It is suggested that some reinforcement of the wave motion generated in each end of the test piece will occur as the draw length approaches a critical value, viz. $\lambda/4$. This would be expected to lead to an enhanced motional amplitude The subject is discussed in greater depth in section 9.3.2.4.

9.2.5 The effect of flexural vibrations on the plastic bending stress

9.2.5.1 General considerations

The effect of superimposed oscillatory stresses and strains at the planes of plastic bending and unbending are shown qualitatively in Figs. 9.16a and b. If plastic bending is assumed to occur instantaneously at the die exit plane the oscillatory stress acting at this section will be superimposed on the distribution of axial stress and strain due to bending. This is illustrated in Fig. 9.16a for a non-work hardening material subjected to an oscillatory stress amplitude σ_m.

Each element experiences a mean axial stress given by $\sigma_1' = \frac{2}{\sqrt{3}}\bar{\sigma} - \sigma_m$ where $\frac{2}{\sqrt{3}}\bar{\sigma}$ is the effective stress which is assumed to be the same under oscillatory and non-oscillatory conditions. The mean elementary stress under oscillatory conditions is less than the non-oscillatory value by an amount equal to the superimposed stress amplitude since yielding is assumed to occur at the same level of effective stress.

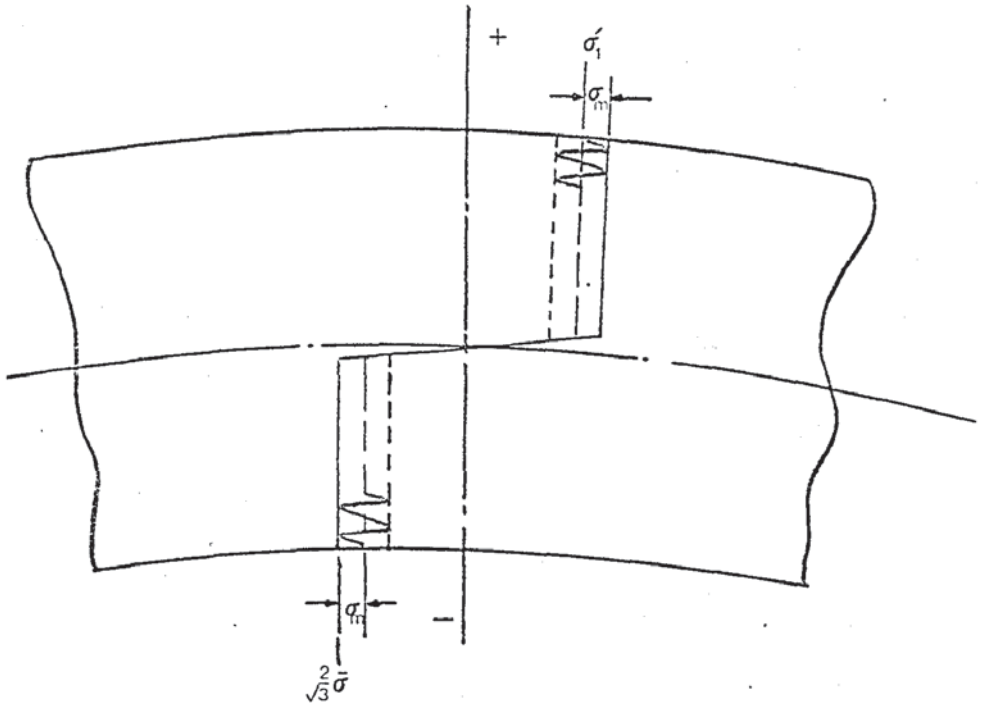

Fig. 9·16 a Plastic bending of non-work hardening material with superposed uniform oscillatory stress of amplitude, σ_m.

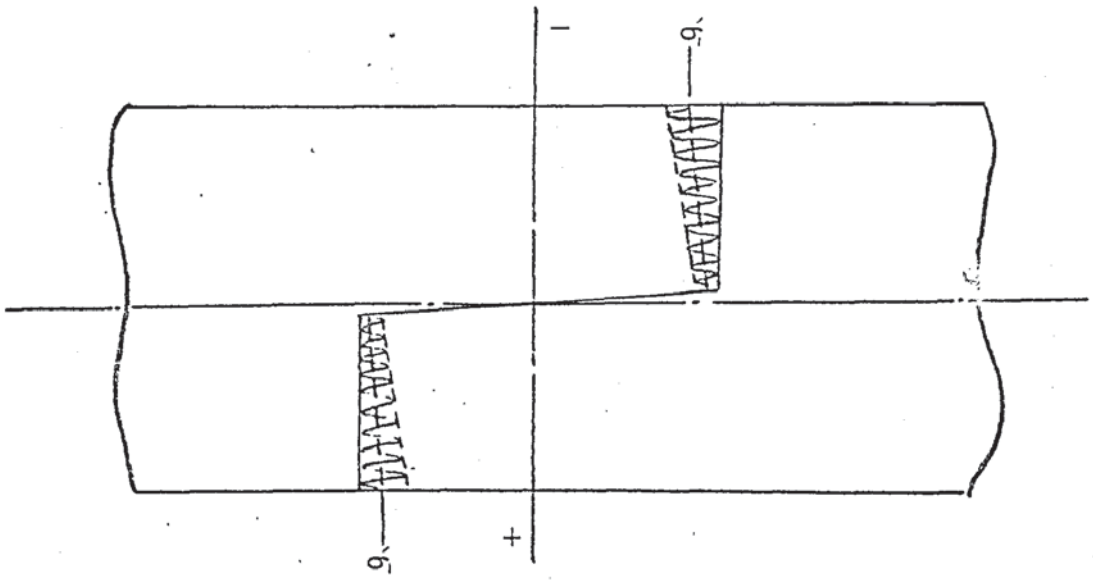

Fig. 9·16 b Plastic unbending of non-work hardening material with superposed oscillatory bending moment

The situation at the plane of plastic unbending is different from the radial section, since in this regime the material is subjected to an oscillatory bending moment and the elastic stress and strain amplitudes vary across the section as they are zero at the neutral axis. The elementary stress and strain distribution is therefore as shown in Fig. 9.16b.

9.2.5.2 Determination of oscillatory bending moments

In order to determine the state of axial stress resulting from cyclic bending at a particular section of the partially drawn specimen, it is necessary to examine the transverse wave motion induced in the specimen by the oscillatory motion of the dies. Particular solutions to the wave equation defining transverse motion then permit the determination of the bending moment and hence the axial stress distribution at any given section.

The wave equation defining the motional state of a vibrating bar of uniform cross section may be simply derived by considering the differential equations of static bending. By equating the downward acting static force producing the deflection with the upward inertial force exerted by the deflected particle under an acceleration the basic equation may be derived as follows:

Taking the familiar equations for a statically loaded beam we have[46], bending moment $M = E.I.\frac{d^2z}{dx^2}$ and q, the mean rate of loading given by:

$$q = \frac{d^2M}{dx^2} = \frac{d^2}{dx^2}\left(E.I.\ \frac{d^2z}{dx^2}\right) = E.I.\ \frac{d^4z}{dx^4} \quad \text{---------- (9.43)}$$

Since E and I (Young's Modulus and the second moment of area respectively) are independent of x.

If we now equate the deflecting load q with the counter-acting inertial force we obtain the familiar equation

$$q = EI \frac{d^4z}{dx^4} = - \rho s \frac{d^2z}{dt^2} \quad \text{---------- (9.44)}$$

where ρ is the density of the beam material and S the cross sectional area. Assuming a simple harmonic motion, equation (9.44) becomes:

$$E.I. \frac{d^4z}{dx^4} = - \rho s \omega^2 z$$

or $$\frac{d^4z}{dx^4} - n^4 z = 0 \quad \text{---------- (9.45)}$$

where $n = \sqrt{\frac{k}{\chi}}$ and χ, the radius of gyration is given by $(\frac{I}{S})^{1/2}$.

The general solution to equation (9.45) is of the form

$$z = A\cosh nx + B \sinh nx + C \cos nx + D \sin nx \quad \text{--- (9.46)}$$

where A, B, C and D are arbitrary constants determined by the boundary conditions at the ends of the vibrating beam.

If the type of end fixing is specified this in turn determines the boundary conditions, viz. for a pinned end the slope and displacement of the beam are zero:- $\frac{dz}{dx} = 0$ and $z = 0$, for a free end the shear stress and bending moment are zero:-

$$\frac{d^3z}{dx^3} = 0 \text{ and } \frac{d^2z}{dx^2} = 0$$

For a simply supported end the deflection and bending moment are zero:

$$\frac{d^2z}{dx^2} = 0 \text{ and } z = 0$$

In the present case it will be assumed that the test piece is fixed at the end in contact with the punch radius and that the conditions at the die exit plane may be represented by the mid-plane conditions of a uniform beam pinned at each end. See Fig. (9.17).

The natural frequencies of the system may be determined by taking the general solution, equation (9.46) and substituting the appropriate end conditions, viz.

$$x = 0,\ z = \dot{z} = o \text{ and } x = 2l,\ z = \dot{z} = o.$$

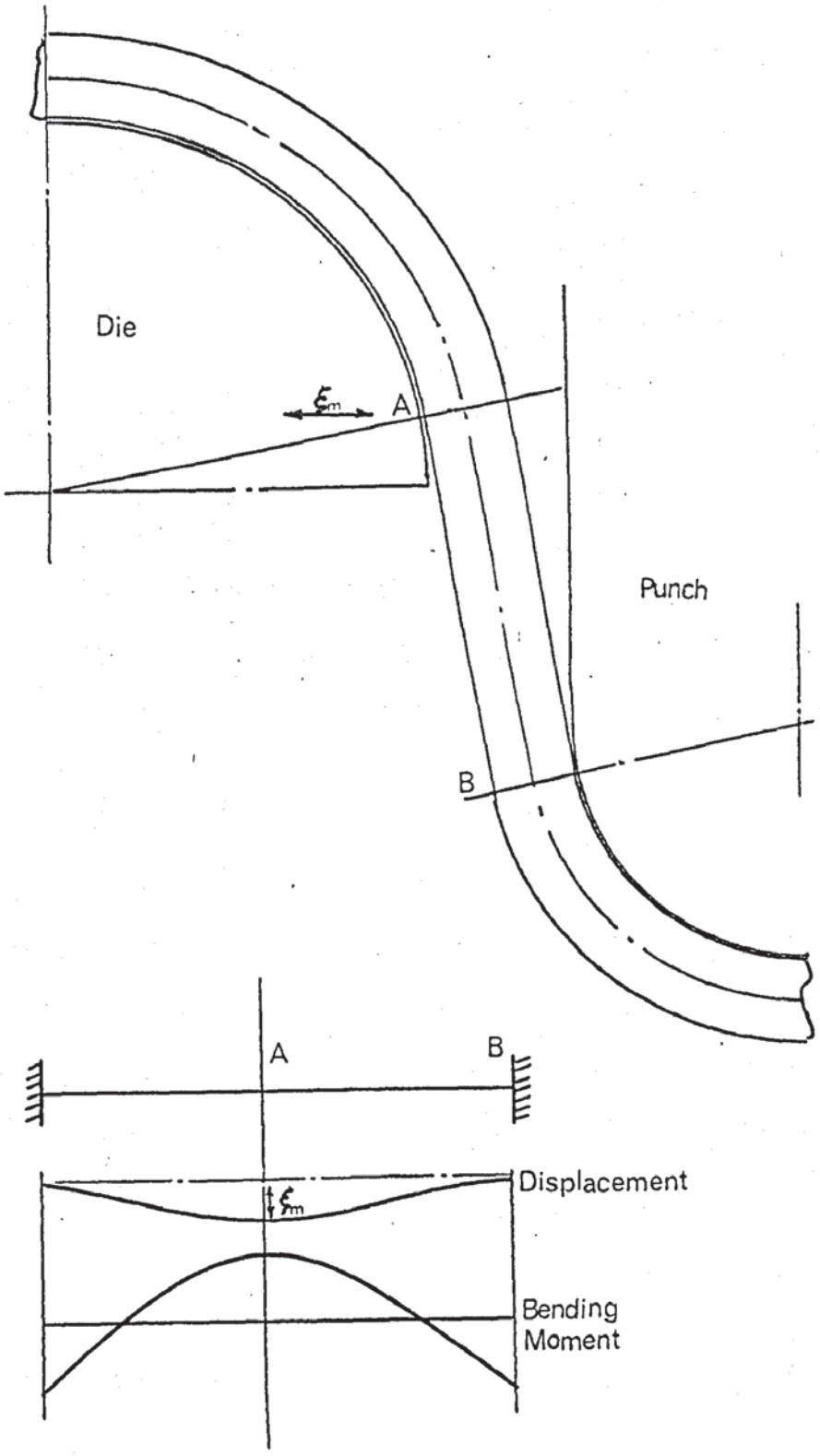

Fig. 9.17 Oscillatory bending of the testpiece between the die and punch radii during wedge drawing.

This gives

$$A + C = 0, \quad B + D = 0$$

and

$$\left.\begin{aligned} &A\cosh 2n\ell + B\sinh 2n\ell + C.\cos.2n\ell + D.\sin.2n\ell = 0 \\ &2n[A.\sinh 2n\ell + B.\cosh 2n\ell - C.\sin 2n\ell + D.\cos 2n\ell] = 0 \end{aligned}\right\} \text{-(9.47)}$$

Eliminating the constants between equations (5) gives;

$$\frac{\cos.2n\ell - \cosh.2n\ell}{\sinh.2n\ell + \sin.2n\ell} = \frac{\sin.2n\ell - \sinh.2n\ell}{\cosh 2n\ell - \cos.2n\ell}$$

which simplifies to yield

$$\cos 2n\ell.\ \cosh 2n\ell = 1 \qquad (9.48)$$

The values of $2n\ell$ which satisfy this expression may be determined graphically thus providing a simple relationship between the beam dimensions and resonant frequencies, viz:

$$(2n\ell)_K = 2\sqrt{\frac{\omega\ell^2}{C.X}}$$

where K refers to the overtone mode.

This analysis enables us to predict at what stage of drawing the conditions satisfying flexural resonance in the unsupported portion of the testpiece, will occur. At these specific intervals it is then possible to predict the distribution of bending moment and axial stress along the test piece.

The bending moment is given by:

$$M = E.I.\frac{d^2z}{dx^2} = n^2|A\cosh nx + B\sinh nx - C.\cos nx - D.\sin nx|E.I. \qquad (9.49)$$

If it is assumed that the distribution of bending moment is of the form shown in Fig. (9.17) then, as in the case of a statically loaded beam the maximum value will coincide with the mid-point and at this section we may therefore write;

$$\frac{d^3z}{dx^3} = n^3[A.\sinh nx + B.\cosh nx + C.\sin nx - D.\cos nx]$$

and $\frac{d^3z}{dx^3} = 0$ when $x = \ell$

Therefore

$$A.\sinh nl + B.\cosh nl + C.\sin nl - D.\cos nl = 0 \text{ ----- } (9.50)$$

From the end conditions described by equation (9.47), we may re-write equation (9.50);

$$A(\sinh nl - \sin nl) + B(\cosh nl + \cos nl) = 0 \text{ ------- } (9.51)$$

also at the mid-section, if the oscillatory displacement amplitude is ξ_{m_1} we have;

$$\xi_{m_1} = A(\cosh nl - \cos nl) + B(\sinh nl - \sin nl) \text{ --------- } (9.52)$$

Eliminating the constants between equation (9.47), (9.50), (9.51) and (9.52) we obtain an expression for the bending moment at the mid-section of the beam. (This, in the present case, coincides with the plane of exit from the die radius).

The maximum bending moment is given by

$$M = E.I.\ n^2 \xi_{m_1} \left[\frac{(\cosh nl + \ln nl)^2 - \sinh^2 nl + \sin^2 nl}{(\cosh^2 nl - \cos^2 nl) - (\sin nl - \sinh nl)^2} \right] (9.53)$$

which on expanding simplifies to give

$$M = E.I.n^2.\xi_{m_1} \left[\frac{1 + \cosh nl . \cos nl}{\sin nl \ . \ \sinh nl} \right] \text{ ---------- } (9.54)$$

The stress in any element of the section, at a distance y from the neutral axis is given by:

$$\sigma_m = \frac{M}{I} . \ y \text{ ---------- } (9.55)$$

The presence of an oscillatory axial stress component at the plane of plastic unbending results in a superposition effect which reduces this component of the drawing stress. The magnitude of this effect may be determined in the following way by considering the basic expression for the work done in plastic bending defined in section 3.

It will be recalled that the work done per unit width in

bending an element dy at distance y from the neutral axis is given by:

$$dw = \sigma_1 . d\varepsilon \ (Q_c + y)\ dy . d\theta \quad \text{---------- (9.56)}$$

where as before σ_1 is the axial stress in the element and $d\varepsilon$ the strain increment.

If an elastic oscillatory stress of amplitude σ_m is superimposed at this section, the elementary stress under oscillatory conditions is determined from

$$\sigma'_1 = \frac{2}{\sqrt{3}} \bar{\sigma} - \sigma_m \quad \text{---------- (9.56(A)}$$

where $\bar{\sigma}$ is the effective stress, which may be replaced by the mean yield stress $\bar{\sigma}_o$ and σ'_1 represents the mean axial stress in the element. The stress increment due to unbending, is found by considering the drawing stress required to provide the bending strain work per unit width, viz.

$$W = \sigma_U . t . Q_c . d\theta \quad \text{---------- (9.57)}$$

where $Q_c . d\theta$ represents the mean element length in the plane of bending.

If σ'_U represents the axial stress producing unbending under oscillatory conditions then substituting for σ_1 in equation (9.56) we may write:

$$\frac{w}{d\theta} = \int_o^{t/2} (Q_c + y) \int_o^{\ln(\frac{1+y}{Q_c})} (\frac{2}{\sqrt{3}} \bar{\sigma}_o - \sigma_m)\, d\varepsilon . dy + \int_o^{t/2} (Q_c - y) \int_o^{\ln(\frac{1+y}{Q_c})} (\frac{2}{\sqrt{3}} \bar{\sigma}_o - \sigma_m)\, d\varepsilon . dy$$

and from equation (9.57) above we find:

$$\sigma'_U = \frac{1}{tQ_c} \left\{ \int_o^{t/2} (Q_c + y) \int_o^{\ln\frac{(1+y)}{Q_c}} (\frac{2}{\sqrt{3}} \bar{\sigma}_o - \sigma_m)\, d\varepsilon . dy + \int_o^{t/2} (Q_c - y) \int_o^{\ln\frac{(1+y)}{Q_c}} (\frac{2}{\sqrt{3}} \bar{\sigma}_o - \sigma_m)\, d\varepsilon . dy \right\} \quad \text{------- (9.58)}$$

writing for $\ln\frac{(1+y)}{Q_c}$ the approximation $\bar{\varepsilon} \simeq \frac{2}{\sqrt{3}} . \frac{y}{Q_c}$ and replacing σ_m by $\frac{M}{I} . y$ from (9.55), equation (9.58) may be evaluated to give:

$$\sigma_U' = \frac{t}{9Q_c} \left| 3\bar{\sigma}_o - \frac{\sqrt{3}}{2} \cdot \frac{M.t}{I} \right| \quad \text{---------- (9.59)}$$

Substituting for M, given by equation (9.54) in equation (9.59), the reduction in unbending stress, represented by the second term, becomes;

$$\Delta\sigma_U = \frac{E.n^2t^2}{6\sqrt{3}.Q_c} \cdot \xi m_1 \left[\frac{1+\cosh.nl.\cos^{nl}}{\sin^{nl}.\sinh^{nl}} \right] \quad \text{---------- (9.60)}$$

where ξ_{m_1} is the component of the testpiece displacement normal to the die radius at the plane of plastic unbending.

Equation (9.60) may be used to determine the reduction in unbending stress at the die exit plane, at specific stages of drawing satisfying the conditions for flexural resonance. These are defined by equation (9.48) from which the value of nl at fundamental resonance was determined graphically as 4.730. Calculating n from the expression $n = (\frac{\sqrt{12}.k}{t})^{1/2}$, the half wavelength for flexural resonance at 13 kHz was determined as 0.378 in. At drawn lengths not satisfying flexural resonance the bending moment may be determined with reasonable accuracy using the equation for a statically deflected beam clamped at its ends[32]. This is readily found to be;

$$M = \frac{6.E.I.z}{l^2}. \quad \text{---------- (9.61)}$$

where z is the deflection given in this case by ξ_{m_1} and it is defined as above. Substituting in the second term of equation (9.59) the reduction in unbending stress, for non-resonant conditions is determined from:

$$\Delta\sigma_u = \frac{1}{\sqrt{3}} \cdot \frac{t^2.E}{Q_c.l^2} \cdot \xi_m \sin\phi \quad \text{---------- (9.62)}$$

Under resonant conditions the bending moment predicted by equation (9.61) is approximately 26% greater than the dynamic

value. This is illustrated in the graph of Fig. 9.18, showing the bending moment distribution at fundamental resonance using both dynamic and static models.

At values of 1 not satisfying the conditions for flexural resonance, the error in calculating M from the 'static' model will be less. It is proposed therefore, that the superposition effect produced at the die exit plane may be determined at any stage of drawing using the appropriate equation.

The reduction in strip tension due to the effect of an oscillatory bending moment on the unbending stress has been calculated using equation (9.62) and plotted as a function of punch displacement, h, in Fig. 9.19. The relationship between h and 1, the length of unsupported testpiece, was calculated using the expression derived in Appendix (9). Equation (9.62) is applicable at punch displacement of between 0.2 and 0.85 in. which avoid the resonant conditions predicted to occur at h = 0.185 and 0.885 in. Fig. 9.19 shows the reduction in strip tension ΔT_u, considering both sides of the testpiece, for die amplitudes of 10, 20 and 30 x 10^{-5} in. It will be noted that a maximum value occurs at punch displacement between 0.5 and 0.6 in.

The effect of die oscillations on the stress producing plastic bending at the die entry plane was shown qualitatively in Fig. 9.16a. If the oscillatory stress acting in this plane σ_m, is given by the reduction in radial drawing stress $\Delta\sigma_r$, the bending stress is found by replacing the elementary bending stress σ_1, in equation (9.56a) by the expression:

$$\sigma_1' = \frac{2}{\sqrt{3}} \bar{\sigma} - \Delta\sigma_r$$

where σ_1', $\bar{\sigma}$ and $\Delta\sigma_r$ are as defined earlier.

The bending stress under oscillatory conditions is then

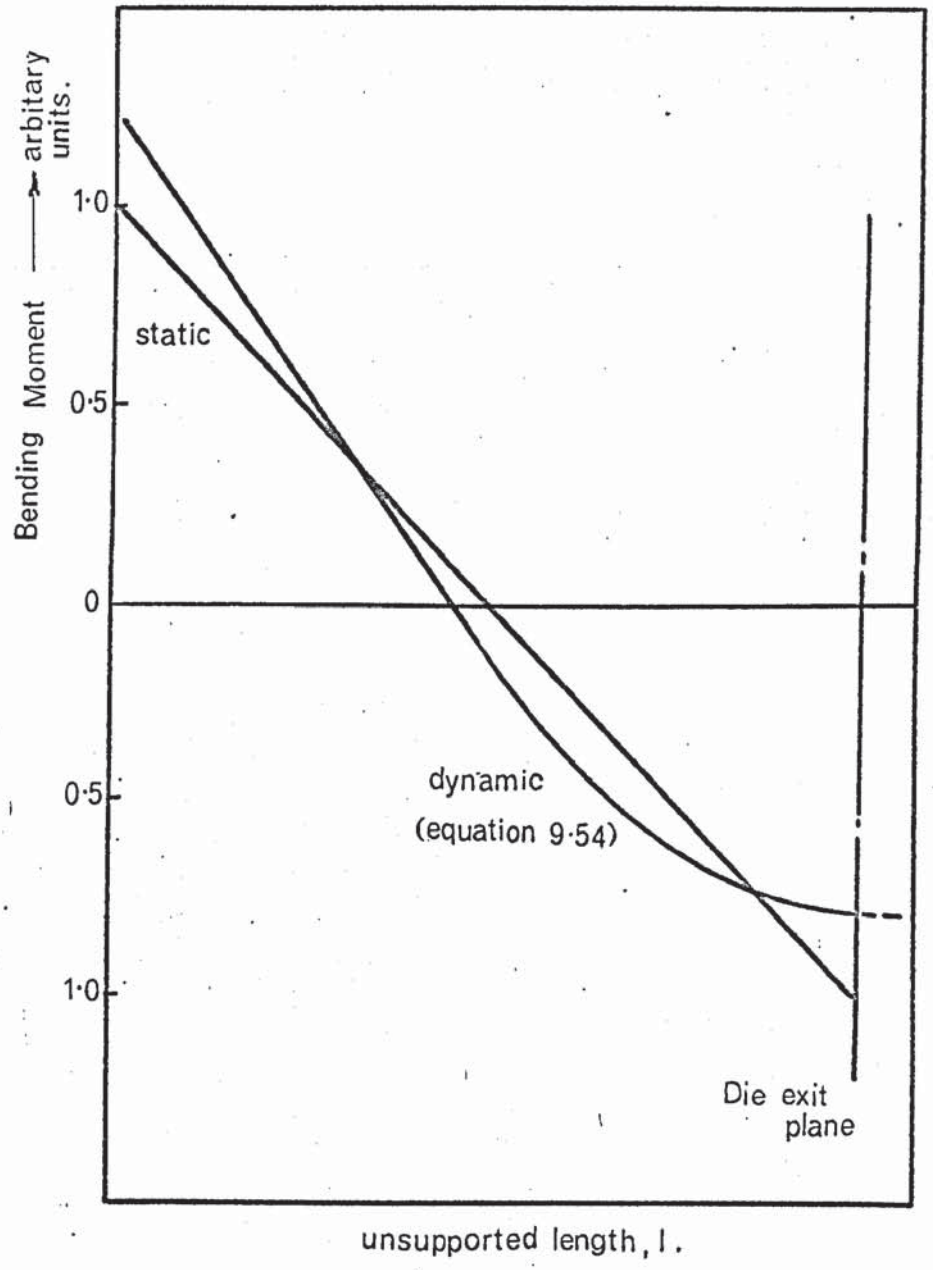

Fig. 9.18 Comparison of bending moment distribution predicted by static and dynamic theories.

Theoretical Relationship between the Reduction in Strip Tension, due to change in unbending stress, $\Delta\sigma_u$, and the Punch displacement, for different values of Die Amplitude 'a'.

Fig. 9·19

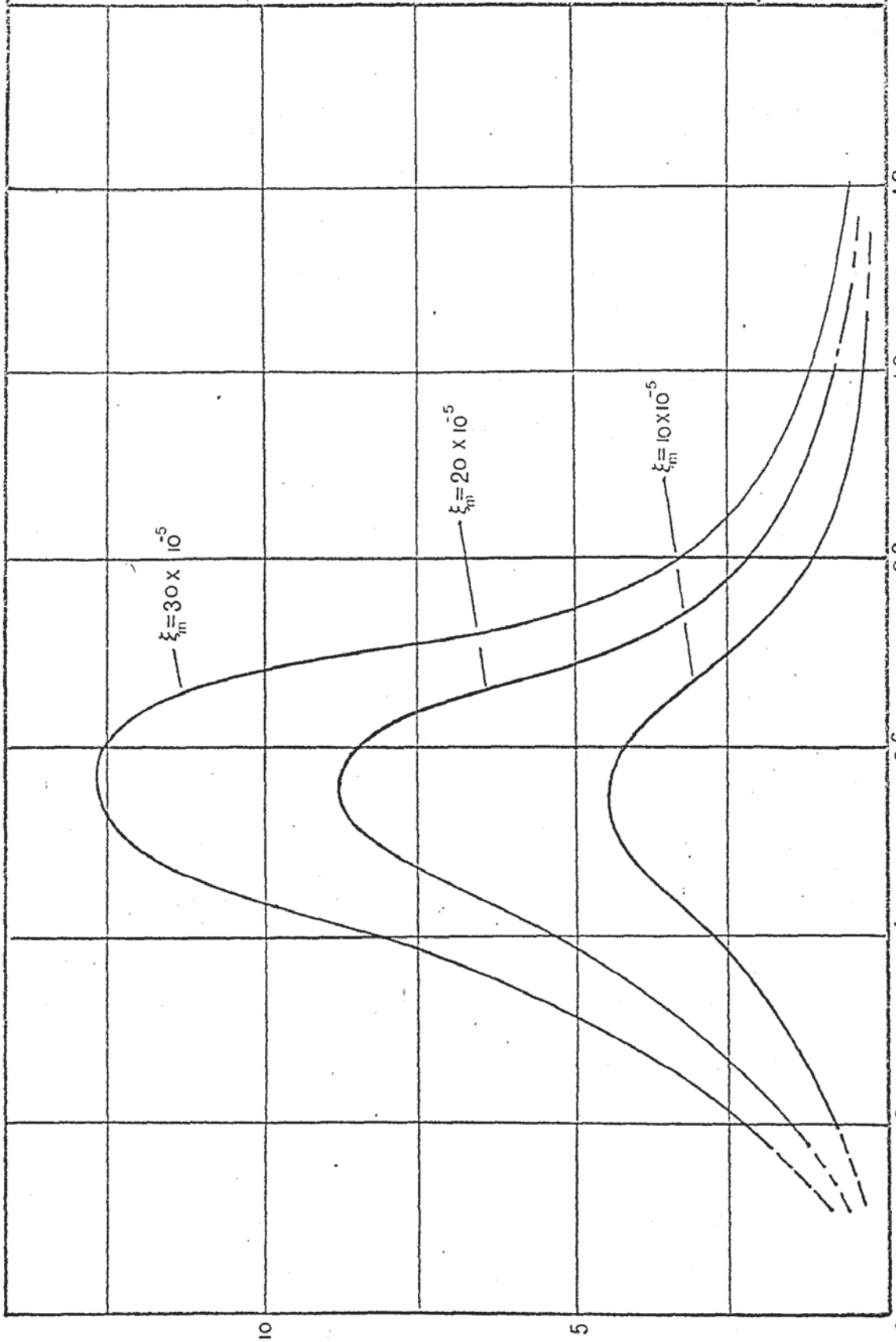

Punch Displacement, h, ------ in.

Reduction in Strip Tension, ΔT_u ····· lbf.

found from equation (9.58) in which σ_m is replaced by $\Delta\sigma_r$. In this instance the oscillatory stress is constant over the section and the equation is readily evaluated to give:

$$\Delta\sigma_b = \frac{1}{2\sqrt{3}} \Delta\sigma_r . \frac{t}{Q_c} \quad \text{---------- (9.64)}$$

9.3 Comparison of Theoretical and Measured Punch Load Reductions

9.3.1 Summary of Friction and Superposition Effects

The general form of the punch load reduction curves shown in Figs. 8.13 - 8.21 indicated two distinct regions. A rapid increase in punch load reduction was observed with increasing die amplitude upto a value of approximately 5×10^{-5} in. Beyond this value, which remained constant for all reductions examined and at each stage of drawing, the effect was linear. However, the magnitude of the linear effect, indicated by the slope of the line, was found to vary throughout the drawing cycle being at a maximum for punch displacements between 0.5 and 0.6 in. This characteristic was common to each drawing ratio.

The analysis undertaken in sections 9.2.3 - 9.2.5 considered the effect of die oscillations on each component of the punch load. It was demonstrated that the non-linear portion of the punch load reduction curve could be accurately accounted for by the sum of the reduction in friction force at the testpiece/blank holder interface and between the testpiece and die radius.

Examination of the effects of die oscillations on the radial drawing-in stress and on the components of force related to plastic bending and unbending around the die radius indicated, in each case, a linear dependance on die amplitude. The reduction in radial drawing in stress, $\Delta\sigma_r$, was predicted

by equation (9.42) to vary with punch displacement, the effect being greatest at the start of drawing. However, it did not predict a maximum value with increasing punch displacement. In order to calculate the total linear effect, attributable to stress superposition, it is necessary to consider also the reduction in bending and unbending stresses. It will be seen from equation (9.59) that the reduction in unbending stress is linearly dependent on M, the oscillatory bending moment and that this in turn is a function of the die amplitude and unsupported length of the test piece, l.

The reduction in unbending stress, determined from equation (9.62) reaches a sharply defined maximum at punch displacements between 0.5 and 0.6 in, Fig. (9.19). This value agrees closely with the observed punch displacement at which the slope of the linear portion of the punch load reduction curves shows a sudden increase. The effect is illustrated in Fig. 8.18 - 8.21, showing punch load reduction with increasing die amplitude at different stages of drawing. At punch displacements beyond 0.5 in, the strip tension is only slightly different from the punch load and by considering the sum of the bending and unbending stress reductions and the radial stress superposition effect it is possible to account for the linear portion of the punch load reduction curves from equations (9.42), (9.62) and (9.63).

The validity of the analysis developed in section 9.2 was examined by calculating the reduction in maximum punch load over a range of die amplitudes at drawing ratios of 1.5 and 1.8.

Each component of the punch load was considered at the stage of drawing coincident with the maximum value and the effect of increasing die amplitude calculated from the

appropriate expression, viz. equations (9.11),(9.29), (9.42), (9.62) and (9.64). The results of the calculations are given in tables 9.2 and 9.3 where the reduction in strip tension associated with each component of the punch load has been calculated at different values of the reciprocal velocity ratio, $1/a = \dot{\xi}m/V$. The total theoretical punch load reduction, found from the sum of the components, is compared with the punch load reduction determined from experimental data at the same drawing ratios. Figs. 9.20 and 9.21 show the theoretical relationship at ratios of 1.5 and 1.8 respectively with superimposed experimental points, determined from individual tests. The dashed line in each case represents the mean experimental curve. At both drawing ratios the theoretical reduction in punch load showed good agreement with the experimental data for low values of the function 1/a. At increasing values, representing higher die amplitudes the theory predicted significantly smaller reductions in punch load. This divergence can be explained in part, by reference to the experimental phenomenon described in section 9.1.2.2. It was observed during intermittent oscillatory tests carried out at high vibrational amplitudes, that both the punch load and blank holder friction force during the non-oscillatory interval were significantly higher than in corresponding continuous non-oscillatory tests at the same drawing ratio. A qualitative explanation was proposed in section 9.2.3.6 which attributed the effect to the local heating of surface asperities resulting from increased relative motion at the friction interface during the oscillatory interval. No allowance was made for this effect in the analysis of the friction reduction mechanism. It will be seen in Figs. 8.22 - 8.25 that the blank holder friction force was increased by upto

Comparison of theoretical and measured values of the reduction in maximum punch load with increasing die amplitude, expressed as the reciprocal velocity ratio .

Fig. 9·20

D.R. = 1·50

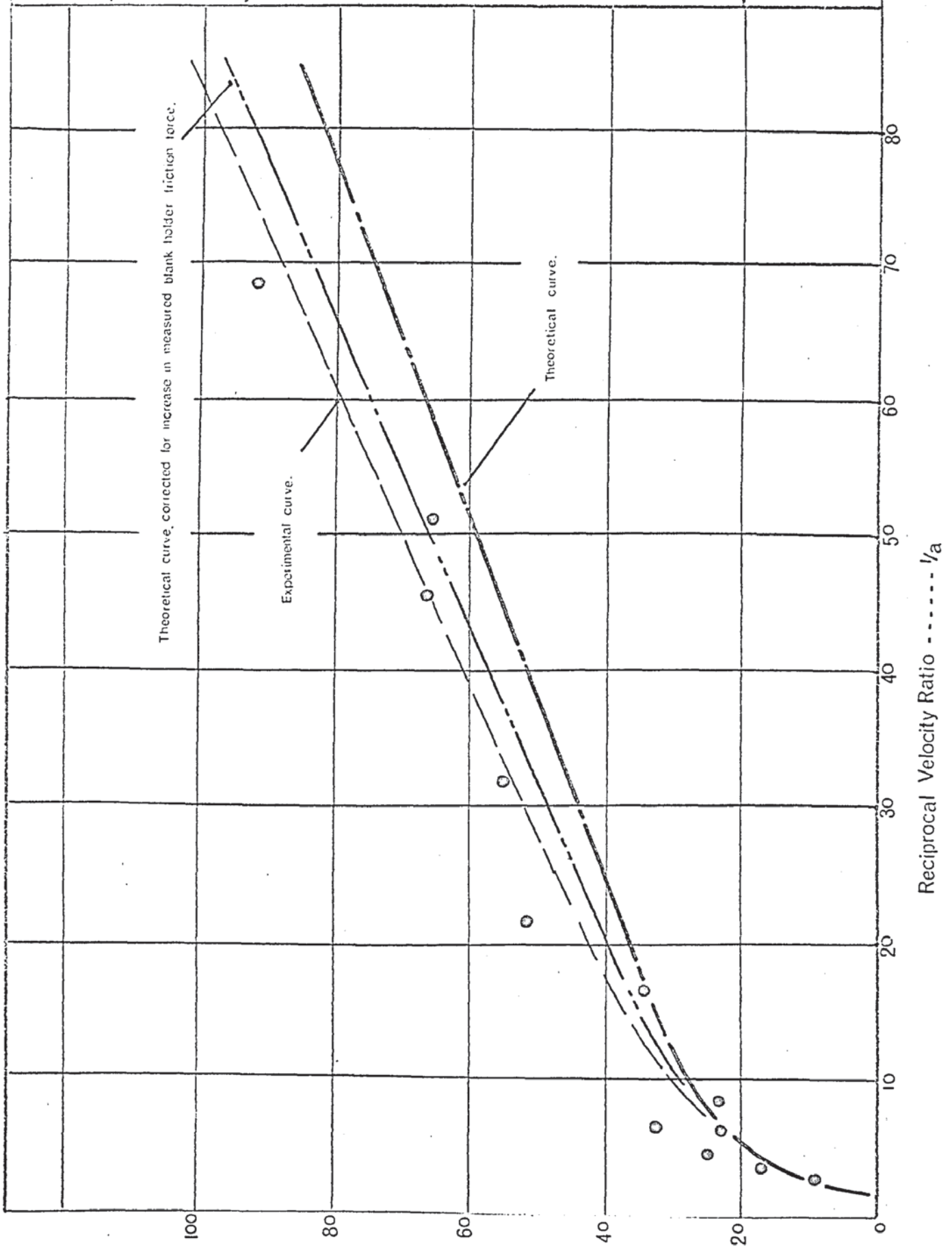

Comparison of theoretical and measured values of the reduction in maximum punch load with increasing die amplitude, expressed as the reciprocal velocity ratio.

Fig. 9·21

D.R. = 1·80

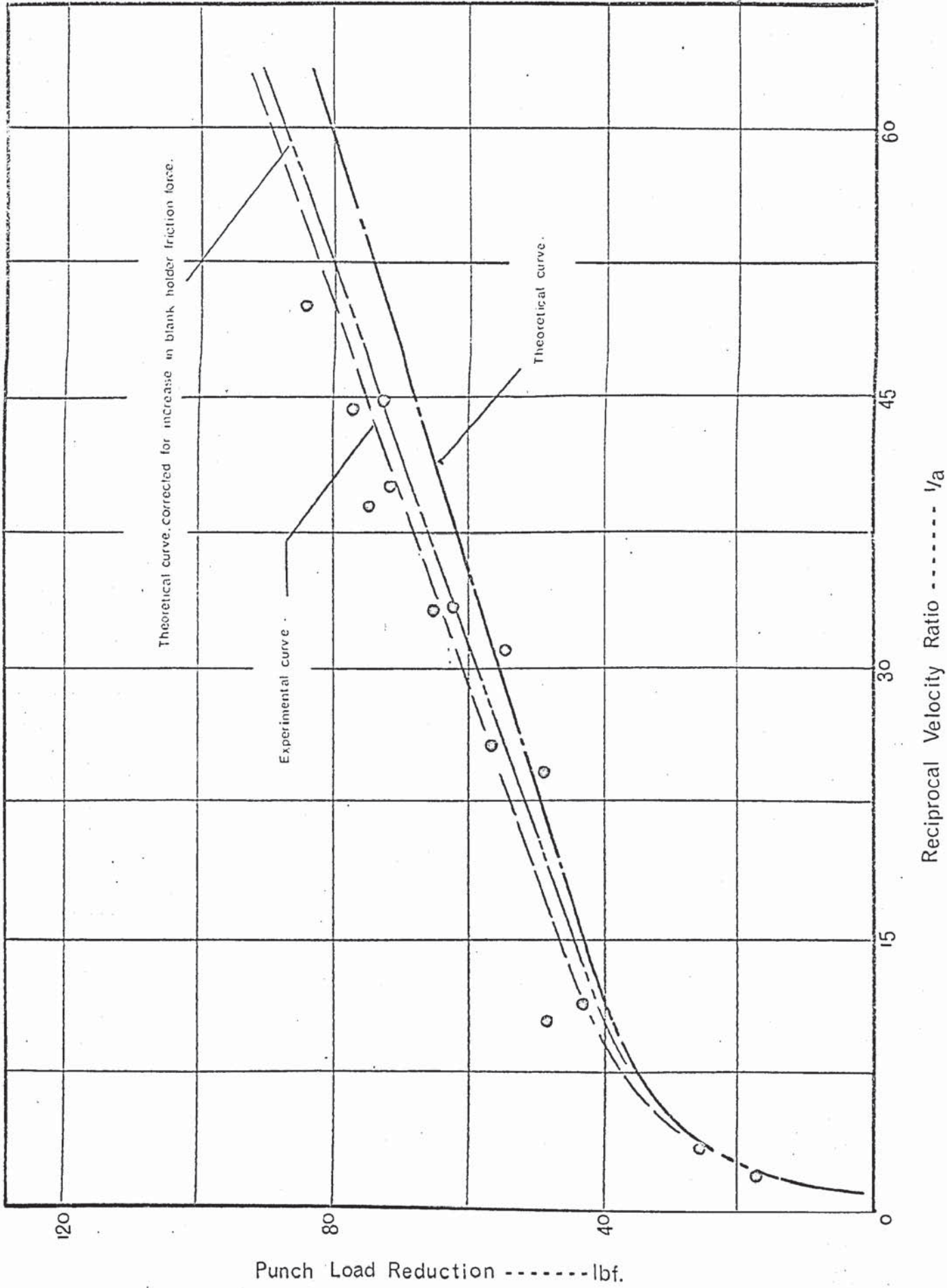

able 9.2 Calculated values of components of the maximum punch load, for a drawing ratio of 1.50:1

Punch load Compo - nent	l/a								D.R. = 1·50	
	1	2	5	10	20	30	40	50	60	70
ΔT_r	0	0.50	2.00	5.00	9.80	14.60	19.50	24.50	29.30	34.50
ΔT_b	0	0	0.09	0.29	0.44	0.61	0.86	1.10	1.31	1.55
ΔT_u	0.19	0.38	0.94	1.89	3.77	5.38	7.55	9.40	10.80	13.20
Δf	0	3.00	9.00	10.90	12.60	13.20	13.70	14.00	14.10	14.20
ΔF	0	5.40	8.80	9.40	9.70	9.80	9.90	9.90	9.90	9.90
ΔP	0.19	9.28	20.73	27.42	36.31	43.59	51.51	58.90	65.41	73.35

Table 9.3 Calculated values of components of the maximum punch load, for a drawing ratio of 1.80:1

Punch load Compo - nent	l/a								D.R. = 1·80	
	1	2	5	10	20	30	40	50	60	70
ΔT_r	0	1.0	2.50	6.50	13.10	19.60	26.00	32.80	39.30	46.00
ΔT_b	0	0.05	0.11	0.28	0.62	0.88	1.17	1.47	1.76	2.06
ΔT_u	0.05	0.08	0.22	0.45	0.88	1.32	1.76	2.20	2.52	3.08
Δf	0	4.50	13.20	16.10	18.50	19.40	20.00	20.50	20.70	20.80
ΔF	0	7.85	12.75	13.60	14.10	14.20	14.35	14.35	14.35	14.38
ΔP	0.05	13.49	28.78	36.93	47.20	55.40	63.28	71.32	78.63	86.32

ΔT_r - strip tension due to radial drawing in stress

ΔT_b - component of strip tension due to bending at entry to the die radius.

ΔT_u - strip tension due to unbending at exit to die radius.

Δf - reduction in die radius friction force

ΔF - reduction in blank holder friction force

ΔP - reduction in maximum punch load.

100 per cent at die amplitudes of 25 x 10^{-5} in. If the theoretical curves in Figs. 9.20 and 9.21 are corrected for this effect, using the experimental data referred to above, quite close agreement is obtained at both drawing ratios for die amplitudes upto 30 x 10^{-5} in, the limit examined in this series. The error is greatest however at the lower drawing ratio which may be explained by the inaccuracy in the assumptions made in predicting the test piece motion during radial drawing. In particular it was assumed in fixed radius drawing that no interaction occurred between the wave forms generated by each vibrator. This is only the case when complete mode conversion occurs around the die radius, causing damping of the longitudinal compression waves.

9.3.2 Effect of vibrations on the limiting drawing ratio

The reduction in punch load achieved under oscillatory conditions would be expected to result in an increased limiting drawing ratio provided that the peak stress at the point of fracture was lower under oscillatory conditions than in the equivalent non-oscillatory test. Failure of the present wedge test pieces was observed to occur always at the necked section close to the plane of initial contact with the punch radius. It is therefore necessary to consider the effect of the various oscillatory mechanisms, on the direct and oscillatory stresses acting in this region, in order to determine their influence on the limiting drawing ratio.

9.3.2.1 Effect of friction force reduction

The reduction in friction force at the blank holder test piece interface during oscillatory drawing resulted in an equal reduction in strip tension, experienced throughout the length of the drawn test piece. This force was not periodic and therefore the resulting punch load reduction

would be expected to contribute to an increased limiting reduction. The effect of die oscillation on the friction force would also be expected to produce a 'true' reduction in punch load.

9.3.2.2 Effects of stress superposition on the limiting draw ratio

The longitudinal wave motion induced in the testpiece during radial drawing-in was considered to be effectively damped as the drawn material passed over the die radius. Under these circumstances, the superposition effect at the plane of tensile failure would be small. However, the situation was complicated by the mode conversion occurring at the exit plane to the die radius, which resulted in a flexural wave form in the unsupported length of the drawn testpiece. The distribution of oscillatory bending moment associated with the flexural motion was determined for the special case when 1 was equal to the half wavelength at flexural resonance. An approximate solution was also given for the general case $1 \neq \lambda b/2$, using static bending theory. Equation (9.62) may be used to determine the mean longitudinal oscillatory stress amplitude at the plane of contact with the punch radius since for the end conditions assumed, the bending moment is the same at both ends of the unsupported length. The longitudinal stress amplitude thus varies between zero at the neutral axis to a maximum value, σ_m, at the surface. If the neutral axis is assumed to coincide with the central plane of the testpiece, the mean oscillatory stress is found by considering one half of the section, viz:

$$\bar{\sigma}_m = \frac{\sigma_{m_1}}{2} = \frac{6E}{1^2}\frac{t}{4}\xi_{m_1} \qquad \text{(9.65)}$$

The mean oscillatory stress amplitude predicted by this equation at a die amplitude of 20×10^{-5} in. varies between

355 lbf/in.^{2} for a punch displacement, h = 0.9 in. and 4000 lbf/in.^{2} for h = 0.55 in. It would be expected therefore that failure of the testpiece would occur at a lower indicated punch load under oscillatory conditions than during the equivalent non-oscillatory reduction, the magnitude of the discrepancy being dependent upon the punch displacement at which failure occurred.

9.3.2.3. Experimentally determined limiting draw ratio

Intermittent oscillatory tests were carried out at draw ratios upto 2.00, a range of die amplitudes being examined in each case. Continuous oscillatory and non-oscillatory tests were also undertaken. At a drawing ratio of 1.90 failure occurred consistently under non-oscillatory conditions, and also at low die amplitudes. However, at values of ξ_m greater than 7×10^{-5} in, the draw was completed. Since the testpiece failed under non-oscillatory conditions it was not possible to obtain an accurate measure of punch load reduction from intermittent tests over the complete drawing cycle. The experimental plot of $\Delta\rho$ vs ξ_m in Fig. 8.17 is therefore based on extrapolated non-oscillatory punch load/displacement data.

At a drawing ratio of 1.95 failure occurred at low die amplitudes even though the measured blank holder friction force was reduced to zero. At amplitudes greater than about 6.4×10^{-5} in. the draw was completed. Further reductions in punch load were achieved by increasing the amplitude upto the maximum attainable value of 18.9×10^{-5} in. Failure occurred consistently at a drawing ratio of 2.00, the maximum attainable die amplitude at this ratio being 14.8×10^{-5} in.

The results of these tests are summarised in Fig. 9.22

Relationship between the maximum oscillatory and non-oscillatory punch loads and the drawing ratio for fixed radius tests.

Fig. 9·22

which shows the variation in maximum punch load with drawing ratio under oscillatory and non-oscillatory conditions, upto the breaking load. It was observed that the breaking load under oscillatory conditions was consistently higher than the non-oscillatory breaking load, which agreed quite closely with the values predicted from the measured ultimate tensile strength of the test material, see appendix X. Furthermore, at a ratio of 2.00 the oscillatory breaking load decreased with increasing die amplitude.

This latter phenomenon can be explained by the superposition effect related to the oscillatory bending moment at the plane of tensile failure. The lowest breaking load occurred at a punch displacement of 0.63 in. and at a die amplitude of 14.8×10^{-5} in. From equation (9.65) the oscillatory force amplitude considering both sides of the testpiece, is found to be 55 lbf which compares quite closely with the observed reduction in breaking load of 65 lbf from Fig. 9.22. Failure occurred in another test at a punch load of 44 lbf. which was approximately 8 lbf. below the oscillatory breaking load established at lower ratios. In this case the punch displacement was 0.87 in. and the die amplitude 9.8×10^{-5} in. The calculated oscillatory force amplitude was found from equation (9.65) to be 7.4 lbf. again showing good agreement with the experimental results.

The observed increase in breaking load, under intermittent oscillatory conditions, could only be caused by either a change in the physical properties of the testpiece, or by a change in the state of stress in the region of failure. It is considered that the application of vibrations would not affect the stress system in the present test and that failure would still occur under uniaxial tension. A more likely

effect may be anticipated from local work hardening under the influence of cyclic oscillatory stresses which approach the yield strength of the material, at some atage in the drawing cycle. The phenomenon of hardening at high ultrasonic intensities was reviewed in section 2.2.3. Fatigue hardening has been observed to occur in the initial stages of the cyclic process and to be virtually complete within 5 per cent of the fatigue life[21]. Significant hardening effects may therefore be produced within 10^4 stress cycles, provided that the stress amplitude is sufficiently high.

In the present test the maximum oscillatory stress amplitude in the failure plane was calculated from equation (9.65) to be about 4000 lbf/in^2. The punch speed and ultrasonic frequency were such as to expose the test piece to something in excess 4×10^4 stress cycles. It is therefore considered probable that some degree of fatigue hardening would occur.

9.3.2.4 Discussion of 'Roller' radius test results

The results of tests incorporating the 'roller' assembly are summarised in the graphs shown in Figs 8.26 - 8.40. Three relationships were plotted to illustrate the main characteristics, viz:

(i) the variation in maximum oscillatory and non-oscillatory punch load with increasing die amplitude, during interrupted tests, Figs. 8.36 - 8.40.

(ii) the reduction in maximum punch load with increasing die amplitude, Figs. 8.26 - 8.30.

(iii) the effect of die amplitude on the magnitude of the punch load reduction at different stages of drawing, Figs. 8.31 - 8.35.

The general characteristics of the relationships examined

were similar to those observed in test series 02, using the standard wedge drawing dies. However several significant differences were observed which are summarised as follows:

(a) the reduction in punch load was greater at a given die amplitude for each drawing ratio examined

(b) comparison of the curves showing the effect of vibration amplitude on the reduction in maximum oscillatory and non-oscillatory punch loads for the two test series, indicated that both the linear and non-linear effects were increased with the roller assembly inserted.

(c) the slope of the linear punch load reduction increased as drawing progressed, at each ratio examined. No evidence was found of an enhanced effect associated with a particular stage of drawing.

(d) extrapolation of the punch load reduction curves to zero reduction indicated a higher threshold amplitude compared with the original tests. This is illustrated in Figs. 8.26 - 8.35 which indicate a threshold amplitude of between 1.0 - 1.5 x 10^{-5} in. compared with a corresponding value of between 0.4 - 0.8 x 10^{-5} in. in the 'fixed' radius tests.

(e) the maximum oscillatory and non-oscillatory punch loads were observed to occur at approximately the same punch displacement, whereas in the original tests the oscillatory punch load/displacement curves were consistently displaced to the left, eg. Fig. 8.10. This was attributed to the removal under oscillatory conditions, of the die radius friction force, which was observed to increase rapidly during the later stages of drawing.

(f) examination of the limiting draw ratio, by plotting the

Relationship between the maximum oscillatory and non-oscillatory punch loads and the drawing ratio for roller radius tests.

Fig. 9·23

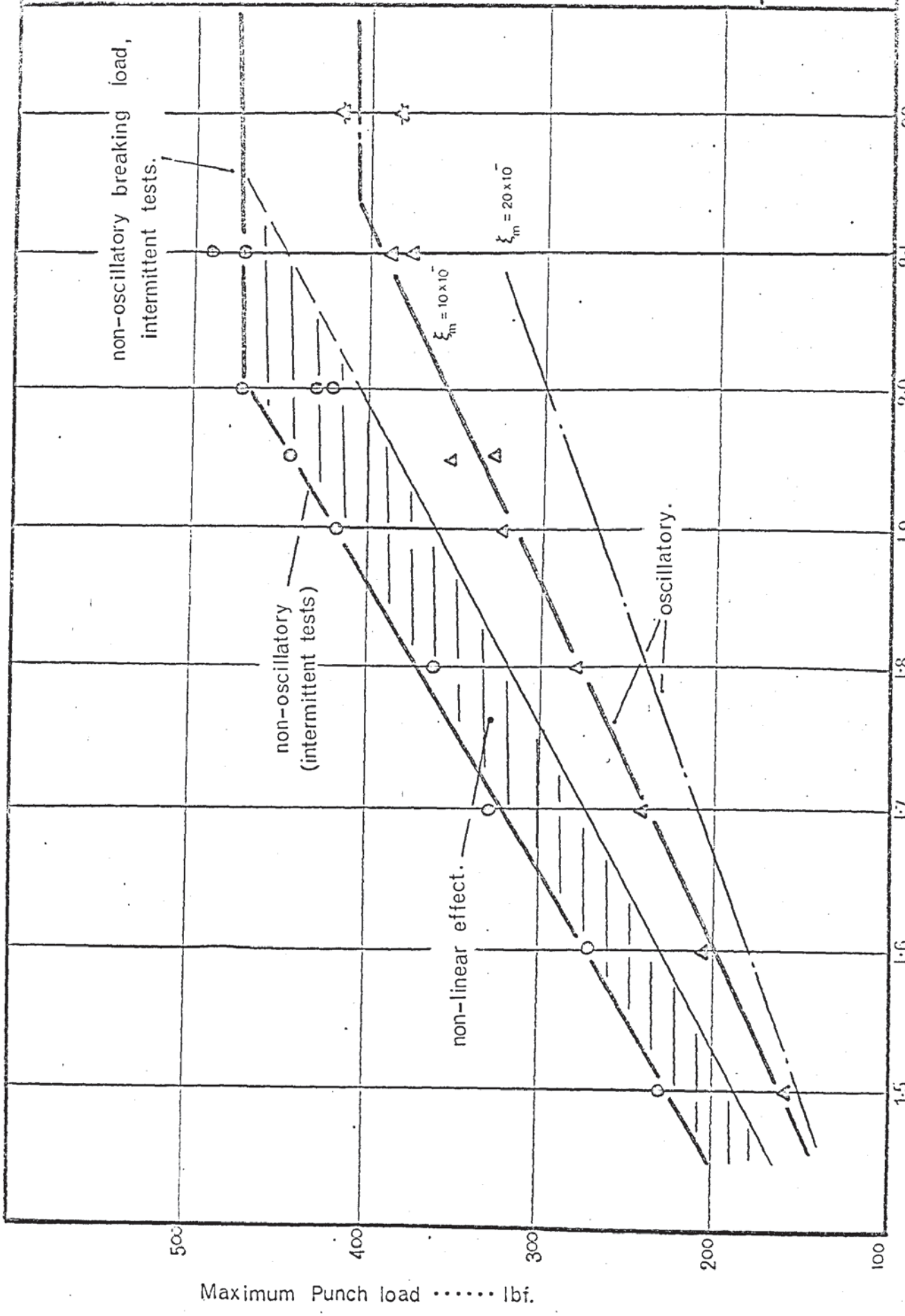

same characteristics as in Fig. 9.22 for the standard wedge drawing test data, showed that the L.D.R. under oscillatory conditions was increased from approximately 2.00 to between 2.10 and 2.15, Fig. 9.23. This increase, unlike the earlier tests was related entirely to the 'non'linear' component of the punch load reduction. It was also noted that the non-oscillatory breaking load during interrupted tests was significantly higher than in the previous series, viz. 475 lbf. compared with 448 lbf. Also, the linear effect attributed to stress superposition, although considerably greater under these conditions, resulted only in lowering the breaking load during continuous oscillatory drawing. These effects can be explained by changes in the motional and stress waveforms associated with the test piece.

In the absence of die radius friction it may be assumed that a transmitted wave will emanate from each vibrator and pass through the drawn portion of the testpiece. It is postulated that on reaching the opposite wedge die, reinforcement of the respective transmitted and incident waves leads to an increase in motional amplitude across the tapered portion of the test piece. The assumption is made that complete absorption of the incident wave occurs at the end of the test piece and that no reflected wave is produced. This situation may be analysed in the following way:

Let the motional amplitude in the two dies be ξm_1 and ξm_2 and the distance between them be given by x. See Fig. 9.24.

Considering the instantaneous displacement ξ_1, due to ξm_1, at some arbitrary point x_1, we may write:

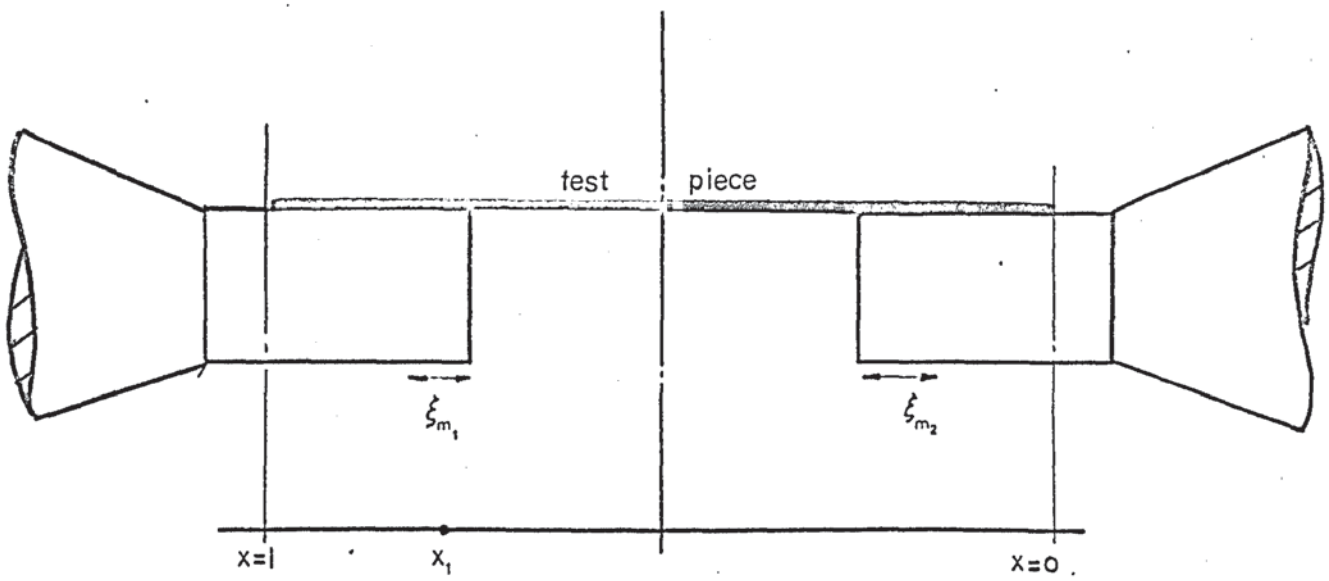

Fig. 9.24 Definition of effective wave path during wedge drawing with the roller radius assembly.

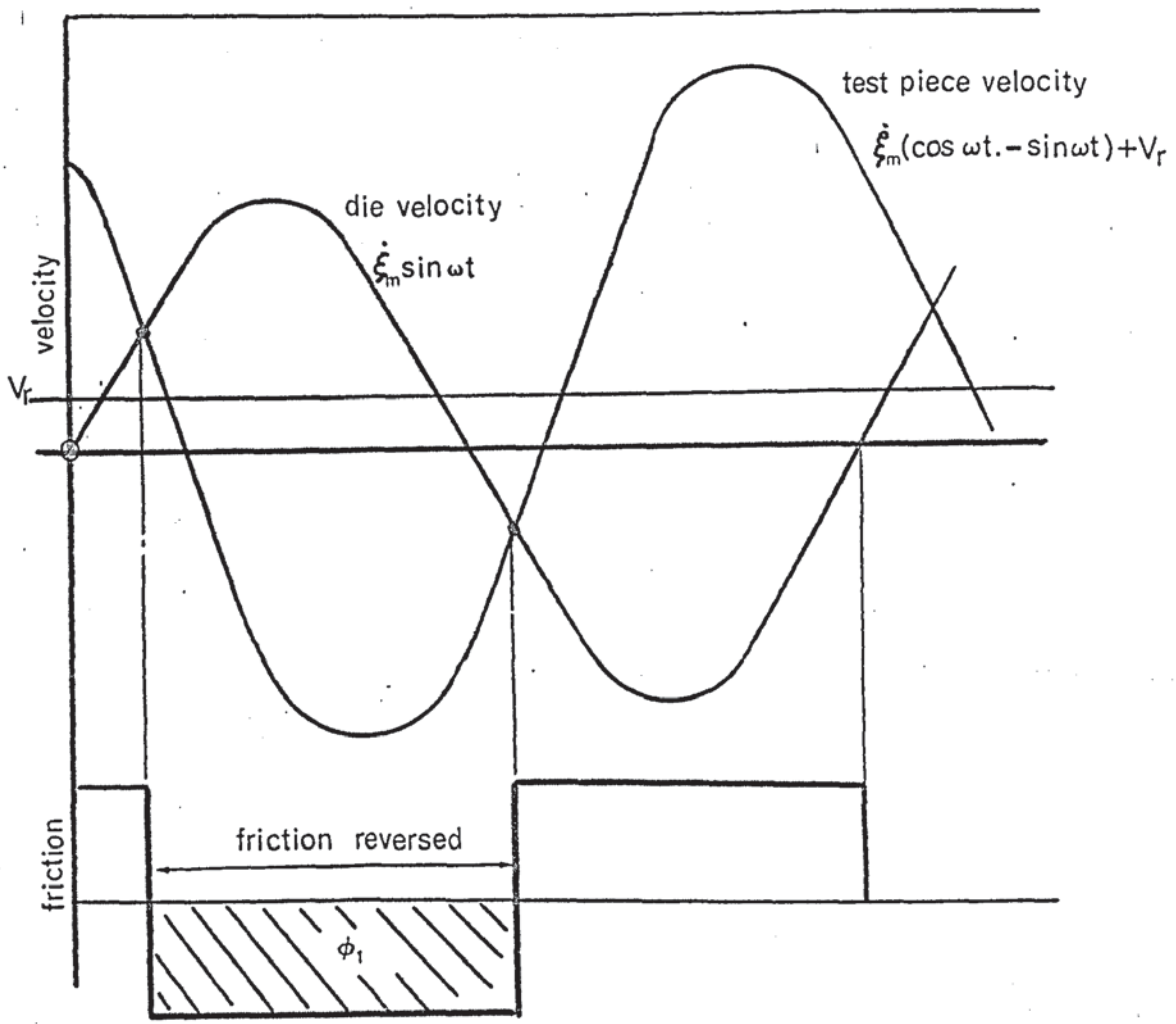

Fig. 9.25 Schematic illustration of friction reduction between the testpiece and die.

$$\xi_1 = \xi m_1 \cos\omega(t - \frac{x_1}{C}) \quad \text{---------- (9.66)}$$

and similarly, due to ξ_{m_2},

$$\xi_2 = \xi m_2 \cos\omega(t - \frac{x - x_1 2}{C}) \quad \text{---------- (9.67)}$$

where C is the wave velocity as defined earlier. The total displacement ξ_{x_1}, is found from the sum of equation (9.66) and (9.67) viz:

$$\xi_{x_1} = \xi_{m_1}\left[\cos\omega(t - \frac{x_1}{C}) + \cos\omega(t - \frac{x - x_1}{C})\right]$$

$$= \xi_{m_1}\left[\cos\omega(t - \frac{x_1}{C}) + \cos\left\{\omega(t + \frac{x_1}{C}) - \frac{\omega}{C}.x\right\}\right] - \quad (9.68)$$

If we now consider the special case when $x = \lambda/4$, then $\frac{\omega x}{C} = \pi/2$ and equation (9.68) may be rewritten:

$$\xi_{x_1} = \xi_{m_1}\left\{\cos.\omega(t - \frac{x_1}{C}) + \sin\omega(t + \frac{x_1}{C})\right\}$$

which on rearranging becomes:

$$\xi_{x_1} = \xi_{m_1}\left[(\cos\omega\frac{x_1}{C} + \sin\frac{\omega x_1}{C})\ (\cos\omega t + \sin\omega t)\right] \quad \text{-------(9.69)}$$

Equation (9.69) implies that the motional amplitude is a maximum mid-way along the drawn test piece, when $x_1 = \lambda/8$, i.e.

as $x_1 \to \lambda/8$, $\frac{\omega x_1}{C} \to \pi/4$

and $$\xi_{x_1} = \sqrt{2}\xi_{m_1}.\ (\cos\omega t + \sin\omega t) \quad \text{---------- (9.70)}$$

the motional amplitude then becomes:

$$\xi_{m_x} = 2\xi_{m_1} \quad \text{---------- (9.71)}$$

This is consistent with the wave form proposed in Fig. 9.4b. Stress discontinuities are assumed at the die exit planes with a constant amplitude throughout the drawn test piece, resulting from addition of the respective incident and transmitted waves. This would lead to an increased

superposition effect which would account for the increased magnitude of the linear punch load reduction and also for the increased discrepancy in the observed oscillatory and non-oscillatory breaking loads, relative to the fixed radius tests.

Furthermore, it can be shown that reinforcement of the motional wave offers the additional possibility of friction vector reversal at the test piece/die interface, viz:

Using an analogous argument to that developed in section 9.2.3.1, the time interval during which the friction force assists the test piece motion is found as follows:

The test piece velocity amplitude at some section x_1, is found by differentiating equation (9.69) with respect to time, viz:

$$\dot{\xi}_{x_1} = \omega \xi m_1 \left[\left(\cos \frac{\omega x_1}{C} + \sin \frac{\omega x_1}{C} \right) \left(- \sin\omega t + \cos\omega t \right) \right] \quad \text{--- (9.72)}$$

but as $x_1 \rightarrow 0$ or $\lambda/4$, i.e. at the ends of the test piece,

$\xi_{m_1} \rightarrow \xi_m$, the die amplitude.

The relative velocity between test piece and die is therefore given by

$$V = \dot{\xi}_m \sin \omega t - \left(V_r + \dot{\xi}_m \left(\cos\omega t - \sin\omega t \right) \right)$$

where V_r is the linear peripheral velocity of the test piece and $\dot{\xi}_m \sin\omega t$ represents the die velocity amplitude.

Friction is removed during the interval in which the die velocity exceeds the test piece velocity, as illustrated in Fig. 9.25. This shows an effective phase shift in the test piece velocity wave relative to the die motion. The friction force under oscillatory conditions is therefore given by:

$$\frac{F_\phi}{F} = 1 - \frac{\phi_1}{2\pi} \quad \text{---------- (9.72)}$$

where ϕ_1 may be determined graphically.

From this analysis it may be assumed that friction reduction

occurs at both the upper and lower surfaces of the test piece during tests with the roller radius in position. This would account for the observed increase in the non-linear punch load reduction relative to the magnitude recorded during fixed radius drawing. The proposed test piece motion is also compatible with friction vector reversal at the edges of the test piece. It might therefore be expected that under oscillatory conditions the L.D.R. would approach that attained in cup drawing. Some discrepancy might still be anticipated however, since in cup drawing, failure occurs under biaxial stress in plane strain, due to the constraint imposed by the punch when necking occurs. The breaking load is thus increased by a factor of $\frac{2}{\sqrt{3}}$ relative to the breaking load in uniaxial tension.

9.3.2.5 Oscillatory tests using parallel test pieces.

In order to examine the characteristics of oscillatory deep drawing, free from the influence of edge effects, which are specific to the wedge drawing test, a series of parallel test pieces were drawn both with and without the roller assembly and covering a range of die amplitudes. The results of these tests are summarised in Figs. 8.41 and 8.42 respectively in which the mean oscillatory and non-oscillatory punch loads are plotted as a function of die amplitude. The effect of increasing die amplitude is also illustrated by plotting the reduction in mean punch load and mean blank holder friction force against die amplitude.

In the tests using the roller assembly, the oscillatory punch load decreased rapidly with increasing die amplitude upto an amplitude of 15×10^{-5} in. and then remained constant at 20 lbf, Fig. 8.42a. The non-oscillatory punch load was observed to increase slightly with increasing die amplitude. Corresponding curves showing the reduction in mean punch load and

blank holder friction force, Fig. 8.42b, indicated that the reduction in punch load was consistently greater than the measured friction force reduction, by a factor of 2. It was therefore concluded that the friction force was effectively removed at both surfaces of the test piece, and that the residual punch load was due to stress increments producing plastic bending and unbending around the roller.

The fixed radius test results showed a similar rapid reduction in punch load but instead of reaching a constant value, the punch load fell linearly as the die amplitude increased beyond a value of approximately $10 \times 10^{-5}_{in}$, Fig. 8.41a. The non-oscillatory punch load also showed a steep increase with increasing die amplitude as in earlier tests, series 02. The pronounced linear effect in the punch load reduction curve shown in Fig. 8.41 b was accounted for largely by a corresponding increase in blank holder friction force during the non-oscillatory test interval. There was however a further effect which was apparent from the variation in mean oscillatory punch load with increasing die amplitude, Fig. 8.41a. This was attributed to the effect of an oscillatory bending moment on the stress producing plastic unbending at the exit to the die radius.

It was not possible to analyse the data quantitatively due to the difficulty in determining the motional amplitude of the test piece. However, the results show qualitative agreement with the original wedge drawing test data and indicate that both friction reduction and superposition mechanisms can occur in the absence of the edge constraint imposed by the wedge profile.

9.3.3 Application of the results of oscillatory wedge drawing to the Axisymmetric Process of Cup Drawing.

The effects of applying vibrations to the tools during the

cup drawing process may be deduced qualitatively by analogy with the wedge drawing data discussed above. A detailed analysis would require that the oscillatory motion of the test piece was established at each stage of drawing which is beyond the scope of the present work. However it is still possible to consider which of the mechanisms observed during wedge drawing are likely to affect the deformation force during cup drawing.

If it is assumed that a pure radial wave motion is established in the cup drawing die (using the design principles described in Appendix I) the test piece, a circular blank in this case, would also acquire an oscillatory motional component. The amplitude of the wave motion induced in the test piece would be determined by the acoustic properties and physical dimensions of the blank and by the operating frequency of the oscillatory system. A considerable change in the resonant characteristics of the test piece would be anticipated during drawing. Initially, resonance would result in a radial stress antinode at the centre. As drawing continued and the centre of the blank became vertically displaced from the plane of radial motion it is anticipated that the conditions of tuning would change due to mode conversion around the die radius.

In the absence of resonance in the test piece its motional amplitude would be expected to be lower than that of the die since the transmission of energy is solely dependent upon the interfacial friction force acting on the lower surface of the blank. In the wedge drawing test it was shown that the test piece motion was influenced principally by the constraint imposed at the edges in contact with the oscillatory die. The series of tests conducted with parallel test pieces, however, clearly indicated that a proportion of the energy dissipated in the dies resulted in a reduced friction force at the upper test

piece surface. If it is assumed that this occurred by a reversal mechanism the high values of threshold and saturation amplitudes recorded, suggest a considerably lower displacement amplitude in the test piece, compared with wedge drawing tests carried out at the same die amplitude. The interfacial conditions are considered to be analogous to those relating to the radial portion of the blank during cup drawing and it is therefore anticipated that the axisymmetric test would show similar oscillatory characteristics.

From the above discussion it may be concluded that relative cyclic motion is possible between the blank and tools at both upper and lower surfaces, during radial drawing in. At sufficiently high vibration amplitudes, relative to the punch velocity, friction vector reversal would therefore occur resulting in a reduction in blank holder friction force. The relationship between friction reduction and the ratio of oscillatory velocity amplitude to linear punch velocity, would be similar to that found in wedge drawing. The expression describing this effect would require to be modified to incorporate the changing relationship between die and blank amplitudes, during drawing and the inherent difference in the motional link between tools and test piece relative to the wedge drawing test.

It is considered that the mechanism defining friction reduction around the die radius during wedge drawing would be equally applicable to the axisymmetric test. However, the analysis is complicated in the latter case by the effects of radial and circumferential strains as each element of the blank passes over the die radius. The simple 'belt pulley' model used to describe the variation in friction force around the die radius is no longer strictly applicable since it

represents the limiting case when σ_θ, the circumferential stress, tends to zero and r, the instantaneous radius tends to infinity. The reduction in die radius friction may therefore be determined more accurately by substituting for df_θ in equation (9.18), the expression derived in section 3, based on Swift's detailed analysis of deformation around the die profile, viz: equation (3.28).

The presence of a radial mode oscillation in the flange of the deforming blank would be expected to cause elastic strain release by a similar mechanism to that described in section 9.2.4. It is therefore anticipated that a radial stress superposition effect would occur, causing a reduction in punch load. The magnitude of the effect would depend upon the amplitude of the wave motion induced in the blank and could therefore be influenced by tuning effects related to changes in the blank geometry during drawing. Superposition would also be anticipated at the planes of plastic bending and unbending at the entry to and exit from the die profile radius. In the latter case it is proposed that stress superposition would result from a complex flexural radial mode causing an oscillatory bending moment, whose magnitude varied along the cup wall. Detailed analysis of the effect would be complicated by the presence of circumferential strains. However, it may be argued qualitatively from the wedge drawing analysis that the maximum effect would coincide with the stage of drawing at which the flexural stiffness in the cup wall was greatest.

It may be concluded therefore that under appropriate oscillatory conditions the punch load will be reduced by the sum of the reduction in friction forces and superposition effects in the flange and at the planes of plastic bending and unbending. The magnitude of the effects is likely to be

influenced by resonant conditions established during drawing and by the geometry of the tools. It is probable that an optimum combination of die and punch profiles exists which maximises the oscillatory effect at a given drawing ratio. This may be selected so that the maximum oscillatory bending moment occurs at the stage of drawing coincident with the maximum punch load. In practice, however, the tool clearance may be reduced so that a controlled degree of ironing occurs. Under these circumstances the radial motion of the die would be expected to have a direct influence on the drawing load by reducing the mean radial stress acting in the plastic zone of the cup wall.

The most significant effect of the reduction in maximum punch load is the increased limiting draw ratio permitted. Each component of the punch load which is lowered under oscillatory conditions, without causing a corresponding cyclic stress at the plane of tensile failure in the cup wall will contribute to an increased L.D.R. The condition is satisfied by both mechanisms of friction reduction and by stress superposition in the flange and at the plane of plastic bending.

However, superposition of an oscillatory bending moment at the plane of plastic unbending is accompanied by an oscillatory stress component at the plane of tensile failure adjacent to the punch radius, causing failure to occur at a lower mean stress. The application of an oscillatory bending moment in the cup wall might therefore be expected to produce fatigue hardening by the mechanism proposed in the wedge drawing tests. This phenomenon could result in an increased L.D.R. if significant hardening occurred before the maximum punch load was achieved and provided that the oscillatory bending stress reached a maximum value and then fell off sharply before the maximum punch load occurred.

10 Conclusions

1. Ultrasonic activation of the dies, during the present wedge drawing test, caused a reduction in punch load which was proportional to the motional amplitude of the vibrating tools.
2. Direct measurement of the blank holder friction force associated with the upper test piece surface, indicated that this was reduced under oscillatory conditions and that at sufficiently high vibration amplitudes it could be effectively eliminated.
3. Comparison of punch load displacement traces for normal wedge drawing, with corresponding traces obtained using a 'frictionless' roller assembly inserted between the dies, permitted an indirect measure of the die radius friction force.
4. The shape of the non-oscillatory punch load displacement curves for 'frictionless' radius tests coincided closely with those of corresponding oscillatory tests, using the standard wedge drawing dies. It was concluded therefore that under the circumstances of these tests, longitudinal oscillation of the dies caused a reduction in die radius friction force.
5. Analysis of the punch load reduction data indicated two specific effects:-
   (i) a pronounced non-linear reduction in punch load at low vibration amplitudes, and
   (ii) a linear punch load reduction with increasing die amplitude which extended upto the limit of amplitude examined.
6. The magnitude of the non-linear effects determined at a

stage of drawing coincident with the maximum punch load, was found to be equal to the sum of the measured blank holder and die radius friction forces for each drawing ratio examined.

7. Theoretical analysis of the test piece motion demonstrated that the observed reduction in blank holder friction force could be quantitatively explained in terms of a simple model based on friction vector reversal at the interface between the test piece and blank holder plate.
8. Physical evidence of the test piece motion during oscillatory drawing was provided by direct observation of various portions of the surface, using a stereoscan electron microscope. The condition of the upper test piece surface which was predicted to experience a cyclic motion, relative to the blank holder plate, showed evidence of localised surface flow and disruption of the oxide flow. This condition was not present on the lower surface or edges of the test piece.
9. Analysis of the test piece motion in the region of the die radius, indicated that cyclic rotation of the friction vector could result in a reduction in the friction force associated with this stage of drawing, and a mathematical model describing the mechanism was derived.
10. In each case, the reduction in friction force predicted by the respective equations was shown to be a function of the velocity ratio - $Vp/\dot{\xi}_m$ where $\dot{\xi}_m$ is the oscillatory velocity amplitude of the die and Vp the linear punch velocity. The model describing the reduction in blank holder friction force predicted a threshold value of the velocity ratio which agreed closely with measured values.
11. Analysis of the oscillatory motion of the test piece during

radial drawing-in predicted a stress superposition effect causing a reduction in the mean stress at the die exit plane.

12. The oscillatory motion of the die resulted in mode conversion in the test piece as it passed over the die radius and it is proposed that this caused a flexural wave form in the drawn portion of the test piece.
13. Analysis of the oscillatory bending moment, associated with flexural vibration of the test piece, lead to a model predicting a reduction in the mean axial stress causing plastic unbending at the exit to the die radius.
14. A simplified model, which ignored inertial effects, indicated a maximum reduction in the unbending stress at a certain stage of drawing. This was found to coincide with experimental results which showed an enhanced linear punch load reduction at a punch displacement between 0.5 and 0.6 in.
15. Superposition of an axial oscillatory stress at the die exit plane was shown theoretically to lower the mean stress producing plastic bending at this plane.
16. The sum of the theoretically determined friction and superposition effects showed good agreement with measured values of the reduction in maximum punch load over the range of die amplitude considered in this investigation.
17. The limiting draw ratio under oscillatory conditions was increased from 1.90 to just below 2.00 at an oscillatory amplitude of 20×10^{-5} in.
18. The non-oscillatory breaking load during 'interrupted' oscillatory tests was approximately 30 lbf higher than the value determined in non-oscillatory tests. This effect was attributed to a fatigue hardening mechanism caused by

oscillatory bending stresses acting locally at the plane of tensile failure.

19. Beyond a certain critical drawing ratio an increase in the amplitude resulted in tensile failure of the test piece at progressively lower punch loads. This was attributed to stress superposition at the plane of tensile failure.

20. The non-oscillatory punch load during 'interrupted' oscillatory tests was observed to be higher than the corresponding value determined during continuous non-oscillatory tests. This was explained by a measured increase in the blank holder friction force during tests with intermittent die activation.

21. The limiting draw ratio in wedge drawing, even under oscillatory conditions, is lower than that for cups drawn in the same material. Two reasons are proposed to account for this.
    (a) the presence of edge friction in the wedge drawing test.
    (b) failure in cup drawing occurs under biaxial stress in plane strain, due to the constraint imposed by the punch when necking commences. The breaking load for a given material would thus exceed the equivalent wedge drawing value by a factor of $2/\sqrt{3}$.

22. Wedge drawing tests with the roller radius inserted, indicated a limiting draw ratio which approached that of the axisymmetric process. This was attributed to additional friction reduction at the edges and lower surface of the test piece, resulting from a phase shift in the velocity wave, relative to the die motion.

23. It is considered that radial vibration of the die during

cup drawing will produce similar effects to those observed in the oscillatory wedge drawing test and that they will result in an increase in the limiting draw ratio.

11. Suggestions for further work.

The current programme of work has indicated a number of areas requiring further investigation. These are considered below under two main headings;

(i) Oscillatory wedge drawing.

(ii) Cup drawing with ultrasonic die activation.

11.1 Oscillatory wedge drawing.

11.1.1 Vibrational mode.

Although the oscillatory configuration used in the current research was chosen as the most likely to yield significant technical improvements there is a need to consider alternative modes of excitation in order to determine the optimum system.

The following configurations should be examined:-

(a) excitation of the blank holder plates in a simulated radial mode. Provision was made for this approach in the design of the present sub-press. This would be expected to reduce the friction force associated with the blank holder but to have only a limited effect on the 'remaining' components of the punch load since the motional and strain amplitudes induced in the blank are likely to be relatively low.

(b) axial vibration of the punch. This would produce stress superposition effects in the cup wall, lowering the mean punch load but might also lead to friction reduction around the die radius and in the wedge die, provided that sufficient energy is transmitted through the test piece to maintain an adequate motional amplitude at the friction interface.

(c) axial excitation of the dies or blank holder plate parallel to the punch axis. This would be expected to have an effect on die radius friction in the case

of die excitation. For thin strip, requiring a high blank holder force to prevent wrinkling, the thickness stress, σ_t would be significant, and superpositions of an oscillatory component would therefore be expected to influence the stress equilibrium producing yielding in the flange. This in turn would produce a true reduction in punch load.

11.1.2 Ironing

The present investigation was concerned with pure deep drawing, sufficient clearance being allowed between punch and die to prevent ironing. The work of Lehfeldt[30] suggests that significant benefits might be obtained with a simulated radial mode, if the clearance were adjusted to permit a controlled degree of thickness reduction during oscillatory wedge drawing.

11.1.3 Measurement of oscillatory force amplitude at the die exit plane.

Attempts to measure the input impedance of the conical horns during the present series of experiments proved unsuccessful, due principally to the restricted access permitted in the sub-press design. It is suggested that the oscillatory force amplitude could be measured by inserting a half-wave parallel section between the concentrator and wedge die. This would incorporate an antinodal bridge (see Appendix VIII) capable of measuring the travelling wave force amplitude directly.

11.2 Oscillatory cup drawing.

11.2.1 Development of radial resonator.

The design concepts of radial resonators, discussed in Appendix I could be used to develop a resonant die system having a sufficiently homogeneous motional field to permit a

systematic evaluation of the mechanics of cup drawing. The validity of the arguments considered in section 9.3.3 could then be assessed.

11.2.2 Cup drawing with wall ironing.

The effect of radial stress superposition in the cup wall during ironing should be examined. It is believed that this could produce a true reduction in punch load leading to a significant increase in the limiting draw ratio.

11.2.3 Examination of the influence of blank thickness on the effectiveness of the oscillatory process.

It is suggested that a series of tests be undertaken in which a wide range of blank thicknesses is examined. As the blank thickness decreases it is anticipated that the blank holder friction force will account for an increasing proportion of the punch load. The effectiveness of radial vibrations, which are assumed to reduce the effective blank holder friction force, should therefore increase with decreasing blank thickness. This would be expected to produce an increase in the limiting draw ratio as the thickness was reduced.

In addition to the aspects considered above, it is suggested that a special series of tests is undertaken to examine the effect of high intensity ultrasound on the post deformation mechanical properties of different materials. It was proposed in section 9.3.2.3 that under certain circumstances the yield strength of the workpiece could be increased locally under the influence of a sufficiently high oscillatory stress amplitude. If, as suggested by other researchers[18,21] this is associated with a vacancy hardening mechanism, the phenomenon could be examined by resistivity measurements, since electrical resistivity is particularly sensitive to changes in the vacancy density. It should there-

fore be possible to demonstrate a fundamental difference between testpieces deformed under non-oscillatory conditions and those deformed with a superimposed cyclic stress, which would be expected to generate a higher vacancy density.

Acknowledgements

The author expresses his sincere thanks to Dr. D.H. Sansome for his continued help and encouragement throughout this research programme. He wishes also to thank Dr. Colin Winsper for his guidance during the early part of the work and Dr. Graham Dawson and Mr. A. Grange (of Ultrasonics Ltd) for their many helpful discussions.

Thanks are also given to the Science Research Council who financed the programme, to Professor Ede, who kindly permitted the work to be undertaken in his department and to ALCO Ltd. who supplied the test material.

The author gratefully acknowledges the help given by the workshop staff in the Mechanical Engineering Department at Aston, in particular Mr. E. Denchfield and Mr. H. Pratt. Thanks also to Mrs. A. Csertan for her care in typing the final manuscript, to Miss J. Hartwell for her assistance with some of the drawings and to Mr. O.M. Blunn for his considerable efforts in translating the Russian text of Professor Teumin's book into English.

Finally, but by no means least, thanks to my wife for her painstaking preparation of the draft manuscript from what can only be described as 'the most unruly handwriting'.

BIBLIOGRAPHY

1. Winsper, C.E. Ph.D. Thesis - University of Aston in Birmingham, 1966.

2. Dawson, G. 'Application of high and low frequency oscillations to the plastic deformation of metals.' Metal Forming, 1970, p. 234.

3. Blaha, F. & Langenecker, B. 'Elongation of zinc single crystals under ultrasonic action'. Die Naturwissenschaften, 1955, 42 (20) p. 556.

4. Blaha, F. & Langenecker, B. 'Plasticity tests on metal crystals in an ultrasonic field'. Acta Metallurgia, 1959, 7, p.93.

5. Nevill, G.E. & Brotzen, F.R. 'The effect of vibrations on the state yield strength of a low carbon steel'. Proc. Am. Soc. for testing materials, 1957, 57, p. 751.

6. Bozarth, R.M. 'Ferromagnetism', D. van Nostrand Co., Inc, New York, 1951.

7. Pohlman, R. & Lehfeldt, E. 'Influence of ultrasonic vibration on metallic friction'. Ultrasonics, 1966, October, p.178.

8. Winsper, C.E. & Sansome, D.H. 'The influence of Oscillatory energy on the stresses during plastic deformation', J.I.M. 1968, 96, p.353.

9. Langenecker, B. 'Effects of ultrasound on deformation characteristics of metals', I.E.E.E. Transaction, Sonics and Ultrasonics, 1966, SU-13 (1) p.1.

10. Langenecker, B. 'The effect of sonic and ultrasonic radiation on the safety factors of rockets

and missiles'. AIAAJ, 1963, Jan. 1. p.80.

11. Langenecker, B. et al. 'Effects of ultrasound on deformation characteristics of structural metals'. U.S. Naval Ord. Test Stn., China Lake, Calif., NAVWEPS, Rept. 8482, NOTS TP 3447, 1964, March, p.53.

12. Oelschlügel, D. & Weiss, B. 'Hardening by intense ultrasonics in single crystals'. Berg. u. Hüttenm, 1966, 111 (3) p 116.

13. Lester, W. & Whymark, R. 'Plastic flow in acoustically and statically loaded nickel'. J.Acoust. Soc. Am. 1970, 48, 3(2) p.671.

14. Mason, W.P. 'Low and high amplitude internal friction measurements in solids and their relation to imperfection motions'. 1967, March, DDC Rep. AD652 p.793.

15. Merkulov, L.G. 'Design of ultrasonic concentrations' Soviet Physics - Acoustics, 1956, p.246.

16. Friedrich, R., Kaiser, G. & Pechhold, W. 'Effect of Mechanical oscillations of the plastic behaviour of metals' Zeitschrift für Metallkunde, 1969, 60 (5) p.390.

17. Seeger, A. Encyclopaedia of Physics, (S. Flügge) 1958, VII, 2 Crystal Physics II, Springer.

18. Langenecker, B. 'Work hardening of zinc crystals by high amplitude ultrasonic wave', Proc. ASTM, 1962, 62, p.602.

19. Seeger, A. & Träuble, H. 'Die plastische verformung von Zinkeinkristallen' Zeitschrift für Metallkunde, 1960, 51, p.435.

20. Kralik, G. 'Ultrasonic hardening of copper at 90°K'.

Z. Metallkde, 1968, 59 (12) p.924.

21. Smallman, R.E. 'Modern Physical Metallurgy' Butterworths, 1963.

22. Severdenko, V.P. and Elin, V.I. 'The effect of ultrasonic vibrations on the microstructure of Armco Iron'. Metallov i Term. Obrabotka Metallov 1966, 9, p.14.

23. Boyd, C.A. & Maropis, N. DMIC report, 187, 1963 August.

24. Pohlman, R. & Lehfeldt, E. Draht-Welt 1966, 52, p.277.

25. Robinson, A.T. 'The application of ultrasonic energy to metal wire drawing', Wire and Wire Prods. 1964, 39 (12) p.1925

26. Severdenko, V.P. & Klubovich, V.V. 'Drawing a copper wire in an ultrasonic field', Doklady Akad. Nauk, B.S.S.R. 1963 7 (2) p.95.

27. Winsper, C.E. & Sansome, D.H. 'A study of the mechanics of wire drawing with a superimposed ultrasonic stress. 10th International M.T.D.R. Conference, 1969, September.

28. Thompson, F.C. J. of the Iron and Steel Inst. 1933, 128 p369

29. Winsper, C.E. & Sansome, D.H. 'Application of ultrasonic Vibrations to the plug drawing of tube' Metal Forming, 1971, (March) p.71.

30. Lehfeldt, E. 'Wire drawing with superimposed ultrasonic vibrations' Wire, Coburg, 1969, (August), 102 p.205.

31. Oelschlägel, D. and Weiss, B. 'Easing of wire by means of ultrasonics', Acta Physica, Austria, 1965, 20, p.363.

32. Ryder, G.H. 'Strength of Materials' Macmillan & Co. Ltd., 1965, Chap.9.

33. Rozner, A.G. 'Effect of ultrasound on stresses during strip drawing' NOL Report No. NOLTR70-45, 1970. March.

34. Winsper, C.E. & Sansome, D.H. 'Fundamentals of "Ultrasonic" wire drawing' J.I.M. 1969, 97, p.274.

35. Butler, L.H. 'A study of lubrication in relation to continuous metal deformation processes.' Sheet Metal Ind. 1956, (Aug), p.571.

36. Ford, H. 'The role of friction in metal cracking processes' Symposium on metal working oils Part II Metal Forming, J.Inst. Petrol., 1954, 40, p.291.

37. Fridman, H.D. & Levesque, P. 'Reduction of static friction by sonic vibration'. J.Appl.Phys.1959, (October) p.1572.

38. Waller, M.D. Acoustica 1953, 3, p.370.

39. Godfrey, D. 'Vibration reduces metal to metal contact and apparent reduction in friction' A.S.L.E. Trans., 1967, 10(2) p.183.

40. Lenkiewicz, W. 'The sliding friction process - effect of external vibrations'. Wear, 1969, 13,p.99.

41. Sirotyuk, M.G. et al. 'Reduction of drawing force in the pressure of ultrasound'. Ul'trazuuk tekhn., 1964, 5, p.18.

42. Nosal, V.V. & Rymsha, O.M. 'Reducing the drawing forces by ultrasonic oscillations of the drawplate and determination of the technological parameters of tube drawing'. Stal (in English), 1966, February, p.135.

43. Golubev, T.M. & Dyadechko, G.P. 'On the problems of contact friction in the deformation zone during vibration drawing', Izv, UUZ, Chernaya Metall. 1965, (2) p.99.

44. Severdenko, V.P. & Reznikov, Y.N. 'How Metal drawing is influenced by ultrasonic oscillation in different directions.' Plasticichnost i Obrabotka Metallov Davleniem, Nauka i Tekhnika, Minsk, 1966, p.247.

45. Weast, R.C. & Selby, S.M. 'Handbook of mathematical Tables', The Chemical Rubber Co. Ohio, U.S.A. 1964, p.559.

46. Den Hartog, J.P. 'Mechanical vibrations', McGraw Hill, 1956, Chap. 4.

47. Balamuth, L. 'Forming goes ultrasonic'. Am. Machinist/ Metal working Manfng. 1961, November, 105, p.83.

48. Langenecker, B. et al 'Ultrasonics - an aid to metal Forming' Metal Progress, 1964, April, 85, p.97.

49. Kristoffy, I. 'Metal Forming with Vibrating Tools' Trans. A.S.M.E. J. Eng. Ind. 1969, Nov. p.1168.

50. Chung, S.Y. and Swift, H.W. Proc. Inst. of Mech. Engs. (Appl. Mech. Div.) 1951, 165, WEP No. 68, p.199.

51. Alexander, J.M. 'An appraisal of the theory of deep drawing' Met. Reviews, 1960, 5 (19) p.349.

52. Hill, R. 'The Mathematical theory of Plasticity', Oxford, (Clarendon Press) 1950.

53. Osgood, W. 'Stress strain formulas' J. of Aeronautical Sci. 1946, 13, p.45.

54. Sachs, G. 'Ein Neues Prüfgerät für Tiefziehlbleche' Metallwirtschaft, 1930, 9. p. 213.

55. Eisenkolb, F. 'Untersuchung über die Prüfung der Tiefziehfähigkeit von Feinblechen' Stahl und Eisen 1932, 52, p.357.

56. Kayseler, H. et al. Stahl und Eisen, 1934, 54 (39) p.993.

57. Brewer, G.A. & Rockwell, M.M. 'Measurement of drawing properties of Aluminium sheet'. Metal Progress 1942, May, p.663.

58. Loxley, E.M. and Swift, H.W. 'The wedge drawing test', Engineering, 1945, January, p.38.

59. Gladwell, G.M.L. & Popplewell, N. 'The vibration of mechanical resonators (1) Uniform rings and discs', J. Sound Vib. 1967, (6) (3) p.343.

60. Friedrich, J.R. Ultrasonic Engineering, (Wylie Interscience) 1965.

61. Mason, W.P. 'Electromechanical tranducers and wave filters' (Van Nostrand, New York) 1942.

62. Eisner, E. 'Design of sonic amplitude transformers for high magnification'. J.Acoust. Soc. Am. 1963, 35, (9) p.1367.

63. Morse, P. 'Vibration and Sound', 1948, Published in New York.

64. Teumin, I.I. 'Ultrasonic vibrating systems' (in Russian) (Moscow,Mashgiz) 1959, Chap. 3.

65. Merkulov, L.G. 'Design of ultrasonic concentrators', Soviet Phys. - Acoustics,1957, 3, p.246.

66. Neppiras, E.A. 'Very High energy ultrasonics' British J. of Appl. Phys. 1960, 11,p.143.

67. Teumin, I.I. 'Ultrasonic vibrating systems', (in Russian), (Moscow Mashgiz), 1959, Chap. 8.

68. Merkulov, L.G. & Kharitonov, A.V. 'Theory and Analysis of

sectional concentrators', Soviet Phys. - Acoustics, 1959, 5, p.183.

69. Young, M.J.R. et al. 'The effect of tool attachment on the resonant characteristics of ultrasonic wave-guides' Appl. Acoust. 1970, 3 p.217.

70. Young, M.J.R. et al. 'The design of high intensity radial vibrators for metal working application! J. Phys.D. Appl. Phys. 1971, 4, p.212.

71. Young, M.J.R. et al. 'Radial mode vibrators for oscillatory metal forming', Appl. Acoust. 1970, 3, p.299.

72. Brown, B. & Grange, A. 'An investigation into the performance of nickel alloy magnetostrictive transducers prepared for commercial use'. Appl. Acoust. 1969, (2) p.111.

73. Markov, A.I. 'Ultrasonic Machining of intractable materials' Iliffe Books, 1966.

74. Ryder, G.H. 'Strength of Materials' Macmillan & Co. Ltd., 1965, Chapter 3.

75. Watson, G.N. 'Theory of Bessel Functions', (Cambridge University Press, 1962).

76. Rozenberg, L.D. et al 'Ultrasonic Cutting', Translation from Russian by J.E.S. Bradley. (Consultants Bureau 1964), Chap. 1.

Appendix I Radial Resonators

A1.1 Radial Resonance in a Continuous Annular Ring[70]

The wave equation defining the particle motion in a thin annular disc may be derived from consideration of the elastic stresses induced in a radial element under the action of an applied oscillatory force[59]. Consider an element dr in a perfectly elastic medium at a radius r from the centre of a thin annular disc of inner and outer radii R_1 and R_2 respectively; then if the circumferential and radial stresses induced by the application of an oscillatory force F_m are as shown in Fig. A1.1 the steady state equation defining the particle motion may be stated as follows:

$$F_m = \rho.r.d\theta.dr.h\,\frac{\partial^2\xi_r}{\partial t^2} = (\sigma_r + d\sigma_r)\,(r + dr)\,h.d\theta - \sigma r.r.h.d\theta$$

$$- 2\sigma\theta.\sin\frac{d\theta}{2}\,dr.h. \qquad \text{----------A.1.1}$$

where ξ_r is the radial displacement at any radius r and h is the ring thickness; the particle acceleration imparted by the oscillatory force F_m is thus $\frac{\partial^2\xi_r}{dt^2}$ and ρ is the density of the disc.

Neglecting products of small increments and assuming that $\sin\frac{d\theta}{2} \simeq \frac{d\theta}{2}$ we may rewrite equation A.1.1 as follows:

$$\rho.\frac{\partial^2\xi_r}{\partial t^2} = \frac{\partial\sigma_r}{\partial r} - \frac{\sigma_r}{r} - \frac{\sigma_\theta}{r} \qquad \text{----------A.1.2}$$

In the biaxial elastic system defined above, the principal stresses can be expressed in terms of their respective strains, which leads to the following relationships[59]:

$$\left.\begin{aligned}\sigma_r &= \frac{E}{1-\nu^2}\cdot(\varepsilon_r + \nu\varepsilon\theta)\\ \sigma_\theta &= \frac{E}{1-\nu^2}\cdot(\varepsilon_\theta + \nu\varepsilon_r)\end{aligned}\right\} \qquad \text{---------- A.1.3}$$

where E and ν are the elastic modulus and Poisson's ratio, ε_θ and ε_r the circumferential and radial strain respectively.

From Fig. A.1.1 we may write $\varepsilon_r = \frac{\partial \xi_r}{\partial_r}$ and considering only pure radial motion in the annular disc the circumferential strain may be written:

$$\varepsilon_\theta = \frac{(r + \xi_r)\, d\theta - r d\theta}{r.d\theta} = \frac{\xi_r}{r}$$

Substituting the above strain relationships into equation A.1.3 gives:

$$\left.\begin{aligned} \sigma_r &= \frac{E}{1-\nu^2}\left(\frac{\partial \xi_r}{\partial_r} + \frac{\nu \xi_r}{r}\right) \\ \sigma_\theta &= \frac{E}{1-\nu^2}\left(\frac{\xi_r}{r} + \frac{\nu \partial \xi_r}{\partial r}\right) \end{aligned}\right\} \quad \text{---------- A.1.4}$$

The first derivative of σ_r with respect to r is

$$\frac{\partial \sigma_r}{\partial_r} = \frac{E}{1-\nu^2}\left[\frac{\partial^2 \xi_r}{\partial r^2} + \frac{\nu}{r}\left(r.\frac{\partial \xi_r}{\partial r} - \xi_r\right)\right] \quad \text{----------A.1.5}$$

and substituting equation A.1.4 and A.1.5 into A.1.2 gives:

$$\rho .\frac{\partial^2 \xi_r}{\partial t^2} = \frac{E}{1-\nu^2}\left[\frac{1}{r}.\frac{\partial \xi_r}{\partial_r} + \frac{\nu \xi_r}{r^2} + \frac{\partial^2 \xi_r}{\partial r^2} + \frac{\nu}{r}.\frac{\partial \xi_r}{r} - \frac{\nu \xi_r}{r^2} - \frac{\xi_r}{r^2} - \frac{\nu}{r}.\frac{\partial \xi_r}{\partial r}\right]$$

If we assume simple harmonic motion in which $\frac{\partial^2 \xi_r}{\partial t^2} = -\omega^2 \xi_r$ the above equation may be rewritten:

$$\frac{\partial^2 \xi_r}{\partial r^2} + \frac{1}{r}.\frac{\partial \xi_r}{\partial r} - \frac{\xi_r}{r^2} = -\left(\frac{1-\nu^2}{E}\right)\rho.\omega^2 \xi_r \quad \text{---------- A.1.6}$$

where ω is the angular velocity given by $\omega = 2\pi f$. The wave equation defining the particle motion in a radial direction at any radius r across the ring width then becomes:

$$\frac{d^2 \xi_r}{dr^2} + \frac{1}{r}.\frac{d\xi_r}{dr} + \left(k^2 - \frac{1}{r^2}\right).\xi_r = 0 \quad \text{---------- A.1.7}$$

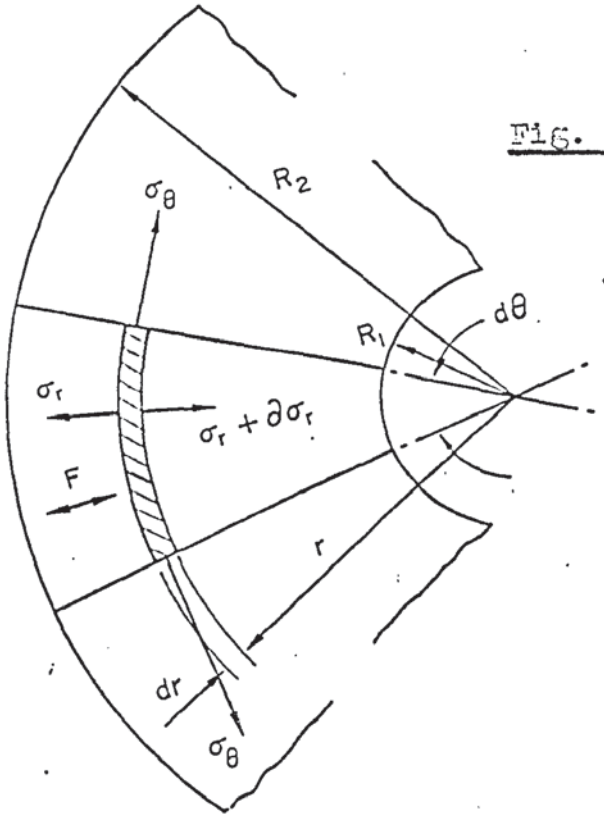

Fig. A1.1 Stresses acting on an elementary ring in a continuous annular plate.

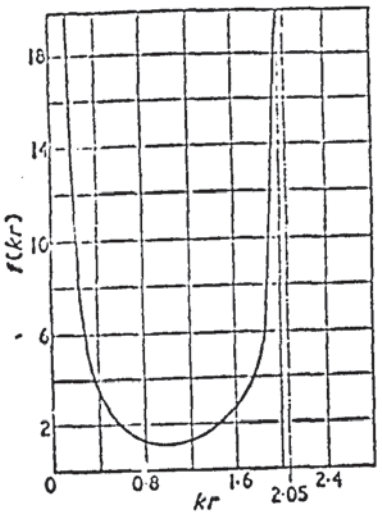

Fig. A1.2 Plot of f(kr) against kr showing the relationship for fundamental resonance in an annular plate.

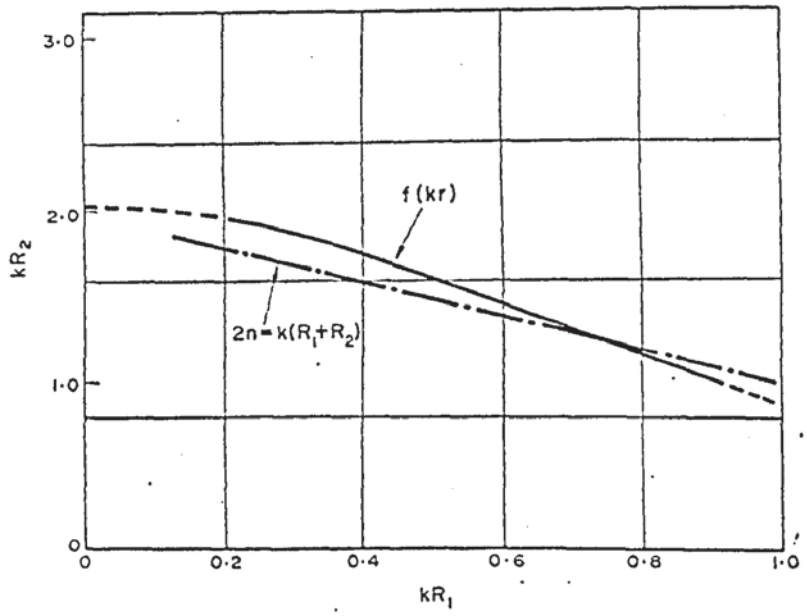

Fig. A1.3 Relationship between inner and outer radii for resonance in a continuous annular ring.

(where $k = \frac{2\pi}{\lambda} = \frac{\omega}{C_r}$ and C_r is the wave velocity taking account of transverse strains.) Viz. $C_r = \sqrt{\frac{E}{\rho(1-\nu^2)}}$. This is a first order Bessel equation having the general solution[75],

$$\xi_r = A\,J_1(kr) + BY_1(kr) \qquad \text{---------- A.1.8}$$

where J_1 and Y_1 are Bessel functions of the first and second kind, first order and A and B are arbitrary constants.

The standing wave state may be specified by applying certain boundary conditions. Such a state exists when the radial stress σ_r, is zero at the inner and outer surfaces of the annulus, namely when $r = R_1$ and R_2 respectively.

From equation A.1.4 the radial stress is defined by:

$$\sigma_r = \frac{E}{1-\nu^2}\cdot\left(\frac{\partial \xi_r}{\partial r} - \frac{\nu \xi_r}{r}\right)$$

Differentiating equation A.1.8 with respect to r gives:

$$\frac{d\xi_r}{dr} = \frac{A}{r}\left(k_r.J_o(kr) - J_1(kr)\right) + \frac{B}{r}\left(kr.Y_o(kr) - Y_1(kr)\right) \qquad \text{-- A.1.9}$$

and substituting equations A.1.9 and A.1.8 into A.1.4 yields an expression for the radial stress in terms of the general solution to the wave equation, viz.

$$\sigma_r = \frac{E}{1-\nu^2}\left[\frac{A}{r}\left\{kr.J_o(kr) - J_1(kr)\right\} + \frac{B}{r}\left\{kr.Y_o(kr) - Y_1(kr)\right\}\right.$$

$$\left. + \frac{\nu}{r}\left\{AJ_1(kr) + BY_1(kr)\right\}\right]$$

$$\therefore \sigma_r = \left[A\left\{kr.J_o(kr) - (1-\nu).J_1(kr)\right\} + B\left\{kr.Y_o(kr) - (1-\nu).Y_1(kr)\right\}\right]$$

$$\cdot\frac{E}{(1-\nu^2)r} \qquad \text{----------A.1.10}$$

A and B may be eliminated by inserting the boundary conditions

$\sigma_r = 0$ when $r = R_1$ and $r = R_2$ which gives:

$$A = -B\left(\frac{kR_1 Yo(kR_1) - (1-\nu).Y(kR_1)}{kR_1.Jo(kR_1) - (1-\nu).J(kR_1)}\right)$$

$$\text{and } \frac{kR_2 Yo(kR_2) - (1-\nu)Y_1(kR_2)}{kR_2 Jo(kR_2) - (1-\nu)J_1(kR_2)} = \frac{kR_1 Yo(kR_1) - (1-\nu)Y_1(kR_1)}{kR_1 Jo(kR_1) - (1-\nu)J_1(kR_1)}$$

-- A.1.11

From the symmetry of the above equation, it is clear that each value of the function: $\frac{krYo(kr) - (1-\nu)Y_1(kr)}{krJo(kr) - (1-\nu)J_1(kr)} = f(kr)$ provides two discreet values of the argument kr, corresponding to the inner and outer radii of the annulus. Fig. A.1.2 shows a plot of f(kr), against kr for fundamental resonance, from which values of kR_1 and kR_2 were taken, enabling the relationship between inner and outer radii to be plotted as shown in Fig. A.1.3.

It is of interest to note that for radial resonance, an approximation simply derived by making the mean circumference of the annular ring equal to an integral number of wavelengths, agrees closely with the accurate solution within the range $1 > kR_1 > 0.3$.

The simplified relationship is written:

$$k(R_1 + R_2) = 2n \qquad \text{---------- A.1.12}$$

which follows from the equation:

$$\pi(R_1 + R_2) = n\lambda = \frac{2\pi n}{k}$$

Equation A.1.12 is plotted in Fig. A.1.3 and may be seen to predict the frequency for fundamental resonance (defined by k) within ± 3.0% for values of kR_1 between 0.58 and 0.75. Overtone modes may be determined by extending the plot of f(kr) against kr in Fig. A.1.2 and in the simplified model by inserting higher values of the integer n into equation A.1.12. The graph in Fig. A.1.2 is based on a constant value of $\nu = 0.30$. Consideration of a range of ν values would result in a family of curves but the single value chosen was considered adequate for most applications involving common die steels.

A.1.2 Radial Resonance in a segmental Ring[71]

When an annular ring is considered as a series of discontinuous radial segments, the circumferential strain normally associated with a radial wave motion may be ignored. If we consider the stresses acting on an element dr in a segment of the ring, Fig. A.1.4, then assuming plane wave propagation, the steady state equation of motion can be written:

$$\sigma_r S - (\sigma_r + \frac{\partial \sigma_r}{\partial r} .dr)\ (S + \frac{\partial S}{\partial r})\ dr + F_m = 0 \quad \text{------ A.1.13}$$

where S is the cross sectional area of the segment at any radius r and Fm is the oscillatory driving force applied to the element dr.

If as before, we assume simple harmonic motion then we may write:

$$Fm = m\frac{\partial^2 \xi_r}{\partial t^2} = S\rho.dr.\ \frac{\partial^2 \xi_r^2}{\partial t^2} = -S\rho.dr.\omega^2 \xi_r$$

and substitution in equation A.1.13 gives:

$$-\sigma_r \frac{\partial S}{\partial r} .dr - S\ \frac{\partial \sigma_r}{\partial r}\ .\ dr - (\frac{\partial \sigma_r}{\partial r}\ .\frac{\partial S}{\partial r}.dr^2) = -S\rho.dr\omega^2 \xi_r$$

where ξ_r is the radial displacement of an element at radius r. Ignoring products of small increments this may be rewritten:

$$-\sigma_r \frac{\partial S}{\partial r} - S\frac{\partial \sigma_r}{\partial r} = -S\rho.\omega^2 \xi_r \quad \text{---------- A.1.14}$$

Substituting $\sigma_r = E\frac{\partial \xi_r}{\partial r}$ and $\frac{\partial \sigma_r}{\partial r} = E\frac{\partial^2 \xi_r}{\partial r^2}$ into equation A.1.14 gives:

$$\frac{d^2 \xi_r}{dr^2} + \frac{d\xi_r}{dr}\ .\frac{dS}{dr}.\frac{1}{S} - k^2 \xi_r = 0 \quad \text{---------- A.1.15}$$

where $k = \frac{\omega}{C}$, and finally the wave equation is found by inserting the appropriate expression for the cross sectional area of a wedge, viz. S = r.θ.t. which gives:

$$\frac{d^2 \xi_r}{dr^2} + \frac{1}{r}.\ \frac{d\xi_r}{dr} + k^2 \xi_r = 0 \quad \text{----------A.1.16}$$

This is a Bessel equation of zero order having the general

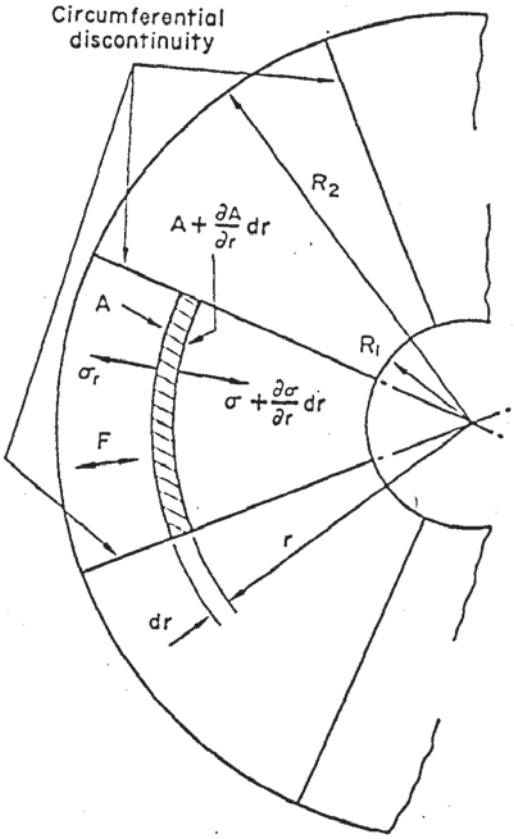

Fig. A1.4 Stresses acting on an element in a segmental annular ring.

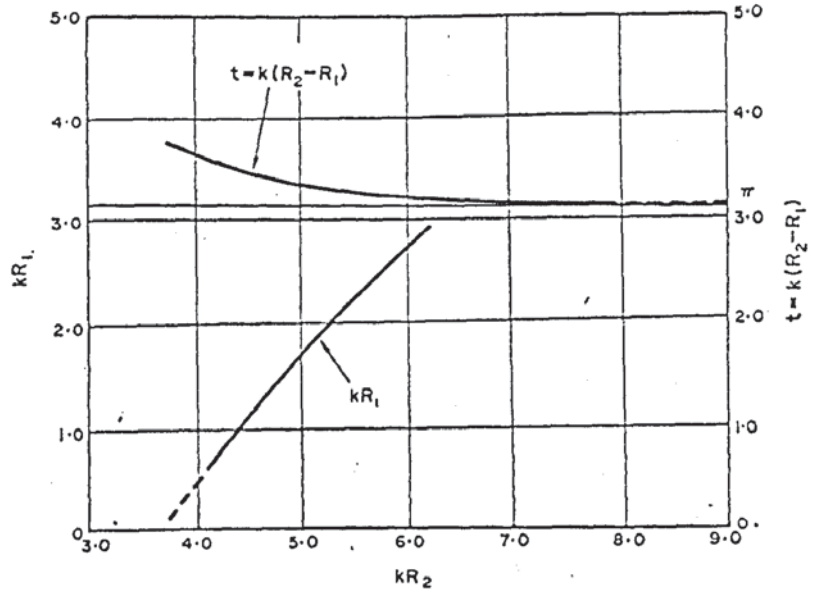

Fig. A1.5 Relationship between inner and outer radii for resonance in a segmental annular ring.

solution:

$$\xi_r = C_1 J_o(kr) + C_2 Y_o(kr) \qquad \text{---------- A.1.17}$$

where Jo and Yo are Bessel functions of the first and second kind zero order and C_1 and C_2 are arbitrary constants.

The particular solution for unloaded radial resonance may be found by considering the boundary condition: $\sigma_r = 0$ at the inner and outer ring surfaces, that is, when $r = R_1$ and $r = R_2$. This defines a state of zero stress at the free surfaces which are thus displacement antinodes.

Differentiating equation A.1.17 and equating to zero gives:

$$\frac{d\xi_r}{dr} = C_1 J_1(kr) + C_2 Y_1(kr) = 0 \qquad \text{---------- A.1.18}$$

and inserting the boundary conditions we have:

$$C_1 J_1(kR_1) + C_2 Y_1(kR_1) = C_1 J_1(kR_2) + C_2 Y_1(kR_2)$$

therefore $C_1 = \dfrac{-C_1 Y_1(kR_1)}{J_1(kR_1)}$

and $C_2 \left(Y_1(kR_2) - \dfrac{Y_1(kR_1) J_1(kR_2)}{J_1(kR_1)} \right) = 0$

and the boundary conditions are satisfied when

$$Y_1(kR_1 p) . J_1(kR_1) = Y_1(kR_1) . J_1(kR_1 p) \qquad \text{---------- A.1.19}$$

where $p = \dfrac{R_2}{R_1} > 1$

Equation A.1.19 may be solved graphically by plotting the functions $Y_1(kR_1 p) . J_1(kR_1)$ and $Y_1(kR_1) . J_1(kR_1 p)$ against p., for various values of kR_1.

This enables the values of R_1 and R_2 which satisfy equation A1.19 to be determined and the final solution may then be presented graphically, by plotting kR_1 against kR_2 as in Fig. A.1.5. Thus for any given value of k, having specified for example the inner radius, it is possible to determine the corresponding outer radius consistent with radial resonance.

The function $k(R_2-R_1)$, representing the ring width is also plotted against kR_2 in Fig. A1.5 and it will be seen that as the outer radius increases, the ring width tends towards the definite value π. That is, since the wave number, $k = \omega/C_r = 2\pi/\lambda$, $R_2 - R_1$ becomes equal to the half-wavelength in a parallel waveguide at the resonant frequency. Examination of the waveform given by the general solution to equation A.1.16 indicates the presence of the radial displacement node at an intermediate radius between R_1 and R_2 - Fig. A.1.6. It is possible to determine the nodal radius R_N from the boundary equation referred to above, by using either graphical or analytical techniques. The relationship between nodal position and inner radius R_1 is shown in Fig. A.1.7 by plotting $M = (R_2 - R_N)/R_2 - R_1)$ against kR_1. The parameter M clearly defines the position of the nodal ring and it can be seen that for high values of kR_1 and kR_2 it tends towards the mean ring radius. This corresponds to the limiting value of ring width $\lambda/2$, when a displacement node would therefore be expected at $\lambda/4$; that is, the mean radius.

Consideration of the general waveform, Fig. A.1.6 indicates that the displacement amplitude is increased at the inner radius, relative to that at the outer radius. Each segment of the ring therefore acts as a velocity transformer, which might be anticipated from the form of the wave equation. A vibrator based on this design therefore offers the possibility of producing greater radial displacement amplitudes than might be achieved in the continuous ring described in section A.1.3.

It should be noted that in adopting this solution it is important to ensure that the maximum circumferential wavepath is less than the half-wavelength of longitudinal waves in the annular material, i.e. $\theta < \frac{\lambda}{2R_2}$; where θ is the angular interval

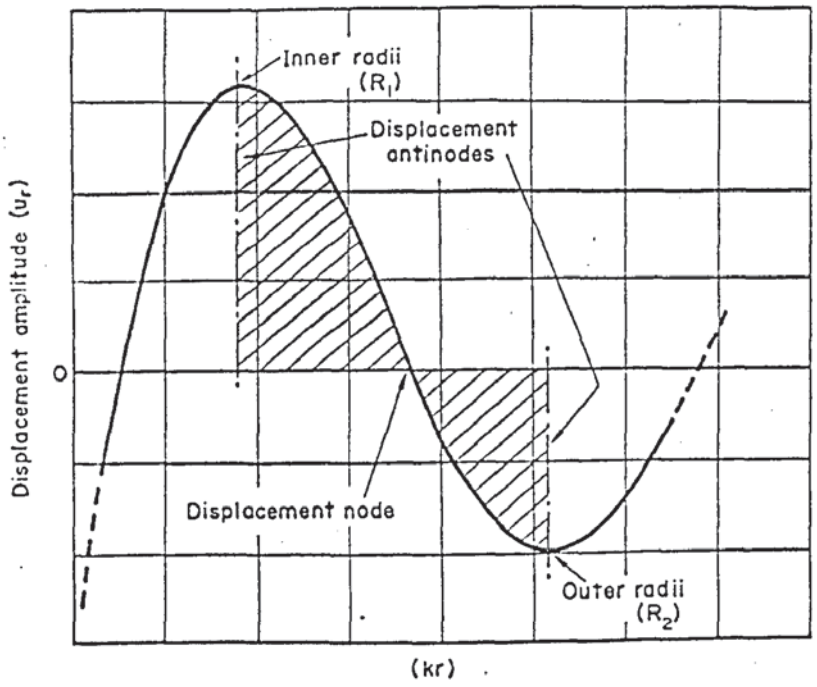

Fig. A1.6 Waveform of general solution to equation A1.16

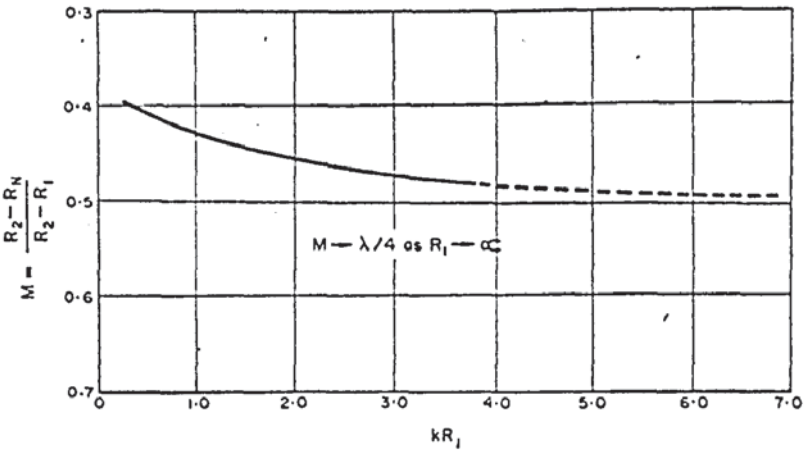

Fig. A1.7 Modal position in a radially resonant segmental ring.

between radial slots. If this criterion is not maintained the assumption of plane wave propagation in the ring segments becomes invalid.

A.1.3 Design of practical resonators.

Three designs of radial resonator were considered, the first two being based on the 'continuous ring' theory in section A1.1 and the third incorporating a segmental annulus, as discussed in the previous section. Resonators based on two of these designs were constructed in order to verify the predicted resonance conditions.

Diagrams showing these designs are given in Figs. A1.8 and A1.9. The first of these, Fig. A1.8(a), depends on the 'Poisson effect' at the displacement node of an exponential concentrator. Attachment of the flange is effected so that both inner and outer surfaces become radial displacement anti-nodes. The radial displacement amplitude of such a system however, is likely to be low in spite of the inherent axial amplification of the transformer, since the radial displacement depends on the transverse strain, which is reduced by comparison with the axial strain, in proportion to Poisson's ratio. An alternative design, also incorporating a continuous ring is shown in Fig. A1.8(b) and employs two cylindrical vibrators attached tangentially to a tuned disc such that acoustic energy at the appropriate frequency is transmitted to the disc, which then adopts its natural mode of vibration.

The third design was based on the segmental disc, Fig. A1.9 and in this system, acoustic energy was provided by a number of transducers attached to the outer periphery of the ring in a radial configuration.

A1.4 Experimental results.

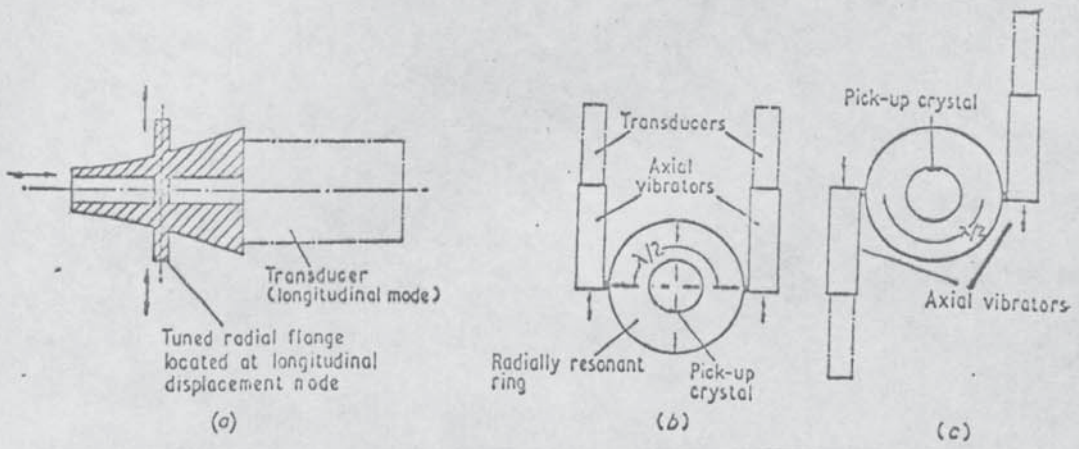

Fig. A1.8 Schematic illustration of radially resonant systems.
a) Mode conversion at a longitudinal displacement node.
b) Radially resonant ring with two axial vibrators driven in phase.
c) Radially resonant ring with vibrators driven in anti-phase.

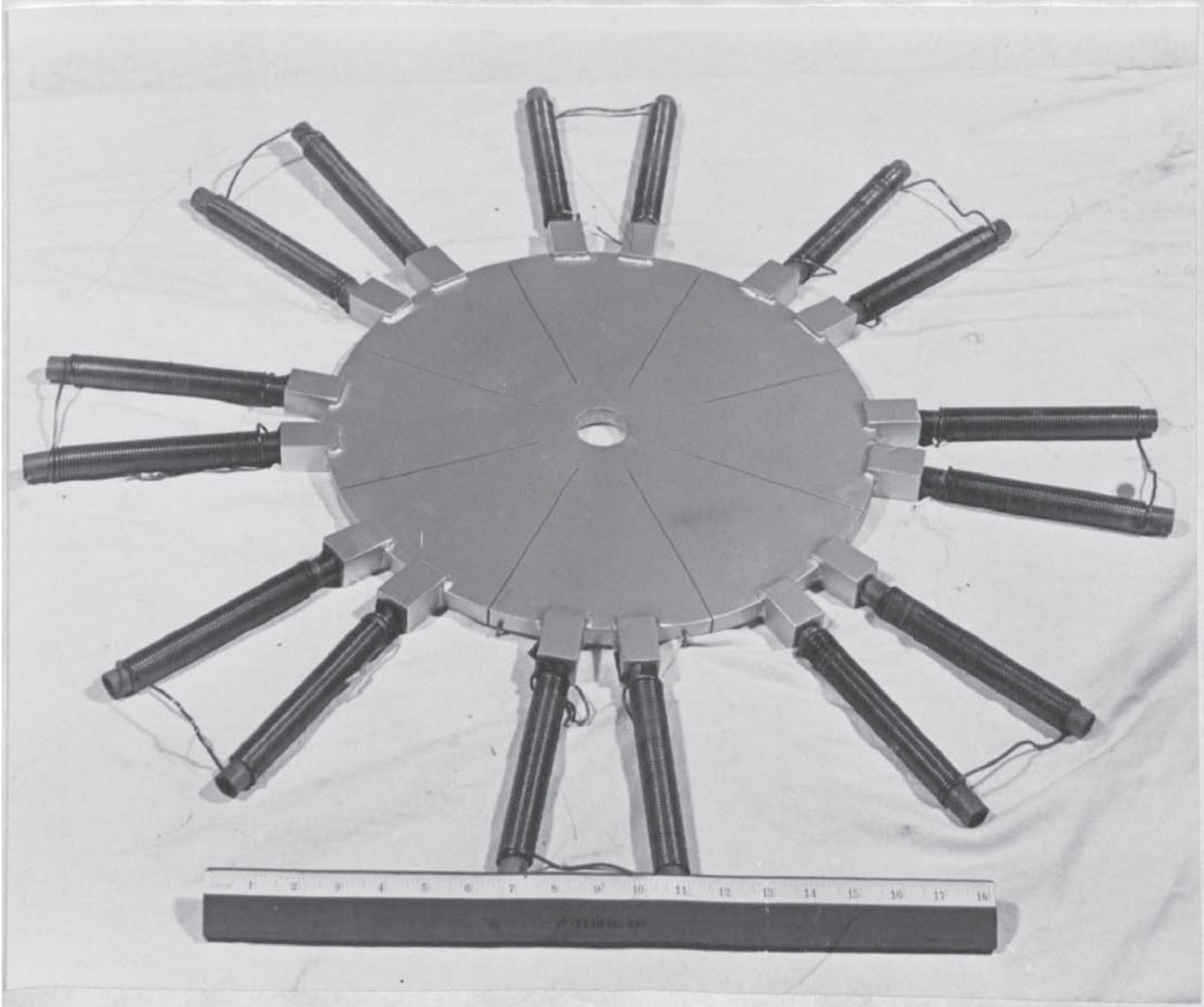

Fig. A1.9 Photograph of segmental resonator showing attached transducers.

A.1.4.1 Continuous-ring vibrator.

A resonator based on the design in Fig. A1.8(b) was constructed using mild steel for the disc and each of the cylindrical vibrators. The ring dimensions were selected in accordance with the accurate solution in Fig. A1.3. The inner radius R_1 was chosen arbitrarily as 2.0 in, which for the appropriate wave number k gave the corresponding outer radius R as 2.98 in, (compared with 3.10 in. for the simplified approximation). The disc thickness was 0.75 in. Laminated nickel stack transducers were attached to the free ends of the cylindrical vibrators using threaded connections and each assembly was then welded onto short radial stubs protruding from the outer surface of the disc, (Fig. A1.8 (b)). Electrical power was provided by a manually tuned 3 kw valve generator. The frequency was measured using a digital counter and radial resonance detected by observation of the output voltage from a Mullard type MB1048 piezoelectric crystal, cemented to the inner surface of the disc, Fig. A1.8(b). The resonant frequency of the system was found to be 13.46 kHz, which agreed closely with the calculated value of 13.30 kHz.

The mode of vibration in the annular ring was examined qualitatively by observing the movement of fine powder sprinkled on the horizontal surface. Some departure from a pure radial motion was noted in the region of the vibrator attachment points and it is considered that secondary vibrational modes, associated with the geometry of these junctions contributed to the discrepancy between calculated and measured values of the resonant frequency. Such a phenomenon might be anticipated since the theoretical model considers only the annular disc in isolation; no allowance was made for the attachment of the driving system.

The simplified approximation defining radial resonance was

found to contribute to an understanding of the physical situation in the system described above. It is apparent that symmetrical attachment of the axial vibrators driven from the same power source as shown in Fig. A1.8(b) results in their being spaced at a distance $\frac{\lambda}{2}$ apart. This introduces a 180-degree phase shift between the oscillatory waves transmitted to the ring from the two vibrators. If these are attached in the manner shown in Fig. A1.8(b) the respective waves are complementary and reinforcement occurs resulting in a radial standing wave. However, when one of the axial vibrators is reversed, Fig. A1.8(c), radial resonance does not occur in the annulus. In order to obtain a standing wave in the latter case it is necessary to drive the vibrators from separate power sources with a 180-degree phase difference.

A.1.4.2 'Segmental -ring' vibrator.

A resonator based on the solution derived in section A1.2 was constructed using a $\frac{5}{8}$in. thick mild steel plate, Fig. A1.9. The inner diameter was chosen arbitrarily as 1.50 in. and using the design curve in Fig. A1.5 for a required resonant frequency of 18 kHz, the corresponding outer diameter was found to be 14.75 ins. In accordance with the assumptions made in this analysis the ring was divided into eight equal segments by machining radial slots from the outer periphery, to within 1.5 in of the inner radius. Laminated nickel alloy transducers were then attached at the outer periphery, as shown in Fig. A1.9. These were screwed into lugs of 1.0 in. square section which were brazed onto each segment of the ring as indicated. The transducer coils were then wired in series and connected to the 3 kw generator. Initial tests failed to produce resonance in the ring within the frequency range of the generator. It was decided therefore, to extend the radial slots symmetrically

towards the inner periphery. Resonance was achieved at a frequency of 22 kHz when the slots were within 1.0 in. of the inner circumference. The vibrational mode was examined using fine powder sprinkled over the surface of the ring which was resting on a horizontal surface. The general particle motion indicated maximum displacement at the inner radius, in a substantially radial direction. There was however, a noticeable torsional component within the continuous ring near the inner periphery.

A.1.4.3 Conclusion

Within the scope of these limited experiments it was concluded that both designs examined could be developed into useful practical resonators. The segmental ring produced greater displacement amplitudes at the inner radius but presented difficulties in predicting the resonant frequency with sufficient accuracy. Unless the analysis is modified to take account of the circumferential strain in the central ring final tuning adjustments are necessary, involving adjustment of the machined slot lengths or inner and outer diameters.

Appendix II

Calculation of Concentrator Dimensions.

A2.1 Determination of gain: $\frac{\dot{\xi}_{ml}}{\dot{\xi}_{mo}}$

The gain of a conical horn is given by:

$$\frac{\dot{\xi}_{ml}}{\dot{\xi}_{mo}} = N(\cos k1 - \frac{N-1}{Nk1} \sin.k1) \quad \text{----------}$$

For a value of N = 9 this may be evaluated using the equivalent value of k1 determined by interpolation in the graph of Fig. 4.11, viz. k1 = 4.03.

and $\frac{\dot{\xi}_{ml}}{\dot{\xi}_{mo}} = 9(-0.629 + \frac{8}{36.27} \times 0.77)$

$= \underline{4.12}$

A2.2 Determination of concentrator length:

From the value of k1 in A.2.1 above, l is given by:

$$l = \frac{4.03}{k},$$

where $k = \frac{2\pi}{\lambda} = 0.419$

$\therefore l = \underline{9.61 \text{ in}}$

A2.3 Determination of included angle β;

The radius of the wide end of the horn, R_1, was fixed at 5.0 in and since $N = R_1/R_2 = 9$, (where R_2 is the radius of the narrow end), $R_2 = \frac{5.0}{9} = 0.556$ in.

and $\beta = 2.\tan^{-1} \frac{(R_1 - R_2)}{(21)}$

$\beta = \underline{26^\circ}$

Appendix III

Heat Treatment of Wedge Drawing tools and Concentrators

(All machined from Carr's P552 alloy steel)

A3.1 Component heat treatment

Component	Heat treated condition
1. Blank holder plates and wedge drawing dies	Hardened and tempered to Rockwell C45. Case hardened to Rockwell C54/56.
2. Concentrators and mounting rings	Heat treated to 60 tonf/in^2 U.T.S.
3. Hydraulic blank holder assembly	Cylinders and load cells hardened and tempered to 100/110 tonf/in^2 U.T.S. Remaining components tempered to 60 tonf/in^2 U.T.S.
4. Punch assembly	Hardened and tempered to 100/110 tonf/in^2 U.T.S.
5. Load cells	Hardened and tempered to 110/110 tonf/in^2 U.T.S.

A3.2 Heat treatment procedure

A3.2.1 Hardening treatment.

(i) Soak at 300/400^{o}C - 1 hour per inch of ruling section

(ii) Raise temperature to 820/830^{o}C and maintain at temperature for a sufficient time to allow the tools to 'equalise'.

(iii) Oil quench and temper immediately, whilst still hand warm.

A3.2.2 Tempering treatment

100/110 tonf U.T.S. Temper at 150/200°C

60 tonf U.T.S. Temper at 550/650°C

A3.2.3. Case Hardening (cyanide bath)

Pre-heat to 300/400°C and soak thoroughly.

Immerse in cyanide bath at 830°C, allow to equalise and soak for two hours.

Cool in still air and temper immediately tools are hand warm.

Tempering: Heat to 200°C and soak for one hour per inch of ruling section. This gives a hardness of Rockwell C54/56.

A.3.3 Nominal Composition of tool steel

C	Mn	Ni	Cr	Mo
0.30	0.50	4.25	1.25	0.30

Appendix IV

Determination of the mounting plate dimensions.

The fundamental frequency of flexural mode vibrations in a circular plate clamped at its outer edge is given by the following equation.(76)

$$fo = 1.88 \frac{h}{D^2} \sqrt{\frac{E}{\rho(1 - \nu^2)}} \qquad \text{---------- A.12}$$

Where E is the modulus of elasticity, ρ the density, ν Poisson's ratio and h and D the thickness and diameter respectively.

For use in overtone modes the natural frequencies are:

fo, 3.88 fo, 8.8 fo.

Overtone operation permits the location of the actual point of support far from the centre of the disc and also the use of quite large diameter oscillatory systems.

In the present design the diameter of the concentrator at the longitudinal displacement node is 3.50 in and for maximum efficiency this should coincide with a flexural antinode in the disc. This will ensure that minimum damping will occur in a partially travelling wave regime.

Since the frequency of operation is fixed at 13 kHz only the thickness h, can be varied in order to find an acceptable value of D, the disc diameter.

This was calculated for three thicknesses, $\frac{1}{8}$ in., 3/16 in. and $\frac{1}{4}$ in., deliberately made small in order to minimise transmission losses at the outer mounting plane. In each case the appropriate diameter was determined for 1st and 2nd overtone operation.

The results of these calculations are given in Table A4.1 which also indicates the position of the first antinodal line for reference to the attachment diameter of the concentrator.

Table A4.1

Relationship between thickness and diameter for flexural resonance in a circular plate clamped at the outer periphery. (frequency: 13 kHz)

h	overtone mode	D ins	Position of antinode, in *
	fo	1.94	)
$\frac{1}{8}$ in.	3.88 fo	3.82	) ---------- 2.88
	8.8 fo	5.75	)
	fo	2.37	)
3/16 in.	3.88 fo	4.67	) ---------- 3.52
	8.8 fo	7.04	)
	fo	2.74	)
$\frac{1}{4}$ in.	3.88 fo	5.39	) ----------4.06
	8.8 fo	8.12	)

* The mid-point between 1st and 2nd nodal planes is taken as a first approximation to the antinodal plane.

From the above table it will be seen that the conditions are quite accurately fulfilled by a mounting flange of 7.04 in. dia. and 3/16 in. thick.

Appendix V

Calibration of Instruments

A.5.1 Punch load cell.

Calibration of the punch load cell was carried out using the 1 tonf range of a 50 tonf Denison mechanical testing machine. The Avery machine on which the sub-press was mounted would have been ideal, but the lowest range was 5 tonf which was not considered sufficiently accurate. The punch assembly was therefore placed between the bottom plate and fixed cross head of the testing machine and the D.C. Supply switched on. After allowing 30 minutes to achieve steady state conditions, a compressive load was applied in 0.05 tonf increments upto a maximum of 0.40 tonf and then successively reduced in similar steps. The deflection of the galvanometer in the U/V recorder was noted at each load setting during the complete cycle. This procedure was repeated six times to ensure reproducibility
A typical calibration curve showing both loading and unloading results is shown in Fig. A5.1.

A.5.2 Blank holder load cells.

The blank holder cylinders with integral load cells were calibrated on the Denison machine in a similar manner to that described above. Some difficulty was experienced however, with non-axial loading due to slight warping of the mounting flanges during heat treatment. It was therefore decided to reduce the contact area of the upper flange surface, by machining from the outer periphery until an annular ring $\frac{1}{8}$ in. wide remained at the centre. This not only corrected the distortion, but by shortening the radius, reduced any bending moment caused by slight misalignment of the cylinder body in its seating. Calibration curves for the left and right hand blank holder load cells are given in Fig. A5.2. An in-situ calibration check was carried out, with the complete blank

holder assembly mounted in the sub-press, using the hydraulic power unit. The common line pressure, indicated by a bourdon gauge, was varied in 100 lbf/in^2 steps, and the corresponding galvanometer deflections noted during loading and unloading. Using the calibration curves in Fig. A5.2 two further graphs were obtained by plotting blank holder force against line pressure. These curves were then compared with the calculated blank holder force/line pressure relationship based on the piston area. This is shown superimposed on the individual blank holder curves in Fig. A5.3. This test showed that the blank holders were evenly loaded over the working range of line pressures and that the pressure gauge was apparently giving a reading which was approximately 10 per cent high. The zero effect on the blank holder force curves was attributed to friction associated with the piston seals.

A.5.3 Master load cell calibration.

The load cell, shown in Fig. 5.17, was calibrated in tension using a Denison dead weight testing machine. In order to avoid damage and also to facilitate gripping in the sliding jaws of the test machine, the hardened ground plates were replaced by identical members machined from mild steel bar.

The bridge leads were connected to the instrumentation shown in the circuit diagram of Fig. 5.21. The DC bridge input was set at 15 volts, which for an amplification factor of X5000 on the DC amplifier, gave a satisfactory galvanometer deflection for loads of the order of 100 lbf. After allowing sufficient time for steady state conditions to be achieved in instrumentation, load increments of 20 lbf were applied, upto a maximum of 160 lbf, and the galvanometer deflection noted during both loading and unloading. The test was repeated

several times to ensure reproducibility; a typical calibration curve being given in Fig. A.5.4.

A.5.4 Friction Load Cell Calibration.

In order to calibrate the friction load cell under the same conditions of loading as experienced in the wedge test, the subpress was assembled without the conical horns and wedge dies and the master load cell positioned between the blank holder plates and die thrust blocks as shown in Fig. 5.18a. The two bridges were then connected to their respective instrumentation circuits, and allowed to warm up before commencing the calibrations test. Testing was carried out at blank holder line pressures of 400 and 800 lbf/in^2 to ensure that variation in the blank holder force did not influence the friction load cell signal. The bridge output from the friction load cell, master and blank holder load cells were monitored on the u/v recorder throughout the calibration tests.

With the blank holder pressure held constant, the master load cell tensioning sleeve was rotated, thus inducing a frictional force at the interface between the blank holder plates and the upper surfaces of the hardened steel strips, attached to the master load cell. The resulting compressive force between the blank holder plates was applied to the friction load as described in Section 5.5.3. The load cell tension was increased in small increments until slipping occurred between the adjacent surfaces. In subsequent tests, the tension was unloaded before reaching this point thus providing calibration data for loading and unloading. The test was repeated several times with the blank holder pressure at 400 lbf/in^2 and then at 800 lbf/in^2. Calibration data was extracted from the resulting u/v recorder traces using the master load cell calibration relationship determined previously. Fig. A.5.5 shows the

Punch load cell calibration curve. Fig. A5.1

Galvanometer no. A/2411. (Calibration factor: 11.9)

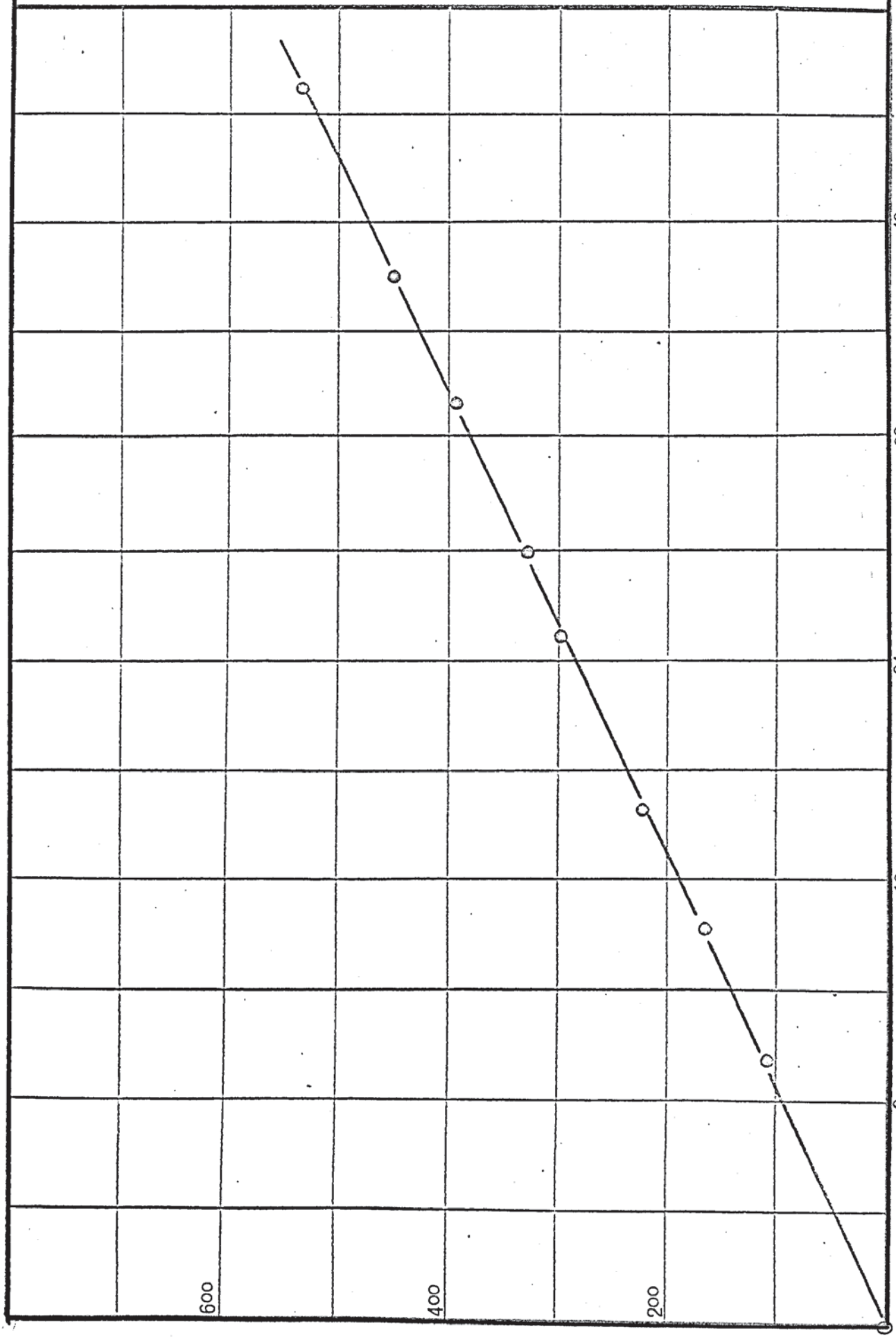

Blank holder load cell calibration curves. Fig. A5.2

Galvanometer nos. left hand A 2418
right hand A 2404

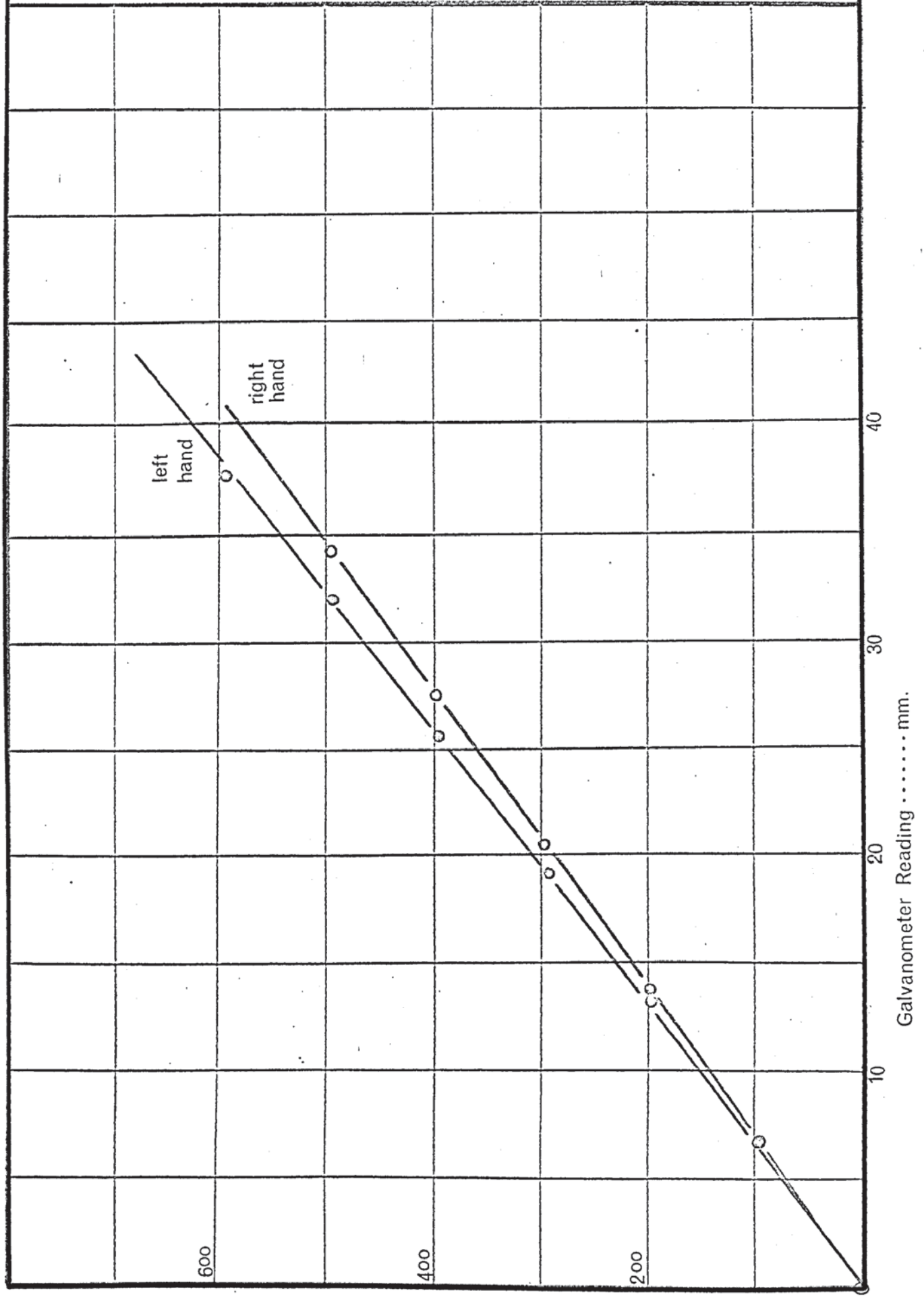

In-situ calibration of blank holder load cells. (Calibration factors - L/H - 15.8)
R/H - 18.3)

Fig. A5.3

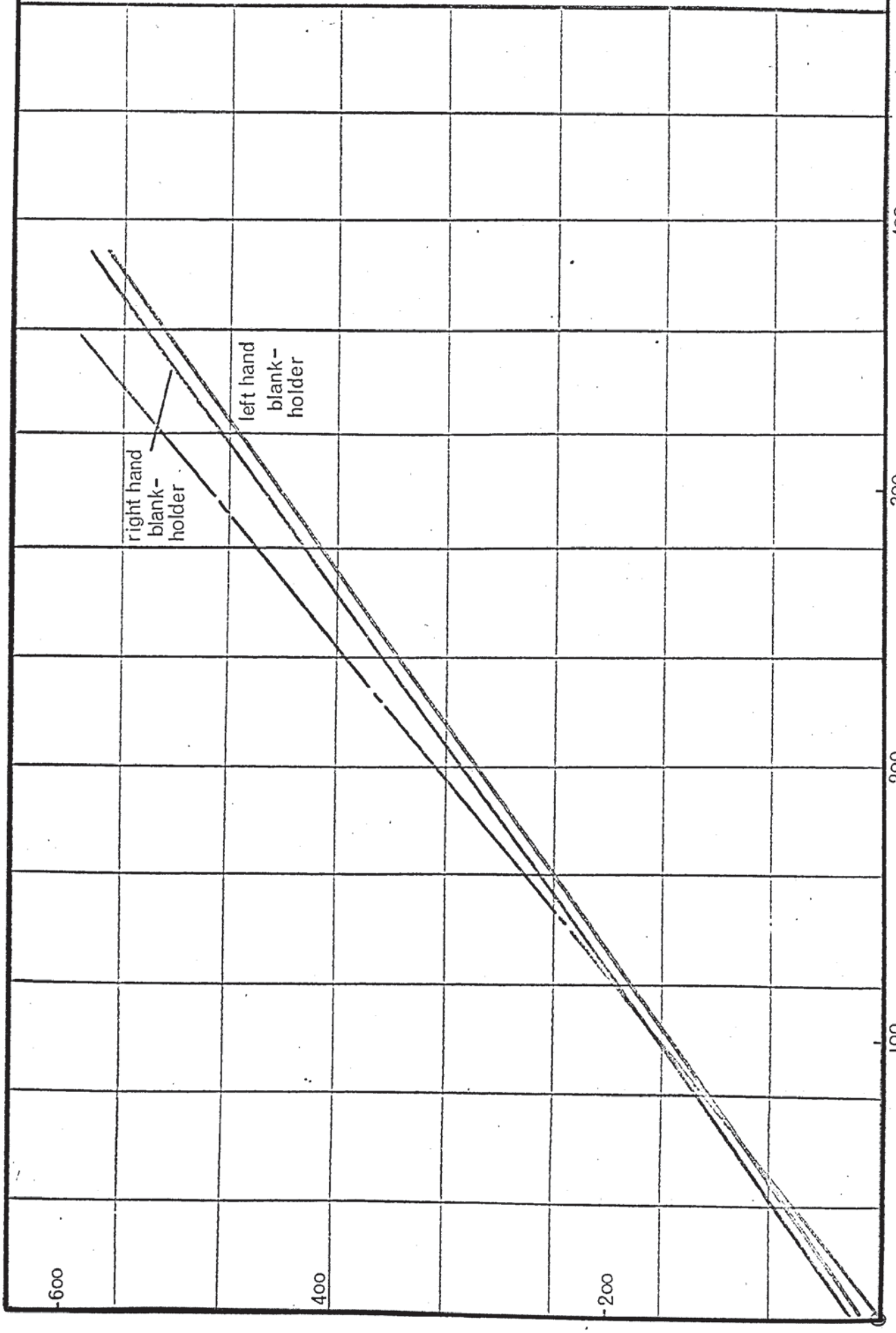

Master load cell calibration curve. Fig. A5.4

Galvanometer no. B880 (Calibration factor 1.42)

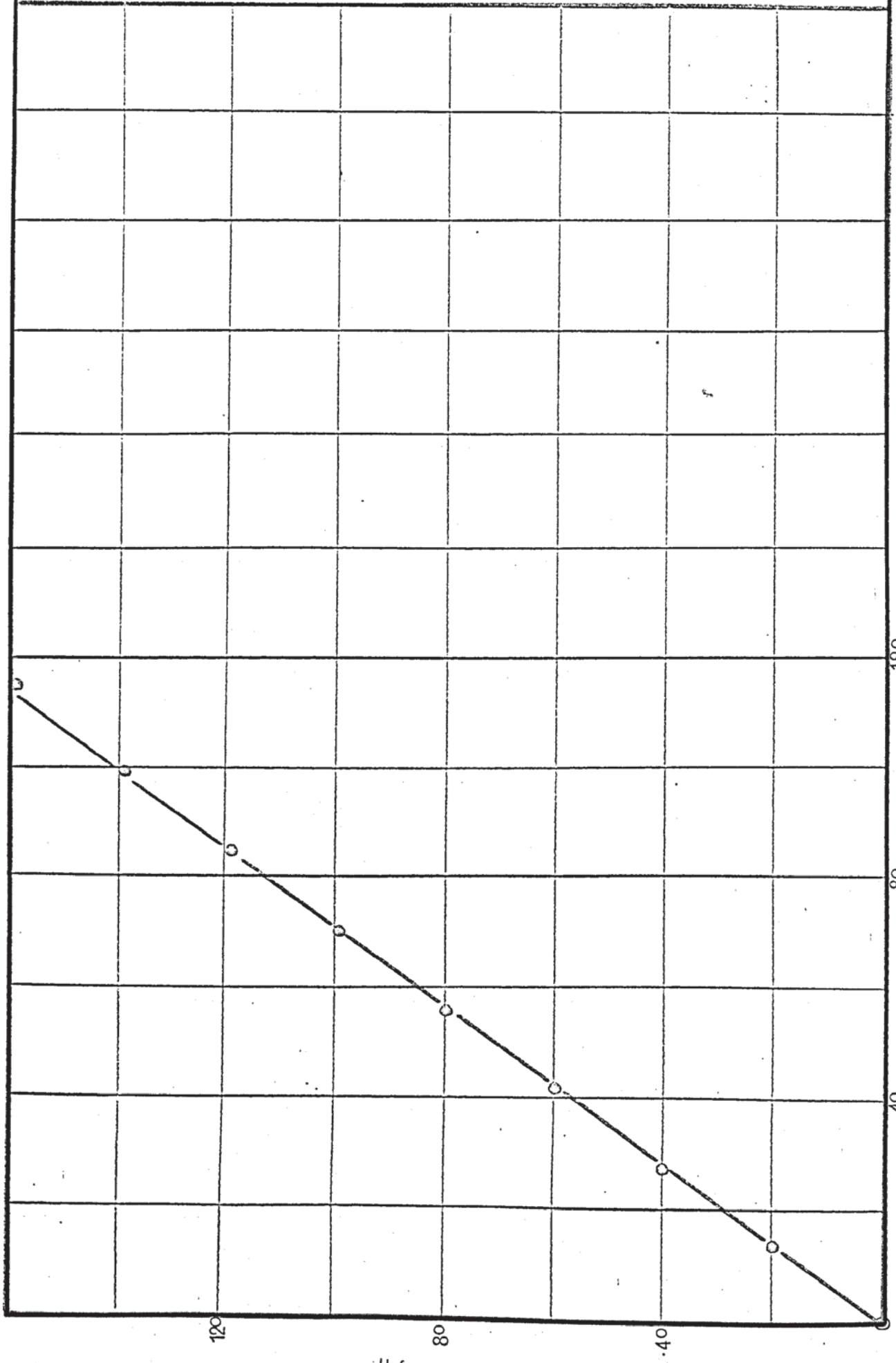

Friction load cell calibration curve. Fig. A5.5

Galvanometer no. MA 129 (Calibration factor 2.23)

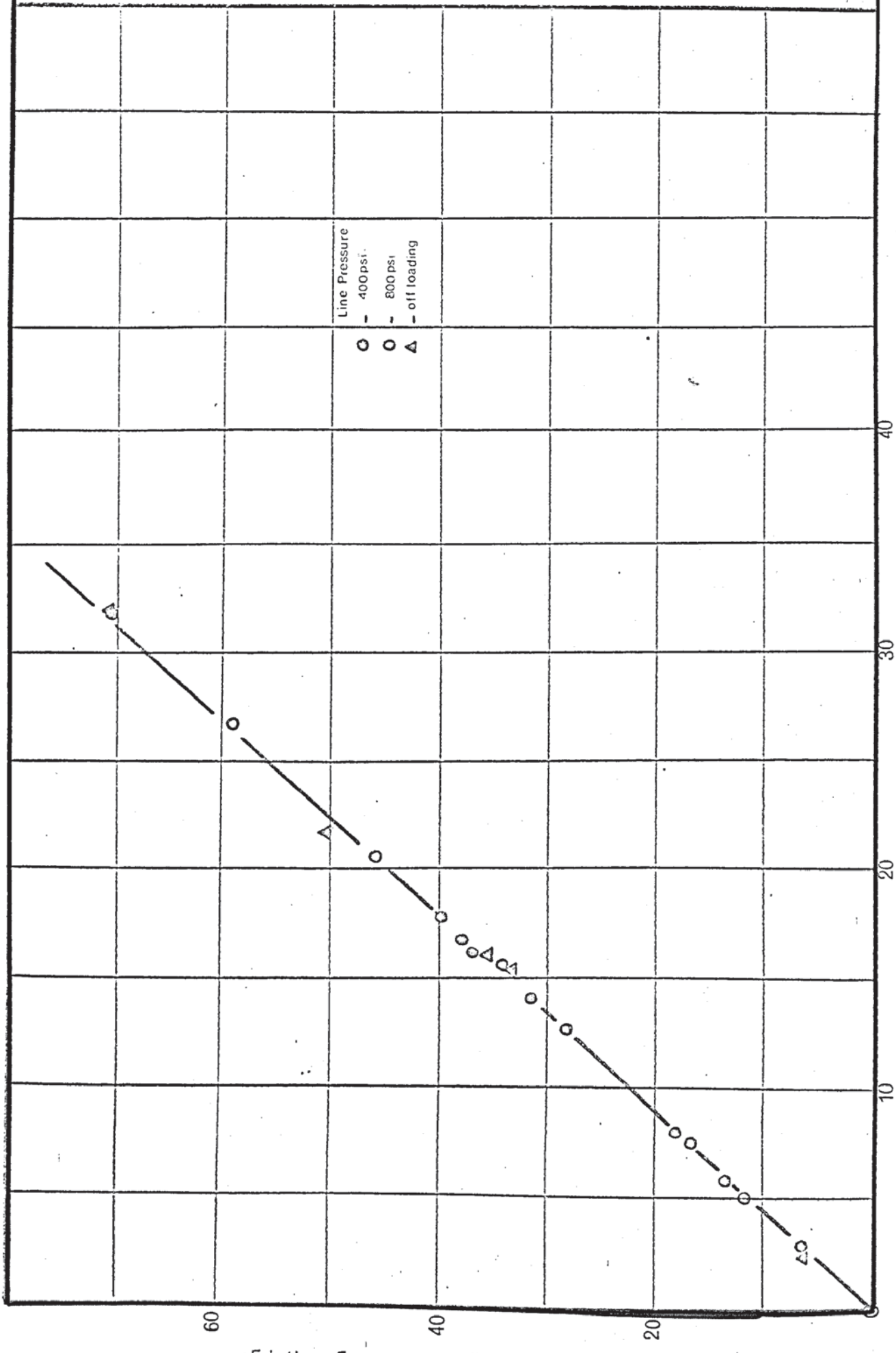

superimposed data from these tests and indicates a linear calibration relationship for the friction load cell, which was independent of blank holder pressure over the range 0 - 800 lbf/in^2.

A.5.5 Calibration of die Motional Sensors.

The most direct and perhaps the simplest method of calibrating the die motional amplitude pick-ups, was by an optical technique using a conventional metallurgical microscope. Such an instrument was modified by attaching the optical column, to a stage specially constructed so that it could be secured by a magnetic clamp to the upper thrust plate of the sub-press. This permitted direct calibration measurements to be taken under operating conditions. The microscope was fitted with a x 40 objective lens and a micrometer eyepiece incorporating a x 10 lens. Fig. A5.6 shows the complete instrument in position, with the objective lens inserted through the inspection slot in the sub-press frame. The micrometer eyepiece contained two parallel cross wires, one fixed and one which traversed the eyepiece field in response to rotation of the micrometer barrel, the distance between the cross wires being indicated by the micrometer reading.

In order to obtain an accurate measurement of the motional amplitude at the end of wedge dies, small pieces of polished stainless steel strip were cemented onto the side of each tool. These were prepared using standard metallurgical polishing techniques, finishing with 1 micron grade diamond paste which produced a highly reflective surface. A series of fine scratches was made on each mirror by lightly drawing a razor blade over the surface, and the mirrors mounted so that the scribed lines were perpendicular to the horn axis. The thickness of the lines was measured with the microscope and

micrometer eyepiece and found to be 5×10^{-6} ins.

It should be mentioned at this stage that the microscope and micrometer eyepiece were calibrated against a standard 1mm grid subdivided into 100 divisions. The micrometer barrel was calibrated in 0.01 mm divisions, which in conjunction with the x 40 microscope objective lens enabled readings to be taken, to the nearest half division, with an accuracy of 5×10^{-6} in.

The microscope and eyepiece calibration curve is given in Fig. A5.7.

Leads from the die-mounted piezo-electric crystals were connected to their respective milli-voltmeters and thence to the u/v recorder. The 'nodal' pick-ups were in turn connected to a twin channel oscilloscope for visual display and calibration of displacement amplitude against amplitudinal pick-up voltage. Calibration was carried out with the friction load cell in place, and the blank holder plates loaded, in order to maintain the same oscillatory conditions as during wedge testing. The resonant oscillatory amplitude of the dies was varied by altering the voltage of the high frequency power supply to the transducers, (this system is dealt with in detail in Appendix A.6). Under oscillatory conditions the fine grid of scribed lines on the stainless steel mirrors became blurred into a series of bands at right angles to the horn axis. The width of each band represented the peak to peak oscillatory amplitude at that particular transverse plane and since the variation of the motional amplitude over the end $\frac{1}{4}$ in. of the horn was negligible, this value was taken as the displacement amplitude of the end face of the horn. Peak to peak die amplitudes between 0.4×10^{-4} and 2.0×10^{-4} in. were measured for each horn and corresponding traces of the galvanometer deflections obtained with the AC milli-voltmeters set to the

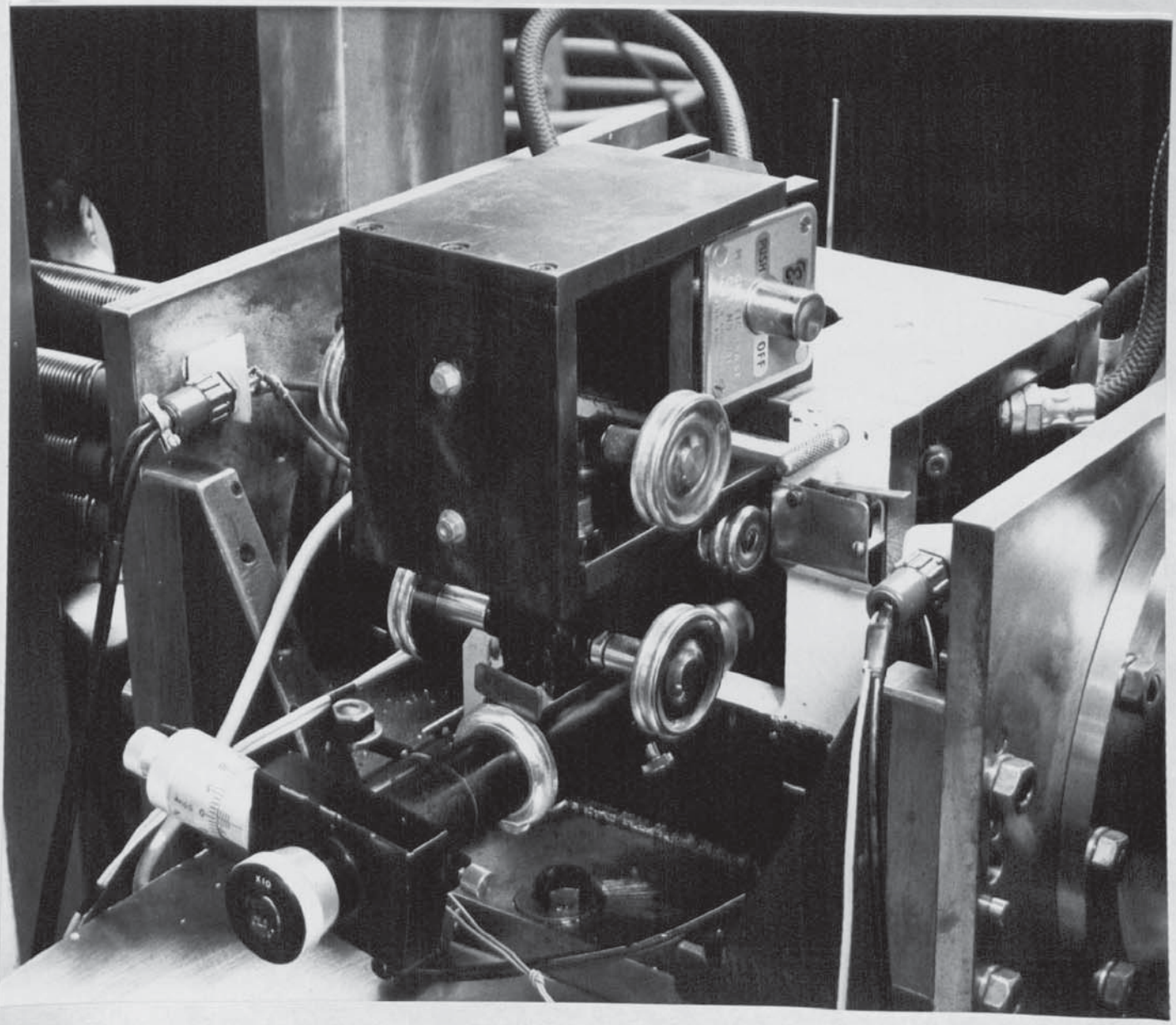

Fig. A5.6 Microscope used to calibrate the die mounted motional sensors.

Optical micrometer calibration. Fig. A5.7

Objective magnification; x 40

Eyepiece magnification; x 10

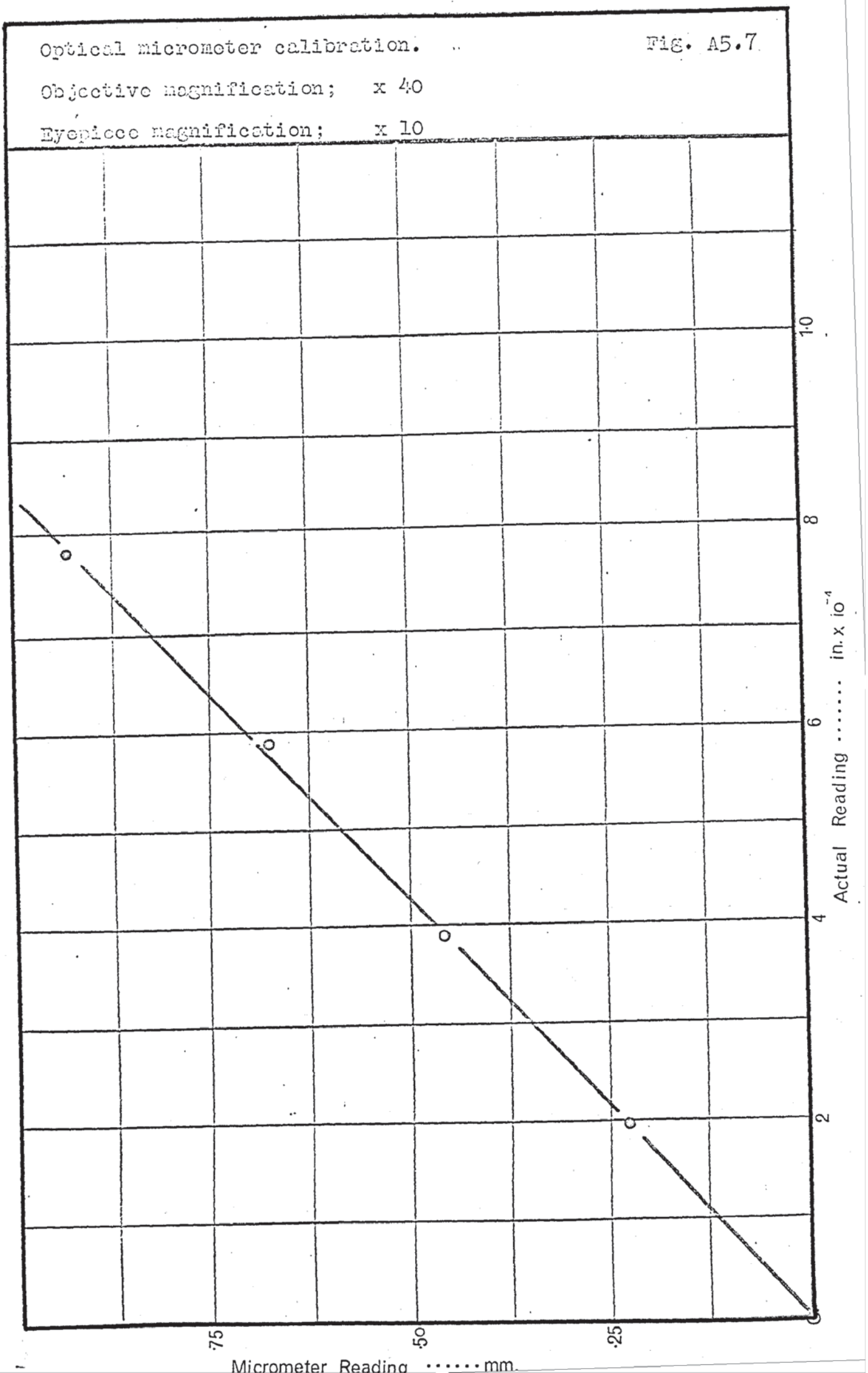

Die amplitude calibration curve. Fig. A5·8

Right hand vibrator

Galvanometer no. S511 (Calibration factor; 0.0885 x 10^{-5})

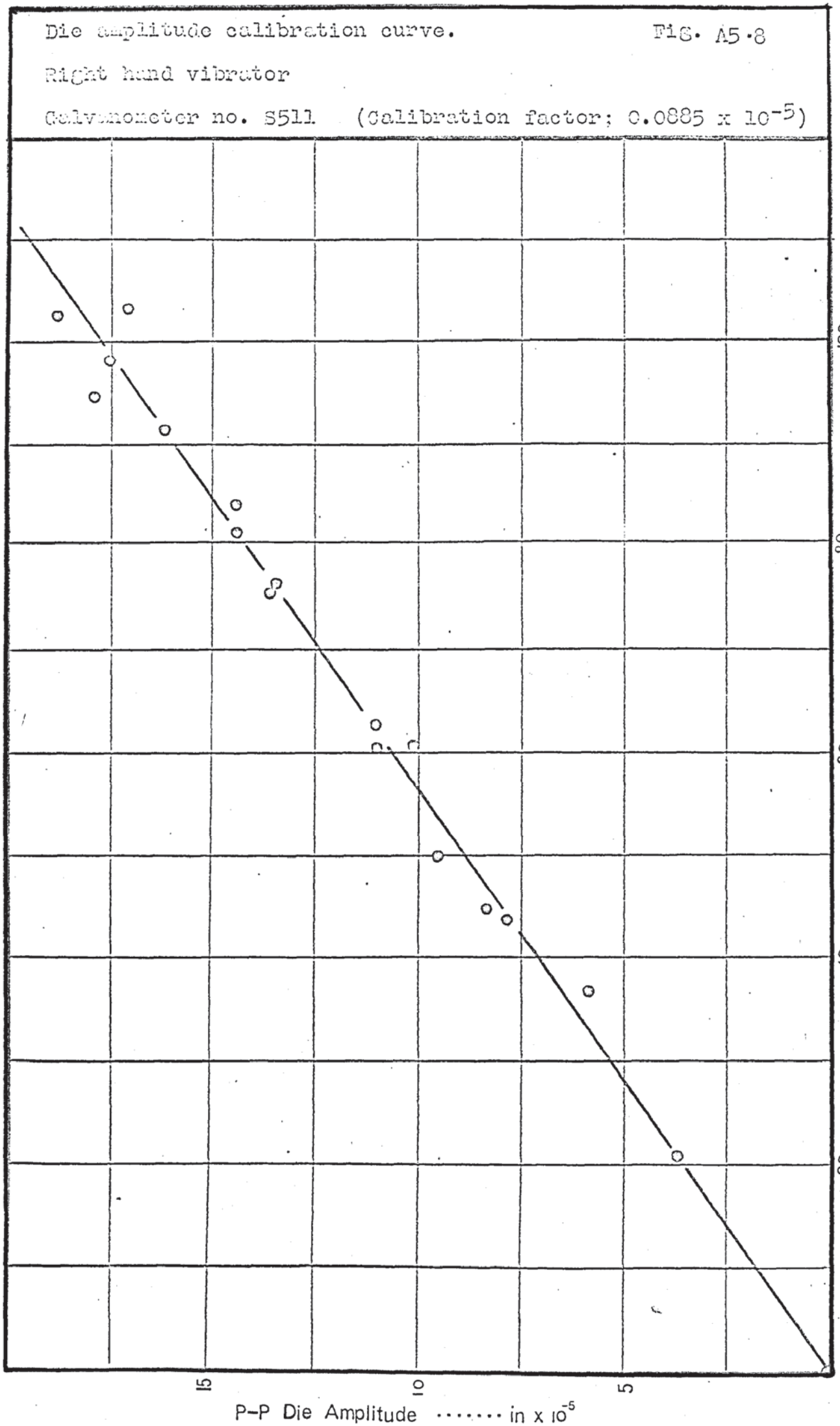

Die amplitude calibration curve. Fig. A5.9

Left hand vibrator

Galvanometer no. P466 (Calibration factor; 0.0925×10^{-5})

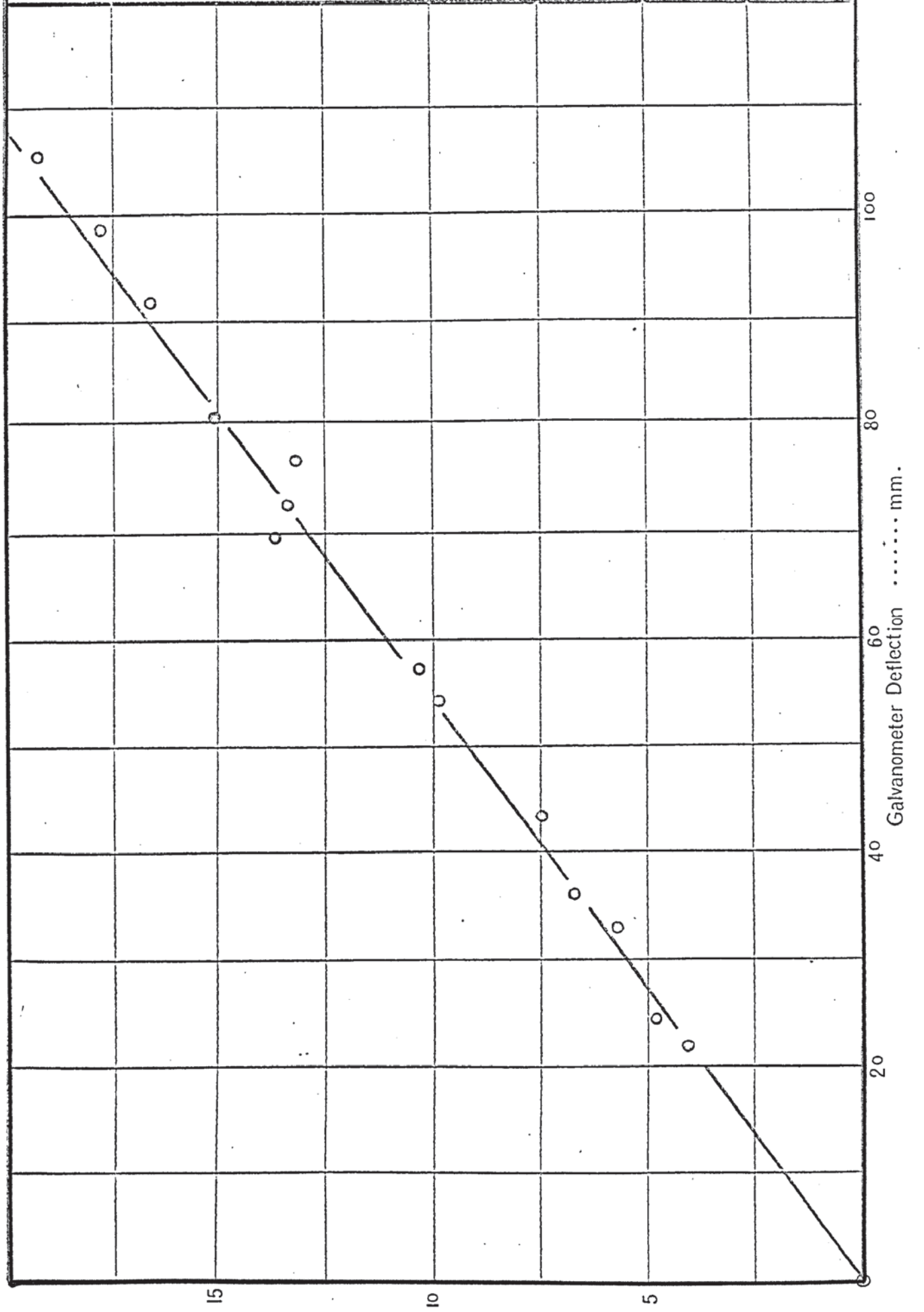

3 volt range. Records were also made of the amplitudinal voltage from the 'nodal' pick-ups, using the twin channel oscilloscope. During the tests minor tuning adjustments were required to accommodate slight changes in the resonant frequency of the system, related to variations in the transducer power input. The resonant frequency in fact varied between 12.85 and 13.04 kHz but this was not found to have a significant effect on the crystal output and the calibration curves for each die pick-up were linear. These are shown in Figs. A5.8 and A5.9.

A.5.6 Calibration of the punch displacement transducers.

The punch displacement transducer was calibrated by scribing a series of lines on the front face of the punch at intervales of 0.1 in. The first line was drawn to coincide with the top surface of the upper thrust plate when the punch was just in contact with an undeformed test piece placed between the dies. Subsequent movement of the punch was then monitored by observation of the progress of successive scribed lines through the punch access hole in the thrust plate. The output from the displacement transducer was simultaneously recorded and the corresponding punch motion noted on the recorder trace using the event marker facility. The calibration curve is shown for this instrument in Fig. A.5.10.

A.5.7 Calibration of the punch velocity transducer.

In order to obtain a significant range of punch velocities the main ram of the tensile testing machine was controlled using the fast return control valve. This gave a maximum velocity an order of magnitude greater than the fastest speed using the fine control valve. For ease of operation and in order to facilitate accurate selection of a given punch

Punch displacement calibration curve. Fig. A5.10

Galvanometer no. N661

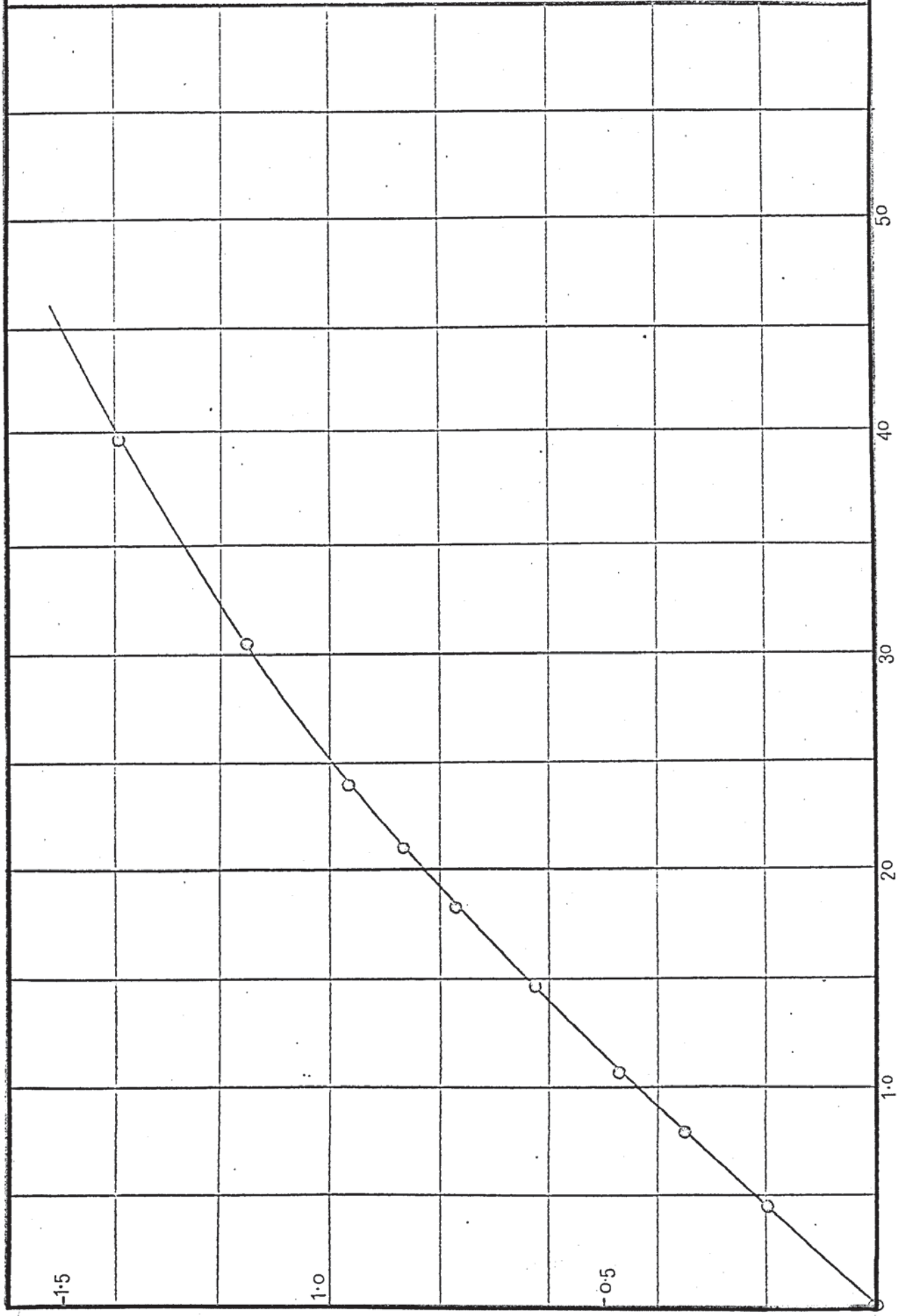

Calibration curve for punch velocity transducer. Fig. A5 .11

Galvanometer no. Z621 (Calibration factor; 0.014)

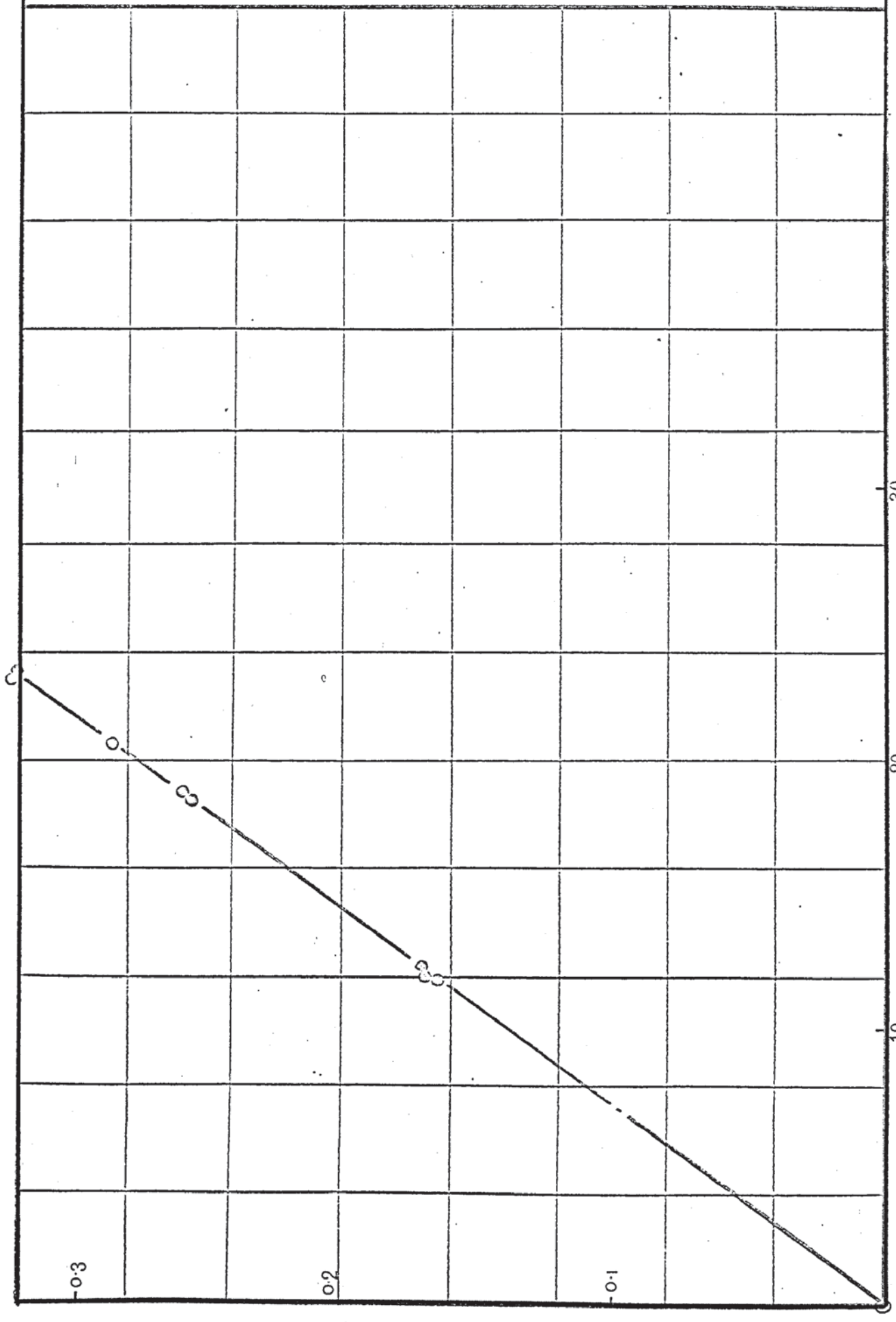

velocity a nine position selector was attached to the main control valve. This consisted essentially of a lever with a spring loaded ball attached at its midpoint, which located in a series of holes drilled in the back plate and disposed in an arc around the axis of rotation of the control lever. Each hole was numbered so that a given valve position could readily be selected. Calibration was carried out using the scribed lines on the punch, as described in the previous section and the time interval, corresponding to some convenient punch displacement, was measured; the transducer output was fed to a galvanometer of suitable sensitivity, in the u/v recorder. Measurements were taken at four positions of the valve selector switch and the velocity calculated from stop watch readings. The tests were repeated several times at each valve setting to ensure reproducibility of the valve position selector. The calibration curve produced from these results was linear as will be seen from Fig. A.5.11.

TABLE A5.1

Instrumentation

Instrument	Type	Serial No.	Make	Function	Associated Circuit
Recorder	Ultra-Violet P10-201	800	Southern Instruments	Load, Velocity and displacement monitoring	Strain gauge bridges and transducers
D.C. Amplifiers	M1266 Power supply:- M1267	-	Southern Instruments	Voltage amplification (load cells)	Strain gauge bridges
A.C. mV Meters 1.	VM 78M	01193	Advance Electronics	Oscillatory forces, tuned punch	Bridges and D.C. Amplifier
2.	VM 78A	426	Advance Electronics	R/H die amplitude	Piezo electric crystal mounted on die.
Valve volt meter	314	1117	Airmec	L/H die amplitude	Crystal P/U
Stabilised Voltage Supply 1.		2494	Farrell	Load cell input voltage	0-30V(Visual display 0.5 v calibrations)
2.		-	Nash & Thompson	Tuned punch load cell input	0-24V
3.		269	Nash & Thompson	Displacement Transducer	0-24V
Scope	02319	OS 25A	Advance Electronics	Vibration amplitude visual display	Piezo-electric crystals attached rear mounting plates of each concentrator.
Timer Counter	SC 3	00382	Advance Electronics	Indicating main generator frequency	-

TABLE A5.1 continued INSTRUMENTATION

Instrument	Type	Serial No.	Make	Function	Associated Circuit
Oscillator	TG 1507	5959	Level1	Travelling wave load cell calibrator	
Muirhead Tunable Filter	D-925-B	351965	Muirhead	"Noise" filter on punch velocity transducer.	

TABLE A5.2

DETAILS OF GALVANOMETERS

U.V. Recorder Channel	1	2	3	4	5	6	7	8	9	10	11	12
Galvo No.	A2404	Z621	A2411	P2563 -2	MA129		P466	M1182	A2468		S511	N661
Measureing Instrument	R/H blank holder load cell	Punch velo- city trans- ducer	Punch load cell	Osc. force load cell	Friction load cell		L/H die amp- litude pick- up		L/H blank holder load cell		R/H die amp- litude pick- up	Punch displace- ment trans- ducer

Appendix VI

Ultrasonic Generator

A.6.1 Oscillator Circuit

The oscillator and drive chassis circuit is shown in Fig. A.6.1. An EF91 RF pentode is employed as the oscillator valve and the output fed to an 807 beam power tetrode drive valve. An additional switched jack socket (c) was inserted in the grid circuit of the 807 in order that an external oscillator could be used when it was necessary to extend the frequency range of the generator. Normal control of the frequency was effected via VRI. This component was mounted on a separate control panel close to the testing machine, for convenience. By adjusting the values of VRI and R12 the frequency range of the oscillator was increased to cover the 8 kHz to 16 kHz band, which adequately catered for most experimental configurations encountered in the design of radial and axial resonators. A coaxial socket was also connected to the 807 control grid which provided a convenient output for frequency monitoring, (B). During initial tests some form of feed back system was attempted in order to improve the tuning characteristics of the vibrators. The output from one of the 'nodal' pick-up crystals attached to the conical horns was connected at socket (A) via a 100 k ohm series resistor into the anode circuit of the oscillator. The appropriate point between capacitances C8 and C11 was determined by comparison of the voltage phase with that of the pick up crystal. Although this system improved the 'locking in' response of the vibrators at their resonant frequency it was difficult to maintain an equal motional amplitude in each horn due to slight differences in the resonance characteristics of the vibrators and also to the fact that the feed back signal was related

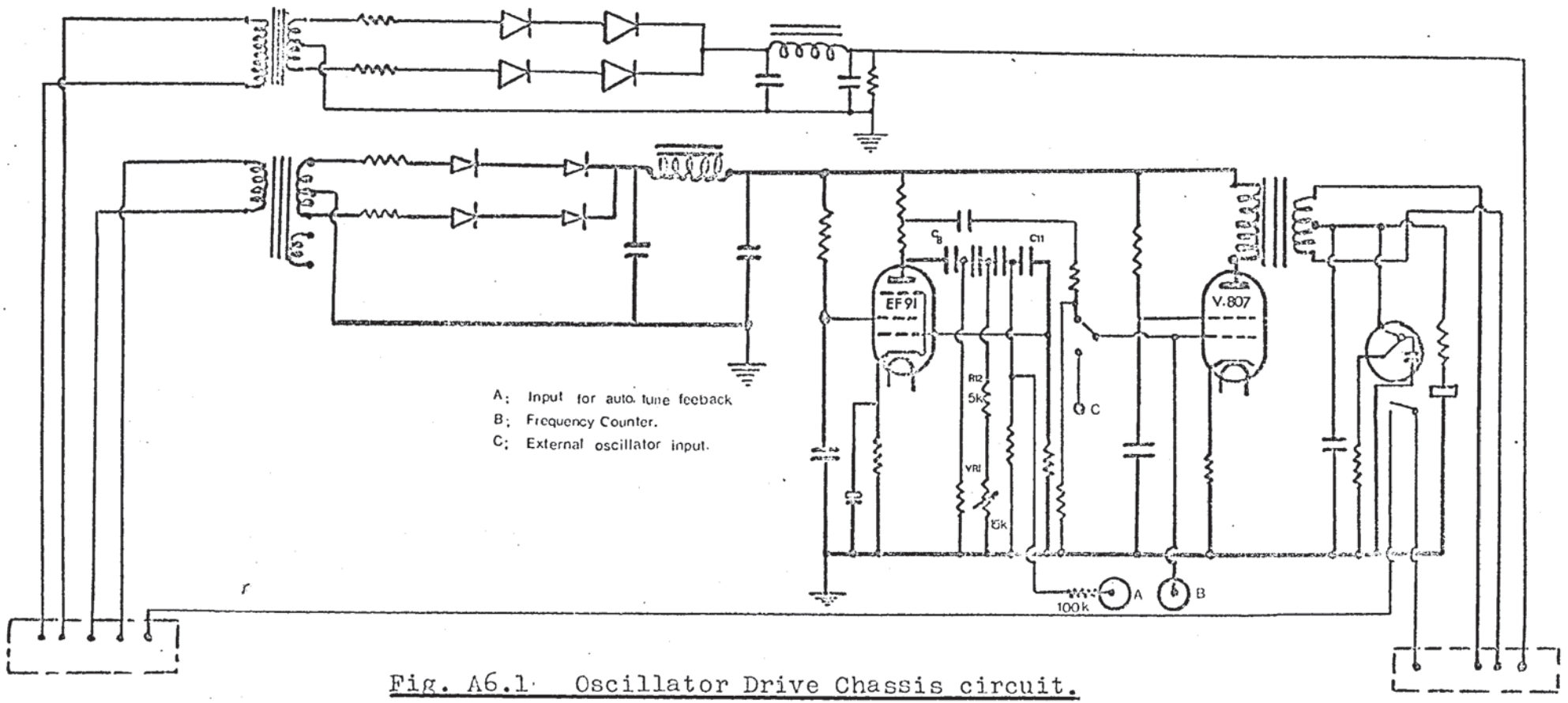

Fig. A6.1 Oscillator Drive Chassis circuit.

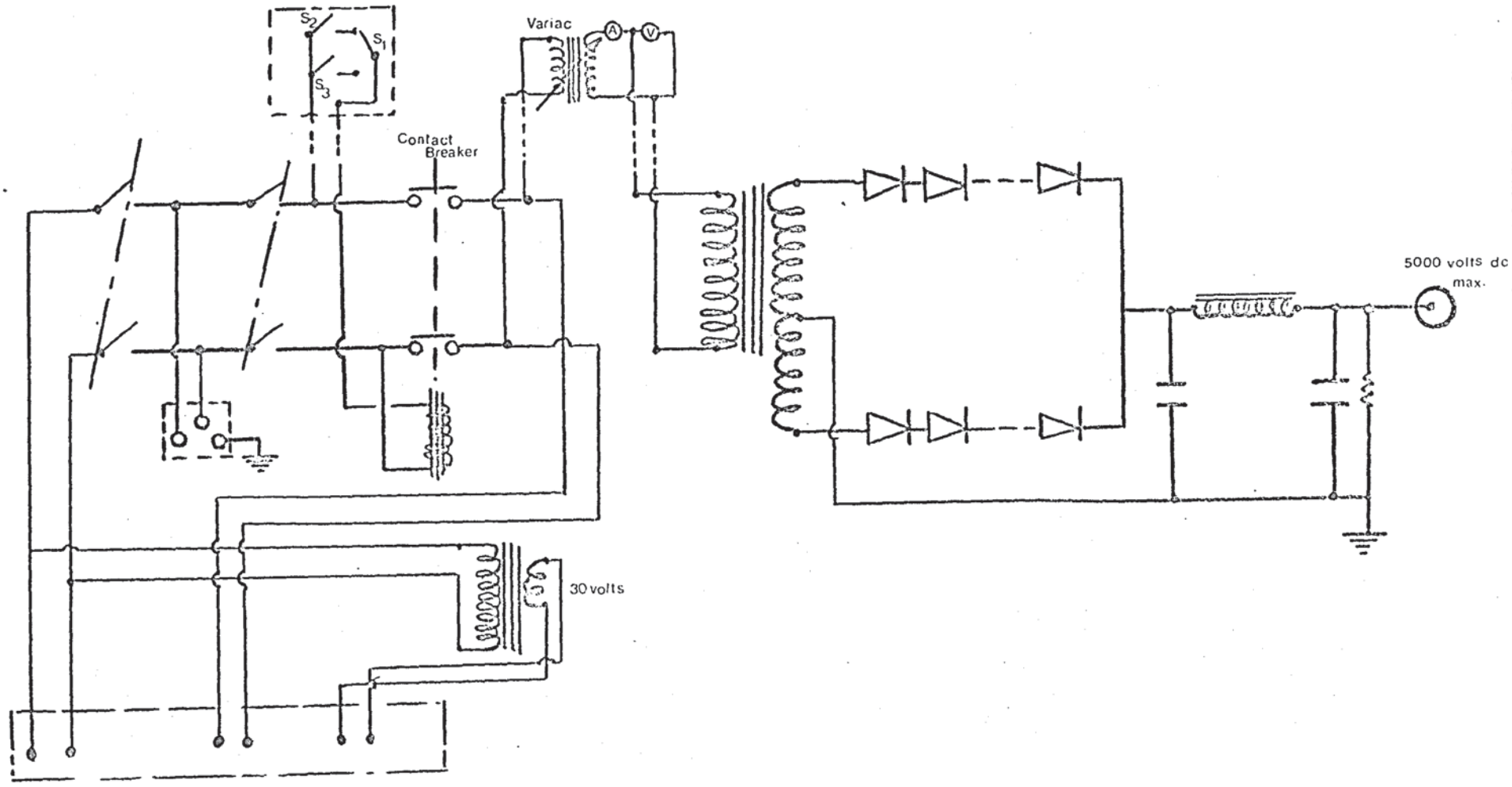

Fig. A6.2 Power Chassis circuit.

particularly to the oscillatory strain in only one of the units. It was therefore decided to rely on manual tuning using the oscilloscope trace as a visual indication of the resonance condition.

A.6.2 Output Chassis.

This consisted essentially of two QY5 - 500 high voltage tetrodes operated in push-pull with an oil cooled output transformer.

The circuit is given in the generator handbook. A thermostat, THI was positioned between the valves. This was included in the original unit to prevent applying HT to the output valves before the heaters were warm. However, in order to simplify operation of the generator, the 4 pole contactor controlling the mains input to the power chassis was removed, which made THI unnecessary. A coaxial socket was fitted to the output chassis and connected with screened lead directly to the control grid of one of the output valves. This allowed the output waveform to be checked and served as an alternative output for frequency monitoring.

A.6.3 Power Chassis.

The main function of this unit was to provide upto 5000 volts, D.C. for the output chassis and a 30 volt. A.C. high current supply to the magnetisation circuit. A 'Variac' voltage transformer was added in order to control the HT transformer primary voltage and hence the power output from the generator. A two pole contactor energised via switches S1, S2 and S3 positioned on the remote control panel was also included in addition to the main LT and HT cutouts. These are shown in the circuit diagram of Fig. A.6.2.

A micro-switch, S_2 positioned on the sub-press automatically operated the generator by closing the HT contactor.

The position of the microswitch and spring loaded push rod were adjusted so that the switch was closed just prior to the start of drawing. This minimised the danger of 'burning' the test piece at high acoustic intensities by ensuring that there was relative linear motion between the test piece and tools, before the latter were ultrasonically activated. For intermittent activation the microswitch was isolated by S_1 and a third switch, S_3, operated manually provided the main control.

The power input to the transformer T6 and the AC current and voltage were monitored by the instruments shown in Fig. A.6.2.

A.6.4 Magnetisation Chassis.

This unit was designed to provide a DC bias current of upto 10 amps to the transducer coils. A heavy duty linear potentiometer permitted selection of the appropriate bias current which was indicated on a 0 - 20 amps moving coil ammeter. The output from the magnetisation chassis was fed to the transducers via chokes CH1 and CH2 in order to isolate the DC circuit from the high voltage, alternating output of the main amplifier. (Details of the circuit are given in the generator handbook.) The purpose of the magnetic bias is to increase the efficiency of the transducers by modifying the B-H hysteresis loop. This also has the effect of reducing the strain frequency by a factor of two so that it equals the electrical frequency. In practice, the optimum bias current was determined by observation of the motional amplitude of the conical horns, the chosen value corresponding to the maximum vibrator amplitude for a given variac setting.

Appendix VII

Test Piece Manufacture.

A.7.1 Drilling the Central locating Hole.

The rectangular blanks were drilled in batches of 12-15 using the jig illustrated in Fig. A.7.1(a).

A.7.2 Machining the wedge profile.

The test piece profile was produced on each drilled batch of blanks, using an Elliot NC milling machine fitted with a standard $\frac{7}{8}$ in. end miller. The jig used to hold the test pieces is shown in Fig. A.7.2. It consisted simply of a mild steel base plate with a 3/16 in. diameter x 1.0 in steel locating pin mounted at the centre and an upper plate machined to the test piece profile. The upper clamping plate was machined initally using a slightly modified programme to give 0.005 in. all round clearance. The basic programme was determined using the scale drawing of the test piece shown in Fig. 6.1. Initial tests showed that in order to obtain a satisfactory surface finish on the milled edge, a roughing cut followed by a 0.005 in. finishing cut were necessary. It was also observed that 'climb' milling gave the best results and the programme was written to ensure that this cutting relationship was maintained around both sides of the test piece. Details of the machining programme are shown in Table A.7.1

A.7.3 End Milling.

The outer radius of the test piece was determined according to the draw ratio required. Batches of test pieces were produced to a given radius using the jig illustrated in Fig. A.7.1(b)

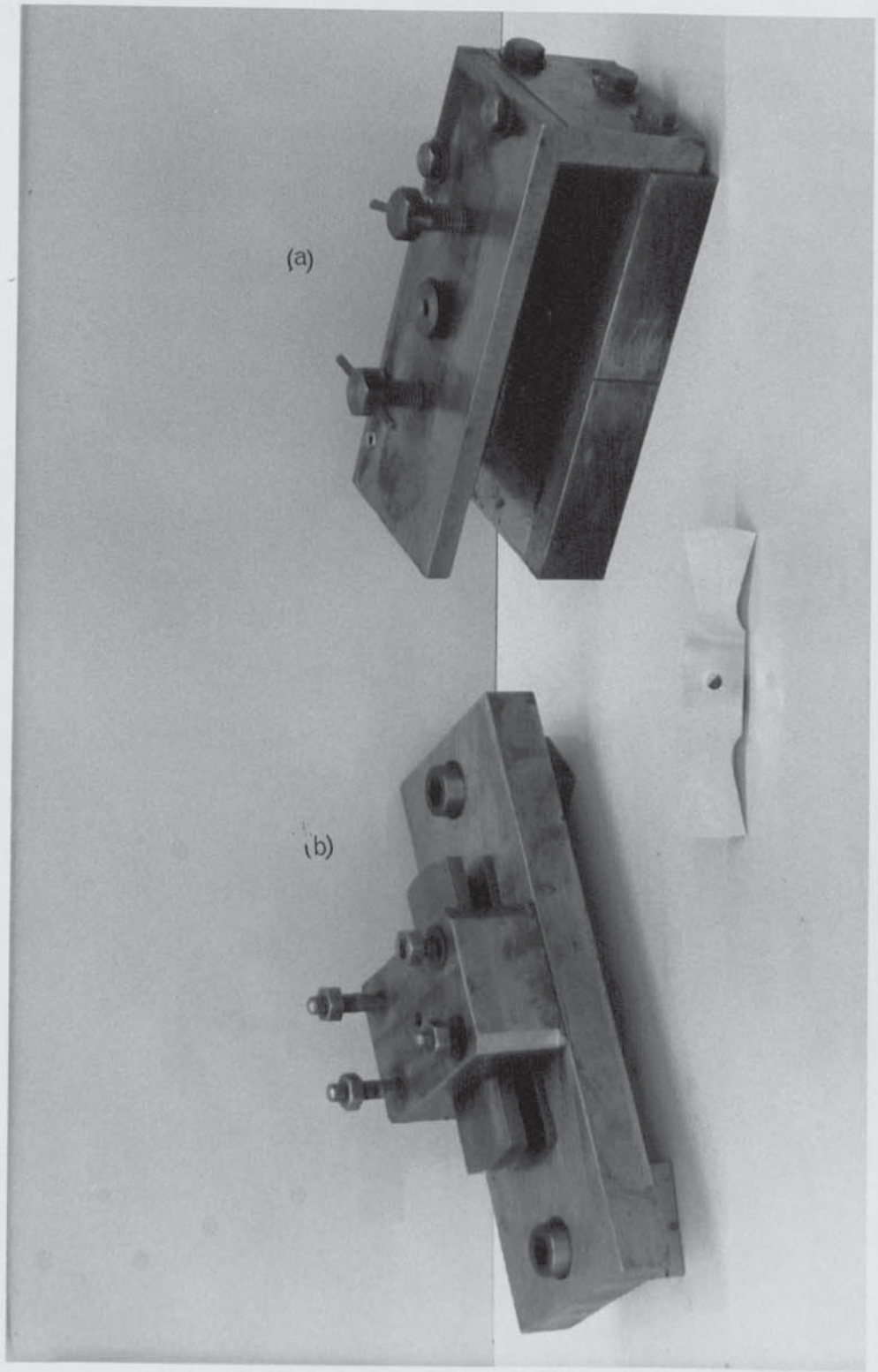

Fig. A7.1 Jigs used in the manufacture of testpieces.

a) drilling operation

b) end mill operation.

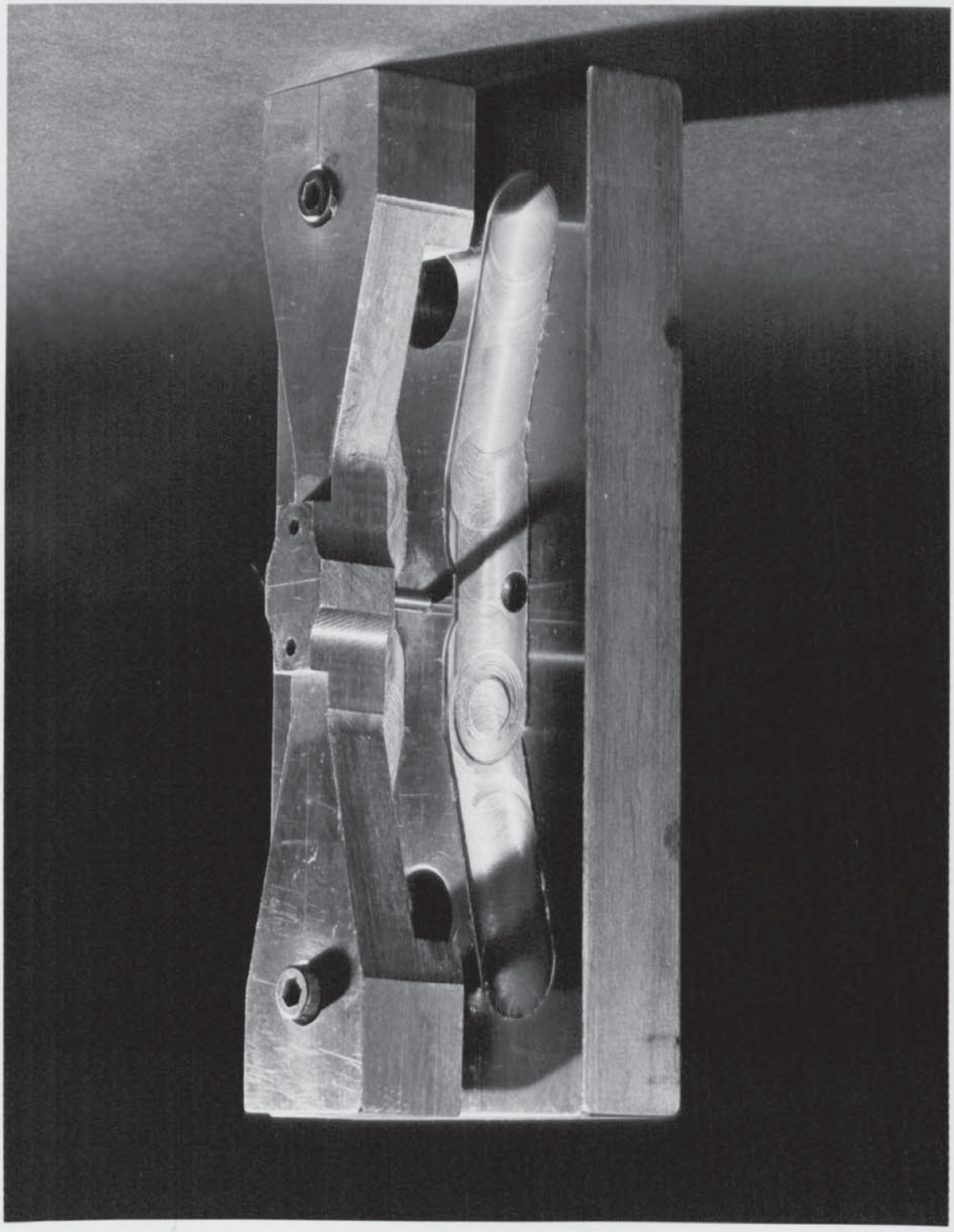

Fig. A7.2 Jig used for N.C. milling of testpieces.

SEQUENCE NUMBER	FUNCTIONS	X AXIS CO-ORDINATES	Y AXIS CO-ORDINATES	TOOL OFFSETS (Z AXIS)	Z AXIS CO-ORDINATES	FEED RATE	MISCELLANEOUS FUNCTIONS
		INCHES	INCHES		INCHES	INCHES/MINUTE	
N OR O 000	G 00	Y±000.0000	Y±000.000	T 001 OR T 002 OR T 003	Z OR R(RAPID ± 000.0000	F 000.00	M 00
N001	G 54	X-0028981	Y0011834				M03
N002	G 55			T001	R-0014000		M08
N003					Z-0015000	F00200	
N004		X-0009466	Y0006942			F00300	
N005			Y0008192				
N006		X0009466					
N007			Y0006942				
N008		X0028981	Y0011834				
N009				T000	R00000000		
N010	G 54		y-0011834				
N011	G55			T001	R-0014000		
N012					Z-0015000		
N013		X0009466	Y-0006942				
N014			Y-0008192				
N015		X-0009466					
N016			Y-0006942				
N017		X-0028981	Y-0011834				

N018				T 000	R00000000	
N019	G 54	X-0028981	Y0011734			
N020	G 55			T 001	R-0014000	
N021					Z-0015000	
N022		X-0009466	Y0006842			
N023			Y0008092			
N024		X0009466				
N025			Y0006842			
N026		X0028981	Y0011734			
N027				T000	R00000000	
N028	G54		Y-0011734			
N029	G55			T001	R-0014000	
N030					Z-0015000	
N031		X0009466	Y-0006842			
N032			Y-0008092			
N033		X-0009466				
N034			Y-0006842			
N035		X-0028981	Y-0011734			
N036				T000	R00000000	M05
N037	G54	X00000000	Y00000000			M30

TABLE A.7.1. NC. PROGRAMME.

Appendix VIII

Measurement of Oscillatory Forces.

A.8.1 Measurement of the input impedance of the loaded vibrators.

The oscillatory force and displacement amplitudes at the narrow end of the conical horn are essentially equal to the values in the die exit plane. Although it was not possible to measure the strain amplitude directly, in this region, from a knowledge of the impedance characteristics of the conical velocity transformer it was intended to deduce this value by measuring the input impedance. In Section 4.2 the mechanical impedance was defined as $Z = \dot{\xi}_m/F_m$; therefore if the velocity amplitude in the die exit plane is known, the force amplitude can be determined from impedance measurements.

A.8.1.1 Impedance transformation characteristics of a conical horn.

The complex input impedance of a loaded conical horn was derived in Section 4.5.2. This was defined by equation (4.67) At resonance the reactive component of the input impedance is zero and only the real part of equation (4.67) need be considered. This is readily evaluated to give:

$$R_{IN} = \frac{Z_H . W_o'/W_{o1}'}{(\cos kl + \frac{N-1}{kl}.\sin kl)^2 + (\frac{Z_H}{W_{o1}'})^2 . \sin^2 kl} \quad \text{--- A.8.1}$$

If the load is assumed to be resistive, (which is justified in this case by the small observed frequency shift in the loaded system) equation A.8.1 may be rewritten:

$$\frac{R_{IN}}{W_o'} = \frac{R_L/W_{o1}'}{(\cos kl + \frac{N-1}{kl}.\sin kl)^2 + (\frac{R_L}{W_{o1}'})\sin^2 kl} \quad \text{--- A.8.2}$$

The transformation characteristics were defined by

plotting the relationship between R_{in}/R_L and N, for different values of the ratio of load impedance to the wave impedance at the narrow end of the horn, viz. R_L/W_{o1}'. These curves are presented in Fig. A.8.1 which also shows the equivalent relationship for an exponential horn. It will be seen that the exponential horn is a more effective transformer for values of N > 2. The coincidence of the curves at low ratios would be expected from comparison of the respective taper laws, viz:

exponential: $So_{exp} = S_{1_{exp}} . e^{b1}$ ---------- A.8.3

Conical $S_{o_c} = S_{1_c} (1 + dx)^2$ ---------- A.8.4

at low values of N, equations A.8.3 and 8.4 may be rewritten: N (1 + b1) and N (1 + 2 α1) respectively. These expressions coincide when $\alpha = \frac{b}{2}$.

In the present case, N = 9 and it is therefore inappropriate to use the single exponential transformation function, $\frac{Z_{IN}}{Z_H} = N^2$. From Fig. A.8.1 the ratio R_{IN}/R_L varies between 15 and 17 depending on the value R_L/W_{o1}'. As a first approximation a mean value of 16 is assumed. We may therefore write:

$$\frac{R_{IN}}{R_L} = \frac{F_{mo}}{\dot{\xi}_{mo}} . \frac{\dot{\xi}_{m1}}{F_{m1}} = 16 \qquad \text{---------- A.8.5}$$

If the displacement amplitudes are determined at each end of the system, then the force amplitude at the die exit plane can be related to the amplitude at the input end of the horn, using equation A.8.5.

An experimental system was designed for measuring the travelling wave force amplitude produced by a single laminated nickel transducer. The apparatus, shown schematically in Fig. A.8.2, consisted essentially of a 1.0 in. diameter cylindrical

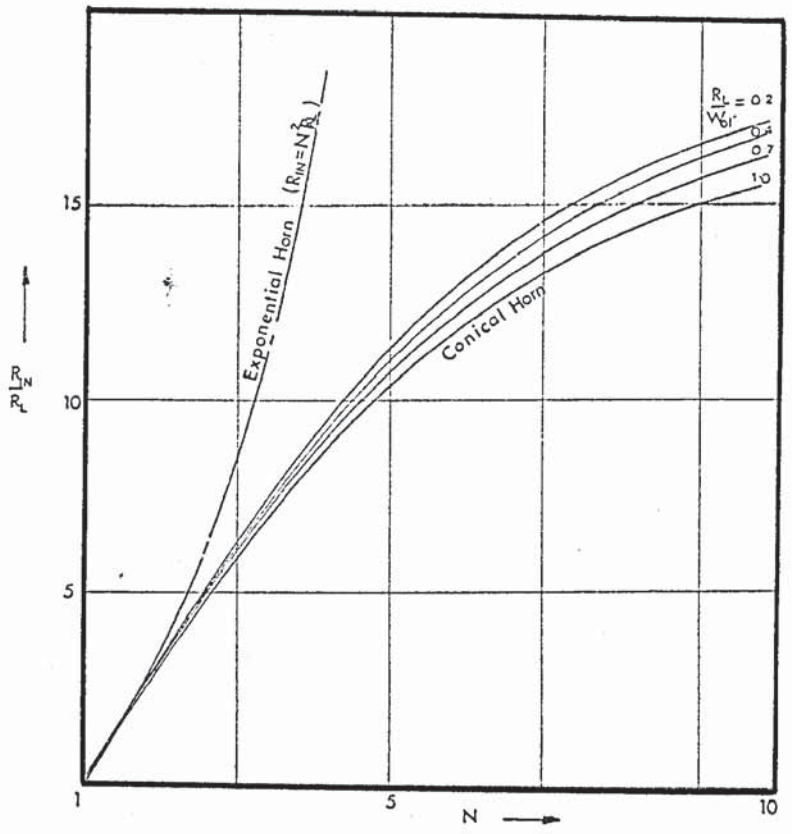

Fig. A8.1 Impedance transformation characteristics for a conical horn with active load, R_L.

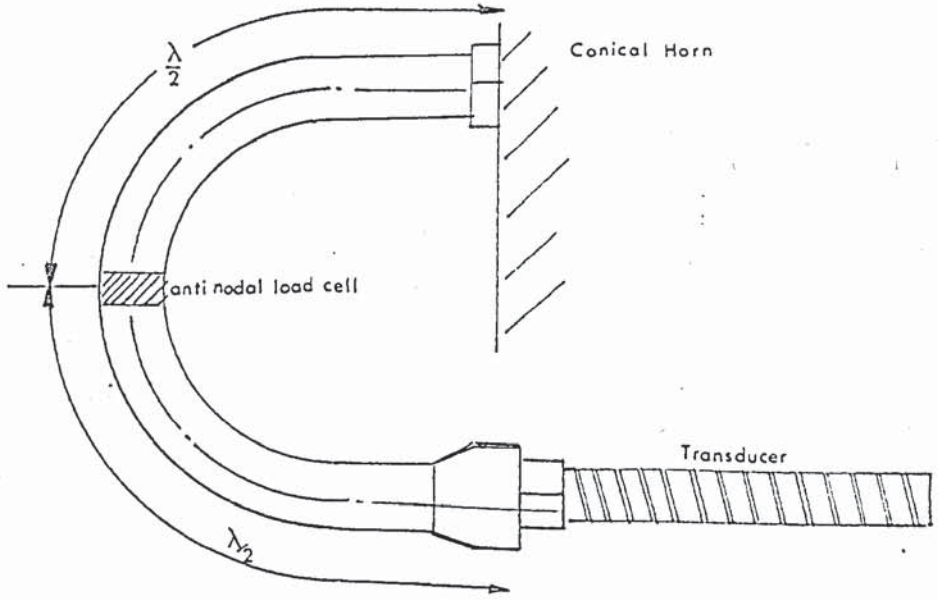

Fig. A8.2 Waveguide for measuring the input impedance of conical horn.

steel waveguide which was inserted between the conical horn and transducer. The length of this measuring waveguide was made equal to $\lambda/2$ at 13 kHz, but due to the restricted access at the rear of each vibrator it was necessary to bend the rod through 180^{o} in order to accommodate the transducer. This required an adjustment to be made to the length of the rod in order to achieve resonance at 13 kHz. The travelling wave force amplitude was measured by a strain gauge bridge positioned at a motional antinode in the unloaded system. The presence of an active load at the output end of the conical horn, resulted in travelling waves giving rise to an oscillatory force coincident with the previous stress node.

In practice it was found that the signal amplitude from the strain gauge bridge was erratic due principally to the difficulty in accurately matching the resonant frequency of the curved waveguide to that of the concentrators. Severe 'pick-up' problems were also encountered due to the close proximity of the bridge to transducers and their associated fields. It was concluded that this technique may be successfully employed if a straight measuring waveguide were incorporated. However, this was not possible on the present sub-press without major alterations and the experiments were discontinued.

A.8.2 Measurement of Oscillatory Force in the partly drawn testpiece.

A.8.2.1 Tuned punch system.

It was considered that energy absorption in the deformation zone, could result in the transmission of travelling waves through the drawn test piece. An attempt was therefore made to examine this possibility using a specially designed tuned punch. This is illustrated in

Fig. A.8.3 and consisted essentially of two quarter wave stepped transformers, the lower one incorporating the geometrical requirements of the punch. Strain gauge bridges were mounted at both nodal and antinodal displacement planes in order to measure the mean and peak punch loads respectively, on independent instruments. The location of the bridges and acoustic properties of the punch assembly are illustrated schematically in Fig. A.8.4.

The system was tuned to resonate at 13.00 kHz using the transducer attached to the upper transformer. It was anticipated that if travelling waves occurred in the test piece they would pass through the punch producing an oscillatory strain in the plane of the 'antinodal' bridge, (see Fig. A.8.4). Tests were carried out at draw ratios of 1.60 and 1.70 with die amplitudes of upto 25×10^{-5} in. In each case the signal from the antinodal bridge rose to a maximum value at a punch displacement of approximately 0.3 in. and fell abruptly to zero beyond this point. Examination of the geometry of the reduction indicated that this coincided with a die radius contact angle of 45°. The unsupported test piece length was also close to the minimum value indicating that its stiffness was approaching the maximum. It was therefore considered that conditions were most favourable for energy transfer to the punch at this stage.

As the draw continued, damping of the wave motion was thought to occur around the profile radius, accompanied by mode conversion which led to bending waves in the drawn test piece. This aspect was considered in Section 9.2.5.2. If this was in fact the case longitudinal travelling waves would not be expected during the later stages of drawing.

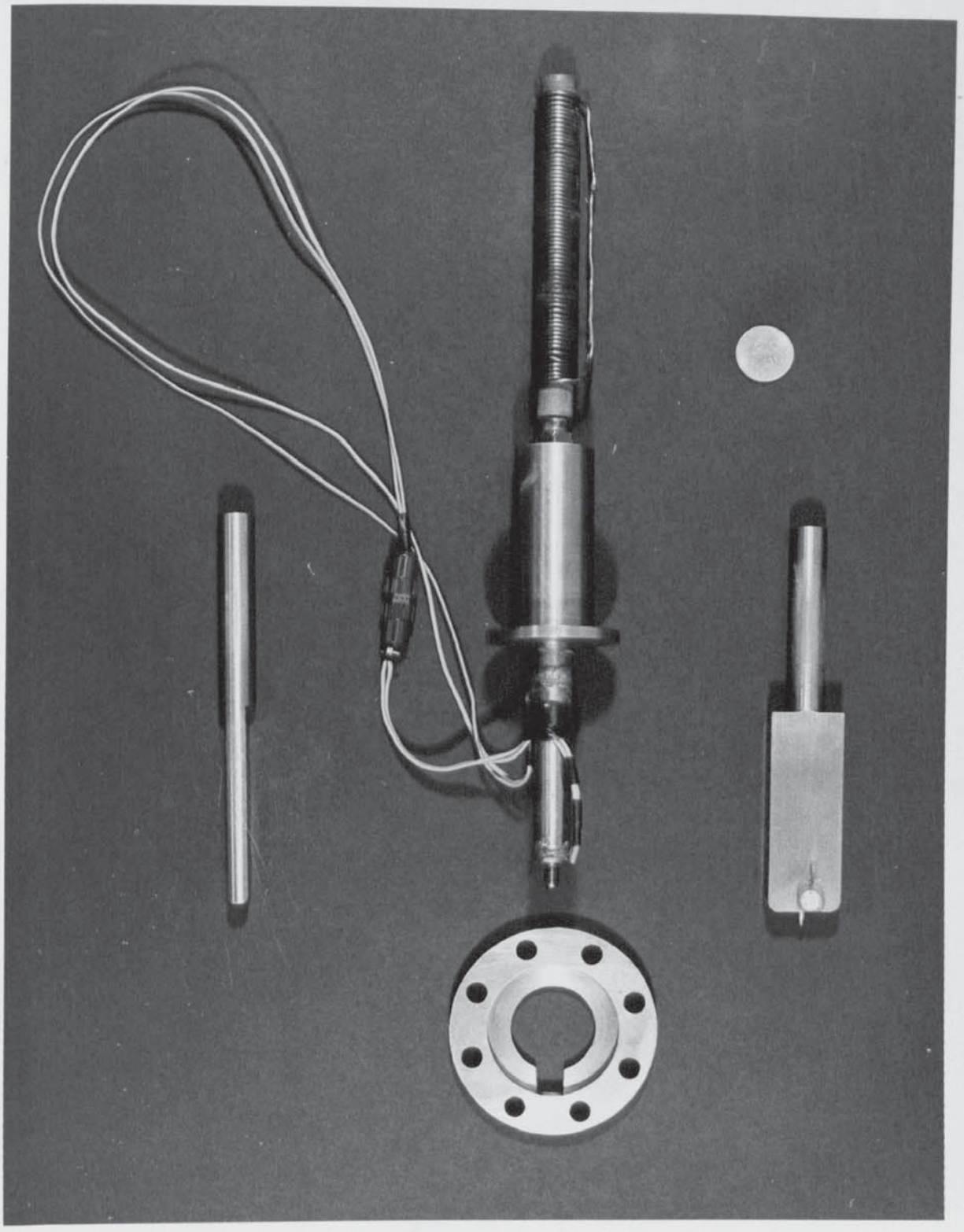

Fig. A8.3 Tuned punch system with mounting plate.

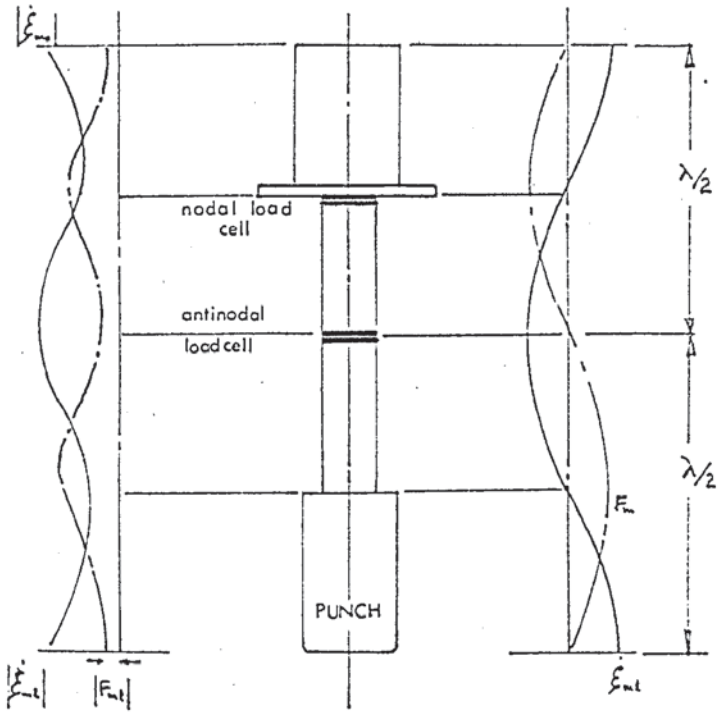

Fig. A8.4 Wave characteristics of tuned punch system

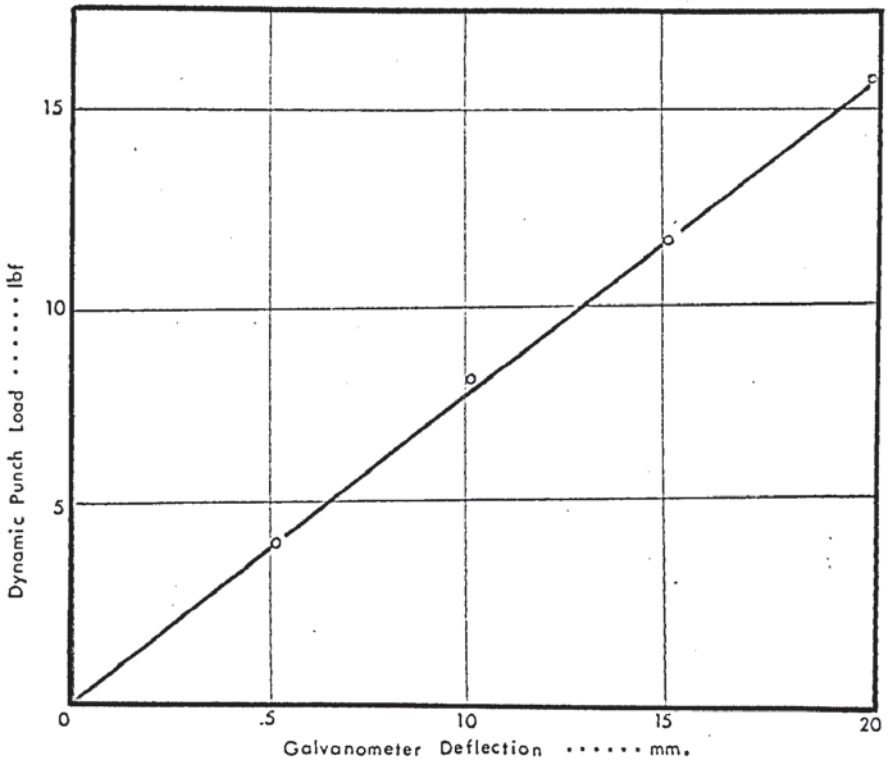

Fig. A8.5 Calibration curve for tuned punch load cell, mounted at displacement antinode.

The presence of bending waves in the drawn test piece was examined by attaching strain gauges to the partly drawn test piece. This is discussed in the following section.

A.8.2.2. Strain gauge measurement of oscillatory force in the test piece.

An attempt was made to measure the oscillatory force in the partly drawn test piece by attaching matched pairs of strain gauges to the upper and lower surfaces and completing the reduction. It was hoped in this way to confirm the results obtained using the tuned punch. In these tests it was necessary to draw sufficient material to permit the gauges to be attached away from regions of plastic deformation, viz. at the die radius exit plane. This made it impossible to examine the stage of drawing in which the travelling wave amplitude reached a maximum.

The results of tests relating to the later stages of deformation indicated force amplitudes of upto only 8 lbf peak to peak. At low die amplitudes negligible strain was detected.

The gauges were connected in series in one arm of a bridge and 3 'dummy' gauges used to complete the circuit. The bridge output was measured with an oscilloscope and calibrated under static loading conditions using the D.C. input facility.

In order to confirm the presence of bending waves in the partly drawn test piece single gauges were attached and the draw completed. These were not calibrated. The results of tests conducted under similar conditions to the earlier series indicated signals which were an order of magnitude greater, furthermore the amplitude varied as the draw progressed reaching a clearly defined maximum at about the

mid-point of the reduction. Both features were consistent with the presence of bending waves.

A.8.2.3 Calibration of Tuned Punch load Cell.

It was necessary to amplify the bridge output by a factor of x 5000 in order to produce a measurable output voltage for force amplitudes in the order of 5-10 lbf. A Southern Instruments D.C. amplifier with a flat frequency response between 15 and 30 kHz was used for this purpose and the output taken to an oscilloscope and sensitive A.C. voltmeter connected in parallel. The voltmeter was used to give an R.M.S. voltage output which could be applied to a standard galvanometer in the U.V. recorder thus providing a continuous monitoring facility in addition to the visual oscilloscope display.

The instrumentation was calibrated using a transistorised wave generator capable of delivering 0 - 2.5 volts over a frequency range of 1 - 150 kHz. The frequency of this instrument was adjusted to 13.06 kHz (the resonant frequency of the complete system under load) and the galvanometer deflection noted over a range of input voltages from 0.01 to 0.05 volts.

The assembled punch system with the load cell in its operating position was calibrated statically using a dead weight testing machine. The bridge output voltage, after amplification, was measured on an oscilloscope, set for D.C. operation. This provided a load/voltage relationship, which when combined with the instrumentation calibration data, allowed the final static calibration curve to be plotted, Fig. A.8.5.

Details of the calibration data are given in Table A.8.1.

TABLE A.8.1

DYNAMIC PUNCH LOAD CELL CALIBRATION DATA

A: Force Calibration B: Instrument Calibration

LOAD (lbf)	OSCILLOSCOPE VOLTAGE: V	EQUIV. RMS VOLTAGE V_X 1/2	RMS VOLTS at 13kHz	GALVO. DEFL. (mm)
22.4	0.30	0.212	0.050	8.40
44.8	0.55	0.388	0.750	12.40
67.2	0.75	0.530	0.100	16.50
112.0	1.25	0.884	0.125	20.70
156.8	1.60	1.130	0.150	25.00
224.0	2.40	1.695		
336.0	3.30	2.335		
448.0	4.40	3.104		

Relationship between punch displacement contact angle ϕ and unsupported length l, for standard and narrow punches. Fig. A9.2.

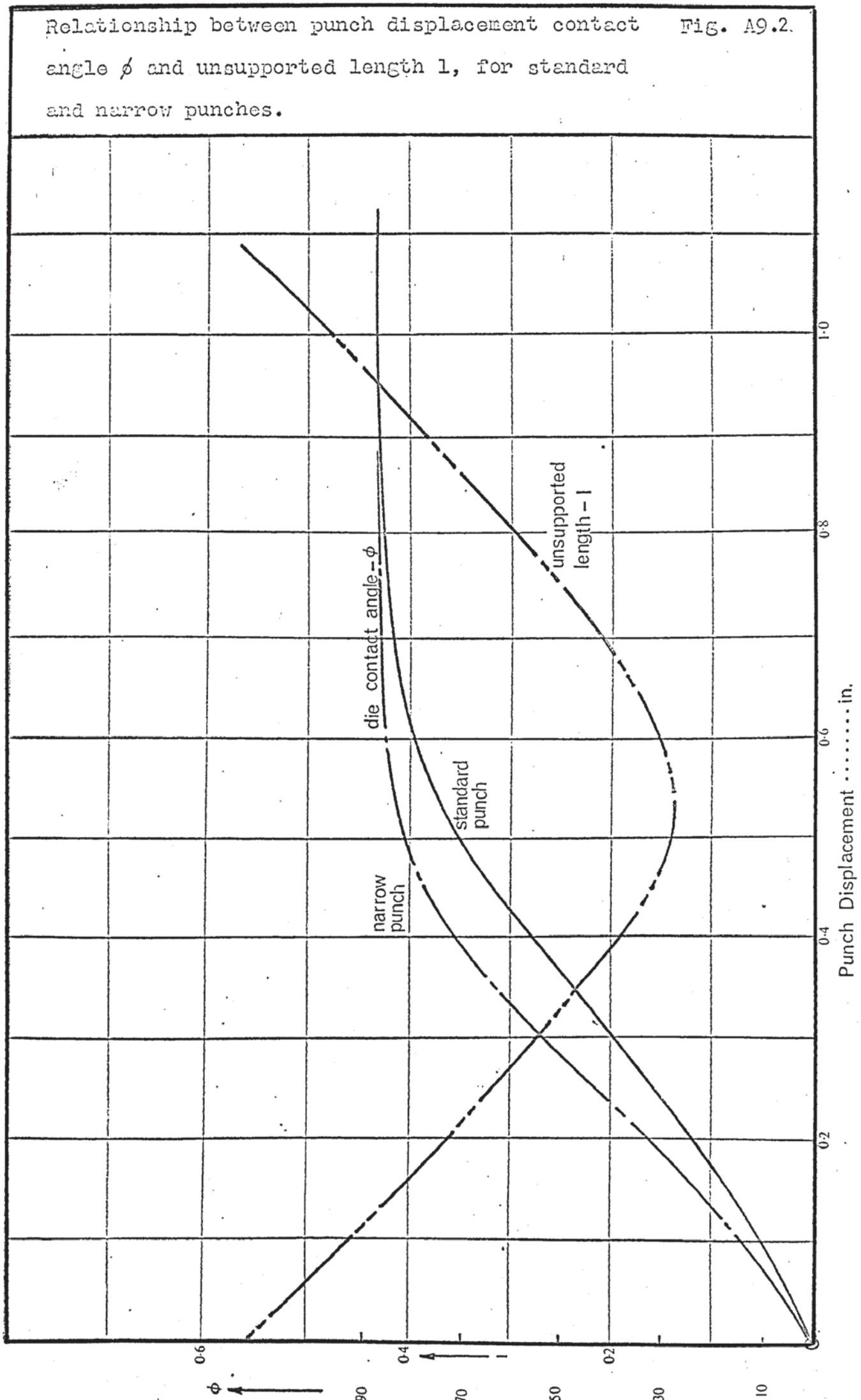

Appendix IX

Relationship between punch displacement, h, die contact angle, ϕ, and the unsupported test piece length, 1.

Fig. A.9.1 Wedge drawing geometry.

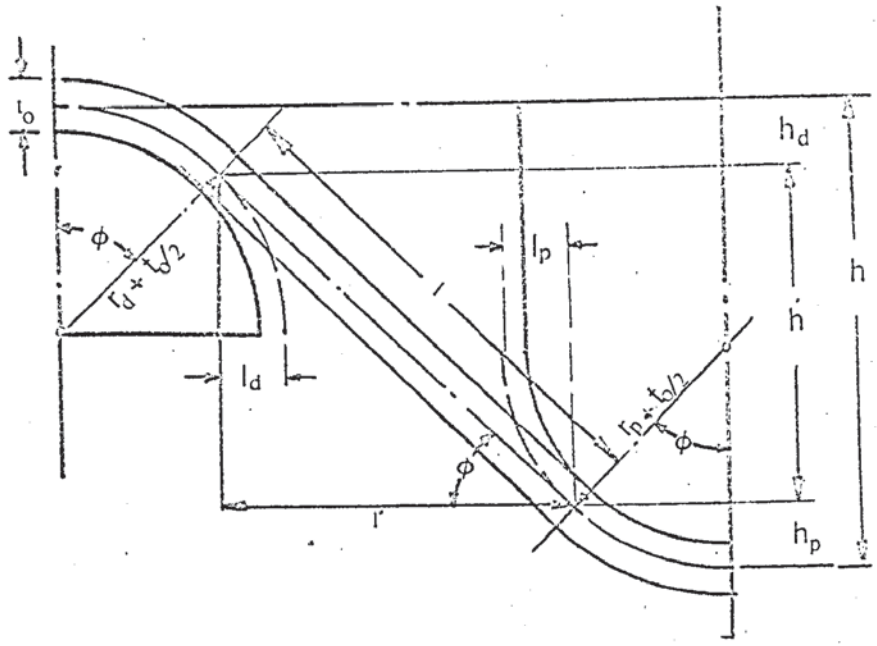

From Fig. A.9.1 the following relationships may be stated:

The punch displacement, h, is given by:

$$h = h' + hp + hd \qquad \text{---------- A.9.1.}$$

$$\left.\begin{aligned} hp &= (r_p + \tfrac{t_o}{2})(1-\cos\phi) \\ h_d &= (r_d + \tfrac{t_o}{2})(1-\cos\phi) \end{aligned}\right\} \qquad \text{---------- A.9.2}$$

$$\left.\begin{aligned} l_p &= (r_p + \tfrac{t_o}{2})(1-\sin\phi) \\ l_d &= (r_d + \tfrac{t_o}{2})(1-\sin\phi) \end{aligned}\right\} \qquad \text{---------- A.9.3}$$

Assuming the clearance between die and punch to be 1.5 t_o

$$h' = \left[\frac{t_o}{2} + (r_p + r_d + t_o)(1-\sin\phi)\right] \tan\phi$$

$$\therefore h = (r_p + r_d + t_o)(1-\cos\ ) + \left[\frac{t_o}{2} + (r_p + r_d + t_o)(1-\sin\phi)\right]$$

$$\times\tan\phi \qquad \text{----------A.9.4}$$

$$\text{and } l = \frac{\frac{t_o}{2} + (r_p + r_d + t_o)(1-\sin\phi)}{\cos\phi} \quad \text{---------- A.9.5}$$

The relationship between h, l and ϕ has been plotted from equations A.9.4 and A.9.5 and is shown in Fig. A.9.2. Tabulated calculations are given in Table A.9.1 which also illustrates the variation in the length of the test piece during drawing, for ratios of 1.50 and 1.80.

Table A9.1 Relationship between h, l, ϕ and test piece length, x, during wedge drawing.

Punch Displacement h, in.	Contact Angle ϕ^o	Unsupported length l, in.	Test piece length, in.	
			$x_{1.50}$	$x_{1.80}$
0	0	0.554	3.000	3.600
0.2	24.0	0.365	3.020	3.828
0.4	55.5	0.195	3.040	3.860
0.6	79.2	0.155	3.110	3.728
0.8	85.0	0.300	3.140	3.764
1.0	86.1	0.485	-	3.854
1.2	86.9	0.682	-	3.920

APPENDIX X.

Tensile Test Data on Commercially Pure Aluminium Sheet.

Tensile tests were carried out on longitudinal samples cut from the original sheet material, using a Hounsfield tensometer with a 250 lbf. beam and x 8 chart magnification. A typical load/extension curve is shown in Fig. A10.1

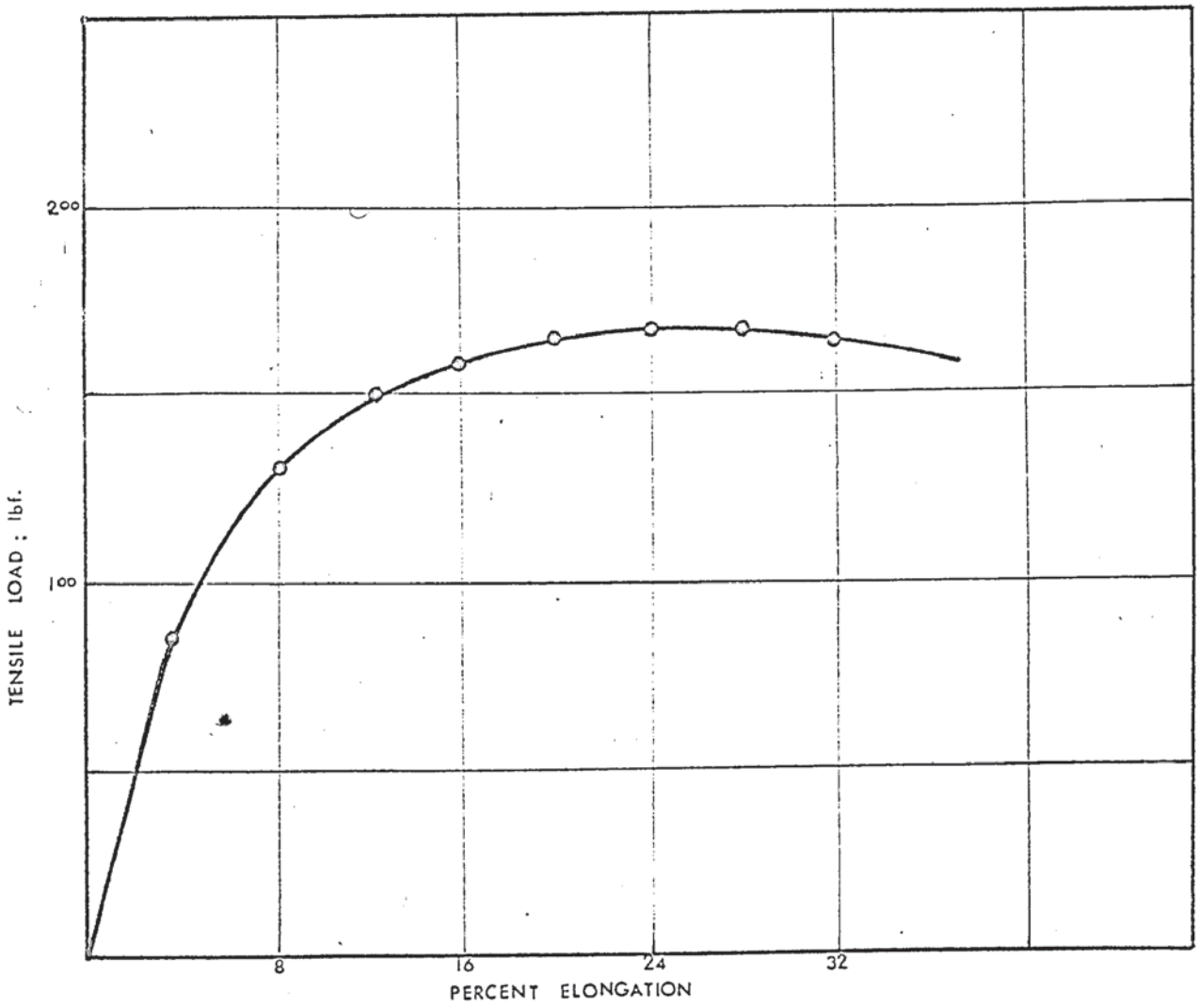

Fig. A10.1 Load/extension curve for c.p. Al.

The UTS and approximate elongation were determined in each case, the mean values being:

U.T.S. - 5.10 tonf/in.^{2}

Elongation - 41% (on 2in. gauge length).

Specimen dimensions:

width	- 0.410in.
thickness	- 0.036in.
gauge length	- 2.0in.
parallel length	- 2.5in.
overall length	- 5.0in.

APPENDIX XI

Tabulated Results

NON-OSCILLATORY WEDGE DRAWING TEST DATA.

TEST NUMBER	DRAW RATIO; 1.60:1					BLANK HOLDER FORCE; 380 lbf.						PUNCH VELOCITY; 0.15 in./sec.					
	Punch Travel, in	0.1	0.2	0.3	0.4	0.5	0.6	0.7	0.8	0.9	1.0	1.1	1.2	1.3	1.4	1.5	1.6
010300	Punch load; lbf	44	95	178	245	292	323	313	275	218	163						
	Blank Holder Friction Force	36.8	26.3	12.9	13.8	17.4	20.5	20.0	19.6	19.6	21.2						
010300/1	Punch load; lbf	-	85	149	214	268	295	309	275	228	178						
	B/H Friction Force; lbf.	-	24.5	20.5	19.0	13.6	16.0	18.1	21.1	22.2	16.0						
	Punch load; lbf																
	B/H Friction Force; lbf.																
	DRAW RATIO; 1.65:1					BLANK HOLDER FORCE; 401 lbf.						PUNCH VELOCITY; 0.14 in./sec.					
010400	Punch load; lbf	69	152	226	275	312	333	336	295	232	172	67					
	B/H Friction Force; lbf.	22.3	18.0	18.4	12.2	15.6	20.0	24.0	25.0	27.3	22.3	-					
010400/1	Punch load; lbf	72	155	228	286	323	345	345	308	238	178	65					
	B/H Friction Force; lbf.	29.0	25.5	16.0	15.0	18.0	24.5	26.7	26.2	21.3	16.7	-					
	Punch load; lbf																
	B/H Friction Force; lbf.																

TABLE No: 1

NON-OSCILLATORY WEDGE DRAWING TEST DATA.

TEST NUMBER	DRAW RATIO; 1.70:1					BLANK HOLDER FORCE; 445 lbf.						PUNCH VELOCITY; 0.16 in./sec.					
	Punch Travel, in	0.1	0.2	0.3	0.4	0.5	0.6	0.7	0.8	0.9	1.0	1.1	1.2	1.3	1.4	1.5	1.6
010500	Punch load; lbf	74	173	262	312	357	384	381	352	309	262	226	83				
	Blank Holder Friction Force	36.8	26.8	18.3	17.8	20.5	22.5	24.6	25.0	25.0	24.1	20.1	-				
010500/1	Punch load; lbf	71	155	226	297	333	357	357	357	316	252	214					
	B/H Friction Force; lbf.	31.0	24.5	16.5	13.5	16.5	20.0	23.0	26.0	28.0	22.5	23.0					
	Punch load; lbf																
	B/H Friction Force; lbf.																
	DRAW RATIO;					BLANK HOLDER FORCE; lbf.						PUNCH VELOCITY; in./sec.					
	Punch load; lbf																
	B/H Friction Force; lbf.																
	Punch load; lbf																
	B/H Friction Force; lbf.																
	Punch load; lbf																
	B/H Friction Force; lbf.																

TABLE No: 2

WEDGE DRAWING TEST DATA.

TEST NUMBER : 010301	MATERIAL : ALUMINIUM .	DRAW RATIO : 1.60:1	TABLE No. 3

Punch Velocity; in/sec.	Blank Holder Force ; lbf	Variac Voltage	Frequency ; kHz.
0.17	385	14	13.36

Punch Travel; in.		0·1	0·2	0·3	0·4	0·5	0·6	0·7	0·8	0·9	1·0	1·1	1·2	1·3	1·4	1·5	1·6
Punch Load P; lbf	non-osc.	60	143	214	267	307	313	286	238	179							
	osc.	-	129	190	250	284	298	273	220	169							
	ΔP	-	14	24	17	23	15	13	18	10							
Blank Holder Friction Force F, lbf.	non-osc.	24.5	20.8	16.8	16.0	16.0	18.0	19.5	22.0	16.0							
	osc.	6.2	7.6	6.0	5.0	7.0	10.0	13.5	18.0	12.0							
	ΔF %	75	64	64	69	56	45	31	18	25							
Die Motional Amplitude, ξ_m in. x 10^{-5}	left hand	-	-	0.55	0.45	0.35	0.40	0.35	0.40	0.35							
	right hand	-	-	0.65	0.63	0.65	0.65	0.60	0.60	0.55							
	mean	-	-	0.60	0.54	0.50	0.53	0.48	0.50	0.45							
Velocity Ratio	$V/\dot{\xi}_m$	-	-	.344	.386	.413	.392	.438	.413	.458							

WEDGE DRAWING TEST DATA.

TEST NUMBER: 010302	MATERIAL: ALUMINIUM.	DRAW RATIO: 1.60:1	TABLE No. 4

Punch Velocity; in/sec.	Blank Holder Force; lbf	Variac Voltage	Frequency; kHz.
0.16	391	14	13.24

Punch Travel; in.		0·1	0·2	0·3	0·4	0·5	0·6	0·7	0·8	0·9	1·0	1·1	1·2	1·3	1·4	1·5	1·6
Punch Load P; lbf	non-osc.	-	-	-	-	-	300	268	214	153							
	osc.	62	119	190	244	270	276	238	190	131							
	ΔP	-	-	-	-	-	24	30	24	24							
Blank Holder Friction Force F, lbf.	non-osc.	-	-	-	-	-	17.9	18.9	17.9	14.1							
	osc.	4.9	3.3	2.3	2.3	5.1	11.8	12.5	10.1	8.3							
	ΔF %	-	-	-	-	-	34	34	44	41							
Die Motional Amplitude, ξ_m in. x 10^{-5}	left hand	0.97	0.74	0.60	0.55	0.55	0.55	0.55	0.65	0.74							
	right hand	1.24	1.02	0.84	0.93	0.84	0.66	0.66	0.75	0.80							
	mean	1.11	0.88	0.72	0.74	0.69	0.60	0.60	0.70	0.77							
Velocity Ratio	v/ξ_m	.173	.218	.267	.260	.277	.318	.318	.275	.250							

WEDGE DRAWING TEST DATA.

TEST NUMBER : 010303	MATERIAL : ALUMINIUM .	DRAW RATIO : 1.60:1	TABLE No. 5

Punch Velocity; in/sec.	Blank Holder Force ; lbf	Variac Voltage	Frequency ; kHz.
0.18	366	20	13.26

Punch Travel; in.		0·1	0·2	0·3	0·4	0·5	0·6	0·7	0·8	0·9	1·0	1·1	1·2	1·3	1·4	1·5	1·6
Punch Load P; lbf	non-osc.	76	154	216	276	310	310	274	214	155							
	osc.	66	132	197	250	277	273	238	191	131							
	ΔP	10	22	19	26	33	37	36	23	24							
Blank Holder Friction Force F, lbf.	non-osc.	24.5	20.5	12.0	14.5	19.6	22.0	22.6	19.0	16.0							
	osc.	7.0	4.6	1.6	3.4	5.0	7.0	12.0	8.9	5.0							
	ΔF %	72	74	87	77	75	68	47	53	69							
Die Motional Amplitude, ξ_m in. x 10^{-5}	left hand	-	0.95	1.20	1.00	0.90	0.85	0.95	1.00	1.00							
	right hand	-	1.30	1.25	1.20	1.10	1.00	1.00	1.00	1.05							
	mean	-	1.13	1.23	1.10	1.00	0.93	0.98	1.00	1.03							
Velocity Ratio	$v/\dot{\xi}_m$	-	.191	.175	.196	.216	.232	.220	.216	.210							

WEDGE DRAWING TEST DATA.

TEST NUMBER : 010304	MATERIAL : ALUMINIUM .	DRAW RATIO : 1.60:1	TABLE No. 6

Punch Velocity; in/sec.	Blank Holder Force ; lbf	Variac Voltage	Frequency ; kHz.
0.17	369	20	13.20

Punch Travel; in.		0·1	0·2	0·3	0·4	0·5	0·6	0·7	0·8	0·9	1·0	1·1	1·2	1·3	1·4	1·5	1·6
Punch Load P; lbf	non-osc.	85	157	218	276	315	327	286	240	168							
	osc.	75	143	202	254	280	283	250	202	149							
	ΔP	10	14	16	22	35	44	36	38	19							
Blank Holder Friction Force F, lbf.	non-osc.	-	-	-	12.5	15.2	19.4	22.3	32.1	-							
	osc.	6.7	2.7	2.2	2.2	2.7	3.3	8.9	8.0	-							
	ΔF %	-	-	-	82	82	83	60	64	-							
Die Motional Amplitude, ξ_m in. x 10^{-5}	left hand	1.46	1.39	1.30	1.22	1.10	1.10	1.25	1.39	1.30							
	right hand	-	-	-	-	-	-	-	-	-							
	mean	1.46	1.39	1.30	1.22	1.10	1.10	1.25	1.39	1.30							
Velocity Ratio	$V/\dot{\xi}_m$	.140	.147	.158	.138	.186	.186	.164	.147	.158							

WEDGE DRAWING TEST DATA.

TEST NUMBER : 010305	MATERIAL : ALUMINIUM .	DRAW RATIO : 1.60:1	TABLE No. 7

Punch Velocity; in/sec.	Blank Holder Force ; lbf	Variac Voltage	Frequency ; kHz.
0.17	389	30	13.22

Punch Travel; in.		0·1	0·2	0·3	0·4	0·5	0·6	0·7	0·8	0·9	1·0	1·1	1·2	1·3	1·4	1·5	1·6
Punch Load P; lbf	non-osc.	59	133	202	259	288	300	264	204	143	-						
	osc.	59	111	180	228	249	250	213	185	123	-						
	ΔP	0	22	22	31	39	50	51	19	20	-						
Blank Holder Friction Force F, lbf.	non-osc.	24.5	21.0	12.0	13.5	16.9	20.0	20.5	20.0	16.0	-						
	osc.	2.3	0	1.4	2.6	2.6	3.5	3.2	1.6	1.2	0.8						
	ΔF %	91	100	89	81	85	83	85	92	93	-						
Die Motional Amplitude, ξ_m in. x 10^{-5}	left hand	1.65	2.25	2.30	2.20	1.85	1.65	1.90	2.00	2.05	2.20						
	right hand	2.10	2.00	1.95	1.85	1.80	1.70	1.75	1.95	2.30	2.55						
	mean	1.88	2.13	2.13	2.03	1.83	1.68	1.83	1.98	2.18	2.35						
Velocity Ratio	$v/\dot{\xi}_m$	.109	.096	.096	.101	.112	.122	.112	.103	.094	.087						

WEDGE DRAWING TEST DATA.

TEST NUMBER : 010306	MATERIAL : ALUMINIUM .	DRAW RATIO : 1.60:1	TABLE No. 8

Punch Velocity; in/sec.	Blank Holder Force ; lbf	Variac Voltage	Frequency ; kHz.
0.15	392	30	13.26

Punch Travel; in.		0·1	0·2	0·3	0·4	0·5	0·6	0·7	0·8	0·9	1·0	1·1	1·2	1·3	1·4	1·5	1·6
Punch Load P; lbf	non-osc.	68	121	181	250	290	312	274	214	145							
	osc.	58	106	159	226	252	261	226	176	118							
	ΔP	10	15	22	24	38	51	48	38	27							
Blank Holder Friction Force F, lbf.	non-osc.	-	-	11.0	14.5	18.5	20.5	20.5	-	-							
	osc.	2.4	0.8	0.8	1.1	1.4	2.2	2.2	-	2.5							
	ΔF %	-	-	93	93	93	90	90	-	-							
Die Motional Amplitude, ξ_m in. x 10^{-5}	left hand	2.40	2.60	2.35	1.90	1.65	1.60	1.90	2.00	2.10							
	right hand	1.90	2.05	1.90	1.85	1.85	1.90	2.05	2.05	2.05							
	mean	2.15	2.33	2.13	1.88	1.75	1.75	1.98	2.02	2.08							
Velocity Ratio	$V/\dot{\xi}_m$	.084	.077	.085	.096	.103	.103	.091	.089	.087							

WEDGE DRAWING TEST DATA.

TEST NUMBER : 010307	MATERIAL : ALUMINIUM .	DRAW RATIO : 1.60:1	TABLE No. 9

Punch Velocity; in/sec.	Blank Holder Force ; lbf	Variac Voltage	Frequency ; kHz.
0.16	392	40	13.18

Punch Travel; in.		0·1	0·2	0·3	0·4	0·5	0·6	0·7	0·8	0·9	1·0	1·1	1·2	1·3	1·4	1·5	1·6
Punch Load P; lbf	non-osc.	54	127	202	262	300	315	280	232	173							
	osc.	54	105	169	222	252	250	202	163	107							
	ΔP	0	22	33	40	48	65	78	69	66							
Blank Holder Friction Force F, lbf.	non-osc.	-	13.0	11.0	13.7	19.0	23.0	24.5	22.0	13.5							
	osc.	-	-	1.0	1.2	1.4	1.4	1.4	-	-							
	ΔF %	-	-	91	91	92.5	94	94	-	-							
Die Motional Amplitude, ξ_m in. x 10^{-5}	left hand	3.80	4.05	4.60	3.15	2.75	3.05	3.70	3.80	3.85							
	right hand	3.80	3.90	3.70	3.45	3.20	3.00	3.05	3.60	3.90							
	mean	3.80	3.95	3.65	3.30	2.95	3.03	3.35	3.70	3.87							
Velocity Ratio	$V/\dot{\xi}_m$	.057	.049	.053	.059	.066	.064	.058	.052	.050							

WEDGE DRAWING TEST DATA.

TEST NUMBER : 010308	MATERIAL : ALUMINIUM .	DRAW RATIO : 1.60:1	TABLE No. 10

Punch Velocity; in/sec.	Blank Holder Force ; lbf	Variac Voltage	Frequency; kHz.
0.17	381	60	13.16

Punch Travel; in.		0·1	0·2	0·3	0·4	0·5	0·6	0·7	0·8	0·9	1·0	1·1	1·2	1·3	1·4	1·5	1·6
Punch Load P; lbf	non-osc.	61	131	202	262	292	292	264	214	155							
	osc.	54	108	167	220	240	232	190	145	77							
	ΔP	7	23	35	42	52	60	74	69	78							
Blank Holder Friction Force F, lbf.	non-osc.	-	-	8.0	9.0	14.5	22.1	22.5	20.0	17.6							
	osc.	0	0	0	0	0	0	0	0	0							
	ΔF %	-	-	100	100	100	100	100	100	100							
Die Motional Amplitude, ξ_m in. x 10^{-5}	left hand	5.5	5.8	5.6	4.8	4.4	4.2	4.1	4.7	5.3	5.4						
	right hand	4.2	3.8	3.6	3.4	3.3	3.4	3.6	3.9	4.2	5.1						
	mean	4.85	4.80	4.60	4.10	3.85	3.80	3.85	4.30	4.75	5.25						
Velocity Ratio	V/ξ_m	.042	.043	.045	.050	.053	.054	.053	.048	.043	.039						

WEDGE DRAWING TEST DATA.

TEST NUMBER : 010401	MATERIAL : ALUMINIUM .	DRAW RATIO : 1.65:1	TABLE No. 11

Punch Velocity; in/sec.	Blank Holder Force ; lbf	Variac Voltage	Frequency ; kHz.
0.15	405	10	13.49

Punch Travel; in.		0·1	0·2	0·3	0·4	0·5	0·6	0·7	0·8	0·9	1·0	1·1	1·2	1·3	1·4	1·5	1·6
Punch Load P; lbf	non-osc.	–	–	–	–	–	–	–	–	–	–	–					
	osc.	67	140	225	284	332	350	345	302	235	176	72					
	ΔP	–	–	–	–	–	–	–	–	–	–	–					
Blank Holder Friction Force F, lbf.	non-osc.*	29.0	26.0	16.0	15.0	18.0	24.5	26.7	26.2	21.3	16.7	–					
	osc.	22.2	20.3	11.0	9.0	10.0	15.5	22.6	22.6	18.0	13.5	–					
	ΔF %	24	22	31	40	44	37	16	14	16	–	–					
Die Motional Amplitude, ξ_m in. x 10^{-5}	left hand	0.29	0.18	0.23	0.29	0.24	0.23	0.22	0.21	0.19	0.22	0.19					
	right hand	0.84	0.62	0.62	0.42	0.35	0.34	0.30	0.28	0.29	0.27	0.28					
	mean	0.57	0.40	0.43	0.36	0.30	0.29	0.26	0.25	0.24	0.25	0.24					
Velocity Ratio	$V/\dot{\xi}_m$	.311	.442	.412	.494	.590	.610	.682	.708	.738	.708	.738					

* Mean of non-oscillatory test results.

WEDGE DRAWING TEST DATA.

TEST NUMBER : 010402	MATERIAL : ALUMINIUM .	DRAW RATIO : 1.65:1	TABLE No. 12

Punch Velocity ; in/sec.	Blank Holder Force ; lbf	Variac Voltage	Frequency ; kHz.
0.17	396	10.0	13.45

Punch Travel ; in.		0·1	0·2	0·3	0·4	0·5	0·6	0·7	0·8	0·9	1·0	1·1	1·2	1·3	1·4	1·5	1·6
Punch Load P ; lbf	non-osc.	73	153	217	283	320	335	322	285	242	177						
	osc.	63	140	203	266	300	317	310	273	227	171						
	ΔP	10	13	14	17	20	18	12	12	15	6						
Blank Holder Friction Force F, lbf.	non-osc.	–	16.3	11.4	12.3	17.0	23.2	27.6	26.6	24.5	16.8						
	osc.	13.5	7.8	4.5	5.1	9.2	14.1	22.3	20.0	20.3	13.5						
	ΔF %	–	52.0	60.5	58.5	46.0	39.3	19.2	24.8	17.1	19.6						
Die Motional Amplitude, ξ_m in. x 10^{-5}	left hand	0.53	0.45	0.38	0.23	0.26	0.28	0.33	0.37	0.38	0.33						
	right hand	0.88	0.75	0.53	0.44	0.31	0.35	0.31	0.44	0.44	0.44						
	mean	0.70	0.60	0.45	0.33	0.28	0.31	0.32	0.40	0.41	0.38						
Velocity Ratio	v/ξ_m	.294	.343	.415	.526	.592	.535	.518	.451	.472	.482						

WEDGE DRAWING TEST DATA.

TEST NUMBER : 010403	MATERIAL : ALUMINIUM .	DRAW RATIO : 1.65:1	TABLE No. 13

Punch Velocity; in/sec.	Blank Holder Force ; lbf	Variac Voltage	Frequency ; kHz.
0.150	421	20.0	13.16

Punch Travel; in.		0·1	0·2	0·3	0·4	0·5	0·6	0·7	0·8	0·9	1·0	1·1	1·2	1·3	1·4	1·5	1·6
Punch Load P; lbf	non-osc.	77	140	211	275	320	337	326	296	247	154						
	osc.	66	128	188	258	287	302	289	250	200	130						
	ΔP	11	12	23	17	33	35	37	46	47	24						
Blank Holder Friction Force F, lbf.	non-osc.	-	18.7	14.7	14.1	13.8	16.7	18.9	20.7	23.4	18.1						
	osc.	-	2.9	2.2	2.2	2.5	2.6	3.3	2.5	4.9	5.6						
	ΔF %	-	84.5	85.0	84.5	82.0	84.0	82.5	88.0	79.0	69.0						
Die Motional Amplitude, ξ_m in. x 10^{-5}	left hand	0.93	0.94	0.93	0.90	0.87	0.90	1.06	1.39	1.58	1.48						
	right hand	1.40	1.24	1.15	0.96	0.87	0.78	0.80	0.97	1.33	1.68						
	mean	1.16	1.09	1.04	0.93	0.87	0.84	0.93	1.18	1.45	1.58						
Velocity Ratio	v/ξ_m	.156	.167	.181	.195	.208	.216	.195	.154	.125	.115						

WEDGE DRAWING TEST DATA.

TEST NUMBER : 010404	MATERIAL : ALUMINIUM .	DRAW RATIO : 1.65:1	TABLE No. 14

Punch Velocity; in/sec.	Blank Holder Force ; lbf	Variac Voltage	Frequency ; kHz.
0.14	404	20.0	13.15

Punch Travel; in.		0·1	0·2	0·3	0·4	0·5	0·6	0·7	0·8	0·9	1·0	1·1	1·2	1·3	1·4	1·5	1·6
Punch Load P; lbf	non-osc.	–	–	–	–	–	–	–	–	–	–						
	osc.	50	122	192	254	289	307	287	236	177	111						
	ΔP	–	–	–	–	–	–	–	–	–	–						
Blank Holder Friction Force F, lbf.	non-osc.*	29.0	26.0	16.0	15.0	18.0	24.5	28.7	26.2	21.3	16.7						
	osc.	6.5	2.5	1.6	1.9	2.3	10.0	11.4	10.0	2.3	–						
	ΔF %	78	91	90	87	87	59	60	62	89	–						
Die Motional Amplitude, ξ_m in. x 10^{-5}	left hand	0.95	0.90	1.35	1.15	1.10	1.05	1.10	1.40	1.65	1.85						
	right hand	1.45	1.35	1.15	1.05	0.90	0.70	0.80	1.00	1.25	1.75						
	mean	1.20	1.10	1.25	1.10	1.03	1.35	1.45	1.20	1.45	1.80						
Velocity Ratio	v/ξ_m	.141	.154	.136	.154	.165	.126	.117	.141	.117	.094						

* Mean of non-oscillatory test results.

WEDGE DRAWING TEST DATA.

TEST NUMBER : 010405		MATERIAL : ALUMINIUM .						DRAW RATIO : 1.65:1					TABLE No. 15				
Punch Velocity; in/sec.		Blank Holder Force ; lbf						Variac Voltage					Frequency ; kHz.				
0.139		401						40					13.20				
Punch Travel; in.		0·1	0·2	0·3	0·4	0·5	0·6	0·7	0·8	0·9	1·0	1·1	1·2	1·3	1·4	1·5	1·6
Punch Load P; lbf	non-osc.	63	144	218	287	317	338	332	287	242	130						
	osc.	49	117	187	252	277	285	263	215	171	95						
	ΔP	14	27	31	35	40	53	69	72	71	35						
Blank Holder Friction Force F, lbf.	non-osc.	-	28.6	20.1	16.0	17.4	20.5	25.0	25.6	22.8	-						
	osc.	2.7	2.0	1.6	1.6	2.0	2.2	2.2	2.0	-	-						
	ΔF %	-	93	92	90	88	89	91	92	-	-						
Die Motional Amplitude, ξ_m in. x 10^{-5}	left hand	3.1	3.7	3.5	3.0	2.5	2.3	2.4	2.7	3.1	3.2						
	right hand	3.7	2.9	2.6	2.3	2.2	2.3	2.5	2.8	3.1	3.2						
	mean	3.4	3.3	3.0	2.65	2.35	2.3	2.45	2.75	3.10	3.20						
Velocity Ratio	V/ξ_m	.049	.051	.056	.063	.071	.073	.068	.061	.054	.052						

WEDGE DRAWING TEST DATA.

TEST NUMBER : 010406		MATERIAL : ALUMINIUM .						DRAW RATIO : 1.65:1					TABLE No. 16				
Punch Velocity; in/sec.		Blank Holder Force ; lbf						Variac Voltage					Frequency; kHz.				
0.13		398						40					13.14				
Punch Travel; in.		0·1	0·2	0·3	0·4	0·5	0·6	0·7	0·8	0·9	1·0	1·1	1·2	1·3	1·4	1·5	1·6
Punch Load P; lbf	non-osc.	–	–	–	–	–	–	–	–	–	–						
	osc.	57	103	188	245	272	278	250	217	160	81						
	ΔP	–	–	–	–	–	–	–	–	–	–						
Blank Holder Friction Force F, lbf.	non-osc.*	29.0	26.0	16.0	15.0	18.0	24.5	26.7	26.2	21.3	16.7						
	osc.	5.7	3.6	1.5	1.0	2.6	2.2	2.0	1.0	0	0						
	ΔF %	80	86	90	94	86	91	92	96	100	100						
Die Motional Amplitude, ξ_m in. x 10^{-5}	left hand	3.4	3.7	3.5	3.1	3.1	3.0	3.2	3.6	3.9	4.4						
	right hand	3.7	3.4	3.4	3.5	3.1	2.8	2.9	3.3	3.8	3.9						
	mean	3.55	3.55	3.45	3.30	3.10	2.90	3.05	3.45	3.85	4.15						
Velocity Ratio	$V/\dot{\xi}_m$	.044	.044	.046	.048	.051	.054	.052	.046	.044	.038						

* Mean of non-oscillatory test results

WEDGE DRAWING TEST DATA.

TEST NUMBER : 010407	MATERIAL : ALUMINIUM .	DRAW RATIO : 1.65:1	TABLE No. 17

Punch Velocity; in/sec.	Blank Holder Force ; lbf	Variac Voltage	Frequency ; kHz.
0.125	408	60	13.14

Punch Travel; in.		0·1	0·2	0·3	0·4	0·5	0·6	0·7	0·8	0·9	1·0	1·1	1·2	1·3	1·4	1·5	1·6
Punch Load P; lbf	non-osc.	60	138	212	281	320	335	320	285	235	135						
	osc.	45	105	176	241	266	270	245	203	153	72						
	ΔP	15	33	36	40	54	65	75	82	82	63						
Blank Holder Friction Force F, lbf.	non-osc.	32.2	30.0	24.2	15.6	15.5	18.0	20.5	21.2	22.5	24.5						
	osc.	2.5	1.2	1.2	1.2	1.0	2.0	0	0	0	0						
	ΔF %	91	96	95	93	94	95	100	100	100	100						
Die Motional Amplitude, ξ_m in. x 10^{-5}	left hand	5.45	5.75	5.70	4.90	4.65	4.65	4.70	5.00	5.35	5.75						
	right hand	4.35	4.35	4.40	4.25	3.80	3.95	4.75	4.65	5.10	5.55						
	mean	4.90	5.05	5.05	4.58	4.22	4.30	4.73	4.82	5.23	5.65						
Velocity Ratio	v/ξ_m	.031	.030	.030	.033	.036	.035	.032	.031	.029	.027						

WEDGE DRAWING TEST DATA.

TEST NUMBER : 010408	MATERIAL : ALUMINIUM .	DRAW RATIO : 1.65:1	TABLE No. 18

Punch Velocity; in/sec.	Blank Holder Force ; lbf	Variac Voltage	Frequency ; kHz.
0.13	403	60	13.20

Punch Travel; in.		0·1	0·2	0·3	0·4	0·5	0·6	0·7	0·8	0·9	1·0	1·1	1·2	1·3	1·4	1·5	1·6
Punch Load P; lbf	non-osc.	-	-	-	-	-	-	-	-	-	-						
	osc.	56	105	194	255	287	292	260	206	155	66						
	ΔP	-	-	-	-	-	-	-	-	-	-						
Blank Holder Friction Force F, lbf.	non-osc.	29.0	26.0	16.0	15.0	18.0	24.5	26.7	26.2	21.3	16.7						
	osc.	0	0	0	0	0	0	0	0	0	0						
	ΔF %	100	100	100	100	100	100	100	100	100	100						
Die Motional Amplitude, ξ_m in. x 10^{-5}	left hand	5.6	5.6	5.3	4.1	3.9	4.1	4.6	4.8	5.1	4.8						
	right hand	4.1	4.9	4.6	4.4	4.0	4.2	4.5	4.7	5.3	4.9						
	mean	4.85	5.25	4.95	4.25	3.95	4.15	4.55	4.75	5.15	4.85						
Velocity Ratio	v/ξ_m	.032	.030	.032	.037	.040	.038	.035	.033	.030	.032						

WEDGE DRAWING TEST DATA.

TEST NUMBER : 010501	MATERIAL : ALUMINIUM .	DRAW RATIO : 1.70:1	TABLE No. 19

Punch Velocity; in/sec.	Blank Holder Force ; lbf	Variac Voltage	Frequency ; kHz.
0.16	442	10	13.30

Punch Travel; in.		0·1	0·2	0·3	0·4	0·5	0·6	0·7	0·8	0·9	1·0	1·1	1·2	1·3	1·4	1·5	1·6
Punch Load P; lbf	non-osc.	-	-	-	-	-	-	-	-	-	-	-	-				
	osc.	87	170	262	324	360	380	380	378	340	276	242	95				
	ΔP	-	-	-	-	-	-	-	-	-	-	-	-				
Blank Holder Friction Force F, lbf.	non-osc.*	33.9	25.6	17.4	15.6	18.5	21.3	23.8	25.5	26.5	23.5	21.5	-				
	osc.	16.0	17.4	13.8	12.9	11.8	16.1	20.1	24.5	25.0	20.3	20.3	-				
	ΔF %	53	32	21	17	36	24	16	4	6	14	6	-				
Die Motional Amplitude, ξ_m. in. x 10^{-5}	left hand	0.32	0.28	0.28	0.32	0.28	0.28	0.26	0.26	0.26	0.27	0.28	0.28				
	right hand	0.78	0.58	0.44	0.40	0.37	0.44	0.44	0.40	0.40	0.42	0.40	0.35				
	mean	0.55	0.43	0.36	0.36	0.33	0.36	0.35	0.33	0.33	0.35	0.34	0.32				
Velocity Ratio	V/ξ_m	.345	.442	.530	.530	.575	.530	.543	.575	.575	.543	.560	.594				

* Mean of non-oscillatory Test results.

WEDGE DRAWING TEST DATA.

TEST NUMBER : 010502	MATERIAL : ALUMINIUM .	DRAW RATIO : 1.70:1	TABLE No. 20

Punch Velocity; in/sec.	Blank Holder Force ; lbf	Variac Voltage	Frequency ; kHz.
0.17	438	20	13.15

Punch Travel; in.		0·1	0·2	0·3	0·4	0·5	0·6	0·7	0·8	0·9	1·0	1·1	1·2	1·3	1·4	1·5	1·6
Punch Load P; lbf	non-osc.	83	169	250	315	357	381	375	357	320	248	161					
	osc.	76	143	219	283	322	346	343	321	275	206	135					
	ΔP	7	26	31	32	35	35	32	36	45	42	26					
Blank Holder Friction Force F, lbf.	non-osc.	-	-	-	-	-	23.5	28.5	29.0	29.0	28.5	-					
	osc.	15.5	5.5	3.5	5.0	8.0	11.0	11.5	17.2	17.2	4.5	-					
	ΔF %	-	-	-	-	-	53	57	41	41	84	-					
Die Motional Amplitude, ξ_m in. x 10^{-5}	left hand	0.25	0.40	0.60	0.80	0.80	0.80	0.65	0.70	1.20	1.60	-					
	right hand	0.95	0.70	1.45	1.35	1.05	0.70	0.70	0.80	0.95	1.45	-					
	mean	0.60	0.55	1.03	1.08	0.93	0.75	0.67	0.75	1.07	1.53	-					
Velocity Ratio	$v/\dot{\xi}_m$	.343	.374	.200	.190	.221	.274	.308	.274	.192	.134	-					

WEDGE DRAWING TEST DATA.

TEST NUMBER : 010503	MATERIAL : ALUMINIUM .	DRAW RATIO : 1.70:1	TABLE No. 21

Punch Velocity; in/sec.	Blank Holder Force ; lbf	Variac Voltage	Frequency ; kHz.
0.14	439	20	13.20

Punch Travel; in.		0·1	0·2	0·3	0·4	0·5	0·6	0·7	0·8	0·9	1·0	1·1	1·2	1·3	1·4	1·5	1·6
Punch Load P; lbf	non-osc.	-	-	-	-	-	-	-	-	-	-	-	-				
	osc.	48	119	184	250	285	307	310	316	291	262	219	184				
	ΔP	-	-	-	-	-	-	-	-	-	-	-	-				
Blank Holder Friction Force F, lbf.	non-osc.*	33.9	25.6	17.4	15.6	18.5	21.3	13.8	25.5	26.5	23.5	21.5	-				
	osc.	6.7	2.7	2.5	2.5	2.7	3.1	5.6	7.2	8.3	10.7	15.1	15.4				
	ΔF %	80	89	86	84	86	85	76	72	69	56	30	-				
Die Motional Amplitude, ξ_m in. x 10^{-5}	left hand	-	1.10	0.97	0.83	0.74	0.74	0.83	0.92	1.02	1.11	1.16	1.16				
	right hand	-	1.33	1.33	1.02	0.93	0.97	1.28	1.42	1.55	1.59	1.48	1.46				
	mean	-	1.21	1.15	1.93	0.84	0.86	1.06	1.17	1.28	1.35	1.32	1.31				
Velocity Ratio	$v/\dot{\xi}_m$	-	.140	.147	.088	.201	.196	.160	.145	.132	.125	.128	.129				

* Mean of non-oscillatory Test results.

WEDGE DRAWING TEST DATA.

TEST NUMBER : 010504	MATERIAL : ALUMINIUM .	DRAW RATIO : 1.70:1	TABLE No. 22

Punch Velocity; in/sec.	Blank Holder Force ; lbf	Variac Voltage	Frequency ; kHz.
0.16	449	20	13.20

Punch Travel; in.		0·1	0·2	0·3	0·4	0·5	0·6	0·7	0·8	0·9	1·0	1·1	1·2	1·3	1·4	1·5	1·6
Punch Load P; lbf	non-osc.	-	-	-	-	-	-	-	-	-	-	-	-				
	osc.	59	128	217	280	336	345	358	358	336	287	232	167				
	ΔP	-	-	-	-	-	-	-	-	-	-	-	-				
Blank Holder Friction Force F, lbf.	non-osc.*	33.9	25.6	17.4	15.6	18.5	21.3	23.8	25.5	26.5	23.5	21.5	-				
	osc.	13.5	8.5	8.0	7.0	6.8	9.0	11.0	15.6	18.0	19.0	18.0	13.5				
	ΔF %	60	67	54	55	63	58	54	39	32	19	16	-				
Die Motional Amplitude, ξ_m in. x 10^{-5}	left hand	1.00	1.15	0.95	0.70	0.60	0.55	0.50	0.55	0.65	0.60	0.55	-				
	right hand	1.05	1.05	0.70	0.60	0.50	0.55	0.60	0.75	0.90	1.05	1.00					
	mean	1.03	1.10	0.83	0.65	0.55	0.55	0.55	0.65	0.78	0.83	0.78					
Velocity Ratio	v/ξ_m	.188	.175	.232	.296	.350	.350	.350	.296	.247	.232	.247					

* Mean of non-oscillatory test results.

WEDGE DRAWING TEST DATA.

TEST NUMBER : 010505	MATERIAL : ALUMINIUM .	DRAW RATIO : 1.70:1	TABLE No. 23

Punch Velocity; in/sec.	Blank Holder Force ; lbf	Variac Voltage	Frequency ; kHz.
0.16	451	40	13.10

Punch Travel; in.		0·1	0·2	0·3	0·4	0·5	0·6	0·7	0·8	0·9	1·0	1·1	1·2	1·3	1·4	1·5	1·6
Punch Load P; lbf	non-osc.	96	180	256	321	360	381	369	345	301	226	107					
	osc.	82	149	231	288	314	321	310	276	226	161	77					
	ΔP	14	31	25	33	46	60	59	69	75	65	30					
Blank Holder Friction Force F, lbf.	non-osc.	-	-	18.1	19.5	22.0	25.5	29.5	31.0	28.0	-	-					
	osc.	3.5	3.4	3.3	2.7	3.3	4.0	5.5	3.3	1.8	-	-					
	ΔF %	-	-	82	86	85	84	83	89	93	-	-					
Die Motional Amplitude, ξ_m in. x 10^{-5}	left hand	1.80	2.10	2.60	2.60	2.50	2.40	2.25	2.35	2.55	3.60	3.70					
	right hand	1.80	2.05	2.05	2.00	1.90	1.75	1.75	1.70	1.85	2.80	3.35					
	mean	1.80	2.08	2.32	2.30	2.70	2.08	2.00	2.03	3.20	3.20	3.53					
Velocity Ratio	$v/\dot{\xi}_m$	.108	.094	.084	.085	.072	.094	.097	.096	.088	.061	.055					

WEDGE DRAWING TEST DATA.

TEST NUMBER : 010506	MATERIAL : ALUMINIUM .	DRAW RATIO : 1.70:1	TABLE No. 24

Punch Velocity; in/sec.	Blank Holder Force ; lbf	Variac Voltage	Frequency ; kHz.
0.13	442	60	13.41

Punch Travel; in.		0·1	0·2	0·3	0·4	0·5	0·6	0·7	0·8	0·9	1·0	1·1	1·2	1·3	1·4	1·5	1·6
Punch Load P; lbf	non-osc.	71	157	230	302	347	364	370	363	330	258	151					
	osc.	56	123	188	248	286	281	293	268	224	174	112					
	ΔP	15	34	42	54	61	83	77	95	106	84	39					
Blank Holder Friction Force F, lbf.	non-osc.	-	-	14.9	17.8	23.4	25.0	25.7	27.4	30.1	33.5	34.6					
	osc.	-	-	0	0	0	0	0	0.9	1.6	1.3	0					
	ΔF%	-	-	100	100	100	100	100	97	95	96	100					
Die Motional Amplitude, ξ_m in. x 10^{-5}	left hand	5.0	5.4	5.2	5.0	4.8	4.7	4.6	4.7	5.0	5.4	6.0					
	right hand	4.4	4.3	4.1	3.8	3.5	3.5	3.6	3.8	4.3	4.7	4.8					
	mean	4.7	4.8	4.7	4.4	4.2	4.1	4.1	4.3	4.7	5.1	5.4					
Velocity Ratio	$V/\dot{\xi}_m$	.034	.033	.034	.036	.038	.039	.038	.037	.034	.031	.029					

WEDGE DRAWING TEST DATA.

TEST NUMBER : 010507	MATERIAL : ALUMINIUM .	DRAW RATIO : 1.70:1	TABLE No. 25

Punch Velocity; in/sec.	Blank Holder Force ; lbf	Variac Voltage	Frequency ; kHz.
0.16	433	60	13.40

Punch Travel; in.		0·1	0·2	0·3	0·4	0·5	0·6	0·7	0·8	0·9	1·0	1·1	1·2	1·3	1·4	1·5	1·6
Punch Load P; lbf	non-osc.	83	150	226	291	351	375	381	370	338	286	214	83				
	osc.	60	119	185	244	291	307	302	286	244	196	137	60				
	ΔP	23	31	41	47	60	68	79	84	94	90	77	23				
Blank Holder Friction Force F, lbf.	non-osc.	-	-	11.0	15.5	19.0	24.0	28.0	32.0	35.5	31.0	18.0	10.0				
	osc.	-	-	0.5	0.9	0.9	1.8	2.3	2.3	2.9	0.7	-	-				
	ΔF %	-	-	96	95	95	95	92	93	92	98	-	-				
Die Motional Amplitude, ξ_m in. x 10^{-5}	left hand	4.40	5.75	6.05	5.85	5.90	5.90	5.65	5.35	5.45	6.20	6.75	6.95				
	right hand	4.30	5.30	5.80	5.40	4.95	4.50	4.25	4.00	4.00	4.35	5.05	5.40				
	mean	4.35	5.53	5.93	5.63	5.48	5.20	4.95	4.68	4.73	5.28	6.40	6.18				
Velocity Ratio	$v/\dot{\xi}_m$	.044	.034	.032	.034	.035	.036	.038	.041	.040	.036	.030	.031				

WEDGE DRAWING TEST DATA.

TEST NUMBER : 010508	MATERIAL : ALUMINIUM .	DRAW RATIO : 1.70:1	TABLE No. 26

Punch Velocity ; in/sec.	Blank Holder Force ; lbf	Variac Voltage	Frequency ; kHz.
0.14	437	60	13.14

Punch Travel ; in.		0·1	0·2	0·3	0·4	0·5	0·6	0·7	0·8	0·9	1·0	1·1	1·2	1·3	1·4	1·5	1·6
Punch Load P ; lbf	non-osc.	74	134	201	272	308	325	336	314	246	185	–					
	osc.	50	107	177	235	266	268	246	218	167	123	–					
	ΔP	24	27	24	37	42	57	90	96	79	62	–					
Blank Holder Friction Force F, lbf.	non-osc.	44.5	38.0	24.5	20.1	21.2	22.3	26.8	26.8	22.3	–	–					
	osc.	3.3	1.1	1.2	1.8	1.6	0	0	0	0	–	–					
	ΔF %	93	97	95	90	88	100	100	100	100	–	–					
Die Motional Amplitude, ξ_m in. x 10^{-5}	left hand	6.3	5.2	4.6	4.3	4.0	3.9	4.1	4.3	4.6	5.0	5.0					
	right hand	4.3	4.0	4.2	3.7	3.7	3.7	3.9	4.1	4.5	4.6	4.4					
	mean	5.3	4.6	4.4	4.0	3.9	3.8	4.0	4.2	4.6	4.8	4.7					
Velocity Ratio	$v/\dot{\xi}_m$	.032	.037	.039	.043	.044	.045	.043	.041	.037	.035	.036					

NON-OSCILLATORY WEDGE DRAWING TEST DATA.

TEST NUMBER	DRAW RATIO; 1.50:1					BLANK HOLDER FORCE; 220 lbf.						PUNCH VELOCITY; 0.34 in./sec.					
	Punch Travel, in	0.1	0.2	0.3	0.4	0.5	0.6	0.7	0.8	0.9	1.0	1.1	1.2	1.3	1.4	1.5	1.6
020100	Punch load; lbf	46	88	156	204	233	218	179	135								
	Blank Holder Friction Force	24.0	17.6	11.1	9.0	10.1	12.0	11.5	10.0								
020100/1	Punch load; lbf	43	102	161	209	235	216	179	129								
	B/H Friction Force; lbf.	22.0	16.4	12.1	8.9	9.0	11.0	10.6	8.1								
	Punch load; lbf																
	B/H Friction Force; lbf.																
	DRAW RATIO; 1.60:1					BLANK HOLDER FORCE; 340 lbf.						PUNCH VELOCITY; 0.35 in./sec.					
020300	Punch load; lbf	33	78	145	208	252	278	278	280	230	193	96					
	B/H Friction Force; lbf.	-	18.5	13.5	8.0	7.0	8.0	10.0	12.0	17.0	14.5	-					
020300/1	Punch load; lbf	41	80	151	208	256	286	306	285	230	181						
	B/H Friction Force; lbf.	20.1	15.1	9.6	8.8	10.2	13.4	16.0	17.5	16.1	14.2						
	Punch load; lbf																
	B/H Friction Force; lbf.																

TABLE No: 27

NON-OSCILLATORY WEDGE DRAWING TEST DATA.

TEST NUMBER	DRAW RATIO; 1.70:1					BLANK HOLDER FORCE; 415 lbf.						PUNCH VELOCITY; 0.31 in./sec.					
	Punch Travel, in	0.1	0.2	0.3	0.4	0.5	0.6	0.7	0.8	0.9	1.0	1.1	1.2	1.3	1.4	1.5	1.6
020500	Punch load; lbf	30	108	224	284	324	338	342	336	306	248	193	56				
	Blank Holder Friction Force	21.8	12.7	4.5	6.3	9.1	12.3	12.9	16.3	16.1	20.2	16.5	-				
020500/1	Punch load; lbf	45	110	180	256	295	316	324	328	305	253	209	46				
	B/H Friction Force; lbf.	32.5	25.5	12.5	9.7	9.0	11.0	13.5	16.0	17.5	17.8	18.4	-				
020500/2	Punch load; lbf	67	128	210	266	305	328	336	336	312	252	208	76				
	B/H Friction Force; lbf.	30.0	26.4	11.2	8.9	11.2	12.9	14.5	16.7	18.9	19.6	17.9	-				
	DRAW RATIO; 1.80:1					BLANK HOLDER FORCE; 502 lbf.						PUNCH VELOCITY; 0.34 in./sec.					
020700	Punch load; lbf	37	96	183	263	319	347	364	364	364	356	314	246	179	50		
	B/H Friction Force; lbf.	29.0	23.4	10.1	7.8	10.7	11.2	12.3	13.4	14.9	19.6	20.1	16.1	15.6	-		
020700/1	Punch load; lbf	31	106	190	262	319	360	375	375	370	364	328	263	201	67		
	B/H Friction Force; lbf.	31.2	16.7	17.8	11.6	12.9	13.4	14.3	14.5	14.5	16.7	19.0	17.8	16.7	-		
	Punch load; lbf																
	B/H Friction Force; lbf.																

TABLE No: 28

NON-OSCILLATORY WEDGE DRAWING TEST DATA.

TEST NUMBER	DRAW RATIO ; 1.90:1					BLANK HOLDER FORCE; 620 lbf.						PUNCH VELOCITY; 0.33 in./sec.					
	Punch Travel, in	0.1	0.2	0.3	0.4	0.5	0.6	0.7	0.8	0.9	1.0	1.1	1.2	1.3	1.4	1.5	1.6
020900	Punch load; lbf	77	147	228	308	362	403	422									
	Blank Holder Friction Force	38.4	15.6	12.1	10.7	11.6	13.2	16.1									
020900/1	Punch load; lbf	45	123	224	297	358	402	416									
	B/H Friction Force; lbf.	26.8	22.3	11.4	9.1	8.9	10.0	11.1									
	Punch load; lbf																
	B/H Friction Force; lbf.																
	DRAW RATIO;					BLANK HOLDER FORCE; lbf.						PUNCH VELOCITY; in./sec.					
	Punch load; lbf																
	B/H Friction Force; lbf.																
	Punch load; lbf																
	B/H Friction Force; lbf.																
	Punch load; lbf																
	B/H Friction Force; lbf.																

TABLE No: 29

WEDGE DRAWING TEST DATA.

TEST NUMBER : 020101	MATERIAL : ALUMINIUM .	DRAW RATIO : 1.50:1	TABLE No. 30

Punch Velocity; in/sec.	Blank Holder Force ; lbf	Variac Voltage	Frequency ; kHz.
0.341	225	15	12.98

Punch Travel; in.		0·1	0·2	0·3	0·4	0·5	0·6	0·7	0·8	0·9	1·0	1·1	1·2	1·3	1·4	1·5	1·6
Punch Load P; lbf	non-osc.	46	90	157	202	223	224	179	139								
	osc.	36	78	148	191	224	211	166	126								
	ΔP	10	12	9	11	9	13	13	13								
Blank Holder Friction Force F, lbf.	non-osc.	-	-	-	-	9.0	11.0	10.0	7.9								
	osc.	-	-	-	-	3.6	6.3	5.6	4.5								
	ΔF %	-	-	-	-	60	43	44	43								
Die Motional Amplitude, ξ_m in. x 10^{-5}	left hand	-	-	.56	.69	.79	.70	.65	.7								
	right hand	1.00	1.25	1.1	1.37	1.75	1.15	1.2	1.45								
	mean	1.00	1.25	.83	.91	1.02	.92	.92	1.07								
Velocity Ratio	V/ξ_m	.418	.336	.502	.457	.410	.455	.455	.391								

WEDGE DRAWING TEST DATA.

TEST NUMBER : 020102	MATERIAL : ALUMINIUM .	DRAW RATIO : 1.50:1	TABLE No.31

Punch Velocity; in/sec.	Blank Holder Force ; lbf	Variac Voltage	Frequency ; kHz.
0.348	220	20	12.99

Punch Travel; in.		0·1	0·2	0·3	0·4	0·5	0·6	0·7	0·8	0·9	1·0	1·1	1·2	1·3	1·4	1·5	1·6
Punch Load P; lbf	non-osc.	39	106	168	210	235	212	179	129								
	osc.	-	90	154	192	218	195	159	101								
	ΔP	-	16	14	18	17	17	20	28								
Blank Holder Friction Force F, lbf.	non-osc.	-	-	-	6.9	11.1	14.0	12.9	-								
	osc.	-	-	-	1.1	3.4	6.3	6.3	-								
	ΔF %	-	-	-	84	69	55	51									
Die Motional Amplitude, ξ_m in. x 10^{-5}	left hand	-	0.62	1.0	1.2	1.27	1.1	0.8	0.7								
	right hand	0.9	1.5	1.95	1.65	1.6	1.45	1.4	1.4								
	mean	0.9	1.06	1.45	1.5	1.45	1.25	1.1	1.05								
Velocity Ratio	V/ξ_m	.474	.402	.294	.285	.294	.341	.388	.406								

WEDGE DRAWING TEST DATA.

TEST NUMBER : 020103	MATERIAL : ALUMINIUM .	DRAW RATIO : 1.50:1	TABLE No. 32

Punch Velocity; in/sec.	Blank Holder Force ; lbf	Variac Voltage	Frequency ; kHz.
0.348	218	30	12.99

Punch Travel; in.		0·1	0·2	0·3	0·4	0·5	0·6	0·7	0·8	0·9	1·0	1·1	1·2	1·3	1·4	1·5	1·6
Punch Load P; lbf	non-osc.	45	95	166	211	235	218	179	112								
	osc.	34	84	145	190	211	190	145	101								
	ΔP	11	11	21	21	24	28	34	11								
Blank Holder Friction Force F, lbf.	non-osc.	-	-	-	-	8.9	11.2	13.4	-								
	osc.	0	-	-	0	0	0	0	0								
	ΔF %	-	-	-	-	100	100	100	-								
Die Motional Amplitude, ξ_m in. x 10^{-5}	left hand	-	1.55	2.10	2.40	2.55	2.40	2.30	2.25								
	right hand	-	1.85	2.10	2.75	2.55	2.50	2.55	2.45								
	mean	-	1.70	2.10	2.55	2.55	2.45	2.42	2.35								
Velocity Ratio	$v/\dot{\xi}_m$		.257	.204	.168	.168	.174	.172	.182								

WEDGE DRAWING TEST DATA.

TEST NUMBER : 020104	MATERIAL : ALUMINIUM .	DRAW RATIO : 1.50:1	TABLE No. 33

Punch Velocity; in/sec.	Blank Holder Force ; lbf	Variac Voltage	Frequency ; kHz.
0.348	218	40	12.99

Punch Travel; in.		0·1	0·2	0·3	0·4	0·5	0·6	0·7	0·8	0·9	1·0	1·1	1·2	1·3	1·4	1·5	1·6
Punch Load P; lbf	non-osc.	57	118	191	246	258	235	179	146								
	osc.	42	99	174	218	235	202	151	95								
	ΔP	15	19	17	28	23	33	28	51								
Blank Holder Friction Force F, lbf.	non-osc.	-	-	-	-	9.0	12.5	13.5	11.0								
	osc.	0	0	0	0	0	0	0	0								
	ΔF %	-	-	-	-	100	100	100	100								
Die Motional Amplitude, ξ_m in. x 10^{-5}	left hand	-	2.08	2.68	3.20	3.70	3.80	3.70	3.70								
	right hand	2.55	3.30	3.00	3.70	3.62	3.55	3.62	3.70								
	mean	2.55	2.69	2.83	3.45	3.66	3.68	3.66	3.70								
Velocity Ratio	$v/\dot{\xi}_m$	.167	.158	.151	.124	.117	.116	.117	.115								

WEDGE DRAWING TEST DATA.

TEST NUMBER : 020105	MATERIAL : ALUMINIUM .	DRAW RATIO : 1.50:1	TABLE No. 34

Punch Velocity; in/sec.	Blank Holder Force ; lbf	Variac Voltage	Frequency ; kHz.
0.338	220	40	13.09

Punch Travel; in.		0·1	0·2	0·3	0·4	0·5	0·6	0·7	0·8	0·9	1·0	1·1	1·2	1·3	1·4	1·5	1·6
Punch Load P; lbf	non-osc.	37	102	170	217	240	222	180	116								
	osc.	22	70	123	179	206	179	140	79								
	ΔP	15	32	47	38	34	43	40	37								
Blank Holder Friction Force F, lbf.	non-osc.	-	-	-	-	10.1	11.0	-	-								
	osc.	0	0	0	0	0	0	0	0								
	ΔF %	-	-	-	-	100	100	-	-								
Die Motional Amplitude, ξ_m in. x 10^{-5}	left hand	-	0.85	2.60	3.20	2.95	2.70	2.60	2.55								
	right hand	-	1.10	2.20	2.50	2.30	2.15	2.50	2.66								
	mean	-	0.97	2.40	2.85	2.62	2.42	2.55	2.60								
Velocity Ratio	v/ξ_m	-	.422	.171	.158	.157	.169	.161	.158								

WEDGE DRAWING TEST DATA.

TEST NUMBER : 020106	MATERIAL : ALUMINIUM .	DRAW RATIO : 1.50:1	TABLE No. 35

Punch Velocity; in/sec.	Blank Holder Force ; lbf	Variac Voltage	Frequency ; kHz.
0.348	190	60	12.86

Punch Travel; in.		0·1	0·2	0·3	0·4	0·5	0·6	0·7	0·8	0·9	1·0	1·1	1·2	1·3	1·4	1·5	1·6
Punch Load P; lbf	non-osc.	50	112	174	215	239	218	179	67								
	osc.	31	90	146	191	206	179	123	51								
	ΔP	19	22	28	24	33	39	56	16								
Blank Holder Friction Force F, lbf.	non-osc.	-	-	-	8.3	9.0	12.2	15.4	-								
	osc.	0	0	0	0	0	0	0	0								
	ΔF%	-	-	-	100	100	100	100	-								
Die Motional Amplitude, ξ_m in. x 10^{-5}	left hand	-	4.0	5.2	7.2	7.4	7.5	7.2	7.0								
	right hand	-	4.5	7.4	7.4	7.2	7.2	7.0	7.2								
	mean	-	4.25	6.3	7.3	7.3	7.35	7.1	7.1								
Velocity Ratio	V/ξ_m	-	.101	.168	.059	.059	.059	.061	.061								

WEDGE DRAWING TEST DATA.

TEST NUMBER : 020107	MATERIAL : ALUMINIUM .	DRAW RATIO : 1.50:1	TABLE No. 36

Punch Velocity; in/sec.	Blank Holder Force ; lbf .	Variac Voltage	Frequency ; kHz.
0.350	210	80	12.87

Punch Travel; in.		0·1	0·2	0·3	0·4	0·5	0·6	0·7	0·8	0·9	1·0	1·1	1·2	1·3	1·4	1·5	1·6
Punch Load P; lbf	non-osc.	45	101	163	217	240	196	168	101								
	osc.	28	73	129	168	174	146	107	56								
	ΔP	17	28	34	49	66	50	61	45								
Blank Holder Friction Force F, lbf.	non-osc.	21.4	-	-	-	14.5	14.5	12.2	5.4								
	osc.	0	0	0	0	0	0	0	0								
	ΔF %	100	-	-	-	100	100	100	100								
Die Motional Amplitude, ξ_m in. x 10^{-5}	left hand	-	-	9.4	10.5	10.5	10.5	9.9	9.2								
	right hand	3.9	6.9	9.5	8.5	8.9	9.2	9.2	9.2								
	mean	3.9	6.9	9.45	9.5	9.7	9.85	9.55	9.2								
Velocity Ratio	V/ξ_m	.111	.063	.046	.046	.045	.044	.053	.047								

WEDGE DRAWING TEST DATA.

TEST NUMBER : 020108	MATERIAL : ALUMINIUM .	DRAW RATIO : 1.50:1	TABLE No. 37

Punch Velocity; in/sec.	Blank Holder Force ; lbf	Variac Voltage	Frequency ; kHz.
0.342	205	80	12.86

Punch Travel; in.		0·1	0·2	0·3	0·4	0·5	0·6	0·7	0·8	0·9	1·0	1·1	1·2	1·3	1·4	1·5	1·6
Punch Load P; lbf	non-osc.	44	107	163	218	246	213	162	34								
	osc.	28	79	125	179	194	162	118	-								
	ΔP	16	28	38	39	52	51	44	-								
Blank Holder Friction Force F, lbf.	non-osc.	28.1	18.9	15.2	12.6	13.4	13.4	14.0	11.2								
	osc.	0	0	0	0	0	0	0	0								
	ΔF %	100	100	100	100	100	100	100	100								
Die Motional Amplitude, ξ_m in. x 10^{-5}	left hand	-	2.0	5.2	7.9	8.5	9.7	9.9	9.7								
	right hand	-	5.9	10.3	10.7	9.4	9.4	9.4	9.7								
	mean	-	3.95	7.75	9.30	8.95	9.55	9.65	9.7								
Velocity Ratio	$V/\dot{\xi}_m$	-	.107	.055	.045	.047	.044	.044	.044								

WEDGE DRAWING TEST DATA.

TEST NUMBER : 020109	MATERIAL : ALUMINIUM .	DRAW RATIO : 1.50:1	TABLE No. 38

Punch Velocity; in/sec.	Blank Holder Force ; lbf	Variac Voltage	Frequency ; kHz.
0.348	223	100	12.79

Punch Travel; in.		0·1	0·2	0·3	0·4	0·5	0·6	0·7	0·8	0·9	1·0	1·1	1·2	1·3	1·4	1·5	1·6
Punch Load P; lbf	non-osc.	36	84	148	196	225	213	176	146								
	osc.	21	62	112	146	168	146	104	62								
	ΔP	15	22	36	50	57	67	72	84								
Blank Holder Friction Force F, lbf.	non-osc.	20.5	14.5	10.0	10.7	11.4	14.5	17.4	13.8								
	osc.	0	0	0	0	0	0	0	0								
	ΔF %	100	100	100	100	100	100	100	100								
Die Motional Amplitude, ξ_m in. x 10^{-5}	left hand	-	5.7	11.3	13.5	13.7	14.8	14.0	-								
	right hand	-	8.3	11.5	13.3	13.3	13.3	13.3	-								
	mean	-	7.0	11.4	13.4	13.5	14.1	13.7	-								
Velocity Ratio	V/ξ_m	-	.062	.038	.032	.032	.031	.032									

WEDGE DRAWING TEST DATA.

TEST NUMBER : 020110	MATERIAL : ALUMINIUM .	DRAW RATIO : 1.50:1	TABLE No. 39

Punch Velocity ; in/sec.	Blank Holder Force ; lbf	Variac Voltage	Frequency ; kHz.
0.350	226	140	12.75

Punch Travel ; in.		0·1	0·2	0·3	0·4	0·5	0·6	0·7	0·8	0·9	1·0	1·1	1·2	1·3	1·4	1·5	1·6
Punch Load P ; lbf	non-osc.	45	100	157	201	230	213	179	134								
	osc.	20	68	123	157	162	135	101	45								
	ΔP	25	32	34	44	68	78	78	89								
Blank Holder Friction Force F, lbf.	non-osc.	-	-	-	-	20.1	21.2	-	-								
	osc.	0	0	0	0	0	0	0	0								
	ΔF %	-	-	-	-	100	100	-	-								
Die Motional Amplitude, ξ_m in. x 10^{-5}	left hand	-	9.2	15.7	18.0	19.5	19.5	19.2	20.0								
	right hand	-	18.4	19.2	19.7	20.4	21.4	22.2	22.5								
	mean	-	13.8	17.5	18.9	20.0	20.5	20.7	21.3								
Velocity Ratio	v/ξ_m	-	.032	.025	.023	.022	.021	.021	.020								

WEDGE DRAWING TEST DATA.

TEST NUMBER : 020111	MATERIAL : ALUMINIUM .	DRAW RATIO : 1.50:1	TABLE No. 40

Punch Velocity; in/sec.	Blank Holder Force ; lbf	Variac Voltage	Frequency ; kHz.
0.344	252	160	12.79

Punch Travel; in.		0·1	0·2	0·3	0·4	0·5	0·6	0·7	0·8	0·9	1·0	1·1	1·2	1·3	1·4	1·5	1·6
Punch Load P; lbf	non-osc.	36	90	157	207	236	207	174	33.6								
	osc.	20	62	112	151	168	129	95	-								
	ΔP	16	28	45	56	68	78	79	-								
Blank Holder Friction Force F, lbf.	non-osc.	15.2	-	-	14.0	17.5	18.9	18.9	-								
	osc.	0	0	0	0	0	0	0	0								
	ΔF %	100	-	-	100	100	100	100	-								
Die Motional Amplitude, ξ_m in. x 10^{-5}	left hand	-	5.5	13.5	18.9	21.0	21.0	21.4	21.5								
	right hand	-	13.4	23.4	23.5	22.7	22.7	22.7	23.5								
	mean	-	9.5	18.5	21.2	21.9	21.9	22.1	22.5								
Velocity Ratio	$v/\dot{\xi}_m$	-	.045	.023	.020	.019	.019	.019	.019								

WEDGE DRAWING TEST DATA.

TEST NUMBER : 020112	MATERIAL : ALUMINIUM .	DRAW RATIO : 1.50:1	TABLE No. 41

Punch Velocity; in/sec.	Blank Holder Force ; lbf	Variac Voltage	Frequency ; kHz.
0.342	207	180	12.75

Punch Travel; in.		0·1	0·2	0·3	0·4	0·5	0·6	0·7	0·8	0·9	1·0	1·1	1·2	1·3	1·4	1·5	1·6
Punch Load P; lbf	non-osc.	39	103	168	218	249	235	191	95								
	osc.	19	64	123	150	157	123	84	34								
	ΔP	20	39	45	68	92	112	107	61								
Blank Holder Friction Force F, lbf.	non-osc.	20.5	-	-	-	22.3	23.4	-	-								
	osc.	0	0	0	0	0	0	0	0								
	ΔF %	100	-	-	-	100	100	-	-								
Die Motional Amplitude, ξ_m in. x 10^{-5}	left hand	-	16.0	24.2	29.9	30.2	30.9	30.9	32.2								
	right hand	-	25.0	27.2	27.8	28.0	29.2	30.0	29.8								
	mean	-	20.5	25.7	28.9	29.1	30.1	30.5	31.0								
Velocity Ratio	v/ξ_m	-	.021	.017	.015	.015	.014	.014	.014								

WEDGE DRAWING TEST DATA.

TEST NUMBER : 020301	MATERIAL : ALUMINIUM .	DRAW RATIO : 1.60:1	TABLE No. 42

Punch Velocity; in/sec.	Blank Holder Force ; lbf	Variac Voltage	Frequency ; kHz.
0.348	339	15	13.17

Punch Travel; in.		0·1	0·2	0·3	0·4	0·5	0·6	0·7	0·8	0·9	1·0	1·1	1·2	1·3	1·4	1·5	1·6
Punch Load P; lbf	non-osc.	41	80	151	210	257	288	300	250	234	196	-					
	osc.	39	78	142	204	251	280	294	274	228	192	-					
	ΔP	2	2	9	7	6	8	6	6	6	4	-					
Blank Holder Friction Force F, lbf.	non-osc.	20.0	14.5	9.4	9.4	12.3	17.4	19.0	18.3	17.0	-	-					
	osc.	-	5.6	4.9	6.5	10.0	14.3	16.0	16.0	14.5	-	-					
	ΔF%	-	61	48	31	19	18	16	13	15	-	-					
Die Motional Amplitude, ξ_m in. x 10^{-5}	left hand	-	0.19	0.42	0.42	0.37	0.23	0.23	0.23	0.23	-	-					
	right hand	-	0.80	0.75	0.67	0.62	0.58	0.44	0.44	0.44	-	-					
	mean	-	0.50	0.58	0.54	0.50	0.40	0.34	0.34	0.34	-	-					
Velocity Ratio	$v/\dot{\xi}_m$	-	.840	.725	.781	.840	1.05	1.24	1.24	1.24	-	-					

WEDGE DRAWING TEST DATA.

TEST NUMBER : 020302	MATERIAL : ALUMINIUM .	DRAW RATIO : 1.60:1	TABLE No. 43

Punch Velocity; in/sec.	Blank Holder Force ; lbf	Variac Voltage	Frequency ; kHz.
0.348	328	20	13.27

Punch Travel; in.		0·1	0·2	0·3	0·4	0·5	0·6	0·7	0·8	0·9	1·0	1·1	1·2	1·3	1·4	1·5	1·6
Punch Load P; lbf	non-osc.	45	97	156	217	259	284	280	253	216	181						
	osc.	36	85	144	204	246	269	269	240	199	169						
	ΔP	9	12	12	13	13	15	11	13	17	12						
Blank Holder Friction Force F, lbf.	non-osc.	-	-	-	-	-	-	17.0	20.0	19.0	-						
	osc.	0	0	0	0	0	5.5	8.0	14.0	14.0	-						
	ΔF %	-	-	-	-	-	-	53	28	24	-						
Die Motional Amplitude, ξ_m in. x 10^{-5}	left hand	-	1.00	0.90	0.80	0.90	0.65	0.60	0.57	0.60	-						
	right hand	0.60	0.60	0.90	1.00	1.00	1.02	1.00	1.00	0.90							
	mean	0.60	0.80	0.90	0.90	0.95	0.84	0.80	0.79	0.75							
Velocity Ratio	$V/\dot{\xi}_m$	.694	.521	.462	.462	.438	.491	.521	.529	.555							

WEDGE DRAWING TEST DATA.

TEST NUMBER : 020303	MATERIAL : ALUMINIUM .	DRAW RATIO : 1.60:1	TABLE No. 44

Punch Velocity; in/sec.	Blank Holder Force ; lbf	Variac Voltage	Frequency ; kHz.
0.328	336	30	13.28

Punch Travel; in.		0·1	0·2	0·3	0·4	0·5	0·6	0·7	0·8	0·9	1·0	1·1	1·2	1·3	1·4	1·5	1·6
Punch Load P; lbf	non-osc.	41	78	150	228	266	291	291	273	234	194						
	osc.	31	65	132	210	252	270	265	240	204	169						
	ΔP	10	13	18	18	14	21	26	33	30	25						
Blank Holder Friction Force F, lbf.	non-osc.	22.3	20.7	8.5	8.9	10.0	12.2	15.6	18.3	15.6	-						
	osc.	-	3.3	2.2	2.2	2.2	2.7	2.9	6.7	7.6	-						
	ΔF %	-	84	74	75	78	78	82	63	51	-						
Die Motional Amplitude, ξ_m in. x 10^{-5}	left hand	-	-	0.80	1.20	1.15	1.15	1.10	1.15	-	-						
	right hand	-	-	1.80	1.75	1.65	1.50	1.60	1.60	1.55	1.50						
	mean	-	-	1.30	1.48	1.40	1.31	1.35	1.36	1.55	1.50						
Velocity Ratio	v/ξ_m	-	-	.303	.266	.281	.301	.292	.290	.254	.262						

WEDGE DRAWING TEST DATA.

TEST NUMBER : 020304	MATERIAL : ALUMINIUM .	DRAW RATIO : 1.60:1	TABLE No. 45

Punch Velocity; in/sec.	Blank Holder Force ; lbf	Variac Voltage	Frequency ; kHz.
0.342	348	50	13.21

Punch Travel; in.		0·1	0·2	0·3	0·4	0·5	0·6	0·7	0·8	0·9	1·0	1·1	1·2	1·3	1·4	1·5	1·6
Punch Load P; lbf	non-osc.	38	60	115	173	228	270	294	294	270	216	–					
	osc.	27	48	96	150	204	246	264	252	228	174	126					
	ΔP	11	12	19	23	24	24	30	42	42	42	–					
Blank Holder Friction Force F, lbf.	non-osc.	25.5	24.5	15.0	11.0	11.0	13.5	16.0	16.7	16.7	12.5	–					
	osc.	0	0	0	0	0	0	0	0	0	0	–					
	ΔF %	100	100	100	100	100	100	100	100	100	100	–					
Die Motional Amplitude, ξ_m in. x 10^{-5}	left hand	–	–	–	2.05	2.60	2.62	2.50	2.25	2.20	2.20						
	right hand	–	–	2.90	3.55	3.20	3.00	2.85	2.85	3.00	3.15						
	mean	–	–	2.90	2.80	2.90	2.80	2.70	2.55	2.60	2.70						
Velocity Ratio	$V/\dot{\xi}_m$	–	–	.142	.147	.142	.147	1.53	1.62	.159	.153						

WEDGE DRAWING TEST DATA.

TEST NUMBER : 020305	MATERIAL : ALUMINIUM .	DRAW RATIO : 1.60:1	TABLE No. 46

Punch Velocity; in/sec.	Blank Holder Force ; lbf	Variac Voltage	Frequency ; kHz.
0.292	324	110	12.93

Punch Travel; in.		0·1	0·2	0·3	0·4	0·5	0·6	0·7	0·8	0·9	1·0	1·1	1·2	1·3	1·4	1·5	1·6
Punch Load P; lbf	non-osc.	48	102	187	255	294	300	282	247	192	-	-					
	osc.	30	78	157	210	240	234	210	168	115	-	-					
	ΔP	18	24	30	45	54	66	72	79	77	-	-					
Blank Holder Friction Force F, lbf.	non-osc.	-	-	-	9.0	10.5	13.5	15.0	15.5	15.5	-	-					
	osc.	0	0	0	0	0	0	0	0	0	0	0					
	ΔF %	-	-	-	100	100	100	100	100	100	-	-					
Die Motional Amplitude, ξ_m in. x 10^{-5}	left hand	-	7.20	8.50	11.2	11.5	11.5	11.3	11.7	11.7	11.7						
	right hand	6.85	6.50	7.70	9.40	9.35	8.85	8.50	8.50	8.85	9.20						
	mean	6.85	6.85	8.10	10.3	10.4	10.2	9.90	10.1	10.2	10.4						
Velocity Ratio	v/ξ_m	.052	.052	.045	.035	.035	.035	.036	.036	.035	.035						

WEDGE DRAWING TEST DATA.

TEST NUMBER : 020306	MATERIAL : ALUMINIUM .	DRAW RATIO : 1.60:1	TABLE No. 47

Punch Velocity; in/sec.	Blank Holder Force ; lbf	Variac Voltage	Frequency ; kHz.
0.300	338	180	12.84

Punch Travel; in.		0·1	0·2	0·3	0·4	0·5	0·6	0·7	0·8	0·9	1·0	1·1	1·2	1·3	1·4	1·5	1·6
Punch Load P; lbf	non-osc.	62	133	208	272	306	312	290	243	196	-						
	osc.	35	87	162	209	238	232	196	151	104	-						
	ΔP	27	46	46	63	68	80	94	92	92	-						
Blank Holder Friction Force F, lbf.	non-osc.	18.0	-	-	-	11.0	12.5	15.5	15.5	14.5	-						
	osc.	0	0	0	0	0	0	0	0	0	0						
	ΔF %	100	-	-	-	100	100	100	100	100	-						
Die Motional Amplitude, ξ_m in. x 10^{-5}	left hand	-	-	17.3	22.4	24.5	24.7	24.5	23.7	23.8	24.4						
	right hand	-	17.4	21.0	19.7	19.3	18.3	18.7	20.0	20.7	20.4						
	mean	-	17.4	19.1	21.0	21.9	21.5	21.6	21.8	22.2	22.4						
Velocity Ratio	V/ξ_m	-	.021	.017	.018	.017	.017	.017	.017	.017	.017						

WEDGE DRAWING TEST DATA.

TEST NUMBER : 020307	MATERIAL : ALUMINIUM .	DRAW RATIO : 1.60:1	TABLE No. 48

Punch Velocity; in/sec.	Blank Holder Force ; lbf	Variac Voltage	Frequency ; kHz.
0.300	332	160	13.41

Punch Travel; in.		0·1	0·2	0·3	0·4	0·5	0·6	0·7	0·8	0·9	1·0	1·1	1·2	1·3	1·4	1·5	1·6
Punch Load P; lbf	non-osc.	36	127	197	254	296	304	296	255	214	64						
	osc.	19	81	144	196	233	231	208	162	116	29						
	ΔP	17	46	53	58	63	73	88	93	98	35						
Blank Holder Friction Force F, lbf.	non-osc.	28.0	-	-	-	13.5	18.0	22.0	22.0	22.0	-						
	osc.	0	0	0	0	0	0	0	0	0	0						
	ΔF%	100	-	-	-	100	100	100	100	100	-						
Die Motional Amplitude, ξ_m in. x 10^{-5}	left hand	-	-	16.0	18.2	19.5	19.3	19.3	19.3	19.5	20.0						
	right hand	17.8	16.2	15.1	18.5	18.5	17.0	16.7	16.5	17.7	18.3						
	mean	17.8	16.2	15.6	18.4	19.0	18.2	18.0	17.9	18.6	19.2						
Velocity Ratio	$v/\dot{\xi}_m$	.020	.022	.023	.019	.019	.020	.020	.020	.019	.019						

WEDGE DRAWING TEST DATA.

TEST NUMBER : 020308	MATERIAL : ALUMINIUM .	DRAW RATIO : 1.60:1	TABLE No. 49

Punch Velocity; in/sec.	Blank Holder Force ; lbf	Variac Voltage	Frequency ; kHz.
0.31	337	180	12.83

Punch Travel; in.		0·1	0·2	0·3	0·4	0·5	0·6	0·7	0·8	0·9	1·0	1·1	1·2	1·3	1·4	1·5	1·6
Punch Load P; lbf	non-osc.	36	101	174	235	280	302	280	241	190	-						
	osc.	17	73	140	185	224	230	202	151	112	-						
	ΔP	19	28	34	50	56	72	78	90	78	-						
Blank Holder Friction Force F, lbf.	non-osc.	28.0	-	-	-	18	21.5	21.5	22.0	-	-						
	osc.	0	0	0	0	0	0	0	0	0	-						
	ΔF %	100	-	-	-	100	100	100	100	-	-						
Die Motional Amplitude, ξ_m in. x 10^{-5}	left hand	-	-	10.8	-	22.4	21.8	21.4	21.4	21.4	23.5						
	right hand	-	13.3	12.3	26.7	22.2	20.4	19.9	20.4	21.2	21.5						
	mean	-	13.3	11.5	26.7	22.3	21.1	20.6	20.9	21.3	22.5						
Velocity Ratio	$v/\dot{\xi}_m$	-	.029	.033	.014	.017	.018	.019	.018	.018	.017						

WEDGE DRAWING TEST DATA.

TEST NUMBER : 020309	MATERIAL : ALUMINIUM .	DRAW RATIO : 1.60:1	TABLE No. 50

Punch Velocity; in/sec.	Blank Holder Force ; lbf	Variac Voltage	Frequency ; kHz.
0.335	346	160	12.88

Punch Travel; in.		0·1	0·2	0·3	0·4	0·5	0·6	0·7	0·8	0·9	1·0	1·1	1·2	1·3	1·4	1·5	1·6
Punch Load P; lbf	non-osc.	36	108	168	228	277	288	270	240	192	-						
	osc.	18	72	127	180	214	216	180	145	108	-						
	ΔP	18	36	41	48	63	71	90	95	84	-						
Blank Holder Friction Force F, lbf.	non-osc.	20.0	-	-	-	10.0	13.0	15.5	18.0	-	-						
	osc.	0	0	0	0	0	0	0	0	0	0						
	ΔF %	100	-	-	-	100	100	100	100	-	-						
Die Motional Amplitude, ξ_m in. x 10^{-5}	left hand	-	-	19.5	19.5	20.7	21.4	21.7	20.0	20.7	21.0						
	right hand	-	19.7	22.0	21.2	20.7	20.0	20.0	20.0	20.3	20.0						
	mean	-	19.7	20.8	20.4	20.7	20.7	20.9	20.0	20.5	20.5						
Velocity Ratio	v/ξ_m	-	.021	.020	.020	.020	.020	.020	.021	.020	.020						

WEDGE DRAWING TEST DATA.

TEST NUMBER : 020310	MATERIAL : ALUMINIUM .	DRAW RATIO : 1.60:1	TABLE No. 51

Punch Velocity; in/sec.	Blank Holder Force ; lbf	Variac Voltage	Frequency ; kHz.
0.335	324	130	12.83

Punch Travel; in.		0·1	0·2	0·3	0·4	0·5	0·6	0·7	0·8	0·9	1·0	1·1	1·2	1·3	1·4	1·5	1·6
Punch Load P; lbf	non-osc.	32	105	174	226	273	290	279	244	209	-						
	osc.	17	69	128	181	215	227	192	163	111	-						
	ΔP	13	36	46	45	58	63	87	81	98	-						
Blank Holder Friction Force F, lbf.	non-osc.	24.0	-	-	-	19.0	20.0	22.0	24.0	-	-						
	osc.	0	0	0	0	0	0	0	0	0	0						
	ΔF %	100	-	-	-	100	100	100	100	-	-						
Die Motional Amplitude, ξ_m in. x 10^{-5}	left hand	-	13.8	15.7	18.5	18.5	18.5	17.8	16.8	16.8	-						
	right hand	-	13.7	13.3	15.8	17.0	16.2	15.8	16.0	16.5	16.8						
	mean	-	13.8	14.5	17.2	17.8	17.4	16.8	16.4	16.7	16.8						
Velocity Ratio	$v/\dot{\xi}_m$	-	.030	.029	.024	.023	.023	.025	.025	.025	.025						

WEDGE DRAWING TEST DATA.

TEST NUMBER : 020311	MATERIAL : ALUMINIUM .	DRAW RATIO : 1.60 : 1	TABLE No.52

Punch Velocity; in/sec.	Blank Holder Force ; lbf	Variac Voltage	Frequency ; kHz.
0.348	352	60	12.86

Punch Travel; in.		0·1	0·2	0·3	0·4	0·5	0·6	0·7	0·8	0·9	1·0	1·1	1·2	1·3	1·4	1·5	1·6
Punch Load P; lbf	non-osc.	38	111	180	241	272	290	281	242	210							
	osc.	27	87	148	210	244	250	226	176	140							
	ΔP	11	23	32	31	28	40	55	66	70							
Blank Holder Friction Force F, lbf.	non-osc.	27.0	-	-	-	-	16.3	18.2	18.7	17.4							
	osc.	0	0	0	0	0	0	0	0	0							
	ΔF %	100	-	-	-	-	100	100	100	100							
Die Motional Amplitude, ξ_m in. x 10^{-5}	left hand	-	-	-	7.35	7.70	7.70	6.50	6.20	6.35							
	right hand	-	4.20	5.85	8.85	7.70	6.85	6.20	5.85	6.50							
	mean	-	4.20	5.85	8.10	7.70	6.93	6.35	6.02	6.42							
Velocity Ratio	$V/\dot{\xi}_m$	-	.102	.074	.053	.056	.062	.068	.071	.067							

WEDGE DRAWING TEST DATA.

TEST NUMBER : 020312	MATERIAL : ALUMINIUM .	DRAW RATIO : 1.60:1	TABLE No. 53

Punch Velocity; in/sec.	Blank Holder Force ; lbf	Variac Voltage	Frequency ; kHz.
0.348	340	50	12.92

Punch Travel; in.		0·1	0·2	0·3	0·4	0·5	0·6	0·7	0·8	0·9	1·0	1·1	1·2	1·3	1·4	1·5	1·6
Punch Load P; lbf	non-osc.	40	105	174	235	272	295	284	246	214	-						
	osc.	29	84	150	209	238	254	232	185	145	46						
	ΔP	11	21	24	26	34	41	52	61	69	-						
Blank Holder Friction Force F, lbf.	non-osc.	27	-	-	-	-	12.5	15.5	18.0	19.5	-						
	osc.	0	0	0	0	0	0	0	0	0	0						
	ΔF %	100	-	-	-	-	100	100	100	100	-						
Die Motional Amplitude, ξ_m in. x 10^{-5}	left hand	-	-	4.00	4.50	4.67	5.18	5.00	4.67	4.18	4.85						
	right hand	-	2.17	3.34	3.84	4.00	3.84	3.68	3.84	4.50	5.35						
	mean	-	2.17	3.67	4.17	4.34	5.01	9.34	4.25	4.34	5.10						
Velocity Ratio	$v/\dot{\xi}_m$	-	.198	.117	.103	.099	.086	.099	.101	.099	.084						

WEDGE DRAWING TEST DATA.

TEST NUMBER : 020501	MATERIAL : ALUMINIUM .	DRAW RATIO : 1.70:1	TABLE No.54

Punch Velocity; in/sec.	Blank Holder Force ; lbf	Variac Voltage	Frequency ; kHz.
0.314	418	20	13.62

Punch Travel; in.		0·1	0·2	0·3	0·4	0·5	0·6	0·7	0·8	0·9	1·0	1·1	1·2	1·3	1·4	1·5	1·6
Punch Load P; lbf	non-osc.	-	-	-	-	-	317	330	330	306	258	199					
	osc.	40	132	198	252	298	310	324	320	293	250	189					
	ΔP	-	-	-	-	-	7	6	10	13	8	10					
Blank Holder Friction Force F, lbf.	non-osc.	19	-	5.5	8.5	12.5	17.0	18.5	17.0	17.0	-	-					
	osc.	13.5	13.5	3.5	5.5	10.0	14.5	15.5	15.0	14.5	13.5	-					
	ΔF %	29	-	36	35	21	15	16	12	15	-	-					
Die Motional Amplitude, ξ_m in. x 10^{-5}	left hand	0.10	0.15	0.15	0.15	0.20	0.20	0.25	0.25	0.20	0.20	0.20					
	right hand	0.55	0.50	0.57	0.65	0.60	0.65	0.60	0.65	0.65	0.60	0.60					
	mean	0.32	0.32	0.36	0.40	0.40	0.42	0.42	0.45	0.42	0.40	0.40					
Velocity Ratio	v/ξ_m	1.15	1.15	1.02	.915	.915	.876	.876	.812	.876	.915	.915					

WEDGE DRAWING TEST DATA.

TEST NUMBER : 020502	MATERIAL : ALUMINIUM .	DRAW RATIO : 1.70:1	TABLE No. 55

Punch Velocity; in/sec.	Blank Holder Force ; lbf	Variac Voltage	Frequency ; kHz.
0.314	422	30	13.31

Punch Travel; in.		0·1	0·2	0·3	0·4	0·5	0·6	0·7	0·8	0·9	1·0	1·1	1·2	1·3	1·4	1·5	1·6
Punch Load P; lbf	non-osc.	44	106	188	262	293	320	325	313	274	232	182					
	osc.	32	94	175	250	282	296	303	281	243	206	156					
	ΔP	12	12	13	12	11	24	22	32	31	26	26					
Blank Holder Friction Force F, lbf.	non-osc.	24.0	20.0	14.5	8.0	6.5	10.0	15.5	18.0	20.0	20.0	-					
	osc.	-	-	-	-	-	-	-	2.9	4.5	6.9	-					
	ΔF %	-	-	-	-	-	-	-	84	78	66	-					
Die Motional Amplitude, ξ_m in. x 10^{-5}	left hand	-	-	0.43	0.43	0.50	0.50	0.60	0.50	0.60	0.43	0.43					
	right hand	-	0.45	0.65	0.90	1.05	1.15	1.15	1.25	1.40	1.50	1.70					
	mean	-	0.45	0.54	0.66	0.78	0.82	0.87	0.87	1.00	0.96	1.06					
Velocity Ratio	$V/\dot{\xi}_m$	-	.834	.694	.568	.481	.459	.432	.432	.373	.390	.355					

WEDGE DRAWING TEST DATA.

TEST NUMBER : 020503	MATERIAL : ALUMINIUM .	DRAW RATIO : 1.70:1	TABLE No. 56

Punch Velocity; in/sec.	Blank Holder Force ; lbf	Variac Voltage	Frequency ; kHz.
0.314	418	40	13.17

Punch Travel; in.		0·1	0·2	0·3	0·4	0·5	0·6	0·7	0·8	0·9	1·0	1·1	1·2	1·3	1·4	1·5	1·6
Punch Load P; lbf	non-osc.	48	125	208	266	304	328	334	315	279	236	166	405				
	osc.	38	108	191	247	293	303	298	270	229	183	121	-				
	ΔP	10	17	17	19	11	25	36	45	50	53	44	-				
Blank Holder Friction Force F, lbf.	non-osc.	14.5	-	-	-	4.5	8.5	15.5	17.5	18.0	18.0	11.0	-				
	osc.	0	0	0	0	0	0	0	0	0	0	0	0				
	ΔF %	100	-	-	-	100	100	100	100	100	100	100	-				
Die Motional Amplitude, ξ_m in. x 10^{-5}	left hand	-	-	0.7	1.1	1.4	1.4	1.3	1.3	1.2	1.1	1.2	-				
	right hand	-	1.6	2.0	2.5	2.5	2.5	2.5	2.5	2.7	2.9	3.1	-				
	mean	-	1.6	1.4	1.8	2.0	2.0	1.9	1.9	2.0	2.0	2.2	-				
Velocity Ratio	$V/\dot{\xi}_m$	-	.237	.272	.212	.191	.191	.200	.200	.191	.191	.173	-				

WEDGE DRAWING TEST DATA.

TEST NUMBER : 020504	MATERIAL : ALUMINIUM .	DRAW RATIO : 1.70:1	TABLE No. 57

Punch Velocity; in/sec.	Blank Holder Force ; lbf	Variac Voltage	Frequency ; kHz.
0.320	409	60	13.40

Punch Travel; in.		0·1	0·2	0·3	0·4	0·5	0·6	0·7	0·8	0·9	1·0	1·1	1·2	1·3	1·4	1·5	1·6
Punch Load P; lbf	non-osc.	48	119	191	257	299	322	334	322	284	226	156					
	osc.	36	101	172	229	268	284	292	255	215	167	107					
	ΔP	12	18	19	28	31	38	42	67	69	59	49					
Blank Holder Friction Force F, lbf.	non-osc.	20.0	-	-	15.0	12.5	13.5	15.5	23.0	23.0	23.0	-					
	osc.	0	0	0	0	0	0	0	0	0	0	0					
	ΔF %	100	-	-	100	100	100	100	100	100	100	-					
Die Motional Amplitude, ξ_m in. x 10^{-5}	left hand	-	-	5.3	6.3	6.3	6.3	6.2	5.9	5.8	5.8	6.0					
	right hand	-	4.8	5.5	5.2	4.8	4.5	4.4	4.4	4.6	4.8	5.0					
	mean	-	4.8	5.4	5.8	5.5	5.4	5.3	5.1	5.2	5.3	5.5					
Velocity Ratio	$v/\dot{\xi}_m$	-	.079	.070	.066	.069	.073	.072	.075	.073	.072	.069					

WEDGE DRAWING TEST DATA.

TEST NUMBER : 020505	MATERIAL : ALUMINIUM .	DRAW RATIO : 1.70:1	TABLE No. 58

Punch Velocity; in/sec.	Blank Holder Force ; lbf	Variac Voltage	Frequency ; kHz.
0.32	428	80	12.81

Punch Travel; in.		0·1	0·2	0·3	0·4	0·5	0·6	0·7	0·8	0·9	1·0	1·1	1·2	1·3	1·4	1·5	1·6
Punch Load P; lbf	non-osc.	42	108	179	239	287	317	317	299	262	214	-					
	osc.	28	88	150	210	257	270	262	233	191	131	-					
	ΔP	14	20	29	29	30	47	55	66	71	83	-					
Blank Holder Friction Force F, lbf.	non-osc.	13.5	18.0	-	-	-	13.5	13.5	14.5	15.5	18.0	-					
	osc.	0	0	-	-	-	0	0	0	0	0	-					
	ΔF %	100	100	-	-	-	100	100	100	100	100	-					
Die Motional Amplitude, ξ_m in. x 10^{-5}	left hand	-	-	3.33	3.33	3.00	2.66	3.50	3.33	3.33	2.84	2.00					
	right hand	-	3.50	7.34	4.83	3.50	7.67	7.34	7.67	7.00	8.00	10.3					
	mean	-	3.50	5.34	4.08	3.25	5.18	5.41	5.50	5.17	5.42	6.16					
Velocity Ratio	V/ξ_m	-	.114	.074	.097	.122	.076	.074	.073	.077	.073	.065					

WEDGE DRAWING TEST DATA.

TEST NUMBER : 020506	MATERIAL : ALUMINIUM .	DRAW RATIO : 1.70:1	TABLE No.59

Punch Velocity; in/sec.	Blank Holder Force ; lbf	Variac Voltage	Frequency ; kHz.
0.320	418	120	12.89

Punch Travel; in.		0·1	0·2	0·3	0·4	0·5	0·6	0·7	0·8	0·9	1·0	1·1	1·2	1·3	1·4	1·5	1·6
Punch Load P; lbf	non-osc.	47	122	209	265	306	330	330	306	267	209	162					
	osc.	35	87	180	232	261	272	254	232	185	138	82					
	ΔP	12	35	29	32	45	58	76	74	82	72	80					
Blank Holder Friction Force F, lbf.	non-osc.	24.5	21.5	-	-	14.5	15.5	21.5	23.5	25.5	22.5	-					
	osc.	0	0	0	0	0	0	0	0	0	0	-					
	ΔF %	100	100	-	-	100	100	100	100	100	100	-					
Die Motional Amplitude, ξ_m in. x 10^{-5}	left hand	-	-	-	-	9.8	9.5	9.5	9.3	9.3	8.5	8.8					
	right hand	-	8.4	10.0	10.5	11.5	11.5	11.5	11.5	11.2	11.8	12.7					
	mean	-	8.4	10.0	10.5	10.7	10.5	10.5	10.4	10.3	10.2	10.8					
Velocity Ratio	v/ξ_m	-	.047	.040	.038	.037	.038	.038	,038	.038	,039	,037					

WEDGE DRAWING TEST DATA.

TEST NUMBER : 020507	MATERIAL : ALUMINIUM .	DRAW RATIO : 1.70:1	TABLE No. 60

Punch Velocity; in/sec.	Blank Holder Force ; lbf	Variac Voltage	Frequency ; kHz.
0.30	409	140	12.88

Punch Travel; in.		0·1	0·2	0·3	0·4	0·5	0·6	0·7	0·8	0·9	1·0	1·1	1·2	1·3	1·4	1·5	1·6
Punch Load P; lbf	non-osc.	38	97	184	254	319	335	340	330	292	244	173					
	osc.	21	70	140	200	244	259	265	238	194	152	98					
	ΔP	17	27	44	54	75	76	75	92	98	92	75					
Blank Holder Friction Force F, lbf.	non-osc.	–	–	–	–	16.5	15.5	21.0	23.0	23.0	21.0	15.5					
	osc.	0	0	0	0	0	0	0	0	0	0	0					
	ΔF %	–	–	–	–	100	100	100	100	100	100	100					
Die Motional Amplitude, ξ_m in. x 10^{-5}	left hand	–	–	14.2	16.3	17.5	17.9	18.2	18.5	17.9	17.5	17.0					
	right hand	–	13.3	13.3	14.5	14.7	13.8	13.7	13.8	14.2	14.7	15.3					
	mean	–	13.3	13.8	15.4	16.1	15.8	15.9	16.2	16.0	16.1	16.2					
Velocity Ratio	$v/\dot{\xi}_m$	–	.028	.027	.024	.023	.023	.023	.023	.023	.023	.023					

WEDGE DRAWING TEST DATA.

TEST NUMBER : 020508	MATERIAL : ALUMINIUM .	DRAW RATIO : 1.70:1	TABLE No. 61

Punch Velocity ; in/sec.	Blank Holder Force ; lbf	Variac Voltage	Frequency ; kHz.
0.320	420	180	12.91

Punch Travel ; in.		0·1	0·2	0·3	0·4	0·5	0·6	0·7	0·8	0·9	1·0	1·1	1·2	1·3	1·4	1·5	1·6
Punch Load P ; lbf	non-osc.	54	113	202	262	305	328	335	320	292	246	186					
	osc.	24	84	155	222	262	275	275	239	191	156	96					
	ΔP	30	29	47	40	43	53	60	81	101	90	90					
Blank Holder Friction Force F, lbf.	non-osc.	21.0	17.0	12.5	10.0	13.5	17.0	20.5	26.5	26.5	26.5	22.0					
	osc.	0	0	0	0	0	0	0	0	0	0	0					
	ΔF %	-	-	-	-	-	-	-	-	-	-	-					
Die Motional Amplitude, ξ_m in. x 10^{-5}	left hand	-	-	11.6	12.7	13.7	14.8	14.8	15.2	14.8	14.5	14.5					
	right hand	-	15.5	17.0	17.7	18.3	18.0	16.8	16.2	16.2	16.7	16.8					
	mean	-	15.5	14.3	15.2	16.1	16.4	15.8	15.7	15.5	15.6	15.7					
Velocity Ratio	$V/\dot{\xi}_m$	-	.025	.028	.026	.025	.024	.025	.025	.025	.025	.025					

WEDGE DRAWING TEST DATA.

TEST NUMBER : 020509	MATERIAL : ALUMINIUM .	DRAW RATIO : 1.70:1	TABLE No. 62

Punch Velocity; in/sec.	Blank Holder Force ; lbf	Variac Voltage	Frequency ; kHz.
0.30	418	200	12.86

Punch Travel; in.		0·1	0·2	0·3	0·4	0·5	0·6	0·7	0·8	0·9	1·0	1·1	1·2	1·3	1·4	1·5	1·6
Punch Load P; lbf	non-osc.	43	98	173	246	308	332	345	339	296	234	135					
	osc.	25	68	143	204	253	264	264	247	197	135	74					
	ΔP	18	30	30	42	55	68	81	92	99	99	61					
Blank Holder Friction Force F, lbf.	non-osc.	15.5	–	–	–	10.0	17.0	21.5	27.0	29.0	29.0	–					
	osc.	0	0	0	0	0	0	0	0	0	0	0					
	ΔF %	100	–	–	–	100	100	100	100	100	100	–					
Die Motional Amplitude, ξ_m in. x 10^{-5}	left hand	–	–	–	21.6	25.6	29.3	29.4	31.6	31.2	31.2	30.5					
	right hand	–	23.0	22.3	21.2	20.3	20.0	20.0	19.9	18.8	18.5	20.8					
	mean	–	23.0	22.3	21.4	23.0	24.6	24.8	25.7	25.0	24.8	25.6					
Velocity Ratio	v/ξ_m	–	.016	.017	.017	.016	.015	.015	.014	.015	.015	.015					

WEDGE DRAWING TEST DATA.

TEST NUMBER : 020715	MATERIAL : ALUMINIUM .	DRAW RATIO : 1.80:1	TABLE No. 63

Punch Velocity; in/sec.	Blank Holder Force ; lbf	Variac Voltage	Frequency ; kHz.
0.344	506	200	12.80

Punch Travel; in.		0·1	0·2	0·3	0·4	0·5	0·6	0·7	0·8	0·9	1·0	1·1	1·2	1·3	1·4	1·5	1·6
Punch Load P; lbf	non-osc.	51	117	218	296	359	390	394	397	386	370	336	292	212			
	osc.	26	90	179	235	286	314	320	312	300	263	213	151	101			
	ΔP	25	27	39	61	73	76	74	85	86	107	123	141	111			
Blank Holder Friction Force F, lbf.	non-osc.	31.2	-	-	-	-	22.3	20.1	21.2	22.3	26.8	30.1	-	-			
	osc.	0	0	0	0	0	0	0	0	0	0	0	0	0			
	ΔF %	100	-	-	-	-	100	100	100	100	100	100	-	-			
Die Motional Amplitude, ξ_m in. x 10^{-5}	left hand	-	-	-	18.5	21.7	22.4	22.5	23.8	23.5	24.2	22.5	22.5	21.7			
	right hand	-	16.9	17.0	19.2	21.2	20.7	19.5	19.2	18.8	18.5	18.7	19.2	-			
	mean	-	16.9	17.0	18.8	21.4	21.5	21.0	21.5	21.2	21.3	20.6	20.8	21.7			
Velocity Ratio	V/ξ_m	-	.025	.025	.023	.020	.020	.202	.020	.020	.020	.021	.021	.020			

WEDGE DRAWING TEST DATA.

TEST NUMBER : 020714	MATERIAL : ALUMINIUM .	DRAW RATIO : 1.80:1	TABLE No. 64

Punch Velocity ; in/sec.	Blank Holder Force ; lbf	Variac Voltage	Frequency ; kHz.
0.335	486	180	12.87

Punch Travel ; in.		0·1	0·2	0·3	0·4	0·5	0·6	0·7	0·8	0·9	1·0	1·1	1·2	1·3	1·4	1·5	1·6
Punch Load P ; lbf	non-osc.	39	90	168	258	319	347	357	368	368	353	314	258	157	62		
	osc.	18	56	134	207	263	291	297	296	285	246	199	146	90	-		
	ΔP	21	34	34	51	56	56	60	72	83	107	115	112	67	-		
Blank Holder Friction Force F, lbf.	non-osc.	-	-	-	-	13.4	13.4	15.6	17.7	22.3	26.7	27.9	23.4	15.6			
	osc.	0	0	0	0	0	0	0	0	0	0	0	0	0			
	ΔF %	-	-	-	-	100	100	100	100	100	100	100	100	100			
Die Motional Amplitude; ξ_m in. x 10^{-5}	left hand	-	-	15.5	18.5	20.0	20.4	20.5	20.6	20.6	20.4	20.4	20.2				
	right hand	-	15.3	12.7	18.5	18.4	17.3	17.0	16.9	16.9	16.9	17.0	17.7				
	mean	-	15.3	14.1	18.5	19.2	18.8	18.5	18.7	18.7	18.6	18.7	18.9				
Velocity Ratio	V/ξ_m	-	.027	.029	.023	.022	.022	.023	.022	.022	.022	.022	.022				

WEDGE DRAWING TEST DATA.

TEST NUMBER : 020713	MATERIAL : ALUMINIUM .	DRAW RATIO : 1.80:1	TABLE No. 65

Punch Velocity; in/sec.	Blank Holder Force ; lbf	Variac Voltage	Frequency ; kHz.
0.328	512	160	12.89

Punch Travel; in.		0·1	0·2	0·3	0·4	0·5	0·6	0·7	0·8	0·9	1·0	1·1	1·2	1·3	1·4	1·5	1·6
Punch Load P; lbf	non-osc.	56	146	230	306	372	392	403	412	408	386	341	271	157	112		
	osc.	31	101	190	252	308	330	336	334	319	293	240	168	90	-		
	ΔP	15	45	40	54	64	62	67	78	89	93	101	103	67	-		
Blank Holder Friction Force F, lbf.	non-osc.	35.7	-	-	-	16.0	16.7	20.1	22.3	24.6	25.6	26.8	26.8	-			
	osc.	0	0	0	0	0	0	0	0	0	0	0	0	0			
	ΔF %	100	-	-	-	100	100	100	100	100	100	100	100	-			
Die Motional Amplitude, ξ_m in. x 10^{-5}	left hand	-	-	-	15.9	18.5	18.7	19.4	19.5	18.8	19.0	18.5	17.7	-			
	right hand	-	15.0	13.0	16.5	16.8	16.5	15.9	15.7	15.7	15.7	15.7	-	-			
	mean	-	15.0	13.0	16.2	17.7	17.6	17.6	17.6	17.3	17.3	17.1	17.7	-			
Velocity Ratio	v/ξ_m	-	.027	.031	.025	.023	.023	.023	.023	.024	.024	.024	.023	-			

WEDGE DRAWING TEST DATA.

TEST NUMBER : 020712	MATERIAL : ALUMINIUM .	DRAW RATIO : 1.80:1	TABLE No. 66

Punch Velocity; in/sec.	Blank Holder Force ; lbf	Variac Voltage	Frequency ; kHz.
0.334	498	160	12.90

Punch Travel; in.		0·1	0·2	0·3	0·4	0·5	0·6	0·7	0·8	0·9	1·0	1·1	1·2	1·3	1·4	1·5	1·6
Punch Load P; lbf	non-osc.	47	114	201	296	350	386	398	397	386	353	319	252	168	45		
	osc.	31	84	168	252	308	330	336	325	308	275	224	168	101	-		
	ΔP	16	30	33	35	42	56	62	72	78	78	95	84	62	-		
Blank Holder Friction Force F, lbf.	non-osc.	-	-	-	-	-	14.5	19.0	20.1	22.3	23.4	24.5	22.3	-	-		
	osc.	0	0	0	0	0	0	0	0	0	0	0	0	-	-		
	ΔF %	-	-	-	-	-	100	100	100	100	100	100	100	-	-		
Die Motional Amplitude, ξ_m in. x 10^{-5}	left hand	-	-	16.0	17.4	17.5	18.2	18.5	18.2	18.2	17.9	18.2	16.7	14.9	-		
	right hand	-	15.3	15.7	16.2	15.7	15.3	14.9	14.5	14.2	13.5	13.5	12.0	9.2	-		
	mean	-	15.3	15.8	16.8	16.6	16.7	16.7	16.3	16.2	15.7	15.8	14.3	12.0	-		
Velocity Ratio	$V/\dot{\xi}_m$	-	.027	.026	.025	.025	.025	.025	.025	.026	.026	.026	.029	.034	-		

WEDGE DRAWING TEST DATA.

TEST NUMBER : 020711	MATERIAL : ALUMINIUM .	DRAW RATIO : 1.80:1	TABLE No. 67

Punch Velocity ; in/sec.	Blank Holder Force ; lbf	Variac Voltage	Frequency ; kHz.
0.328	484	140	12.85

Punch Travel ; in.		0·1	0·2	0·3	0·4	0·5	0·6	0·7	0·8	0·9	1·0	1·1	1·2	1·3	1·4	1·5	1·6
Punch Load P ; lbf	non-osc.	39	125	213	286	340	368	374	371	364	352	320	-	-			
	osc.	17	84	165	230	280	302	308	296	282	258	213	145	67			
	ΔP	22	41	48	56	60	66	66	75	82	94	10	-	-			
Blank Holder Friction Force F, lbf.	non-osc.	-	-	-	-	-	12.3	13.8	15.5	18.5	21.2	23.3	24.4				
	osc.	0	0	0	0	0	0	0	0	0	0	0	0				
	ΔF %	-	-	-	-	-	100	100	100	100	100	100	100				
Die Motional Amplitude, ξ_m in. x 10^{-5}	left hand	-	-	12.3	13.3	15.8	17.0	17.2	17.2	17.0	17.0	16.3	15.7	16.0			
	right hand	-	9.7	12.3	12.0	14.5	13.8	13.3	13.5	13.3	13.0	13.3	13.5	14.8			
	mean	-	9.7	12.3	12.7	15.2	15.4	15.2	15.3	15.2	15.0	14.8	14.6	15.4			
Velocity Ratio	V/ξ_m	-	.042	.033	.032	.027	.026	.027	.026	.027	.027	.027	.028	.026			

WEDGE DRAWING TEST DATA.

TEST NUMBER : 020710	MATERIAL : ALUMINIUM .	DRAW RATIO : 1.80:1	TABLE No. 68

Punch Velocity; in/sec.	Blank Holder Force ; lbf	Variac Voltage	Frequency ; kHz.
0.325	496	140	12.91

Punch Travel; in.		0·1	0·2	0·3	0·4	0·5	0·6	0·7	0·8	0·9	1·0	1·1	1·2	1·3	1·4	1·5	1·6
Punch Load P; lbf	non-osc.	36	101	179	252	325	364	381	381	375	364	325	258	168			
	osc.	21	84	157	224	286	314	314	314	308	269	224	168	95			
	ΔP	15	17	22	28	39	50	67	67	67	95	101	90	73			
Blank Holder Friction Force F, lbf.	non-osc.	-	-	-	-	-	20.0	17.9	21.2	24.6	24.6	20.0	6.7	-			
	osc.	0	0	0	0	0	0	0	0	0	0	0	0	0			
	ΔF %	-	-	-	-	-	100	100	100	100	100	100	100	-			
Die Motional Amplitude, ξ_m in. x 10^{-5}	left hand	-	-	-	11.7	13.5	13.2	16.0	15.7	16.0	17.0	16.7	16.0	15.7			
	right hand	-	8.5	9.7	10.8	11.5	12.8	12.7	12.7	12.7	12.3	12.3	12.3	13.0			
	mean	-	8.5	9.7	11.3	12.5	13.0	14.3	14.2	14.3	14.6	14.5	14.2	14.3			
Velocity Ratio	$V/\dot{\xi}_m$	-	.047	.041	.035	.032	.031	.028	.028	.028	.028	.028	.028	.028			

WEDGE DRAWING TEST DATA.

TEST NUMBER : 020709	MATERIAL : ALUMINIUM .	DRAW RATIO : 1.80:1	TABLE No. 69

Punch Velocity; in/sec.	Blank Holder Force ; lbf	Variac Voltage	Frequency ; kHz.
0.330	498	120	12.84

Punch Travel; in.		0·1	0·2	0·3	0·4	0·5	0·6	0·7	0·8	0·9	1·0	1·1	1·2	1·3	1·4	1·5	1·6
Punch Load P; lbf	non-osc.	47	112	210	290	348	387	392	398	390	370	334	269				
	osc.	29	81	178	248	298	331	336	336	314	282	226	160				
	ΔP	18	31	32	42	50	56	56	62	76	88	108	109				
Blank Holder Friction Force F, lbf.	non-osc.	-	-	-	-	-	-	6.7	11.1	15.6	21.8	25.0	22.3				
	osc.	0	0	0	0	0	0	0	0	0	0	0	0				
	ΔF %	-	-	-	-	-	-	100	100	100	100	100	100				
Die Motional Amplitude, ξ_m in. x 10^{-5}	left hand	-	-	9.9	9.2	11.7	13.8	14.5	15.2	15.7	15.7	15.2	14.9	15.2			
	right hand	-	7.7	8.5	8.3	14.7	15.0	14.7	14.2	13.3	11.9	11.5	12.0	14.2			
	mean	-	7.7	9.2	8.7	13.2	14.4	14.6	14.7	14.5	13.8	13.3	13.3	14.7			
Velocity Ratio	$V/\dot{\xi}_m$	-	.053	.044	.047	.031	.028	.028	.028	.028	.030	.030	.030	.028			

WEDGE DRAWING TEST DATA.

TEST NUMBER : 020708	MATERIAL : ALUMINIUM .	DRAW RATIO : 1.80:1	TABLE No. 70

Punch Velocity; in/sec.	Blank Holder Force ; lbf	Variac Voltage	Frequency ; kHz.
0.325	504	110	12.96

Punch Travel; in.		0·1	0·2	0·3	0·4	0·5	0·6	0·7	0·8	0·9	1·0	1·1	1·2	1·3	1·4	1·5	1·6
Punch Load P; lbf	non-osc.	45	112	179	258	325	363	381	386	386	358	319	260	157			
	osc.	25	84	151	225	280	319	330	330	314	280	224	166	90			
	ΔP	20	28	28	33	45	44	51	56	72	78	95	94	67			
Blank Holder Friction Force F, lbf.	non-osc.	-	-	-	-	-	14.5	14.5	16.7	21.2	22.3	23.4	21.2	15.6			
	osc.	0	0	0	0	0	0	0	0	0	0	0	0	0			
	ΔF %	-	-	-	-	-	100	100	100	100	100	100	100	100			
Die Motional Amplitude, ξ_m in. x 10^{-5}	left hand	-	-	9.5	11.2	12.0	13.5	13.2	13.2	13.9	13.2	13.2	13.5	13.2			
	right hand	-	8.3	9.7	8.3	11.8	12.0	11.8	11.5	11.5	10.7	10.4	11.0	11.7			
	mean	-	8.3	9.6	9.6	11.9	12.7	12.5	12.3	12.7	11.9	11.8	12.2	12.4			
Velocity Ratio	$V/\dot{\xi}_m$	-	.048	.042	.041	.034	.031	.032	.032	.031	.034	.034	.033	.032			

WEDGE DRAWING TEST DATA.

TEST NUMBER : 020707	MATERIAL : ALUMINIUM .	DRAW RATIO : 1.80:1	TABLE No. 71

Punch Velocity; in/sec.	Blank Holder Force ; lbf	Variac Voltage	Frequency ; kHz.
0.342	505	80	12.98

Punch Travel; in.		0·1	0·2	0·3	0·4	0·5	0·6	0·7	0·8	0·9	1·0	1·1	1·2	1·3	1·4	1·5	1·6
Punch Load P; lbf	non-osc.	48	108	190	257	317	350	375	386	386	366	324	263	168	-		
	osc.	36	101	168	241	291	322	337	336	324	300	241	179	86	31		
	ΔP	12	7	22	16	26	28	38	50	62	66	83	84	82	-		
Blank Holder Friction Force F, lbf.	non-osc.	14	-	-	-	-	8.5	6.7	9.6	13.4	17.8	17.8	15.6	-	-		
	osc.	0	0	0	0	0	0	0	0	0	0	0	0	0	0		
	ΔF %	-	-	-	-	-	100	100	100	100	100	100	100	-	-		
Die Motional Amplitude, ξ_n in. x 10^{-5}	left hand	-	-	-	6.7	7.3	8.3	8.7	8.9	8.7	8.7	8.3	8.2	7.3	-		
	right hand	-	-	4.8	5.7	6.5	6.8	6.5	6.7	6.8	6.5	6.2	6.7	-	-		
	mean	-	-	4.8	6.2	6.9	7.6	7.6	7.8	7.7	7.6	7.2	7.4	7.3	-		
Velocity Ratio	v/ξ_n	-	-	.087	.068	.061	.055	.055	.054	.054	.055	.058	.057	.057	-		

WEDGE DRAWING TEST DATA.

TEST NUMBER : 020706	MATERIAL : ALUMINIUM .	DRAW RATIO : 1.80:1	TABLE No. 72

Punch Velocity; in/sec.	Blank Holder Force ; lbf	Variac Voltage	Frequency ; kHz.
0.334	496	80	12.89

Punch Travel; in.		0·1	0·2	0·3	0·4	0·5	0·6	0·7	0·8	0·9	1·0	1·1	1·2	1·3	1·4	1·5	1·6
Punch Load P; lbf	non-osc.	31	101	185	263	319	358	383	394	384	370	325	274	201			
	osc.	17	76	151	230	292	325	336	336	319	297	252	196	123			
	ΔP	14	25	34	33	27	33	47	58	65	73	73	78	78			
Blank Holder Friction Force F, lbf.	non-osc.	-	-	-	-	-	10.3	14.5	16.1	21.2	23.4	22.3	13.4	13.4			
	osc.	0	0	0	0	0	0	0	0	0	0	0	0	0			
	ΔF %	-	-	-	-	-	100	100	100	100	100	100	100	100			
Die Motional Amplitude, ξ_m in. x 10^{-5}	left hand	-	-	6.3	7.7	8.5	9.5	9.9	8.9	8.7	8.3	7.7	7.3	8.0			
	right hand	-	6.2	7.7	8.0	8.4	8.5	7.7	8.0	7.7	7.0	7.0	7.3	8.0			
	mean	-	6.2	7.0	7.8	8.5	9.0	8.8	8.4	8.2	7.6	7.3	7.3	8.0			
Velocity Ratio	v/ξ_m	-	.067	.059	.053	.048	.046	.047	.049	.051	.054	.060	.060	.051			

WEDGE DRAWING TEST DATA.

TEST NUMBER : 020705	MATERIAL : ALUMINIUM .	DRAW RATIO : 1.80:1	TABLE No. 73

Punch Velocity; in/sec.	Blank Holder Force ; lbf	Variac Voltage	Frequency ; kHz.
0.334	498	60	13.01

Punch Travel; in.		0·1	0·2	0·3	0·4	0·5	0·6	0·7	0·8	0·9	1·0	1·1	1·2	1·3	1·4	1·5	1·6
Punch Load P; lbf	non-osc.	39	110	201	280	336	370	381	386	380	364	336	285	168			
	osc.	29	87	179	260	316	345	347	336	334	302	246	182	101			
	ΔP	10	23	22	20	20	25	34	50	46	62	90	103	67			
Blank Holder Friction Force F, lbf.	non-osc.	-	-	-	-	9.4	11.2	13.8	15.6	20.1	22.3	23.4	-	-			
	osc.	0	0	0	0	0	0	0	0	0	0	0	0	0			
	ΔF %	-	-	-	-	100	100	100	100	100	100	100	-	-			
Die Motional Amplitude, ξ_m in. x 10^{-5}	left hand	-	2.7	2.7	4.2	4.9	4.7	5.2	4.9	4.5	4.5	4.2	4.5	5.2			
	right hand	3.0	3.0	4.2	4.3	4.2	4.0	3.9	3.7	3.7	3.5	3.0	4.2	4.3			
	mean	3.0	2.8	3.4	4.3	4.5	4.3	4.5	4.3	4.1	4.0	3.6	4.3	4.7			
Velocity Ratio	V/ξ_m	.136	.146	.120	.095	.091	.095	.091	.095	.099	.102	.112	.095	.087			

WEDGE DRAWING TEST DATA.

TEST NUMBER : 020704		MATERIAL : ALUMINIUM .							DRAW RATIO : 1.80:1				TABLE No. 74				
Punch Velocity; in/sec.		Blank Holder Force ; lbf						Variac Voltage					Frequency ; kHz.				
0.344		492						60					12.85				
Punch Travel; in.		0·1	0·2	0·3	0·4	0·5	0·6	0·7	0·8	0·9	1·0	1·1	1·2	1·3	1·4	1·5	1·6
Punch Load P; lbf	non-osc.	42	110	201	280	336	370	383	383	378	356	317	253	-			
	osc.	20	88	166	251	304	334	342	339	330	304	258	184	84	58		
	ΔP	12	22	35	29	32	36	41	44	48	52	59	69	-	-		
Blank Holder Friction Force F, lbf.	non-osc.	-	-	-	-	-	-	12.2	13.4	15.6	18.5	20.1	22.3	-	-		
	osc.	0	0	0	0	0	0	0	0	0	0	0	0	0	0		
	ΔF %	-	-	-	-	-	-	100	100	100	100	100	100	-	-		
Die Motional Amplitude, ξ_m in. x 10^{-5}	left hand	-	-	2.7	3.3	3.7	4.2	5.2	5.5	5.5	4.0	4.0	3.0	4.0	-		
	right hand	-	1.8	2.0	1.0	1.8	3.0	4.0	4.3	4.3	2.7	2.3	-	-	-		
	mean	-	1.8	2.3	2.1	2.7	3.6	4.6	4.9	4.9	3.3	3.1	3.0	4.0	-		
Velocity Ratio	V/ξ_m	-	.237	.185	.203	.157	.118	.093	.087	.087	.129	.137	.142	.107	-		

WEDGE DRAWING TEST DATA.

TEST NUMBER : 020703	MATERIAL : ALUMINIUM .	DRAW RATIO : 1.80:1	TABLE No. 75

Punch Velocity; in/sec.	Blank Holder Force ; lbf	Variac Voltage	Frequency ; kHz.
0.334	496	40	13.40

Punch Travel; in.		0·1	0·2	0·3	0·4	0·5	0·6	0·7	0·8	0·9	1·0	1·1	1·2	1·3	1·4	1·5	1·6
Punch Load P; lbf	non-osc.	41	118	213	275	325	353	364	368	364	352	302	252	-	-		
	osc.	34	103	201	267	314	336	345	342	330	314	268	218	162	95		
	ΔP	7	15	12	8	11	17	19	26	34	38	34	34	-	-		
Blank Holder Friction Force F, lbf.	non-osc.	-	29	-	-	-	-	11.2	13.4	17.8	20.5	18.9	22.3	15.6	-		
	osc.	0	0	0	0.7	1.1	1.1	1.6	1.6	3.1	7.1	6.5	10.0	6.7	-		
	ΔF %	-	100	-	-	-	-	86	88	83	65	66	55	51	-		
Die Motional Amplitude, ξ_m in. x 10^{-5}	left hand	-	-	2.2	2.5	2.0	1.6	1.6	1.4	1.4	1.4	1.4	1.3	1.2	-		
	right hand	-	3.0	0.6	1.2	0.9	1.1	1.3	1.3	1.4	1.6	1.7	1.7	1.6	-		
	mean	-	1.5	1.4	1.9	1.4	1.3	1.4	1.3	1.4	1.5	1.6	1.5	1.4	-		
Velocity Ratio	$v/\dot{\xi}_m$	-	.264	.284	.209	.274	.294	.274	.294	.284	.264	.248	.264	.278			

WEDGE DRAWING TEST DATA.

TEST NUMBER : 020702	MATERIAL : ALUMINIUM .	DRAW RATIO : 1.80:1	TABLE No. 76

Punch Velocity; in/sec.	Blank Holder Force ; lbf	Variac Voltage	Frequency ; kHz.
0.334	494	30	13.46

Punch Travel; in.		0·1	0·2	0·3	0·4	0·5	0·6	0·7	0·8	0·9	1·0	1·1	1·2	1·3	1·4	1·5	1·6
Punch Load P; lbf	non-osc.	50	113	202	269	325	358	373	375	375	358	319	258	–			
	osc.	–	110	199	264	319	350	358	358	356	347	298	244	168			
	ΔP	–	3	3	5	6	8	15	17	19	11	21	14	–			
Blank Holder Friction Force F, lbf.	non-osc.	–	17.8	–	–	–	10.0	12.2	13.4	16.7	19.0	18.3	21.2	–			
	osc.	–	2.9	1.1	2.2	2.7	3.1	4.5	5.8	9.4	12.5	15.2	16.1	10.0			
	ΔF %	–	84	–	–	–	69	63	57	44	34	17	24	–			
Die Motional Amplitude, ξ_m in. x 10^{-5}	left hand	–	–	0.45	0.6	0.65	0.75	0.7	0.7	0.8	0.75	0.85	0.7	0.7			
	right hand	–	–	0.45	0.55	0.6	0.7	0.75	0.85	1.0	1.05	1.1	0.95	0.85			
	mean	–	–	0.45	0.58	0.63	0.73	0.73	0.78	0.9	0.9	0.98	0.82	0.80			
Velocity Ratio	v/ξ_m	–	–	.876	.680	.633	.546	.546	.507	.438	.438	.403	.481	.492			

WEDGE DRAWING TEST DATA.

TEST NUMBER : 020701	MATERIAL : ALUMINIUM .	DRAW RATIO : 1.80:1	TABLE No. 77

Punch Velocity; in/sec.	Blank Holder Force ; lbf	Variac Voltage	Frequency ; kHz.
0.328	513	25	13.37

Punch Travel; in.		0·1	0·2	0·3	0·4	0·5	0·6	0·7	0·8	0·9	1·0	1·1	1·2	1·3	1·4	1·5	1·6
Punch Load P; lbf	non-osc.	34	103	190	258	314	353	370	372	370	364	325	258	-			
	osc.	24	88	178	246	302	336	353	353	348	338	302	246	179	90		
	ΔP	10	15	12	12	12	17	17	19	22	26	23	12	-	-		
Blank Holder Friction Force F, lbf.	non-osc.	33.4	-	-	-	-	11.1	12.2	15.6	18.5	22.3	21.9	20.0	-	-		
	osc.	-	2.7	2.2	2.2	1.8	2.4	4.5	6.9	9.6	13.4	14.5	15.8	13.0	-		
	ΔF %	-	-	-	-	-	78	63	56	48	40	34	21				
Die Motional Amplitude, ξ_m in. x 10^{-5}	left hand	-	0.28	0.60	0.69	0.74	0.85	0.86	0.78	0.78	0.78	0.78	0.78	0.65	0.65		
	right hand	-	0.91	0.80	0.71	0.84	0.86	0.86	0.86	0.93	0.88	0.97	0.93	0.78	0.79		
	mean	-	0.59	0.70	0.70	0.79	0.85	0.86	0.82	0.85	0.83	0.87	0.85	0.71	0.72		
Velocity Ratio	V/ξ_m	-	.660	.558	.558	.494	.460	.454	.476	.460	.471	.450	.460	.550	.542		

WEDGE DRAWING TEST DATA.

TEST NUMBER : 020906	MATERIAL : ALUMINIUM .	DRAW RATIO : 1.90:1	TABLE No. 78

Punch Velocity; in/sec.	Blank Holder Force ; lbf	Variac Voltage	Frequency ; kHz.
0.328	622	200	12.90

Punch Travel; in.		0·1	0·2	0·3	0·4	0·5	0·6	0·7	0·8	0·9	1·0	1·1	1·2	1·3	1·4	1·5	1·6
Punch Load P; lbf	non-osc.	77	147	228	308	362	403	-	-	440	-	-	-	-	-		
	osc.	52	122	200	275	312	336	350	347	336	312	278	240	172	134		
	ΔP	25	25	28	33	50	67	-	-	104	-	-	-	-	-		
Blank Holder Friction Force F, lbf.	non-osc.	36.8	18.0	12.0	10.7	11.6	13.2	16.1	-	-	-	-	-	-	-		
	osc.	-	0	0	0	0	0	0	0	0	0	0	0	0	0		
	ΔF %	100	100	100	100	100	100	100	-	-	-	-	-	-	-		
Die Motional Amplitude, ξ_m in. x 10^{-5}	left hand	-	-	14.5	17.1	18.2	19.5	20.6	21.7	22.0	22.4	22.2	21.7	21.7	21.0		
	right hand	-	18.3	18.5	18.8	18.8	18.5	18.5	18.5	18.5	18.3	17.2	16.5	17.2	19.2		
	mean	-	18.3	16.5	18.0	18.5	19.0	19.6	20.1	20.3	20.4	19.7	19.1	19.5	20.1		
Velocity Ratio	$v/\dot{\xi}_m$	-	.024	.024	.022	.022	.021	.021	.020	.020	.020	.021	.020	.021	.020		

WEDGE DRAWING TEST DATA.

TEST NUMBER : 020905	MATERIAL : ALUMINIUM .	DRAW RATIO : 1.90:1	TABLE No. 79

Punch Velocity; in/sec.	Blank Holder Force ; lbf	Variac Voltage	Frequency ; kHz.
0.334	615	180	13.04

Punch Travel; in.		0·1	0·2	0·3	0·4	0·5	0·6	0·7	0·8	0·9	1·0	1·1	1·2	1·3	1·4	1·5	1·6
Punch Load P; lbf	non-osc.	50	-	-	-	-	-	-	-	-	-	-	-	-	-		
	osc.	22	90	179	258	330	360	370	375	375	362	336	241	224	168		
	ΔP																
Blank Holder Friction Force F, lbf.	non-osc.	46	-	-	-	-	-	-	-	-	-	-	-	-	-		
	osc.	0	0	0	0	0	0	0	0	0	0	0	0	0	0		
	ΔF %																
Die Motional Amplitude, ξ_m in. x 10^{-5}	left hand	-	-	7.7	9.3	10.4	11.4	12.0	12.3	12.7	12.7	12.3	12.0	12.3	12.7		
	right hand	-	8.5	8.8	8.0	9.2	9.2	9.2	9.2	9.2	9.2	9.2	9.2	9.5	10.3		
	mean	-	8.5	8.3	8.7	9.8	10.3	10.6	10.8	10.9	10.9	10.8	10.6	10.9	11.5		
Velocity Ratio	v/ξ_m	-	.048	.049	.047	.042	.039	.038	.038	.038	.038	.038	.038	.037	.035		

WEDGE DRAWING TEST DATA.

TEST NUMBER : 020904	MATERIAL : ALUMINIUM .	DRAW RATIO : 1.90:1	TABLE No. 80

Punch Velocity; in/sec.	Blank Holder Force ; lbf	Variac Voltage	Frequency ; kHz.
0.334	618	180	12.80

Punch Travel; in.		0·1	0·2	0·3	0·4	0·5	0·6	0·7	0·8	0·9	1·0	1·1	1·2	1·3	1·4	1·5	1·6
Punch Load P; lbf	non-osc.	95	187	274	330	381	416	428									
	osc.	67	155	230	280	325	353	-									
	ΔP	28	32	44	50	56	63	-									
Blank Holder Friction Force F, lbf.	non-osc.	29.0	-	-	-	-	-	16.3									
	osc.	0	0	0	0	0	0	0									
	ΔF %	100	-	-	-	-	-	100									
Die Motional Amplitude, ξ_m in. x 10^{-5}	left hand	-	9.4	10.9	14.8	17.7	19.3										
	right hand	10.8	12.7	15.8	22.6	25.7	25.4										
	mean	10.8	11.0	13.3	18.7	21.7	22.3										
Velocity Ratio	V/ξ_m	.038	.038	.031	.022	.019	.019										

WEDGE DRAWING TEST DATA.

TEST NUMBER : 020903		MATERIAL : ALUMINIUM .						DRAW RATIO : 1.90:1					TABLE No. 81				
Punch Velocity; in/sec.		Blank Holder Force ; lbf						Variac Voltage					Frequency ; kHz.				
0.342		601						100					13.03				
Punch Travel; in.		0·1	0·2	0·3	0·4	0·5	0·6	0·7	0·8	0·9	1·0	1·1	1·2	1·3	1·4	1·5	1·6
Punch Load P; lbf	non-osc.	43	-	-	-	-	-	-	-	-	-	-	-	-	-		
	osc.	17	78	177	252	316	353	372	372	364	345	324	292	241	179		
	ΔP,	26	-	-	-	-	-	-	-	-	-	-	-	-	-		
Blank Holder Friction Force F, lbf.	non-osc.	23.4	-	-	-	-	-	-	-	-	-	-	-	-	-		
	osc.	0	0	0	0	0	0	0	0	0	0	0	0	0	0		
	ΔF %	100	-	-	-	-	-	-	-	-	-	-	-	-	-		
Die Motional Amplitude, ξ_m in. x 10^{-5}	left hand	-	-	5.8	7.3	7.7	7.7	7.3	8.0	8.3	8.3	8.7	8.3	8.3	8.7		
	right hand	-	5.7	5.8	6.2	6.2	5.0	5.8	6.2	6.2	6.5	6.5	6.5	6.5	6.8		
	mean	-	5.7	5.8	6.8	7.0	6.4	6.6	7.1	7.3	7.4	7.6	7.4	7.4	7.8		
Velocity Ratio	$V/\dot{\xi}_m$	-	.073	.072	.061	.059	.065	.063	.059	.057	.056	.055	.056	.056	.053		

WEDGE DRAWING TEST DATA.

TEST NUMBER : 020902	MATERIAL : ALUMINIUM .	DRAW RATIO : 1.90:1	TABLE No. 82

Punch Velocity; in/sec.	Blank Holder Force ; lbf	Variac Voltage	Frequency ; kHz.
0.334	610	30	13.06

Punch Travel; in.		0·1	0·2	0·3	0·4	0·5	0·6	0·7	0·8	0·9	1·0	1·1	1·2	1·3	1·4	1·5	1·6
Punch Load P; lbf	non-osc.	33	-	-	-	-	-	-	-	-	-	-	-	-	-	-	
	osc.	-	100	207	280	348	390	412	420	425	408	392	381	314	235	157	
	ΔP																
Blank Holder Friction Force F, lbf.	non-osc.	51.5	29.0	-	-	-	-	-	-	-	-	-	-	-	-	-	
	osc.	17.8	10.0	2.5	2.5	2.5	2.2	2.5	3.3	4.5	3.3	5.8	4.9	-	-	-	
	ΔF %	66	66	-	-	-	-	-	-	-	-	-	-	-	-	-	
Die Motional Amplitude, ξ_m in. x 10^{-5}	left hand	-	-	-	1.0	1.2	1.5	1.7	1.7	1.6	1.7	2.0	2.0	2.0	2.1	2.3	
	right hand	-	0.7	1.4	1.8	1.8	1.8	1.7	1.5	1.4	1.4	1.6	1.5	1.7	2.2	2.6	
	mean	-	0.7	1.4	1·4	1.5	1.7	1.7	1.6	1.5	1.5	1.8	1.8	1.9	2.1	2.4	
Velocity Ratio	$V/\dot{\xi}_m$	-	.529	.291	.291	.271	.239	.239	.254	.271	.272	.293	.293	.272	.194	.169	

WEDGE DRAWING TEST DATA.

TEST NUMBER : 020901	MATERIAL : ALUMINIUM .	DRAW RATIO : 1.90:1	TABLE No. 83

Punch Velocity; in/sec.	Blank Holder Force ; lbf	Variac Voltage	Frequency ; kHz.
0.341	615	30	13.01

Punch Travel; in.		0·1	0·2	0·3	0·4	0·5	0·6	0·7	0·8	0·9	1·0	1·1	1·2	1·3	1·4	1·5	1·6
Punch Load P; lbf	non-osc.	–	–	–	–	–	–	–	–	–							
	osc.	28	98	190	258	330	392	425	342	453							
	ΔP	–	–	–	–	–	–	–	–	–							
Blank Holder Friction Force F, lbf.	non-osc.	–	–	–	–	–	–	–	–	–							
	osc.	0	0	0	0	0	0	0	0	0							
	ΔF %	–	–	–	–	–	–	–	–	–							
Die Motional Amplitude, ξ_m in. x 10^{-5}	left hand	–	–	2.8	2.8	3.0	3.0	3.0	3.0	2.5	2.2						
	right hand	–	–	4.0	2.7	3.0	2.3	2.5	2.6	2.9	2.5						
	mean	–	–	3.40	2.75	3.00	2.65	2.75	2.80	2.70	2.35						
Velocity Ratio	V/ξ_m	–	–	.122	.152	.139	.157	.151	.149	.155	.177						

WEDGE DRAWING DATA.

TEST NUMBER.	DRAW RATIO,	FREQUENCY kHz	PUNCH VELOCITY in/sec.	MEAN DIE AMPLITUDE in. x 10^{-5}	MAX. PUNCH LOAD; lbf.		PUNCH TRAVEL, h; in.	DREW / FAILED
					OSC.	NON-OSC.		
020801	1.95:1	13.04	0.34	2.25	448		0.90	F
020802	1.95:1	12.91	0.34	6.35	412		0.90	D
020803	1.95:1	12.92	0.34	12.90	408		0.80	D
020804	1.95:1	12.91	0.34	18.20	403		0.80	D
020901	2.00:1	12.96	0.34	4.00	448		0.76	F
020902	2.00:1	12.96	0.32	9.80	440		0.88	F
020903	2.00:1	12.96	0.32	10.35	438		0.62	F
020904	2.00:1	12.96	0.34	14.80	386		0.63	F

TABLE: 84

NON-OSCILLATORY WEDGE DRAWING TEST DATA.

TEST NUMBER	DRAW RATIO; 1.50:1					BLANK HOLDER FORCE; 228 lbf.						PUNCH VELOCITY; 0.34 in./sec.					
	Punch Travel, in	0.1	0.2	0.3	0.4	0.5	0.6	0.7	0.8	0.9	1.0	1.1	1.2	1.3	1.4	1.5	1.6
030100	Punch load; lbf	45	96	177	219	224	190	135	80	39							
	Blank Holder Friction Force	20.0	8.0	5.2	9.5	14.5	13.0	10.6	5.0	-							
030100/1	Punch load; lbf	49	98	185	221	233	172	146	78	45							
	B/H Friction Force; lbf.	2.1	8.5	6.8	9.5	10.6	11.4	10.6	8.4	-							
	Punch load; lbf																
	B/H Friction Force; lbf.																
	DRAW RATIO; 1.90:1					BLANK HOLDER FORCE; 631 lbf.						PUNCH VELOCITY; 0.34 in./sec.					
030700	Punch load; lbf	56	146	258	340	381	396	403	405	404	392	375	356	314	251	190	45
	B/H Friction Force; lbf.	45.4	29.9	15.2	13.4	13.4	13.4	15.6	17.8	20.1	22.5	23.4	22.8	21.2	14.5	15.6	
030700/1	Punch load; lbf	34	123	239	316	365	386	398	407	393	400	384	363	353	286	213	95
	B/H Friction Force; lbf.	47.0	42.0	26.8	19.0	15.6	16.7	17.6	21.2	24.8	25.0	25.6	27.0	29.0	25.6	19.0	
030700/2	Punch load; lbf	55	144	281	358	392	403	408	415	408	398	383	371	314	255	190	67
	B/H Friction Force; lbf.	47.0	38.8	19.2	20.7	16.7	10.9	13.4	18.8	21.9	22.3	20.3	23.4	20.3	22.1	17.9	

TABLE No: 85

NON-OSCILLATORY WEDGE DRAWING TEST DATA.

TEST NUMBER	DRAW RATIO; 1.60:1					BLANK HOLDER FORCE; 331 lbf.						PUNCH VELOCITY; 0.33 in./sec.					
	Punch Travel, in	0.1	0.2	0.3	0.4	0.5	0.6	0.7	0.8	0.9	1.0	1.1	1.2	1.3	1.4	1.5	1.6
030300	Punch load; lbf	46	110	186	242	275	280	255	209	154	88						
	Blank Holder Friction Force	-	-	-	4.0	11.2	16.0	19.9	16.3	12.9	-						
030300/1	Punch load; lbf	37	105	182	236	268	272	247	203	149	70	28					
	B/H Friction Force; lbf.	-	6.3	3.3	5.2	10.0	15.4	16.7	14.7	11.6	-						
	Punch load; lbf																
	B/H Friction Force; lbf.																
	DRAW RATIO; 1.60:1					BLANK HOLDER FORCE; 346 lbf.						PUNCH VELOCITY; 0.34 in./sec.					
030300N	Punch load; lbf	42	132	254	344	394	410	392	340	282	215	101					
	B/H Friction Force; lbf.	-	27.9	27.9	29.0	31.2	35.2	33.0	33.0	31.2	29.0	13.8					
030300N/1	Punch load; lbf	51	145	274	370	425	442	420	370	302	238	132					
	B/H Friction Force; lbf.	25.4	29.4	31.2	30.2	29.0	29.0	29.5	29.0	27.2	26.8	20.0					
	Punch load; lbf																
	B/H Friction Force; lbf.																

TABLE No: 86

NON-OSCILLATORY WEDGE DRAWING TEST DATA.

TEST NUMBER	DRAW RATIO; 1.70:1					BLANK HOLDER FORCE; 420 lbf.						PUNCH VELOCITY; 0.34 in./sec.					
	Punch Travel, in	0.1	0.2	0.3	0.4	0.5	0.6	0.7	0.8	0.9	1.0	1.1	1.2	1.3	1.4	1.5	1.6
030500	Punch load; lbf	67	145	235	288	310	320	322	310	274	212	155	35				
	Blank Holder Friction Force	30.8	20.0	14.5	10.0	10.9	15.4	19.0	21.2	19.6	15.6	14.5	-				
030500/1	Punch load; lbf	45	112	195	276	297	314	316	308	276	213	147	35				
	B/H Friction Force; lbf.	26.8	23.0	10.0	8.9	9.4	11.2	13.4	16.0	19.8	16.3	13.6	-				
	Punch load; lbf																
	B/H Friction Force; lbf.																
	DRAW RATIO; 1.70:1					BLANK HOLDER FORCE; 428 lbf.						PUNCH VELOCITY; 0.32 in./sec.					
030500N	Punch load; lbf	34	112	246	352	415	436	436	436	420	376	314	246	134			
	B/H Friction Force; lbf.	-	16.7	13.4	18.3	26.8	31.2	31.7	31.2	29.0	26.8	22.3	17.9	-			
030500N/1	Punch load; lbf	28	118	248	336	386	386	375	370	348	291	224	146				
	B/H Friction Force; lbf.	30.0	35.7	34.6	31.6	30.1	30.1	29.0	30.1	31.2	32.4	32.4	24.5				
	Punch load; lbf																
	B/H Friction Force; lbf.																

TABLE No: 87

NON-OSCILLATORY WEDGE DRAWING TEST DATA.

TEST NUMBER	DRAW RATIO; 1.80:1					BLANK HOLDER FORCE; 503 lbf.						PUNCH VELOCITY; 0.32 in./sec.					
	Punch Travel, in	0.1	0.2	0.3	0.4	0.5	0.6	0.7	0.8	0.9	1.0	1.1	1.2	1.3	1.4	1.5	1.6
030600	Punch load; lbf	62	148	225	302	338	352	358	356	338	325	291	228	121			
	Blank Holder Friction Force	19.4	14.7	10.7	11.1	12.9	14.2	16.5	17.6	17.4	17.8	18.9	13.4	13.8			
030600/1	Punch load; lbf	39	130	214	284	318	334	340	330	325	313	258	202	138			
	B/H Friction Force; lbf.	32.4	22.3	12.3	11.2	11.8	14.5	18.7	21.8	22.5	25.9	22.0	15.8	15.6			
030600/2	Punch load; lbf	34	106	201	280	327	352	358	358	350	342	296	233	170	54		
	B/H Friction Force; lbf.	-	32.3	15.2	11.6	11.6	13.8	16.7	19.2	19.6	22.3	20.5	15.6	14.5	-		
	DRAW RATIO; 1.80:1					BLANK HOLDER FORCE; 506 lbf.						PUNCH VELOCITY; 0.34 in./sec.					
030600N	Punch load; lbf	28	121	252	348	405	469	485	462	401	381	334	252	177			
	B/H Friction Force; lbf.	-	27.2	23.4	25.7	30.1	32.4	33.4	33.6	33.9	38.4	35.7	27.9	17.8			
	Punch load; lbf																
	B/H Friction Force; lbf.																
	Punch load; lbf																
	B/H Friction Force; lbf.																

TABLE No: 88

WEDGE DRAWING TEST DATA.

TEST NUMBER : 030101	MATERIAL : ALUMINIUM .	DRAW RATIO : 1.50:1	TABLE No. 89

Punch Velocity; in/sec.	Blank Holder Force ; lbf	Variac Voltage	Frequency ; kHz.
0.34	225	30	13.37

Punch Travel; in.		0·1	0·2	0·3	0·4	0·5	0·6	0·7	0·8	0·9	1·0	1·1	1·2	1·3	1·4	1·5	1·6
Punch Load P; lbf	non-osc.	50	123	188	230	235	170	148	79	25							
	osc.	44	107	174	213	216	179	134	67	-							
	ΔP	6	16	14	17	19	11	14	12	-							
Blank Holder Friction Force F, lbf.	non-osc.	-	-	-	-	6.7	8.0	6.0	5.6	-							
	osc.	-	-	1.1	2.2	2.5	3.1	3.2	-	-							
	ΔF %	-	-	-	-	63	61	47	-	-							
Die Motional Amplitude, ξ_m in. x 10^{-5}	left hand	-	-	1.53	1.62	1.46	1.29	1.20	1.11	0.83							
	right hand	-	-	1.07	1.20	1.29	1.38	1.38	1.24	1.29							
	mean	-	-	1.30	1.41	1.38	1.33	1.29	1.17	1.16							
Velocity Ratio	V/ξ_m	-	-	.312	.287	.294	.304	.314	.347	.350							

WEDGE DRAWING TEST DATA.

TEST NUMBER : 030102	MATERIAL : ALUMINIUM .	DRAW RATIO : 1.50:1	TABLE No. 90

Punch Velocity; in/sec.	Blank Holder Force ; lbf	Variac Voltage	Frequency ; kHz.
0.32	224	50	13.36

Punch Travel; in.		0·1	0·2	0·3	0·4	0·5	0·6	0·7	0·8	0·9	1·0	1·1	1·2	1·3	1·4	1·5	1·6
Punch Load P; lbf	non-osc.	31	112	179	218	241	207	157	101	36							
	osc.	22	100	162	199	207	174	123	78	-							
	ΔP	9	12	17	19	34	33	34	23	-							
Blank Holder Friction Force F, lbf.	non-osc.	-	-	-	3.0	10.5	11.0	9.5	-	-							
	osc.	-	-	-	-	0.8	1.2	2.0	-	-							
	ΔF %	-	-	-	-	83	89	79	-	-							
Die Motional Amplitude, ξ_m in. x 10^{-5}	left hand	-	-	1.5	1.65	1.65	1.3	1.2	1.25								
	right hand	-	2.0	1.8	2.1	2.25	2.1	2.0	1.95								
	mean	-	2.0	1.65	1.87	1.95	1.70	1.6	1.6								
Velocity Ratio	$V/\dot{\xi}_m$	-	.188	.228	.201	.193	.221	.235	.235								

WEDGE DRAWING TEST DATA.

TEST NUMBER : 030103	MATERIAL : ALUMINIUM .	DRAW RATIO : 1.50:1	TABLE No. 91

Punch Velocity; in/sec.	Blank Holder Force ; lbf	Variac Voltage	Frequency ; kHz.
0.33	229	80	13.20

Punch Travel; in.		0·1	0·2	0·3	0·4	0·5	0·6	0·7	0·8	0·9	1·0	1·1	1·2	1·3	1·4	1·5	1·6
Punch Load P; lbf	non-osc.	39	102	168	213	224	202	143	92	31							
	osc.	26	82	140	175	177	148	103	57	-							
	ΔP	13	20	28	38	47	54	40	35	-							
Blank Holder Friction Force F, lbf.	non-osc.	-	-	-	-	12.3	12.5	10.0	5.6	-							
	osc.	0	0	0	0	0	0	0	0	-							
	ΔF %	-	-	-	-	100	100	100	100	-							
Die Motional Amplitude, ξ_m in. x 10^{-5}	left hand	-	-	-	4.15	4.80	4.60	4.25	4.00	3.80							
	right hand	-	4.10	4.20	4.25	4.70	4.30	4.10	3.90	4.00							
	mean	-	4.10	4.20	4.20	4.25	4.45	4.18	3.95	3.90							
Velocity Ratio	$v/\dot{\xi}_m$	-	.097	.094	.094	.083	.089	.095	.100	.102							

WEDGE DRAWING TEST DATA.

TEST NUMBER : 030104	MATERIAL : ALUMINIUM .	DRAW RATIO : 1.50:1	TABLE No. 92

Punch Velocity; in/sec.	Blank Holder Force ; lbf	Variac Voltage	Frequency ; kHz.
0.33	231	120	13.21

Punch Travel; in.		0·1	0·2	0·3	0·4	0·5	0·6	0·7	0·8	0·9	1·0	1·1	1·2	1·3	1·4	1·5	1·6
Punch Load P; lbf	non-osc.	42	110	181	222	233	199	147	83	33							
	osc.	-	89	157	199	183	151	107	65	-							
	ΔP	-	21	24	23	50	48	40	18	-							
Blank Holder Friction Force F, lbf.	non-osc.	-	-	-	-	-	11.6	7.8	5.6	-							
	osc.	0	0	0	0	0	0	0	0	0							
	ΔF %	-	-	-	-	-	100	100	100	-							
Die Motional Amplitude, ξ_m in. x 10^{-5}	left hand	-	-	-	4.3	4.9	6.5	5.9	6.2								
	right hand	-	-	5.6	5.3	6.1	6.5	5.8	5.6								
	mean	-	-	5.6	4.8	5.5	6.5	5.9	5.9								
Velocity Ratio	$v/\dot{\xi}_m$	-	-	.071	.083	.072	.061	.068	.068								

WEDGE DRAWING TEST DATA.

TEST NUMBER : 030105	MATERIAL : ALUMINIUM .	DRAW RATIO : 1.50:1	TABLE No. 93

Punch Velocity; in/sec.	Blank Holder Force ; lbf	Variac Voltage	Frequency ; kHz.
0.33	218	120	13.17

Punch Travel; in.		0·1	0·2	0·3	0·4	0·5	0·6	0·7	0·8	0·9	1·0	1·1	1·2	1·3	1·4	1·5	1·6
Punch Load P; lbf	non-osc.	39	108	174	222	230	201	146	-	-							
	osc.	29	90	147	172	168	138	101	51	34							
	ΔP	10	18	27	50	62	63	45	-	-							
Blank Holder Friction Force F, lbf.	non-osc.	-	-	-	-	12.3	14.1	10.0	-	-							
	osc.	0	0	0	0	0	0	0	0	0							
	ΔF %	-	-	-	-	100	100	100	-	-							
Die Motional Amplitude, ξ_m in. x 10^{-5}	left hand	-	-	5.9	6.2	7.4	7.1	7.7	6.5	-							
	right hand	-	6.2	6.5	6.8	7.2	7.1	6.8	6.2	-							
	mean	-	6.2	6.2	6.5	7.3	7.1	7.3	6.4	-							
Velocity Ratio	v/ξ_m	-	.064	.064	.061	.055	.056	.055	.063								

WEDGE DRAWING TEST DATA.

TEST NUMBER : 030106	MATERIAL : ALUMINIUM .	DRAW RATIO : 1.50:1	TABLE No. 94

Punch Velocity; in/sec.	Blank Holder Force ; lbf	Variac Voltage	Frequency ; kHz.
0.34	226	150	12.15

Punch Travel; in.		0·1	0·2	0·3	0·4	0·5	0·6	0·7	0·8	0·9	1·0	1·1	1·2	1·3	1·4	1·5	1·6
Punch Load P; lbf	non-osc.	34	90	168	218	240	208	152	90								
	osc.	22	73	140	164	168	137	101	56								
	ΔP	12	17	28	54	72	71	51	34								
Blank Holder Friction Force F, lbf.	non-osc.	-	-	-	-	12.3	11.2	8.9	6.7								
	osc.	0	0	0	0	0	0	0	0								
	ΔF %	-	-	-	-	100	100	100	100								
Die Motional Amplitude, ξ_m in. x 10^{-5}	left hand	-	-	7.4	8.3	9.3	8.6	9.3	8.6								
	right hand	-	8.3	7.4	8.9	9.2	8.9	8.6	8.0								
	mean	-	8.3	7.4	8.6	9.2	8.8	8.9	8.3								
Velocity Ratio	$v/\dot{\xi}_m$	-	.050	.056	.048	.045	.047	.046	.050								

WEDGE DRAWING TEST DATA.

TEST NUMBER : 030107	MATERIAL : ALUMINIUM .	DRAW RATIO : 1.50:1	TABLE No. 95

Punch Velocity ; in/sec.	Blank Holder Force ; lbf	Variac Voltage	Frequency ; kHz.
0 .33	238	170	13.25

Punch Travel ; in.		0·1	0·2	0·3	0·4	0·5	0·6	0·7	0·8	0·9	1·0	1·1	1·2	1·3	1·4	1·5	1·6
Punch Load P ; lbf	non-osc.	34	107	179	215	224	188	140	69								
	osc.	20	90	140	167	159	129	90	42								
	ΔP	14	17	39	48	65	59	50	27								
Blank Holder Friction Force F, lbf.	non-osc.	18	-	-	12.9	14.5	15.2	13.4	-								
	osc.	0	0	0	0	0	0	0	0								
	ΔF %	100	-	-	100	100	100	100	-								
Die Motional Amplitude, ξ_m in. x 10^{-5}	left hand	-	-	5.2	6.5	6.5	6.5	6.2	6.5	6.2							
	right hand	-	6.8	6.8	7.4	7.1	6.8	6.5	6.2	5.9							
	mean	-	6.8	6.0	7.0	6.8	6.7	6.4	6.4	6.1							
Velocity Ratio	V/ξ_m	-	.058	.066	.057	.058	.060	.062	.062	.065							

WEDGE DRAWING TEST DATA.

TEST NUMBER : 030108	MATERIAL : ALUMINIUM .	DRAW RATIO : 1.50:1	TABLE No. 96

Punch Velocity; in/sec.	Blank Holder Force ; lbf	Variac Voltage	Frequency ; kHz.
0.33	230	200	13.27

Punch Travel; in.		0·1	0·2	0·3	0·4	0·5	0·6	0·7	0·8	0·9	1·0	1·1	1·2	1·3	1·4	1·5	1·6
Punch Load P; lbf	non-osc.	39	95	168	222	249	218	157	95								
	osc.	25	78	140	172	176	143	103	58								
	ΔP	14	17	28	50	73	75	54	37								
Blank Holder Friction Force F, lbf.	non-osc.	-	-	-	10.0	13.8	14.5	14.5	-								
	osc.	0	0	0	0	0	0	0	0								
	ΔF %	-	-	-	100	100	100	100	-								
Die Motional Amplitude, ξ_m in. x 10^{-5}	left hand	-	-	6.5	7.7	7.1	6.8	6.8	6.5								
	right hand	-	7.4	7.4	7.4	7.1	7.1	6 .8	6.5								
	mean	-	7.4	7.0	7.7	7.1	7.0	6.8	6.5								
Velocity Ratio	v/ξ_m	-	.054	.057	.052	.056	.057	.050	.061								

WEDGE DRAWING TEST DATA.

TEST NUMBER : 030301	MATERIAL : ALUMINIUM .	DRAW RATIO : 1.60:1	TABLE No. 97

Punch Velocity ; in/sec.	Blank Holder Force ; lbf	Variac Voltage	Frequency ; kHz.
0.32	342	30	13.03

Punch Travel ; in.		0·1	0·2	0·3	0·4	0·5	0·6	0·7	0·8	0·9	1·0	1·1	1·2	1·3	1·4	1·5	1·6
Punch Load P ; lbf	non-osc.	43	112	188	246	273	273	258	204	146	54						
	osc.	34	99	169	224	246	246	218	168	114	39						
	ΔP	11	13	19	22	27	27	40	36	32	15						
Blank Holder Friction Force F, lbf.	non-osc.	17.8	-	-	-	-	11.6	16.7	-	-	-						
	osc.	-	0	0	0	0.9	2.2	4.5	4.0	4.2	-						
	ΔF %	-	-	-	-	-	81	73	-	-	-						
Die Motional Amplitude, ξ_m in. x 10^{-5}	left hand	-	-	1.65	1.75	1.85	1.55	1.65	1.2	1.55	1.65						
	right hand	-	1.80	1.85	1.75	1.95	1.85	1.75	1.75	1.95	2.40						
	mean	-	1.80	1.75	1.75	1.90	1.85	1.70	1.50	1.75	2.00						
Velocity Ratio	v/ξ_m	-	.217	.223	.223	.205	.211	.230	.260	.223	.195						

WEDGE DRAWING TEST DATA.

TEST NUMBER : 030302	MATERIAL : ALUMINIUM .	DRAW RATIO : 1.60:1	TABLE No. 98

Punch Velocity; in/sec.	Blank Holder Force ; lbf	Variac Voltage	Frequency ; kHz.
0.33	341	50	13.16

Punch Travel; in.		0·1	0·2	0·3	0·4	0·5	0·6	0·7	0·8	0·9	1·0	1·1	1·2	1·3	1·4	1·5	1·6
Punch Load P; lbf	non-osc.	47	119	195	249	270	264	226	183	129	30						
	osc.	33	97	162	200	222	210	178	140	92	-						
	ΔP	14	22	33	49	48	54	48	43	37	-						
Blank Holder Friction Force F, lbf.	non-osc.	21.8	-	-	-	13.5	17.6	16.7	13.4	11.2	-						
	osc.	-	0	0	0	1.1	1.3	1.8	1.3	-	-						
	ΔF %	-	-	-	-	92	93	89	90	-	-						
Die Motional Amplitude, ξ_m in. x 10^{-5}	left hand	-	-	3.5	4.45	4.0	3.7	2.8	2.95	2.05	-						
	right hand	-	2.9	3.55	3.8	3.35	3.25	3.45	3.45	3.35	3.35						
	mean	-	2.90	3.5	4.12	3.70	3.50	3.12	3.20	2.70	3.35						
Velocity Ratio	$V/\dot{\xi}_m$	-	.138	.114	.097	.108	.114	.128	.125	.148	.119						

WEDGE DRAWING TEST DATA.

TEST NUMBER : 030303	MATERIAL : ALUMINIUM .	DRAW RATIO : 1.60:1	TABLE No. 99

Punch Velocity; in/sec.	Blank Holder Force ; lbf	Variac Voltage	Frequency ; kHz.
0.33	346	110	13.03

Punch Travel; in.		0·1	0·2	0·3	0·4	0·5	0·6	0·7	0·8	0·9	1·0	1·1	1·2	1·3	1·4	1·5	1·6
Punch Load P; lbf	non-osc.	45	110	194	240	276	276	253	202	151	65						
	osc.	33	87	168	194	210	200	168	129	92	27						
	ΔP	12	23	26	46	66	76	85	73	59	38						
Blank Holder Friction Force F, lbf.	non-osc.	13.4	-	-	6.7	10.7	13.4	16.9	16.1	10.0	-						
	osc.	0	0	0	0	0	0	0	0	0	0						
	ΔF %	100	-	-	100	100	100	100	100	100	100						
Die Motional Amplitude, ξ_m in. x 10^{-5}	left hand	-	-	5.9	7.4	9.0	9.0	9.0	8.7	8.7	8.3						
	right hand	-	6.5	5.7	8.3	8.0	8.0	7.7	7.7	7.4	7.2						
	mean	-	6.5	5.8	7.85	8.5	8.5	8.35	8.20	8.05	7.75						
Velocity Ratio	$V/\dot{\xi}_m$	-	.062	.067	.051	,047	.047	.048	.049	.050	.052						

WEDGE DRAWING TEST DATA.

TEST NUMBER : 030304	MATERIAL : ALUMINIUM .	DRAW RATIO : 1.60:1	TABLE No. 100

Punch Velocity; in/sec.	Blank Holder Force ; lbf	Variac Voltage	Frequency ; kHz.
0.34	340	150	12.86

Punch Travel; in.		0·1	0·2	0·3	0·4	0·5	0·6	0·7	0·8	0·9	1·0	1·1	1·2	1·3	1·4	1·5	1·6
Punch Load P; lbf	non-osc.	43	103	168	237	270	274	250	206	152	60						
	osc.	25	71	133	173	186	180	154	119	71	33						
	ΔP	18	32	35	64	84	94	96	87	81	27						
Blank Holder Friction Force F, lbf.	non-osc.	20.0	-	-	11.1	15.2	15.2	16.3	17.2	12.9	-						
	osc.	0	0	0	0	0	0	0	0	0	-						
	ΔF %	100	-	-	100	100	100	100	100	100	-						
Die Motional Amplitude, ξ_m in. x 10^{-5}	left hand	-	-	-	20.7	23.8	23.5	23.2	-	-	-						
	right hand	-	11.8	12.7	14.7	14.5	14.2	13.7	-								
	mean	-	11.8	12.7	17.7	19.2	18.8	18.4	-								
Velocity Ratio	V/ξ_m	-	.036	.033	.024	.022	.023	.023	-								

WEDGE DRAWING TEST DATA.

TEST NUMBER : 030305	MATERIAL : ALUMINIUM .	DRAW RATIO : 1.60:1	TABLE No. 101

Punch Velocity; in/sec.	Blank Holder Force ; lbf	Variac Voltage	Frequency ; kHz.
0.33	375	170	12.89

Punch Travel; in.		0·1	0·2	0·3	0·4	0·5	0·6	0·7	0·8	0·9	1·0	1·1	1·2	1·3	1·4	1·5	1·6
Punch Load P; lbf	non-osc.	27	-	-	238	270	274	241	208	162	70						
	osc.	11	65	120	162	183	173	146	114	78	21						
	ΔP	16	-	-	76	87	101	95	94	84	49						
Blank Holder Friction Force F, lbf.	non-osc.	-	-	-	-	-	14.2	16.3	15.0	13.4	-						
	osc.	0	0	0	0	0	0	0	0	0	0						
	ΔF %	-	-	-	-	-	100	100	100	100	100						
Die Motional Amplitude, ξ_m in. x 10^{-5}	left hand	-	-	-	25.8	24.7	21.0	20.0	21.9	23.2	21.9						
	right hand	-	12.0	13.8	17.3	18.0	17.3	17.3	18.0	18.5	17.7						
	mean	-	12.0	13.8	21.6	21.4	19.2	18.7	19.9	20.8	19.8						
Velocity Ratio	$v/\dot{\xi}_m$	-	.034	.029	.019	.019	.021	.022	.020	.020	.021						

WEDGE DRAWING TEST DATA.

TEST NUMBER : 030306	MATERIAL : ALUMINIUM .	DRAW RATIO : 1.60:1	TABLE No. 102

Punch Velocity; in/sec.	Blank Holder Force ; lbf	Variac Voltage	Frequency ; kHz.
0.32	326	130	13.27

Punch Travel; in.		0·1	0·2	0·3	0·4	0·5	0·6	0·7	0·8	0·9	1·0	1·1	1·2	1·3	1·4	1·5	1·6
Punch Load P; lbf	non-osc.	26	96	170	229	264	278	246	204	146	67						
	osc.	12	75	146	188	212	202	173	134	78	34						
	ΔP	14	21	24	41	57	76	73	70	68	33						
Blank Holder Friction Force F, lbf.	non-osc.	-	-	-	-	15.9	17.8	16.7	16.0	-	-						
	osc.	0	0	0	0	0	0	0	0	0	0						
	ΔF %	-	-	-	-	100	100	100	100	-	-						
Die Motional Amplitude, ξ_m in. x 10^{-5}	left hand	-	-	5.5	6.2	6.4	6.2	4.9	5.2	5.5	4.5						
	right hand	-	5.8	5.7	5.3	5.7	5.3	5.0	5.0	5.0	4.5						
	mean	-	5.8	5.6	5.8	6.0	5.8	4.9	5.1	5.2	4.5						
Velocity Ratio	$v/\dot{\xi}_m$	-	.066	.069	.066	.064	.066	.078	.075	.074	.085						

WEDGE DRAWING TEST DATA.

TEST NUMBER : 030307	MATERIAL : ALUMINIUM .	DRAW RATIO : 1.60:1	TABLE No. 103

Punch Velocity; in/sec.	Blank Holder Force ; lbf	Variac Voltage	Frequency ; kHz.
0.34	338	70	13.27

Punch Travel; in.		0·1	0·2	0·3	0·4	0·5	0·6	0·7	0·8	0·9	1·0	1·1	1·2	1·3	1·4	1·5	1·6
Punch Load P; lbf	non-osc.	26	95	179	235	268	264	235	202	146	67						
	osc.	15	79	157	201	224	218	190	151	107	48						
	ΔP	11	16	22	34	44	46	45	51	39	19						
Blank Holder Friction Force F, lbf.	non-osc.	-	-	-	-	8.5	11.8	12.3	11.2	8.9	-						
	osc.	0	0	0	0	0	0	0	0	0	0						
	ΔF %	-	-	-	-	100	100	100	100	100	-						
Die Motional Amplitude, ξ_m in. x 10^{-5}	left hand	-	1.85	2.8	2.95	3.15	2.3	2.8	2.95	2.6	2.3						
	right hand	-	3.25	3.0	3.35	3.5	3.45	3.35	3.35	.325	4.3						
	mean	-	2.55	2.90	3.15	3.32	2.87	3.07	3.15	2.90	3.0						
Velocity Ratio	V/ξ_m	-	.160	.140	.129	.123	.142	.133	.129	.140	.136						

WEDGE DRAWING TEST DATA.

TEST NUMBER : 030308	MATERIAL : ALUMINIUM .	DRAW RATIO : 1.60:1	TABLE No.104

Punch Velocity; in/sec.	Blank Holder Force ; lbf	Variac Voltage	Frequency ; kHz.
0.34	341	40	13.27

Punch Travel; in.		0·1	0·2	0·3	0·4	0·5	0·6	0·7	0·8	0·9	1·0	1·1	1·2	1·3	1·4	1·5	1·6
Punch Load P; lbf	non-osc.	22	91	177	235	269	271	244	201	165	73						
	osc.	11	33	148	213	235	235	208	168	136	50						
	ΔP	11	18	29	22	34	36	36	33	29	23						
Blank Holder Friction Force F, lbf.	non-osc.	17.8	-	-	-	11.2	15.6	16.0	14.2	11.6							
	osc.	0	0	0	0	0.9	1.3	2.5	3.1	3.3							
	ΔF %	100	-	-	-	92	92	85	78	72							
Die Motional Amplitude, ξ_m in. x 10^{-5}	left hand	-	-	1.55	1.55	1.65	1.65	1.55	1.55	1.55	1.45						
	right hand	-	1.70	1.70	1.50	1.75	1.75	1.75	1.95	2.05	1.85						
	mean	-	1.70	1.62	1.52	1.70	1.70	1.65	1.75	1.80	1.65						
Velocity Ratio	$v/\dot{\xi}_m$	-	.240	.252	.268	.240	.240	.247	.233	.227	.247						

WEDGE . DRAWING TEST DATA.

TEST NUMBER : 030501	MATERIAL : ALUMINIUM .	DRAW RATIO : 1.70:1	TABLE No. 105

Punch Velocity ; in/sec.	Blank Holder Force ; lbf	Variac Voltage	Frequency ; kHz.
0.34	421	30	13.31

Punch Travel ; in.		0·1	0·2	0·3	0·4	0·5	0·6	0·7	0·8	0·9	1·0	1·1	1·2	1·3	1·4	1·5	1·6
Punch Load P ; lbf	non-osc.	56	145	230	287	315	325	323	293	252	201	132					
	osc.	47	125	207	269	299	302	292	271	230	185	121					
	ΔP	9	20	23	18	16	23	31	22	22	16	11					
Blank Holder Friction Force F, lbf.	non-osc.	30	20.1	13.4	11.6	11.6	13.8	19.0	19.6	17.8	15.6	12.2					
	osc.	-	3.3	2.2	2.7	4.5	6.2	8.7	8.9	10.0	9.4	7.8					
	ΔF %	-	84	84	77	62	55	54	55	44	40	36					
Die Motional Amplitude, ξ_m in. x 10^{-5}	left hand	-	-	1.02	1.30	1.30	1.30	1.30	1.25	1.25	1.20	1.20					
	right hand	-	1.50	1.86	1.77	1.59	1.72	1.68	1.64	1.68	1.72	1.76					
	mean	-	1.50	1.44	1.54	1.44	1.51	1.50	1.45	1.46	1.46	1.48					
Velocity Ratio	$v/\dot{\xi}_m$	-	.270	.283	.264	.283	.270	.270	.281	.279	.279	.275					

WEDGE DRAWING TEST DATA.

TEST NUMBER : 030502	MATERIAL : ALUMINIUM .	DRAW RATIO : 1.70:1	TABLE No. 106

Punch Velocity; in/sec.	Blank Holder Force ; lbf	Variac Voltage	Frequency ; kHz.
0.33	428	30	13.41

Punch Travel; in.		0·1	0·2	0·3	0·4	0·5	0·6	0·7	0·8	0·9	1·0	1·1	1·2	1·3	1·4	1·5	1·6
Punch Load P; lbf	non-osc.	45	-	-	277	303	330	319	308	268	212	137	-				
	osc.	-	112	197	249	280	297	288	278	236	180	112	36				
	ΔP	45	112	197	28	23	33	31	30	32	32	25	-				
Blank Holder Friction Force F, lbf.	non-osc.	17.8	-	-	-	-	-	18.5	20.9	20.1	15.6	9.0	-				
	osc.	-	-	-	-	0.7	2.7	7.8	7.8	7.6	4.9	-	-				
	ΔF %	-	-	-	-	-	-	58	63	62	69	-	-				
Die Motional Amplitude, ξ_m in. x 10^{-5}	left hand	-	-	1.1	1.3	1.5	1.45	1.25	1.35	1.4	1.45	1.45					
	right hand	1.1	1.2	0.8	1.1	1.4	1.3	1.4	1.5	1.5	1.4	1.4					
	mean	1.1	1.2	1.0	1.2	1.4	1.4	1.3	1.4	1.4	1.4	1.4					
Velocity Ratio	$v/\dot{\xi}_m$	.360	.347	.400	.333	.281	.296	.302	.285	.285	.285	.285					

WEDGE DRAWING TEST DATA.

TEST NUMBER : 030503	MATERIAL : ALUMINIUM .	DRAW RATIO : 1.70:1	TABLE No. 107 .

Punch Velocity; in/sec.	Blank Holder Force ; lbf	Variac Voltage	Frequency ; kHz.
0.34	409	40	13.20

Punch Travel; in.		0·1	0·2	0·3	0·4	0·5	0·6	0·7	0·8	0·9	1·0	1·1	1·2	1·3	1·4	1·5	1·6
Punch Load P; lbf	non-osc.	28	96	187	258	309	336	336	314	280	224	157					
	osc.	-	80	163	228	269	287	285	279	230	174	146	39				
	ΔP	28	16	24	30	40	49	51	44	50	50	11	39				
Blank Holder Friction Force F, lbf.	non-osc.	20.2	-	-	-	-	-	18.7	21.2	20.7	18.6	13.6	-				
	osc.	-	2.2	1.1	1.1	1.8	2.2	3.3	4.5	4.7	3.8	4.5	-				
	ΔF %	-	-	-	-	-	-	82	79	77	80	67	-				
Die Motional Amplitude, ξ_m in. x 10^{-5}	left hand	-	-	1.75	2.5	2.9	2.7	2.5	2.4	2.35	2.1	2.0	1.65				
	right hand	1.7	1.0	1.25	1.35	1.35	1.4	1.4	1.35	1.35	1.7	1.6	1.35				
	mean	1.7	1.0	1.5	1.92	2.12	2.05	1.95	1.87	1.85	1.90	1.80	1.50				
Velocity Ratio	V/ξ_m	.241	.410	.273	.214	.193	.200	.210	.219	.221	.216	.228	.273				

WEDGE DRAWING TEST DATA.

TEST NUMBER : 030504	MATERIAL : ALUMINIUM .	DRAW RATIO : 1.70:1	TABLE No. 108

Punch Velocity; in/sec.	Blank Holder Force ; lbf	Variac Voltage	Frequency ; kHz.
0.33	417	50	13.10

Punch Travel; in.		0·1	0·2	0·3	0·4	0·5	0·6	0·7	0·8	0·9	1·0	1·1	1·2	1·3	1·4	1·5	1·6
Punch Load P; lbf	non-osc.	45	123	204	263	294	312	305	292	220	-	-					
	osc.	-	104	180	236	258	260	255	238	151	106	29					
	ΔP	45	19	24	27	36	52	50	54	69	-	-					
Blank Holder Friction Force F, lbf.	non-osc.	18.9	-	-	-	11.2	14.5	19.6	22.3	20.8	17.8						
	osc.	-	-	-	-	1.6	2.2	2.7	3.3	2.9	1.0						
	ΔF %	-	-	-	-	86	85	86	85	86	95						
Die Motional Amplitude, ξ_m in. x 10^{-5}	left hand	-	-	2.55	3.1	3.7	3.8	3.5	3.25	2.95	3.05	3.05					
	right hand	2.4	2.85	3.05	3.1	3.85	3.45	3.45	3.25	3.25	3.2	3.35					
	mean	2.4	2.9	2.8	3.1	3.7	3.6	3.5	3.3	3.1	3.1	3.2					
Velocity Ratio	v/ξ_m	.167	.140	.143	.129	.118	.111	.114	.123	.129	.129	.125					

WEDGE DRAWING TEST DATA.

TEST NUMBER : 030505	MATERIAL : ALUMINIUM .	DRAW RATIO : 1.70:1	TABLE No. 109

Punch Velocity; in/sec.	Blank Holder Force ; lbf	Variac Voltage	Frequency ; kHz.
0.32	419	80	13.11

Punch Travel; in.		0·1	0·2	0·3	0·4	0·5	0·6	0·7	0·8	0·9	1·0	1·1	1·2	1·3	1·4	1·5	1·6
Punch Load P; lbf	non-osc.	54	134	218	271	308	327	328	305	271	196	135					
	osc.	45	112	185	241	258	263	249	224	188	134	90					
	ΔP	9	22	33	30	50	64	79	81	83	62	45					
Blank Holder Friction Force F, lbf.	non-osc.	=	=	=	=	=	13.8	17.8	20.5	19.6	15.6	6.7					
	osc.	0	0	0	0	0	0	0	0	0	0	0					
	ΔF %	-	-	-	-	-	100	100	100	100	100	100					
Die Motional Amplitude, ξ_m in. x 10^{-5}	left hand	-	-	3.7	5.6	6.8	6.3	5.6	5.1	4.9	4.8	4.6					
	right hand	-	-	6.5	6.5	6.5	6.5	6.2	5.9	5.6	5.8	5.9					
	mean	-	-	5.1	6.1	6.7	6.4	5.9	5.5	5.3	5.3	5.3					
Velocity Ratio	$v/\dot{\xi}_m$	-	-	.076	.064	.058	.061	.066	.071	.077	.073	.073					

WEDGE DRAWING TEST DATA.

TEST NUMBER : 030506	MATERIAL : ALUMINIUM .	DRAW RATIO : 1.70:1	TABLE No.110

Punch Velocity; in/sec.	Blank Holder Force ; lbf	Variac Voltage	Frequency ; kHz.
0.33	426	90	13.10

Punch Travel; in.		0·1	0·2	0·3	0·4	0·5	0·6	0·7	0·8	0·9	1·0	1·1	1·2	1·3	1·4	1·5	1·6
Punch Load P; lbf	non-osc.	45	111	202	274	319	338	347	337	304	247	-					
	osc.	-	90	179	224	250	258	250	234	193	146	85					
	ΔP	45	21	23	50	69	80	97	103	111	101	-					
Blank Holder Friction Force F, lbf.	non-osc.	22.3	21.2	-	-	-	17.8	20.1	22.5	23.0	20.3	13.8					
	osc.	0	0	0	0	0	0	0	0	0	0	0					
	ΔF %	100	100	-	-	-	100	100	100	100	100	100					
Die Motional Amplitude, ξ_m in. x 10^{-5}	left hand	-	-	3.5	4.9	8.0	8.7	8.3	8.0	7.3	7.7	8.3					
	right hand	-	3.5	3.5	5.9	6.9	6.9	6.5	6.2	6.2	7.0	7.2					
	mean	-	3.5	3.5	5.4	7.4	7.8	7.4	7.1	6.7	7.4	7.8					
Velocity Ratio	v/ξ_m	-	.114	.114	.074	.054	.057	.054	.056	.060	.054	.051					

WEDGE DRAWING TEST DATA.

TEST NUMBER : 030507	MATERIAL : ALUMINIUM .	DRAW RATIO : 1.70:1	TABLE No. 111

Punch Velocity; in/sec.	Blank Holder Force ; lbf	Variac Voltage	Frequency ; kHz.
-0.33	416	110	13.14

Punch Travel; in.		0·1	0·2	0·3	0·4	0·5	0·6	0·7	0·8	0·9	1·0	1·1	1·2	1·3	1·4	1·5	1·6
Punch Load P; lbf	non-osc.	54	129	218	275	315	332	336	314	270	204	140					
	osc.	36	102	188	224	254	254	247	216	174	123	68					
	ΔP	18	27	30	51	61	78	89	98	96	81	72					
Blank Holder Friction Force F, lbf.	non-osc.	27.8	14.5	-	-	10.5	12.1	15.4	20.1	19.2	14.5	-					
	osc.	0	0	0	0	0	0	0	0	0	0	0					
	ΔF %	100	100	-	-	100	100	100	100	100	100	-					
Die Motional. Amplitude, ξ_m in. x 10^{-5}	left hand	-	-	5.9	6.3	6.9	7.2	7.4	7.4	7.5	7.4	7.4					
	right hand	6.9	7.9	6.5	7.4	7.7	7.7	8.0	7.7	7.4	7.4	6.7					
	mean	6.9	7.9	6.2	6.9	7.3	7.5	7.7	7.6	7.5	7.4	7.1					
Velocity Ratio	$V/\dot{\xi}_m$	.058	.051	.064	.058	.055	.053	.052	.053	.053	.054	.056					

WEDGE DRAWING TEST DATA.

TEST NUMBER : 030508	MATERIAL : ALUMINIUM .	DRAW RATIO : 1.70:1	TABLE No. 112

Punch Velocity; in/sec.	Blank Holder Force ; lbf	Variac Voltage	Frequency ; kHz.
0.34	419	130	12.98

Punch Travel; in.		0·1	0·2	0·3	0·4	0·5	0·6	0·7	0·8	0·9	1·0	1·1	1·2	1·3	1·4	1·5	1·6
Punch Load P; lbf	non-osc.	45	107	187	262	300	321	319	303	272	213	146					
	osc.	-	80	157	207	235	245	233	211	175	114	70					
	ΔP	45	27	30	55	65	76	86	92	97	99	76					
Blank Holder Friction Force F, lbf.	non-osc.	26.8	-	-	-	12.5	14.5	18.4	22.8	22.8	18.1	11.8					
	osc.	0	0	0	0	0	0	0	0	0	0	0					
	ΔF %	100	-	-	-	100	100	100	100	100	100	100					
Die Motional Amplitude, ξ_m in. x 10^{-5}	left hand	-	10.2	10.5	12.0	11.7	11.4	9.2	8.7	8.7	10.5	12.3					
	right hand	-	8.5	8.9	10.7	10.0	9.7	8.9	8.3	9.2	13.0	16.2					
	mean	-	9.3	9.7	11.3	10.8	10.5	9.0	8.5	8.9	11.7	14.3					
Velocity Ratio	$V/\dot{\xi}_m$	-	.045	.043	.037	.039	.040	.046	.049	.047	.035	.029					

WEDGE DRAWING TEST DATA.

TEST NUMBER : 030509	MATERIAL : ALUMINIUM .	DRAW RATIO : 1.70:1	TABLE No. 113

Punch Velocity; in/sec.	Blank Holder Force ; lbf	Variac Voltage	Frequency ; kHz.
0.33	418	140	13.01

Punch Travel; in.		0·1	0·2	0·3	0·4	0·5	0·6	0·7	0·8	0·9	1·0	1·1	1·2	1·3	1·4	1·5	1·6
Punch Load P; lbf	non-osc.	45	112	196	260	294	314	308	292	258	190	112					
	osc.	28	90	152	202	224	227	213	192	155	109	65					
	ΔP	17	22	44	58	70	87	95	100	103	81	47					
Blank Holder Friction Force F, lbf.	non-osc.	25.6	20.3	-	-	14.5	14.5	16.7	17.8	21.8	-	-					
	osc.	0	0	0	0	0	0	0	0	0	-	-					
	ΔF %	100	100	-	-	100	100	100	100	100	-	-					
Die Motional Amplitude, ξ_m in. x 10^{-5}	left hand	-	-	7.6	9.7	11.2	11.9	11.7	11.4	11.1	10.5	10.5					
	right hand	-	7.4	10.0	9.7	8.0	9.2	9.4	10.3	10.9	10.9	10.6					
	mean	-	7.4	10.0	9.7	9.6	10.0	10.6	10.8	11.0	10.7	10.6					
Velocity Ratio	$V/\dot{\xi}_m$	-	.055	.040	.042	.042	.040	.038	.037	.037	.038	.038					

WEDGE DRAWING TEST DATA.

TEST NUMBER : 030510	MATERIAL : ALUMINIUM .	DRAW RATIO : 1.70:1	TABLE No. 114

Punch Velocity; in/sec.	Blank Holder Force ; lbf	Variac Voltage	Frequency ; kHz.
0.32	420	180	12.93

Punch Travel; in.		0·1	0·2	0·3	0·4	0·5	0·6	0·7	0·8	0·9	1·0	1·1	1·2	1·3	1·4	1·5	1·6
Punch Load P; lbf	non-osc.	50	125	207	274	320	337	328	306	274	202	118					
	osc.	-	95	162	207	228	229	224	191	155	103	56					
	ΔP	50	30	45	67	92	108	104	115	119	99	62					
Blank Holder Friction Force F, lbf.	non-osc.	-	-	-	-	-	13.5	17.4	20.1	21.2	17.8	-					
	osc.	0	0	0	0	0	0	0	0	0	0						
	ΔF %	-	-	-	-	-	100	100	100	100	100						
Die Motional Amplitude, ξ_m in. x 10^{-5}	left hand	-	-	-	18.0	21.5	21.9	20.0	18.4	16.7	18.4	15.2					
	right hand	-	-	16.2	13.0	14.5	13.3	13.0	13.5	14.3	14.2	13.9					
	mean	-	-	16.2	15.5	18.0	17.6	16.5	15.9	15.5	16.3	14.5					
Velocity Ratio	V/ξ_m	-	-	.024	.025	.022	.022	.024	.025	.025	.024	.027					

WEDGE DRAWING TEST DATA.

TEST NUMBER : 030511	MATERIAL : ALUMINIUM .	DRAW RATIO : 1.70:1	TABLE No. 115

Punch Velocity; in/sec.	Blank Holder Force ; lbf	Variac Voltage	Frequency ; kHz.
0.32	421	200	12.99

Punch Travel; in.		0·1	0·2	0·3	0·4	0·5	0·6	0·7	0·8	0·9	1·0	1·1	1·2	1·3	1·4	1·5	1·6
Punch Load P; lbf	non-osc.	62	129	213	280	316	338	336	314	271	201	114					
	osc.	44	100	165	212	224	224	212	190	155	110	58					
	ΔP	18	29	48	68	92	114	124	124	116	91	56					
Blank Holder Friction Force F, lbf.	non-osc.	29.0	-	-	-	-	26.8	26.8	26.8	25.6	-	-					
	osc.	0	0	0	0	0	0	0	0	0	0	0					
	ΔF %	100	-	-	-	-	100	100	100	100	-	-					
Die Motional Amplitude, ξ_m in. x 10^{-5}	left hand	-	-	14.7	14.3	15.1	16.0	16.0	15.9	15.4	14.5	12.7					
	right hand	12.7	13.8	17.1	13.5	15.7	14.7	14.2	13.9	13.9	13.9	13.6					
	mean	12.7	13.8	15.9	13.9	15.4	15.7	15.1	14.9	14.7	14.2	13.2					
Velocity Ratio	$v/\dot{\xi}_m$	.031	.028	.025	.028	.025	.025	,026	,026	.027	.028	.030					

WEDGE DRAWING TEST DATA.

TEST NUMBER : 030512	MATERIAL : ALUMINIUM .	DRAW RATIO : 1.70:1	TABLE No. 116

Punch Velocity; in/sec.	Blank Holder Force ; lbf	Variac Voltage	Frequency ; kHz.
0.33	414	220	12.96

Punch Travel; in.		0·1	0·2	0·3	0·4	0·5	0·6	0·7	0·8	0·9	1·0	1·1	1·2	1·3	1·4	1·5	1·6
Punch Load P; lbf	non-osc.	56	128	215	282	303	317	319	304	276	213	150	35				
	osc.	25	74	135	181	214	218	206	182	148	102	56	-				
	ΔP	31	54	80	101	89	99	113	127	128	111	94	-				
Blank Holder Friction Force F, lbf.	non-osc.	29	21.5	12.5	9.5	10.0	13.0	16.0	18.5	20.0	16.0	14.5					
	osc.	0	0	0	0	0	0	0	0	0	0	0					
	ΔF %	100	100	100	100	100	100	100	100	100	100	100					
Die Motional Amplitude, ξ_m in. x 10^{-5}	left hand	-	-	-	26.2	26.2	26.8	25.0	24.7	26.5	31.0	28.2					
	right hand	13.3	13.8	16.8	17.7	16.2	19.2	19.2	18.5	19.2	20.2	20.0					
	mean	13.3	13.8	16.8	21.9	21.2	23.0	22.1	21.6	22.8	25.6	24.1					
Velocity Ratio	$v/\dot{\xi}_m$	.031	.029	.024	.019	.019	.018	.018	.019	.018	.016	.019					

WEDGE DRAWING TEST DATA.

TEST NUMBER : 030601		MATERIAL : ALUMINIUM .						DRAW RATIO : 1.80:1					TABLE No. 117				
Punch Velocity; in/sec.		Blank Holder Force ; lbf						Variac Voltage					Frequency ; kHz.				
0.32		499						200					12.99				
Punch Travel; in.		0·1	0·2	0·3	0·4	0·5	0·6	0·7	0·8	0·9	1·0	1·1	1·2	1·3	1·4	1·5	1·6
Punch Load P; lbf	non-osc.	71	125	205	286	330	356	364	367	360	326	274	218	-	-		
	osc.	40	92	166	222	241	250	246	235	224	193	152	107	59	36		
	ΔP	31	33	39	64	89	106	118	132	136	133	122	111	-	-		
Blank Holder Friction Force F, lbf.	non-osc.	-	-	-	-	-	18.0	19.0	23.0	11.8	11.9	11.0	10.0	-	-		
	osc.	0	0	0	0	0	0	0	0	0	0	0	0	0	0		
	ΔF %	-	-	-	-	-	100	100	100	100	100	100	100	-	-		
Die Motional Amplitude, ξ_m in. x 10^{-5}	left hand	-	-	21.6	24.7	26.2	25.8	25.8	25.7	26.5	24.7	21.4	16.7	15.3			
	right hand	-	12.7	12.7	13.9	14.2	14.2	14.2	14.2	14.5	14.2	14.3	14.2	14.7			
	mean	-	12.7	17.2	19.3	20.2	20.0	20.0	19.9	20.5	19.4	17.8	15.4	15.0			
Velocity Ratio	v/ξ_m	-	.307	.228	.203	.194	.197	1.97	1.97	.192	.202	.221	.255	.262			

WEDGE DRAWING TEST DATA.

TEST NUMBER : 030602		MATERIAL : ALUMINIUM .						DRAW RATIO : 1.80:1					TABLE No.118				
Punch Velocity; in/sec.		Blank Holder Force ; lbf						Variac Voltage					Frequency ; kHz.				
0.33		501						160					12.96				
Punch Travel; in.		0·1	0·2	0·3	0·4	0·5	0·6	0·7	0·8	0·9	1·0	1·1	1·2	1·3	1·4	1·5	1·6
Punch Load P; lbf	non-osc.	66	123	202	280	325	346	356	357	346	314	267	202				
	osc.	39	100	159	215	242	251	251	235	224	194	150	101				
	ΔP	27	23	43	65	83	95	105	122	122	120	117	101				
Blank Holder Friction Force F, lbf.	non-osc.	35.2	-	-	-	7.9	14.0	18.0	22.5	22.8	23.4	22.3	-	-			
	osc.	0	0	0	0	0	0	0	0	0	0	0	0	0			
	ΔF %	100	-	-	-	100	100	100	100	100	100	100	-	-			
Die Motional Amplitude, ξ_m in. x 10^{-5}	left hand	-	-	-	21.9	25.4	22.5	22.5	21.9	21.7	21.0	19.7	17.9				
	right hand	-	11.2	14.7	13.5	12.8	12.0	11.7	11.7	11.5	12.0	12.5	13.0				
	mean	-	11.2	14.7	17.7	19.1	17.2	17.1	16.8	16.6	16.5	16.1	15.4				
Velocity Ratio	v/ξ_m	-	.036	.038	.023	.021	.024	.024	.024	.024	.025	,025	.026				

WEDGE DRAWING TEST DATA.

TEST NUMBER : 030603		MATERIAL : ALUMINIUM .						DRAW RATIO : 1.80:1					TABLE No. 119				
Punch Velocity; in/sec.		Blank Holder Force ; lbf						Variac Voltage					Frequency ; kHz.				
0.32		504						120					13.14				
Punch Travel; in.		0·1	0·2	0·3	0·4	0·5	0·6	0·7	0·8	0·9	1·0	1·1	1·2	1·3	1·4	1·5	1·6
Punch Load P; lbf	non-osc.	56	122	213	288	339	365	368	366	354	324	274	211				
	osc.	34	99	177	241	269	275	271	263	242	222	173	117				
	ΔP	22	23	36	47	70	90	97	103	112	102	101	94				
Blank Holder Friction Force F, lbf.	non-osc.	40	-	-	-	-	16	16	19.5	25.0	25.0	18.0	-				
	osc.	0	0	0	0	0	0	0	0	0	0	0	0				
	ΔF %	100	-	-	-	-	100	100	100	100	100	100	-				
Die Motional Amplitude, ξ_m in. x 10^{-5}	left hand	-	-	10.9	12.3	10.9	11.6	12.0	11.6	11.3	10.9	9.9	11.0				
	right hand.	-	7.0	7.3	9.2	9.5	9.9	9.9	9.7	10.2	10.7	11.2	12.2				
	mean	-	7.0	9.1	10.8	10.2	10.8	10.9	10.7	10.8	10.8	10.5	11.6				
Velocity Ratio	V/ξ_m	-	.055	.043	.036	.038	.036	.035	.036	.036	.036	.037	.033				

WEDGE DRAWING TEST DATA.

TEST NUMBER : 030604		MATERIAL : ALUMINIUM .						DRAW RATIO : 1.80:1					TABLE No. 120				
Punch Velocity; in/sec.		Blank Holder Force ; lbf						Variac Voltage					Frequency ; kHz.				
0.33		491						80					13.06				
Punch Travel; in.		0·1	0·2	0·3	0·4	0·5	0·6	0·7	0·8	0·9	1·0	1·1	1·2	1·3	1·4	1·5	1·6
Punch Load P; lbf	non-osc.	-	-	-	-	-	-	-	-	-	-	-	-	-			
	osc.	39	115	196	250	272	277	271	263	252	217	164	116	39			
	ΔP	-	-	-	-	-	-	-	-	-	-	-	-	-			
Blank Holder Friction Force F, lbf.	non-osc.	-	-	-	-	-	-	-	-	-	-	-	-	-			
	osc.	0	0	0	0	0	0	0	0	0	0	0	0	0			
	ΔF %	-	-	-	-	-	-	-	-	-	-	-	-	-			
Die Motional Amplitude, ξ_m in. x 10^{-5}	left hand	5.6	4.3	3.7	3.4	4.0	5.3	5.3	6.1	6.1	5.8	5.9	5.8	5.6			
	right hand	2.5	2.8	2.1	3.1	4.6	5.5	5.8	5.3	5.0	5.3	5.9	6.2	6.5			
	mean	4.1	3.6	2.9	3.3	4.3	5.4	5.6	5.7	5.6	5.6	5.9	6.0	6.1			
Velocity Ratio	v/ξ_m	.098	.112	.139	.122	.094	.075	.072	.071	.072	.072	.068	.067	.066			

WEDGE DRAWING TEST DATA.

TEST NUMBER : 030605	MATERIAL : ALUMINIUM .	DRAW RATIO : 1.80:1	TABLE No. 121

Punch Velocity; in/sec.	Blank Holder Force ; lbf	Variac Voltage	Frequency ; kHz.
0.32	498	25	13.50

Punch Travel; in.		0·1	0·2	0·3	0·4	0·5	0·6	0·7	0·8	0·9	1·0	1·1	1·2	1·3	1·4	1·5	1·6
Punch Load P; lbf	non-osc.	56	135	218	296	326	342	347	347	336	325	269	218	163	-		
	osc.	-	119	197	280	312	325	327	325	312	293	246	194	146	55		
	ΔP	-	16	21	16	14	17	20	22	24	32	23	24	17	-		
Blank Holder Friction Force F, lbf.	non-osc.	36	29	-	-	-	12.9	15.8	18.2	18.9	21.2	19.6	16.1	-	-		
	osc.	-	11.2	2.2	4.5	3.6	4.5	7.8	10.0	11.2	11.2	9.4	10.0				
	ΔF %	-	61	-	-	-	65	51	45	41	47	52	38				
Die Motional Amplitude, ξ_m in. x 10^{-5}	left hand	-	-	0.9	0.75	0.95	1.0	1.0	1.0	0.95	0.9	1.05	0.9				
	right hand	-	0.9	1.0	0.8	0.85	1.0	1.0	1.05	1.05	1.15	1.25	1.25	1.05			
	mean	-	0.9	0.95	0.78	0.9	1.0	1.0	1.02	1.0	1.02	1.15	1.07	1.05			
Velocity Ratio	V/ξ_m	-	.416	.397	.482	.418	.376	.376	.368	.376	.368	.371	.350	.358			

WEDGE DRAWING TEST DATA.

TEST NUMBER : 030606	MATERIAL : ALUMINIUM .	DRAW RATIO : 1.80:1	TABLE No. 122

Punch Velocity; in/sec.	Blank Holder Force ; lbf	Variac Voltage	Frequency ; kHz.
0.26	495	40	13.14

Punch Travel; in.		0·1	0·2	0·3	0·4	0·5	0·6	0·7	0·8	0·9	1·0	1·1	1·2	1·3	1·4	1·5	1·6
Punch Load P; lbf	non-osc.	39	129	233	303	347	381	390	381	370	343	292	227	-	-		
	osc.	20	98	197	275	312	336	336	325	308	286	235	168	118	42		
	ΔP	19	31	36	28	35	45	54	56	62	57	57	59	-	-		
Blank Holder Friction Force F, lbf.	non-osc.	-	-	-	-	-	-	20.1	22.3	23.4	24.1	22.3	18.3	-	-		
	osc.	-	6.7	-	1.1	2.5	3.1	4.5	4.7	4.7	2.7	1.1	1.8	4.0	-		
	ΔF %	-	-	-	-	-	-	77	79	84	89	95	90				
Die Motional Amplitude, ξ_m in. x 10^{-5}	left hand	-	-	1.45	1.95	2.1	2.3	2.2	2.05	2.1	2.1	2.2	2.2				
	right hand	-	1.2	1.95	1.95	2.1	2.1	2.1	2.05	2.05	2.1	2.3	2.4	2.4			
	mean	-	1.2	1.70	1.95	2.1	2.2	2.15	2.05	2.07	2.1	2.25	2.3	2.4			
Velocity Ratio	v/ξ_m	-	.263	.185	.162	.150	.143	.147	.154	.152	.150	.140	.137	.132			

WEDGE DRAWING TEST DATA.

TEST NUMBER : 030607		MATERIAL : ALUMINIUM .						DRAW RATIO : 1.80:1						TABLE No. 123				
Punch Velocity; in/sec.		Blank Holder Force ; lbf						Variac Voltage						Frequency ; kHz.				
0.33		506						60						13.26				
Punch Travel; in.		0·1	0·2	0·3	0·4	0·5	0·6	0·7	0·8	0·9	1·0	1·1	1·2	1·3	1·4	1·5	1·6	
Punch Load P; lbf	non-osc.	34	125	225	310	346	380	391	390	375	346	280	202	-				
	osc.	28	101	191	270	303	314	320	309	293	260	211	155	78				
	ΔP	6	24	34	40	43	66	71	81	82	86	69	47	78				
Blank Holder Friction Force F, lbf.	non-osc.	23.4	-	-	-	-	-	-	-	26.3	26.3	22.3	16.1	-				
	osc.	-	1.1	1.3	1.3	1.1	1.3	2.7	2.5	2.0	2.2	2.5	2.9	-				
	ΔF %	-	-	-	-	-	-	-	-	93	92	89	82	-				
Die Motional Amplitude, ξ_m in. x 10^{-5}	left hand	-	-	3.15	3.7	6.95	4.65	4.15	3.7	3.5	3.35	3.05	2.8	2.5				
	right hand	-	2.1	3.0	3.0	2.8	2.85	2.65	2.65	2.75	2.9	3.1	3.1	2.5				
	mean	-	2.1	3.07	3.35	4.87	3.75	3.4	3.17	3.12	3.12	3.07	2.95	2.5				
Velocity Ratio	v/ξ_m	-	.190	.130	.119	.082	.107	.118	.125	.133	.133	.130	.136	.160				

WEDGE DRAWING TEST DATA.

TEST NUMBER : 030608		MATERIAL : ALUMINIUM .						DRAW RATIO : 1.80:1					TABLE No. 124				
Punch Velocity; in/sec.		Blank Holder Force ; lbf						Variac Voltage					Frequency ; kHz.				
0.34		503						140					13.01				
Punch Travel; in.		0·1	0·2	0·3	0·4	0·5	0·6	0·7	0·8	0·9	1·0	1·1	1·2	1·3	1·4	1·5	1·6
Punch Load P; lbf	non-osc.	45	128	235	302	360	392	403	403	394	376	318	263	155			
	osc.	–	90	181	241	280	280	283	272	258	235	196	150	95			
	ΔP	–	38	54	61	80	112	120	131	136	141	122	113	60			
Blank Holder Friction Force F, lbf.	non-osc.	–	–	–	–	–	–	19.2	21.4	24.1	26.4	25.4	21.2	–			
	osc.	0	0	0	0	0	0	0	0	0	0	0	0	0			
	ΔF %	–	–	–	–	–	–	100	100	100	100	100	100	–			
Die Motional Amplitude, ξ_m in. x 10^{-5}	left hand	–	–	–	8.3	9.2	9.5	9.5	9.5	9.9	10.0	10.2	10.2	9.9			
	right hand	–	–	8.5	9.2	8.5	9.2	9.3	9.3	9.2	8.5	8.0	7.7	7.7			
	mean	–	–	8.5	8.75	8.85	9.35	9.4	9.4	9.55	9.25	9.1	8.95	8.8			
Velocity Ratio	$V/\dot{\xi}_m$	–	–	.488	.475	.468	.415	.442	.442	.435	.415	.456	.456	.470			

WEDGE DRAWING TEST DATA.

TEST NUMBER : 030701	MATERIAL : ALUMINIUM .	DRAW RATIO : 1.90:1	TABLE No. 125

Punch Velocity; in/sec.	Blank Holder Force ; lbf	Variac Voltage	Frequency ; kHz.
0.32	637	50	13.05

Punch Travel; in.		0·1	0·2	0·3	0·4	0·5	0·6	0·7	0·8	0·9	1·0	1·1	1·2	1·3	1·4	1·5	1·6
Punch Load P; lbf	non-osc.	67	165	302	376	415	427	431	430	422	412	399	370	320	263	157	
	osc.	-	135	274	336	367	381	381	372	373	362	345	318	249	180	102	
	ΔP	-	30	28	40	48	46	50	53	49	50	54	52	71	83	55	
Blank Holder Friction Force F, lbf.	non-osc.	44.5	43.5	36.8	31.2	25.6	18.3	17.4	19.0	21.0	23.4	25.6	25.6	23.4	19.6	12.9	
	osc.	-	11.6	8.5	6.9	4.4	3.8	3.3	4.0	4.9	7.1	6.7	5.6	3.3	2.2	-	
	ΔF %	-	74	77	78	83	79	81	79	77	70	74	78	85	86	-	
Die Motional Amplitude, ξ_m in. x 10^{-5}	left hand	-	-	-	-	1.35	1.85	2.1	2.3	2.4	2.5	2.3	2.1	2.3	2.65	2.75	
	right hand	-	-	1.7	2.05	2.4	2.5	2.55	2.6	2.6	2.5	2.25	2.05	2.4	2.05	2.55	
	mean	-	-	1.7	2.05	1.9	2.17	2.3	2.45	2.5	2.5	2.3	2.07	2.35	2.35	2.65	
Velocity Ratio	V/ξ_m	-	-	.230	.195	.205	.188	.170	.159	.152	.156	.169	.188	.166	.166	.147	

WEDGE DRAWING TEST DATA.

TEST NUMBER : 030702	MATERIAL : ALUMINIUM .	DRAW RATIO : 1.90:1	TABLE No. 126

Punch Velocity; in/sec.	Blank Holder Force ; lbf	Variac Voltage	Frequency ; kHz.
0.33	641	100	12.96

Punch Travel; in.		0·1	0·2	0·3	0·4	0·5	0·6	0·7	0·8	0·9	1·0	1·1	1·2	1·3	1·4	1·5	1·6
Punch Load P; lbf	non-osc.	50	134	246	327	381	411	431	431	425	408	392	364	302	224	112	
	osc.	-	101	188	268	304	318	336	328	317	297	280	241	174	132	67	
	ΔP	-	33	58	59	77	93	95	103	108	111	112	123	128	92	45	
Blank Holder Friction Force F, lbf.	non-osc.	-	-	-	-	-	-	-	15.6	21.2	25.7	27.2	26.8	23.4	17.9	-	
	osc.	0	0	0	0	0	0	0	0	0	0	0	0	0	0	0	
	ΔF %	-	-	-	-	-	-	-	100	100	100	100	100	100	100	100	
Die Motional Amplitude, ξ_m in. x 10^{-5}	left hand	-	-	-	8.8	9.2	9.0	9.0	8.7	7.7	7.0	6.5	6.5	7.0	8.0		
	right hand	-	-	7.7	5.7	6.5	6.5	6.5	5.8	5.8	5.7	6.2	6.5	7.7	8.8		
	mean	-	-	7.7	7.25	7.85	7.75	7.75	7.25	6.75	6.35	6.35	6.5	7.35	8.4		
Velocity Ratio	$V/\dot{\xi}_m$	-	-	.053	.056	.052	.052	.052	.052	.060	.064	.064	.062	.055	.048		

WEDGE DRAWING TEST DATA.

TEST NUMBER : 030703	MATERIAL : ALUMINIUM .	DRAW RATIO : 1.90:1	TABLE No. 127

Punch Velocity; in/sec.	Blank Holder Force ; lbf	Variac Voltage	Frequency ; kHz.
0.33	636	120	13.02

Punch Travel; in.		0·1	0·2	0·3	0·4	0·5	0·6	0·7	0·8	0·9	1·0	1·1	1·2	1·3	1·4	1·5	1·6
Punch Load P; lbf	non-osc.	67	161	269	338	386	418	429	435	432	420	403	375	320	246	-	
	osc.	39	123	212	260	314	330	340	336	319	297	280	241	179	123	45	
	ΔP	28	38	57	58	72	88	89	99	113	123	123	134	141	123	-	
Blank Holder Friction Force F, lbf.	non-osc.	-	-	-	-	17.8	18.9	21.2	23.0	23.2	24.6	26.8	28.5	-	-	-	
	osc.	0	0	0	0	0	0	0	0	0	0	0	0	0	0	0	
	ΔF %	-	-	-	-	100	100	100	100	100	100	100	100	-	-	-	
Die Motional Amplitude, ξ_m in. x 10^{-5}	left hand	-	-	-	9.2	10.2	10.0	9.7	9.5	9.2	8.8	8.8	9.2	10.2	10.0	10.2	
	right hand	-	-	7.8	6.8	6.8	6.8	6.5	6.5	6.5	7.0	7.0	7.3	8.3	9.5	9.7	
	mean	-	-	7.8	8.0	8.5	8.4	8.1	8.0	7.8	7.9	7.9	8.2	9.2	9.7	9.9	
Velocity Ratio	V/ξ_m	-	-	.052	.050	.049	.048	.050	.050	.051	.051	,051	.049	.044	.041	.041	

WEDGE DRAWING TEST DATA.

TEST NUMBER : 030704	MATERIAL : ALUMINIUM .	DRAW RATIO : 1.90:1	TABLE No. 128

Punch Velocity; in/sec.	Blank Holder Force ; lbf	Variac Voltage	Frequency ; kHz.
0.33	631	140	12.91

Punch Travel; in.		0·1	0·2	0·3	0·4	0·5	0·6	0·7	0·8	0·9	1·0	1·1	1·2	1·3	1·4	1·5	1·6
Punch Load P; lbf	non-osc.	45	140	246	325	384	415	428	431	431	424	398	364	308	246	134	
	osc.	-	110	202	264	304	322	325	325	315	293	274	246	185	129	56	
	ΔP	-	30	44	61	80	93	103	106	116	131	124	118	123	117	78	
Blank Holder Friction Force F, lbf.	non-osc.	43.5	33.8	24.1	17.4	13.4	12.3	16.8	20.5	22.3	23.4	23.4	25.0	19.0	14.5	-	
	osc.	0	0	0	0	0	0	0	0	0	0	0	0	0	0	0	
	ΔF %	100	100	100	100	100	100	100	100	100	100	100	100	100	100	100	
Die Motional Amplitude, ξ_m in. x 10^{-5}	left hand	-	-	12.8	12.3	11.3	10.5	9.5	8.5	8.3	8.0	8.5	9.8	10.2	12.0	12.3	
	right hand	-	7.3	9.5	8.5	8.3	7.7	7.3	7.3	7.7	8.3	9.2	10.0	11.5	12.3	14.7	
	mean	-	7.3	11.1	10.4	9.8	9.1	8.4	7.9	8.0	8.1	8.8	9.9	10.8	12.1	13.5	
Velocity Ratio	$V/\dot{\xi}_m$	-	.058	.038	.040	.043	.046	.050	.053	.053	.052	.047	.042	.043	.035	.031	

WEDGE DRAWING TEST DATA.

TEST NUMBER : 030705	MATERIAL : ALUMINIUM .	DRAW RATIO : 1.90:1	TABLE No. 129

Punch Velocity; in/sec.	Blank Holder Force ; lbf	Variac Voltage	Frequency ; kHz.
0.33	630	180	12.94

Punch Travel; in.		0·1	0·2	0·3	0·4	0·5	0·6	0·7	0·8	0·9	1·0	1·1	1·2	1·3	1·4	1·5	1·6
Punch Load P; lbf	non-osc.	65	151	263	345	398	420	431	442	442	434	423	382	324	252	157	
	osc.	43	110	202	260	300	314	319	323	312	264	263	230	177	117	62	
	ΔP	22	41	61	85	98	106	112	119	130	170	160	152	147	135	95	
Blank Holder Friction Force F, lbf.	non-osc.	-	-	-	-	-	26.8	27.9	30.6	33.4	32.4	34.8	34.3	26.8	23.4	14.3	
	osc.	0	0	0	0	0	0	0	0	0	0	0	0	0	0	0	
	ΔF %	-	-	-	-	-	100	100	100	100	100	100	100	100	100	100	
Die Motional Amplitude, ξ_m in. x 10^{-5}	left hand	-	-	10.8	13.8	16.0	15.0	14.2	13.5	13.5	14.2	14.5	15.3	16.3	17.3		
	right hand	-	10.3	9.5	13.0	11.7	11.2	11.2	11.3	11.2	11.7	11.7	12.3	13.3	15.0		
	mean	-	10.3	10.1	13.4	13.8	13.1	12.7	12.2	12.3	12.9	13.1	13.8	14.8	16.1		
Velocity Ratio	V/ξ_m	-	.039	.040	.030	.029	.031	.032	.033	.030	.031	.031	.029	.027	.025		

WEDGE DRAWING TEST DATA.

TEST NUMBER : 030706	MATERIAL : ALUMINIUM .	DRAW RATIO : 1.90:1	TABLE No. 130

Punch Velocity; in/sec.	Blank Holder Force ; lbf	Variac Voltage	Frequency ; kHz.
0.34	629	200	13.16

Punch Travel; in.		0·1	0·2	0·3	0·4	0·5	0·6	0·7	0·8	0·9	1·0	1·1	1·2	1·3	1·4	1·5	1·6
Punch Load P; lbf	non-osc.	-	-	-	-	-	-	-	-	-	-	-	-	-	-	-	
	osc.	35	121	207	258	282	292	292	286	276	264	242	262	146	107	39	
	ΔP	-	-	-	-	-	-	-	-	-	-	-	-	-	-	-	
Blank Holder Friction Force F, lbf.	non-osc.	-	-	-	-	-	-	-	-	-	-	-	-	-	-	-	
	osc.	0	0	0	0	0	0	0	0	0	0	0	0	0	0	0	
	ΔF %	-	-	-	-	-	-	-	-	-	-	-	-	-	-	-	
Die Motional Amplitude, ξ_m in. x 10^{-5}	left hand	-	-	9.5	9.8	10.2	10.5	10.8	10.5	10.7	10.8	11.0	11.0	11.2	11.3	11.3	
	right hand	-	10.0	9.3	9.3	10.0	10.3	10.3	10.5	10.8	11.2	10.7	10.7	10.5	10.7	9.5	
	mean	-	10.0	9.4	9.5	10.1	10.4	10.5	10.5	10.7	11.0	10.8	10.8	10.8	11.0	10.4	
Velocity Ratio	$V/\dot{\xi}_m$	-	.042	.044	.044	.041	.040	.040	.040	.039	.038	.038	.038	.038	.038	.040	

WEDGE DRAWING TEST DATA.

TEST NUMBER : 030707	MATERIAL : ALUMINIUM .	DRAW RATIO : 1.90:1	TABLE No. 131

Punch Velocity; in/sec.	Blank Holder Force ; lbf	Variac Voltage	Frequency ; kHz.
0.33	638	200	12.96

Punch Travel; in.		0·1	0·2	0·3	0·4	0·5	0·6	0·7	0·8	0·9	1·0	1·1	1·2	1·3	1·4	1·5	1·6
Punch Load P; lbf	non-osc.	–	120	230	319	380	412	415	415	412	403	381	342	280	218	112	
	osc.	–	94	190	247	280	297	300	287	280	267	235	196	140	93	31	
	ΔP	–	26	40	72	100	115	115	128	132	136	146	146	140	125	81	
Blank Holder Friction Force F, lbf.	non-osc.	–	–	–	–	–	20.5	17.9	20.5	23.2	25.0	26.8	25.0	22.3	19.6	–	
	osc.	0	0	0	0	0	0	0	0	0	0	0	0	0	0	0	
	ΔF %	–	–	–	–	–	100	100	100	100	100	100	100	100	100	–	
Die Motional Amplitude, ξ_m in. x 10^{-5}	left hand	–	–	73.6	16.1	17.3	19.4	18.2	17.6	16.7	17.0	17.6	18.5	20.1	19.8	18.5	
	right hand	–	10.3	10.6	12.1	12.4	12.4	12.1	11.8	11.8	12.4	12.7	13.0	14.2	15.6	16.8	
	mean	–	10.3	12.1	14.1	14.9	15.9	15.2	14.7	14.3	14.7	15.2	15.8	17.2	17.7	17.7	
Velocity Ratio	V/ξ_m	–	.041	.035	.030	.028	.026	.027	.028	.029	.028	.028	.026	.024	.024	.024	

WEDGE DRAWING TEST DATA.

TEST NUMBER : 030708	MATERIAL : ALUMINIUM .	DRAW RATIO : 1.90:1	TABLE No. 132

Punch Velocity; in/sec.	Blank Holder Force ; lbf	Variac Voltage	Frequency ; kHz.
0.34	630	200	12.96

Punch Travel; in.		0·1	0·2	0·3	0·4	0·5	0·6	0·7	0·8	0·9	1·0	1·1	1·2	1·3	1·4	1·5	1·6
Punch Load P; lbf	non-osc.	34	112	218	292	348	398	407	420	415	403	392	363	286	205	67	
	osc.	-	84	190	245	280	297	296	291	286	264	235	196	146	95	34	
	ΔP	-	28	28	47	68	101	111	117	129	139	157	167	140	110	33	
Blank Holder Friction Force F, lbf.	non-osc.	-	-	-	-	10.0	11.6	14.5	19.4	24.6	25.7	27.9	31.2	28.6	-	-	
	osc.	0	0	0	0	0	0	0	0	0	0	0	0	0	0	0	
	ΔF %	-	-	-	-	100	100	100	100	100	100	100	100	100	100	100	
Die Motional Amplitude, ξ_m in. x 10^{-5}	left hand	-	-	13.0	14.5	15.4	17.0	20.0	19.8	19.8	17.9	17.0	17.3	18.5	19.4	19.4	
	right hand	-	8.6	8.7	10.3	11.8	12.2	12.1	11.8	12.1	12.1	12.1	12.4	14.9	15.6	16.8	
	mean	-	8.6	10.9	12.4	13.6	14.6	16.1	15.8	15.9	15.0	14.6	14.9	16.7	17.5	18.1	
Velocity Ratio	V/ξ_m		.049	.042	.034	.031	.029	.026	.026	.026	.028	.029	.028	.025	.024	.023	

WEDGE DRAWING DATA.

TEST NUMBER.	DRAW RATIO,	FREQUENCY kHz	PUNCH VELOCITY in./sec.	MEAN DIE AMPLITUDE in. x 10^{-5}	MAX. PUNCH LOAD, lbf.		PUNCH TRAVEL, h, in.	DREW/ FAILED
					OSC.	NON-OSC.		
030800	1.95:1	-	0.34	0	-	460	0.94	D
030801	1.95:1	12.93	0.33	5.10	405	448	0.86	D
030802	1.95:1	12.94	0.34	9.70	356	465	0.82	D
030803	1.95:1	12.94	0.11	9.80	330	-	0.73	D
030804	1.95:1	12.96	0.34	18.50	330	471	0.80	D
030900	2.00:1	-	0.35	-	-	432	1.10	F
030901	2.00:1	12.98	0.34	2.58	443	472	1.10	F
031001	2.10:1	13.01	0.34	9.45	370	-	1.07	D

TABLE: 133

WEDGE DRAWING DATA.

TEST NUMBER.	DRAW RATIO,	FREQUENCY kHz	PUNCH VELOCITY in/sec.	MEAN DIE AMPLITUDE in. x 10^{-5}	MAX. PUNCH LOAD; lbf.		PUNCH TRAVEL, h; in.	DREW/ FAILED
					OSC.	NON-OSC.		
031002	2.10:1	13.02	0.35	8.60	386	-	0.85	D
031101	2.10:1	13.04	0.34	10.90	381	-	0.78	F
031102	2.20:1	13.04	0.34	9.8	418	-	0.86	F
031201	2.30:1	13.01	0.34	6.35	434	-	0.7	F

TABLE: 134

WEDGE DRAWING TEST DATA.

TEST NUMBER : 030301N	MATERIAL : ALUMINIUM .	DRAW RATIO : 1.60:1	TABLE No. 135

Punch Velocity; in/sec.	Blank Holder Force ; lbf	Variac Voltage	Frequency ; kHz.
0.34	354	80	13.28

Punch Travel; in.		0·1	0·2	0·3	0·4	0·5	0·6	0·7	0·8	0·9	1·0	1·1	1·2	1·3	1·4	1·5	1·6
Punch Load P; lbf	non-osc.	43	132	230	325	387	403	376	330	246	151						
	osc.	22	101	195	268	292	280	252	213	218	118						
	ΔP	21	31	35	57	95	123	124	117	28	33						
Blank Holder Friction Force F, lbf.	non-osc.	23.4	24.6	26.8	29.0	31.2	32.4	33.9	38.0	34.5	22.3						
	osc.	0	0	0	0	0	0	0	5.6	15.6	15.6						
	ΔF %	100	100	100	100	100	100	100	85	55	30						
Die Motional Amplitude, ξ_m in. x 10^{-5}	left hand	-	-	4.3	4.9	5.1	4.0	4.6	4.9	4.2	4.3						
	right hand	-	4.1	4.0	3.5	4.0	4.0	4.9	5.3	4.1	3.7						
	mean	-	4.1	4.15	4.2	4.55	4.0	4.75	5.10	4.15	4.0						
Velocity Ratio	v/ξ_m	-	.100	.098	.097	.089	.102	.086	.080	.098	.102						

WEDGE DRAWING TEST DATA.

TEST NUMBER : 030501	MATERIAL : ALUMINIUM .	DRAW RATIO : 1.70:1	TABLE No. 136

Punch Velocity; in/sec.	Blank Holder Force ; lbf	Variac Voltage	Frequency ; kHz.
0.34	426	100	13.27

Punch Travel; in.		0·1	0·2	0·3	0·4	0·5	0·6	0·7	0·8	0·9	1·0	1·1	1·2	1·3	1·4	1·5	1·6
Punch Load P; lbf	non-osc.	34	-	-	-	-	-	-	-	-	-	-	-				
	osc.	-	92	190	286	320	335	324	294	260	222	170	118				
	ΔP	-	-	-	-	-	-	-	-	-	-	-	-				
Blank Holder Friction Force F, lbf.	non-osc.	30.0	26.2	24.0	25.0	28.5	30.6	30.3	30.6	30.1	29.6	27.8	-				
	osc.	0	0	0	0	0	0	0	1.1	2.2	6.2	17.8	-				
	ΔF %	100	100	100	100	100	100	100	96	93	79	36	-				
Die Motional Amplitude, ξ_m in. x 10^{-5}	left hand	-	-	6.3	6.6	6.6	6.8	7.2	8.0	8.6	8.3	8.0					
	right hand	-	4.9	5.0	5.0	5.3	6.2	6.8	6.8	6.2	5.0	4.3					
	mean	-	4.9	5.65	5.8	5.95	6.5	7.0	7.4	7.4	6.65	6.15					
Velocity Ratio	v/ξ_m	-	.083	.072	070	.069	.063	.058	.055	.055	.061	.066					

WEDGE DRAWING TEST DATA.

TEST NUMBER : 030601N	MATERIAL : ALUMINIUM .	DRAW RATIO : 1.80:1	TABLE No. 137

Punch Velocity; in/sec.	Blank Holder Force ; lbf	Variac Voltage	Frequency ; kHz.
0.34	493	180	13.20

Punch Travel; in.		0·1	0·2	0·3	0·4	0·5	0·6	0·7	0·8	0·9	1·0	1·1	1·2	1·3	1·4	1·5	1·6
Punch Load P; lbf	non-osc.	34	114	242	358	415	451	470	482								
	osc.	–	56	185	282	348	403	392	397								
	ΔP	–	58	57	76	67	48	78	95								
Blank Holder Friction Force F, lbf.	non-osc.	–	–	23.4	25.7	30.1	32.4	33.4	33.6								
	osc.	–	–	4.5	4.9	5.1	7.8	4.7	4.9								
	ΔF %	–	–	81	81	83	76	86	85								
Die Motional Amplitude, ξ_m in. x 10^{-5}	left hand	–	–	–	9.2	10.8	10.8	11.1	11.7								
	right hand	–	–	5.9	5.3	5.2	3.0	5.2	5.9								
	mean	–	–	5.90	7.25	8.00	6.90	8.15	8.80								
Velocity Ratio	V/ξ_m	–	–	.069	.057	.051	.059	.050	.047								

WEDGE DRAWING TEST DATA.

TEST NUMBER : 030602N	MATERIAL : ALUMINIUM .	DRAW RATIO : 1.80:1	TABLE No. 138

Punch Velocity; in/sec.	Blank Holder Force ; lbf	Variac Voltage	Frequency ; kHz.
0.34	498	120	13.2

Punch Travel; in.		0·1	0·2	0·3	0·4	0·5	0·6	0·7	0·8	0·9	1·0	1·1	1·2	1·3	1·4	1·5	1·6
Punch Load P; lbf	non-osc.	50	151	–	–	–	–	–	–	–	–	–	–				
	osc.	–	123	230	323	370	381	375	360	342	308	260	202				
	ΔP	–	18	–	–	–	–	–	–	–	–	–	–				
Blank Holder Friction Force F, lbf.	non-osc.	–	38.0	–	–	–	–	–	–	–	–	–	–				
	osc.	–	0	0	0	0	0	0	0	0	0	0	0				
	ΔF %	–	100	100	100	100	100	100	100	100	100	100	100				
Die Motional Amplitude, ξ_m in. x 10^{-5}	left hand	–	–	–	–	7.1	7.6	7.7	8.0	8.6	9.6	10.2	10.5				
	right hand	–	3.8	4.4	4.4	4.7	5.0	5.3	6.2	7.4	8.3	9.2	9.4				
	mean	–	3.8	4.4	4.4	5.9	6.3	6.5	7.1	8.0	8.9	9.7	9.9				
Velocity Ratio	v/ξ_m	--	.108	.093	.093	.069	.065	.063	.058	.051	.046	.042	.041				

WEDGE DRAWING TEST DATA.

TEST NUMBER : 030603N	MATERIAL : ALUMINIUM .	DRAW RATIO : 1.80:1	TABLE No. 139

Punch Velocity; in/sec.	Blank Holder Force ; lbf	Variac Voltage	Frequency ; kHz.
- 0.34	496	200	13.21

Punch Travel; in.		0·1	0·2	0·3	0·4	0·5	0·6	0·7	0·8	0·9	1·0	1·1	1·2	1·3	1·4	1·5	1·6
Punch Load P; lbf	non-osc.	34	-	-	-	-	-	-	-	-	-	-	-	-	-		
	osc.	-	62	113	202	260	336	398	388	372	346	282	226	163	123		
	ΔP	-	-	-	-	-	-	-	-	-	-	-	-	-	-		
Blank Holder Friction Force F, lbf.	non-osc.	34.5	-	-	-	-	-	-	-	-	-	-	-	-	-		
	osc.	-	0	0	0	0	0	0	-	-	-	-	-	-	-		
	ΔF %	-	100	100	100	100	100	100	-	-	-	-	-	-	-		
Die Motional Amplitude, ξ_m in. x 10^{-5}	left hand	-	-	7.1	8.3	9.6	10.5	11.4	11.7	12.0	12.0	12.0	12.0	11.1	10.8		
	right hand	-	7.7	7.7	7.1	6.8	8.0	10.0	11.2	12.4	12.1	11.5	9.2	7.7	7.4		
	mean	-	7.70	7.40	7.70	8.20	9.25	10.7	11.4	12.2	12.0	11.7	10.6	9.4	9.1		
Velocity Ratio	v/ξ_m	-	.053	.055	.053	.050	.044	.038	.036	.033	.034	.035	.039	.044	.045		

WEDGE DRAWING DATA - PARALLEL TEST PIECES.

TEST NUMBER	FREQUENCY kHz.	PUNCH VELOCITY in./sec.	MEAN DIE AMPLITUDE in. x 10^{-5}	MEAN PUNCH LOAD; lbf.		ΔP lbf.	MEAN FRICTION FORCE		ΔFx2 lbf.
				OSC.	NON-OSC.		OSC.	NON-OSC.	
P0201	13.29	0.34	0.25	54.0	54.0	0	13.4	13.4	0
P0202	13.13	0.34	1.01	53.0	68.0	15	8.7	15.6	13.8
P0203	12.89	0.33	1.45	42.5	56.0	13.5	3.4	9.6	12.4
P0204	13.15	0.35	2.22	39.0	59.5	20.5	2.5	15.4	25.8
P0205	12.91	0.34	3.70	33.5	49.0	15.5	0	6.3	12.6
P0206	12.93	0.34	5.50	31.4	58.0	26.6	0	16.1	32.2
P0207	12.89	0.32	8.85	32.5	65.0	32.5	0	17.0	34.0
P0208	12.85	0.34	18.60	22.4	74.0	51.6	0	17.9	35.8
P0209	12.85	0.34	22.50	18.0	82.0	64.0	0	32.4	64.8

TABLE No: 140

WEDGE DRAWING DATA - PARALLEL TEST PIECES.

TEST NUMBER	FREQUENCY kHz.	PUNCH VELOCITY in./sec.	MEAN DIE AMPLITUDE in. x 10^{-5}	MEAN PUNCH LOAD; lbf.		ΔP lbf.	MEAN FRICTION FORCE		ΔFx2 lbf.
				OSC.	NON-OSC.		OSC.	NON-OSC.	
P0300	-	0.34	0	-	59.5	-	-	17.8	-
P0301	13.19	0.34	0.65	74.0	87.5	13.5	17.6	23.0	10.8
P0302	13.29	0.33	0.88	45.0	56.0	11.0	7.8	13.4	11.2
P0303	13.23	0.32	2.20	36.0	59.5	23.5	2.2	16.0	27.6
P0304	12.98	0.34	7.70	20.1	50.5	30.4	0	11.2	22,4
P0305	13.05	0.34	8.10	22.4	48.0	25.6	0	16.7	33.4
P0306	13.01	0.33	8.75	23.5	62.0	38.5	0.7	21.2	41.0
P0307	12.98	0.34	13.8	19.0	56.0	37.0	0	24.5	49.0
P0308	12.97	0.34	17.5	20.1	76.0	55.9	0	29.8	59.6
P0309	12.93	0.33	18.2	28.0	67.0	39.0	0	18.9	37.8

TABLE No: 141

WEDGE DRAWING DATA - PARALLEL TEST PIECES.

TEST NUMBER	FREQUENCY kHz.	PUNCH VELOCITY in./sec.	MEAN DIE AMPLITUDE in. x 10^{-5}	MEAN PUNCH LOAD; lbf.		ΔP lbf.	MEAN FRICTION FORCE		ΔFx2 lbf.
				OSC.	NON-OSC.		OSC.	NON-OSC.	
P0310	12.84	0.34	18.8	20.1	65.0	44.9	0	18.9	37.8
P0311	12.81	0.34	29.6	19.0	65.0	46.0	0	18.9	37.8

TABLE No: 142